

Active elastic solids : collective motion, collective actuation & polarization

Paul Baconnier

▶ **To cite this version:**

Paul Baconnier. Active elastic solids : collective motion, collective actuation & polarization. Mechanics of materials [physics.class-ph]. Université Paris sciences et lettres, 2023. English. ⟨NNT : 2023UPSLS002⟩. ⟨tel-04081179⟩

HAL Id: tel-04081179

https://pastel.hal.science/tel-04081179v1

Submitted on 25 Apr 2023

HAL is a multi-disciplinary open access archive for the deposit and dissemination of scientific research documents, whether they are published or not. The documents may come from teaching and research institutions in France or abroad, or from public or private research centers.

L'archive ouverte pluridisciplinaire **HAL**, est destinée au dépôt et à la diffusion de documents scientifiques de niveau recherche, publiés ou non, émanant des établissements d'enseignement et de recherche français ou étrangers, des laboratoires publics ou privés.



HAL Authorization

PSL
UNIVERSITÉ PARIS

THÈSE DE DOCTORAT
DE L'UNIVERSITÉ PSL

Préparée à l'ESPCI Paris, laboratoire Gulliver

Solides actifs élastiques : mouvements collectifs, actuation collective & polarisation

Active elastic solids: collective motion, collective actuation & polarization

Soutenue par
Paul Baconnier
Le 23 Janvier 2023

École doctorale n°564
EDPIF

Spécialité
Physique

Composition du jury :

M. Hamid Kellay Professeur, Université de Bordeaux	*Président*
M. Vincenzo Vitelli Professor, University of Chicago	*Examinateur*
Mme. Françoise Brochard Professeur, UPMC-Institut Curie	*Examinatrice*
M. Denis Bartolo Professeur, ENS Lyon	*Rapporteur*
Mme. Silke Henkes Associate Professor, University of Bristol	*Rapportrice*
M. Olivier Dauchot Directeur de recherche, CNRS-ESPCI Paris PSL	*Directeur de thèse*

ESPCI PARIS
EDUCATION SCIENCE INNOVATION

Solides actifs élastiques :
mouvements collectifs, actuation collective & polarisation

Résumé : Les solides actifs sont constitués d'unités hors équilibre couplées élastiquement. Ils sont centraux dans de nombreux processus biologiques comme la locomotion, les oscillations spontanées et la morphogenèse. De plus, leurs propriétés mécaniques et leur capacité à fournir du travail permettent d'imaginer de nouveaux métamatériaux, multifonctionnels, et dotés d'une véritable autonomie. Néanmoins, les mécanismes de rétroaction entre les forces actives et élastiques et la possible émergence de comportements collectifs, restent encore peu explorés. En tirant profit d'unités actives centimétriques, nous construisons une réalisation minimale de solide actif élastique. Les unités actives polaires exercent des forces sur les nœuds d'un réseau élastique bidimensionnel, et le champ de déplacement induit réoriente non-linéairement les agents actifs. De ce couplage, dit élasto-actif, émergent quantités de nouveaux comportements. Dans la première partie, nous montrons que, pour un faible couplage, la présence de modes zéros dicte la nature et la géométrie des comportements collectifs. Sans conditions aux limites, les solides actifs fournissent ainsi un moyen de mettre en mouvement collectif une population d'unités actives couplées rigidement. Dans un second temps, nous constatons, pour un couplage suffisamment grand, l'émergence d'une oscillation collective des nœuds du réseau autour de leurs positions d'équilibres. Nous appelons ce phénomène l'actuation collective. Seuls quelques modes élastiques sont activés et, de manière cruciale, ils ne sont pas nécessairement les modes de plus basses énergies. En combinant des expériences modèles avec l'analyse numérique et théorique d'un modèle d'agents, nous expliquons le scénario de bifurcation et le mécanisme de sélection par lequel l'actuation collective a lieu. Nous proposons une théorie hydrodynamique des solides actifs pour décrire leurs propriétés à grande échelle, et analysons certaines de ses conséquences. En jouant avec les propriétés de vibrations du réseau, nous explorons également la grande variété d'actuations collectives, et mettons en évidence les paramètres qui contrôlent la dynamique. Enfin, nous étudions la manière dont le couplage avec un champ extérieur polarise les solides actifs et affecte l'émergence de l'actuation collective. En définitive, au-delà de la compréhension de notre système particulier, ce manuscrit tente d'établir les fonctions mécaniques de la matière active à grande échelle.

Mots-clés : Matière active, solides actifs, mouvements collectifs, actuation collective, métamatériaux.

Active elastic solids:
collective motion, collective actuation & polarization

Abstract : Active solids consist of elastically coupled out-of-equilibrium units performing work. They are central to autonomous processes in biological systems, e.g. locomotion, self-oscillations and morphogenesis. Moreover, their shape-preserving property and their intrinsic non-equilibrium nature make active solids a promising framework to create multifunctional metamaterials with bona fide autonomy. Yet, the feedback mechanism between elastic and active forces, and the possible emergence of collective behaviors remains poorly understood. We take advantage of centimetric models of self-propelled active units and introduce a minimal realization of an active elastic solid. Polar active agents exert forces on the nodes of a two-dimensional elastic lattice, and the resulting displacement field nonlinearly reorients the active agents. From this so-called elasto-active feedback emerges numerous new collective behaviors. In the first part, we show that for weak enough coupling, the presence of zero modes dictates the nature and the geometry of the collective behaviors. Rigid body motions in free boundary conditions thus provide a way to set a population a rigidly coupled active units into collective motion. Then, we find that for large enough coupling, a collective oscillation of the lattice nodes around their equilibrium position emerges, the so-called collective actuation. We find that only a few elastic modes are actuated and, crucially, they are not necessarily the lowest energy ones. Combining experiments with the numerical and theoretical analysis of an agents model, we unveil the bifurcation scenario and the selection mechanism by which the collective actuation takes place. We propose a hydrodynamic theory of active solids to describe their large-scale properties, and analyze some of its consequences. Playing with the vibrational properties of the lattice, we also explore the wide variety of collective actuations, and find control parameters and design strategies for the emerging dynamics. Finally, we study how the coupling with an external field polarizes active solids and affects the emergence of collective actuation. Altogether, beyond the understanding of our particular system, this manuscript is an attempt to unveil the mechanical functionality of active matter as a continuum.

Keywords : Active matter, active solids, collective motion, collective actuation, metamaterials.

Laboratoire Gulliver, ESPCI Paris, UMR 7083 CNRS/Université PSL
10, rue Vauquelin, 75005, Paris

Remerciements

Je nourris à l'issue de ces trois années un fort sentiment de reconnaissance. J'ai tant de personnes à remercier pour leur soutien et leur aide pendant ma thèse ! D'abord, ceux qui m'ont montré ce que je ne voulais pas être. Mais surtout, ceux qui m'ont inspiré, m'ont fait grandir, et m'ont aidé à surmonter les nombreux défis auxquels j'ai fait face.

J'adresse mes premiers remerciements à Olivier Dauchot. Franchement, pas de bonne thèse sans un bon directeur. Merci pour ton soutien constant, ta confiance et tes conseils avisés. Merci pour les leçons d'humilité, au baby-foot et devant le tableau noir. Mais surtout, merci de m'avoir initié au monde et au métier de la recherche.

Un très chaleureux merci à Vincent Démery, non seulement pour ton évidente et précieuse aide technique, mais aussi pour tout le reste : les opportunités d'enseignement, les bons moments partagés autour de nos pizzas préférées, les discussions politiques... Tu as clairement joué un rôle de modèle pendant ma thèse. Quand je serai grand, j'espère être comme toi.

Merci aux deux rapporteurs de ma thèse, Silke Henkes et Denis Bartolo, pour leur relecture attentive de mon manuscrit, ainsi qu'à Hamid Kellay, Françoise Brochard et Vincenzo Vitelli pour avoir accepté de faire partie de mon jury et d'évaluer mon travail. Merci aussi à Benoît Roman, et encore une fois à Vincent Démery, pour avoir participé à mon comité de suivi de thèse chaque année.

Je tiens également à remercier les nombreux chercheurs, en herbe ou accomplis, avec qui j'ai eu la chance de travailler ou d'interagir. D'abord, Corentin Coulais, qui nous a accueillis une semaine à Amsterdam en février 2022. Cette visite a été extrêmement bénéfique pour la suite de ma thèse : c'est à cette occasion que nous avons mesuré pour la première fois l'effet de la gravité et les propriétés mécaniques de nos solides actifs. Merci pour ton implication, pour tous nos échanges, et pour avoir enfanté mon projet de thèse avec Olivier. Merci aussi à Jonas Veenstra, qui nous a permi de réaliser le programme de manips dans les temps, et pour son enthousiasme communicatif. Un grand merci à Gustavo Düring et Claudio Hernández López pour vos contributions à ce manuscrit, et pour toutes nos délicieuses discussions scientifiques, toujours dans la bonne humeur. Je tiens aussi à remercier chaleureusement Vincenzo Vitelli. Je garde un souvenir exaltant de notre visite à Chicago et de cette pause digestive pendant laquelle tu m'expliquas comment faire une présentation "avec le bide". Merci à Guillaume Briand pour la formation grains marcheur le premier jour de ma thèse. Merci à mon camarade Dor Shohat, avec qui j'ai étroitement collaboré pendant sa visite à Gulliver. J'espère de tout cœur avoir à nouveau la chance de faire de la physique avec toi, sans vraiment en douter. Finalement, merci à tous les étudiants que j'ai eu la chance d'encadrer : Roméo Troubat, Jules Craquelin, Alice Marché, Henri Fabre, Maxime Vinteler et Mathéo Aksil.

Je souhaite remercier tous les membres du laboratoire Gulliver, qui m'ont offert le meilleur environnement dont un doctorant peut rêver pour ses années de labeur. Merci à Élie Raphaël et Mathilde Reyssat pour votre bienveillance et votre affection à mon égard depuis ma première année à l'ESPCI, il y a sept ans. Merci aussi à Matthieu Labousse et Zorana Zeracvic, pour votre aide précieuse à chaque fois qu'il y en a eu besoin, et pour tous nos échanges. Merci à Ludwik Leibler pour les cafés partagés de bon matin et pour ton enthousiasme vis-à-vis de mon travail. Merci aux ingénieures de l'équipe,

Aurélie Lloret et Justine Laurent, et aux gestionnaires du labo, Fée Sorrentino et Elisa Silveira, pour avoir fait de ma vie au labo un long fleuve tranquille. Pour finir, merci à l'infatigable équipe des non-permanents de Gulliver. Je vous suis très reconnaissant pour tous les bons moments passés, toutes les discussions, et pour toute la confiance que vous m'avez témoignée. Merci à Antoine et Coline pour m'avoir prêté vos mains. Merci à Hag, Charlo, Mats, Armand, Margarida, Rocio, Juliane, Thibault, Kostas, Zerihun, Vincent, et Pierre pour la bonne ambiance au quotidien. Merci à Matan et Jéméry pour les discussions autour de nos robots. Vous êtes bien nombreux pour être tous cités ici, mais vous restez exhaustivement dans mon cœur.

Je ne peux pas non plus oublier de remercier tous les membres de l'atelier de mécanique de l'ESPCI, sans lesquels j'aurais eu bien du mal à imprimer mes centaines de pièces $3d$. Un merci tout particulier à Jean-Claude Mancer. Merci pour tes apprentissages, ta bonne humeur, et toutes les opportunités que tu m'as offertes. Je te souhaite la plus heureuse des retraites, bien méritée.

Merci à tous mes amis. Merci à Sacha, Seb et Clément, mes copains de toujours et comparses d'aventure devant l'éternel. Merci à mes potes de prépa, en particulier à Enki, mon premier binôme de TP. Un énorme merci à Joachim pour avoir mis à contribution ses compétences de photographe, et pour son amitié sans faille. Merci à mes potes de PC, en particulier mon acolyte Rami et à mon deuxième mais tout aussi génial binôme de TP, Sam. Merci à Vincent et Antoine pour avoir joué, peut-être sans le savoir, un rôle de grand-frère dans ce monde de fous qu'est la recherche.

Enfin, je tiens à remercier ma famille pour leur soutien indéfectible au travers des vingt-sept dernières années. Un grand merci à ma grand-mère pour m'avoir accueilli et nourri pendant une partie de la rédaction de ce manuscrit. Rien de tel qu'une salade corrézienne pour vous stimuler les neurones.

Mes derniers mots vont à Marie. Tu me donnes tellement de force qu'avec toi, rien ne me semble impossible. Merci pour ça, mais pas seulement.

Contents

Introduction **8**

1 State of the art **16**
1.1 Active liquids . . . 17
1.1.1 Scalar active matter . . . 17
1.1.2 Collective motion . . . 19
1.2 Dense biological systems . . . 24
1.2.1 Cell monolayers experiments . . . 24
1.2.2 Bacterial biofilms . . . 28
1.3 Dense active matter phases . . . 30
1.3.1 Jamming of active particles . . . 30
1.3.2 Active crystals . . . 32
1.3.3 Self-propelled Voronoi model . . . 33
1.4 Active elastic structures . . . 35
1.4.1 Actuation of rigid body motions . . . 35
1.4.2 Actuation of non-trivial zero modes . . . 37
1.4.3 Frustrated active chain . . . 39
1.4.4 Odd elastic solids . . . 41
1.4.5 Non-reciprocal metametarials . . . 43
1.5 Conclusion . . . 44

2 Experimental systems **48**
2.1 Active units . . . 48
2.1.1 How to make active particles? . . . 48
2.1.2 *Hexbugs* as active particles . . . 48
2.1.3 Anatomy . . . 49
2.1.4 Propulsion mechanism . . . 49
2.1.5 Left/right bias . . . 51
2.1.6 Self-alignment . . . 51
2.1.7 *Hexbugs* eugenics . . . 52
2.2 Active elastic building blocks . . . 53
2.2.1 Design principle . . . 53
2.2.2 Anatomy . . . 53
2.2.3 Main physical ingredients . . . 54
2.3 Measurement of the microscopic parameters . . . 55
2.3.1 Inertia . . . 55
2.3.2 Self-alignment . . . 57
2.3.3 Active force . . . 60
2.3.4 Elasto-active coupling . . . 60
2.3.5 Tuning springs stiffness . . . 61
2.4 Active networks . . . 61

2.4.1 Active mechanical metamaterial . . . 61
2.4.2 Boundary condition . . . 62
2.4.3 Mechanical tension . . . 62
2.5 Tracking algorithm . . . 63
2.5.1 Image cleaning step . . . 63
2.5.2 Annulus detection step . . . 63
2.5.3 Orientation detection step . . . 65
2.5.4 Matching step . . . 66
2.5.5 Finding the correct directions . . . 66
2.5.6 Determining the displacement field . . . 66
2.5.7 Error estimates . . . 68
2.6 Conclusion . . . 69

3 Agent-based model 72
3.1 Single particle in a harmonic trap . . . 72
3.2 Mechanics of passive networks . . . 74
3.2.1 Mechanical stability . . . 74
3.2.2 Equations of motion . . . 76
3.2.3 Harmonic approximation . . . 77
3.2.4 Symmetry considerations . . . 80
3.2.5 Dynamics . . . 83
3.2.6 Thermodynamics . . . 84
3.3 Active networks . . . 85
3.3.1 Equations of motion . . . 85
3.3.2 Projection on the normal modes . . . 87
3.3.3 Numerical simulations . . . 88

4 Stress-induced collective motion 90
4.1 Introduction . . . 90
4.2 Experiments . . . 91
4.3 Rigid equations . . . 93
4.4 Single pinning point . . . 95
4.4.1 Rigid equation in the co-rotating frame . . . 95
4.4.2 Steady rotation regime . . . 96
4.4.3 Rigid experiments . . . 96
4.5 Free boundary condition . . . 98
4.5.1 Rigid equation in the co-rotating frame . . . 98
4.5.2 Steady translation regime . . . 99
4.5.3 Steady rotation regime . . . 99
4.6 Influence of noise . . . 100
4.6.1 Fokker-Planck equation . . . 101
4.6.2 Free-energy . . . 101
4.6.3 Application to free boundary conditions . . . 103
4.7 Conclusion . . . 105

5 Selective and collective actuation 108
5.1 Introduction . . . 108
5.2 Collective actuation in active networks . . . 108
5.2.1 CA regime . . . 109
5.2.2 Transition to CA . . . 110
5.2.3 Large N systems . . . 112

5.2.4 Role of noise . . . 114
5.2.5 Summary of observations . . . 115
5.3 A few exact results for N particles systems . . . 115
5.3.1 Fixed points stability analysis . . . 115
5.3.2 Symmetry considerations . . . 117
5.3.3 N particles dynamics restricted to two modes . . . 119
5.4 Single particle in a harmonic potential . . . 120
5.4.1 Experiments . . . 120
5.4.2 Governing ODEs . . . 122
5.4.3 Fixed Points . . . 122
5.4.4 Orbiting solutions in the degenerate case . . . 123
5.4.5 Bifurcation scenario . . . 123
5.4.6 Influence of the bias . . . 123
5.5 Simple models with heterogeneity . . . 125
5.5.1 Linear structures . . . 125
5.5.2 Two coupled particles in a parabolic potential . . . 130
5.6 Coarse-grained description . . . 134
5.6.1 Continuous fields . . . 134
5.6.2 Strain dynamics . . . 134
5.6.3 Polarity dynamics . . . 135
5.6.4 Polarization relaxation . . . 136
5.6.5 Disordered phase . . . 136
5.6.6 Homogeneous phases . . . 138
5.6.7 Phase diagram . . . 140
5.6.8 Relation to non-reciprocal systems . . . 140
5.7 Conclusion . . . 141

6 Tension-controlled switch between collective actuation 144
6.1 Introduction . . . 144
6.2 Boundary-condition-controlled dynamics . . . 145
6.3 Active *Gerris* . . . 146
6.3.1 Structure . . . 147
6.3.2 Normal mode spectrum . . . 147
6.3.3 Tension-controlled switch . . . 148
6.3.4 Numerical model . . . 148
6.4 Material-scale switch . . . 152
6.4.1 Homogeneously dilating structures . . . 152
6.4.2 Large honeycomb . . . 153
6.5 Conclusion . . . 154

7 Polarization by an external field 156
7.1 Introduction . . . 156
7.2 Gravity-induced polarization . . . 157
7.2.1 Experimental observations . . . 157
7.2.2 Discussion . . . 159
7.3 N particle systems with a polarizing field . . . 161
7.3.1 Triangular lattices pinned at the edges . . . 161
7.3.2 Square lattices pinned at opposite ends . . . 163
7.3.3 Summary of observations . . . 165
7.4 Single particle actuation with a polarizing field . . . 168
7.4.1 Experimental observations . . . 168

7.4.2 Numerical simulations . . . 170
7.4.3 Discussion . . . 170
7.5 Coarse-grained description . . . 180
7.5.1 Noise-induced collective actuation at zero-gravity . . . 181
7.5.2 Fixed points with a polarizing field . . . 182
7.5.3 Stability of the frozen phase . . . 182
7.5.4 Beyond fixed points . . . 184
7.6 Conclusion . . . 185

8 Perspectives **188**
8.1 Counter-rotating squares mechanism . . . 188
8.1.1 Case of a zero mode . . . 188
8.1.2 Case of a harmonic mode . . . 190
8.2 Mechanical response . . . 191
8.2.1 Setup . . . 191
8.2.2 Discussion . . . 193
8.3 Walking grains experiments . . . 195
8.3.1 Setup . . . 195
8.3.2 Design principle . . . 196
8.3.3 Linear chains . . . 197
8.3.4 Large honeycomb . . . 199

Conclusion **202**

A Normal modes **210**

B Rigid limit **216**
B.1 Rigid theoretical framework . . . 216
B.1.1 Dimensionless scheme . . . 216
B.1.2 Force determination . . . 216
B.2 Stability of translational and rotational solutions in rigid structures . . . 219
B.2.1 Pinned structure . . . 219
B.2.2 Non-pinned structure translational solution . . . 220
B.2.3 Non-pinned structure rotating solution . . . 221
B.3 Fokker-Planck equation . . . 221
B.4 Statistics of the adiabatic approximation . . . 223

C Fixed point stability analysis for mechanically stable structures **226**
C.1 Dynamics linearized around a given fixed point . . . 226
C.2 Properties of the spectrum valid for all fixed points . . . 226
C.3 Stability threshold of a given fixed point . . . 227
C.4 First linear destabilization . . . 228
C.5 Upper bound of the stability thresholds . . . 229

D Zero-rest-length chains **232**
D.1 Single-frequency limit cycles. . . . 232
D.2 Stability of the limit cycles. . . . 233
D.3 Geometrical restriction on the existence of rotating solutions . . . 233
D.4 Application to the chains . . . 234

E Two coupled particles in a harmonic potential **236**

F Single particle mapping to non-reciprocal systems **240**
F.1 Single particle dynamics . . . 240
F.2 Exceptional points . . . 240
F.3 Mapping of j_+ and j_- . . . 241

G Dynamical matrix of an homogeneously dilated structure **244**

H Active *Gerris*' equations of motion **246**
H.1 Full elasticity level . . . 249
H.2 Harmonic approximation level . . . 249
H.3 Additionally considering angular noise . . . 249

I Asymmetric single particle **250**
I.1 Fixed points stability analysis . . . 250
I.2 Dynamical regimes . . . 251
I.2.1 Degenerate case . . . 251
I.2.2 General case . . . 251

J Single particle in 3d **256**
J.1 General equations . . . 256
J.1.1 In cartesian coordinates . . . 256
J.1.2 In spherical coordinates . . . 257
J.2 Oscillating regime on the equatorial plane . . . 257
J.2.1 Stationary solution . . . 258
J.2.2 Stability . . . 258

K Perspective distortions **260**

L Perturbative approaches **262**
L.1 Multiple-scale analysis . . . 262
L.1.1 Coarse-grained toy model: NICA regime at zero-gravity . . . 262
L.1.2 Single-particle: WW regime . . . 264
L.2 Linear response in the CO regime . . . 267

M Blueprints **270**

Bibliography **281**

Introduction

This manuscript is the result of my doctoral research, which I carried out at the Gulliver laboratory (ESPCI Paris/PSL University), under the supervision of Olivier Dauchot. Our work has given rise to the writing of five articles: [*Stress-induced collective motion in active solids*, In preparation], [*Selective and collective actuation in active solids*, 2022] [1], [*Discontinuous tension-controlled transition between collective actuations in active solids*, 2023] [2], [*Noise-induced collective actuation in active solids*, In preparation], [*Polarization-induced reentrance transition to collective actuation in active solids*, In preparation], two of which being published [1, 2].

General context

Active matter is composed of a large number of *active agents*, each of which consumes energy in order to move or exert mechanical forces. We consider that an *active agent* is an object that breaks spatial and time-reversal symmetries, or, said differently, an anisotropic object whose dynamics break detailed balance. Such systems are therefore intrinsically out of thermal equilibrium, and activity endows the agents with an additional free degree of freedom in the form of polar, or dipolar, active forces. *Active matter* designates a multidisciplinary field of research at the interface between biology and physics, as most examples of active matter systems are of biological origin and span all the scales of the living world, from self-organizing bio-polymers such as microtubules and actin, to schools of fish and flocks of birds. It was progressively popularized since the pioneering work of Tamás Vicsek in 1995 and the extensive study of his celebrated model [9].

For the past 25 years, a large amount of work has dealt with studying active liquids, which are relatively dilute phases of active matter, allowing for the spatial reorganization of the active agents. They led the physics community to understand deeply the nature of two important phenomena occurring in active systems: *collective motion*, and *motility-induced phase separation*. However, for a broad class of active matter systems, the description in terms of free-to-move agents does not hold anymore, for example, because of the presence of strong position-based interactions, and new theoretical frameworks are required. This situation generally arises when repulsive active units are put under strong confinement, or for attractive active units, which spontaneously cluster together.

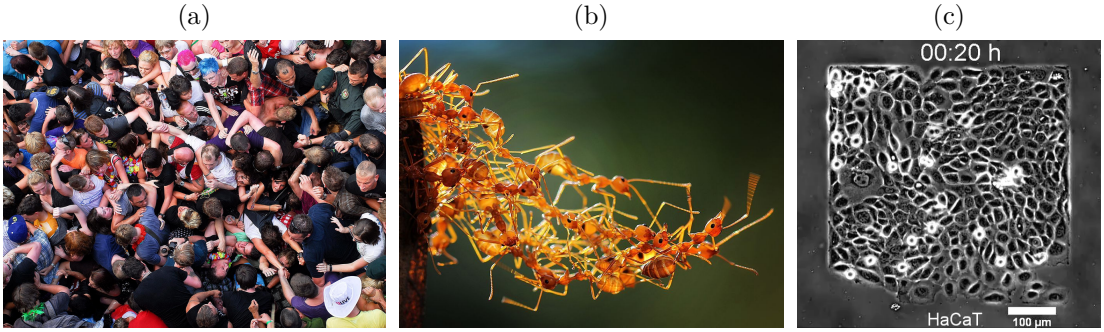


FIG. 1. **Examples of systems combining activity and elasticity in the living world.** (a) Dense human crowd during the catastrophic stampede of the 2010 Duisburg Love Parade [3, 4]. (b) Fire ants forming living structures out of their bodies [5–7]. Credit: Adhi Prayoga. (c) Cell monolayer under square confinement. The dynamics cannot be appreciated in this picture, but the cells perform a collective oscillation around their reference configuration. Adapted from [8].

One can think about dense human crowds, ant colonies forming living structures, or epithelial cells in confinement (Fig. 1). In such systems, the existence of a reference configuration calls for a description in terms of active solids rather than active liquids. Active solids are also interesting as they shed light on the physics of biological tissues, which play crucial roles in physiology and morphogenesis. However, they remain largely unexplored, and only very few experimental systems allow for strong elastic couplings between active agents.

Material sciences have recently experienced its own revolution. Playing with the architecture of the underlying structure, or with the constitutive laws of its constitutive elementary "springs", physicists and engineers have unveiled new behavior breaking the laws of standard elasticity. Such features allow for the design of programmable materials, displaying multiple elastic response, or peculiar responses such as negative Poisson ratio. Yet, to date, such metamaterials are passive, limiting their properties and their range of application. In particular, they are not robust to fluctuations and attenuation. Active solids are therefore a promising framework for fabricating autonomous mechanical metamaterials, because they could provide a controllable and completely endogenous actuation mechanism for the mechanical functions of classical metamaterials. Understanding the mechanical functionality of active matter is essential to bridge the gap between practical applications and the fundamental knowledge learned in the two fields over the past decades.

Throughout this work, we focus on *dry* and *polar* active solids: *polar* because the active units exert polar forces, and *dry* because momentum is taken from the ground to generate such forces. Therefore, neither energy nor momentum is conserved, and space dimension $d = 2$. In such systems, the active and elastic forces combine to produce an active strain. Generically, this active strain tensor will act on the polarities of the active units and reorient them, which in turn modifies the active strain. What we shall call this elasto-active feedback is likely to provide mechanisms for interesting new collective behaviors, which are the focus of this work, and shall be called *Collective Actuation* (CA). Emerging collective behaviors in living active solids can be incredibly complex, because of the large number of agents involved and of the nonlinearity of the couplings, but also because additional processes might take place, like spatial reorganization, chemical communication, or dipolar forces between agents. Nonetheless, as is often the case in physics, our approach consists of reducing the complexity through the use of model systems, the objective being to derive simple and fundamental principles governing the physics of active solids.

Taking advantage of centimetric models of self-propelled particles, we build new model active solids experiments, and study the collective behaviors that emerge in systems with various sizes, shapes, and boundary conditions. In the presence of zero modes, activity leads to the emergence of collective steady states dictated by said modes. In contrast, we find that polar agents embedded in a mechanically stable spring network spontaneously perform synchronized oscillations around their reference configuration. Only a few normal modes are actuated, and crucially, they are not necessarily the lowest energy ones. Combining experiments with the numerical and theoretical analysis of an agents model, we unveil the minimum ingredients at the origin of CA, and find control parameters and design strategies for the emerging dynamics. We show that mechanical tension can be used to jump abruptly between different collective dynamics, and that polarization by an external field, e.g. gravity, favors transverse oscillations. Finally, we

derive a hydrodynamic theory of active solids aiming for their large-scale properties, and analyze some of its consequences.

Presentation and summary of the results

This manuscript is articulated around eight chapters.

Chapter 1 : State of the art.
In this first chapter, we present the current common knowledge on active solids, with particular emphasis on *dry* and *polar* active solids with *self-alignment* interactions. Starting with a historical discussion about active liquids, we review experimental and theoretical approaches to understand *motility-induced phase separation* and the transition to *collective motion*. Then, we present dense biological systems, whose phenomenology clearly falls outside the scope of active liquids, and claim that new theoretical frameworks are required. Finally, we elaborate on the two strategies explored to construct active structures: increasing the confinement or density of an active fluid, and doping a genuine elastic structure with active units. Overall, the two hallmarks of active solids are autonomous actuation and odd elastic moduli, which give rise to locomotion, self-oscillating behavior, and non-Hermitian skin effects.

Chapter 2 : Experiments.
In this chapter, we provide details on the experimental system, which is both the first achievement and the central topic of this work. Each active unit is a so-called *hexbug*, a centimetric self-propelled robotic cockroach. We introduce a general design principle for making active solid systems, which consists of trapping active units in cylindrical structures, so that the units can both push and freely reorient, while being embedded in a spring network. The key ingredient of this system is the presence of a self-aligning torque of the active unit's polarity toward the velocity vector, which provides the so-called elasto-active feedback. We also describe the measurement of the "microscopic" parameters with simple experiments, and, eventually, elaborate on the tracking algorithm.

Chapter 3 : Agent-based model.
In this chapter, we first elaborate on the physics of passive spring networks, from their stability to their dynamics, paying particular attention to the harmonic approximation and the normal modes picture. Then, we introduce the model of elastically coupled active particles, by doping every node of the passive network with active units. We show that, in the harmonic approximation, this model is governed by a single dimensionless parameter, namely the elasto-active coupling $\pi = F_0/kl_a$; where F_0 is the amplitude of the active forces, k is the stiffness of the springs, and l_a characterizes the self-alignment property. In this pedestrian chapter, we analyze how active solids differ from their passive counterpart, and provide details on the numerical simulations.

Chapter 4 : Stress-induced collective motion.
For small enough activity, the vibrational modes of the solid are barely excited, and the network can be considered effectively rigid. We thus theoretically study strictly rigid structures, and show that in the presence of zero modes, any finite amount of activity leads to the emergence of collective steady states, whose properties and stability are governed by the geometry of the zero modes. Combining this framework with numerical simulations and with the experimental study of rigid active solids, we show

that our predictions are robust to imperfections and a finite amount of elasticity. We demonstrate that translating states are unconditionally stable, while rotating states' stability depends on the structure's geometry and the alignment length. Eventually, we investigate the effect of noise and show that the dynamics of active solids can map to equilibrium situations, for which exact results exist in the thermodynamic limit. In particular, mode selection and the existence of collective motion are determined by the minima of a Landau-Guinzberg-like free energy. Eventually, we demonstrate that the polarity dynamics of a large translating rigid active solid maps to a genuine mean-field XY model; and thus, supports long-range order for finite noise amplitude.

Chapter 5 : Selective and collective actuation.

We characterize the emergence of selective and collective actuation in active networks pinned at the edges. For large enough elasto-active coupling π, Synchronized Chiral Oscillations (SCO) of the lattice nodes around their equilibrium position emerges. Only a few elastic modes are actuated and, crucially, they are not necessarily the lowest energy ones. Combining experiments with the numerical and theoretical analysis of an agents model, we unveil the bifurcation scenario and the selection mechanism by which this specific CA takes place. Using simple toy models, we demonstrate that the spatial heterogeneity of the selected modes governs the nature of the transition to CA, and in particular, leads to discontinuous transitions and heterogeneous dynamical regimes. Moreover, we show that the dynamics preferentially selects pairs of relatively low-energy, but most importantly, extended and locally-orthogonal normal modes, two properties at the root of the selection mechanism. Finally, we derive a coarse-grained model describing the physics of active solids at large scales, study its mean field predictions, and propose a scenario for the fates of the SCO phase in the thermodynamic and continuum elasticity limits.

Chapter 6 : Tension-controlled switch.

This chapter is motivated by the recent observations of CA in dense biological systems. On the one hand, Synchronized Chiral Oscillations (SCO) were reported in confined epithelial cells and dense bacterial suspensions. On the other hand, a collective dynamics with the system performing Global Alternating Rotation (GAR) around its center, was reported in bacterial bio-films. From a biomimetic point of view, active metamaterials are therefore a promising framework for creating multifunctional materials with bona fide autonomy. However, an explicit realization of active metamaterials exhibiting different CA regimes, with good control of the transition between these regimes, is still lacking. In this chapter, we bridge this gap by (i) demonstrating the existence of both SCO and GAR in the same active elastic structure, (ii) showing how mechanical tension can be harnessed to manipulate the vibrational spectrum of an active solid and control the transition between these different CA regimes. We first establish the experimental proof of concept using a toy-model active solid. We then dissect the underlying mechanism and extend our findings to more general geometries, on the basis of an agents model and theoretical arguments. The presence of hysteresis when varying tension back and forth highlights the non-trivial selectivity of CA.

Chapter 7 : Polarization by an external field.

Living systems have the ability to respond to various types of environmental cues and can polarize towards or away from these signals, e.g. by chemotaxis or galvanotaxis. Yet, the effect of an external field on the collective dynamics of active solids remains, until today, largely unexplored. In this chapter, we combine model experiments, numerical

simulations of an agent-based model, and theory to investigate the effect of a polarizing gravity field on the dynamics of active elastic structures. First, we reveal the existence of a third CA regime, different from SCO and GAR, denoted *Noise-Induced CA* (NICA). In this regime, the system performs CA along the lowest-energy mode, emerging from the balance between activity, elasticity, and angular noise. Then we apply homogeneous polarizing fields to SCO, NICA, and *frozen* regimes. We show that active unis tend to polarize against the polarizing gravity field, and that this polarization decreases the activity threshold for CA, leading to *Polarization-Induced Reentrance* (PIR). We then establish the complete analysis of the single-particle case, and fully map out the interplay between activity, elasticity, and polarization. Eventually, using the coarse-grained model derived in chapter 5, we explain the origin of NICA, and show that PIR is a purely collective effect, inherited from the differential stability of the *Frozen-Disordered* (FD) and *Frozen-Polarized* (FP) phases.

Chapter 8 : Perspectives.
In the last chapter, we discuss exciting future directions and ongoing work. The first section links active solids and metamaterial, as we study the counter-rotating squares mechanism, a paradigmatic mechanical metamaterial, with embedded active units. We show that it is possible to excite selectively and periodically the soft mode of this structure using elasto-active feedback and angular noise. In the second section, we describe experiments conducted to measure the mechanical properties of square lattices, and show that, in this case, activity can be seen as a negative friction relaxing toward motion direction. Finally, in the third section, we show that our design principle can be extended to other dry active matter systems, namely the vibrated polar disks, paving the way for the downsizing of active solids.

Appendix A presents the normal modes spectrum of all the structures presented in this manuscript. Appendix B is complementary to chapter 4. Appendices C, D, E, and F provide complementary results to chapter 5. Appendices G, H, I, and J provide complementary results to chapter 6. Appendices K and L are complementary to chapter 7. Finally, the reader may find the blueprints for $3d$ printed structures in Appendix M.

Chapter 1

State of the art

We consider that an *active agent* is an object that breaks spatial and time reversal symmetries; or, said differently, an anisotropic object whose dynamics break detailed balance. Active matter, in turn, is composed of many such individual active units, essentially identical, which all individually perform some work and interact with each other. At the macroscopic level, these intrinsically out of equilibrium materials are prone to develop new and interesting macroscopic physics. Looking for symmetries and conserved quantities is an excellent way to classify the systems we are interested in. Because the agents are able to perform work, energy conservation is broken at the microscopic level, and such systems are intrinsically out of thermodynamic equilibrium. Moreover, from the broken spatial symmetry, activity endows the agents with an additional free degree of freedom in the form of *polar* (arrows $\hat{\boldsymbol{n}}$), or *dipolar* (tensors $\mathbb{Q}$), active forces. For completeness' sake, one should mention that the active agents can also be *chiral*. The nature of the active agents (*polar*/*dipolar*/*chiral*) constitutes the first classification of active matter systems. Moreover, we call *wet* an active system immersed in a fluid, while we call it *dry* if it evolves on a substrate. This second characteristic (*dry*/*wet*) of active systems is crucial: it tells whether or not linear momentum is conserved. The last characteristic of active systems is the nature of the interactions between the active agents. They can, for instance, have *nematic* or *polar* alignment interactions with each other or, conversely, have only isotropic repulsion interactions. In that case, the active system is said *scalar*, as density is the only relevant macroscopic parameter. Eventually, the active degree of freedom can be coupled with the position dynamics. This last case, termed *self-alignment*, will be thoroughly discussed. The different classes of active matter systems are illustrated below using three simple questions on the system's properties.

Classes of active matter systems:

- What is the nature of the active agents? *polar*, *dipolar*, or *chiral*.
- Is linear momentum conserved? *wet* or *dry*.
- What is the nature of the interactions between the active agents? *nematic*, *polar*, *scalar*, or *self-alignment*.

Throughout this work, we focus on *dry* and *polar* active solids with *self-alignment* interactions. We start by introducing active liquids and the two important phenomena occurring in those systems: *motility-induced phase separation*, and *collective motion*, with particular emphasis on agent-based models, hydrodynamics theories, and model experiments. For a broad class of dense biological systems, however, a description in

terms of free-to-move agents does not hold because of the presence of strong position-based interactions. In such systems, the existence of a reference configuration calls for a description in terms of active strain/active solids rather than active flows/active liquids. We show that confined cell monolayers and bacterial biofilms are relatively faithful realizations of *dry* and *polar* active solids, and introduce the main phenomena specific to those systems. Finally, we focus on model active matter systems, and discuss two strategies to fabricate active solids: first, by compacting dense active liquids, and second, by constructing elastic structures doped with active agents.

1.1 Active liquids

For the past 25 years, a large amount of work has dealt with the study of active liquids, which are relatively dilute phases of active matter, allowing for the spatial reorganization of the active agents. Let us discuss the cases of *polar* particles with *scalar* interactions or *polar* alignment in such dilute regimes separately.

1.1.1 Scalar active matter

When the active units interact only through *scalar*, position-based repulsive interactions, the system boils down to a disordered active gas. Nonetheless, self-propelled particles tend to accumulate where they move more slowly. They may also slow down at high density for either biochemical [10, 11] or steric reasons [12, 13]. This creates a positive feedback, which can lead to Motility-Induced Phase Separation (MIPS), a spontaneous phase separation between a dense and a dilute fluid phase via steric or excluded volume repulsion [14]. In microbiological studies, the formation of dense clusters from a uniform initial population of motile bacterial cells is often encountered, and usually called aggregation, or fruiting body formation rather than phase separation [15]. Note that bacteria aggregation generally involves chemical communication between individual cells, but this effect may still be representable partly as a density-dependent swim speed, $v(\rho)$.

Agent-based model

The MIPS phenomenology has been confirmed in simulations of self-propelled particles with *scalar* interactions [10, 13, 16–19]. In particular, in 2008, *Tailleur et al.* studied a $1d$ model of interacting run-and-tumble particles [10] and showed that it exhibits a spontaneous phase separation between a dense and a dilute phase for great enough density. Later, models of interacting active Brownian particles (ABPs) were simulated in $2d$ by *Fily et al.* [13] and in $3d$ by *Stenhammar et al.* [18] with similar conclusions. In general, agent-based models for MIPS are formulated as a set of overdamped equations of motion for the position $\boldsymbol{r}_i$ and orientation $\hat{\boldsymbol{n}}_i$ of particle i:

$$\gamma_t \dot{\boldsymbol{r}}_i = F_0 \hat{\boldsymbol{n}}_i + \boldsymbol{F}^{int}, \tag{1.1a}$$

$$\gamma_r \dot{\theta}_i = \xi_i, \tag{1.1b}$$

where θ_i is the angle of the unit vector $\hat{\boldsymbol{n}}_i$ with respect to the x-axis, γ_t (resp. γ_r) is the translational (resp. rotational) friction, F_0 is the amplitude of the active *polar* force, $\boldsymbol{F}^{int}$ are repulsive position-based interactions, and ξ_i are i.i.d Gaussian white noise, with zero mean $\langle \xi_i \rangle = 0$ and correlations $\langle \xi_i(t)\xi_j(t') \rangle = 2D\delta_{ij}\delta(t-t')$. Note that steric interactions $\boldsymbol{F}^{int}$ are considered isotropic. In Eq. (1.1b), the absence of interactions forbids the emergence of orientational order.

Nature of the instability

The mechanism underlying MIPS can be intuitively captured by a relatively simple argument, well known in the literature [14, 20].

On the one hand, as stated above, self-propelled particles tend to accumulate where they move more slowly. This follows directly from the master equation of a self-propelled particle of spatially varying speed $v(\boldsymbol{r}) = F_0/\gamma_t$, where $\boldsymbol{r}$ indicates the spatial coordinate:

$$\dot{P}(\boldsymbol{r},\theta) = -\boldsymbol{\nabla}_{\boldsymbol{r}}\left[v(r)\hat{\boldsymbol{n}}P(\boldsymbol{r},\theta)\right] + D\Delta_\theta P(\boldsymbol{r},\theta) \tag{1.2}$$

where the first term accounts for self-propulsion, and the second for angular diffusion. For isotropic processes, $P_{\text{stat}}(\boldsymbol{r},\theta) \propto 1/v(r)$ is always a steady-state solution of Eq. (1.2), highlighting the propensity of the system to be denser where it is slower. On the other hand, crucially, MIPS arises in assemblies of active particles exhibiting a propulsion speed v that depends on the local particle density ρ, which is reminiscent of the interactions between the particles. However, this dependence must be strong enough, which is illustrated by the following criterion:

$$\frac{dv}{d\rho}(\rho_0) < -\frac{v(\rho_0)}{\rho_0}, \tag{1.3}$$

corresponding to the linear instability of the homogeneous state, with density ρ_0. Interestingly, this equation correctly identifies the region where macroscopic MIPS is initiated by spinodal decomposition.

Hydrodynamics theory

An equilibrium system undergoing diffusive fluid-fluid phase separation is governed on continuum scales by the so-called *Model B* in the classification of *Hohenberg and Halperin* [21]. It consists of constructing a Landau free energy F as a quartic polynomial in the conserved quantity ϕ, linearly related to the local density ρ, with square-gradient terms, and assuming local diffusive dynamics. Such scalar ϕ^4 field theories (or phase-field models) have played a crucial role in understanding phase separation in systems with time-reversal symmetry [21, 22]. In 2014, to create phenomenologically an active version of the model, *Wittkowski et al.* added the simplest "non-integrable" gradient term to what is otherwise the standard *Model B* [23]. The chosen gradient term breaks detailed balance, which implies that the resulting *Active Model B* (AMB) cannot be derived from any free-energy functional. The model can be formulated as:

$$\dot{\phi} = -\boldsymbol{\nabla}\cdot\left(\boldsymbol{J} + \sqrt{2D}\boldsymbol{\Lambda}\right), \tag{1.4a}$$

$$\boldsymbol{J} = -\boldsymbol{\nabla}\left[\frac{\delta F}{\delta\phi} + \lambda|\nabla\phi|^2\right], \tag{1.4b}$$

$$F[\phi] = \int\left\{\underbrace{\frac{a}{2}\phi^2 + \frac{b}{4}\phi^4}_{f(\phi)} + \frac{K}{2}|\nabla\phi|^2\right\}d\boldsymbol{r}, \tag{1.4c}$$

where $f(\phi)$ is the bulk free-energy density, $K > 0$ governs the energetic cost of interfaces, and $\boldsymbol{\Lambda}$ is Gaussian white noise with zero mean and unit variance. The composition variable ϕ is related to the number density $\rho(\boldsymbol{r},t)$ of active particles by a linear transform $\phi = (2\rho - \rho_H - \rho_L)/(\rho_H - \rho_L)$, where ρ_H and ρ_L are the densities of the high- and low-density coexisting phases, respectively. Thus, the local bulk contribution of the free

energy f is even to quartic order, with the critical point at $a = 0$ and phase separation for $a < 0$. Neglecting terms in f beyond quartic is justified only when the order parameter ϕ remains small. The coexisting mean-field binodal densities $\pm\phi_b$ obey $\phi_b = \sqrt{-a/b}$; these terms should therefore map under the linear transform onto $\rho = \rho_c \pm \Delta\rho_b$, with $\Delta\rho_b \ll \rho_c$. *Wittkowski et al.* find that the additional non-integrable λ-term has modest effects on coarsening dynamics, but alters the static phase diagram by creating a jump in (thermodynamic) pressure across flat interfaces. Nonetheless, simulations of repulsive ABPs reveal that during coarsening, the macroscopic droplets of dense liquid arising via MIPS host a population of mesoscopic vapor bubbles that are continuously created in the bulk, coarsen, and are ejected into the exterior vapor [18, 24]. The "boiling liquid" is thus itself a microphase-separated state of vapor bubbles surrounded by dense liquid (or "bubble phase"). Recently, a refined version of *Active Model B*, so-called *Active Model B+* (AMB+), was introduced to explain the origin of the bubble phases observed in the phase separation [24].

Model experiments

In terms of model experiments, MIPS was exciting because it allowed the reusing of experimental systems that were not aligning enough for collective motion (described below). One can think about Janus colloids experiments [25–27], in which cluster formation is reported. Note that it might be caused in part by attractive interactions rather than a purely MIPS scenario. Moreover, in such systems, no "real" MIPS is observed, as cluster formation ends up being interrupted. It is generally interpreted as a consequence of remaining *polar* alignment interactions [28], or additional hydrodynamics interactions [29, 30]. In summary, there is some evidence for MIPS in systems of bacteria and synthetic colloidal swimmers, although more experimental work is needed to understand the effect of alignment and hydrodynamics on MIPS interruption.

1.1.2 Collective motion

Collective Motion (CM), the spontaneous, macroscopic ordering of the velocities of a system of many particles, is a phenomenon observed in real-life systems ranging from bird flocks [31–37] and fish schools [38], to locus swarms [39, 40], down to bacterial suspensions [41, 42]. It is specific to active systems composed of *polar* agents, interacting with *ferromagnetic*-like, *polar* alignment. The observation of spectacular collective dynamics in such systems of self-propelled *polar* objects led the physics community to devise models able to capture their full richness and qualitative features.

Agent-based model

The transition to CM was first investigated in 1995 in an effective model, the so-called *Vicsek* model. It describes the discrete-time evolution of self-propelled point-like particles moving at a constant speed, and aligning their velocities when they encounter:

$$\boldsymbol{r}_i(t + \Delta t) = \boldsymbol{r}_i(t) + \boldsymbol{v}_i(t)\Delta t, \tag{1.5a}$$

$$\theta_i(t + \Delta t) = \sum_{j \in v(i)} (\theta_j - \theta_i) + \xi_i, \tag{1.5b}$$

where $\boldsymbol{r}_i(t)$ is the position of particle i at time t, $\boldsymbol{v}_i(t) = v_0\hat{\boldsymbol{n}}_i(t) = v_0\left(\cos\theta_i(t), \sin\theta_i(t)\right)$ represents the instantaneous velocity of particle i at time t, oriented along its polarity

$\hat{\boldsymbol{n}}_i(t)$, and $v(i)$ denotes some kind of neighborhood of particle i, which originally designates all the particles within a circle of radius r surrounding particle i (Fig. 1.15-left). The term ξ_i on the right-hand side of Eq. (1.5b) accounts for i.i.d. Gaussian variables with zero mean $\langle \xi_i \rangle = 0$ and correlations $\langle \xi_i(t)\xi_j(t') \rangle = 2D\delta_{ij}\delta(t-t')$, modeling an angular noise. The *Vicsek* model displays a nonequilibrium phase transition from a disordered state at low density or high noise to an ordered, coherently moving state at high density or low noise [9, 43]. The orientational order is characterized by the classical order parameter:

$$\Psi(t) = \left| \frac{1}{N} \sum_{i=1}^{N} \frac{\boldsymbol{v}_i(t)}{|\boldsymbol{v}_i(t)|} \right|. \tag{1.6}$$

For high density or low noise, all velocities are aligned, thus $\Psi = 1$, while for low density or high noise, the system is completely disordered, and $\Psi = 0$. Importantly, the transition is discontinuous and occurs via the nucleation of elongated propagating bands [44, 45]. The *Vicsek* model is very similar to the $2d$ XY model for magnetism [46] because the active unit's velocity, like the local spin of the classical XY model, also has a fixed norm and continuous rotational symmetry. In the limit of zero self-propulsion $v_0 \to 0$, on each time step the particles' orientations evolve, but never actually move, and thus the model reduces precisely to the dynamics of a $2d$ XY model, with the (small) particle's velocity playing the role of the XY spin. Since the $2d$ XY model does not exhibit a long-range ordered phase at finite temperatures, its observation in the *Vicsek* model seems very surprising. Indeed, in light of the Mermin-Wagner theorem[1] for equilibrium systems [47], its existence must depend on fundamentally dynamical, non-equilibrium aspects of the model; or, somewhat equivalently, on some effective long-range interactions coming from the flying nature of the active spins.

Hydrodynamics theory

A continuum effective theory for the flocking model of *Vicsek et al.* was proposed four months after the original paper by *Toner and Tu* [48, 49] (see also [50]). They formulated the continuum model phenomenologically, solely based on symmetry considerations. A few years later, the same equations were derived in [51, 52] by explicitly coarse-graining a binary-interaction version of the *Vicsek* model. These derivations provide a microscopic basis for the hydrodynamic theory and lead to a deterministic coarse-grained description, with the stochasticity of the *Vicsek* model reflected in an average sense through the diffusion and relaxation terms. Let us introduce the continuum equations in their simplest form and analyze some of their consequences. We consider that the particles are moving on a frictional substrate, thus the only conserved field is the number density $\rho(\boldsymbol{r}, t)$ of active particles. In addition, to describe the possibility of states with *polar* orientational order, one must consider the dynamics of a polarization vector field $\boldsymbol{p}(\boldsymbol{r}, t)$, that is a broken symmetry, therefore slow, variable. These continuum fields can be defined as follows:

$$\rho(\boldsymbol{r}, t) = \sum_i \delta(\boldsymbol{r} - \boldsymbol{r}_i(t)), \tag{1.7a}$$

$$\boldsymbol{p}(\boldsymbol{r}, t) = \frac{1}{\rho(\boldsymbol{r}, t)} \sum_i \hat{\boldsymbol{n}}_i(t)\delta(\boldsymbol{r} - \boldsymbol{r}_i(t)), \tag{1.7b}$$

[1] which states that continuous symmetries cannot be spontaneously broken at finite temperatures in systems with sufficiently short-range interactions in dimensions $d \leq 2$.

the dynamical equations of which are written as:

$$\partial_t \rho + v_0 \boldsymbol{\nabla} \cdot (\rho \boldsymbol{p}) = 0, \tag{1.8a}$$

$$\partial_t \boldsymbol{p} + \lambda_1 (\boldsymbol{p} \cdot \boldsymbol{\nabla}) \boldsymbol{p} = -\left[\alpha(\rho) + \beta |\boldsymbol{p}|^2\right] \boldsymbol{p} + K \nabla^2 \boldsymbol{p} - v_1 \boldsymbol{\nabla} \frac{\rho}{\rho_0} + \lambda_2 \boldsymbol{p} (\boldsymbol{\nabla} \cdot \boldsymbol{p}) + \frac{\lambda_3}{2} \boldsymbol{\nabla} |\boldsymbol{p}|^2 + \boldsymbol{f}. \tag{1.8b}$$

The first two terms on the right-hand side of Eq. (1.8b) control the mean-field continuous order-disorder transition that takes place as the parameter α goes through zero. In the derivation of *Bertin et al.* [51], α depends on the local density ρ and the noise strength in the underlying microscopic model and turns negative at large enough ρ. A reasonable phenomenological approach to describe the physics near the transition is to take $\alpha(\rho) = a_0(1 - \rho/\rho_c)$, changing sign at a characteristic density ρ_c. The coefficient β happens to be positive, ensuring the stability of the bifurcated solution with respect to homogeneous peturbations. The third term captures the energy cost for spatially inhomogeneous deformations of the order parameter $\boldsymbol{p}$, and the so-called Frank constant K is positive. The three following terms are allowed in equilibrium systems with *polar* symmetry [53, 54]. Finally, the last term on the right-hand side of Eq. (1.8b) captures the fluctuations and is taken to be white, Gaussian noise, with zero mean and correlations: $\langle f_\alpha(\boldsymbol{r}, t) f_\beta(\boldsymbol{r}', t') \rangle = 2D\delta_{\alpha\beta}\delta(\boldsymbol{r} - \boldsymbol{r}')\delta(t - t')$; where the indices represent the axis.

The dynamical model described by Eqs. (1.8) exhibits by construction, in a mean-field treatment of homogeneous solutions, a continuous transition from a disordered to an ordered state. For $\alpha > 0$, corresponding to an equilibrium density $\rho_0 < \rho_c$, the homogeneous steady state of the system is disordered or isotropic, with $\boldsymbol{p} = \boldsymbol{0}$ and a corresponding zero mean velocity. For $\alpha < 0$, corresponding to $\rho_0 > \rho_c$, the system orders in a state with uniform orientational order, with $|\boldsymbol{p}_0| = \sqrt{-\alpha_0/\beta}$, where $\alpha_0 = \alpha(\rho_0)$. In the ordered state, which is also a moving state, with $\boldsymbol{v} = v_0 \boldsymbol{p}_0$, continuous rotational symmetry is spontaneously broken. This mean-field analysis survives fluctuation corrections in two dimensions [48, 49], evading the *Mermin-Wagner* theorem. Finally, similarly to the original *Vicsek* model, inhomogeneous perturbations destabilize the polar phase close to the onset of CM, leading to fully nonlinear solutions in the form of solitary bands, and making the transition generically discontinuous in large enough systems.

Model experiments

The development of model experiments like vibrated *polar* disks [55–58], colloid rollers [59–61], or actin filaments on a molecular motor carpet [62, 63], in parallel with theoretical models, allowed for a better understanding of the mechanisms at the origin of collective motion of real-life systems. Let us elaborate on the two first.

Large populations of colloid rollers were realized experimentally for the first time in 2013 by *Bricard et al.* [59]. The system consists of spherical colloidal particles of diameter 5 μm, which self-propel by rolling on solid surfaces. The self-propulsion results from an electro-hydrodynamic phenomenon referred to as the Quincke rotation [64]: when an electric field is applied to an insulating sphere immersed in a conducting fluid, the charge distribution at the sphere surface is unstable above a critical field amplitude $E > E_Q$. This spontaneous symmetry breaking results in a net electrostatic torque on the sphere, which thus rotates at a constant speed around a randomly picked direction transverse to the electric field. When the sphere lies on a rigid surface, this spinning motion turns into self-propulsion. The electric and hydrodynamic interactions rule the alignment and

repulsion between the rolling colloids.

The motion of the rollers is confined to racetrack channels of width 500 μm $< W <$ 5 mm (Fig. 1.1-a), by adding a patterned insulating film at the surface of the upper transparent electrodes. When the area fraction ϕ of colloid rollers is small, the population of rollers behaves as a gaseous phase (Fig. 1.1-b). All the particles move in random directions at the same speed. When the area fraction is increased above a critical value ϕ_c, collective motion emerges spontaneously: a macroscopic fraction of the population moves coherently in the same direction. For area fraction greater but close to ϕ_c, the system phase separates into a homogeneous isotropic phase and a denser polar phase, which typically consists of a single macroscopic band that propagates at a constant velocity (Fig. 1.7-c). Increasing further the area fraction, a homogeneous band-less polar state develops, with the entire population of rollers cruising coherently along the same direction and with homogeneous polarization Ψ (Fig. 1.7-d). These observations are very much reminiscent of the transition to collective motion reported in the *Vicsek* model [9, 44, 45] (Fig. 1.7-e). However, one specificity of the ordered polar phase obtained in the *Vicsek* model [9] and at the level of the large-scale hydrodynamics theory [48, 49] is the presence of anomalously large density fluctuations. The first quantitative analysis of the polar phase of colloidal rollers concluded they were absent; and it is only recently, that it was shown that they are indeed present, conducting new experiments with larger statistics and weaker confinement [61].

The second worth-mentioning model experimental system is that of walking grains. The system consists of a collection of vibrated micro-machined disks of diameter $d = 4$ cm, with a built-in *polar* asymmetry (Fig. 1.2-a). Polar alignment emerges from the

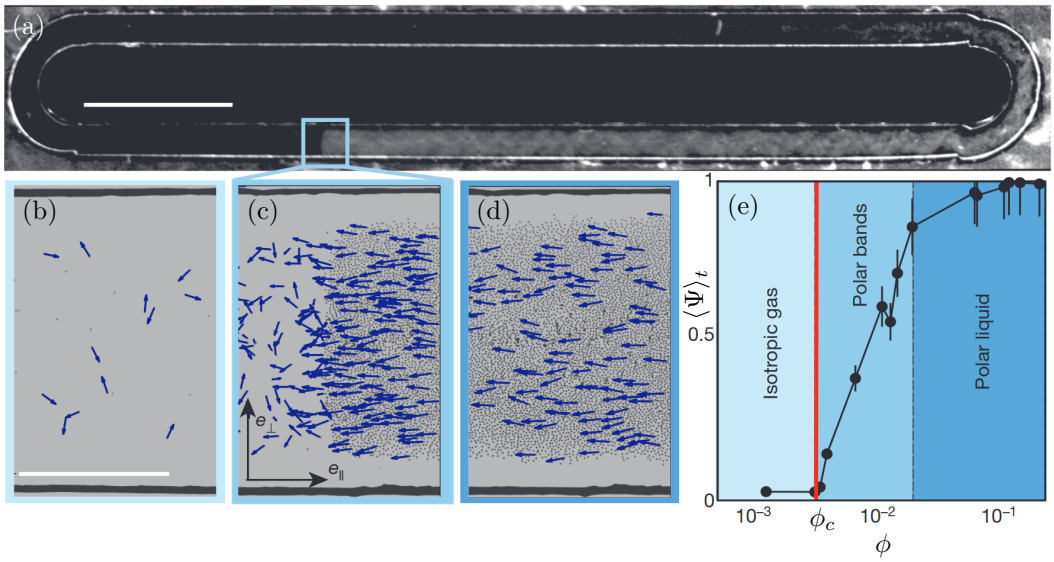


FIG. 1.1. **Transition to directed collective motion in populations of Quincke rollers.** (a) Dark-field pictures of a roller population that spontaneously forms a macroscopic band propagating along the racetrack; scale bar 5 mm. (b-d) Close-up views. The arrows correspond to the roller displacement between two subsequent video frames. (b) Isotropic gas, (c) propagating band, (d) homogeneous polar liquid; scale bar 500 mm. (e) Average order parameter $\langle\Psi\rangle_t$ as a function of the area fraction ϕ. Collective motion occurs as ϕ exceeds $\phi_c = 3.10^{-3}$; error bars, 1 s.d.; $e_\parallel$ (resp. $e_\perp$) is the unit vector oriented along the tangent (resp. the normal) of the racetrack confinement. Adapted from [59].

dynamical relaxation of the particle polarity towards its velocity after each collision, and induces collective motion at a moderate packing fraction (Fig. 1.2-b and [55, 58]). The system is described as N self-propelled hard disks, with position $\boldsymbol{r}_i$, velocity $\boldsymbol{v}_i$, and a body axis, or polarity, given by the unit vector $\hat{\boldsymbol{n}}_i$. Between collisions, these parameters evolve according to the dimensionless equations:

$$\dot{\boldsymbol{r}}_i = \boldsymbol{v}_i, \tag{1.9a}$$

$$\tau_v \dot{\boldsymbol{v}}_i = \boldsymbol{n}_i - \boldsymbol{v}_i, \tag{1.9b}$$

$$\tau_n \dot{\theta}_i = (\hat{\boldsymbol{n}}_i \times \boldsymbol{v}_i) \times \hat{\boldsymbol{n}}_i. \tag{1.9c}$$

In Eq. (1.9b), the competition between self-propulsion $\hat{\boldsymbol{n}}$ and viscous damping $-\boldsymbol{v}$ lets the velocity relax to $\hat{\boldsymbol{n}}$ on a timescale τ_v. Similarly, in Eq. (1.9c), the polarity $\hat{\boldsymbol{n}}$ undergoes an overdamped *self-alignment* torque that reorients it toward $\boldsymbol{v}$ on a timescale τ_n. Note that the latter is proportional to the velocity, giving rise to an alignment length rather than an alignment time. Interactions between particles are considered elastic hard-disk collisions, which change $\boldsymbol{v}$ but not $\hat{\boldsymbol{n}}$. After such a collision, $\boldsymbol{v}$ and $\hat{\boldsymbol{n}}$ are not collinear, and the particles undergo curved trajectories which are interrupted by another collision. Simulations of Eqs. (1.9) very well reproduce the phenomenology observed in experiments. Within periodic boundary conditions, varying only the noise level and the packing fraction, a phase diagram akin to the Vicsek one was obtained (Fig. 1.2-c), thereby establishing the evidence of truly long-range collective motion in an experimentalo-silico system of self-propelled particles. This system is also conceptually powerful because it demonstrates that collective motion arises even in the absence of explicit aligning interactions between the active agents; ingredient that was historically introduced to model birds flocks or fish schools but that is not generic to all active matter; indicating that genuine physical interactions at the individual level are sufficient

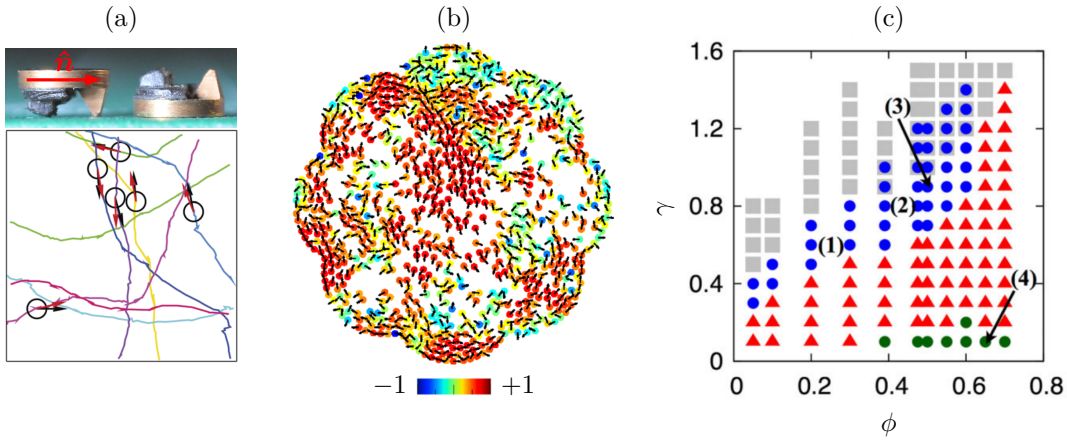


FIG. 1.2. **Transition to directed collective motion in populations of self-propelled hard disks.** (a) Picture of a walking grain (top): a hard metallic disc with an off-center tip and a glued rubber skate located at diametrically opposite positions; the velocity $\boldsymbol{v}$ is in general not perfectly aligned with the polarity $\hat{\boldsymbol{n}}$. Under proper vertical vibration, the walker performs a persistent random walk (bottom). (b) Snapshot of the experimental system. A thousand of such discs confined in a flower-shaped arena, interacting through collisions, develop large-scale collective motions. The black arrows indicate the particles' polarity. The color-code ranges from -1 (blue) to $+1$ (red), and corresponds to the relative alignment with the neighboring particles. (c) Complete phase diagram, from simulations of Eqs. (1.9) in periodic boundary conditions in a domain of size $L = 200d$, with γ the noise amplitude and ϕ the area fraction (gray square: disordered phase; red triangles: homogeneous polar ordered phase; blue bullet: polar bands; green bullets: inverse polar bands). Adapted from [55, 57].

to set homogeneous active populations into stable collective motion [58].

1.2 Dense biological systems

In polar active liquids, free-to-move agents interact through explicit or effective aligning interactions, leading to collective motion. However, for a broad class of active matter systems, the description in terms of free-to-move agents does not hold anymore because of the presence of strong position-based interactions. This situation generally arises when repulsive active units are put under strong confinement, or for attractive active units, which can spontaneously cluster together at any density. In such systems, the existence of a reference configuration calls for a description in terms of active strain/active solids rather than active flows/active liquids: new theoretical frameworks are required. Let us illustrate this idea using two biological systems which have recently attracted the attention of the physics community: (i) cell monolayers, and (ii) bacterial biofilms.

1.2.1 Cell monolayers experiments

One-cell-thick monolayers are the simplest tissues in multicellular organisms, yet they fulfill critical roles in development and normal physiology. In early development, embryonic morphogenesis results largely from rearrangements and deformations of such monolayers due to internal stresses. Later, monolayers act as physical barriers separating the internal environment of organs from the exterior and must withstand externally applied forces. Resisting and generating mechanical forces is an essential part of monolayer functions, highlighting the combined roles of elasticity and activity in those systems. Moreover, the presence of elasto-active feedback between tissue deformations and cell polarizations, a typical realization of which is the contact inhibition of locomotion (CIL) of cells[2] [65–67] is likely to allow for the emergence of collective behaviors. There exists a rich literature on cell monolayer experiments [8, 68–74]. We first elaborate on collective migration experiments, somewhat reminiscent of the transition to CM in the *Vicsek* model; and then discuss spontaneous self-oscillations, which arise when the spatial confinement applied to the cell monolayer is strong enough.

Collective motion

Collective motion of cells has been observed experimentally and numerically in a pioneering work by *Szabó et al.* [68]. The authors studied the collective migration of a large number of keratocytes[3] using long-term videomicroscopy. By increasing the overall density of the migrating cells, they observed experimentally a phase transition from a disordered into an ordered, coherently moving state (Figs. 1.3-a to f). As done in flocking active liquids or magnetism, the orientational order is characterized by the classical order parameter $\Psi(t)$ (Eq. (1.6)). A sharp increase of $\langle\Psi\rangle_t$ is observed around $\rho = 5 \times 10^{-4}$ cells/μm^2 (Fig. 1.3-j), highlighting the propensity of cells to organize coherently when density is large enough. These experiments motivated the construction of a flocking model that exhibits a continuous transition to the ordered phase, while assuming only short-range interactions and no explicit information about the knowledge of the directions of motion of neighbors. The overdamped equations describing the $2d$ dynamics of model cell i with position $\boldsymbol{r}_i$ and polarity orientation $\hat{\boldsymbol{n}}_i$ are:

[2]Process whereby a cell ceases motility or changes its trajectory upon collision with another cell.
[3]Keratinocytes are the primary type of cell found in the epidermis, the outermost layer of the skin.

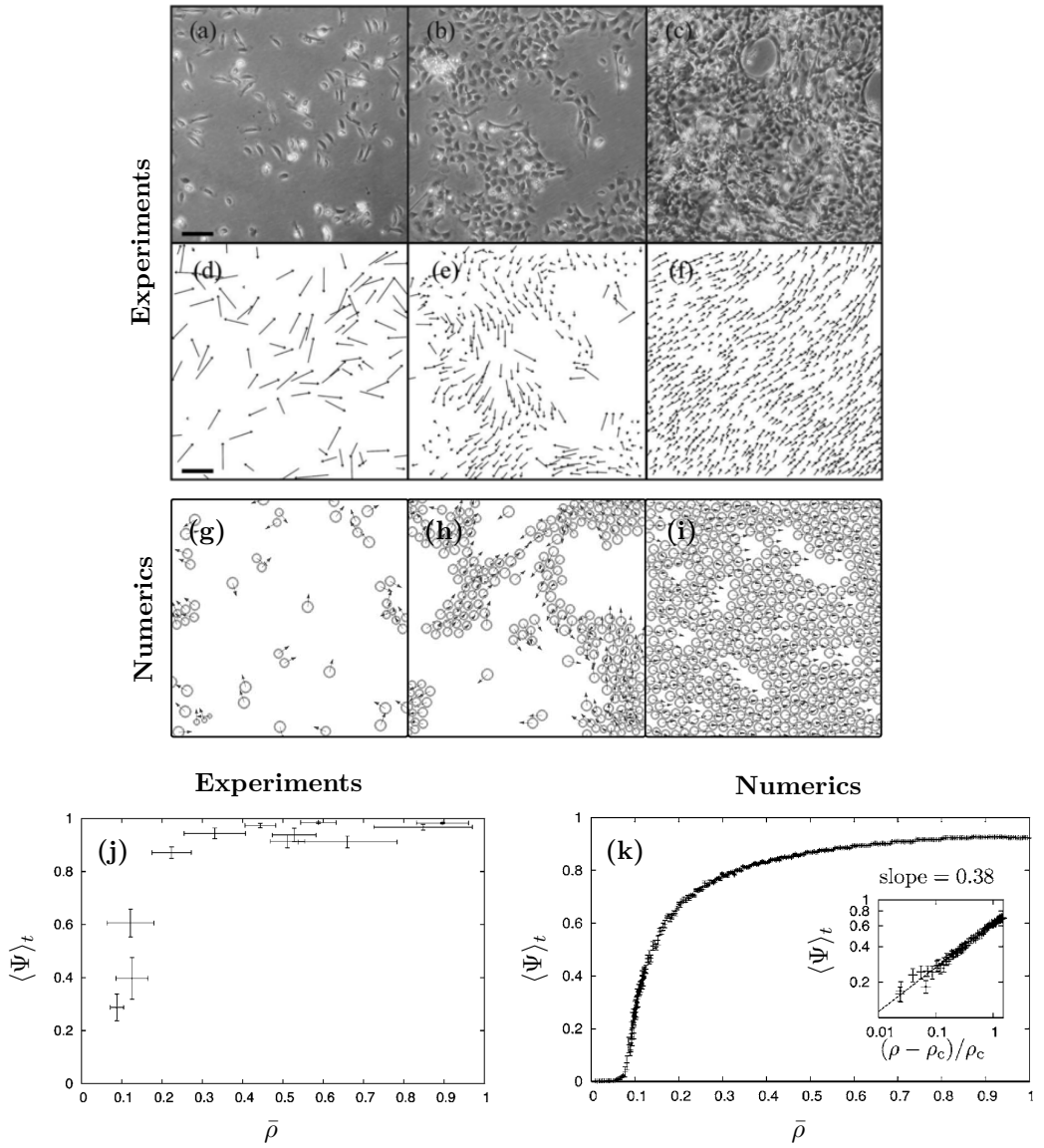


FIG. 1.3. **Emergence of orientational order in systems of migrating cells.** (a-c) Phase contrast images showing the typical behavior of cells for three different densities. (a) 1.8, (b) 5.3, (c) 14.7 cells/100×100 μm^2; scale bar 200 μm. (d-f) Velocity of cells; scale bar 50 μm/min. (g-i) Numerical simulations for different densities. The normalized number density $\bar{\rho} = \rho/\rho_{\max}$ are respectively 0.12 (g), 0.4 (h), 0.8 (i) (with $\rho_{\max} = 2$, which is approximately the density where cells reach tight packing in simulations). (j) Average order parameter $\langle\Psi\rangle_t$ as a function of the normalized cell density $\bar{\rho}$, as obtained from experiments. Cell density is normalized with the maximal observed density of 2.5×10^{-3} cells/μm^2 and error bars indicate the standard error of the density and order parameter. (k) Average order parameter $\langle\Psi\rangle_t$ as a function of the normalized number density $\bar{\rho}$, as obtained from numerical simulations. Each data point was obtained from at least 10 independent simulation runs with $N = 1000$ and $\eta = 0.6$. The insets show the dependence of $\langle\Psi\rangle_t$ on $[\rho - \rho_c(\eta)]/\rho_c$. Adapted from [68].

$$\dot{\boldsymbol{r}}_i = v_0 \hat{\boldsymbol{n}}_i + \mu \sum_{j=1}^{N} \boldsymbol{F}(\boldsymbol{r}_i, \boldsymbol{r}_j), \tag{1.10a}$$

$$\dot{\theta}_i = \frac{1}{\tau} \arcsin \left[\left(\hat{\boldsymbol{n}}_i \times \frac{\boldsymbol{v}_i(t)}{|\boldsymbol{v}_i(t)|} \right) \cdot \boldsymbol{e}_z \right] + \xi, \tag{1.10b}$$

where $\boldsymbol{e}_z$ is a unit vector orthogonal to the plane of motion, and ξ is a delta correlated

Gaussian white noise term with zero mean and correlations $\langle \xi(t)\xi(t')\rangle = \eta^2/12\delta(t-t')$. Thus, each cell with mobility μ attempts to maintain a self-propelling velocity of magnitude v_0 in the direction of the unit vector $\hat{\boldsymbol{n}}_i$ and experiences intercellular forces $\boldsymbol{F}(\boldsymbol{r}_i, \boldsymbol{r}_j)$. Note that $\boldsymbol{F}(\boldsymbol{r}_i, \boldsymbol{r}_j)$ are not simple elastic interactions: they are repulsive at short distances, attractive at longer distances, and cells do not interact when they are too far apart. Therefore, cells interact through forces deriving from a rather realistic but complicated potential. Importantly, the direction of the polarity vector $\hat{\boldsymbol{n}}_i$ relaxes toward the direction of motion $\boldsymbol{v}_i = \dot{\boldsymbol{r}}_i$ with a relaxation time τ, while also experiencing angular noise ξ.

Simulations of Eqs. (1.10) show that a continuous transition to the ordered phase arises when density is large enough (Figs. 1.3-g,h,i, and k), in line with the experimental observations, and that this transition also occurs as η decreases while ρ is held fixed. The growing importance of position-based interactions leads to discrepancies with the *Vicsek* model: the authors claim that the transition is continuous, and observed neither polar bands nor density fluctuations at the transition to CM. This is quite surpringing and might be attributed to a finite size effect. Eventually, modulo a few deviations from the *Vicsek* scenario, collective migration can still be interpreted as emerging CM.

Note that once again, the polarity dynamics is assumed to evolve via a self-alignment term. To our knowledge, the first flocking model to introduce a torque reorienting the polarity of an active unit toward its motion direction was introduced as early as 1996 [75]. However, like in the work of *Szabó et al.*, they considered a speed-independent reorientation rate of the polarity vector.

Self-oscillation

In a recent paper [8], *Peyret et al.* describe a form of collective oscillations in confined epithelial tissues in which the oscillatory motion is the dominant contribution to cellular movements. The authors deposited human keratinocytes on square areas surrounded by a nonadherent surface, imposing a confinement. Cells are initially sparse but progressively expand within the square through cell proliferation until the tissue is confluent and occupies all the available space. Individual cells then move along parallel elliptical trajectories with little net relative motion of cells with respect to each other, and no swirling behavior is observed (Figs. 1.4-a). This highlights the emergence of a layer-scale coordinated movement in which all the cells move together in a direction that rotates slowly with time. The oscillatory nature of these collective movements is best revealed by considering the total velocity $\langle \boldsymbol{v} \rangle_{\mathrm{ROI}}$ averaged over a region of interest (ROI) at the center of the system. Although the magnitude $|\langle \boldsymbol{v} \rangle_{\mathrm{ROI}}|$ is almost constant and nonzero, the individual components $\langle v_x \rangle_{\mathrm{ROI}}$ and $\langle v_y \rangle_{\mathrm{ROI}}$ show clear oscillations (Fig. 1.4-c), with a phase shift of $\pi/2$. The period of this rotation is typically 6 hrs, and was found to grow linearly with the square domain size [8]. Finally, in rectangular, thus anisotropic confinement, it has been shown that the motion along the long direction exhibits a transition from global to multinodal standing wave as the aspect ratio of the rectangle increases [8, 73].

An active phase-field model is introduced to describe the dynamics of the cell monolayers. They consider a $2d$ tissue and describe each cell i independently by a polarity $\hat{\boldsymbol{n}}_i$ and a phase field ϕ_i, where $\phi_i = 1$ indicates the interior of the cell and $\phi_i = 0$ its exterior. Each cell is described implicitly, and its boundary is defined to lie at the midpoint $\phi_i = 1/2$.

The phase fields satisfy an overdamped dynamics given by:

$$\partial_t \phi_i + \boldsymbol{v}_i \cdot \boldsymbol{\nabla} \phi_i = -\frac{\delta F}{\delta \phi_i}, \tag{1.11}$$

where $\boldsymbol{v}_i = (\alpha \hat{\boldsymbol{n}}_i + \boldsymbol{F}_i^{\text{tot}})/\zeta$ is the speed of the cell i, F is the free energy, α is the strength of the motility, ζ is a friction coefficient, and $\boldsymbol{F}_i^{\text{tot}} = \boldsymbol{F}_i^{\text{ster}} + \boldsymbol{F}_i^{\text{visc}}$ is the total force acting on one cell's surface (including steric and viscous interactions, the first one deriving from the free energy F, and the second one from polarity imbalance between neighboring cells).

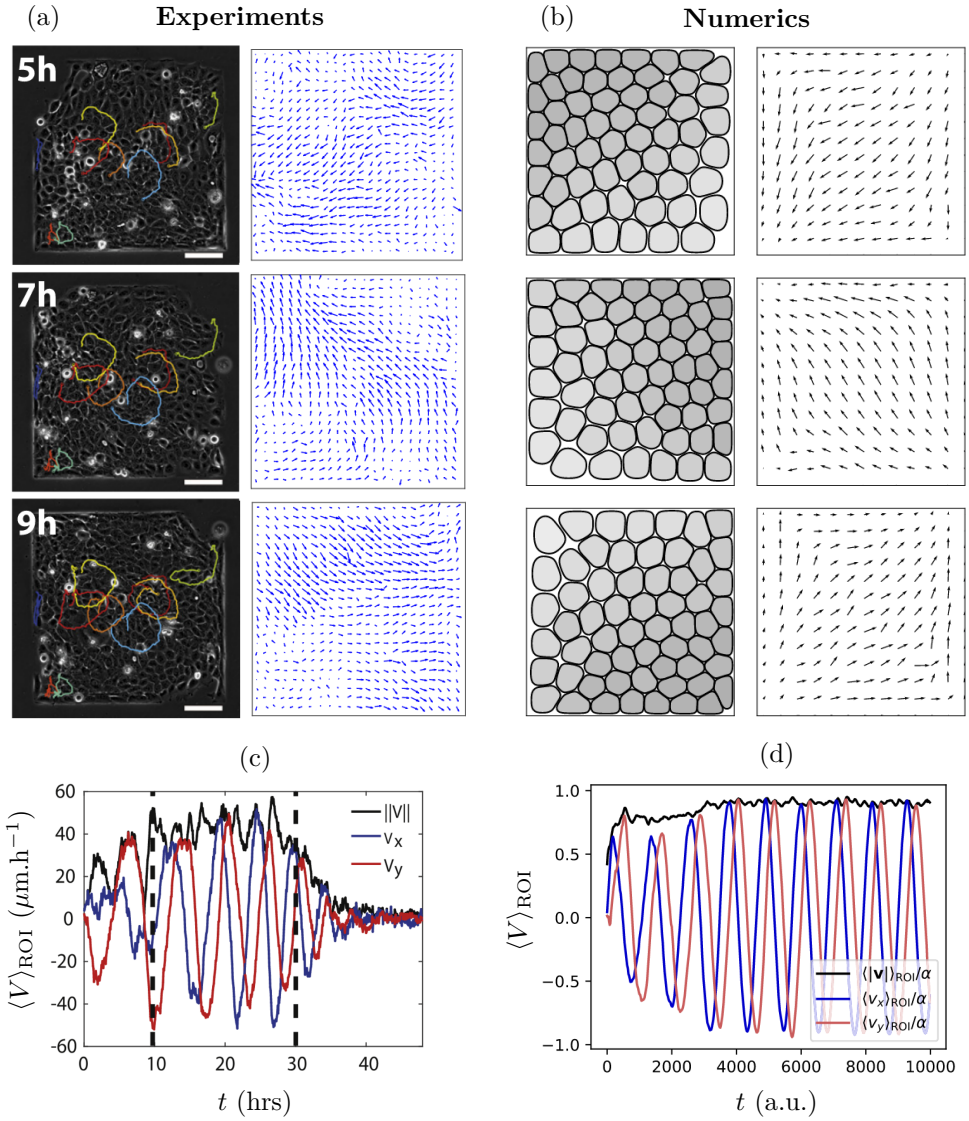


FIG. 1.4. **Coordinated oscillations of a confined cell monolayer.** (a) Left column shows snapshots of a confluent HaCaT layer in square confinement at various times and representative trajectories of single cells; scale bar: 100 mm. Right column shows velocity fields from PIV measurement at the corresponding times. (b) Snapshots of simulations showing an oscillating tissue at different times. The left-hand panels show the individual cells, darker cells being more compressed, and the right-hand panels show the corresponding velocity fields. (c) Time evolution of the two projected components, $V_x = \langle v_x \rangle_{\text{ROI}}$ and $V_y = \langle v_y \rangle_{\text{ROI}}$, and norm of the velocity $|V| = \left(V_x^2 + V_y^2\right)^{1/2}$, computed on a cropped area in the center of the square of panels (a). (d) Average velocity projected on the x and y axes for the numerical system of panels (b). Adapted from [8].

The role of the total free energy F is both to maintain the cell integrity as well as to define interactions between cells. It can be decomposed as follows: a Ginzburg-Landau free-energy term responsible for the stabilization of the diffuse interfaces, a quadratic soft constraint enforcing area conservation, and finally, two terms giving rise to repulsion forces between cells and with the confining walls [76]. The sole source of activity in the model is provided by α, which induces a propulsion in the direction of $\hat{\boldsymbol{n}}_i$. The polarity vectors are normalized, i.e. $\hat{\boldsymbol{n}}_i = (\cos\theta_i, \sin\theta_i)$, and the authors define the following alignment dynamics for the angle:

$$\partial_t \theta_i = -J|\boldsymbol{F}_i^{\text{tot}}|\Delta\theta_i + \sqrt{2D}\eta_i, \tag{1.12}$$

where $\Delta\theta_i \in [-\pi, \pi]$ is the angle between $\hat{\boldsymbol{n}}_i$ and $\boldsymbol{F}_i^{\text{tot}}$; and η_i is a Gaussian white noise. The positive constant J represents the strength of the *self-alignment* torque. Interestingly, as compared to the previous model of *Szabó et al.* (Eqs. 1.10), the *self-alignment* term is now inducing a torque rotating the polarity vector $\hat{\boldsymbol{n}}_i$ toward $\boldsymbol{F}_i^{\text{tot}}$, with an amplitude proportional to its norm $|\boldsymbol{F}_i^{\text{tot}}|$, and linearly related to the angle between the two vectors (while it is non-linear and independent of the amplitude in the work of *Szabó et al.*, see Eq. (1.10b)). Simulations of confluent monolayers in square confinement show the emergence of sustained oscillations (Fig. 1.4-b and d). As the cells move toward one of the edges, they start to compress each other, increasing the steric repulsion force in the direction opposite to their motion, which then induces the reorientation of their polarity. The authors pinpoint that the period T decreases with increasing J, and diverges as J vanishes, demonstrating that the oscillations effectively disappear when the alignment mechanism is absent.

Such observations fall outside of the scope of active liquids and their phenomenologies. When density is large enough and forbids spatial rearrangements, given that cells exert polar forces and propel on a substrate, the above cell monolayers are faithful realizations of *dry* and *polar* active solids[4]. Interestingly, they could shed a new light on the mechanisms at play during in vivo wound healing and embryonic development, in particular tissue invagination, an essential but poorly understood process. Indeed, this self-oscillation results in regular spatial and temporal patterns of deformations, which translate into molecular signals at the cell level and could thus be relevant to several shape-defining events. However, in such complex living systems, it is hard to disentangle the feedback induced by chemicals, mechanotransduction, and elasto-active effects. This strongly motivates the study of model and simpler systems.

1.2.2 Bacterial biofilms

A few months before this manuscript's publication, the pioneering work of *Xu et al.* demonstrated that bacterial bio-films are very convenient experimental systems to study biological active solids on large scales [77]. They study quasi-2d and disk-shaped biofilms composed of densely-packed bacteria, encased in a viscoelastic cell-derived extracellular polymer matrix. A rim of immotile cells laterally confines the system. Strikingly, they show that the biofilms are self-driven into local oscillatory motion, which self-organizes into a pair of topologically-distinct global motion modes (Fig. 1.5). In one mode, all tracked bacteria follow periodic and synchronized quasi-circular trajectories (Fig. 1.5-a), similar to the observation of *Peyret et al.* [8], and referred to as *oscillatory translation.*

[4]Note that because of cell deformations, there is a *nematic* symmetry shape coupling too, but it seems to be relatively small.

In the other mode, all tracked bacteria follow periodic and synchronized concentric circular arcs around the center of the disk (Fig. 1.5-b), referred to as *oscillatory rotation*. These two self-driven global modes are also evident from the temporal dynamics of the spatially averaged velocity field (Figs. 1.5-c and d). The *oscillatory translation* is a chiral regime reminiscent of a spontaneous chiral symmetry breaking. In this regime, the two orthogonal Cartesian coordinate components of the spatially averaged velocity oscillate periodically with $\pi/2$ or $3\pi/2$ phase shifts depending on the spontaneous chirality chosen by the system. On the other hand, in the *oscillatory rotation*, the polar coordinate azimuthal component of the spatially averaged velocity oscillates periodically, while the radial component is negligible. The most exciting feature of this system is that elasticity and activity can be tuned independently: the extracellular matrix viscoelastic moduli depend on temperature, and the activity of the bacteria can be decreased with violet light illumination [78].

The above observations, amongst others, are rationalized using simulations of an agent-based model. They consider a collection of self-propelled particles connected by Hookean springs and arranged in a 2d triangular lattice. The position $\boldsymbol{r}_i$ and polarity vector $\boldsymbol{n}_i$

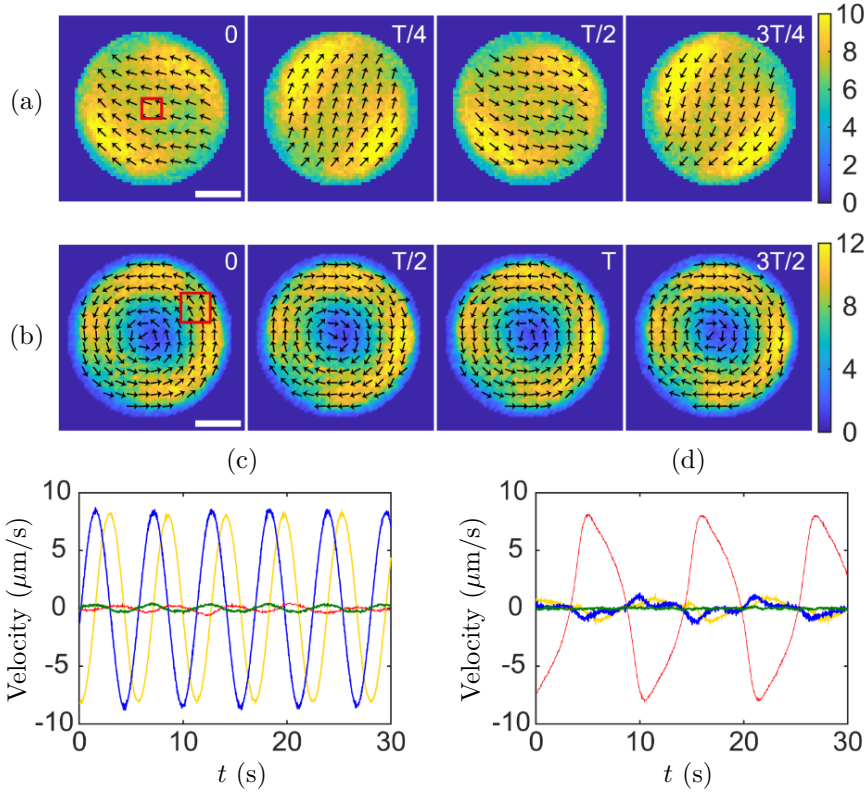


FIG. 1.5. **Spontaneous self-oscillation of bacteria-based active solids under isotropic lateral confinement.** (a/b) Time sequences of collective velocity field in the global *oscillatory translation* mode (panel a, period $T = 5.6$ s) and *oscillatory rotation* mode (panel b, $T = 11.0$ s). Arrows represent velocity direction, and the colormap indicates velocity magnitude in μm/s; scale bar: 500 μm. (c/d) Temporal dynamics of spatially averaged collective velocity in the global *oscillatory translation* mode (c) and *oscillatory rotation* mode (d). The spatially averaged collective velocity is decomposed as Cartesian (yellow and blue traces) and polar-coordinate components (red: azimuthal component, green: radial component). In the *oscillatory translation* mode, the polar-coordinate components are negligible; in the *oscillatory rotation* mode, both the radial and the Cartesian components are negligible. Adapted from [77].

of particle i evolve according to the following governing equations:

$$\dot{\boldsymbol{r}}_i = v_0 \boldsymbol{n}_i + \Xi_i \left(\boldsymbol{F}_i + D_r \hat{\boldsymbol{\xi}}_r \right), \tag{1.13a}$$

$$\dot{\boldsymbol{n}}_i = \beta \left[\left(\boldsymbol{F}_i + D_r \hat{\boldsymbol{\xi}}_r \right) \cdot \boldsymbol{n}_i^{\perp} \right] \boldsymbol{n}_i^{\perp} + D_\theta \hat{\boldsymbol{\xi}}_\theta - \Gamma \frac{\delta F_n}{\delta \boldsymbol{n}_i}, \tag{1.13b}$$

where Ξ_i is the motility tensor, $\boldsymbol{F}_i$ is the total external elastic force acting on the particle, $\hat{\boldsymbol{\xi}}_r$ and $\hat{\boldsymbol{\xi}}_\theta$ are randomly oriented and delta-correlated unit vectors, and where D_r, D_θ, β and Γ are constants. The polarity dynamics is controlled by three terms in Eq. (1.13b): a force-induced *self-alignment*, a noise term, and a term involving a Landau-type free energy $F_n = A \left(-2\boldsymbol{n}_i \cdot \boldsymbol{n}_i + (\boldsymbol{n}_i \cdot \boldsymbol{n}_i)^2 + \frac{1}{2}\kappa \left(\nabla \boldsymbol{n}_i \right)^2 \right)$ that penalizes the deviation of $\boldsymbol{n}_i$ from being a unit vector. The gradient part in F_n allows for extending the model to active solids with microscopic geometrical anisotropy and orientational elasticity, by associating an energetic cost to inhomogeneous polarity fields, but the authors focus on $\kappa = 0$. Simulations of Eqs. (1.13) show clear evidence that such an agent-based model captures the emerging collective behaviors of bacteria-based active solids at the quantitative level.

1.3 Dense active matter phases

Motivated by the observation of new interesting collective dynamics in dense biological systems, the physics community, and especially the active matter community, started designing models able to understand more deeply the nature of these phenomena. Starting from active liquids, the simplest way to make an active solid is to enforce mechanical rigidity by compacting the system. When density becomes large enough, the active units cannot reorganize spatially, and the system as a whole starts exhibiting elastic properties. Depending on the microscopic model, this process can give rise to jammed active solids, active crystals, or active glasses. We will omit a lengthy discussion on active glasses for conciseness, and also because this literature focuses on the glassy dynamics, which is not our priority here. We then elaborate on self-propelled Voronoi models, which have played a crucial role in understanding the mechanical rigidity of dense cell monolayers. Throughout this section, we put particular emphazise on systems for which *self-alignment*-like interactions dictate the polarity dynamics, consistently with the above biological systems.

1.3.1 Jamming of active particles

In 2011, *Henkes et al.* [79] introduced a seminal model of self-propelled particles at jamming, motivated by previous experiments on confluent monolayers of migratory epithelial and endothelial cells [68, 80–85]. They consider a collection of N *polar* soft disks of polydisperse radii a_i, positions $\boldsymbol{r}_i$, and polarity vectors $\hat{\boldsymbol{n}}_i = \cos\theta_i \hat{\boldsymbol{x}} + \sin\theta_i \hat{\boldsymbol{y}}$, which evolve according to the overdamped equations:

$$\dot{\boldsymbol{r}}_i = v_0 \boldsymbol{n}_i + \mu \sum_j \boldsymbol{F}_{ij}, \tag{1.14a}$$

$$\dot{\theta}_i = \frac{1}{\tau} \left(\psi_i - \theta_i \right) + \eta_i, \tag{1.14b}$$

where ψ is the orientation of the velocity vector $\boldsymbol{v}_i = \dot{\boldsymbol{r}}_i$, η_i are Gaussian white noises with zero mean and correlations $\langle \eta_i(t) \eta_j(t') \rangle = \sigma^2 \delta_{ij} \delta(t - t')$, and $\boldsymbol{F}_{ij}$ is the repulsive contact force particle j exerts on particle i. Particles repulse each other at small enough

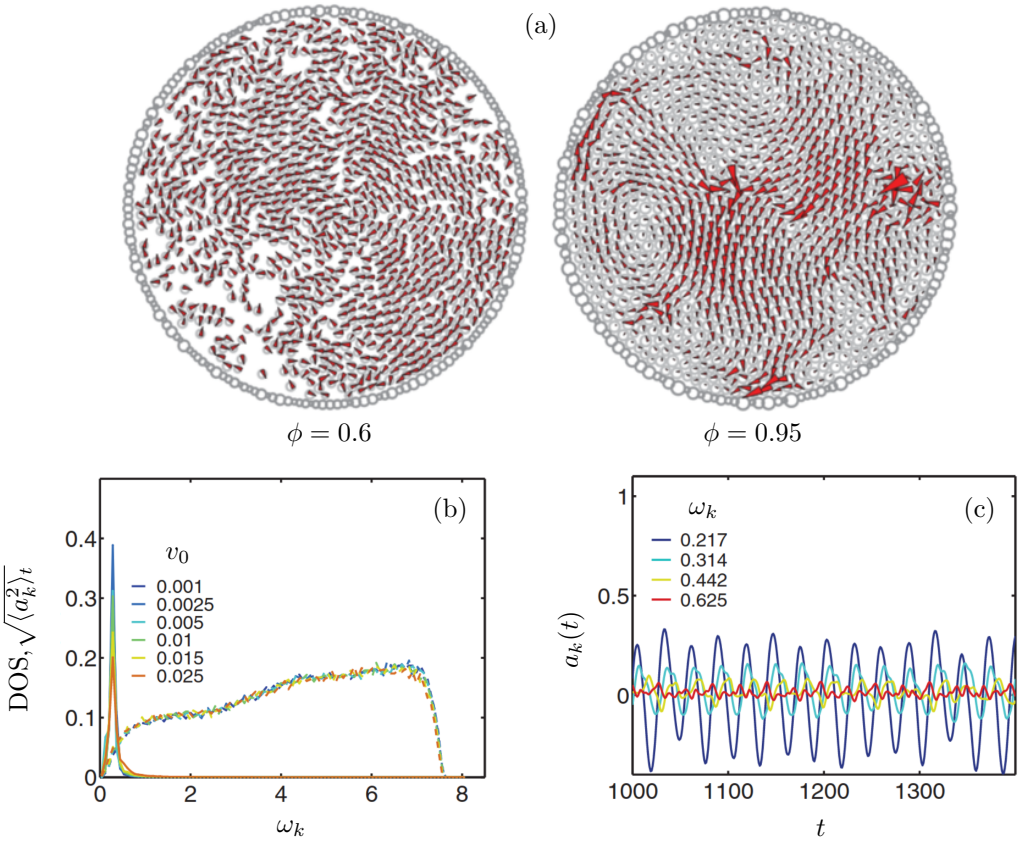


FIG. 1.6. **Active jamming of self-propelled soft particles.** (a) Sample snapshots of the system in the liquid phase ($\phi = 0.6$, left) and in the jammed phase ($\phi = 0.95$, right) for $v_0 = 0.025$. The glued boundary is shown in dark gray. The red arrows represent the instantaneous velocity field, with $v = v_0$ corresponding to an arrow of length 1 in units of the particle diameter. (b) Histogram of normal modes (DOS) as a function of modes' frequency ω_k (dashed) and mean squared projections of the displacements on the modes (solid, scaled for visibility) for $\phi = 0.86$. (c) Time projection of the displacements on the modes $a_k(t)$ for four representative modes in the undamped and damped regions ($\phi = 0.86$, $v_0 = 0.025$). Adapted from [79].

distances: $\boldsymbol{F}_{ij} = -k\,(a_i + a_j - r_{ij})\,\hat{\boldsymbol{e}}_{ij}$ if $r_{ij} < a_i + a_j$; and $\boldsymbol{F}_{ij} = \boldsymbol{0}$ otherwise, corresponding to soft disks. The relaxation time τ accounts for a linear[5] *self-alignment* term, similar to the work of *Peyret et al.* [8], but here the *self-alignment* torque is again speed-independent. Moreover, particles are confined within a circular box with soft repulsive boundary conditions, implemented using a row of immobile soft disks attached to the boundary. They perform simulations at various densities and find that, while the system is flowing for dilute regimes, at large density, particles are trapped in a cage formed by their neighbors (Fig. 1.6-a). In the jammed, solid phase, they observe regular oscillations of the particle displacements around their reference position, with a pattern that strikingly resembles the low-frequency modes of jammed packings.

This observation is rationalized by projecting the agents model on the normal modes' eigenbasis. They introduce the displacement field $\boldsymbol{u}_i = \boldsymbol{r}_i - \boldsymbol{r}_i^0$, where $\{\boldsymbol{r}_i^0\}$ is the reference configuration at mechanical equilibrium (and $v_0 = 0$). We denote ω_k^2 (resp. $\boldsymbol{\varphi}_k^i$) the eigenvalues (resp. eigenvectors) of the corresponding dynamical matrix. Importantly, they consider that the angle $\psi_i - \theta_i$ is very small, thus neglecting nonlinearities coming

[5] In the difference of angle.

from Eq. (1.14b); assume homogeneous solutions, that is $|\dot{\boldsymbol{r}}_i| = v_i = \left[\frac{1}{N}\sum_i v_i^2\right]^{1/2} = v_{rms}$; and somewhat, average over the angular noise. With such approximations, they find the equation for the projection of the displacement field on a given normal mode $a_k = \langle \boldsymbol{\varphi}_k | \boldsymbol{u} \rangle = \sum_i \boldsymbol{\varphi}_k^i \cdot \boldsymbol{u}_i$:

$$\ddot{a}_k + \mu \left[\omega_{\min}^2 - \omega_k^2\right] \dot{a}_k + \frac{\mu\omega_k^2}{\tau} a_k = 0, \tag{1.15}$$

where $\omega_{\min}^2$ is the smallest eigenfrequency. On long times, the dynamics is dominated by undamped oscillations corresponding to the lowest energy mode of the jammed packing. This is confirmed by observations in silico (Figs. 1.6-b and c): after a transient, the lowest energy mode dominates the dynamics, and the projections on higher energy modes describe strongly damped forced oscillations at the same frequency.

As a final remark, note that this work is historically the first to introduce self-oscillations of a genuine *dry* and *polar* model active solid with *self-alignment* interactions, and, remarkably, already intuited the crucial role played by the normal mode spectrum of the underlying elastic structure.

1.3.2 Active crystals

In the work discussed above, the polydispersity of the disks forbids the formation of an ordered packing at large density. Understanding how active processes transform the equilibrium picture of $2d$ crystallization [86] is also an important question. In the absence of alignment, it was shown that the crystallization of self-propelled disks with *scalar* interactions follows a two-step melting scenario similar to the one reported at equilibrium[6]. However, there is an absence of coexistence between the hexatic and the liquid phase for large enough activity [87], and the transitions shift to higher density as activity increases [87–89]. Finally, at large enough activity, in the liquid phase, a critical point opens up a MIPS region, indicating that the two-step melting and MIPS are independent phenomena.

The situation is far less clear when *polar* alignment between particles overcomes rotational diffusion. On the one hand, a mesoscopic field theory [90] predicts a transition from a resting crystal to a traveling crystalline polar state, where the particles migrate collectively while keeping their crystalline order. On the other hand, simulations [91] of a generalized *Vicsek* model with alignment as well as short-ranged repulsive interactions, report a mutual exclusion of the polar and the structural order and thus refute the generality of the theory. Crystallization with *polar* alignment and short-range repulsion is still an open debate.

Let us mention, as an example, a traveling phase found experimentally by *Briand et al.* with the walking grains experiments [92], discussed above. They demonstrate that alignment survives at high density. In hexagonal confinement, the system develops both polar and structural ordering on the experimental length scales, and organizes into a coherent sheared flow, which is made possible by the localization of shear along intermittent stacking faults (Fig. 1.7). Simulations of Eqs. (1.9) very well reproduce the

[6] One transition separates the liquid phase (short-range positional and orientational order) from a hexatic phase (short-range positional yet quasi-long-range orientational order), and a second transition at larger density separates the latter from a solid phase (quasi-long-range positional order and long-range orientational order).

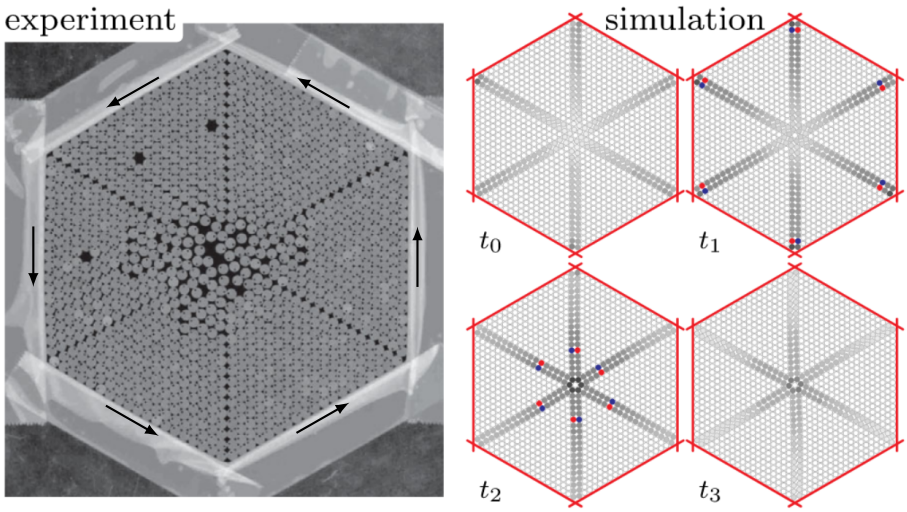


FIG. 1.7. **Spontaneously flowing crystal of self-propelled particles.** Flowing crystal configurations in the experiment at a finite noise level with geometrical frustration ($N = 1104$, $\phi = 0.86$), and in simulations at successive times, without noise and without geometrical frustration. The gray levels code for the orientational order parameter; the colors blue and red code for five and seven neighbors, respectively ($N = 1141$, $\phi = 0.88$). Adapted from [92].

phenomenology observed in experiments. Moreover, within periodic boundary conditions, they confirm the existence of a traveling ordered structure up to the largest scale that was investigated. Note that the emergence of orientational order near close packing is not trivial. Indeed, in this system, *polar* alignment arises effectively from the dynamical relaxation of the particle polarity after each collision; however, those collision are extremely frequent, and orientations do not have the time to relax following binary collisions.

1.3.3 Self-propelled Voronoi model

Arguably, a more refined description of cell monolayers should also account for the inherent confluence of the layer and the anisotropic shape deformability of the cells. These aspects are naturally incorporated in the so-called vertex or Voronoi models, which represent cells as polygons that collectively tesselate the entire space [93] (Fig. 1.8-a). The main difference between these models lies in the choice of the relevant degrees of freedom. In vertex models, the dynamical equations of motion are solved for the polygon vertices, while in Voronoi models, the equations of motion apply to the Voronoi centers of each cell (Fig. 1.8-a).

Vertex models got popularized since the pioneering work of *Bi et al.* [95, 96]. On the one hand, the mechanical energy of each cell is governed by its perimeter P and surface area A, effectively accounting for the bulk elasticity of the cell. On the other hand, activity is taken into account by considering an active contractility, and a net line tension. In cell monolayers, the latter arises from a competition between the cortical tension of the active actomyosin layer near the cortex, which tends to minimize the area of cell-cell contact, and intercellular adhesion forces, which maximize the area of cell-cell contact. The cell shape can be non-dimensionalized in terms of the so-called shape index $p = P/\sqrt{A}$. Based on their simulations, it was predicted that the confluent cell layer undergoes a fluid-to-solid-like transition at an average value of $\bar{p} \simeq 3.81$. This value could also be

associated with a change in the energy barrier heights of so-called T1 transitions, which govern cell rearrangements in confluent layers.

For the incorporation of active cell motility, the Voronoi model is generally preferred over a vertex model simulation, as the Voronoi centers provide a natural way to assign a single active force to every individual cell. A later study by *Bi et al.* [94] focused on the glassy dynamics of confluent cell layers using the so-called self-propelled Voronoi model. The mechanical energy of the system was assumed to be the same as in the vertex model, i.e. controlled by the cells' perimeters and areas. In contrast with vertex models, activity is taken into account by additionally considering self-propulsion forces. They invoke an ABP-like equation of motion: the cells' self-propulsive forces have a constant magnitude v_0, and do not interact with each other. The main result of this study is the phase diagram shown in Figs. 1.8-b and c, which indicates regions of parameter space in which the dynamics are glass-like and fluid-like, respectively. The role of the rotational diffusion constant was also explored, revealing a monotonic shift in the glass-transition line. Note that the rigidity transition of the Voronoi model in $3d$ is similarly controlled by the surface-to-volume ratio of the cells [97].

Even more interesting in our case, several studies considered a *self-alignment* term in the polarity dynamics of the self-propelled Voronoi model [72, 73, 98, 99]. In all cases, they include the same *self-alignment* interactions as *Henkes et al.* [79], with an alignment timescale τ of the polarity toward the velocity vector. In periodic boundary conditions, *Giavazzi et al.* showed that when self-alignment is small as compared to angular noise, the standard liquid and amorphous solid phases remain, and when self-alignment dominates, it leads to the emergence of an amorphous flocking solid, and a flocking liquid phase, both exhibiting collective directed motion or migration. Interestingly, using simple effective temperature and caging timescales arguments, they could understand and predict the location of the transitions between these different phases [72]. In contrast,

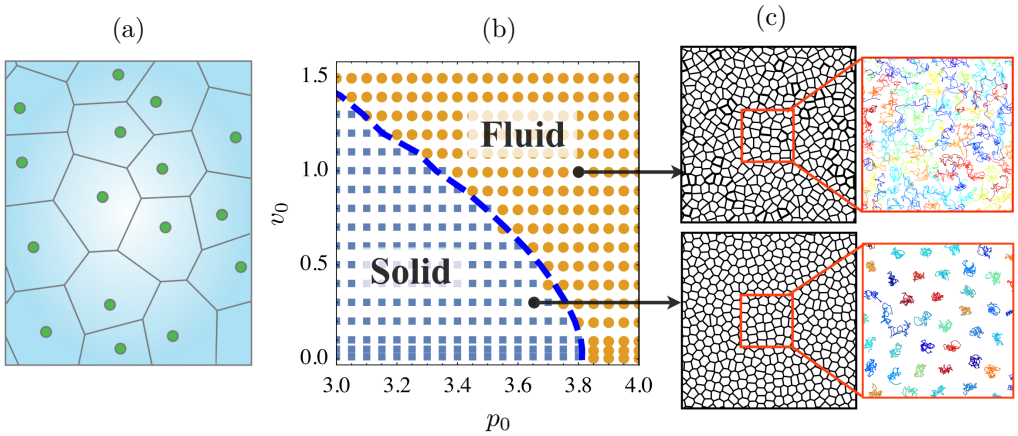


FIG. 1.8. **Motility-driven glass and jamming transitions in a self-propelled Voronoi model.** (a) Illustration of the Voronoi model for confluent cells. (b) Glassy phase diagram for confluent tissues as a function of cell motility v_0 and target shape index p_0 at fixed angular noise. Blue data points correspond to solid-like tissue; orange points correspond to flowing tissues. The dynamical glass transition boundary also coincides with the locations in phase space where the structural order parameter $q = \langle p \rangle = 3.81$ (dashed line). In the solid phase, $q \simeq 3.81$, and $q > 3.81$ in the fluid phase. (c) Instantaneous tissue snapshots show the difference in cell shape across the transition. Cell tracks also show dynamical arrest due to caging in the solid phase and diffusion in the fluid phase. Adapted from [93] and [94].

in the presence of confinement, *Petrolli et al.* found a transition between a global and a multinodal standing wave, controlled by the confinement size, and identified two crucial conditions to produce these oscillations: (i) a small enough self-alignment timescale, and (ii) a very limited number of cellular rearrangement, in the solid-like regime [73].

1.4 Active elastic structures

We have seen that active systems under strong confinement can exhibit collective behaviors incompatible with an active liquid description. However, other strategies exist besides increasing density or confinement to reach active solids physics. A more convenient way consists of designing authentic solid structures, intrinsically out-of-equilibrium due to active actuators, embedded in the elastic matrix. In this case, the structure is genuinely an elastic solid, and active forces induce deformations that may couple with the forces and start a feedback loop.

Interestingly, the physics of elastic materials has recently experienced its own revolution. Playing with the mesoscale architecture of the underlying structure, or with the constitutive laws of its constitutive elementary "springs", physicists and engineers have unveiled new behavior breaking the laws of standard elasticity. Such features allow for the design of programmable materials, displaying multiple elastic response, or peculiar responses such as negative Poisson ratio [100–108]. Yet, to date, such meta-materials are passive, limiting their properties and their range of application. In particular, they are not robust to fluctuations and attenuation. One strategy to solve this problem consists of actuating metamaterials using an external field that interacts with the structure, e.g. using hydrodynamic pressure [109] or magnetic fields [110]. However, this requires fine-tuning the externally driven actuation mechanism, and is not readily adaptable to a new mechanical function. In this context, active solids are a promising framework to fabricate autonomous mechanical metamaterials, because they could provide a controllable and completely endogeneous actuation mechanism for the mechanical functions of classical metamaterials [111].

Over the past years, numerous experimental, numerical, and theoretical approaches have been attempted to conceive active structures and revealed two essential features of those systems: autonomous actuation, and odd elastic moduli.

1.4.1 Actuation of rigid body motions

Doping an elastic structure with active units was pioneered by *Ferrante et al.* in 2013 [112]. In their active crystal model, so-called Active Elastic Sheet (AES), N active agents are embedded in a springs network in the $2d$ plane, and the position $\boldsymbol{r}_i$ and orientation θ_i of agent i follow the overdamped equations of motion:

$$\dot{\boldsymbol{r}}_i = v_0\hat{\boldsymbol{n}}_i + \alpha\left[(\boldsymbol{F}_i + D_r\boldsymbol{\xi}_r)\cdot\hat{\boldsymbol{n}}_i\right]\hat{\boldsymbol{n}}_i, \tag{1.16a}$$

$$\dot{\theta}_i = \beta\left[(\boldsymbol{F}_i + D_r\boldsymbol{\xi}_r)\cdot\hat{\boldsymbol{n}}_i^{\perp}\right] + D_\theta\xi_\theta, \tag{1.16b}$$

where v_0 is the self-propulsion speed, $\hat{\boldsymbol{n}}_i$ and $\hat{\boldsymbol{n}}_i^{\perp}$ are two unit vectors pointing parallel and perpendicular to the heading direction of agent i, and parameters α and β are the inverse translational and rotational damping coefficients, respectively. The total force over agent i is given by $\boldsymbol{F}_i = \sum_{j\in\partial i}(-k/l_{ij})(|\boldsymbol{r}_{ij}| - l_{ij})\boldsymbol{r}_{ij}/|\boldsymbol{r}_{ij}|$ (with $\boldsymbol{r}_{ij} = \boldsymbol{r}_j - \boldsymbol{r}_i$), a

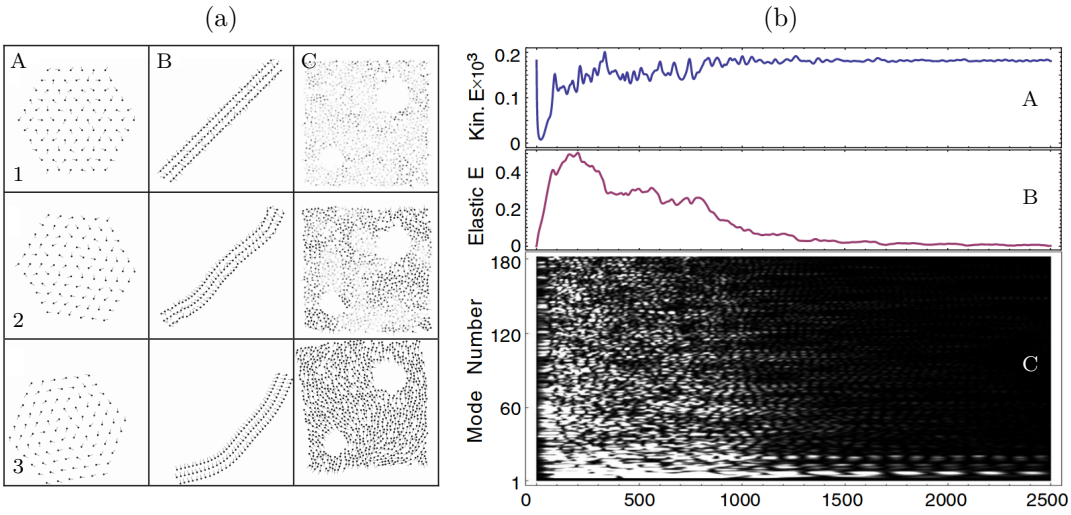


FIG. 1.9. **Elasticity-based mechanism for the collective motion of self-propelled particles with spring-like interactions.** (a) Active elastic sheet simulations of Eqs. (1.16). (A) Hexagonal active triangular lattice at $t = 0$ (A1), 240 (A2), and 1700 (A3). (B) Rod-like active square lattice with next-nearest neighbors interactions at $t = 0$ (B1), 400 (B2), and 1700 (B3). (C) Active solid at same times as column B; darker agents symbolize higher local alignment. (b) Kinetic energy (A), elastic energy (B), and spectral decomposition of the elastic energy (C) as a function of time for an hexagonal $N = 91$ active triangular lattice simulation (with zero noise and same initial condition as (a)) that converges to the translating state. Brighter points on C indicate higher energies. Adapted from [112].

sum of linear spring-like forces with equilibrium distances l_{ij} and spring constants k/l_{ij}. Each set ∂i contains all agents interacting with agent i and remains fixed throughout the dynamics. This system is thus akin to a spring-mass model of elastic sheet where masses are replaced by self-propelled agents that turn according to $\boldsymbol{F}_i \cdot \hat{\boldsymbol{n}}_i^{\perp}$ and move forward or backward following $\boldsymbol{F}_i \cdot \hat{\boldsymbol{n}}_i$ and their self-propulsion. Note that this model being motivated by swarms of autonomous robots on wheels [43, 113], the elastic forces are projected on the heading direction in Eq. (1.16a) to forbid for gliding, which is very specific to this model. They also include two types of noise. First, an actuation noise (fluctuations of the individual motion) by adding a term $D_\theta \xi_\theta$ to Eq. (1.16b), where D_θ is the angular noise amplitude and ξ_θ a random variable with zero mean and correlations $\langle \xi_\theta(t)\xi_\theta(t')\rangle = \delta(t - t')$; and second, a sensing noise (errors in the measured forces) by adding a term $D_r \boldsymbol{\xi}_r$ to $\boldsymbol{F}_i$ in Eq. (1.16a), where D_r is the noise amplitude and $\boldsymbol{\xi}_r$ is a randomly oriented unit vector.

Simulating Eqs. (1.16) on different mechanically stable spring networks with random initial orientations of agents (Fig. 1.9-a panels 1), they find that regions of coherent motion develop (Fig. 1.9-a panels 2), deforming the elastic structure, until the group starts translating or rotating collectively in steady state (Fig. 1.9-a panels 3). Remarkably, the rotating states are metastable and relax to the translating state on long times. One hallmark of this work is the characterization of the nonlinear energy cascade giving rise to collective motion (Figs. 1.9-b). In the initial condition, the system has zero potential energy and kinetic energy $E_k = Nv_0^2/2$ (setting the agent mass to 1). As the sheet deforms during the transient, potential energy grows and becomes broadly distributed over all modes, while kinetic energy drops. As time advances, the system rearranges itself into configurations with lower elastic energy and higher kinetic energy. The elastic energy in each mode oscillates while decaying, with the higher energy modes decaying faster than

the lower ones. Self-propulsion thus feeds energy to lower and lower energy modes, until eventually reaching selectively the translational or rotational zero modes, achieving CM. Interestingly, the AES model also displays a discontinuous order-disorder transition with noise similar to that of the *Vicsek* model, and supports long-range order at small enough but finite noise amplitude. Note that the latter is far from trivial. Indeed, in section 1.1 we invoked the existence of effective long-range interactions coming from the flying nature of the active units to violate the Mermin-Wagner theorem. However, here, the active units only interact with their nearest neighbors.

1.4.2 Actuation of non-trivial zero modes

In the work above, the active dynamics is driving the system to actuate autonomously the rigid body motions of the structure, i.e. translations and rotations. In a recent paper, *Woodhouse et al.* demonstrate that activity also enables autonomous actuation of coordinated mechanisms engineered through the network topology [114]. On the one hand, they show that active *Ornstein-Uhlenbeck* particles activate selectively Infinitesimal Zero Modes (IZM), which are normal modes with zero energy but resistance at nonlinear order. On the other hand, they show that so-called *Rayleigh* activity (defined below) can mobilize complex mechanisms, which also have zero energy but a finite range of costless motion. The normal modes classification will be clarified in chapter 3.

The AES model from *Woodhouse et al.* differs from the one of *Ferrante et al.* in the family of active particles embedded in the springs network, which are first chosen to be Active Ornstein-Uhlenbeck Particles (AOUPs) [115]. The position $\boldsymbol{r}_i$ of agent i obeys the following overdamped equations:

$$\dot{\boldsymbol{r}}_i = \boldsymbol{\xi}_i + \boldsymbol{F}_i, \tag{1.17a}$$

$$\tau\dot{\boldsymbol{\xi}}_i = -\boldsymbol{\xi}_i + \boldsymbol{\eta}_i, \tag{1.17b}$$

where $\boldsymbol{F}_i$ is the total elastic force applied to agent i, $\eta_{i,\alpha}$ are Gaussian white noises with zero mean and correlations $\langle \eta_{i,\alpha}(t)\eta_{j,\beta}(t')\rangle = 2D\delta_{ij}\delta_{\alpha\beta}\delta(t-t')$, and $\boldsymbol{\xi}_i$ is an Ornstein-Uhlenbeck noise[7]. Note that in the limit $\tau \to 0$, the latter transforms back into thermal

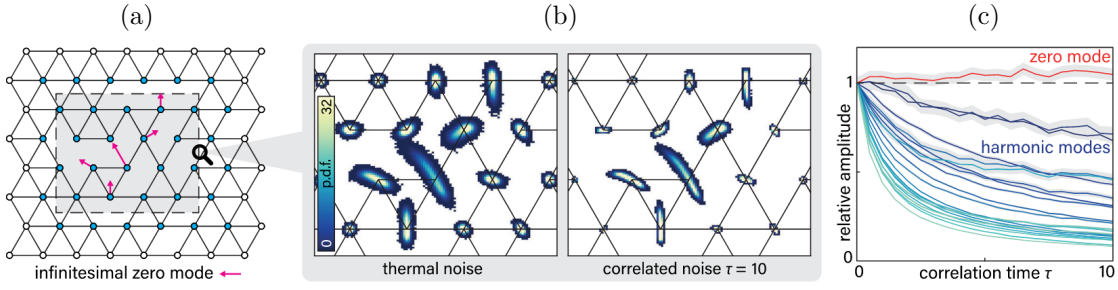


FIG. 1.10. **Active noise actuates an IZM while suppressing harmonic modes in a pruned mechanical network.** (a) A network of unit length, unit stiffness springs is designed to contain exactly one IZM (arrows). White nodes are pinned. (b) Histograms of node positions in the highlighted area of (a) when actuated by thermal noise (left) and correlated noise with $\tau = 10$ (right) of strength $T = 10^{-3}$. (c) Thermal-relative amplitude $\langle u_i^2\rangle_\tau / \langle u_i^2\rangle_{\tau=0}$ of the 21 lowest eigenvalue modes u_i of (a) from numerical integration at $0 \leq \tau \leq 10$, with $T = 10^{-3}$ fixed. The IZM (red) is barely affected, while harmonic modes (blues) diminish. Grey areas are estimated 95 % confidence intervals from 20 realizations. Adapted from [114].

[7]The two-point correlation function of the active force expresses as $\langle \xi_{i,\alpha}(t)\xi_{j,\beta}(t')\rangle = \delta_{ij}\delta_{\alpha\beta}\frac{D}{\tau}e^{-|t-t'|/\tau}$ [114, 115].

noise. The AOUPs are embedded into a triangular lattice, pinned at the edges to eliminate rigid body translations and rotations, and pruned so that the lattice exhibit a single non-trivial IZM (Fig. 1.10-a). Simulating Eqs. (1.17) on this network, they find that while thermal noise ($\tau = 0$) actuates the IZM with significant surrounding fluctuations (Fig. 1.10-b left), the active process with $\tau > 0$ damps harmonic modes fluctuations with respect to those of the IZM (Fig. 1.10-b right). This effect is best illustrated in Fig. 1.10-c, which represents the mean squared fluctuations of the displacement field projections on the normal modes, relatively to the thermal case. The IZM amplitude remains at its $\tau = 0$ level, while harmonic modes excitations decay as τ increases.

The second system is the linear chain inspired by the Su-Schrieffer-Heeger (SSH) model for polyacetylene [116]. This molecule has topologically protected electronic states localized at its edges, and its mechanical analog, built from rigid bars and elastic springs (Fig. 1.11-a), has zero-energy vibrational modes with a non-trivial topological index, whose eigenvectors are localized at one of the edges [117]. Remarkably, it was shown that this zero mode can propagate along the chain in the form of a soliton of finite deformations [100]. However, an external energy input is needed, either in the form of a "kick" on one of the nodes, or in the form of global force field. Yet, propagation is difficult: motion by a "kick" will inevitably slow down and stop due to dissipation, while an external field needs regular adjustments to keep the mechanism moving. The authors embed *Rayleigh* activity in this structure [118, 119], which takes the form of an active force $\boldsymbol{F}_i^a$ along the

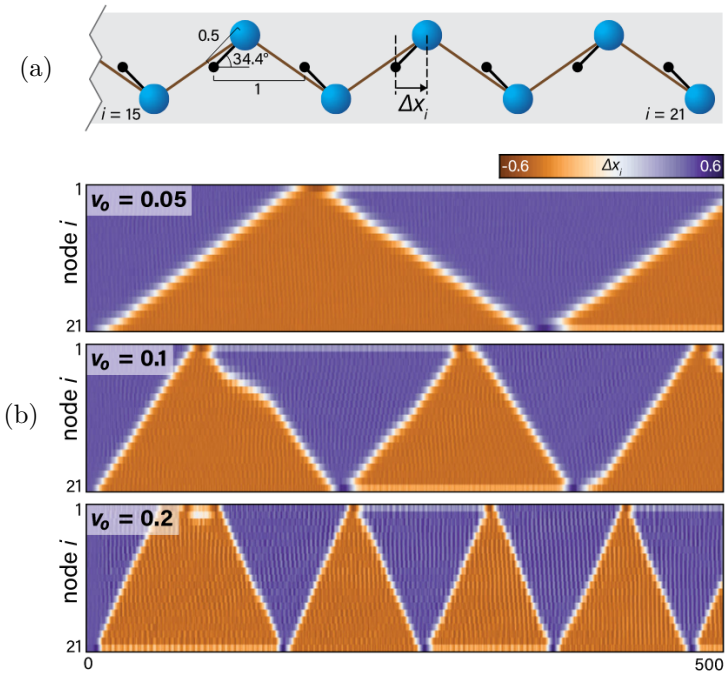


FIG. 1.11. **Rayleigh activity spontaneously mobilizes a complex mechanism** (a) Mechanical SSH model, which has a periodic mechanism comprising progressive flipping of the masses from right to left and back again. Black (resp. blue) nodes are fixed (resp. mobile), black (resp. red) lines are rigid bars (resp. elastic springs). (b) Endowing a 21-node chain with *Rayleigh* activity spontaneously mobilizes the mechanism. The propagation speed depends on the propulsion v_0, seen through the time-dependent offsets Δx_i of mobile nodes from their pinning points. Adapted from [114].

particles' velocity:

$$\boldsymbol{F}_i^a = \gamma_f \left(1 - \frac{|\dot{\boldsymbol{r}}_i|^2}{v^2}\right) \dot{\boldsymbol{r}}_i, \tag{1.18}$$

where v is a characteristic speed, and γ_f sets the amplitude of the polar force. This term can be interpreted as a negative friction coefficient, balancing with genuine friction force $-\gamma\dot{\boldsymbol{r}}_i$ to give rise to a cruise velocity $v_0 = v|\frac{\gamma_f-\gamma}{\gamma_f}|^{1/2}$. Note that here the overdamped limit is not assumed. Not only does this activity model provide the same selection of IZM in pruned triangular lattices as AOUPs, but it can also mobilize the free-moving mechanism of the mechanical SSH chain (Fig. 1.11-b). The soliton cleanly propagates at speed v_0 for multiple cycles up and down the chain, with occasional stalls or reversals caused by the complex interactions of the fluctuating active nodes.

It is now clear that activity can autonomously actuate the zero-modes of a structure, whether they are rigid body motions or engineered through the network topology [112, 114]. Nevertheless, the work of *Henkes et al.* also demonstrated the autonomous actuation of a harmonic mode [79], the lowest energy one, asking the general question of the mechanical functionality of active matter, which remains an open question. In the next section, we discuss one of the very few systems where the interplay between elasticity and activity was studied experimentally, providing more insights into understanding the physics of mechanically stable active solids.

1.4.3 Frustrated active chain

Motivated by the observations of self-oscillations in biological systems such as flagella and cilia [121–123], *Zheng et al.* recently constructed a model system of *dry* and *polar* active chain [120]. It is made of 7 centimetric self-propelled particles[8], exerting *polar* forces of amplitude F_a along their heading directions, and elastically coupled by a laser-cut silicon rubber chain pinned at one end (Fig. 1.12-a). Interestingly, they can manipulate the stiffness of the chain by tuning the width W of the connections. The authors model this system with coupled active pendulums, represented by N non-linear coupled ODEs that describe the motion of the elasto-active chain[9]. There are two dimensionless parameters: the elasto-active number $\sigma = F_a l/C$, and the characteristic damping timescale $\tau = \gamma l^2/C$, where l (resp. C) is the length (resp. the torsional stiffness) of the connections, and where γ is an effective friction coefficient.

[8] Hexbugs Nano, which is the former design of commercially available Hexbugs toys.

[9] Denoting θ_i the orientation of active agent i, the ODEs are:

$$0 = 2\theta_1 - \theta_2 - \sigma \sum_{j=1}^{N} \sin(\theta_1 - \theta_j) + \tau \left(N\dot{\theta}_1 + \sum_{j=2}^{N} \theta_j \cos(\dot{\theta}_1 - \theta_j) \right) \text{ for } i = 1, \tag{1.19}$$

$$\begin{aligned} 0 =& 2\theta_i - \theta_{i-1} - \theta_{i+1} - \sigma \sum_{j=1}^{N} \sin(\theta_i - \theta_j) \\ &+ \tau \left((N-i+1) \sum_{j=1}^{i} \dot{\theta}_j \cos(\theta_i - \theta_j) + \sum_{j=i+1}^{N} (N-j+1)\, \dot{\theta}_j \cos(\theta_i - \theta_j) \right) \text{ for } i \in [2, N-1], \end{aligned} \tag{1.20}$$

$$0 = \theta_N - \theta_{N-1} + \tau \sum_{j=1}^{N} \dot{\theta}_j \cos(\theta_N - \theta_j) \text{ for } i = N. \tag{1.21}$$

For the chain with the widest connection, i.e. the smallest elasto-active number σ, any perturbation is damped (Fig. 1.12-b). As σ increases and exceeds the threshold σ_c, spontaneous self-oscillations of the chain emerge (Figs. 1.12-c and d). This transition is illustrated by the abrupt increase of the amplitude $\Theta = \theta_7 - \theta_1$ as σ increases (Fig. 1.12-e), where θ_i represents the orientation of the i^{th} active unit with respect to the vertical direction. Notably, the transition is characterized by a finite frequency at the onset of self-oscillations, monotonically increasing for larger activity (Fig. 1.12-f). Combining the above experimental observations with the linear stability analysis of the chain in its rest state, they demonstrate that a supercritical Hopf bifurcation governs

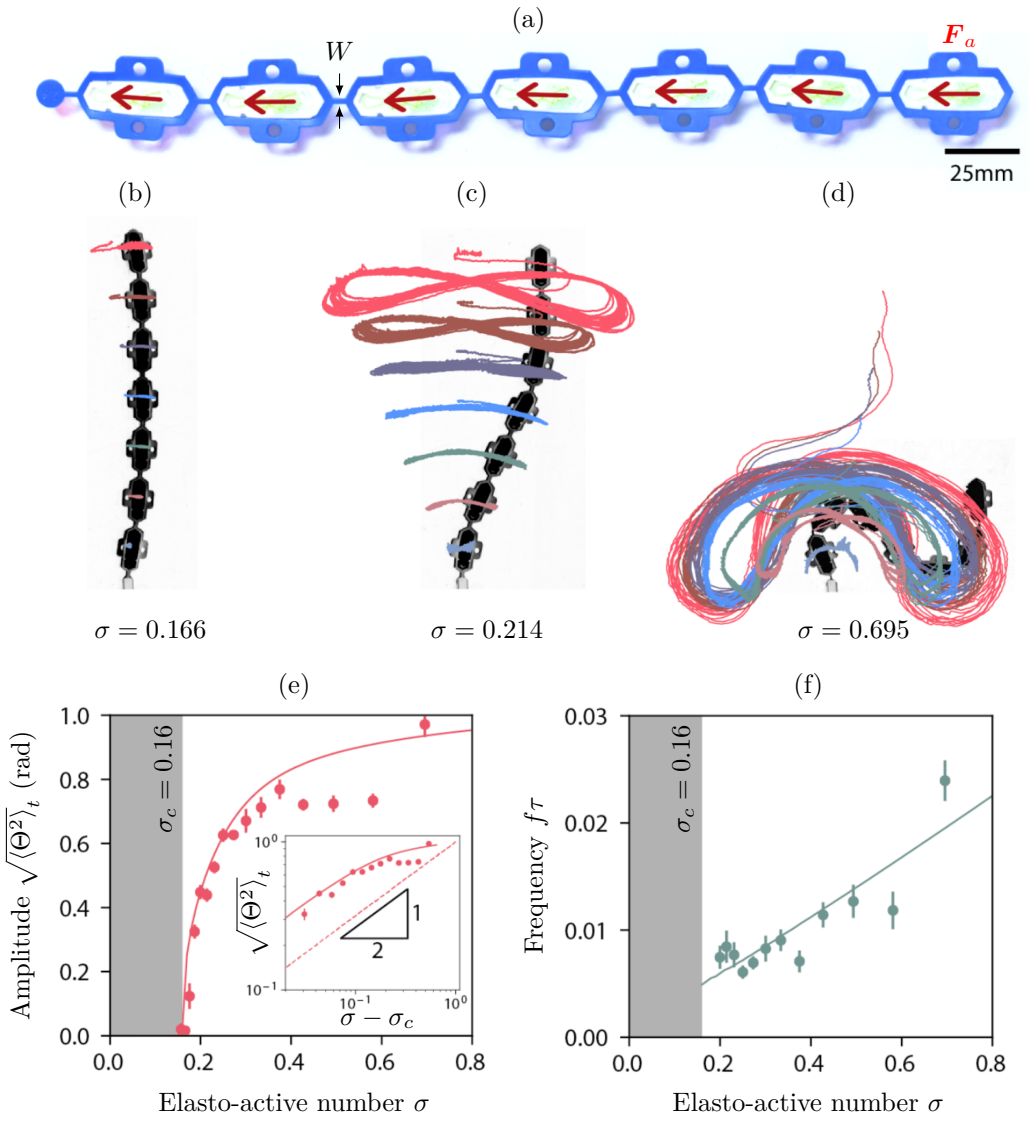


FIG. 1.12. **Emergence of self-oscillations in frustrated elasto-active chains.** (a) Configurations of 7 active particles connected by a flexible rubber chain, each exerting a *polar* force $\boldsymbol{F}_a$ in the chain's direction. The width of the chain's connections is denoted W. (b-d) Snapshots of the trajectories of the active particles showing the oscillations changed from self-amplified to overdamped with elasto-active number $\sigma = 0.166$, 0.214 and 0.695 respectively. (e-f) Hopf bifurcation at $\sigma = 0.16$. Simulation (solid lines) and experimental (markers) results showing the evolution of the amplitude $\sqrt{\langle\Theta^2\rangle_t}$ (e) and of the dimensionless frequency $f\tau$ (f) of oscillation with increasing σ. Inset: oscillation's amplitude as a function of distance to the threshold in log-log. The dashed gray line represents the 1/2 power-law. Adapted from [120].

this transition. Here, non-linear elasticity is crucial as the underlying mechanism at the origin of the transition is a nonlinear elasto-active feedback between the direction of the active forces and the non-linear elastic deflections. Eventually, this active structure is said here to be frustrated because active forces can only point along the chain's direction.

Having discussed autonomous actuation, which results in locomotion or self-oscillating behavior, we now elaborate on the second hallmark of active solids: odd moduli.

1.4.4 Odd elastic solids

One of the central assumptions of classical elasticity is that the work needed to quasistatically deform a solid depends only on its initial and final states, putting strong constraints on the allowed elastic moduli [124]. However, if the microscopic constituents of the solid are active, then the work can be path-dependent. Very recently, *Scheibner et al.* revealed that the presence of active, non-conservative interactions, can give rise to new elastic moduli that would be absent in passive elasticity [125]. They consider the network of masses connected by active bonds depicted in Fig. 1.13-a. When the bond elongates or contracts, a gear system rotates the battery-powered propellers to produce transverse forces. For small strains, the force law is linear in the displacements and is given by

$$\boldsymbol{F}(r) = (-k\hat{\boldsymbol{r}} + k^a\hat{\boldsymbol{r}}^\perp)\delta r, \tag{1.22}$$

where $\delta r = r - r_0$ is the radial displacement from the equilibrium length r_0, and $\hat{\boldsymbol{r}}$ and $\hat{\boldsymbol{r}}^\perp$ are respectively the unit vectors parallel and perpendicular to the bond. Eq. (1.22) describes a Hookean spring of stiffness k with an additional chiral, transverse force proportional to k^a. Note that the presence of such forces everywhere in the springs network requires the system to be active, e.g. by providing power to the propellers. Nonetheless, the interaction conserves linear momentum because the forces on each end of the bond are equal and opposite.

The authors introduce a convenient representation of the additional elastic moduli of a material built out of many such components (Eq. 1.23). While elastic potential energy is not well defined because of the microscopic path dependence (Figs. 1.13-d and e), a stress-strain relation exists and can be linearized for small deformations. This approximation, known as Hooke's law, is captured by the continuum equation $\sigma_{ij}(\boldsymbol{x}) = C_{ijmn}u_{mn}(\boldsymbol{x})$, where $u_{mn}(\boldsymbol{x})$ are the gradients $\partial_m u_n(\boldsymbol{x})$ of the displacement vector $u_n(\boldsymbol{x})$ and C_{ijmn} is the elastic modulus tensor. In the absence of an elastic potential energy, the most general linear relationship between stress and displacement gradient for a $2d$ isotropic solid reads[10]:

$$\begin{pmatrix} \\ \\ \\ \end{pmatrix} = \begin{pmatrix} B & 0 & 0 & 0 \\ A & 0 & 0 & 0 \\ 0 & 0 & \mu & K^0 \\ 0 & 0 & -K^0 & \mu \end{pmatrix} \begin{pmatrix} \\ \\ \\ \end{pmatrix}. \tag{1.23}$$

The displacement gradients on the right-hand side (resp. the stress vector on the left-hand side) are decomposed into dilation, rotation, and the two shear deformations (resp. pressure, torque, and the two shear stresses). For passive elasticity, only the bulk modulus B and shear modulus μ are present. In contrast, when lifting energy conservation, two new moduli arise: A and K^0. A couples compression to internal torque density,

[10] Adapted from [125].

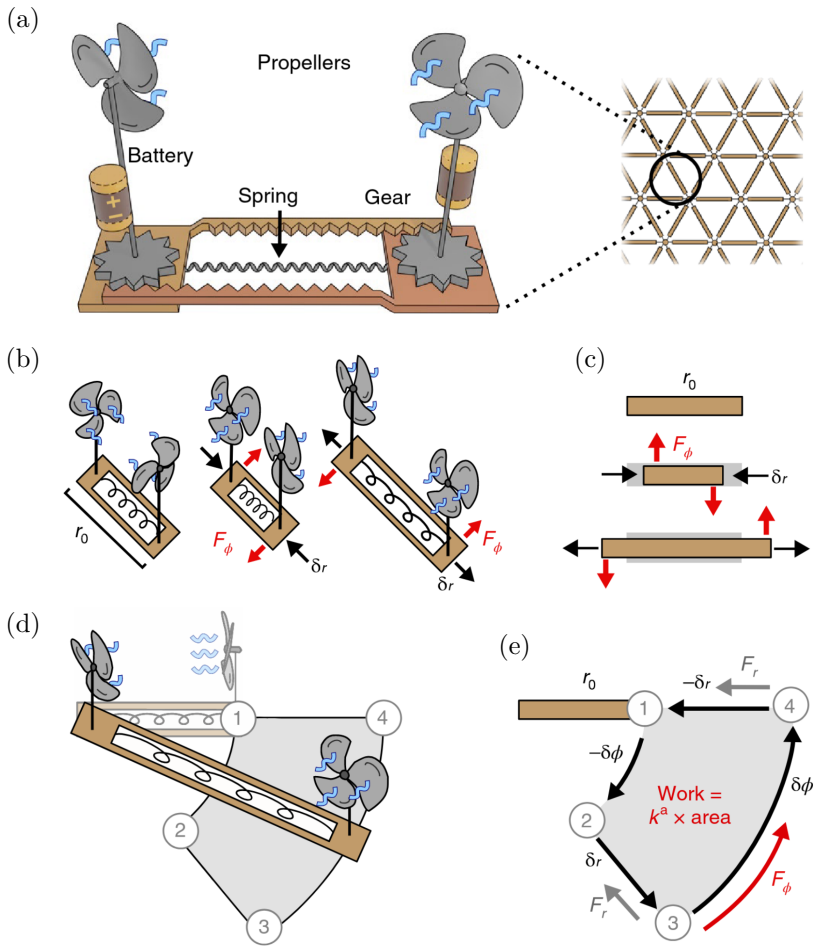


FIG. 1.13. **Quasistatic work cycles with non-conservative active bonds.** (a) A mechanical realization of Eq (1.22). Two propellers, mounted on platforms connected by a Hookean spring, are powered by batteries and blow air at a constant rate. As the platforms slide together (or apart), a gear system rotates the propellers, giving rise to transverse forces. An elongated configuration is shown. A triangular lattice built out of such active bonds exhibits odd elasticity. (b-c), The concrete schematic (b) and conceptual diagram (c) illustrate the linearized force law, given by Eq. (1.22). The key feature is an active transverse force (red arrows) proportional to strain (black arrows). (d-e) When the bond is brought on a strain-controlled quasistatic cycle, the work done by the radial forces F_r during legs 2-3 and 4-1 sums to zero. However, the transverse force F_ϕ does work during leg 3-4 that is not compensated elsewhere during the cycle. For small angles $\delta\phi$ and strains $\delta r/r_0$, the work done by the bond on a quasistatic cycle is equal to k^a times the area enclosed. Adapted from [125].

while K^0, like shear modulus μ, is a proportionality constant between shear stress and shear strain. However, K^0 mixes the two independent shears in an antisymmetric way. Note that such an odd elasticity framework applies to active systems for which the active forces derive from a stress tensor. Interestingly, this is not possible for the *dry* and *polar* active solids that will be considered in this work, asking the question of the generalization of odd elastic moduli to systems that do not conserve linear momentum.

In terms of phenomenology, odd elasticity emerging from microscopic non-conservative interactions was shown to be at the origin of auxetic behavior and wave propagation in overdamped media [125], self-sustained oscillations in living chiral crystals [126], and non-Hermitian skin effects and work-generating limit cycles in non-reciprocal metama-

terials [127–129]. Notwithstanding such systems conserve linear momentum, they are of great interest as they allow for experimental platforms to explore the physics of active solids in a more general sense. In the next section, we discuss an experimental system that was designed to reproduce the type of microscopic interactions described above.

1.4.5 Non-reciprocal metametarials

Building on their earlier work on $1d$ active mechanical metamaterials [127, 128], *Brandenbourger et al.* have recently introduced a new experimental platform allowing for non-reciprocal interactions in a $2d$ material [129].

In molecular edifice, ordinary angular or bond-bending interactions are approximated by a potential energy $E = \frac{\kappa}{2}\sum_i \delta\theta_i$, where $\delta\theta_i$ corresponds to the deviation from the equilibrium angle of bond i, and κ is the bending stiffness. The resulting torques τ_i are obtained from the gradients of the potential, and given by the generalized force-displacement relation $\tau_i = -\kappa\delta\theta_i$. *Brandenbourger at al.* construct a mechanical realization with rigid bars and motor-powered connections, described by two bond angles θ_1 and θ_2 (Figs. 1.14-a and d), and whose generalized force-displacement relation reads:

$$\begin{pmatrix}\tau_1\\ \tau_2\end{pmatrix} = \begin{pmatrix}-\kappa & -\kappa^a\\ \kappa^a & -\kappa\end{pmatrix}\begin{pmatrix}\delta\theta_1\\ \delta\theta_2\end{pmatrix}. \tag{1.24}$$

In addition to the diagonal, passive κ-terms, the matrix in Eq. (1.24) also has an off-diagonal component κ^a. These terms are called *odd*, since they are antisymmetric under the exchange of indices i and j. For $\kappa^a > 0$, when θ_1 is contracted, θ_2 contracts too (Figs. 1.14-b and e); but when θ_2 is contracted, θ_1 expands instead (Figs. 1.14-c and f). As discussed in the above section, when the vertices are deformed, the work done by the vertices depends on the path taken and can be positive or negative, which implies that Eq. (1.24) requires a source of energy (provided by the motor-powered connections). If activity (or *oddness*) is large enough, the dynamical system will proceed to a nonlinear limit cycle in which the energy injected by the non-conservative force balance with dissipation. This is made possible by the nonlinear saturation of the motors' torques at $\tau_{\max}$ (Fig. 1.14-g). They show that the instability threshold of the rest state is written in term of a dimensionless parameter $\xi = \kappa^a/I\sqrt{I/\kappa}$, where Γ is a dissipation coefficient, and I is the moment of inertia of the bonds. When $|\xi| < 1$, dissipation and restoring forces win and perturbations are damped (Fig. 1.14-h). In contrast, when $|\xi| > 1$, a Hopf bifurcation occurs and a limit cycle of finite amplitude, proportional to $\tau_{\max}$, emerges (Fig. 1.14-i).

The authors then demonstrate how the above design principle can be used to construct *odd* structures, and how their tendency to cycle can be harnessed to perform mechanical functions. They first focus on an *odd* wheel, made of 6 active vertices connected on a closed hexagon (Fig. 1.14-j). Due to the κ^a couplings, the odd wheel is able to perform spontaneous work cycles between its two shear modes (Figs. 1.14-k and l), providing the structure with the ability to self-propel on a substrate. Eventually, they study the collision of a ball with a wall when either the ball or the wall is odd, and reveal more autonomous functionalities of odd matter such as asymmetric and enhanced rebound and steering of impact vibrations, which are reminiscent of non-Hermitian skin effects [127, 128, 130]. Note that they could construct odd structures up to 120 motorized vertices, getting relatively close to an active material [129].

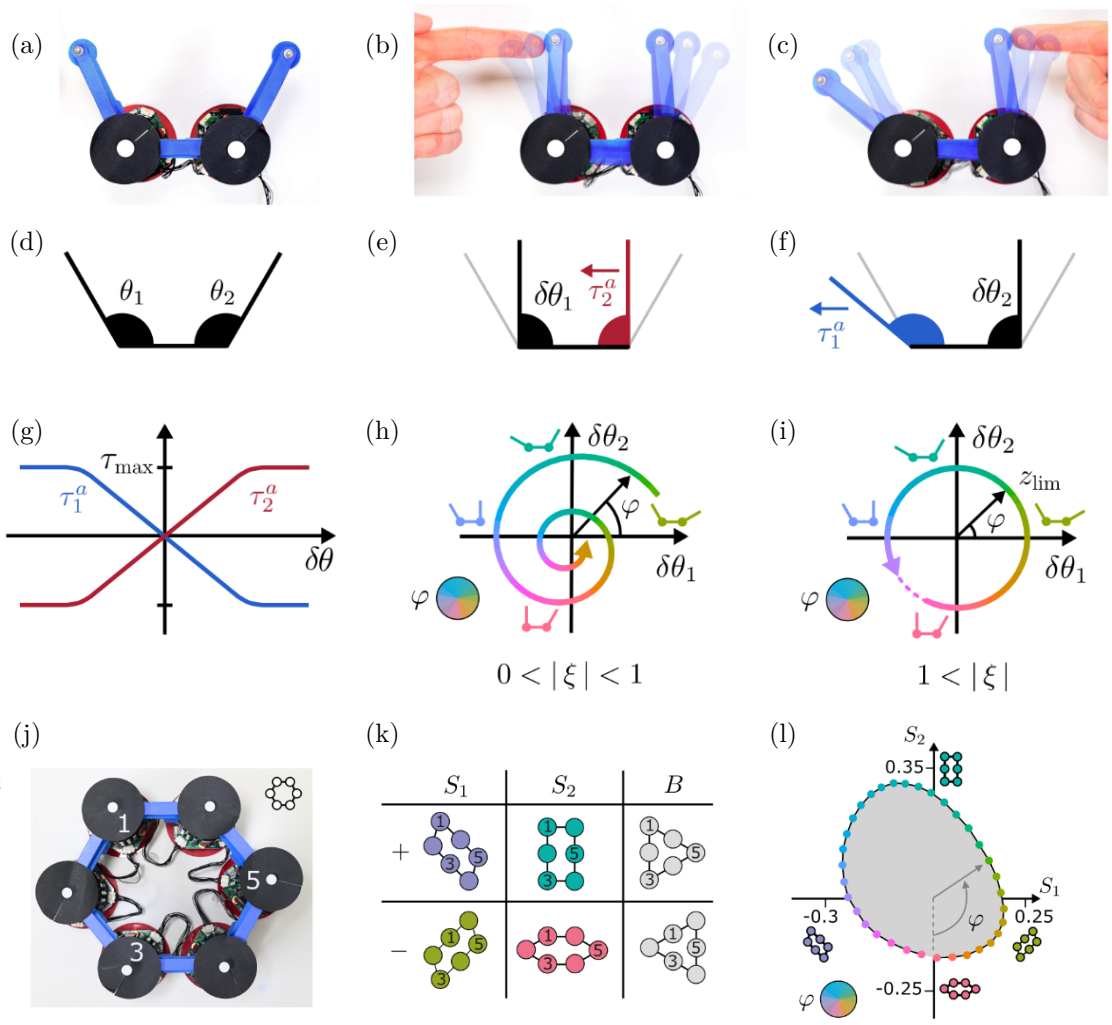


FIG. 1.14. **Odd forces induce nonlinear work generating limit cycles.** (a) Three rigid linkages are connected by motorized vertices. (b) A hand pushes in on the left, and the right vertex contracts. (c) A hand pushes in on the right, and the left vertex expands. (d-f) Schematics summarizing the asymmetric (or odd) stiffness for $\kappa^a > 0$. (g) The non-conservative force is proportional to the angular deflection $\delta\theta$ for small amplitudes but saturates at a value $\tau_{\max}$ at large amplitudes. (h-i) The dynamics are parameterized by the dimensionless quantity $\xi = \kappa^a/\Gamma\sqrt{I/\kappa}$ capturing the strength of the odd forces. For $|\xi| < 1$ the system relaxes to its rest configuration. For $|\xi| > 1$, the interplay of odd stiffness, nonlinearity, and dissipation produces a limit cycle at finite amplitude. Color indicates phase angle φ. (j-k) Six odd vertices are connected in a hexagon, whose shape is summarized by 3 independent angles, θ_1, θ_3, θ_5, or alternatively three deformation modes: two shears S_1 and S_2, and a breathing mode B. (l) When initially perturbed, the system evolves towards a limit cycle in the space of S_1 and S_2. Adapted from [129].

1.5 Conclusion

Active solids consist of elastically coupled out-of-equilibrium units performing work. Conceptually, they combine the central properties of simple elastic solids and active liquids (Fig. 1.15). On the one hand, the positional degrees of freedom of their constituting units have a well-defined reference state. On the other hand, activity endows these units with an additional free degree of freedom in the form of *polar* or *dipolar* active forces, or in the form of an active torque for *chiral* active agents. The active forces deform the

elastic matrix, and induce an active strain $\Gamma(\{\boldsymbol{r}_i\}, \{\hat{\boldsymbol{n}}_i\})$, which depends on the configuration of the forces. This active strain Γ will in turn reorient the forces. This generic nonlinear elasto-active feedback, formulated without the need for explicit aligning interactions, opens the path towards spontaneous collective excitations of the solid, which we shall call collective actuation. Considering *polar* agents, a general agent-based model accounting for the physics of active solids is:

$$\gamma_t \dot{\boldsymbol{r}}_i = F_0 \hat{\boldsymbol{n}}_i + \boldsymbol{F}^{\mathrm{el}}[\{\boldsymbol{r}_i\}], \tag{1.25a}$$

$$\gamma_r \dot{\boldsymbol{n}}_i = \Gamma(\{\boldsymbol{r}_i\}, \{\hat{\boldsymbol{n}}_i\}) \cdot \hat{\boldsymbol{n}}_i, \tag{1.25b}$$

where the interaction forces $\boldsymbol{F}^{\mathrm{int}}$ are now elastic, position-based forces $\boldsymbol{F}^{\mathrm{el}}[\{\boldsymbol{r}_i\}]$. Interestingly, the elasto-active feedback reorients locally the active units according to the active strain, without explicit alignment. In general, active agents do not obviously have the processing and sensor capabilities to access their neighbors' mean orientation, e.g. for biological tissues, and thus such models are more likely to provide realistic mechanisms for the origin of collective behaviors in real-life active solids. Moreover, they are particularly relevant for active systems where elasticity dominates over the spatial reorganization of the agents.

Different communities have constructed active solids, by compacting a dense active liquid or doping a genuine elastic structure with active units, revealing two hallmarks of active solids: autonomous actuation and odd moduli. Autonomous actuation refers to the spontaneous excitation of one or several normal modes, contrasting with equipartition in equilibrium systems. In the presence of zero modes, autonomous actuation resembles collective locomotion. In contrast, for mechanically stable elastic structures, autonomous actuation might be seen as spontaneous self-oscillations. Eventually, the existence of odd elastic moduli was demonstrated in the case of systems that conserve linear momentum.

A myriad of open questions remain:

- How do the mechanical properties of the solid affect the emergence of collective

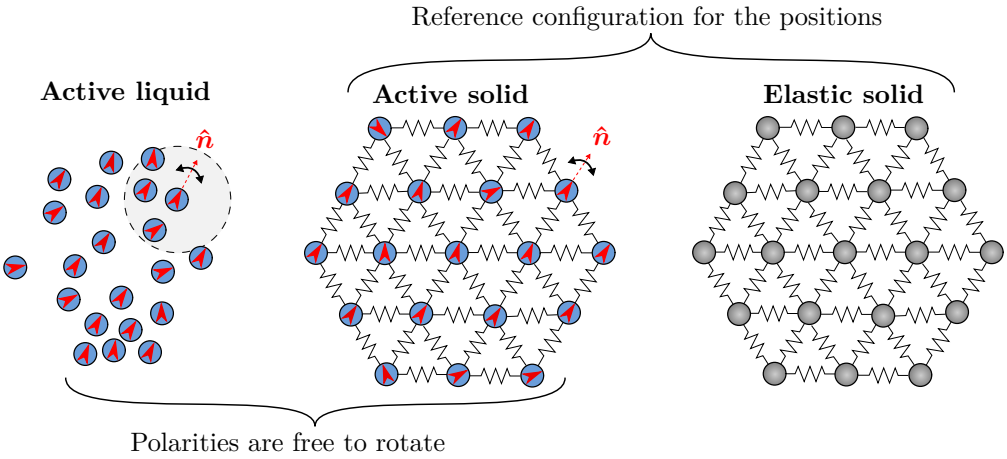


FIG. 1.15. ***Polar* active solids principle.** *Polar* active liquids (left) are composed of a large number of self-propelled interacting spins with no particular spatial order. The gray area illustrates the interaction range between active agents. Conversely, for *polar* active solids (middle), the positional degrees of freedom have a reference configuration, like in the case of standard elastic solids (right), and free-to-rotate polarity vectors.

behaviors? Are zero-mode actuation and self-oscillations two facets of the same phenomenon?

- What mechanisms govern the transition to collective actuation?
- What principles determine the selection rules of the most actuated modes?
- What are the fates of these regimes in the continuum and thermodynamic limits? What is the large-scale physics of active solids? Can one write a hydrodynamics theory?
- How can one control the emerging collective behaviors, whether by design, or external control?
- If odd elastic solids have to be active in some way, are *dry* and *polar* active solids odd elastic? What can we say about the mechanical properties of active solids which do not conserve momentum?
- What are the connections between non-reciprocal systems and active solids?
- Can we design an elasto-active feedback between active units' orientations and structure deformations, different than *Zheng et al.* [120], i.e. not frustrated, and not relying on elastic nonlinearities?

Inspired by the above framework, we aim at addressing some of the above questions by introducing a new experimental platform to investigate the collective dynamics of *dry* and *polar* active solids. We embed centimetric model active units in a genuine spring network, and take advantage of self-alignment to obtain a new feedback between the deformations of the elastic structure and the active force field. We explore the emerging dynamics in systems with various sizes, shapes, and boundary conditions; and combine those findings with the numerical and theoretical analysis of an agents model. Finally, we propose a hydrodynamics theory for *dry* and *polar* active solids with *self-alignment* interactions.

Chapter 2

Experimental systems

In this chapter, we introduce our model active solid experiments, elaborate on their design and physical ingredients, and measure the microscopic parameters. We also provide the full details on processing the experimental data, in particular the tracking algorithm.

2.1 Active units

2.1.1 How to make active particles?

Let us start by answering the first question an active matter experimentalist may wonder: how to construct a model active particle in the lab? Whether working in *dry* or *wet* active matter systems, the requirements are the same: give yourself an object (i) that breaks some spatial symmetries (*polar*, *dipolar*, or *chiral*); and (ii) provide it with an energy supply. The active particles can harvest the energy at the microscopic level from their environment, like in the case of bacteria, robots, and swimming droplets; or it can also be provided by a global energy source, like in light-driven Janus particles [26, 131–133], vibrated polar disks [55–58, 92, 134–137] or colloid rollers [59–61, 138]. Also, note that the broken spatial symmetry the active particles must endow can be broken by design (by explicitly designing asymmetric objects) or spontaneously broken (like swimming droplets [139–141]). From the asymmetry of the particle, energy is dissipated locally and anisotropically, providing the particle with out-of-equilibrium fluctuations, e.g. self-propulsion.

2.1.2 *Hexbugs* as active particles

Hexbugs[1] are centimetric self-propelled robotic cockroaches (Fig. 2.1). When switched on, the vibration produced by the internal motor couples to their flexible legs, allowing for directed motion in the $2d$ plane. Indeed, those robots satisfy the two requirements described above to become self-propelled active particles: their legs are curved to the back, breaking the font/tail symmetry, and the battery they carry supplies the internal motor. The broken front/tail symmetry defines the polarity vector of the active particle, denoted $\hat{\boldsymbol{n}}$ (Fig. 2.1-a). This ultimately defines the self-propulsion direction, oriented forward, along the body's nematic vector. *Hexbugs* were extensively studied in the past years, particularly their individual dynamics in harmonic traps [142, 143], their interactions with walls [144], their clustering in confinement [145, 146], and were used to create chiral active fluids [147] and active elastic structures [120]. Note that a full zoology of such self-propelled cockroaches exists, which differ in their number of legs, the materials

[1] Visit `https://www.hexbug.com/` . Perfect for outreach activities and cats love them.

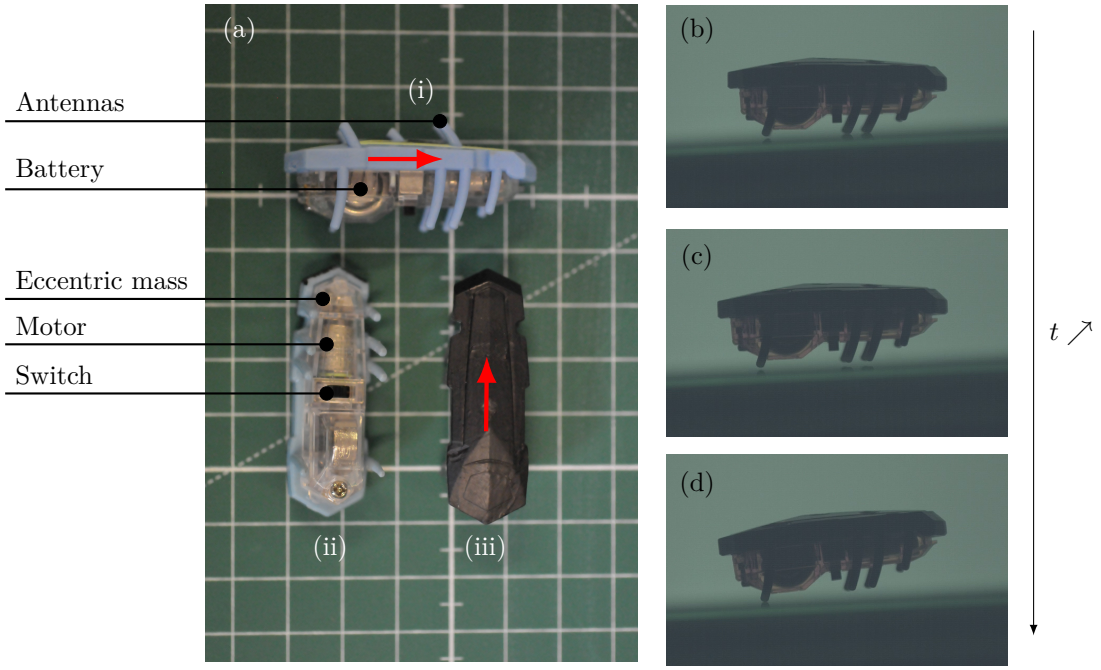


FIG. 2.1. ***Hexbug* anatomy and propulsion mechanism.** (a) *Hexbug nitro* anatomy; (i) side view (ii) bottom view (iii) top view. Polarity vectors are shown with red arrows, and square sides are 1 cm long. In (i), the antennas were not cut, and the body was not painted black. (b-d) Jump phase of a *hexbug nitro*. Pictures spaced by 5.2 ms and 3.4 ms. (b) Motor is up, the *hexbug* is touching the substrate, and its front legs are charged with elastic energy. (c) Motor is down, the *hexbug*'s front takes off as the legs release elastic energy. (d) The *hexbug* is jumping, its front legs are up while its rear legs are touching the substrate.

used, and exact mass distribution, but all have similar physical properties. Unless stated otherwise, we focus on the so-called *hexbug nitro* in the rest of this manuscript.

2.1.3 Anatomy

Hexbugs are somewhat elongated objects: their body length is 45.0 mm, width is 11.5 mm, and height is 14.5 mm (Fig. 2.1-a). The energy supply comes from a 1.5 V AG13/LR44 battery inside the robot, which provides power to a rotating motor connected to an eccentric mass. The majority of the mass lies in the battery, located at the back of the particle; thus, the barycenter is closer to the tail than the front. A switch allows for turning the motor on and off. The *hexbugs* bulk is made of hard plastic, while the legs are made of a soft material that deforms under the action of the motor. When freshly unpacked, the *hexbugs* are provided with antennas that allow the robot to turn around if knocked down. In the following, we cut the antennas as low as possible to avoid future parasitic mechanical coupling. Eventually, we paint the top part of the *hexbugs* in black to easily identify them from the top on a white background.

2.1.4 Propulsion mechanism

Now let us elaborate on the *hexbugs*' propulsion mechanism. As discussed above, when switched on, the internal motor starts rotating the eccentric mass. From linear momentum conservation along the z-direction, and from the position of the motor with respect to the mass barycenter, when the motor's mass goes up, the *hexbug*'s front goes down, and reciprocally, resulting in a vertical vibration of the body's front. Self-propulsion in

the $2d$ plane results from the coupling of this vertical vibration with the curved flexible legs. Indeed, when the *hexbug* stands on a horizontal substrate, as the motor goes up, the body's front goes down, charging elastically the front legs. As the motor goes down, the legs' elastic energy is released, and the body's front is kicked in the legs' direction, i.e. vertically and along the polarity $\hat{\boldsymbol{n}}$ (Figs. 2.1-b and d). The *hexbug* starts its jumping phase, during which the front of the particle is in the air, while the back legs rub on the substrate. This friction and gravity ultimately recall the body's front toward the substrate. As the front legs land, they get charged again, and the process repeats. Note that the motor's frequency is way larger than the jump frequency, and these two processes are not particularly synchronized. Combined with complicated $3d$ effects, the propulsion regime is mostly *chaotic*. Nevertheless, observed on long timescales, *hexbugs* travel at the well-defined cruise velocity, while their polarity $\hat{\boldsymbol{n}}$ diffuses. The repeated kicks given on the substrate, which is held fixed by friction, are at the origin of the overall non-conservation of linear momentum in the $2d$ plane.

To further characterize the propulsion mechanism, we apply different voltages from 0 to 3 V (twice the battery voltage) to the *hexbugs*. We weld copper cables to the *hexbugs* battery pins, and connect them to a tunable DC power supply. The cables[2] are very thin and loose not to disturb the *hexbugs*' motion. Using a standard microphone and Fourier analysis, we first measure the motor's frequency as a function of the applied voltage (Fig. 2.2-a). We find that for a small enough voltage ($< 0.2V$), the motor is at rest. For large enough voltage ($> 0.2V$), the motor starts rotating, and the motor's frequency increases monotonically with voltage. Second, we measure the *hexbugs* speed as a function of the applied voltage, and find a similar observation. Fig. 2.2-b shows how the cruise velocity depends on the motor's frequency, for two species of *hexbugs*, the *nitro*, and the *nano*. In both cases, we find that speed scales mostly linearly with the motor's frequency for small driving, and ends up saturating at roughly 30 cm/s at large driving. This linear relationship at small frequency was observed in other studies on *Bristlebots*[3] locomotion

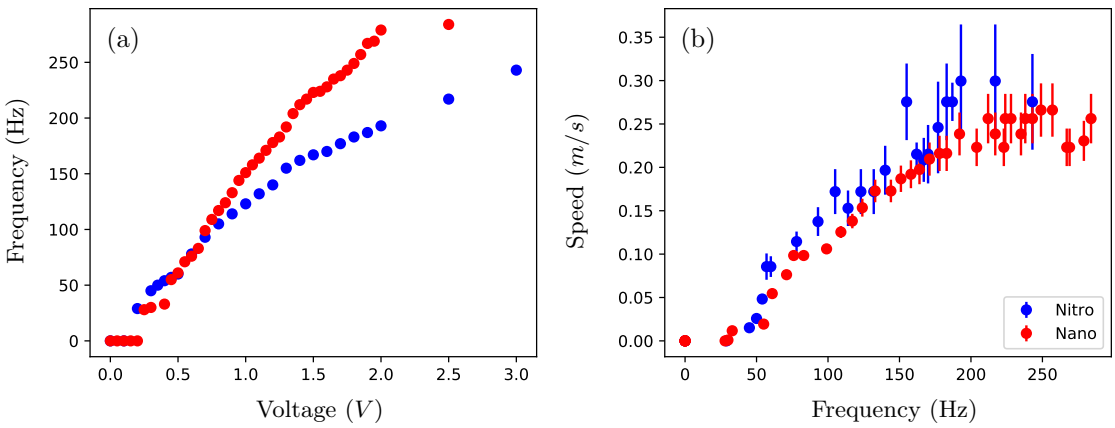


FIG. 2.2. ***Hexbugs*' propulsion as a function of the applied voltage.** (a) Main frequency of the sound emitted by a *hexbug* (as given by the largest peak of its FFT) as a function of the imposed voltage. (b) Cruise velocity of a *hexbug* as a function of its vibration frequency (a). On both figures, blue markers account for the nitro *hexbugs* (6 legs), and red markers for the nano *hexbugs* (10 legs).

[2]BLOCK, 100/0.15∅; 150 μm diameter enameled copper wires.
[3]General name given to vertically vibrated robots propelled thanks to curved flexible legs

[148–150]. In the rest of the manuscript, unless stated otherwise, we restrict to the 1.5 V voltage provided with the batteries.

2.1.5 Left/right bias

It is worth noting that *hexbugs* are generally biased: they turn preferentially to the left or right. This is due to both design and aging of the *hexbugs*. First, the rotating motor already breaks the left/right symmetry of the active particle. To compensate for this effect, the left legs are designed to be stronger than the right ones (slightly wider), resulting in a mostly unbiased motion. However, lousy packaging, manufacturing errors, and components variability give rise to particles biased either to the left or right. Aging also plays a crucial role: emerging chiral behavior in previous experiments can induce long-term bias in the particles involved. In section 2.1.7, we describe the procedure used to select only the less biased *hexbugs*.

2.1.6 Self-alignment

In 2018, *Dauchot and Démery* [143] demonstrated that *hexbugs* exhibit *self-alignment* properties: their polarity vector reorients toward the direction of motion. This ingredient was shown to be at the root of orbital motion for a single *hexbug* embedded in a harmonic trap (see chapters 3 and 5), and originates from the mass distribution of the particle. Because the barycenter lies closer to the tail, when in motion, the particle experiences more friction with the substrate on the back than on the front, resulting in an effective self-alignment torque.

Let us illustrate the *self-alignment* properties of *hexbugs* using another simple benchmark experiment. We explore the effect of gravity on the dynamics of a single active unit in free boundary conditions. Therefore, we study the motion of one *hexbug* freely moving on a substrate, but the latter is also tilted by an angle $\alpha = 5.3°$ with respect to the horizontal plane (Fig. 2.3-a). An *hexbug*'s starting block is designed with cardboard to prepare the initial condition, perpendicular to the slope (Fig. 2.3-b). The dynamics are recorded and tracked 10 times, and the possible left/right bias of the *hexbug* is taken into account by performing each experiment twice, first with the slope running down

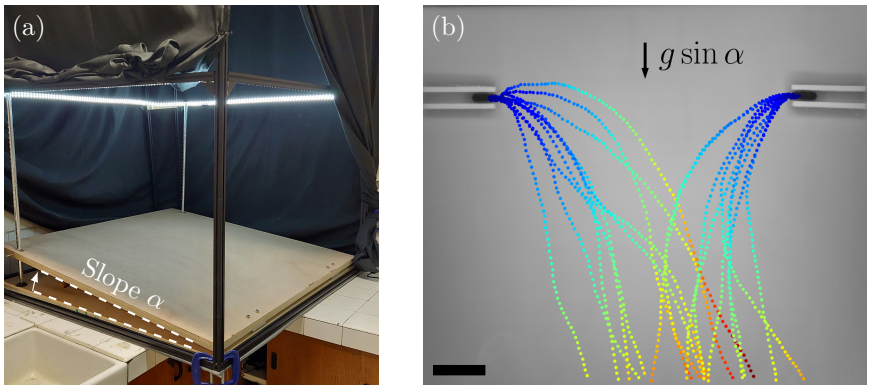


FIG. 2.3. **Tilted experiments with gravity, and benchmark** (a) Experimental setup picture. The tilt generates a gravity acceleration of amplitude $g_\alpha = g \sin \alpha$, where α is the angle of the substrate with respect to the horizontal plane, and g is the gravity acceleration at the earth's surface. (b) Single *hexbug* dynamics in a gravity field. 10 trajectories are color-coded from blue to red by increasing time for the two possible initial orientations of the *hexbug*; scale bar: 10 cm.

on the left and then on the right. We find that the *hexbug*, initially perpendicular to the slope, systematically reorients toward it. This effect is illustrated by the trajectories represented in Fig. 2.3-b. As a matter of fact, we find that the *hexbug* aligns on average toward a direction close to the gravity force direction, but not strictly. As discussed below, this comes from the intrinsic left bias of the *hexbug* used for this experiment.

Inspired by the work of *Dauchot and Démery* [143], we consider the noiseless and overdamped dynamics of a single hexbug in free boundary conditions, simply replacing the central force toward the parabola's origin by a constant gravity force. The position $\boldsymbol{r}$ and orientation $\hat{\boldsymbol{n}}$ of the *hexbug* evolve according to the following equations of motion:

$$\dot{\boldsymbol{r}} = v_0\hat{\boldsymbol{n}} + m\boldsymbol{g}/\gamma, \tag{2.1a}$$

$$\tau\dot{\boldsymbol{n}} = \zeta(\hat{\boldsymbol{n}} \times \dot{\boldsymbol{r}}) \times \hat{\boldsymbol{n}}, \tag{2.1b}$$

where $\boldsymbol{g} = g\sin\alpha\boldsymbol{e}_g$, $\boldsymbol{e}_g$ is a unit vector pointing toward the slope running down, m is the *hexbug*'s mass, and $v_0 = F_0/\gamma$ is the *hexbug* cruise velocity. Importantly, the term on the right-hand side of Eq. (2.1b) is a *self-alignment* term, reorienting the polarity vector toward the direction of motion. Note that this term is proportional to the velocity $\dot{\boldsymbol{r}}$, thus the alignment process is characterized by an alignment length $l_a = \tau/\zeta$. The polar force does not contribute to rotating the polarity vector; only the gravity term does, thus the polarity equation decouples from the position. The dynamical equation for the angle θ between the polarity vector $\hat{\boldsymbol{n}}$ and the slope direction $\boldsymbol{e}_g$ is:

$$\dot{\theta} = -\frac{mg\sin\alpha}{\gamma l_a}\sin\theta. \tag{2.2}$$

The orientation is relaxing toward the gravity direction, the same way an overdamped nonlinear pendulum in a gravity field would. The transitory regime can be computed analytically (see section 2.3), and mostly consists of a relaxation toward $\theta = 0$ (running down the slope) over a typical timescale $\gamma l_a/mg\sin\alpha$. Adding a bias term $\omega\hat{\boldsymbol{n}}^{\perp}$ in the polarity dynamics Eq. (2.1b), we find that independently of the initial orientation θ_0, the stationary angle θ_s reads:

$$\sin\theta_s = \omega\frac{\gamma l_a}{mg\sin\alpha}, \tag{2.3}$$

where ω is the *hexbug* bias rotation rate. For vanishing bias ($\omega = 0$), the stationary orientation is $\theta = 0$, meaning that the polarity vector is aligned with the slope. For finite bias ($\omega > 0$), the polarity vector is misaligned with the gravity force, as given by Eq. (2.3) and observed in the experiments shown in Fig. 2.3-b. Interestingly, *Zion et al.* studied this alignment on gravity in free boundary conditions using kilobots[4] augmented with 3d printed exoskeletons [151]. They have shown that the design of the exoskeleton allows for setting the sign of the alignment length l_a, and can therefore lead to alignment ($l_a > 0$) or anti-alignment ($l_a < 0$) on gravity, according to the same equations as Eqs. (2.1).

2.1.7 *Hexbugs* eugenics

Regardless of morals, in the following, we do eugenics and only keep the best *hexbugs*. This decreases the heterogeneity among the active units and prevents too severe consequences in the experiments. To find the best *hexbugs* among a large set[5], the first step is

[4] *Low-cost* centimetric robots specifically designed for swarm robotics experiments.

[5] Our *hexbugs* fleet typically contains 100 active units.

to change all their batteries. Then, the following criteria should be met to use a *hexbug* in an experiment:

- It should run fast enough. As an arbitrary criterion, we ask the *hexbugs* to run at speeds close enough to 20 cm/s.
- It should not appear to be biased on the length scale of a lab table. A biased *hexbug* performs a circular motion, whose radius is given by $R = v_0/\omega_b$, where v_0 the cruise velocity and ω_b the bias angular rotation rate. We select a *hexbug* only if $R > R_{\text{table}} \simeq 1$ m, which avoids considering too severely biased active units.
- It should adequately self-align when imposing a motion manually with the active elastic building block (see section below). This is a completely arbitrary condition, but it allows discarding *hexbugs* that perpendicular displacements would easily knock down.

2.2 Active elastic building blocks

2.2.1 Design principle

In order to create a mechanical coupling between the *hexbugs*' polarities and motion, we embed them into little cages; made of a 3d printed ABS annulus (Fig. 2.4-a), and covered by an elastic plastic film to restrict the vertical motion of the *hexbugs*. The active unit induces self-propulsion of the whole building block along the polarity $\hat{\boldsymbol{n}}$. At the same time, the effective friction of the *hexbugs* with the top plastic film and substrate reorients the active unit. The annuli were designed to optimize both self-propulsion and reorientation of the active units. On the one hand, the active building blocks are as self-propelled as the annuli are light, because they create additional friction with the substrate. On the other hand, reorientation by motion is as strong as the annuli are heavy and their height is small.

2.2.2 Anatomy

The annuli' internal diameter is 5 cm, their thickness is 3 mm, their height is 14 mm (as the *hexbugs* themselves), and their overall mass (including hat and plastic film)

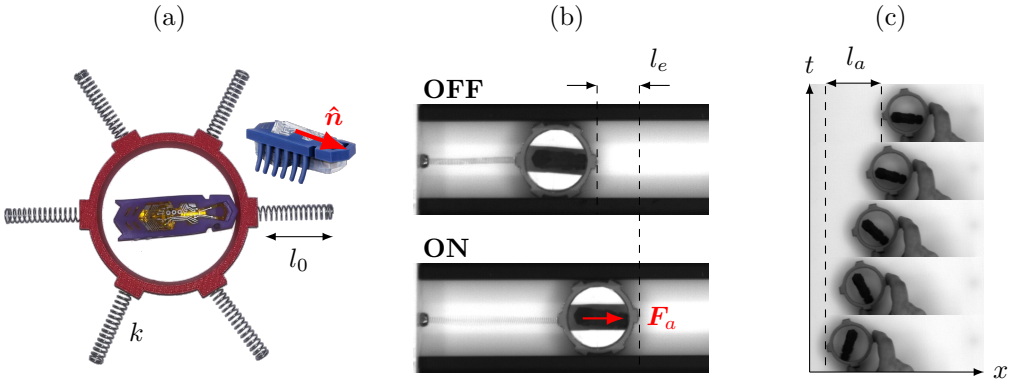


FIG. 2.4. **Active solids design principle.** (a) Active unit: a *hexbug* is trapped in a 3*d* printed annulus. (b) The active component, here confined in a linear track and attached to a spring of stiffness k, produces an active force of amplitude F_0 in the direction of the polarity $\hat{\boldsymbol{n}}$ and elongates the spring by a length $l_e = F_0/k$. (c) The mechanical design of the *hexbug* – mass distribution and shape of the legs – is responsible for its alignment toward its displacement, here imposed manually (see section 2.3 for a quantitative measure of the self-alignment length l_a).

is 9.80 g. These 3d printed annuli have 6 overhangs (3 mm thick), that are pierced with a milling machine in order to hold the edges of the springs. It is also simple to design building blocks with a different number and repartition of overhangs to adapt to other local arrangements, like honeycomb or square lattices. Eventually, we set a thin polypropylene plastic film on the top of the annulus to restrict the vertical motion of the *hexbugs*, which we fix using commercial glue[6] and a 3d printed 1 mm thick ring. The obtained active elastic building block is shown in Fig. 2.4-a. These elementary components are connected by coil springs, fixed with commercial glue to the overhangs. We use two kinds of springs, respectively the *soft* and *stiff* springs. Specifically, in chapter 4, we will also use plastic straws as rigid[7] connectors, which are light enough not to affect the dynamics. All these connectors have the same outer diameters to fit the overhang holes. Their properties are summarized in table 2.1.

Name	Manufacturer	k (N/m)	l_0 (cm)	D (mm)	d (mm)	n
Soft	Schweizer Federntechnik	1.2	8	5	0.18	67
Stiff	Ets. Jean CHAPUIS	120	3	5	0.4	18
Rigid	Dhaikkkd	∞	15	5	-	-

Table 2.1: Properties of the different springs. Stiffness k, rest length l_0, outer diameter D, wire diameter d, and winding number n for the two springs used. Notations are defined in section 2.3.5 and Fig. 2.9

2.2.3 Main physical ingredients

Let us review the two main physical ingredients presented in Figs. 2.4-b and c, at the root of the physics of these model active elastic systems: active force, and self-alignment.

Quite obviously, once springs are attached to form an active elastic network, we find that the polar forces create deformations. This ingredient is illustrated in Fig. 2.4-b, using a single active unit connected to a spring in a quasi-1d channel geometry, and frustrated to point in the channel direction. As the *hexbug* is off, the spring is at its rest length l_0. When switched on, the polar force generated by the *hexbug* elongates the spring by an additional length l_e, namely the elasto-active length. Force balance enforces $l_e = F_0/k$; where F_0 is the amplitude of the polar active force in the direction of the polarity $\hat{\boldsymbol{n}}$, and where k is the spring's stiffness.

Moreover, the *hexbugs* maintain their self-alignment properties when embedded in the active elastic building blocks. Manually imposing a displacement to the outer cylinder, we indeed find that the internal *hexbug* spontaneously aligns toward the direction of motion (Fig. 2.4-c). The self-alignment torque has the same origin as before: *hexbugs* are subjected to more friction on the back than on the front, but here friction arises from both effective contacts with the substrate and the top plastic film. Therefore, when the polarity $\hat{\boldsymbol{n}}$ is not aligned with the displacement, it reorients until the two vectors eventually point the same way. A feathered badminton shuttlecock experiences the same self-aligning torque: when given a velocity, the shuttlecock reorients toward the latter (Fig. 2.5-a). Note, however, that in the case of badminton, the self-alignment process is underdamped, as the polarity overshoots the velocity vector when reorienting, while for *hexbugs*, it is overdamped (Fig. 2.5-b).

[6] SADER, Répare tout.

[7] Rigid enough to neglect any elasticity.

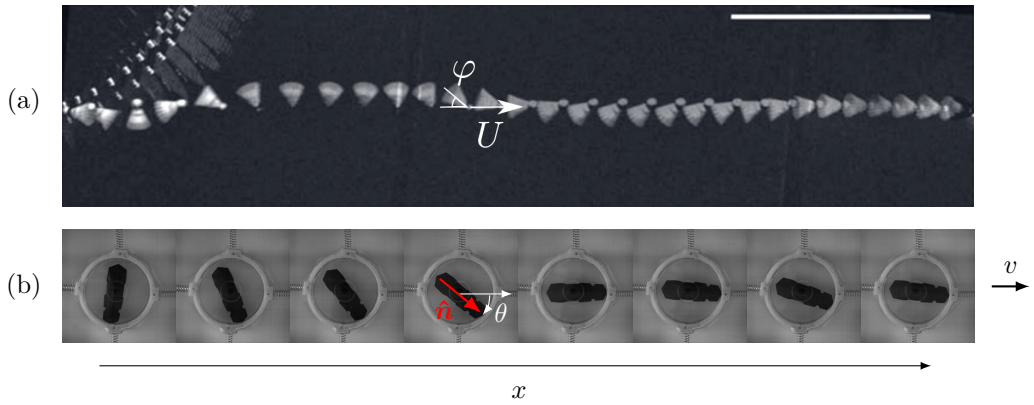


FIG. 2.5. **Self-alignment of a *hexbug* and a feathered shuttlecock.** (a) Chronophotographies of shuttlecocks after an impact with a racket, showing the time evolution of the angle φ between the shuttlecock orientation and its velocity U. The white line indicates 50 cm. The time interval between each position is 5 ms. Adapted from [152]. (b) Reorientation of a *hexbug* toward the imposed direction of motion, showing the time evolution of the angle θ between the *hexbug*'s orientation and its velocity. The time interval between two pictures is 150 ms. The precise figure description can be found in Fig. 2.8.

2.3 Measurement of the microscopic parameters

In this section, we describe three simple experiments we conducted to measure the parameters of the active elastic building blocks. First, we evaluate the influence of inertia and the relevance of the overdamped limit. Then we measure the alignment length l_a, our model's key parameter, as well as the angular noise D_θ. Finally, we measure the active force F_0 the *hexbugs* can exert.

2.3.1 Inertia

Experiments

We consider a single active unit, initially at rest, whose self-propulsion is switched on at $t = 0$ and whose orientation is fixed (Fig. 2.6-a). This experiment cannot be realized using the active elastic building block, as self-propulsion cannot be switched on while the *hexbug* stands on the substrate inside the cage. Consequently, we build a *hacked hexbug* (Fig. 2.6-b), powered by a DC generator[8]. A hole drilled on top of the *hexbug* allows fitting a plastic sheath[9] through which go two copper wires[10], connected to the battery pins. The cables feature a thin covering of enamel which acts as an electrical insulator. To maintain *hexbug*'s mass and mass distribution, the battery is replaced by a bolt with roughly the same mass[11], covered with insulating varnish. Eventually, the active building block is constructed by connecting the *hacked hexbugs* to the DC generator, the wires going through a 21 mm diameter hole pierced in the middle of the top plastic film (Fig. 2.6-a). The DC generator delivers a Heaviside signal of amplitude 1.5 V (same as the *hexbug*'s battery) at $t = 0$. We use two cardboard blockers[12] on the sides of the hexbug to prevent its polarity from rotating with respect to the annulus orientation, setting the orientation $\hat{\boldsymbol{n}}$ essentially constant.

[8] AGILENT, E3631A, Triple Output DC Power Supply, 0-6V,6A/0-±25V,1A
[9] External diameter: 1.6 mm; internal diameter: 0.8 mm.
[10] BLOCK, 100/0.15∅; 150 μm diameter enameled copper wires.
[11] Battery mass: 1.99 g; bolt mass: 2.26 g.
[12] 5 mm thick, negligible mass.

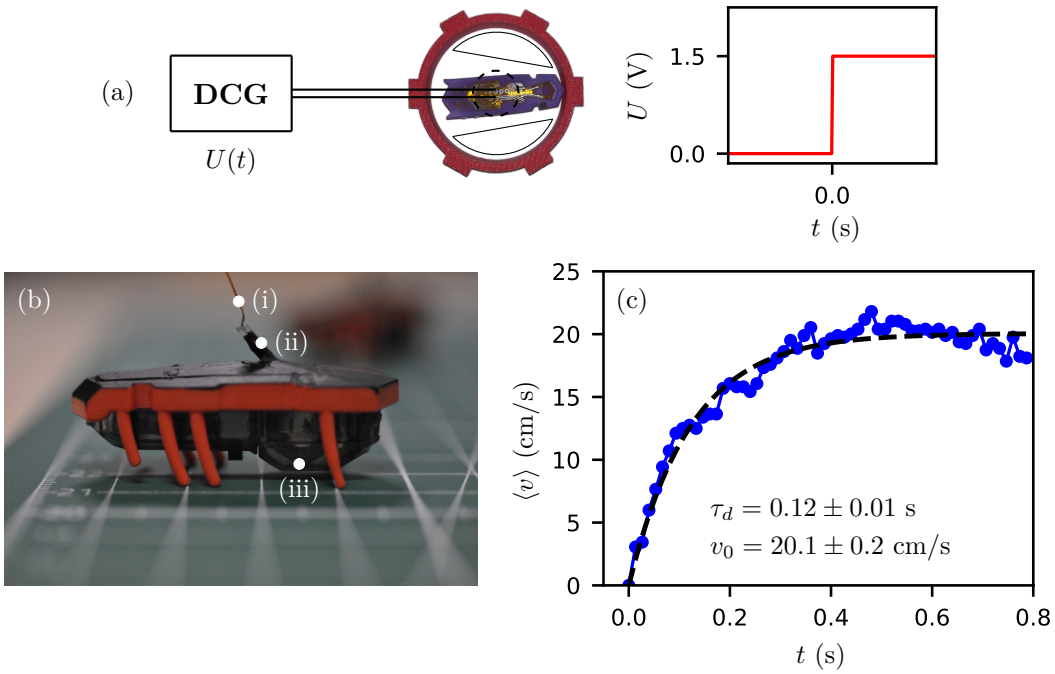


FIG. 2.6. **Inertia measurement.** (a) Experimental setup: an active unit is powered by a DC generator that delivers a Heaviside signal of amplitude 1.5 V at $t = 0$. The *hacked hexbug*'s polarity is fixed during the whole experiment. The dashed black circle indicates the hole pierced in the covering plastic film. (b) A *hacked hexbug*. A hole on the *hexbug*'s top allows fitting a plastic sheath (ii) through which go the two cables (i), connected to the battery pins. A bolt (iii) replaces the battery to maintain mass and mass distribution. (c) Average speed $\langle v \rangle$ as a function of time t for 20 realizations (blue markers), fitted by Eq. (2.5) (dashed black line) with a least-squared method. Inset data are the fit parameters, with 1σ confidence intervals.

The acceleration experiments are performed 20 times, acquired at 75 frames per second. The instantaneous speed is measured by differentiating the building block's position as a function of time. The average speed response to the Heaviside driving is shown in Fig. 2.6-c. The active building block's speed first increases linearly with time and ends up saturating at a cruise velocity $v_0 \simeq 20$ cm/s. For $t >$ 0.6-0.8 s, the wires are less and less loose, and their growing influence leads to a decrease in the average speed.

Discussion

The general equation of motion for the position of a single active unit, without neglecting inertia, expresses as (see chapter 3):

$$m\frac{d\boldsymbol{v}}{dt} = F_0\hat{\boldsymbol{n}} - \gamma\boldsymbol{v}, \tag{2.4}$$

where m is the mass of the active particle, γ the effective friction coefficient, F_0 is the amplitude of the self-propulsive force, $\boldsymbol{v}$ the instantaneous velocity of the active unit, and $\hat{\boldsymbol{n}}$ is the polarity vector. Note that the latter is considered fixed during the experiment, $\hat{\boldsymbol{n}}(t) = \hat{\boldsymbol{n}}_0$. Solving Eq. (2.4) projected on $\hat{\boldsymbol{n}}_0$, for $\boldsymbol{v}(t = 0) = \boldsymbol{0}$, we find:

$$v(t) = |\boldsymbol{v}(t)| = v_0(1 - e^{-t/\tau_d}), \tag{2.5}$$

that is, an exponential relaxation toward the long-time cruise velocity $v_0 = F_0/\gamma$, on a typical acceleration time $\tau_d = m/\gamma = \tau_v t_0$, where $\tau_v = mk/\gamma^2$ and $t_0 = \gamma/k$ are defined

in chapter 3. The experimental data are in good agreement with this prediction (Fig. 2.6-c). The values $v_0 = 20.1 \pm 0.2$ cm/s and $\tau_d = 0.12 \pm 0.01$ s are obtained from a least-squared fit of the averaged speed for $t < 0.6$ s, with $\pm$ indicating the 1σ confidence intervals. For timescales larger than τ_d, such as those considered at the level of the collective dynamics, inertia can be safely neglected.

2.3.2 Self-alignment

Experiments

In order to quantify the self-alignment properties, we measure the response of a *hexbug*'s polarity when imposing a square motion to an active elastic building block (Figs. 2.7-a and b). The motion and speed are controlled using a CNC translating stage[13], and the square's sides are 20 cm long. At each corner of the square, the orientation of the velocity $\boldsymbol{v}$ changes abruptly, and the polarity aligns with the newly imposed velocity. Snapshots of this process are shown in Fig. 2.7-b for an entire square, and in Fig. 2.8-a for a single alignment experiment. The device the *hexbug* is trapped in is designed to reproduce the

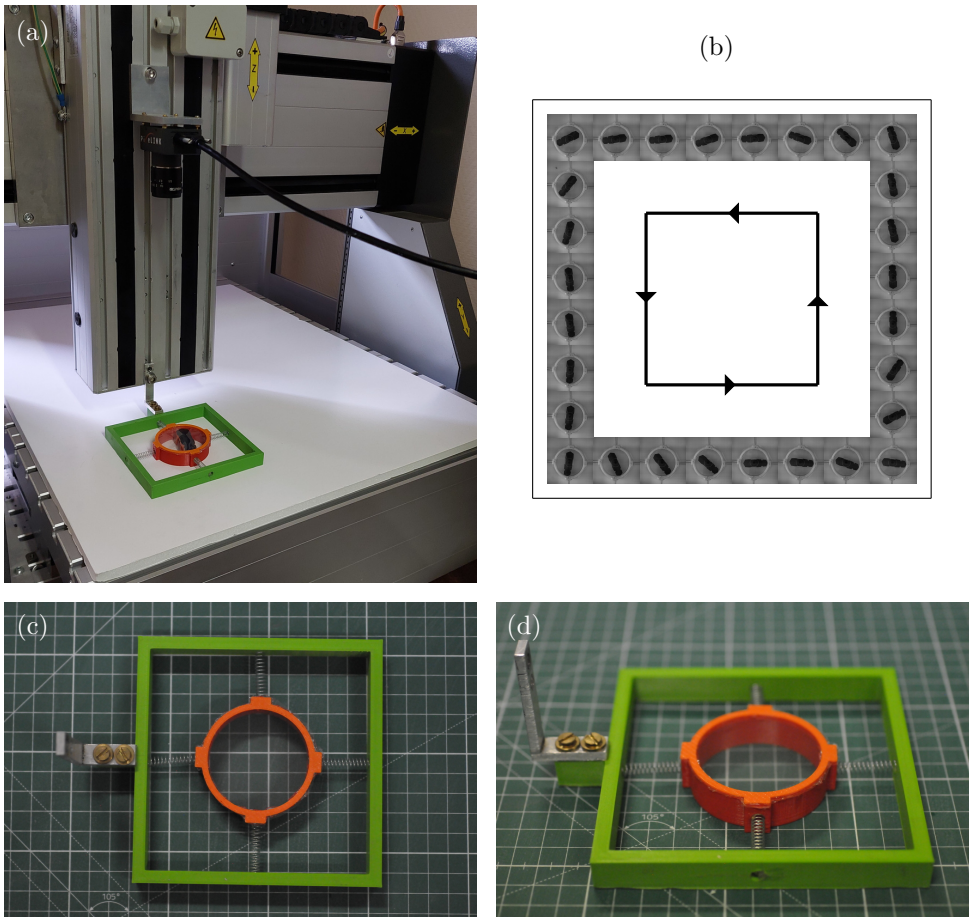


FIG. 2.7. **Self-alignment experimental setup.** (a) A camera is attached to the top of the CNC arm, acquiring the orientation dynamics of a *hexbug* trapped in an alignment device. (b) Reorientation of the active unit along the imposed square motion, at $V = 10$ cm/s. Each side of the square corresponds to an alignment experiment. (c-d) Alignment device: (c) top view; (c) side view.

[13]Translating stage ModuFlat P30; CNC stands for Computerized Numerical Control.

mechanical conditions faced in the active elastic network experiments (Figs. 2.7-c and d). It consists of a stiff square frame, at the middle of which lies a square active elastic building block, connected to the frame with 4 regularly spaced *stiff* springs. The springs' stiffness is such that the *hexbug* cannot displace enough to reorient thanks to its own activity[14], but only through the CNC-generated motion. Note however that the presence of finite stiffness springs is essential, as it gives some springiness along the z-direction, mimicking the conditions in the collective experiments. A camera[15] and the alignment device are both attached to the CNC machine arm, so the alignment process is acquired in the reference frame of motion. The camera is attached to the top of the arm, while the alignment device's frame is positioned as close as possible to the substrate. We set the displacement speed from 5 cm/s to 12 cm/s[16], by steps of 0.5 cm/s, and perform 10 independent realizations for each speed value.

The orientation of the *hexbug* with respect to the direction of motion is denoted θ (Fig. 2.8-a). Several individual alignment processes performed at $V = 10$ cm/s are shown in Fig. 2.8-b, and the average response is shown in Fig. 2.8-c. We find two regimes: (i) the short-time transitory alignment regime ($t < 1$ s), during which the polarity reorients toward the new velocity vector; and (ii) the long-time steady state ($t > 1$ s), during which polarity and velocity are mostly aligned, self-alignment balancing angular noise.

Discussion

The equation of motion for the orientation θ, evolving through self-alignment and angular noise, reads (see chapter 3):

$$\tau \frac{d\theta}{dt} = -V\zeta \sin(\theta) + \sqrt{2\alpha}\xi, \tag{2.6}$$

where V is the imposed speed, $\tau/\zeta = l_a$ is the alignment length, and ξ is a Gaussian random variable with zero mean $\langle \xi(t) \rangle = 0$ and correlations $\langle \xi(t)\xi(t') \rangle = \delta(t - t')$.

The short-time transitory alignment regime has nothing to do with noise, as it comes from the self-alignment torque, reorienting the polarity toward the velocity. In the absence of noise ($\alpha = 0$), Eq. (2.6) transforms into a simple ODE, and the solution to the initial condition problem with $\theta(t = 0) = \theta_0 = 90°$ is:

$$\tan\left(\frac{\theta(t)}{2}\right) = \tan\left(\frac{\theta_0}{2}\right) e^{-t/\tau_a}, \tag{2.7}$$

where the alignment time is $\tau_a = l_a/V$. The polarity thus relaxes toward the velocity vector, on a typical timescale given by the ratio of the alignment length and motion speed. Note that because of the sin non-linearity, it is not the angle θ which exponentially relaxes to zero, but $\tan(\theta/2)$. The average alignment process (Fig. 2.8-c) is well described by the prediction of Eq. (2.7). Fitting the short-time decay of $\log\left[\overline{\tan(\theta/2)/\tan(\theta_0/2)}\right]$ with a linear function, we find the associated alignment time τ_a for a given speed V (Fig. 2.8-c, inset). Performing this measurement for all speeds (Fig. 2.8-d), we find that the alignment time scales as the inverse of the imposed speed, in agreement with Eq. (2.7). The agreement is better at large speed where the influence of noise on the measurements

[14] More precisely, the mechanical structure associated with the four springs and the boundary condition has two degenerated normal modes of energy $\omega_0^2 = 2$; and $\pi \ll \omega_0^2$.

[15] Camera: PixeLink PL-D734MU; Lens: PixeLink, f=25mm/F1.6

[16] Upper limit of the CNC.

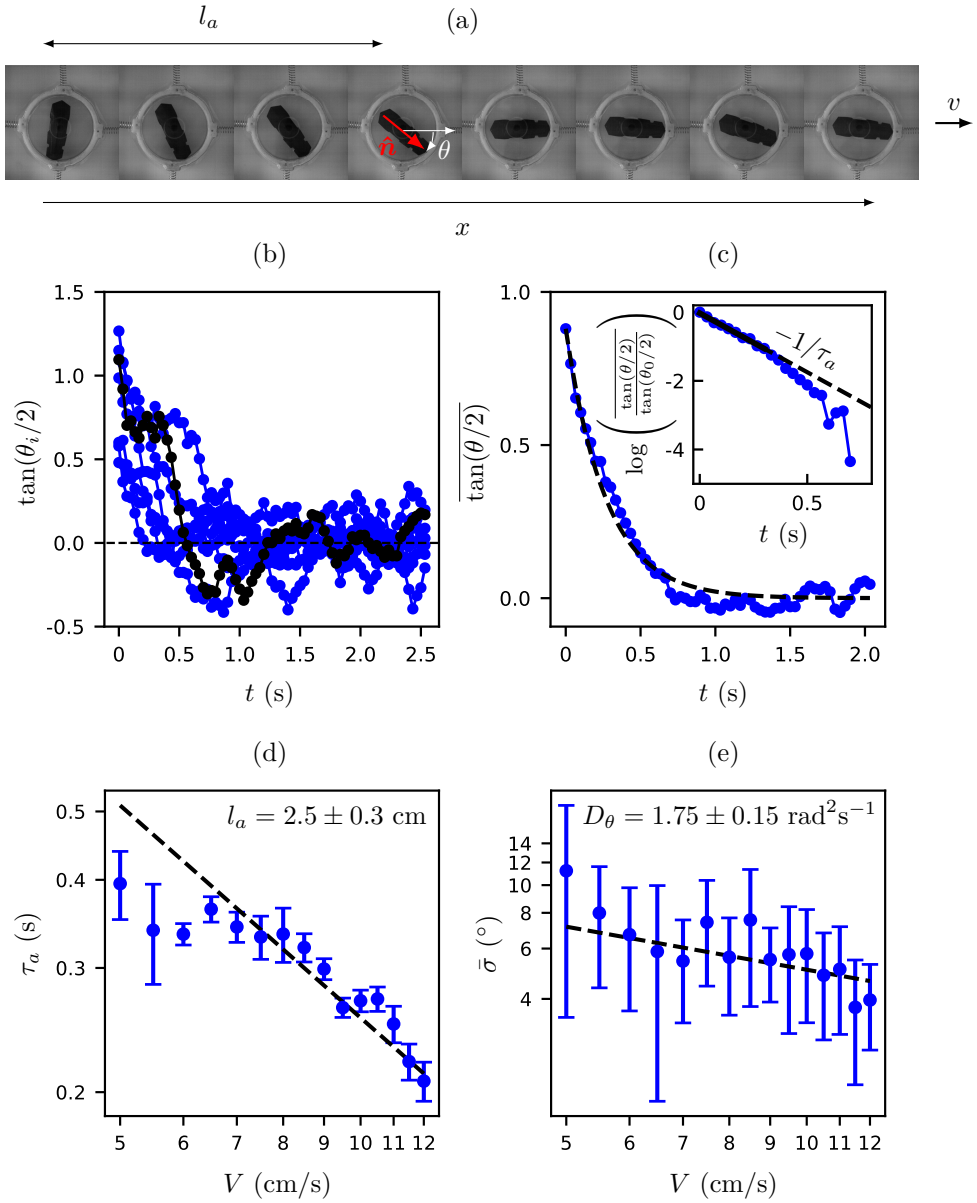


FIG. 2.8. **Self-alignment experiments.** (a) Single alignment experiment at $V = 10$ cm/s, showing the time evolution of the angle θ between the *hexbug*'s orientation $\hat{\boldsymbol{n}}$ and its velocity $\boldsymbol{v}$. The time interval between two pictures is 150 ms. (b) Misalignments $\tan(\theta_i/2)$ as a function of time time, for 10 independent alignment experiments with $V = 10$ cm/s. One of them is highlighted in black. (c) Average misalignment $\overline{\tan(\theta/2)}(t) = \frac{1}{N}\sum_i \tan(\theta_i/2)(t)$ of the 10 independent realizations of (a) (blue markers), superposed with Eq. (2.7) (dashed black line). Inset: the alignment time τ_a is measured by fitting the short times of $\overline{\tan(\theta(t)/2)} \,/\, \overline{\tan(\theta_0/2)}$ with an exponential decay. (d) Alignment time τ_a as a function of the imposed speed V (blue markers). Vertical error bars are the 1σ confidence intervals. The dashed black line is an inverse power law whose prefactor gives an estimate of the alignment length l_a (e) Average standard deviation $\bar{\sigma}$ of misalignments as a function of the imposed speed V (blue markers). Vertical error bars are the standard deviation of the standard deviations σ for each speed. The dashed black line is given by Eq. (2.11).

is the weakest. We end up with a measure of the alignment length $l_a = 2.5 \pm 0.3$ cm, obtained by manually adjusting Eq. (2.7) to the experimental data at large enough speed, with a reasonable confidence interval.

In the long-time steady state, self-alignment balances angular noise, giving rise to a stationary orientation distribution. Note that this state is accessible experimentally, as the square sides are 20 cm, while the alignment length is only 2.5 cm. In the presence of noise, the Fokker-Planck equation associated with Eq. (2.6) is

$$\frac{\partial P}{\partial t}(\theta,t) = \frac{\partial}{\partial \theta}\left(\frac{V\zeta}{\tau}\sin(\theta)P(\theta,t)\right) + \frac{\partial^2}{\partial \theta^2}\left(\frac{\alpha}{\tau^2}P(\theta,t)\right), \tag{2.8}$$

where $P(\theta,t)$ is the probability distribution of the angle θ at time t. The stationary probability density $P_s(\theta)$ satisfies:

$$\frac{d^2P_s}{d\theta^2}(\theta) + \sin(\theta)\frac{V\zeta\tau}{\alpha}\frac{dP_s}{d\theta}(\theta) + \cos(\theta)\frac{V\zeta\tau}{\alpha}P_s(\theta) = 0, \tag{2.9}$$

which has the following solution:

$$P_s(\theta) = \mathcal{N}\exp\left(\frac{V\zeta\tau}{\alpha}\cos(\theta)\right), \tag{2.10}$$

where $\mathcal{N}$ is a normalization factor. In the vicinity of $\theta = 0$ (aligned state), this distribution is a Gaussian with a standard deviation

$$\sigma = \sqrt{\frac{\alpha}{\tau\zeta V}} = \sqrt{\frac{D_\theta l_a}{V}}, \tag{2.11}$$

where $D_\theta = \alpha/\tau^2$ is the angular diffusion coefficient. We measure the average misalignment $\bar{\sigma}$ by averaging the standard deviations of misalignments $\sqrt{\langle\theta^2\rangle}$ for the 10 realizations at a given speed (Fig. 2.8-e). Data are analyzed after two associated τ_a to consider only the stationary distributions. As seen from Fig. 2.8-e, $\bar{\sigma}$ decays in a way that is consistent with the prediction of Eq. (2.11). This allows extracting an angular diffusion coefficient $D_\theta = 1.75 \pm 0.15$ rad$^2 s^{-1}$, by adjusting Eq. (2.11) to the experimental data with a least-squared method, the $\pm$ indicating the 1σ confidence interval.

2.3.3 Active force

To evaluate the amplitude of active force, we restrict the motion of an active elastic building block by trapping it in a sufficiently narrow rectangular channel, and we fix the *hexbug*'s polarity so that it always points in the long direction of the arena, as shown in Fig. 2.4-b. The active unit is attached to one end of the channel by a spring. As activity is switched on, the hexbug moves forward, up to the point where the elastic force balances the active one. As we know the spring's stiffness[17], the extension of the spring in the steady state gives a measure of the active force $F_0 = 43 \pm 3$ mN. The uncertainty is given by the standard deviation of the measurements on 5 different *hexbugs*.

2.3.4 Elasto-active coupling

Having extracted F_0, we can obtain the elasto-active length $l_e = F_0/k$ for the different springs used. Together with l_a, we are therefore in position to have the experimental value for $\pi = l_e/l_a$, the central control parameter of the experiment (see chapter 3). The estimated values are summarized in table 2.2. Using the *soft* or the *stiff* springs thus gives rise to elasto-active coupling values close to unity or one hundredth.

[17] From the manufacturer. *Soft* springs: $k \simeq 1.2$ N/m; *Stiff* springs: $k \simeq 120$ N/m.

Name	l_e (cm)	l_a (cm)	π
Soft	3.6	2.5	1.4
Stiff	0.04	2.5	0.014
Rigid	0^+	2.5	0^+

Table 2.2: Elasto-active coupling π for the different springs. Elasto-active length $l_e = F_0/k$, alignment length l_a, elasto-active coupling $\pi = l_e/l_a$.

2.3.5 Tuning springs stiffness

Playing with the length of the springs allows to obtain intermediate values of π. The springs used to connect the active elastic building blocks are helical compression springs (Fig. 2.9). They are good at standing elongation efforts, however, they bend almost directly when submitted to compression, resulting in a pretty non-linear response[18]. However, we are interested in varying their linear elastic properties. The stiffness k of such a coil spring reads:

$$k = \frac{Gd^4}{8nD^3} = \frac{Gpd^4}{8l_0D^3}, \tag{2.12}$$

where $G = E/2(1+\nu)$ is the wire's material shear modulus, E and ν are respectively the wire's Young modulus and Poisson ratio, d is the wire's diameter, n is the number of windings, D is the winding's diameter, and p is the pitch (Fig. 2.9). We tune the stiffness of *soft* springs by varying their length, the stiffness k of a coil spring being inversely proportional to l_0, all other parameters held constants (Eq. (2.12)). This allows for increasing the spring stiffness, i.e. decreasing the value of π.

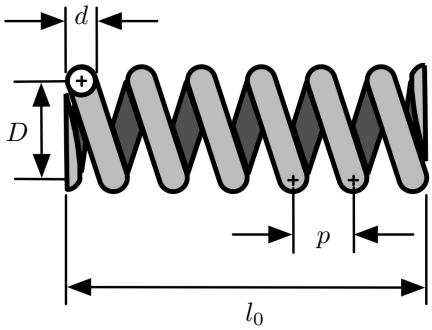


FIG. 2.9. **Helical spring cartoon.** Notations for the rest length l_0, pitch p, wire diameter d and winding diameter D. Adapted from [153].

2.4 Active networks

2.4.1 Active mechanical metamaterial

We create active mechanical metamaterials by combining the active elastic building blocks into $2d$ spring networks (Fig. 2.12-a). We let the system evolve on a white 5 mm thick square PMMA plate, with 130 cm sides. The dynamics of the active elastic structures are captured at 40 frames per second thanks to a camera[19] attached to the ceiling[20], and standard tracking software is used to capture the position and orientation

[18]This is less true for the *stiff* springs, which have a relatively large bending rigidity.
[19]Camera: PixeLink PL-D734MU; Lens: SIGMA ZOOM, 24-70 mm, 1:2.8, EX DG MACRO, ∅82
[20]Distance from the PMMA plate: 255 cm

dynamics of the particles (see section 2.5). Each node has a well-defined reference position in the network, but will be displaced by the active particles. In contrast, the polarity of each particle $\hat{\boldsymbol{n}}_i$ is free to rotate and reorients towards the node's displacement rate $\boldsymbol{v}_i$. This nonlinear elasto-active feedback between deformations and polarities is controlled by the ratio $\pi = l_e/l_a$ (see chapter 3), namely the elasto-active coupling; where l_e (resp. l_a) is the elasto-active length (resp. alignment length). When this coupling is large enough, we find that active units spontaneously organize into fascinating collective steady states (Figs. 2.12-b to j), which are governed by the boundary condition of the elastic structures.

2.4.2 Boundary condition

In the active elastic networks studied experimentally, a given node is either active, meaning that the associated annulus contains an active unit, or pinned, meaning that the associated annulus is empty and some constraints are applied to its degrees of freedom. In the following, we make the distinction between two different pinnings:

Pinned annulus

A *pinned annulus* contains a cylinder of the same height and diameter slightly smaller than the annulus' internal diameter (4.9 cm). This cylinder is fixed in the $2d$ plane, thanks to a small cleat fitting into holes pierced in the PMMA plate. In such a situation, the translational degrees of freedom of the annulus are frozen, but it can still freely rotate. This is the most common pinning condition in this work (Figs. 2.12-f to i), and it kills 2 degrees of freedom simultaneously (the x and y translational degrees of freedom). Note that one of such pinning points forbids any structure to translate, and a second one also kills the possibility of rotating freely. Eventually, a node of the network can be pinned without being an annulus, as shown in Fig. 2.12-e, where a single active unit connects via a rigid spring to a ball bearing (the so-called *abandoned dog* setup).

Embedded annulus

An *embedded annulus* stands below a massive object which forbids said annulus to translate and rotate because of solid friction. In this case, free rotation is killed because of the annulus' finite size and the finite bending rigidity of the real springs used. This pinning condition is illustrated in Fig. 2.12-j, and is only used in the associated experiment. It kills 3 degrees of freedom simultaneously, the x and y translational degrees of freedom and the rotational one.

2.4.3 Mechanical tension

In most of this work's experiments, even in the absence of activity in the network, the pinning condition prevents the springs from being at rest. The set of mechanical efforts in the springs in the reference configuration is called the *pre-stress*. This frustration has significant consequences on the mechanical properties of the networks and must be taken into account (see chapter 3). As we will generally consider regular lattices, the springs deform homogeneously to accommodate the pinning condition, for example, by elongating. We define the extension α of a given spring as the ratio l_{eq}/l_0, where l_0 is the rest length of the spring, and l_{eq} is the length of the spring in the stressed reference configuration. The larger the mechanical tension, the less the springs can explore compression during the dynamics, reducing nonlinearities coming from their non-idealized nature.

2.5 Tracking algorithm

Finally, we discuss the tracking algorithm used to extract data from the experimental movies (Fig. 2.12). Note that it can be found on a Zenodo database[21]. Let us consider a movie of N_{frame} images in greyscale illustrating the dynamics of N active units in an active elastic network. The tracking algorithm converts the set of *.png* images into a *.csv* file containing the trajectories $\{x_i(t), y_i(t), \theta_i(t)\}_{i\in[1,N]}$; where $x_i(t)$ (resp. $y_i(t)$) is particle i's annulus center along the x (resp. y) direction at time t; and where $\theta_i(t)$ is the orientation of the particle i at time t. For each picture of a movie (like Fig. 2.10-a), the algorithm goes through the following steps:

for $t \in [1, N_{frame}]$ **do**
- 1. Load video frame I_t;
- 2. Clean I_t; ▷ section 2.5.1
- 3. Detect circles $\{x_i, y_i, r_i\}_{i\in[1,N]}$; ▷ section 2.5.2
- **for** $i \in [1, N]$ **do**
  - 4. $A_i \leftarrow I_t|_{[x_i-r:x_i+r],[y_i-r:y_i+r]}$;
  - 5. Threshold: $\bar{A}_i \leftarrow A_i$;
  - 6. Detect $\theta_i \mod \pi$; ▷ section 2.5.3
- **end**
- **if** $t > 1$ **then**
  - 7. Mapping from I_t to I_{t-1}; ▷ section 2.5.4
- **end**

end

8. Find the correct directions for the θ_i's; ▷ section 2.5.5
9. Determine the displacement field; ▷ section 2.5.6

Algorithm 1: Main loop of the tracking algorithm

Note that our experimental movies are relatively easy to process because the annuli never touch each other, being in an elastic network, and because the orientations of the *hexbugs* are readily visible by the eye.

2.5.1 Image cleaning step

During this first simple step, one reduces the background noise to ease the annulus detection. One first defines a threshold t (generally equal to 120) and a Region Of Interest (ROI) in the image. Then, there are two stages:

- The image is restricted to the ROI.
- All pixels in the ROI with an intensity brighter than t are given the value t. This step avoids parasitic detection of circles in the white background by suppressing all kinds of fluctuations.

2.5.2 Annulus detection step

During the annulus detection step, the algorithm finds the circles $\{x_i, y_i, r_i\}_{i\in[1,N]}$ in the cleaned image, where the r_i's are the circles' radii. To do so, we use a Hough transform - a feature extraction technique that aims to find imperfect instances of objects within a certain class of shapes by a voting procedure. This voting procedure is carried out in a

[21] `https://zenodo.org/record/6653906`

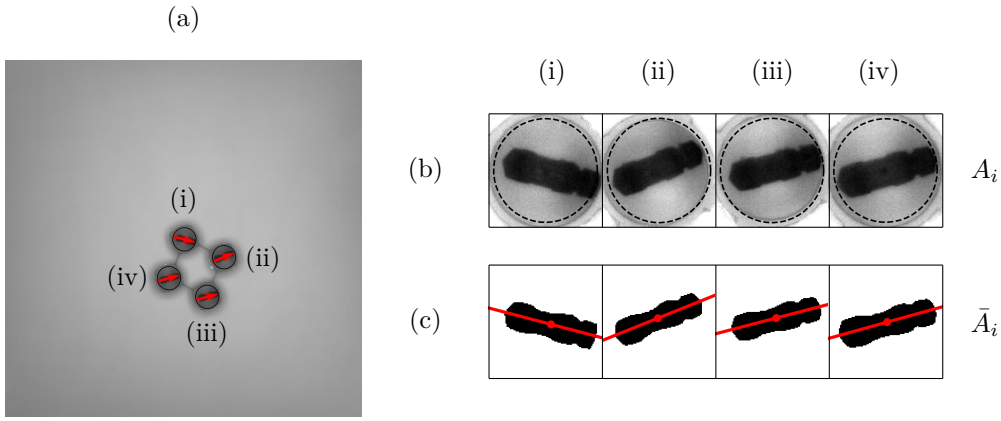


FIG. 2.10. **Tracking algorithm illustration.** (a) Typical image of a square active elastic structure, superimposed with the detected annulus (black circles) and orientations (red arrows). (b) Cleaned image restricted to the detected annulus. The black dashed circle represents the secondary circle for the last cleaning step. (c) Cleaned and thresholded image restricted to the detected annulus, superimposed with the sub-images barycenters (red markers) and main orientations (red lines). Detected annulus are numbered consistently from (i) to (iv).

so-called accumulator space, from which object candidates are obtained as local maxima. We use a built-in function of the Python package *OpenCV* called *cv2.HoughCircles*. This function finds circles in a grayscale image using a modification of the *Hough* transform[22], and has many parameters. Hereafter we detail the most important ones and the way they are set:

- *minDist*. Minimum distance between two detected circles' centers. Set manually by measuring the typical distance between annuli.
- *minRadius*. Minimum radius of detected circles. $minRadius = r - \Delta$, where r is the typical annuli radius, and Δ the accepted variance on the annuli radius (generally 10% of the annuli radius).
- *maxRadius*. Maximum radius of detected circles. $maxRadius = r + \Delta$, where r and Δ are the same parameters as for *minRadius*.
- *param1*. Upper threshold for the internal Canny edge detector (the lower one is twice smaller).
- *param2*. Threshold for center detection.

Nevertheless, the function *cv2.HoughCircles* cannot be given the number of circles trying to be detected. Assuming *param1* is well set to perform the appropriate edge detection, if *param2* is too large, there will not be enough circles detected, and reciprocally. Thus, we algorithmically fine-tune the value of *param2* in order to find the correct number of circles N.

[22] A circle is represented mathematically as $(x - x_i)^2 + (y - y_i)^2 = r_i^2$ where (x_i, y_i) is the center of the circle, and r_i is the radius of the circle. From this equation, we can see we have 3 parameters, so we need a $3d$ accumulator for the Hough transform, which would be highly ineffective. So *OpenCV* uses a trickier method, the Hough Gradient Method, which uses the gradient information of edges.

$\{x_i, y_i, r_i\}_{i\in[1,N_d]} \leftarrow$ *cv2.HoughCircles*(*param2*);
while $N_d \neq N$ **do**
  if $N_d > N$ **then**
    param2 $\leftarrow$ *param2*+1;
    $\{x_i, y_i, r_i\}_{i\in[1,N_d]} \leftarrow$ *cv2.HoughCircles*(*param2*);
  else
    param2 $\leftarrow$ *param2*−1;
    $\{x_i, y_i, r_i\}_{i\in[1,N_d]} \leftarrow$ *cv2.HoughCircles*(*param2*);
  end
end

Algorithm 2: Loop for annulus detection

At the end of this step, we find N sub-images centered on the detected annuli, namely A_i (Fig. 2.10-b).

2.5.3 Orientation detection step

To find the orientations of the *hexbugs*, we proceed by thresholding the sub-images A_i and computing their moments. This step is divided into three stages:

- Last cleaning step. In this stage, we give all pixels outside of a secondary circle of radius $r_i - \Delta$ the value t (Fig 2.10-b). This allows for suppressing any shadows on the annulus' edges which could be confounded with the *hexbug*'s body during the thresholding.

- Thresholding. The threshold is chosen so that the n_b darker pixels are set black, where n_b is set manually by measuring the typical area of a *hexbug*. To make the algorithm as robust as possible to shadows, this value is set to 90% of the measured *hexbug*'s area (typically 2000 pixels).

- Compute image moments. This part of the algorithm is largely inspired from[23]. One can find the main orientation θ_i of a set of black pixels by computing image moments. They are defined as weighted averages of the image pixels' intensities. In a greyscale image with pixel intensities $I(i, j)$, the raw (p,q)-moment $M_{p,q}$ is given by:

$$M_{p,q} = \sum_i \sum_j i^p j^q I(p, q), \tag{2.13}$$

  where the $I(p, q)$ are ones and zeros in a thresholded image. The zero-order moment $M_{0,0}$ gives the total number of pixels in the object, i.e. the object's area. The first-order moments $M_{1,0}$ and $M_{0,1}$, when normalized by $M_{0,0}$ give the coordinates of the barycenter in the horizontal and vertical directions, respectively:

$$\bar{x} = \frac{M_{1,0}}{M_{0,0}} \quad \text{and} \quad \bar{y} = \frac{M_{0,1}}{M_{0,0}}. \tag{2.14}$$

  Extracting the object orientation from the second-order moments $M_{2,0}$, $M_{1,1}$, and $M_{0,2}$ is not as immediate since one has to use the second-order central moments, which differ from the second-order raw moments. They can be written as follows:

$$\mu'_{2,0} = \frac{M_{2,0}}{M_{0,0}} - \bar{x}^2, \quad \mu'_{1,1} = \frac{M_{1,1}}{M_{0,0}} - \bar{x}\bar{y}, \quad \mu'_{0,2} = \frac{M_{0,2}}{M_{0,0}} - \bar{y}^2. \tag{2.15}$$

[23] Raphaël Candelier webpage `http://raphael.candelier.fr/` ; see article *Tracking object orientation with image moments.*

And the orientation θ of the object is given by:

$$\theta = \frac{1}{2} \arctan \left(\frac{2\mu'_{1,1}}{\mu'_{2,0} - \mu'_{0,2}} \right), \tag{2.16}$$

defined modulo π rad. Measured barycenters and orientations are shown in Fig. 2.10-c. The correct direction is eventually determined in the last step.

2.5.4 Matching step

In order to obtain the full trajectories of particles during the movie, we perform the association between the N detected particles at time t and at time $t - \delta t$. Matching is easy to do because of the relatively large frame rate used. Indeed, the annuli move so little between two images that the association can be done by simply identifying the closest annuli between two images. In addition, we correct the possible orientation jumps there could be for all particles between time t and time $t - \delta t$, as the orientations are defined modulo π rad.

2.5.5 Finding the correct directions

Hexbugs tend to move in the forward direction on average, which allows us to find the correct orientation for each active particle. They are determined by integrating $\delta \boldsymbol{r}_i(t) \cdot \hat{\boldsymbol{n}}_i(t)$ along the dynamics, where $\delta \boldsymbol{r}_i(t) = \boldsymbol{r}_i(t + \delta t) - \boldsymbol{r}_i(t)$, and determining its sign for each *hexbug*. If it is positive, then the direction is the correct one, otherwise we add π rad to the time serie of $\theta_i(t)$.

2.5.6 Determining the displacement field

Before to process the experimental trajectories, the last step is to determine the displacement field $\{u_i^x(t), u_i^y(t)\}$ from the positions $\{x_i(t), y_i(t)\}$, which requires the knowledge of the reference configuration $\boldsymbol{R}_i$. The displacements are defined as $\boldsymbol{u}_i = \boldsymbol{r}_i - \boldsymbol{R}_i$.

Active and pinned nodes

Let us determine, from the experimental data, which nodes are pinned and which ones are active. To do so, we apply a simple criterion on the standard deviation of the position time series. If it is smaller than a given threshold (typically 5 pixels), then the associated node is considered pinned. Conversely, it is considered active.

Find the reference configuration

Once the boundary condition is detected, the next step is to find the structure's reference configuration. Because our systems are always symmetric, it can be done by first explicitly measuring the pinned nodes' reference positions, and then interpolating the active nodes' ones, using intersections of segments connecting pinned nodes (Fig. 2.11).

By convention, we consider that the reference position of a pinned node is given by measuring its mean position during the dynamics, which allows averaging the tracking errors on its position. Fig. 2.11-a represents the reference position of the detected pinned nodes (black markers) for a triangular lattice with hexagonal pinned boundaries. Note that all detected active and pinned nodes are numbered consistently from 0 to $N - 1$. To find the reference position of active node i, we then use the symmetry of the lattice. For a regular triangular lattice with hexagonal boundaries, the reference position of any

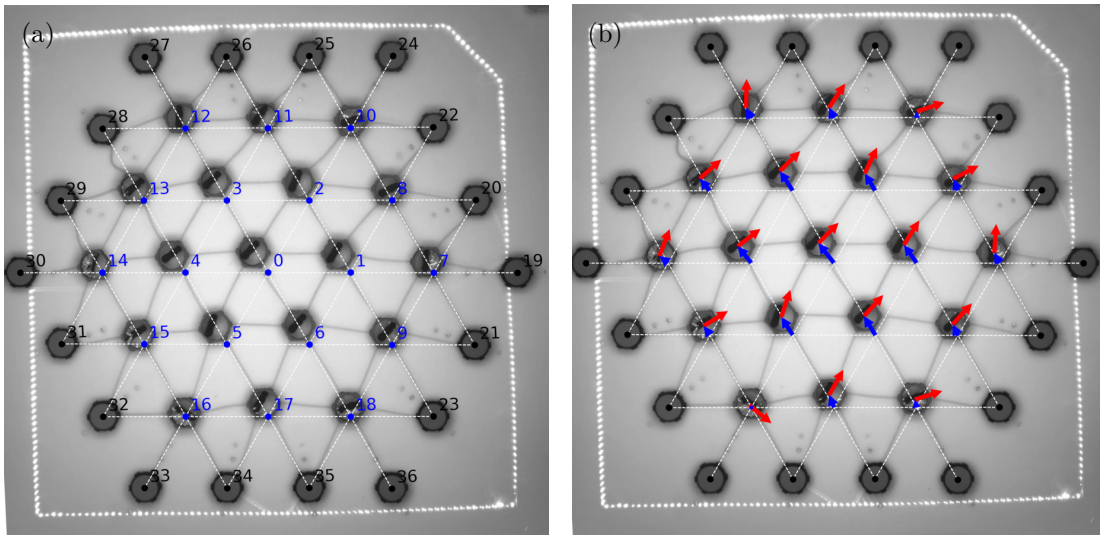


FIG. 2.11. **Reference configuration from experimental data.** Collective dynamics in an active triangular lattice with hexagonal pinned boundaries ($N = 19$, $\alpha = 1.27$), and illustration of the experimental processing. (a) The reference configuration is found by triangulating the equilibrium positions of the free nodes (blue markers) thanks to the intersections between segments of pinned nodes (black markers). (b) Representation of the instantaneous polarity and displacement fields in the experiment. Red arrows: polarities $\hat{\boldsymbol{n}}_i$; blue arrows: displacements $\boldsymbol{u}_i$. Pinned nodes are represented with black markers.

Active node	Segment a	Segment b	Segment c
0	(19,30)	(24,33)	(27,36)
1	(19,30)	(22,34)	(23,26)
2	(24,33)	(20,29)	(23,26)
3	(27,36)	(25,32)	(20,29)
4	(25,32)	(19,30)	(28,35)
5	(28,35)	(21,31)	(24,33)
6	(27,36)	(22,34)	(21,31)
7	(20,35)	(21,25)	(19,30)
8	(22,34)	(21,25)	(20,29)
9	(21,31)	(20,35)	(23,26)
10	(24,33)	(22,28)	(21,25)
11	(23,26)	(22,28)	(25,32)
12	(22,28)	(26,31)	(27,36)
13	(20,29)	(28,35)	(26,31)
14	(19,30)	(29,34)	(26,31)
15	(25,32)	(29,34)	(21,31)
16	(23,32)	(24,33)	(29,34)
17	(28,35)	(23,32)	(22,34)
18	(27,36)	(23,32)	(20,35)

Table 2.3: Mapping between free nodes' reference positions and intersections of segments of pinned nodes. The reference position of node i is given by the triangulation of the intersections between the three segments of pinned nodes a, b and c.

of the free nodes is at the intersection of three segments linking opposite pinned nodes. Table 2.3 gives the mapping between the index of a free node and the three segments of pinned nodes in the case of the structure of Fig. 2.11-a. In experiments, because some spatial disorder is intrinsically present, the three segments do not intersect at a single point but at three locations. The reference position of the associated active node

is triangulated at the barycenter of those intersections. Therefore, we find the complete reference configuration, the $\{x_i^{eq}, y_i^{eq}\}_{i\in[1,N]}$, shown in Fig. 2.11-a (blue markers).

At the end of this process, the trajectories $\{x_i(t), y_i(t), \theta_i(t)\}_{i\in[1,N]}$ are converted into the displacement and polarity field time series $\{u_i^x = x_i(t) - x_i^{eq}, u_i^y = y_i(t) - y_i^{eq}, n_i^x = \cos\theta_i, n_i^y = \sin\theta_i\}_{i\in[1,N]}$; represented in Fig. 2.11-b at a given time.

2.5.7 Error estimates

Positions

The detection errors on the annuli positions mostly come from the possibility of detecting both the internal and external rings of the annulus. Once contours are detected, these two rings are relatively similar, and because of noise in the picture, the tracking algorithm may detect any circle between the two rings (can be slightly witnessed in Fig. 2.10-b, ii). Moreover, the difference in ring radius is roughly 5 pixels. Consequently, the position error on the annulus' positions is typically 5 pixels, to compare with the annulus radius, which is typically 50 pixels. Denoting the error on the detected positions Δu, and the annulus internal diameter d, we have $\Delta u/d \simeq 1/20$.

Orientations

The orientation detection is precise and robust, because it measures the spatial organization of typically 2000 pixels. The bottleneck of orientation detection is related to the annuli position detection. If the annulus' position is measured with a too large error, then the thresholding operation will cut the *hexbug*'s shape and bias the orientation measurement. This error is tough to evaluate, but we estimated it manually, and found that the angles are detected modulo a typical error of $\Delta\theta \simeq 3°$.

Projections

Using the error estimates on the detected positions and orientations, we can also have the error estimates on the displacement/polarity field projections on the normal modes (see chapter 3, where the normal modes are properly defined an characterized). For the normalized polarity field projection on a given mode $\langle\boldsymbol{\varphi}_k|\hat{\boldsymbol{n}}\rangle/\sqrt{N}$, it yields:

$$\Delta\left[\frac{\langle\boldsymbol{\varphi}_k|\hat{\boldsymbol{n}}\rangle}{\sqrt{N}}\right] = \sum_i \Delta\theta_i|\boldsymbol{\varphi}_k^i||\sin\theta_i|/\sqrt{N} \leq \frac{\Delta\theta}{\sqrt{N}}\sum_i|\boldsymbol{\varphi}_k^i| = \Delta\theta\sqrt{Q_k}, \tag{2.17}$$

where we have assumed $\Delta\theta_i = \Delta\theta$ and where $Q_k = \left(\sum_i|\boldsymbol{\varphi}_k^i|\right)^2/N$ is mode k's participation ratio, bounded between 0 and 1 (see chapter 3). Therefore, the error on the polarity field projection on a given mode depends on said mode's extension. As an example, for a plane-wave mode $Q_k \simeq 0.67$, and we find $\Delta\left[\langle\boldsymbol{\varphi}_k|\hat{\boldsymbol{n}}\rangle^2/N\right] = 2\frac{\langle\boldsymbol{\varphi}_k|\hat{\boldsymbol{n}}\rangle}{\sqrt{N}}\Delta\left[\frac{\langle\boldsymbol{\varphi}_k|\hat{\boldsymbol{n}}\rangle}{\sqrt{N}}\right] \simeq 0.05$[24]: the fraction of active force injected in a given mode is thus given modulo a typical 5% error due to tracking inaccuracies. For the normalized displacement field projection on a given mode $\langle\boldsymbol{\varphi}_k|\boldsymbol{u}\rangle/\sqrt{N}$, the error can be written as follows:

$$\begin{aligned}\Delta\left[\frac{\langle\boldsymbol{\varphi}_k|\boldsymbol{u}\rangle}{\sqrt{N}}\right] &= \sum_i\left(|\boldsymbol{\varphi}_{k,x}^i|\Delta u_{i,x} + |\boldsymbol{\varphi}_{k,y}^i|\Delta u_{i,y}\right)/\sqrt{N},\\ &= \Delta u\sum_i\left(|\boldsymbol{\varphi}_{k,x}^i| + |\boldsymbol{\varphi}_{k,y}^i|\right)/\sqrt{N} \simeq \Delta u\sqrt{Q_k},\end{aligned} \tag{2.18}$$

[24] Assuming a condensation fraction $\frac{\langle\boldsymbol{\varphi}_k|\hat{\boldsymbol{n}}\rangle^2}{N} = 1$, that is, all the active force injected in the same mode (error upper bound)

where we have assumed $\Delta u_{i,x} = \Delta u_{i,y} = \Delta u$. Note that the last approximation underestimates the error from the Cauchy-Schwarz inequality, but the final formula is good enough to provide reasonable confidence intervals. Interestingly, both for the projections of the displacement and polarity fields, the error depends on the extension of the mode.

2.6 Conclusion

At the end of this chapter, we constructed model active solids experiments by embedding *hexbugs* within genuine spring networks, and observed fascinating dynamics (Fig. 2.12). The tracking algorithm then allows for determining the experimental trajectories of the displacement and polarity vectors. The next chapter describes the theoretical framework used to analyze those trajectories.

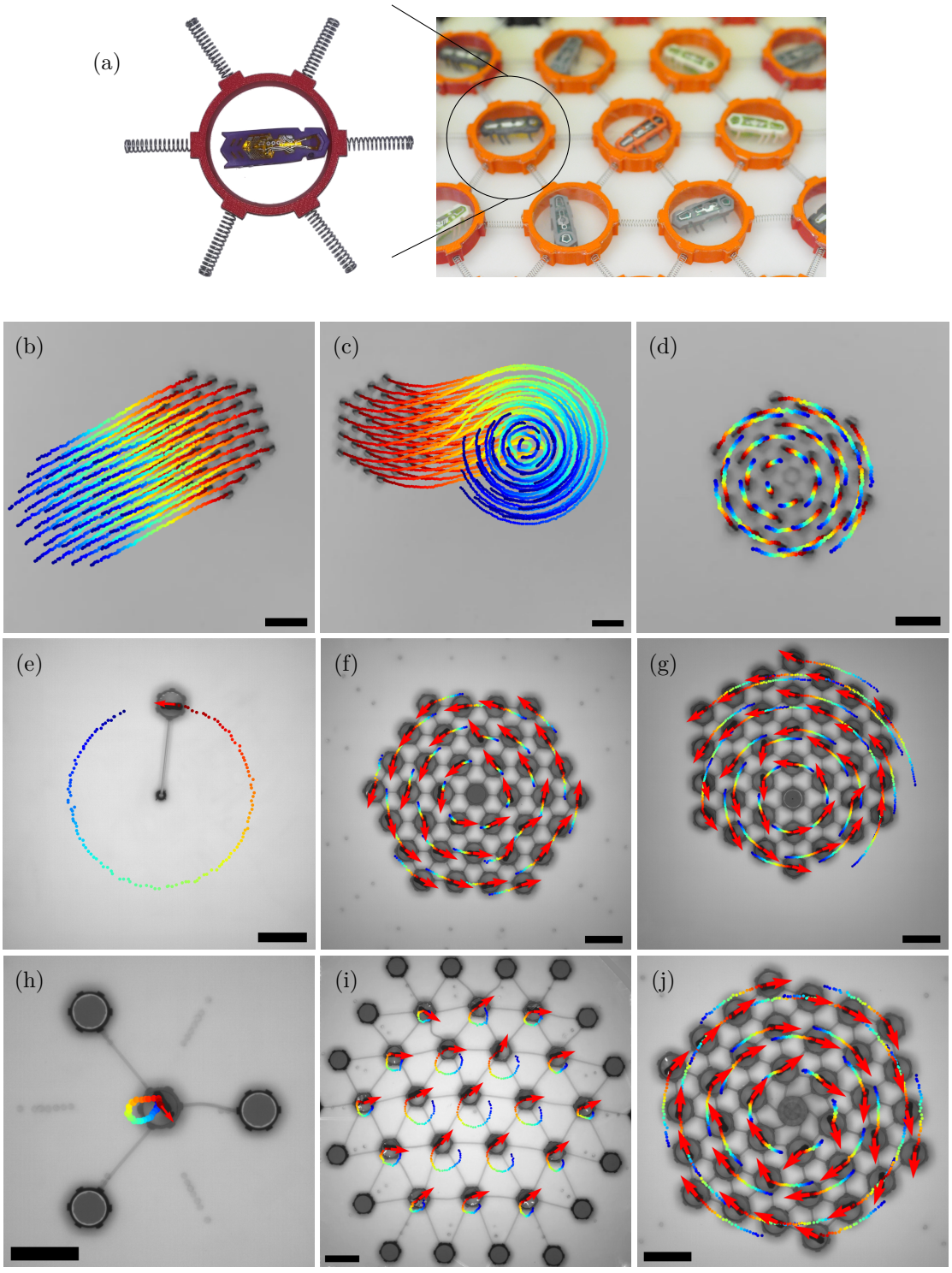


FIG. 2.12. **Overview of the experimental results.** (a) The active elastic building blocks are combined with coil springs to form an active elastic lattice. (b-j) Emerging collective dynamics in model active solids with various boundary conditions. Red arrows: polarities $\hat{\boldsymbol{n}}_i$; trajectories color-coded from blue to red by increasing time; scale bars: 10 cm. (top line) Collective motions in free boundary conditions (see chapter 4). (middle line) Collective rotations around a single pinning point (see chapter 4). (bottom line) Collective actuation in mechanically stable elastic structures (see chapter 5 and 6). (b) Stable translation regime. (c) Unstable rotation regime. (d) Stable rotation regime. (e) Stable rotation of an *abandoned dog*. (f) Stable rotation for central pinning. (g) Stable rotation for arbitrary pinning. (h) Orbiting regime of a single particle embedded in a harmonic trap. (i) CA of a triangular lattice pinned at its edges. (j) CA of a triangular lattice with embedded central pinning.

Date	Type of experiments	Chapter	Number of sub-runs*	Springs type	Local arrangement	Boundaries	Pinning condition**	Pre-stress α***	N	Number of images	Size of images (Go)
Jun. 2021	alignment	3	15	*stiff*	square	square	EPC	1.0	1	15000	2.7
Jul. 2020	acceleration	3	1	-	-	-	FBC	-	1	6000	0.2
Apr. 2021	traction	3	1	*soft*	linear	linear	EPC	1.0	1	13000	6.2
Aug. 2020	dynamics	4	1	*stiff*	triangular	hexagonal	FBC	1.0	[36-37]	72000	86
Jun. 2020	dynamics	4	1	*stiff*	triangular	hexagonal	CPC	1.0	36	10000	21
Oct. 2021	dynamics	4	1	*stiff*	square	square	CPC	1.0	24	10000	21
Sep. 2020	l_0 annealing	4	11	*rigid*	triangular	hexagonal	CPC	1.0	[6-36]	110000	231
Sep. 2021	l_0 annealing	4	6	*rigid*	linear	dumbell	CPC	1.0	1	60000	42
Jul. 2020	π annealing	5	11	*soft*	triangular	hexagonal	EPC	1.27	[7-19]	110000	231
Dec. 2020	π annealing	5	9	*soft*	kagome	hexagonal	EPC	1.02	12	90000	180
Jul. 2020	π annealing	5	6	*soft*	honeycomb	triangular	EPC	1.35	1	60000	126
Oct. 2020	π annealing	5	10	*soft*	linear	linear	EPC	2.45	3	100000	84
Jun. 2020	dynamics	6	1	*stiff*	triangular	hexagonal	ECPC	1.0	36	10000	21
Mar. 2021	α annealing	6	11	*soft*	gerris	hexagonal	EPC	[1.0-1.2]	6	220000	132
Jul. 2022	g annealing	7	11	*stiff*	square	square	EPC	1.0	1	110000	116
Jul. 2022	g annealing	7	11	*soft*	honeycomb	triangular	EPC	1.16	1	110000	116
Jul. 2022	g annealing	7	11	*stiff*	square	rectangular	OSPC	1.28	[24-48]	330000	347
Jun. 2020	dynamics	8	1	*stiff*	square	square	ECPC	1.0	24	10000	21
Feb. 2022	mechanical test	8	5	*stiff*	square	rectangular	OSPC	1.09	20	29000	57
Feb. 2022	mechanical test	8	5	*stiff*	square	square	OSPC	1.0	25	14000	28
Jul. 2022	walking grains	8	16	*soft*	linear	linear	EPC	[1.0-1.3]	18	384000	54
Sep. 2021	walking grains	8	1	*soft*	honeycomb	hexagonal	EPC	1.0	180	10000	21

* Number of experimental runs with for the annealings.
** EPC: Edge Pinning Condition; CPC: Central Pinning Condition; ECPC: Embedded Central Pinning Condition; OSPC: Opposite Sides Pinning Condition.
*** Springs elongation in the reference configuration.

Table 2.4: All the experimental data. Summary of all the experiments runt during the PhD.

Chapter 3

Agent-based model

We complement the experiments discussed in the previous chapter with the numerical simulations and theoretical analysis of a model of elastically coupled self-aligning active particles [1, 143]. This chapter consists of a pedagogical derivation of the following equations, which describe our system within the *overdamped limit* and *harmonic approximation*:

$$\dot{\boldsymbol{u}}_i = \pi \hat{\boldsymbol{n}}_i - \mathbb{M}_{ij}\boldsymbol{u}_j, \tag{3.1a}$$

$$\dot{\boldsymbol{n}}_i = (\hat{\boldsymbol{n}}_i \times \dot{\boldsymbol{u}}_i) \times \hat{\boldsymbol{n}}_i + \sqrt{2D}\xi_i \hat{\boldsymbol{n}}_i^{\perp}, \tag{3.1b}$$

where the $\hat{\boldsymbol{n}}_i$'s are the polarity vectors, the $\boldsymbol{u}_i$'s are the displacements vectors with respect to the reference configuration, $\mathbb{M}$ is the dynamical matrix (see section 3.2.3), and the ratio of the elasto-active and alignment lengths, $\pi = l_e/l_a$, which we refer to as the elasto-active coupling, is the unique microscopic control parameter.

We first discuss the equations of motion for a single active particle in a harmonic trap. We then remind the key concepts of the mechanics of passive discrete networks. By combining these two frameworks, we find Eqs. (3.1), and examine their properties. Finally, we elaborate on the numerical simulations of this agents model.

3.1 Single particle in a harmonic trap

The single active particle in a harmonic trap is the first ingredient of understanding. Let us establish the equations governing its physics.

Experimentally speaking, a single active particle in a harmonic trap consists of a *hexbug* evolving in a parabolic dish (Fig. 3.1). The combination of the surface's geometry and gravity creates a harmonic potential, driving the active unit toward the origin of the parabolic dish. This system is the simplest instance combining activity and elasticity: there is only one active particle, and elasticity is a purely linear restoring force along the radial direction. The dynamics of an active particle in a harmonic potential was studied experimentally, numerically, and theoretically by *Dauchot and Démery* in [143]. Here we mostly adapt the analysis to make a consistent first step toward active solids.

We consider a single active *self-aligning* polar particle such as those described in [57, 58, 143]; and connected by a linear spring of stiffness k and zero-rest-length to the origin. The elastic force can be written $\boldsymbol{F}^{el} = -k\boldsymbol{u}$; where $\boldsymbol{u}$ the displacement of the active particle with respect to the origin; which is equivalent to the force deriving from the

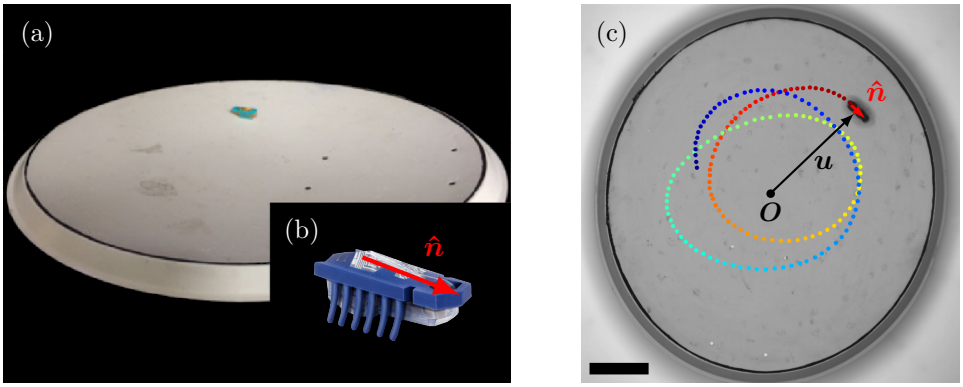


FIG. 3.1. **Single active particle in a harmonic trap.** *Hexbug* (b) running in an actual parabolic dish (a). Adapted from [143]. (c) Orbiting dynamics of a *hexbug* in an actual parabolic dish, and notations. The origin is chosen to be the bottom of the harmonic well $\boldsymbol{O}$. Red arrow: polarity $\hat{\boldsymbol{n}}$; trajectory color-coded from blue to red by increasing time; scale bars: 10 cm.

gravitational potential energy in a parabolic well. The activity takes the form of a force $\boldsymbol{F}_a = F_0\hat{\boldsymbol{n}}$ along the polarity $\hat{\boldsymbol{n}}$ of the particle. The equations describing the dynamics of this system are

$$m\frac{d\boldsymbol{v}}{dt} = F_0\hat{\boldsymbol{n}} - \gamma\boldsymbol{v} - k\boldsymbol{u}, \tag{3.2a}$$

$$\tau\frac{d\hat{\boldsymbol{n}}}{dt} = \zeta(\hat{\boldsymbol{n}}\times\boldsymbol{v})\times\hat{\boldsymbol{n}} + \sqrt{2\alpha}\xi\hat{\boldsymbol{n}}^{\perp}, \tag{3.2b}$$

where m is the mass of the active particle, γ the effective friction coefficient, and k the stiffness of the spring. In the absence of confinement, the particle thus moves with a cruise velocity $v_0 = F_0/\gamma$. The orientation dynamics Eq. (3.2b) contains the key ingredient, specific to the model, namely the presence of a self-aligning torque of the orientation $\hat{\boldsymbol{n}}$ towards the velocity $\boldsymbol{v}$. At a conceptual level, this torque originates from the fact that the dissipative force is not symmetric with respect to the propulsion direction $\hat{\boldsymbol{n}}$ when $\boldsymbol{v}$ is not aligned with $\hat{\boldsymbol{n}}$. Importantly, the *self-alignment* torque is proportional to the velocity, giving rise to an alignment length $l_a = \tau/\zeta$. Finally, the orientation dynamics contains a delta-correlated Gaussian noise $\xi(t)$ with zero mean and correlations $\langle\xi(t)\xi(t')\rangle = \delta(t-t')$; and α/τ^2 is the rotational diffusion coefficient. Those orientation fluctuations are not of thermal origin but model the mechanical noise present in the experiments.

Rescaling length by the alignment length $u_0 = \tau/\zeta = l_a$ and time by $t_0 = \gamma/k$, the characteristic relaxation time of a $1d$ mass-spring system, the dimensionless equations of motion read

$$\tau_v\frac{d\boldsymbol{v}}{dt} = \pi\hat{\boldsymbol{n}} - \boldsymbol{v} - \boldsymbol{u}, \tag{3.3a}$$

$$\frac{d\hat{\boldsymbol{n}}}{dt} = (\hat{\boldsymbol{n}}\times\boldsymbol{v})\times\hat{\boldsymbol{n}} + \sqrt{2D}\xi\hat{\boldsymbol{n}}^{\perp}, \tag{3.3b}$$

with three parameters, $\tau_v = mk/\gamma^2$ the dimensionless inertia; $\pi = F_0/kl_a = l_e/l_a$ the dimensionless activity, or active-elastic coupling; and $D = \alpha\gamma/k\tau^2$, the dimensionless angular noise. Note that $\pi = l_e/l_a$, where $l_a = \tau/\zeta$ is the alignment length, that is the length over which $\hat{\boldsymbol{n}}$ aligns toward $\boldsymbol{v}$, and $l_e = F_0/k$ is the elasto-active length, which is the distance that the active force can drive away the particle from its equilibrium

position, given the elastic restoring force.

Dauchot and Démery demonstrated the existence of two dynamical states for which the particle condensates at a finite distance from the trap center [143]. In the low-activity *climbing* state, also found in other systems[1], the particle points radially outward from the trap, while diffusing along the azimuthal direction. In contrast, as activity increases, the system transitions to the *orbiting* state (Fig. 3.1-b), where the particle performs circular trajectories around the trap's center. At low inertia (small τ_v), the transition happens at $\pi = 1$ and is continuous. Crucially, it originates from the self-alignment torque in the polarity dynamics; an ingredient initially introduced to explain the emergence of collective motion in systems of vibrated polar discs [57, 58] and migrating cells [68]. For large inertia, the transition is discontinuous and a coexistence regime with intermittent dynamics develops. Interestingly, the authors show that the two states survive in the overdamped limit or when the particle is confined by a hard curved wall.

Overdamped limit

In line with the prospect of describing biological systems, and in agreement with the measurements of the experimental parameters, we take the overdamped limit of Eqs. (3.3). It reduces to take $\tau_v \to 0$ in the position dynamics, Eq. (3.3a). It yields:

$$\frac{d\boldsymbol{u}}{dt} = \pi\hat{\boldsymbol{n}} - \boldsymbol{u}, \tag{3.4a}$$

$$\frac{d\hat{\boldsymbol{n}}}{dt} = (\hat{\boldsymbol{n}} \times \dot{\boldsymbol{u}}) \times \hat{\boldsymbol{n}} + \sqrt{2D}\xi\hat{\boldsymbol{n}}^{\perp}. \tag{3.4b}$$

In the overdamped limit, the torque in Eq. (3.4b) reorients the polarity vector towards the elastic force $\boldsymbol{F}^{el} = -\boldsymbol{u}$ acting on the active particle, because the term $\pi\hat{\boldsymbol{n}}$ does not contribute to rotate $\hat{\boldsymbol{n}}$. Note that we have reached the one-particle version of Eqs. (3.1).

3.2 Mechanics of passive networks

In this section, we take a step back and review the basic elements of understanding required to study the statics and dynamics of passive spring networks, from mechanical stability to the harmonic approximation. In the first section, elasticity was a trivial harmonic potential. We now consider a network of N passive masses, or nodes, connected by bonds occupied by central-force springs (also called a *frame*).

3.2.1 Mechanical stability

A crucial property of spring networks is *mechanical stability* - having a well-defined reference configuration satisfying mechanical equilibrium. This requires the spring network to be stable with respect to any set of displacements of the nodes when it lies close to its reference configuration. In the following, we start by discussing the general principles governing the mechanical stability of frames in terms of constraint satisfaction problems.

the Maxwell rule

In 1864, James Clerk Maxwell undertook the first systematic study of the mechanical stability of frames [154]. He defined a *stiff* frame as one in which "the distance between

[1] For example, ABPs in a parabolic trap only exhibit *climbing* dynamics.

two points cannot be altered without changing the length of one or more connections", which is equivalent to the above definition for *mechanical stability*. He showed that a *stiff* frame containing N sites in dimension d requires:

$$N_c = dN - f(d), \tag{3.5}$$

connections, where $f(d) = d(d+1)/2$ is the number of rigid body translations and rotations under free boundary conditions in dimension d. This relation, so-called Maxwell's rule, can be reexpressed as a critical coordination number:

$$z_c = 2d - 2\frac{f(d)}{N}. \tag{3.6}$$

If the coordination $z = 2N_c/N < z_c$, the system is not *stiff*, and if $z > z_c$, it is (in the $2d$ plane, $z_c = 4$). Unfortunately, the simple Maxwell's rule for the stability of frames requires modification [155, 156].

Generalized Maxwell relation

Let us start from scratch: N disconnected points in dimension d. Each site has d independent translational degrees of freedom, and in the absence of connections, they are all decoupled and form dN zero-energy displacement modes (without any restoring force), which we will refer to as *zero modes*. Let us consider that each new connection reduces the number of zero modes by one. Therefore, if there are N_c connections, there are

$$N_0 = dN - N_c, \tag{3.7}$$

zero modes. Of these, $f(d)$ are the trivial ones associated with rigid body translations and rotations. Any other zero modes involve internal displacements of the sites and are generally called *floppy modes* or *mechanisms*. Eq. (3.7), reexpressed in terms of the number of mechanisms M, is

$$M = dN - N_c - f(d), \tag{3.8}$$

which is also called Maxwell's count. A frame is *stiff* if it has no mechanisms. Setting $M = 0$ yields the Maxwell rule, Eq. (3.5). Fig. 3.2-a depicts a simple frame that obeys Maxwell's count. It consists of $N = 6$ nodes and $N_c = 7$ bonds, and it has $N_0 = 2 \times 6 - 7 = 5$ zero modes and $M = N_c = 5 - 3 = 2$ mechanisms. However, the simple Maxwell's count does not apply to all frames, because each new connection does not reduce the number of zero modes by one. Consider the pedagogical example given in [156]: a two-square frame with $N = 6$ sites and $N_c = 8$ bonds, shown in Fig. 3.2-b. It has one mechanism, as expected from the Maxwell count. If an extra bond is added, Maxwell's rule would say that the frame is stiff with no mechanisms. However, the extra bond can be placed as a diagonal in the right square (Fig. 3.2-c), or as an extra diagonal in the left square (Fig. 3.2-d). In the first case, there are no mechanisms, and Maxwell's count applies. In the second case, however, the mechanism present before the extra bond was added remains, and Maxwell's count is violated. Nevertheless, the left square with crossed diagonal bonds has an extra redundant bond not needed for its rigidity. It also has a new and interesting property: the outer bonds of the square can be placed under tension (compression), and the inner diagonal bonds under compression (tension) such that the net force on all sites is zero. This is a state of *self-stress*. This process can clearly be repeated with each added bond, either decreasing the number of zero modes

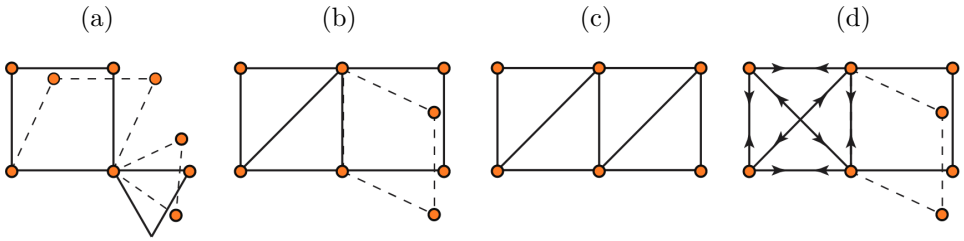


FIG. 3.2. **Floppy modes and self-stress states.** (a-c) Frames satisfying the Maxwell rule. (a) has 6 sites, 7 bonds, and 5 zero modes, among which there are two mechanisms, indicated by the dotted bonds. (b) has 6 sites, 8 bonds, and 4 zero modes, among which there is one mechanism. (c) and (d) are constructed from (b) by adding an additional diagonal bond. (c) satisfies the Maxwell rule with only the three trivial zero modes. (d) has 4 zero modes and one state of self-stress indicated by the arrows on the bonds in the left square. Adapted from [156]

or increasing the number of states of self-stress, to yield the generalized Maxwell relation [156]:

$$M - N_s = dN - N_c - f(d), \tag{3.9}$$

where N_s is the number of self-stress states. Given the number of self-stress states, one can thus say if the structure is *stiff*.

Remarks

However, even the generalized Maxwell relation, Eq. (3.9), is not a sufficient condition to assess the mechanical stability/number of zero modes of a structure. Indeed, as an algebraic constraint counting relationship, it does not consider the *pre-stress*, i.e. the set of stresses in the bonds in the reference configuration [157]. As it increases, the structure's deformation modes and their corresponding energies change via two mechanisms. (i) Tension (compression) stiffens (weaken) the bonds, and the modes' energies increases/decreases/stagnate depending on how the geometry of the normal modes compares to the stress pattern and bond orientations. In particular, the energy of a mode increases if tension increases perpendicularly to its polarization[2]. (ii) Force balance on the nodes changes their equilibrium positions, modifying the structure of the interactions between them, which can have severe consequences on the vibrational properties. These effects can transform a zero mode at the qualitative level, violating all the above rules. In the rest of this work, a *mechanically stable* elastic structure refers to one in which there are no zero modes, the conditions for which are yet to be discussed.

3.2.2 Equations of motion

We now describe spring networks from a dynamical system point of view. Let us consider N passive masses, connected by linear springs of stiffness k and unstressed length l_0. The system's physics reduces to N position dynamics equations:

$$m\frac{d^2\boldsymbol{r}_i}{dt^2} = -\gamma\frac{d\boldsymbol{r}_i}{dt} + \sum_{j\in\partial i} k\left(|\boldsymbol{r}_i - \boldsymbol{r}_j| - l_0\right)\hat{\boldsymbol{e}}_{ij}, \tag{3.10}$$

where $\boldsymbol{r}_i$ is the position vector of particle i, m is the mass of the particles, γ is the friction coefficient, k the stiffness of the springs, ∂i refers to the neighbors of node i, and $\hat{\boldsymbol{e}}_{ij}$ is the unit vector from i to j.

[2]This is commonly experienced when tuning a guitar string.

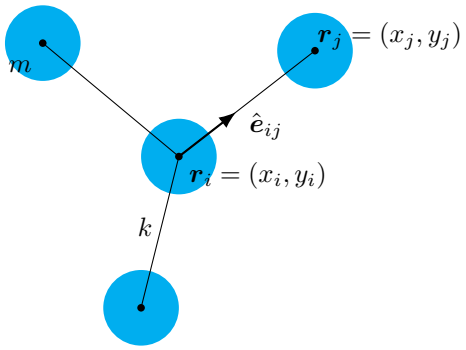


FIG. 3.3. **Notations for passive springs network.** The unit vector $\hat{\boldsymbol{e}}_{ij}$ points from particle i to particle j.

Next, we write down the dimensionless form of Eq (3.10) under two different choices of time units, knowing there is only one length scale in this system ($r_0 = l_0$).

Inertial limit

The regular time scale chosen in elasticity is $t_0 = \sqrt{m/k}$, the typical period of a $1d$ mass-spring oscillator. We call this choice of units the *inertial scheme*:

$$\frac{d^2\boldsymbol{r}_i}{dt^2} + \frac{1}{\sqrt{\tau_v}}\frac{d\boldsymbol{r}_i}{dt} = \sum_{j\in\partial i} \left(|\boldsymbol{r}_i - \boldsymbol{r}_j| - 1\right) \hat{\boldsymbol{e}}_{ij}, \tag{3.11}$$

where $\tau_v = mk/\gamma^2$ is the same dimensionless inertia as in section 3.1. In this scheme, the overdamped limit ($\tau_v \to 0$) is singular and one would instead study the inertial limit ($\tau_v \to \infty$), for which friction becomes negligible:

$$\frac{d^2\boldsymbol{r}_i}{dt^2} = \sum_{j\in\partial i} \left(|\boldsymbol{r}_i - \boldsymbol{r}_j| - 1\right) \hat{\boldsymbol{e}}_{ij}. \tag{3.12}$$

Overdamped limit

When friction dominates over inertia, as in biological active solids, the unit of time is chosen to be $t_0 = \gamma/k$, the typical relaxation time of an overdamped $1d$ mass-spring system. This is indeed more relevant when planning to use the overdamped limit to avoid vanishing time units. We call this choice of units the *frictional scheme*:

$$\tau_v\frac{d^2\boldsymbol{r}_i}{dt^2} + \frac{d\boldsymbol{r}_i}{dt} = \sum_{j\in\partial i} \left(|\boldsymbol{r}_i - \boldsymbol{r}_j| - 1\right) \hat{\boldsymbol{e}}_{ij}, \tag{3.13}$$

where $\tau_v = mk/\gamma^2$ is again the dimensionless inertia. In this scheme, the overdamped limit ($\tau_v \to 0$), for which inertia becomes negligible, is well-defined:

$$\frac{d\boldsymbol{r}_i}{dt} = \sum_{j\in\partial i} \left(|\boldsymbol{r}_i - \boldsymbol{r}_j| - 1\right) \hat{\boldsymbol{e}}_{ij}. \tag{3.14}$$

3.2.3 Harmonic approximation

In this section, we can put ourselves in the most general framework of a heterogeneous springs network. In this case, the elastic force acting on node i can be written as follows:

$$\boldsymbol{F}_i^{\text{el}} = \sum_{j\in\partial i} k_{ij}\left(|\boldsymbol{r}_i - \boldsymbol{r}_j| - l_0^{ij}\right)\hat{\boldsymbol{e}}_{ij} = \sum_{j\in\partial i} k_{ij}\left(1 - \frac{l_0^{ij}}{|\boldsymbol{r}_j - \boldsymbol{r}_i|}\right)(\boldsymbol{r}_j - \boldsymbol{r}_i), \tag{3.15}$$

where k_{ij} (resp. l_0^{ij}) is the dimensionless stiffness (resp. rest length) of the spring between nodes i and j. We introduce the displacement field $\boldsymbol{u}_i$, defined as the set of displacements with respect to the reference configuration $\boldsymbol{R}_i$, $\boldsymbol{r}_i = \boldsymbol{R}_i + \boldsymbol{u}_i$, as done in the Cauchy-Born theory of elastic solids [157]. Notably, in what follows, there is no need for a well-defined reference configuration, as long as the system is in a stable mechanical equilibrium at $\boldsymbol{R}_i$. If, for some bonds $l_0^{ij} \neq l_{\text{eq}}^{ij}$, where l_{eq}^{ij} is the dimensionless equilibrium length of the spring between nodes i and j in the reference configuration; then the reference configuration has *pre-stress*.

The *harmonic approximation* consists of writing an approximate expression of the elastic force close to the configuration $\boldsymbol{R}_i$, written only in terms of the displacement vectors $\boldsymbol{u}_i$.

Geometrical nonlinearities

While the response of the springs is linear along their axis, the elastic force (Eq. (3.15)) is very much nonlinear due to the geometry of the unit vectors $\hat{\boldsymbol{e}}_{ij}$, which express as $(\boldsymbol{r}_j - \boldsymbol{r}_i)/|\boldsymbol{r}_j - \boldsymbol{r}_i|$, and are dynamical quantities. It gives rise to what are called geometrical nonlinearities, the effect of which is discussed in section 3.2.5. The next step is to get rid of these nonlinearities.

Linearized elastic force and mechanical equilibrium

In the harmonic approximation, we linearize the elastic force expression (Eq. (3.15)) around the reference configuration $\boldsymbol{R}_i$, given its existence and knowledge[3]. The expansion requires to assume that gradients of displacements are small: $|\boldsymbol{u}_j - \boldsymbol{u}_i| \ll 1$ ($\Leftrightarrow |\boldsymbol{u}_j - \boldsymbol{u}_i|/l_0 \simeq \nabla \boldsymbol{u} \ll 1$ in physical units). Therefore, while the nodes can move away from their reference configuration, we consider displacements small enough so that the unit vectors $\hat{\boldsymbol{e}}_{\boldsymbol{ij}}$ can be considered fixed, killing all nonlinearities. After some algebra, the elastic force becomes:

$$\boldsymbol{F}_i^{\text{el}} = -\mathbb{M}_{ij}\boldsymbol{u}_j + o(|\boldsymbol{u}_j - \boldsymbol{u}_i|), \tag{3.16}$$

where $\mathbb{M}$ is called the dynamical matrix, and where the summation over repeated indices is implied. *Mechanical equilibrium* is defined by a strictly zero zeroth-order contribution in this expansion for any particle i in the network. Projected onto the x and y axis, it gives:

$$\begin{aligned} \sum_{j\in\partial i} \left(R_j^x - R_i^x\right)\left(1 - \frac{l_0^{ij}}{l_{\text{eq}}^{ij}}\right) = 0, \\ \sum_{j\in\partial i} \left(R_j^y - R_i^y\right)\left(1 - \frac{l_0^{ij}}{l_{\text{eq}}^{ij}}\right) = 0, \end{aligned} \tag{3.17}$$

with $l_{\text{eq}}^{ij} = \sqrt{\sum_\alpha \left(R_i^\alpha - R_j^\alpha\right)^2}$.

Dynamical matrix

The dynamical matrix is the matrix of coefficients connecting the linearized expression of the elastic force to the displacement vectors. Explicitly performing the expansion

[3]The reference consideration is generally obtained by using symmetry arguments to respect mechanical equilibrium everywhere in the network. In the general case of non-crystalline structure, the best hope is to simulate the overdamped dynamics with full elasticity (Eq. (3.14)), and let the system relax and find a reference configuration, which might not be unique.

leading to Eq. (3.16), we find, at first order in small quantities:

$$\begin{aligned}\boldsymbol{F}^{\mathrm{el}}_{j\to i} \simeq &\left[\left(1-\frac{l_0^{ij}}{l_{\mathrm{eq}}^{ij}}\right)\left(u_j^x-u_i^x\right)+\frac{l_0^{ij}}{{l_{\mathrm{eq}}^{ij}}^3}\left(R_j^x-R_i^x\right)^2\left(u_j^x-u_i^x\right)\right.\\ &\left.+\frac{l_0^{ij}}{{l_{\mathrm{eq}}^{ij}}^3}\left(R_j^x-R_i^x\right)\left(R_j^y-R_i^y\right)\left(u_j^y-u_i^y\right)\right]\hat{\boldsymbol{e}}_x\\ &+\left[\left(1-\frac{l_0^{ij}}{l_{\mathrm{eq}}^{ij}}\right)\left(u_j^y-u_i^y\right)+\frac{l_0^{ij}}{{l_{\mathrm{eq}}^{ij}}^3}\left(R_j^y-R_i^y\right)^2\left(u_j^y-u_i^y\right)\right.\\ &\left.+\frac{l_0^{ij}}{{l_{\mathrm{eq}}^{ij}}^3}\left(R_j^x-R_i^x\right)\left(R_j^y-R_i^y\right)\left(u_j^x-u_i^x\right)\right]\hat{\boldsymbol{e}}_y,\end{aligned} \tag{3.18}$$

where $\boldsymbol{F}^{\mathrm{el}}_{j\to i}$ is the force particle j exerts on particle i; and where $\boldsymbol{F}^{\mathrm{el}}_i = \sum_{j\in\partial i}\boldsymbol{F}^{\mathrm{el}}_{j\to i}$. This expression allows to construct the dynamical matrix for any structure, given the reference configuration:

$$\begin{aligned}&\mathbb{M}_{i_\beta j_\gamma} = -\frac{k_{ij}l_0^{ij}}{{l_{\mathrm{eq}}^{ij}}^3}(R_{i_\beta}-R_{j_\beta})(R_{i_\gamma}-R_{j_\gamma}) - k_{ij}\delta_{\alpha\beta}\left(1-\frac{l_0^{ij}}{l_{\mathrm{eq}}^{ij}}\right) \quad \text{if} \quad j\in\partial i, 0 \quad \text{otherwise},\\ &\mathbb{M}_{i_\beta i_\gamma} = -\sum_{j\neq i}\mathbb{M}_{i_\beta j_\gamma},\end{aligned} \tag{3.19}$$

where the indices i, j indicate the nodes considered, and $\beta, \gamma = \hat{x}, \hat{y}$ indicate the axis. In the particular case of a homogeneous structure ($k_{ij} = 1$, $l_0^{ij} = 1$) without pre-stress ($l_0^{ij} = l_{\mathrm{eq}}^{ij}$), the dynamical matrix simply expresses as:

$$\begin{aligned}&\mathbb{M}_{i_\beta j_\gamma} = -(R_{i_\beta}-R_{j_\beta})(R_{i_\gamma}-R_{j_\gamma}) \quad \text{if} \quad j\in\partial i, 0 \quad \text{otherwise},\\ &\mathbb{M}_{i_\beta i_\gamma} = -\sum_{j\neq i}\mathbb{M}_{i_\beta j_\gamma}.\end{aligned} \tag{3.20}$$

Finally, the dynamical matrix is also the matrix of coefficients for the second-order expansion of the elastic energy in small gradients of displacements. The dimensionless elastic energy U^{el} stored in the springs deformations reads, to leading order in small quantities:

$$U^{\mathrm{el}} = U^{\mathrm{el}}(\boldsymbol{r}) \simeq \frac{1}{2}\langle \boldsymbol{u}|\mathbb{M}|\boldsymbol{u}\rangle, \tag{3.21}$$

where the ket $|\boldsymbol{u}\rangle$ is the vector of the dN-components of the displacement field.

Normal modes

The dynamical matrix $\mathbb{M}$ is square, real, and symmetric. Therefore, one can find a complete orthonormal basis in which it is diagonal, namely the *normal modes* $|\boldsymbol{\varphi}_k\rangle$, with corresponding eigenvalues ω_k^2, namely the *squared eigenfrequencies*, also called the modes' energies. We define the scalar product $\langle \boldsymbol{a}|\boldsymbol{b}\rangle$ of two vectors of $\mathbb{R}^{dN}$ as the sum of the node-wise scalar products in $\mathbb{R}^d$: $\langle \boldsymbol{a}|\boldsymbol{b}\rangle = \sum_i \boldsymbol{a}_i\cdot\boldsymbol{b}_i$. Orthonormality expresses as $\langle\boldsymbol{\varphi}_k|\boldsymbol{\varphi}_p\rangle = \delta_{kp}$. By convention, we sort the eigenvalues from the smallest to the largest $\omega_1^2 \leq \cdots \leq \omega_i^2 \leq \cdots \leq \omega_{dN}^2$. Note that there exist two kinds of modes depending on the associated squared eigenfrequency:

- If $\omega_k^2 > 0$, we say mode $|\boldsymbol{\varphi}_k\rangle$ is a *harmonic mode*. The activation of such a mode stretches bonds and induces a restoring force at first order in small displacements. For a $1d$ mass-spring system where one mass connects to a single spring, the only

mode of the system has unity squared eigenfrequency. For an arbitrary $2d$ system, the squared eigenfrequency can thus be understood as the mode's stiffness with respect to a $1d$ spring.

- If $\omega_k^2 = 0$, we say mode $|\boldsymbol{\varphi}_k\rangle$ is a *zero mode*. They can be rigid body motions, or involve internal displacements of the nodes, in which case they are called *floppy modes*, or *mechanisms* (as discussed in section 3.2.1). Among them, two families can be distinguished: *finite* mechanisms, in which finite-amplitude displacements of sites stretch no bonds, and *infinitesimal* mechanisms, in which bond lengths do not change to first order in the magnitude of displacements but do so to second (or higher) order. The latter are also called Infinitesimal Zero Modes (IZM).

If the system's modes are all *harmonic*, it is *mechanically stable*.

Normal modes extension

The concepts of strict *localization* and *delocalization* are reasonably clear when applied to such cases as modes highly localized about defects in lattices, or the plane wave-like vibrations of atoms in perfect crystals. However, the concept of degree of localization is less clear for the more complicated situations which occur in between these two extremes. To measure the spatial extension of normal modes in spring networks, we introduce the *participation ratio* Q_k of mode $|\boldsymbol{\varphi}_k\rangle$:

$$Q_k = \left(\sum_i |\boldsymbol{\varphi}_k^i| \right)^2 / N, \tag{3.22}$$

where Q_k gives some indication about the number of nodes participating in said mode [158]. If the mode is completely *delocalized*, so all particles contribute equally, then $Q_k = 1$. At the other extreme, a mode *localized* on a single particle has $Q_k = 1/N$. In general, a mode *delocalized* on a subset of n nodes (involving only n nodes, with equal amplitudes along each of them) has $Q_k = n/N$. Eventually, one can show that $Q_k \leq 1$[4]. Note that one should not confound Q_k with $P_k = \left[N \sum_i \left(\boldsymbol{\varphi}_k^i \right)^4 \right]^{-1}$, which is also termed participation ratio in other works [159–161], and has similar properties. The *participation ratio* Q_k is an essential property of normal modes for active solids, as discussed in the following chapters.

3.2.4 Symmetry considerations

The structures studied in this work have some sort of symmetry: some transformations, namely the symmetry operations, leave the elastic structures looking the same after they have been carried out. The symmetry of a structure is determined by its point group. We will generally focus on the D_2 and D_6 point groups, which are respectively the symmetry groups of a rectangle and a regular hexagon in the plane. To each point group is associated a set of symmetry operations g. Note that:

$$U^{\mathrm{el}}(\boldsymbol{r}) = U^{\mathrm{el}}(\Gamma_g \boldsymbol{r}), \tag{3.24}$$

[4]This is trivial from Jensen's inequality:

$$Q_k = \frac{1}{N} \left(\sum_i |\boldsymbol{\varphi}_k^i| \right)^2 = N \left(\sum_i \frac{1}{N} |\boldsymbol{\varphi}_k^i| \right)^2 \leq N \sum_i \frac{1}{N} \left(\boldsymbol{\varphi}_k^i \right)^2 = 1. \tag{3.23}$$

for all $\boldsymbol{r} \in \mathbb{R}^{dN}$ and for all symmety operations g of the point group, where Γ_g is the matrix representation of the symmetry operation g. For example, Γ_{C_6} is the block matrix that maps every coordinate to the one rotated by 60 degrees from it, and also rotates each vector by 60 degrees. We can take derivatives twice and find:

$$\Gamma_g \mathbb{M} = \mathbb{M} \Gamma_g, \tag{3.25}$$

and hence

$$[\mathbb{M}, \Gamma_g] = 0. \tag{3.26}$$

The dynamical matrix $\mathbb{M}$ commutes with the matrix representation of symmetry operations Γ_g. The normal modes $|\boldsymbol{\varphi}_k\rangle$ are thus also eigenvectors of the matrix representation of the symmetry operation Γ_g, and are associated with the generalized eigenvalues $\lambda_k^g = \langle \boldsymbol{\varphi}_k | \Gamma_g | \boldsymbol{\varphi}_k \rangle$. This quantity allows to classify the normal modes by symmetry classes, which are modified the same way by the symmetry operations.

Normal modes sorted by class of symmetry in D_6 geometry

The symmetry group of the triangular, kagome and honeycomb lattices with hexagonal boundaries is the dihedral group D_6. It is generated by the rotation τ of angle $\pi/3$ and a reflection σ (say, of axis $y = 0$), which satisfy $\tau^6 = 1$ and $\sigma^2 = 1$. The eigenvalues of σ are ± 1. The eigenvalues of τ are $\exp(ik\pi/3)$ for $k \in \{-2, \dots 3\}$:

$$\mathrm{Spec}_{D_6}(\tau) = \left(1, e^{i\pi/3}, e^{-i\pi/3}, e^{2i\pi/3}, e^{-2i\pi/3}, -1\right).$$

The eigenmodes of D_6 associated with the complex eigenvalues are complex and come in pairs: to a mode $|\boldsymbol{\varphi}_+\rangle$ with eigenvalue $e^{in\pi/3}$ is associated a mode $|\boldsymbol{\varphi}_-\rangle$ with eigenvalue $e^{-in\pi/3}$ and with the same energy. These two modes can be combined into two real modes $|\boldsymbol{\varphi}_1\rangle$ and $|\boldsymbol{\varphi}_2\rangle$ with the same energy as $|\boldsymbol{\varphi}_\pm\rangle$. $|\boldsymbol{\varphi}_1\rangle$ and $|\boldsymbol{\varphi}_2\rangle$ are not eigenvectors of τ, but the 2-dimensional space they span is stable under the action of τ. The action of τ on these modes is characterized by $\langle \boldsymbol{\varphi}_1 | \tau | \boldsymbol{\varphi}_1 \rangle = \langle \boldsymbol{\varphi}_2 | \tau | \boldsymbol{\varphi}_2 \rangle$, which is the real part of the eigenvalue of $|\boldsymbol{\varphi}_\pm\rangle$. Hence, the symmetry of a normal mode $|\boldsymbol{\varphi}_k\rangle$ is characterized by two real numbers,

$$\langle \boldsymbol{\varphi}_k | \tau | \boldsymbol{\varphi}_k \rangle \in \{1, 1/2, -1/2, -1\}, \tag{3.27a}$$
$$\langle \boldsymbol{\varphi}_k | \sigma | \boldsymbol{\varphi}_k \rangle \in \{1, -1\}. \tag{3.27b}$$

For illustration, Fig. 3.4 represents the 30^{th} first modes of a triangular lattice with hexagonal boundaries in free boundary conditions ($N = 331$). The symmetry-classified normal modes are color-coded with respect to their generalized eigenvalues according to operation τ.

Normal modes sorted by class of symmetry in D_2 geometry

The symmetry group of the line is the dihedral group D_2. It is generated by the rotation τ of angle π and a reflection σ (say, of axis $y = 0$). They satisfy $\tau^2 = 1$, $\sigma^2 = 1$. Here, the symmetry of a normal mode $|\boldsymbol{\varphi}_k\rangle$ is thus characterized by two real numbers,

$$\langle \boldsymbol{\varphi}_k | \tau | \boldsymbol{\varphi}_k \rangle \in \{1, -1\}, \tag{3.28a}$$
$$\langle \boldsymbol{\varphi}_k | \sigma | \boldsymbol{\varphi}_k \rangle \in \{1, -1\}. \tag{3.28b}$$

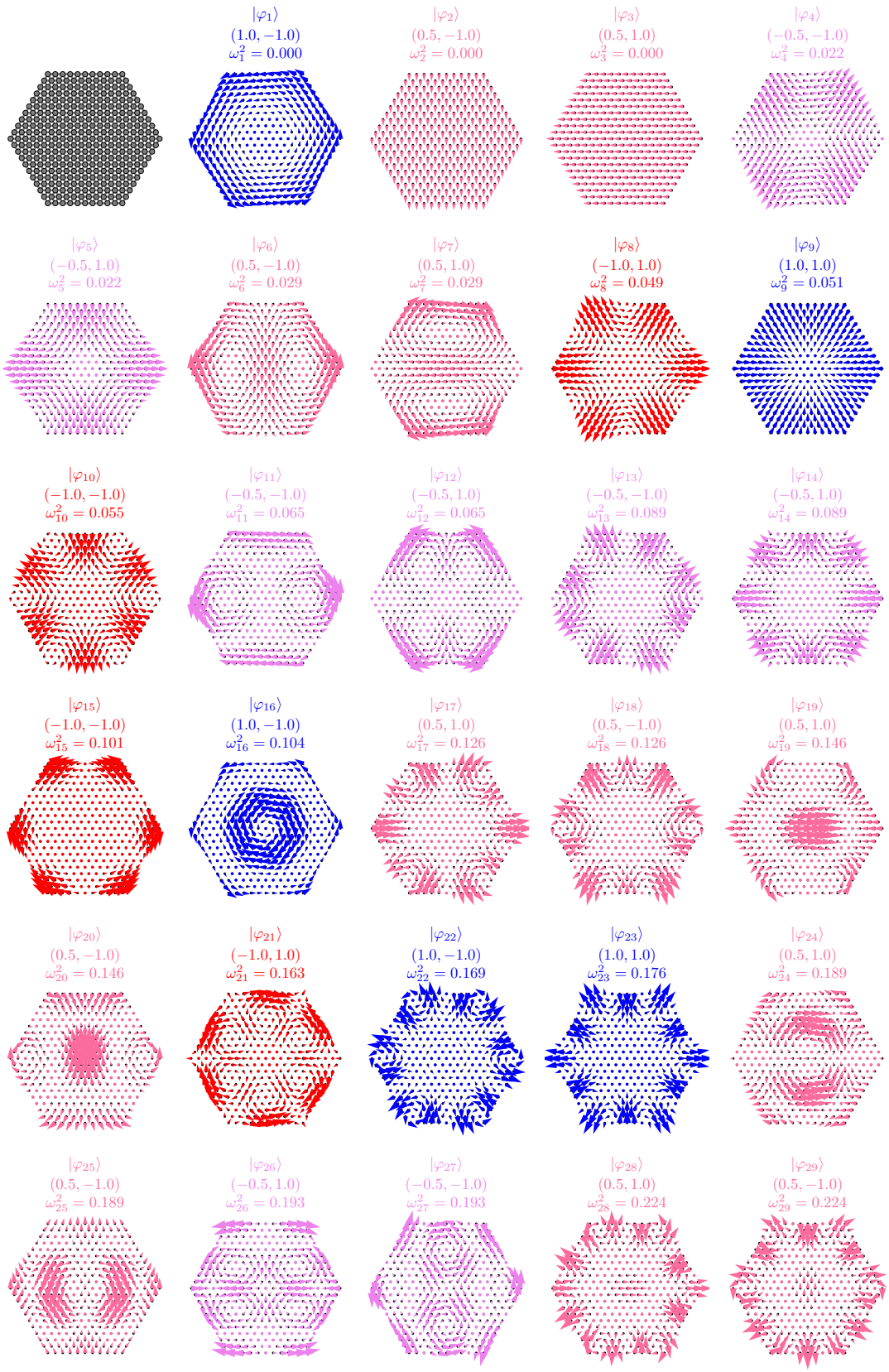


FIG. 3.4. **Normal modes of a triangular lattice in free boundary conditions.** (top left) triangular lattice in free boundary conditions, with hexagonal boundaries ($N = 331$). The modes are sorted by order of growing energies, and colored by their associated eigenvalues with respect to the rotation operation of the dihedral group of symmetry D_6 of the structure. The modes are computed for the experimental values of the tension, and only the 30^{th} first modes are shown. For every mode, the figure highlights the mode's index k, the eigenvalues associated with the symmetry operations (τ, σ), and the associated squared eigenfrequency ω_k^2.

3.2.5 Dynamics

Within the harmonic approximation

Now, let us solve the equations of motion (Eqs. (3.12) and (3.14)) using the elastic force expression in the harmonic approximation (Eq. (3.16)). We introduce the dN projections $a_k = \langle \boldsymbol{\varphi}_k | \boldsymbol{u} \rangle$ of the displacement field $|\boldsymbol{u}\rangle$ on the normal modes $|\boldsymbol{\varphi}_k\rangle$.

Inertial limit. Combining Eqs. (3.12) and (3.16), we find the equation governing the dynamics of a spring network in the inertial limit:

$$\frac{d^2 \boldsymbol{u}_i}{dt^2} = -\mathbb{M}_{ij} \boldsymbol{u}_j, \tag{3.29}$$

for small gradients of displacements. We find a set of N linearly coupled ODEs, which can be solved by projecting on the dN normal modes:

$$\frac{d^2 a_k}{dt^2} = -\omega_k^2 a_k. \tag{3.30}$$

Hence, the projection of the displacement field on the mode $|\boldsymbol{\varphi_k}\rangle$ oscillates at frequency ω_k. This is the common interpretation of the dynamical matrix eigenvalues. Note that the modes are uncoupled: energy does not flow spontaneously from one mode to the other and stays localized where it is initially injected. This is why they are called *normal* modes: their dynamics are orthogonal.

Overdamped limit. Combining Eqs. (3.14) and (3.16), we find the equation governing the dynamics of a spring network in the overdamped limit:

$$\frac{d \boldsymbol{u}_i}{dt} = -\mathbb{M}_{ij} \boldsymbol{u}_j, \tag{3.31}$$

for small gradients of displacements. We again find a set of N linearly coupled ODEs, which can be solved by projecting on the dN normal modes:

$$\frac{d a_k}{dt} = -\omega_k^2 a_k. \tag{3.32}$$

In the overdamped limit, the projection of the displacement field on the mode $|\boldsymbol{\varphi_k}\rangle$ is exponentially relaxing to zero on a time scale $1/\omega_k^2$.

Including geometrical nonlinearities

For small deformations, elasticity is linear, and the normal modes picture is applicable. However, when the deformations of the springs are large, the elasticity is non-linear, and the normal modes can be coupled. Including geometrical nonlinearities results in the addition of higher-order terms in the elastic force expression in mode space. The right-hand side term of Eqs. (3.30) and (3.32) transforms into:

$$-\omega_k^2 a_k + A_{ki} a_k a_i + B_{kij} a_k a_i a_j + o(\boldsymbol{a}^3), \tag{3.33}$$

where the third-order tensor A and forth-order tensor B express the nonlinear modal coupling coefficients. From these couplings, elastic energy can now flow from mode to mode, which opens the way to the thermalization of the elastic structure [162]. Nevertheless, there are symmetry constraints on the allowed energy leaks, which are detailed in section 5. Note, for example, that if the elastic forces derive from a potential invariant under $\boldsymbol{u} \to -\boldsymbol{u}$ ($a_k \to -a_k$), the term A must be zero.

3.2.6 Thermodynamics

Equipartition theorem

The *equipartition theorem* states that for a system whose Hamiltonian H expresses as a sum of quadratic functions of its coordinates p_k; at thermodynamic equilibrium, the averaged energy is evenly spread among all its composants and equals $fk_BT/2$, where f is the number of quadratic terms of the sum:

$$\langle H \rangle = \left\langle \sum_{k=1}^{f} \alpha_k p_k^2 \right\rangle = fk_BT/2. \tag{3.34}$$

As we discuss below, equipartition holds for passive spring networks in contact with a thermostat at temperature T, and gives strong constraints on the repartition of the elastic energy.

Contact with a thermostat in real space

Coming back to the most general Eq. (3.13), and using the elastic force expression within the harmonic approximation (Eq. (3.16)), we find:

$$\tau_v \frac{d^2\boldsymbol{u}_i}{dt^2} + \frac{d\boldsymbol{u}_i}{dt} + \mathbb{M}_{ij}\boldsymbol{u}_j = 0. \tag{3.35}$$

In this system, the total energy reads:

$$H = \sum_{k=1}^{dN} \left(\frac{1}{2}\omega_k^2 a_k^2 + \frac{1}{2}\tau_v \dot{a}_k^2 \right) \tag{3.36}$$

where the first (resp. second) term on the right-hand side is the spectral decomposition of the elastic energy (resp. kinetic energy). Now, we consider that the spring network couples to a thermostat at temperature T. Therefore, Eq. (3.35) is driven by a Langevin term, such that:

$$\tau_v \frac{d^2\boldsymbol{u}_i}{dt^2} + \frac{d\boldsymbol{u}_i}{dt} + \mathbb{M}_{ij}\boldsymbol{u}_j = \boldsymbol{\xi}_i(t), \tag{3.37}$$

where $\boldsymbol{\xi}_i = (\xi_i^x, \xi_i^y)$ is a two-dimensional random variable; and where the ξ_i^β are i.i.d random variables with zero mean $\langle \xi_i^\beta(t) \rangle = 0$, and correlations $\langle \xi_i^\beta(t)\xi_j^\gamma(t') \rangle = 2k_BT\delta_{ij}\delta_{\beta\gamma}\delta(t-t')$[5].

Contact with a thermostat in mode space

The elastic energy is not quadratic in the coordinates $\boldsymbol{u}_i$, but in the displacement field projections on the normal modes a_k. We thus project Eqs. (3.37) on the dN normal modes:

$$\tau_v \frac{d^2 a_k}{dt^2} + \frac{da_k}{dt} + \omega_k^2 a_k = \xi_k(t), \tag{3.38}$$

where $\xi_k = \langle \boldsymbol{\varphi}_k | \boldsymbol{\xi} \rangle$ can be shown to be i.i.d random variables, with zero mean $\langle \xi_k(t) \rangle = 0$, and same correlations as the ξ_i^β, i.e. $\langle \xi_k(t)\xi_{k'}(t') \rangle = 2k_BT\delta_{kk'}\delta(t-t')$. Interestingly, the combined white noises on the particle positions result in i.i.d white noises in mode

[5]To map the canonical ensemble stationary probability distribution to the solution of the associated Fokker-Planck equation, we must take $\langle \xi_i^\beta(t)\xi_j^\gamma(t') \rangle = 2\nu k_BT\delta_{ij}\delta_{\beta\gamma}\delta(t-t')$ where ν is the viscous dissipation, set to 1 in our dimensionless scheme.

space. Computing the time correlation functions $\langle a_k(t)a_k(0)\rangle$ and $\langle \dot{a}_k(t)\dot{a}_k(0)\rangle$ using Fourier transforms, we find:

$$\frac{1}{2}\omega_k^2\langle a_k^2\rangle = \frac{1}{2}\tau_v\langle \dot{a}_k^2\rangle = \frac{1}{2}k_BT, \tag{3.39}$$

and thus, the equipartition theorem holds. At thermodynamic equilibrium, the normal modes of a spring network all bear the same amount of elastic energy, or, said differently, are excited in inverse proportion to their stiffness ($\langle a_k^2\rangle \simeq 1/\omega_k^2$).

3.3 Active networks

3.3.1 Equations of motion

In this section, we combine the results obtained in section 3.1, for the dynamics of a single active unit in a harmonic trap; and in section 3.2, for the dynamics of passive spring networks.

Starting from Eqs. (3.10) for the dynamics of passive springs networks, we consider that an active particle is embedded at every node of the network (Fig. 3.5). For each active component, the activity takes the form of a force $\boldsymbol{F}_a = F_0\hat{\boldsymbol{n}}_i$ along the polarity $\hat{\boldsymbol{n}}_i$ of the particle. The equations describing the dynamics of this system are

$$m\frac{d\boldsymbol{v}_i}{dt} = F_0\hat{\boldsymbol{n}}_i - \gamma\boldsymbol{v}_i + \sum_{j\in\partial i} k\left(|\boldsymbol{r}_i - \boldsymbol{r}_j| - l_0\right)\hat{\boldsymbol{e}}_{ij}, \tag{3.40a}$$

$$\tau\frac{d\hat{\boldsymbol{n}}_i}{dt} = \zeta(\hat{\boldsymbol{n}}_i \times \boldsymbol{v}_i)\times\hat{\boldsymbol{n}}_i + \sqrt{2\alpha}\xi_i\hat{\boldsymbol{n}}_i^{\perp}, \tag{3.40b}$$

where m is the mass of the active particles, γ the friction coefficient, k the stiffness of the spring, ∂i refers to the neighbors of node i, and $\hat{\boldsymbol{e}}_{ij}$ the unit vector from i to j. The orientation dynamics, Eq. (3.40b), is the same as in the single-particle case, and contains a self-alignment and a rotational diffusion term.

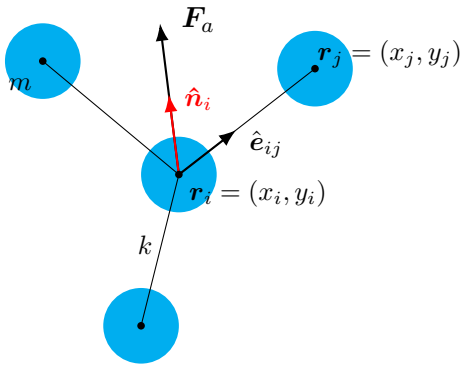


FIG. 3.5. **Notations for active solids.** The unit vector $\hat{\boldsymbol{e}}_{ij}$ points from particle i to particle j. The active force $\boldsymbol{F}_a$ exerted by particle i has amplitude F_0 along $\hat{\boldsymbol{n}}_i$.

Rescaling length by $r_0 = l_0$ and time by $t_0 = \gamma/k$ (frictional scheme of section 3.2), the

dimensionless equations of motion read

$$\tau_v \frac{d\boldsymbol{v}_i}{dt} = \tilde{F}_0 \hat{\boldsymbol{n}}_i - \boldsymbol{v}_i + \sum_{j\in\partial i} \left(|\boldsymbol{r}_i - \boldsymbol{r}_j| - 1\right) \hat{\boldsymbol{e}}_{ij}, \tag{3.41a}$$

$$\tau_n \frac{d\hat{\boldsymbol{n}}_i}{dt} = (\hat{\boldsymbol{n}}_i \times \boldsymbol{v}_i) \times \hat{\boldsymbol{n}}_i + \sqrt{2D}\xi_i \hat{\boldsymbol{n}}_i^{\perp}, \tag{3.41b}$$

with four parameters, $\tau_v = mk/\gamma^2$, $\tau_n = \tau/(\zeta l_0)$, $\tilde{F}_0 = F_0/kl_0$ and $D = \alpha\gamma/k(\zeta l_0)^2$. Note that $\tau_n = l_a/l_0$ and $\tilde{F}_0 = l_e/l_0$, where $l_a = \tau/\zeta$ is the alignment length, and $l_e = F_0/k$ is the elasto-active length.

Overdamped limit

Setting $\tau_v = 0$ in Eq. (3.41a), we find:

$$\boldsymbol{v}_i = \tilde{F}_0 \hat{\boldsymbol{n}}_i + \boldsymbol{F}_i^{\mathrm{el}}, \tag{3.42a}$$

$$\tau_n \frac{d\hat{\boldsymbol{n}}_i}{dt} = (\hat{\boldsymbol{n}}_i \times \boldsymbol{v}_i) \times \hat{\boldsymbol{n}}_i + \sqrt{2D}\xi_i \hat{\boldsymbol{n}}_i^{\perp}, \tag{3.42b}$$

with $\boldsymbol{F}_i^{\mathrm{el}} = \sum_{j\in\partial i} \left(|\boldsymbol{r}_i - \boldsymbol{r}_j| - 1\right) \hat{\boldsymbol{e}}_{ij}$ the dimensionless elastic force acting on particle i, and τ_n, D and $\tilde{F}_0$ being the same quantities as before. In the overdamped limit, the torque in Eq. (3.42b) reorients the polarity vector of particle i towards the elastic force acting on it, because the term $\pi\hat{\boldsymbol{n}}_i$ does not contribute to rotate $\hat{\boldsymbol{n}}_i$.

Harmonic approximation

The last step of the derivation is, as done in the previous section, to introduce the displacement field $\boldsymbol{u}_i$, defined as the set of displacements with respect to the reference configuration $\boldsymbol{R}_i$, $\boldsymbol{r}_i = \boldsymbol{R}_i + \boldsymbol{u}_i$; and to use the linearized expression of the elastic force around $\boldsymbol{R}_i$ (Eq. 3.16). Note that as compared to the passive case, where the amplitude of the displacements is dictated by the initial condition, in active networks, it is dictated by the dimensionless active force $\tilde{F}_0$, Eq. (3.42). The harmonic approximation thus corresponds to assume $\tilde{F}_0 \ll 1$. In that case, Eqs. (3.42) transform into:

$$\boldsymbol{v}_i = \tilde{F}_0 \hat{\boldsymbol{n}}_i - \mathbb{M}_{ij}\boldsymbol{u}_j, \tag{3.43a}$$

$$\tau_n \frac{d\hat{\boldsymbol{n}}_i}{dt} = (\hat{\boldsymbol{n}}_i \times \boldsymbol{v}_i) \times \hat{\boldsymbol{n}}_i + \sqrt{2D}\xi_i \hat{\boldsymbol{n}}_i^{\perp}, \tag{3.43b}$$

where $\mathbb{M}$ is the dynamical matrix. Within the harmonic approximation, the equations of motion have an additional symmetry that reduces the number of parameters by one. Rescaling displacements by $\tau_n = l_a/l_0$, we find back Eqs. (3.1), introduced at the beginning of the chapter:

$$\dot{\boldsymbol{u}}_i = \pi\hat{\boldsymbol{n}}_i - \mathbb{M}_{ij}\boldsymbol{u}_j, \tag{3.44a}$$

$$\dot{\boldsymbol{n}}_i = (\hat{\boldsymbol{n}}_i \times \dot{\boldsymbol{u}}_i) \times \hat{\boldsymbol{n}}_i + \sqrt{2D}\xi_i \hat{\boldsymbol{n}}_i^{\perp}, \tag{3.44b}$$

where $D = \alpha\gamma/k\tau^2$, and the ratio of the elasto-active and alignment lengths, $\pi = l_e/l_a$, which we refer to as the elasto-active coupling, is the unique microscopic control parameter. Note that because of the last rescaling, the displacement field $\boldsymbol{u}_i$ is written in unit of alignment length l_a, the same way it would have been if lengths were rescaled by l_a. At this point, it is worth making several comments on the structure of Eqs. (3.44):

- The first equation describes the dynamics of the displacement vector, which relaxes toward the reference configuration, and is now driven along the direction of the polarity vector, with amplitude π.
- The elasto-active coupling π is the dimensionless activity, or the engines' strength with respect to elasticity. The larger it is, the more particles reorient upon elastic deformations induced by activity. From the equation's structure, π compares to the modes' energies ω_k^2.
- The second equation describes the dynamics of the polarity vector, reorienting through noise and self-alignment, which is a cubic nonlinearity.

Note that equivalently, Eqs. (3.44) can be formulated for the dynamics of the polarity vector orientations θ_i:

$$\dot{\boldsymbol{u}}_i = \pi \hat{\boldsymbol{n}}_i - \mathbb{M}_{ij}\boldsymbol{u}_j, \tag{3.45a}$$

$$\dot{\theta}_i = \left(\hat{\boldsymbol{n}}_i^{\perp} \cdot \dot{\boldsymbol{u}}_i\right) + \sqrt{2D}\xi_i. \tag{3.45b}$$

3.3.2 Projection on the normal modes

As done in section 3.2, we now decompose Eqs. (3.44) on the normal modes $|\boldsymbol{\varphi}_k\rangle$.

Bra-ket notations

For the sake of simplicity, before to project, it is helpful to recast Eqs. (3.44) using bra-ket notations:

$$|\dot{\boldsymbol{u}}\rangle = \pi|\hat{\boldsymbol{n}}\rangle - \mathbb{M}|\boldsymbol{u}\rangle, \tag{3.46a}$$

$$|\dot{\boldsymbol{n}}\rangle = \mathbb{K}^T\mathbb{K}|\dot{\boldsymbol{u}}\rangle = -\mathbb{K}^T\mathbb{K}\mathbb{M}|\boldsymbol{u}\rangle, \tag{3.46b}$$

where $\langle i|\boldsymbol{a}\rangle = \boldsymbol{a}_i$, $\mathbb{K}^T$ is the transpose of the matrix $\mathbb{K}$; and where the matrix $\mathbb{K}$, of dimension $N \times 2N$, with elements $\langle i|\mathbb{K}|j\rangle = \hat{\boldsymbol{n}}_i^{\perp}\delta_{ij}$, explicitly depends on the polarity field configuration $|\hat{\boldsymbol{n}}\rangle$. Therefore, the matrix $\mathbb{K}^T\mathbb{K}$ is the projector on $|\hat{\boldsymbol{n}}^{\perp}\rangle$. Equivalently, Eq. (3.46b) can be formulated for the dynamics of the polarity vector orientations $|\theta\rangle$:

$$|\dot{\boldsymbol{u}}\rangle = \pi|\hat{\boldsymbol{n}}\rangle - \mathbb{M}|\boldsymbol{u}\rangle, \tag{3.47a}$$

$$|\dot{\theta}\rangle = -\mathbb{K}\mathbb{M}|\boldsymbol{u}\rangle. \tag{3.47b}$$

Mode space

We decompose the displacement and polarity fields on the normal modes:

$$|\boldsymbol{u}\rangle = \sum_k a_k^u|\boldsymbol{\varphi}_k\rangle, \tag{3.48a}$$

$$|\hat{\boldsymbol{n}}\rangle = \sum_k a_k^n|\boldsymbol{\varphi}_k\rangle, \tag{3.48b}$$

where the a_k^u's (resp. a_k^n's) are the coefficients of the spectral decomposition of the displacement field (resp. polar force field). The equations of motion (3.46) translate into

$$\frac{da_k^u}{dt} = \pi a_k^n - \omega_k^2 a_k^u, \tag{3.49a}$$

$$\frac{da_k^n}{dt} = -\sum_{lpq} \omega_q^2 \Gamma_{pqlk} a_q^u a_l^n a_p^n + \sqrt{2D}\xi_k, \tag{3.49b}$$

where ξ_k is a Gaussian white noise in mode space (as discussed in section 3.2.6), and where we have introduced the inter-modal geometrical coupling coefficients

$$\Gamma_{pqlk} = \sum_i \boldsymbol{\varphi}_k^i \cdot \left[(\boldsymbol{\varphi}_p^i \times \boldsymbol{\varphi}_q^i) \times \boldsymbol{\varphi}_l^i \right] = \sum_i \left[\boldsymbol{\varphi}_p^i \times \boldsymbol{\varphi}_q^i \right] \cdot \left[\boldsymbol{\varphi}_l^i \times \boldsymbol{\varphi}_k^i \right]. \tag{3.50}$$

Note the cubic nonlinearity of the second equation, inherited from the self-alignment dynamics of the polarity. In contrast with passive spring networks, the normal modes are coupled at the level of the harmonic approximation, and active force can flow from one mode to the other. The coupling coefficients Γ_{pqlk} are antisymmetric under the exchanges $p \leftrightarrow q$ and $l \leftrightarrow k$, and symmetric under the exchange $(p, q) \leftrightarrow (l, k)$. This implies for instance that $\sum_{pl} \Gamma_{pqlk} a_l^n a_p^n$ is symmetric under the exchange $k \leftrightarrow q$.

Note that compared to section 3.2, the geometry of the modes now plays a crucial role in setting the amplitude of the active force transfers (see Eq. (3.49b)). The physics is not only governed by the modes' energies ω_k^2, but also by the inter-modal geometrical coupling tensor Γ, solely set by the modes' geometry. Eventually, the structure of the Γ couplings in Eq. (3.50) highlights that *local-orthogonality*, the property of two modes to be node-wise orthogonal, increases their overall coupling, allowing for a more efficient active force transfer from one mode to the other.

In addition to the dynamical equation, the normalization condition $|\hat{\boldsymbol{n}}_i| = 1$ for all i implies that the $2N$ polarity coefficients a_k^n belong to a N-dimensional manifold isomorphic to the N-torus. Since the normalization condition implies that $\sum_i \boldsymbol{n}_i^2 = \sum_k {a_k^n}^2 = N$, this manifold is included in the $(2N-1)$-sphere of radius $\sqrt{N}$. This is a good reason to define the normalized projections of the displacement and polarity fields, respectively $\tilde{a}_k^u = a_k^u/\sqrt{N}$ and $\tilde{a}_k^n = a_k^n/\sqrt{N}$, the latter satisfying $|\tilde{a}_k^n| < 1$.

3.3.3 Numerical simulations

Let us briefly describe the numerical simulations of the active elastic networks, that were used to vary the parameters more finely and in a broader range than in the experiments. First, we discuss simulations performed within the harmonic approximation, then, considering geometrical nonlinearities, and eventually, considering angular noise in the polarity dynamics.

We simulate the Eqs. (3.1) with a vectorial Runge-Kutta method, already implemented in the Python function *scipy.integrate.solve_ivp*[6]. The time step is adaptative, optimized by the function to ensure a quick convergence while keeping relative local error estimates smaller than 10^{-6}. Unless stated otherwise, the initial condition is always at rest ($\forall i, \boldsymbol{u}_i = \boldsymbol{0}$), with polarities $\hat{\boldsymbol{n}}_i(t=0) = (\cos\theta_i(t=0), \sin\theta_i(t=0))$, where $\theta_i(t=0)$ is the initial orientation of particle i. Remember that within the harmonic approximation, the only microscopic parameter is the elasto-active coupling π. The elastic forces are computed using Eqs. (3.16) and (3.19).

Compared to a simulation within the harmonic approximation, including geometrical nonlinearities first means defining a finite dimensionless active force $\tilde{F}_0$, which sets the amplitude of said nonlinearities. Eventually, we simulate Eqs. (3.42) using $\tau_n = \tilde{F}_0/\pi$, with a vectorial Runge-Kutta method[7]. As in the previous section, the time step is

[6] Documentation at `https://docs.scipy.org/doc/scipy/reference/generated/scipy.integrate.solve_ivp.html` .

[7] *scipy.integrate.solve_ivp* also solves for non-linear ODEs.

adaptative, and the initial condition is at rest unless stated otherwise.

Finally, including angular noise transforms the previous coupled ODEs into coupled SDEs. They are solved numerically using an Euler method with a fixed time step $\delta t = 10^{-3}$, and by adding a noisy angular contribution to each polarity vector at every time step, drawn independently from a Gaussian distribution of zero mean and variance $2D\delta t$.

Chapter 4

Stress-induced collective motion

We choose to start with this mostly theoretical chapter because it makes a natural link between collective motion and elastic structures. A free elastic structure, in the sense that it is not pinned to a substrate, has translational and rotational zero modes corresponding to the rigid body motions. As we shall see, when such a structure is embedded with self-aligning active units, those zero modes are spontaneously excited, and the associated motion takes place. This chapter results from a collaboration with Gustavo Düring and Claudio Hernández López. They derived the rigid limit presented in Appendix B, all the results presented in section 4.6 regarding the effect of noise, and contributed to the analysis of the rigid theory.

4.1 Introduction

Collective motion is a spectacular and widely observed phenomenon in nature. Whether observing bird flocks [36], bacteria colonies [41, 163], cellular tissues undergoing migration [80], locust swarms [39], or schooling fish [38], the common motif is the tendency to move together. Artificial systems of self-propelled particles have played a crucial role in understanding the emergence of ordered movements, such as vibrated polar disks [55–58] or rods [164], interacting robots [165], and motile colloids [25, 59]. Generally, flocking models invoke the existence of polar alignment interactions between the active agents, like in the celebrated *Vicsek* model [9]. When only self-alignment interactions are present, active systems are also known to achieve collective motion via pairwise position-based interactions, such as elastic [112] or intermolecular-like forces [75] (see chapter 1). In particular, it was shown that a traveling phase exists and is stable, with numerical evidence of long-range order [112]. The latter is highly non-trivial, and must violate the Mermin-Wagner theorem while strictly consisting of short-range interactions. Remarkably, for small enough self-propulsion, not only do such systems stay below the active yielding transition [79], remaining genuinely solids, but the vibrational modes of the structure are also barely excited. Therefore, the coherently moving active solid can be considered effectively rigid. However, to date, the mechanisms governing the emergence of collective motion in rigid active solids remain unclear.

Here we develop a new theoretical framework for strictly rigid structures, demonstrating how long-range stress propagation can lead to different forms of collective motion. We show that in the presence of zero modes, any finite amount of activity leads to the emergence of collective steady states, which are dictated by the geometry of said zero modes. Combining this framework with numerical simulations and the experimental study of our model active solids in rigid settings, we show that the predictions are robust

to imperfections and a finite amount of elasticity. Finally, we investigate the effect of noise, and find that the dynamics of rigid active solids can be mapped to equilibrium systems, for which exact results exist. In particular, mode selection and the existence of collective motion are determined by the minima of a Landau-Ginzburg-like free energy.

4.2 Experiments

We start by exploring the free boundary condition dynamics of triangular lattices with a hexagonal shape, made with *stiff* springs (Figs. 4.1-a). As discussed in chapter 3, in the absence of pinning, such systems have translational and rotational zero modes, which are the three rigid body motions of $2d$ structures. Once this structure is doped with active units, we let it evolve on the lab's floor. We find two regimes: collective translation, where all the active units are aligned, and the system coherently moves in a given direction, spontaneously breaking invariance by rotation (Fig. 4.1-d); and collective rotation, where the active units organize into a vortex state that triggers the rotation of the structure clockwise or counter-clockwise, spontaneously breaking the chiral symmetry (Fig. 4.1-f). Translational solutions appear to be stable on the experimental timescales. Conversely, rotational solutions are not always stable. In the presence of an active unit at the center of the structure, the rotation regime destabilizes toward the translation one (Fig. 4.1-e). Removing the central active unit allows for observing stable rotation regimes on the experimental timescales (Fig. 4.1-f). Importantly, no significant deformations of the

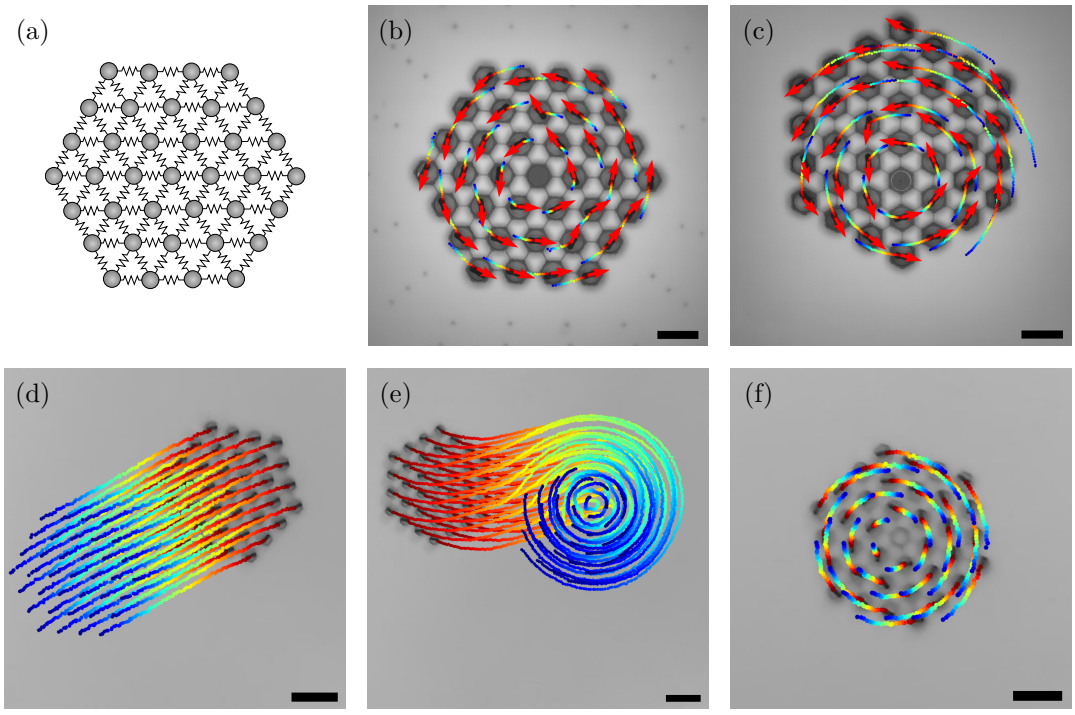


FIG. 4.1. **Stiff active solids with rigid body motions** (a) Elastic architecture cartoon ($N = 37$). (b-c) Only the central node (b) or an arbitrary point of the network (c) is pinned, giving rise to a single rigid body rotation zero mode ($N = 36$). In both cases, the structure collectively and steadily rotates around the pinning point; scale bars: 10 cm (d-f) Free boundary conditions, with all annuli doped with active units (d-e), or all but the central one (f). (d) Stable translation regime ($N = 37$). (e) Unstable rotation regime ($N = 37$). (f) Stable rotation regime ($N = 36$). All trajectories are color-coded from blue to red by increasing time; scale bars: 20 cm

structure are observed during the different dynamics.

We next consider lattices with a single zero mode. The simplest case corresponds to a structure with a single pinning point, i.e a freely rotating structure, with a single rotational zero mode. Indeed, by fixing a solid cylinder to the experimental table, a given node can freely rotate but not displace, as seen in Figs. 4.1-b and c. Independently of the chosen structure and pinning point, only collective rotations are found, and they are always stable on the experimental timescales. We find that the structure rotates with a well-defined average rotation rate $\langle\Omega\rangle$ (Figs. 4.2-a and b), where Ω is obtained by averaging the angular displacement measured between two frames over particles. As discussed below, the latter depends on the geometry and inter-agent distances (Fig. 4.5).

Spectral decomposition of the polarity field in the experiments represented in Fig. 4.1-b reveals that activation of non-zero modes is negligible in comparison with that of zero modes. We introduce the condensation fraction λ_k on mode $|\boldsymbol{\varphi}_k\rangle$:

$$\lambda_k = \left\langle (\tilde{a}_k^n)^2 \right\rangle_t = \frac{1}{T}\int^T \left[\frac{\langle \boldsymbol{\varphi}_k | \hat{\boldsymbol{n}}(t)\rangle}{\sqrt{N}}\right]^2 dt, \tag{4.1}$$

where $\tilde{a}_k^n = \langle \boldsymbol{\varphi}_k | \hat{\boldsymbol{n}}\rangle/\sqrt{N}$ is the normalized projection of the polarity field on mode $|\boldsymbol{\varphi}_k\rangle$, and satisfies $|\tilde{a}_k^n| < 1$ (see chapter 3). λ_k corresponds to the fraction of active force injected on average into mode $|\boldsymbol{\varphi}_k\rangle$. Said differently, it measures how much the polarity field is aligned with mode $|\boldsymbol{\varphi}_k\rangle$ on average and is bounded between 0 and 1. We measure the condensation fraction on the modes for the hexagonal structure with central pinning condition (Fig. 4.2-c). Importantly, the normal modes are computed in the frame co-rotating with the structure (see appendix A for the whole normal mode spectrum). The main peak corresponds to the rotational mode, which is the only zero mode, and contains roughly 80% of the total active force injected. Subsequent smaller peaks correspond to breather modes, which belong to the same symmetry class as the rotation mode. As discussed in the next chapter, the secondary peaks originate from the normalization of the polarity field, which leads to the selection of an entire symmetry class. However, in this chapter, the projection of the polarity field on non-zero modes being very small, and their energies being relatively large, deformations of the structure can be neglected, consistently with observations in real space.

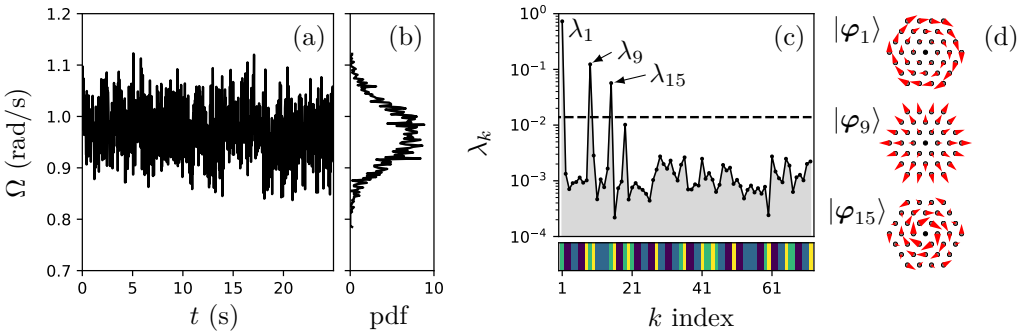


FIG. 4.2. **Properties of collective rotations.** (a) Instantaneous rotation rate of the whole structure Ω as a function of time, for the structure of Fig. 4.1-b; and (b) its probability density function. (c) Condensation fraction λ_k on the normal modes, sorted by order of growing energies. The symmetry classification of the normal modes is highlighted in the bottom panel. The horizontal dashed line indicates equipartition. (d) Geometry of the 3 most activated modes.

In the spirit of deepening our theoretical understanding of the existence, characteristics, and stability of these different collective behaviors, we develop a framework that ignores the contribution of harmonic modes. This amounts to considering the system in the infinitely rigid limit, i.e virtually replacing the *stiff* springs with rigid bars.

4.3 Rigid equations

Our starting point is the standard overdamped dynamic for N active units (see chaper 3). We can safely use the harmonic approximation, given that the structures are rigid and deformations can be neglected:

$$\dot{\boldsymbol{u}}_i = \pi \hat{\boldsymbol{n}}_i - \mathbb{M}_{ij}\boldsymbol{u}_j, \tag{4.2a}$$

$$\dot{\theta}_i = \left(\hat{\boldsymbol{n}}_i^{\perp} \cdot \dot{\boldsymbol{u}}_i\right) + \sqrt{2D}\xi_i, \tag{4.2b}$$

where $\boldsymbol{u}_i$ (resp. θ_i) is the displacement vector with respect to the reference configuration (resp. polarity vector orientation, i.e. $\hat{\boldsymbol{n}}_i = (\cos\theta_i, \sin\theta_i)$) of active unit i; and the elasto-active coupling $\pi = l_e/l_a$ is the ratio between the elasto-active length $l_e = F_0/k$ and the alignment length l_a (see Eqs. (3.45)). Finally, the dimensionless noise amplitude reads $D = \alpha\gamma/k\tau^2$.

On the one hand, the units of length and time respectively read $r_0 = l_a$, and $t_0 = \gamma/k$ (see chapter 3). On the other hand, the rigid limit can be understood as a limiting procedure with $k \to +\infty$, all other parameters being held constant. Therefore, we should change the dimensionless scheme to avoid infinitesimal time units. Choosing the units of time and length such that $r_0 = l_a$ and $t_0 = l_a/v_0 = l_a\gamma/F_0$, Eqs. (4.2) re-cast into:

$$\dot{\boldsymbol{u}}_i = \hat{\boldsymbol{n}}_i - \frac{1}{\pi}\mathbb{M}_{ij}\boldsymbol{u}_j, \tag{4.3a}$$

$$\dot{\theta}_i = \left(\hat{\boldsymbol{n}}_i^{\perp} \cdot \dot{\boldsymbol{u}}_i\right) + \sqrt{2D}\xi_i, \tag{4.3b}$$

where the dimensionless noise amplitude now expresses as $D = D_\theta l_a/v_0$, where $D_\theta = \alpha/\tau^2$ is the rotational diffusion coefficient.

Projecting the position dynamics, Eq. (4.3a), on the eigenmodes of the structure, it re-casts as:

$$\dot{a}_q^u = a_q^n - \frac{\omega_q^2}{\pi}a_q^u, \tag{4.4}$$

where a_q^u (resp. a_q^n) is the projection of the displacement (resp. polarity) field on mode $|\boldsymbol{\varphi}_k\rangle$, and ω_k^2 is the energy of mode $|\boldsymbol{\varphi}_k\rangle$. As $\pi \to 0$, e.g. because the spring stiffness k diverges, the components of the eigenmode expansion of the displacements separate into two disjoint sets depending on their associated eigenvalues. We denote $\mathcal{F}$ the set of zero modes.

- For $q \in \mathcal{F}$, $\omega_q^2 = 0$, and Eq. (4.4) trivially becomes:

$$\dot{a}_q^u = a_q^n. \tag{4.5}$$

  For zero modes, a_q^u evolves solely due to the projection of the polarity field on the mode, a_q^n.

- For $q \notin \mathcal{F}$, $\omega_q^2 > 0$. Asumming $\pi \ll \omega_q^2$, $\forall q \notin \mathcal{F}$, the dominant terms of Eq. 4.4 are:

$$\dot{a}_q^u \simeq -\frac{\omega_q^2}{\pi} a_q^u. \tag{4.6}$$

  For harmonic modes, a_q^u is severely damped and relaxes to zero on a timescale π/ω_q^2, thus it vanishes asymptotically fast in the rigid limit. We place ourselve at times larger than this typically transitory regime, so that displacements along the harmonic modes can be safely neglected.

In the presence of zero modes, for small enough elasto-active coupling $\pi \ll \omega_q^2$, the contributions from the harmonic modes can be neglected and the dynamics is dictated by the structure of the zero modes. Coming back to real space, we can write the final general equations in the rigid limit:

$$\dot{\boldsymbol{u}}_i = \sum_{q \in \mathcal{F}} a_q^n \boldsymbol{\varphi}_i^q, \tag{4.7a}$$

$$\dot{\theta}_i = \left(\hat{\boldsymbol{n}}_i^{\perp} \cdot \dot{\boldsymbol{u}}_i \right) + \sqrt{2D}\xi_i. \tag{4.7b}$$

Eventually, re-injecting Eq. (4.7a) into the polarity dynamics Eq. (4.7b), we end up with a closed equation for the dynamics of the orientations θ_i:

$$\dot{\theta}_i = -\frac{\partial V}{\partial \theta_i} + \sqrt{2D}\xi_i, \tag{4.8}$$

where:

$$V\left(\theta_1, \ldots, \theta_N\right) = -\frac{1}{2} \sum_{q \in \mathfrak{F}} a_q^n \left(\theta_1, \ldots, \theta_N\right)^2. \tag{4.9}$$

A few remarks are in order. First, there is only one dimensionless parameter: the noise amplitude D (the elasto-active coupling π is eliminated in the rigid limit). Second, Eqs. (4.7) and the theoretical framework presented here is quite general; a rigid description can be obtained via a limiting procedure starting from a variety of interaction forces, in particular springs as in the case of *hexbugs*. In Appendix B, we show that the rigid limit can also be obtained starting from pairwise radially symmetric position-based interactions. Third, if the normal modes are fixed throughout the dynamics (i.e. independent of time[1]), the right-hand side of Eq. (4.7a) is slaved to the polarity dynamics, Eq. (4.8), thus this equation is solved for free once the θ_i are known.

In the presence of a single zero mode (the set $\mathcal{F}$ contains a single zero mode), the minimum of the potential given by Eq. (4.9) is realized when the polarity field aligns with said zero mode, leading to a steady state of Eq. (4.8). However, when several zero modes are present, the situation becomes more complicated, and the emerging steady states are dictated by the geometry of the zero modes and their inter-modal geometrical couplings.

As a final remark, the lowest energy harmonic modes of the triangular lattices in free boundary condition (Figs. 4.1-d to f) and central pinning condition (Fig. 4.1-b) have energies $\omega_{\text{min}}^2 = 0.194$ and $\omega_{\text{min}}^2 = 0.046$, respectively. The value of π for *stiff* springs being typically 0.01 (see chapter 2), the rigid limit requirement $\pi \ll \omega_k^2$ for all harmonic modes is satisfied.

[1]This is necessarily true if the structure is mechanically stable, but not always true in the presence of zero modes.

4.4 Single pinning point

We start by considering structures with a single global zero mode, i.e pinned systems. Therefore, the set of zero modes reduces to the rotation mode around the pinning point $\mathcal{F} = \{|\boldsymbol{\varphi}^R\rangle\}$. Let $\boldsymbol{r}_i$ be the vector from the pinning point to particle i (see Fig. 4.3). Defining ϕ_i as the angle between $\boldsymbol{r}_i$ and the horizontal axis, the rotational zero mode reads:

$$\boldsymbol{\varphi}_i^R = \frac{r_i}{\sqrt{I}}\left(-\sin\phi_i\hat{\boldsymbol{x}} + \cos\phi_i\hat{\boldsymbol{y}}\right) = \frac{\boldsymbol{r}_i^\perp}{\sqrt{I}} = \frac{r_i}{\sqrt{I}}\hat{\boldsymbol{e}}_\theta, \tag{4.10}$$

where $I = \sum_i r_i^2$ the massless angular inertia of the structure, and where $\hat{\boldsymbol{e}}_\theta$ is the azimuthal unit vector in polar coordinates. In the following, we aim to solve Eqs. (4.7a) and (4.8), considering that the set $\mathcal{F}$ restricts to the rotation zero mode, given in Eq. (4.10).

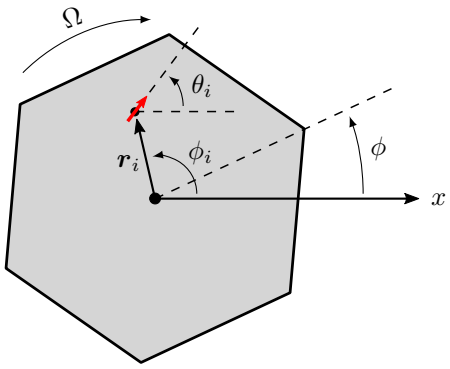


FIG. 4.3. **Notations.** The angle of the solid body with respect to the x-axis is denoted ϕ, and thus rotates at a rate $\Omega = \dot{\phi}$. The angle of the vector $\boldsymbol{r}_i$ (resp. $\hat{\boldsymbol{n}}_i$) is denoted ϕ_i (resp. θ_i).

4.4.1 Rigid equation in the co-rotating frame

In the presence of a rotational zero mode, the structure and the entire normal mode spectrum rotate as the rotation mode is actuated. To avoid contradicting the unicity of the reference configuration and linear elasticity, we place ourselves in the frame co-rotating with the structure. We denote ϕ the angle between this frame and the horizontal axis (see Fig. 4.3). Let us determine the dimensionless rotational speed $\dot{\phi}$ of the structure. Re-injecting Eq. (4.10) into Eq. (4.7a), we find:

$$\dot{\boldsymbol{u}}_i = a_R^n\boldsymbol{\varphi}_i^R = a_R^n\frac{r_i}{\sqrt{I}}\hat{\boldsymbol{e}}_\theta. \tag{4.11}$$

With $\dot{\boldsymbol{u}}_i \cdot \hat{\boldsymbol{e}}_\theta = r_i\dot{\phi}$ from solid body rotation, we find:

$$\dot{\phi} = \frac{a_R^n}{\sqrt{I}} = \frac{1}{I}\left(\sum_i \boldsymbol{r}_i^\perp \cdot \hat{\boldsymbol{n}}_i\right). \tag{4.12}$$

As expected, the structure rotates as quickly as the polarity field projects on the rotation mode, and as slowly as the rotational inertia is large. Note that translation modes, absent in this setting, do not contribute to rotating the structure. Therefore, the above expression is also valid in free boundary conditions. Then we can define $\theta_i' = \theta_i - \phi$ and $\phi_i' = \phi_i - \phi$, where the latter is now a constant quantity. Under this convention,

and using the explicit rotation mode expression in Eq. (4.8), the noiseless equation of motion of the angular variables is:

$$\dot{\theta}_i' = -\frac{\partial V}{\partial \theta_i} - \dot{\phi} = (\boldsymbol{r}_i \cdot \hat{\boldsymbol{n}}_i - 1)\,\dot{\phi}. \tag{4.13}$$

Crucially, in the presence of a rotational zero mode, a new parameter appears, hidden in the definition of the $\boldsymbol{r}_i$. Indeed, we can write $\boldsymbol{r}_i = \tilde{\boldsymbol{r}}_i l_0/l_a = \tilde{\boldsymbol{r}}_i/\tau_n$, where $\tau_n = l_a/l_0$ is the alignment length l_a rescaled by the springs rest length l_0, and where $\tilde{\boldsymbol{r}}_i = \tilde{r}_i \hat{\boldsymbol{e}}_r$ is the positions of the particle i with respect to the pinning point in the unit-length lattice. Therefore, $\dot{\phi}$ scales like τ_n: for $\tau_n \ll 1$, moving with the frame co-rotating with the structure has no effects, because it happens on timescales much larger than those of the polarity dynamics. Otherwise, the system has two parameters: the dimensionless alignment length τ_n, and the noise amplitude D.

4.4.2 Steady rotation regime

A stationary rotating solution exists only if $\dot{\theta}_i' = 0$, imposing the condition:

$$\boldsymbol{r}_i \cdot \hat{\boldsymbol{n}}_i = 1, \tag{4.14}$$

for all particles. Hence

$$\hat{\boldsymbol{e}}_r \cdot \hat{\boldsymbol{n}}_i = \frac{\tau_n}{\tilde{r}_i}. \tag{4.15}$$

This implies that the alignment between the two vectors increases as we look at particles closer to the center of rotation: the closer from the pinning point, the more particles point radially and not azimuthally. Therefore, a stationary solution of Eq. (4.13) exists only if $\tau_n < \tilde{r}_i \ \forall i$. Applying this constraint to the smallest possible $\tilde{r}_i = 1$, we find that a steady rotating solution exists only if $\tau_n \leq 1$, i.e. $l_0 \geq l_a$. Condition (4.14) is enough to determine the orientation of every active unit, and thus the angular speed $\dot{\phi} = \Omega$, Eq. (4.12):

$$\Omega = \pm \frac{\sum_i \sqrt{r_i^2 - 1}}{\sum_i r_i^2}, \tag{4.16}$$

where the $\pm$ indicates the two broken symmetry rotations, turning clockwise and counter-clockwise. In dimensional form, it reads:

$$\Omega = \pm v_0 \frac{\sum_i \sqrt{r_i^2 - l_a^2}}{\sum_i r_i^2}. \tag{4.17}$$

Linear stability analysis reveals that this solution is stable independently of the geometry and pinning point (see Appendix B), which is consistent with experimental observations in Figs. 4.1-b and c for triangular lattices, and Figs. 4.4-a and b for square lattices.

To summarize, in the presence of a single rotational zero mode, a steady collective rotation regime exists for $\tau_n < 1$ and is unconditionally stable.

4.4.3 Rigid experiments

We now compare the prediction from Eq. (4.17) to numerical simulations of the rigid equations in the presence of a single rotational zero mode, Eq. (4.13), and to experiments performed with rigid links.

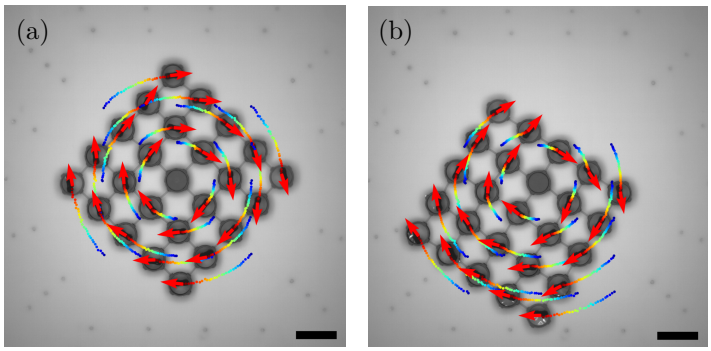


FIG. 4.4. **Collective rotation for pinned square lattices** (a-b) Only the central node (a) or an arbitrary point of the network (b) is pinned, giving rise to a single rigid body rotation zero mode. In both cases, the structure collectively and steadily rotates around the pinning point ($N = 24$). All trajectories are color-coded from blue to red by increasing time; scale bars: 10 cm.

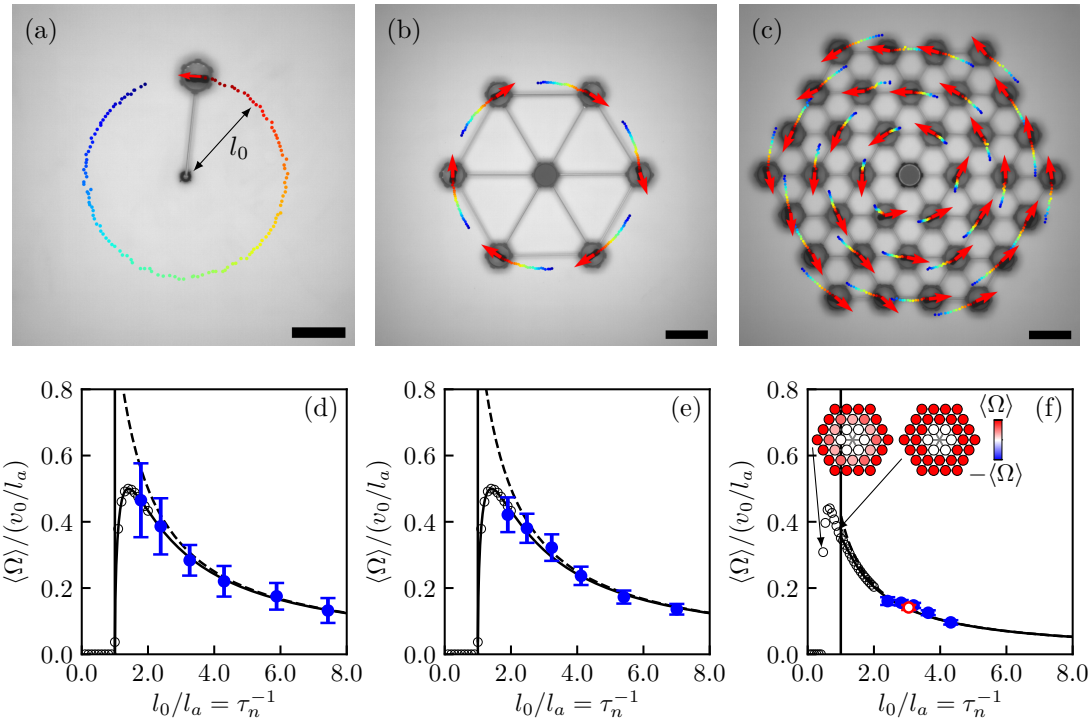


FIG. 4.5. **Rigid active solids with rigid body rotation only** (a) Abandoned dog ($N = 1$). (b) 1-ring triangular lattice with central pinning condition ($N = 6$). (c) 3-ring triangular lattice with central pinning condition ($N = 36$); scale bars: 10 cm. (d-f) Scaled angular speed of the networks depicted in (a-c) as a function of the inter-agent distances. Blue and red dots are experimental data, and correspond respectively to experiments performed with *rigid* and *stiff* connections. Error bars are given by the $1 - \sigma$ width of the instantaneous angular velocity distributions (see Fig. 4.2-b). The solid black line corresponds to the theoretical prediction from Eq. (4.17), and the dashed black line to the $l_0/l_a \to +\infty$ asymptotic expression of the same equation. The open black circles are numerical simulations. (d): $l_a = 2.51$ cm, $v_0 = 29.7$ cm/s (least-squared fit of Eq. (4.17)); (e): $l_a = 2.94$ cm, $v_0 = 20.5$ cm/s (least-squared fit of Eq. (4.17)); (f): $l_a = 2.94$ cm, $v_0 = 20.5$ cm/s. Inset: individual rotation rates ω_i illustrating the spatial coexistence in numerical simulations; (left) $l_0/l_a = 0.47$; (right) $l_0/l_a = 0.93$.

We construct triangular lattices with hexagonal boundaries, replacing the previous *stiff* helical springs with plastic straws, that play the role of very light *rigid* links. Consistently with the above section, the central node is pinned to consider only a single zero energy rotation mode (Figs. 4.5-b and c). We also consider a single active unit, connected to a pinned ball bearing via a *rigid* link, the so-called *abandoned dog* (Fig. 4.5-a), which has one rotation zero mode, and a stiff harmonic mode along the radial direction. The parameter $\tau_n^{-1} = l_0/l_a$ is varied by tuning the *rigid* connectors' length, assuming that the added/removed mass does not affect the other parameters of the system. We find that the average rotation rate $\langle\Omega\rangle$ depends on the geometry and inter-agent distances, in good agreement with the rigid theory (Figs. 4.5-d,e, and f, blue markers). For large l_0/l_a, Ω decreases like $(l_0/l_a)^{-1}$, because angular inertia increases with l_0; and as l_0 approaches l_a, Ω vanishes critically like $(l_0 - l_a)^{1/2}$, because of self-alignment. Moreover, we find that the rotation rate's fluctuations decrease with the number of active units. Note that the rotation rate measured from the experiment with *stiff* springs (Fig. 4.1-b) also matches very well with the prediction (Fig. 4.5-f, red marker), regardless of its residual elasticity. Interestingly, in the rigid experiments, the measurements at the smallest l_0 allow for measuring deviations from the large l_0/l_a asymptotic regime (Figs. 4.5-d and e), emphasizing the role of self-alignment. By construction, however, the inter-agent distance l_0 must be larger than the annulus diameter, which is larger than the alignment length. Therefore, experimentally we cannot explore the range $l_0 \leq l_a$ where the steady collective rotation is expected to disappear.

We thus perform numerical simulations of Eq. (4.13) close to the transition. For the two first structures studied experimentally (Figs. 4.5-a and b), there is only one distance from the pinning point, $\tilde{r}_i = 1$, thus the existence threshold for the steady rotating solution given by Eq. (4.14) is reached everywhere in the lattice at $l_0 = l_a$. It implies that the steady rotation rate Ω continuously goes to zero as l_0 approaches l_a from above. At the transition, all active units point radially, and the rotation stops, as observed numerically (Figs. 4.5-d and e, open black markers). In contrast, for larger structures, as l_0/l_a approaches 1, only the particles the closest to the pinning point stop verifying condition (4.14). For $l_0 < l_a$, the steady collective rotation ceases to exist, but is replaced by unsteady collective rotations (Fig. 4.5-f, open black markers and insets), which exist and are stable up to smaller values of l_0/l_a. They are characterized by a spatial coexistence between a frozen region close to the pinning condition, where polarity vectors do not rotate on average; and a region where polarity vectors are synchronized with the rotation of the whole structure, and rotate on average at the same rate. As l_0/l_a decreases further, the frozen region invades the system layer-by-layer, and the heterogeneous unsteady regimes rotate slower and slower on average. Eventually, for too small l_0/l_a, the system ends up fully frozen and stops turning.

4.5 Free boundary condition

4.5.1 Rigid equation in the co-rotating frame

We will now consider a non-pinned structure, with three zero modes corresponding to rigid body motions, $\mathcal{F} = \{|\boldsymbol{\varphi}^{T_x}\rangle, |\boldsymbol{\varphi}^{T_y}\rangle, |\boldsymbol{\varphi}^{R}\rangle\}$. In this case, the zero mode expressions

are:

$$\begin{aligned}\boldsymbol{\varphi}_i^{T_x} &= \hat{\boldsymbol{x}}/\sqrt{N},\\ \boldsymbol{\varphi}_i^{T_y} &= \hat{\boldsymbol{y}}/\sqrt{N},\\ \boldsymbol{\varphi}_i^{R} &= \frac{r_i}{\sqrt{I}}\left(-\sin\phi_i\hat{\boldsymbol{x}} + \cos\phi_i\hat{\boldsymbol{y}}\right) = \frac{\boldsymbol{r}_i^{\perp}}{\sqrt{I}},\end{aligned} \tag{4.18}$$

where the vectors $\boldsymbol{r}_i$ denote the position of the nodes with respect to the mass barycenter. Re-injecting these expressions into Eqs. (4.7), we find the noiseless equation of motion of the angular variables (see Appendix B):

$$\dot{\theta}_i' = \frac{1}{N}\hat{\boldsymbol{n}}_i^{\perp}\cdot\sum_j \hat{\boldsymbol{n}}_j + \left(\boldsymbol{r}_i\cdot\hat{\boldsymbol{n}}_i - 1\right)\dot{\phi}. \tag{4.19}$$

The first (resp. second) term on the right-hand side originates from the two translation modes zero modes (resp. from the rotational zero mode).

4.5.2 Steady translation regime

Let us first study the translational solutions. They are defined by $\theta_i = \theta\ \forall i$. Clearly, the first term on the right-hand side of Eq. (4.19) vanishes in the translating state. Moreover, from Eq. (4.12), the rotation rate $\dot{\phi}$ must be zero, killing the second right-hand side term of Eq. (4.19). Therefore, independently of the structure, any translating state oriented along θ corresponds to a stationary solution satisfying $\theta_i' = 0\ \forall i$. The linear stability matrix governing the damping of small perturbations has a null eigenvalue corresponding to a global rotation and $N-1$ negative eigenvalues, ensuring the stability of translational solutions (see Appendix B). The null eigenvalue reflects the marginal stability of the latter, and gives rise to a diffusion process of the heading direction θ when angular noise is present, in agreement with experimental observations.

To summarize, in free boundary conditions, the translational solution always exists and is, overall, linearly stable.

4.5.3 Steady rotation regime

For non-pinned rotational solutions, Eqs. (4.14) and (4.17) still hold, where $\boldsymbol{r}_i$ is now the position of particle i with respect to the structure's barycenter. However, stability analysis reveals that there is a strong dependence on geometry (see Appendix B). Considering the hexagon-like experimental structures, from Eq. (4.14), purely rotational solutions do not exist when a central unit is present. This is in agreement with the system observed in Fig. 4.1-e, where an initial pseudo-rotating state transitions to the more stable translational solution. Note that this effect could have been anticipated from symmetry considerations. When the solution exists, i.e. without a central active unit and for $\tau_n < 1$, stability depends on τ_n and the system's size, defined by its number of layers (see Appendix B). As Fig. 4.6-a shows that stability is ensured for $\tau_n < \tau_n^{\star}(N) < 1$. Note that the stability threshold $\tau_n^{\star}$ approaches the rotational solution's existence threshold $\tau_n = 1$ in the thermodynamic limit.

Once again, we turn to numerical simulations to study the destabilization of the rotating solutions as τ_n exceeds the stability threshold. The dynamics is best described by the two order parameters μ_R and μ_T, which respectively characterize the configurations fully

aligned with the rotational and translational modes. As a general expression, the order parameter μ_q characterizing the order along a given mode q can be written as:

$$\mu_q = \frac{\langle a_q^n \rangle}{\sqrt{N}} = \frac{\left\langle \sum_i \boldsymbol{\varphi}_i^q \cdot \hat{\boldsymbol{n}}_i \right\rangle}{\sqrt{N}}, \tag{4.20}$$

where the outer brackets stand for a time average over the stationary state. For the rotation mode, $\mu_R = \langle \dot{\phi} \rangle / \phi_{\max}$, where $\phi_{\max} = \sqrt{N/I}$; and for the translation modes, $\mu_T = \mu_{T_x} + \mu_{T_y} = \langle |\boldsymbol{P}| \rangle$, where the $\boldsymbol{P}$ is the polarization, or orientational order parameter $\boldsymbol{P} = \frac{1}{N} \sum_i \hat{\boldsymbol{n}}_i$.

Similarly to the case with a single pinning point, we find that large enough heterogeneity of the rotation mode allows for the spatial coexistence of rotating and translating solutions as l_0 decreases (Figs. 4.6-b and c). For $l_0/l_a > \tau_n^{\star -1}(N)$, we find homogeneous and stable steady rotation regimes, thus $\mu_T = 0$ and μ_R is finite but below one, in perfect agreement with the rigid theory ($\mu_R \to 1$ in the limit $\tau_n \to 0$). As l_0 decreases below the stability threshold, the steady rotation destabilizes. For a 1-ring structure, with a fully homogeneous rotation mode, the destabilization drives the system toward the stable translation regime, with $\mu_T = 1$ and $\mu_R = 0$ (Fig. 4.6-b). On the contrary, for a 5-ring structure, we find spatial coexistence between the rotating and translating solution (Fig. 4.6-c), the rotating solution being favored close to the edges, where the rotation mode has the largest amplitude. As l_0 decreases further, the heterogeneous rotation regime also destabilizes, and the only remaining solution is a pure translation.

4.6 Influence of noise

The existence of multiple stable equilibrium states raises the natural question of mode selection and the effect of noise. The stochastic angular evolution of each agent should

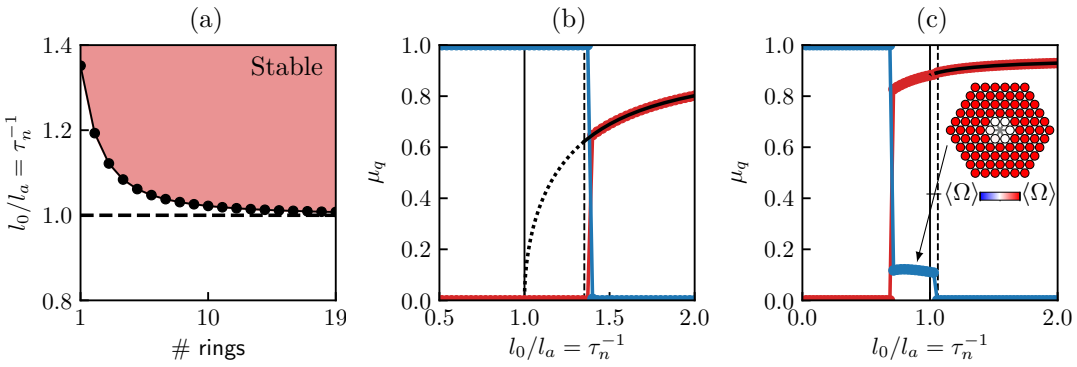


FIG. 4.6. **Collective rotation in free boundary conditions** (a) Stability threshold of the steady rotation regime $1/\tau_n^\star$ (black markers) as a function of the number of rings in a triangular lattice without a central unit. The dashed black line represents the existence threshold of the steady rotation. (b-c) Order parameters μ_R (red markers) and μ_T (blue markers) as a function of inter-agents distance l_0/l_a, as obtained from simulations of Eqs. (4.19). (b) 1-ring triangular lattice ($N = 7$), (c) 5-ring triangular lattice ($N = 91$). The solid (resp. dashed) black vertical lines represent $l_0/l_a = 1$ (resp. the stability threshold of the steady rotation, as given by (a)). The solid black lines represent the predicted value of μ_R from the rigid theory in the range where steady rotation is stable, and the dotted black lines highlight the same prediction in the region where it exists but is unstable. Inset: individual rotation rates ω_i illustrating the spatial coexistence in numerical simulations for $l_0/l_a = 0.86$.

allow the system to explore different polarity field configurations, potentially settling on the most stable ones. Therefore, we now consider the Gaussian white noise ξ_i in the polarity equation (4.7b).

4.6.1 Fokker-Planck equation

The stochastic evolution of the positional and angular degrees of freedom can be studied by considering the probability density function $Q(\boldsymbol{r}_1, \ldots, \boldsymbol{r}_N; \theta_1, \ldots, \theta_N | t)$, characterizing the time-dependent probability of observing a certain spatial/angular arrangement of the system. It evolves according to the Fokker-Planck equation (see Appendix B):

$$\frac{\partial Q}{\partial t} = -\boldsymbol{\nabla}_{\boldsymbol{r}_i} \left(\left(\sum_j \boldsymbol{\varphi}_j^k \cdot \hat{\boldsymbol{n}}_j \right) \boldsymbol{\varphi}_i^k Q \right) + \frac{\partial}{\partial \theta_i} \left(\frac{\partial V}{\partial \theta_i} Q \right) + D \frac{\partial^2 Q}{\partial \theta_i^2}, \tag{4.21}$$

where the sum over repeated indices is implied. The last term on the right-hand side comes from the angular diffusion of the active units, and the first one originates from variations of the zero modes geometry as the system evolves (e.g. the rotation mode rotates with the structure in free boundary conditions). The second term on the right-hand side can be interpreted as a probability current driven by the gradient of a potential, where:

$$V(\theta_1, \ldots, \theta_N) = -\frac{1}{2} \sum_{q \in \mathcal{F}} a_q^n (\theta_1, \ldots, \theta_N)^2 . \tag{4.22}$$

Finding a general solution for the probability density function Q is a complex problem. However, we are mainly interested in the $\tau_n \ll 1$ regime, where multiple equilibrium solutions exist. In this limit, the zero mode variation timescale is expected to be much smaller than the θ_i dynamics timescale. Indeed, $\boldsymbol{r}_i$ scaling like τ_n^{-1}, derivatives with respect to $\boldsymbol{r}_i$ scale like τ_n. This timescale separation, which also depends on the particular geometry of the system, leads to a significant simplification of the dynamics. In such a regime, we could consider the polarity field evolution keeping a frozen, or quasi-static evolution of the zero modes. In practice, this approximation considers that the probability density function Q is different from zero only for combinations of $\boldsymbol{r}_i$ which preserve the same zero modes. Therefore, integrating out positional degrees of freedom in Eq. (4.21):

$$\frac{\partial \mathcal{Q}}{\partial t} = \frac{\partial}{\partial \theta_i} \left(\frac{\partial V}{\partial \theta_i} \mathcal{Q} \right) + D \frac{\partial^2 \mathcal{Q}}{\partial \theta_i^2}, \tag{4.23}$$

where the reduced density probability function $\mathcal{Q} = \int_{-\infty}^{+\infty} Q d\boldsymbol{r}_1 \ldots d\boldsymbol{r}_N$. This Fokker-Planck equation admits a steady-state solution given by:

$$\mathcal{Q} = \frac{1}{Z} e^{-\beta V}, \tag{4.24}$$

where $\beta = 1/D$ and the partition function $Z = \int_{-\pi}^{\pi} e^{-\beta V} d\theta_1 \ldots \theta_N$. Remarkably, the explicit expression of this partition function allows for using all the equilibrium systems' toolbox, as discussed below.

4.6.2 Free-energy

Collective motion can be achieved along a zero mode only if the normalized projection of the polarity vector over that mode is $\mathcal{O}(1)$. Such quantities define the order parameters $\mu_q = \langle a_q^n \rangle / \sqrt{N}$, where the outer parentheses $\langle \bullet \rangle$ stand for the average over the stationary distribution (see Appendix B). Considering extended zero modes only, such

as translations, rotations, or more exotic ones like auxetic modes [166], we can recast the expression of the partition function as:

$$Z = \int_{-\infty}^{+\infty} e^{-N\beta f(\mu_1,\ldots,\mu_M)} d^M\mu, \tag{4.25}$$

where M is the number of zero modes. The method consists of introducing conjugated variables h_q, and reformulating the partition function's expression using Gaussian integrals tricks (see Appendix B). Therefore, mode selection in the stationary state is governed by the minimum of the Landau-Ginzburg-like free energy:

$$f(\mu_1,\ldots,\mu_M) = \frac{1}{2}\sum_{q\in\mathcal{F}} \mu_q^2 - \frac{1}{\beta N}\sum_i \log(I_0(\beta\mathcal{D}_i)), \tag{4.26}$$

where $I_n(z)$ are the modified Bessel functions of first kind, and where:

$$\mathcal{D}_i = \left(N \sum_{q,l\in\mathcal{F}} \mu_q\mu_l \left(\boldsymbol{\varphi}_i^q \cdot \boldsymbol{\varphi}_i^l\right)\right)^{1/2}, \tag{4.27}$$

couples the different zero modes. This description in terms of free energy is valid only in the large N limit. For finite N a similar description can be obtained in terms of simple integrals (as shown in appendix B).

Phase transition

In the following, we show that for a generic rigid structure with $D > 1/2$, the disordered solution is a minimum of Eq. (4.26).

In the large noise limit, one expects that the order parameters are very small. We can thus use the approximation $\ln(I_0(x)) \simeq x^2/4$ and write the free energy close to the disordered solution:

$$\begin{aligned} f\left[\mu_q\right] &\simeq \frac{1}{2}\sum_{q\in\mathcal{F}} \mu_q^2 - \frac{\beta}{4}\sum_i\sum_{q,l} \mu_q\mu_l \left(\boldsymbol{\varphi}_i^q \cdot \boldsymbol{\varphi}_i^l\right), \\ &= \frac{1}{2}\sum_{q\in\mathcal{F}} \mu_q^2 - \frac{\beta}{4}\sum_{q,l} \mu_q\mu_l \langle\boldsymbol{\varphi}^q|\boldsymbol{\varphi}^l\rangle, \\ &= \frac{1}{2}\left(1-\frac{\beta}{2}\right)\sum_q \mu_q^2, \end{aligned} \tag{4.28}$$

where the last equality is obtained from orthonormality. Generically, a phase transition toward the disordered phase happens at $\beta = 2$, thus $D = 1/2$, along every zero mode, with mean-field critical exponents.

Global minimum for small noise

As the noise goes to zero, $\beta \to +\infty$, we can use the asymptotic expression $I_0(x) \simeq e^x$ to approximate Eq. (4.26):

$$f\left[\mu_q\right] \simeq \frac{1}{2}\sum_{q\in\mathcal{F}} \mu_q^2 - \sum_i \left(\frac{1}{N}\sum_{q,l} \mu_q\mu_l \left(\boldsymbol{\varphi}_i^q \cdot \boldsymbol{\varphi}_i^l\right)\right)^{1/2}. \tag{4.29}$$

Let us now minimize the above functional in the presence of a single mode, or said differently, considering that a given mode q_0 is selected by the active dynamics ($\mu_{q_0} \simeq 1$ and $\mu_{q\neq q_0} \simeq 0$). We find:

$$f_{q_0} = \frac{1}{2}\mu_{q_0}^2 - \frac{1}{\sqrt{N}} \sum_i \mu_{q_0} |\boldsymbol{\varphi}_i^{q_0}|, \tag{4.30}$$

which has a minimum corresponding to:

$$\tilde{f}_{q_0} = -\frac{1}{N} \left(\sum_i |\boldsymbol{\varphi}_i^{q_0}| \right). \tag{4.31}$$

We want to maximize $\sum_i |\boldsymbol{\varphi}_i^{q_0}|$, subject to the normalization constraint $\sum_i |\boldsymbol{\varphi}_i^{q_0}|^2 = 1$. We can easily demonstrate that the maximum is achieved when all the components are equal, i.e $|\boldsymbol{\varphi}_i^{q_0}| = 1/\sqrt{N}$. Then, in the $\beta \to +\infty$ limit, collective motion will align with the least localized mode, i.e translations in an unpinned structure. In the case of a 1-ring hexagon without a central active unit, because every particle is at the same distance from the barycenter, translations and rotations result in the exact same minimum value, and there is no preference for one over the other.

4.6.3 Application to free boundary conditions

Mode selection

To get a better insight into the mode selection, let us consider the most common case of an active solid with rigid body motions. Considering the explicit expressions of the translational and rotational zero modes in the Fokker-Plank Eq. (4.21), we can show that the timescale separation approximation is controlled by the small parameter τ_n. A formal perturbative expansion can be performed, where at leading order in small quantities, Eq. (4.23) is obtained (see Appendix B). Thus, the steady state is determined by the minima of the potential:

$$f = \frac{1}{2} \left[\langle \boldsymbol{P} \rangle^2 + \frac{I}{N} \left\langle \dot{\phi} \right\rangle^2 \right] - \frac{1}{\beta N} \sum_i \ln(I_0(\beta \mathcal{D}_i)), \tag{4.32}$$

where

$$\mathcal{D}_i = \left| \langle \boldsymbol{P} \rangle + \boldsymbol{r}_i^{\perp} \left\langle \dot{\phi} \right\rangle \right|. \tag{4.33}$$

We numerically studied the free energy landscape for different geometries, such as triangular lattices arranged as in Fig. 4.1-f with an increasing number of rings, rigid square lattices with different aspect ratios, and rigid rings. Figs. 4.7-a and b show this landscape for a 9-ring hexagonal structure without a central unit for two different noise amplitudes. We observed that purely rotational and purely translational solutions are local minima of the free energy for $D < 1/2$. Interestingly, mixed translational/rotational states are not steady-state solutions. As discussed in the limit $D \to 0$, the translational solution is indeed the global minimum. Despite the complexity of the free energy landscape, we find that minima are separated by an energy barrier proportional to N, hence large-N systems should remain trapped in a local minimum.

When the energy barrier between the two minima becomes comparable with the energy scale β, we expect to see transitions on the experimental timescale between the two states. This opens the possibility of designing structures with particularly tuned actuation behaviors. In Figs. 4.7-c,d, and e, we can see the non-trivial behavior of a 2-ring

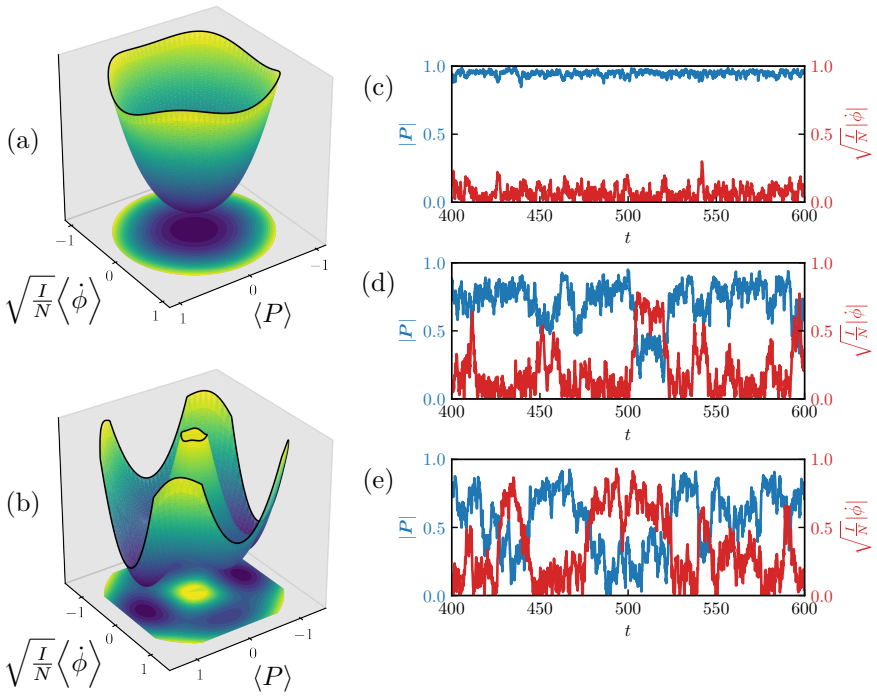


FIG. 4.7. **Finite systems' energy landscape and noise-induced actuation mode switching.** (a) Function f given by Eq. (4.32) for a 9-ring hexagonal structure without a central unit ($N = 270$) as a function of the mean scalar polarization and the mean rotational speed. Landscapes are shown for $D = 0.6$ and (a) $D = 0.1$ (b). (c) Polarization and rotational speed as a function of time for a simulated 2-ring hexagonal configuration similar to Fig. 4.5-c. for $D = 0.10$, (d) $D = 0.32$ and (e) $D = 0.35$. For every system, $\tau_n = 0.1$.

hexagon without a central unit, jumping between translational and rotational states when β is small enough, with a persistence time that decreases with the noise amplitude, and a clear preference for the translating solution. Further studies of geometrical configurations in the finite N limit, i.e explicitly considering the distribution Q, could shed light on the possibility of more complex mode-selection behaviors.

Collective translation

For large enough N, the energy barrier connecting rotational and translational states is large enough for them to be considered separately. If only translational motion is allowed, we can show that the Fokker-Plank Eq. (4.23) is exact, since translational zero modes are position-independent. Furthermore, the free energy follows Eq. (4.32), taking $\dot{\phi} = 0$. An exact realization with only translational degrees of freedom is achieved using a rigid triangular lattice with Periodic Boundary Conditions (PBC). Indeed, in that case, the dynamics take place on the 2-torus, and solid body rotation is topologically forbidden. Remember that in the thermodynamic limit, we have shown above that a phase transition with the mean-field critical exponents generically happens at $D = 1/2$, which therefore applies here. Extracting from simulations the polarization order parameter $\Psi = \langle|\boldsymbol{P}|\rangle$ as a function of the noise amplitude, a very good agreement with the rigid theory is observed (Fig. 4.8-a). For the PBC system, the potential function can be written as follows:

$$V = -\frac{1}{2N}\sum_{i\neq j}\cos(\theta_i - \theta_j), \tag{4.34}$$

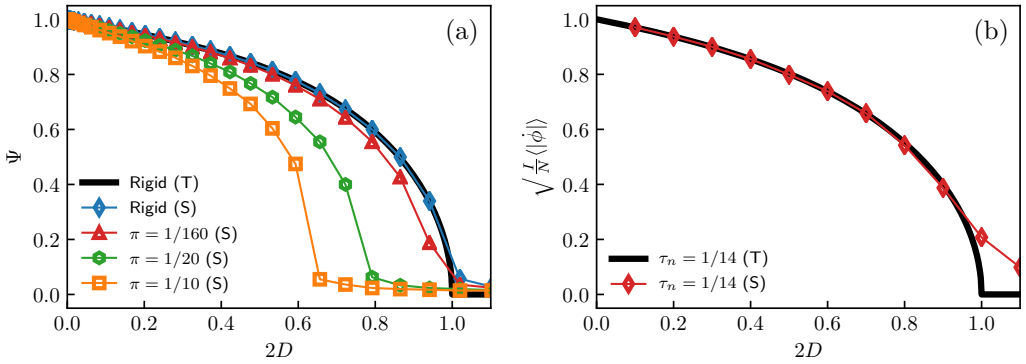


FIG. 4.8. **Noise-induced phase transition.** (a) Polarization order parameter $\Psi = \langle|\boldsymbol{P}|\rangle$ as a function of the noise amplitude for a $N = 100 \times 100$ system with different parameters π, and the same configuration in the rigid limit. (b) Rotational order parameter $\langle|\dot{\phi}|\rangle/\phi_{\max}$ as a function of the noise amplitude for a 9-ring hexagonal structure pinned at the center ($N = 270$), showing the values predicted from the free energy minimization (T) and the average simulation values (S).

which exactly corresponds to the $2d$ mean-field XY model. It is remarkable that, in this case, the mean-field behavior of the system does not arise from an uncontrolled approximation. In a way, as soon as the network connectivity restricts local deformations, stresses can propagate through the whole system without a defined decay length. These stresses are responsible for the emergence of long-range order. This is a consequence of considering perfectly rigid links. We would expect to observe deviations from this behavior if we consider truly elastic springs. Indeed, by increasing $l_e = F_0/k$, for instance by keeping F_0 fixed and decreasing k, the decay length of stress relaxation should decrease, and as a consequence, the system should be more disordered for the same noise level. This is confirmed by our numerical simulations of Eqs. (4.2). As Fig. 4.8-a shows, the critical value $D^\star$ decreases as π increases. Once elasticity is recovered, the nature of the critical behavior and critical exponents remain unclear and call for more numerical and theoretical work.

Collective rotation

In the purely rotational case, i.e a pinned system, the free energy corresponds to Eq. (4.32) with $\boldsymbol{P} = \boldsymbol{0}$. We perform numerical simulations of a 9-ring hexagonal structure with central pinning, extracting the rotational order parameter $\langle|\dot{\phi}|\rangle/\phi_{\max}$ as a function of the noise amplitude. We compare those results with the rotational minimum of the free energy for the same structure, and find a good correspondence between our simulations and theoretical predictions when τ_n is small enough (Fig. 4.8-b). Note that the large-D discrepancy is associated with a finite size effect.

4.7 Conclusion

In this chapter, we have studied the dynamics of non-deformable active solids, where interaction forces are mediated by rigid links constraining the motion of each agent to follow the zero modes of the structure. This stress propagation mechanism is sufficient to induce collective motion along these modes, whose explicit geometry allowed us to make general statements about the properties and stability of translating/rotating regimes, for different boundary conditions. Note that the theoretical framework presented here

is quite general; a rigid description can be obtained via a limiting procedure starting from various interaction forces. Even though perfectly inextensible links are not feasible, our experiments considering hard plastic links and stiff springs imply that the theory is robust against small agent-agent distance variations and residual elasticity. However, the effect of elasticity over the phase transition and the critical phenomena in the thermodynamic limit remains to be elucidated.

We have shown that for large systems and slow timescales of positional evolution, mode selection privileges the least localized modes, e.g pure translations, with a noise-induced continuous phase transition from order to disorder at a well-defined noise amplitude. Previously studied underdamped systems point to a different noise-induced phase transition from a translational-dominated regime to a rotational-dominated one when considering non-fixed topologies and short-range interactions [167, 168]. Further studies of rigid active solids outside of the scope of our theory, i.e with $\tau_n \simeq 1$ or including non-extended modes, could reveal the existence of more complicated noise-induced transitions. Furthermore, it has been observed in other active solids systems that translational collective motion selects particular directions based on the lattice geometry [112]. Our numerical simulations hint at the same phenomenon, which our theory cannot account for. A deeper analysis of the dynamical equations outside of the linear regime could shed light on this selection mechanism.

Chapter 5

Selective and collective actuation

5.1 Introduction

If not held, active solids adopt the translational and/or rotational rigid body motion dictated by the presence of zero modes, as discussed in the previous chapter, and reported in other theoretical models. Nevertheless, the feedback mechanism between elastic and active forces, and the possible emergence of collective behaviors in a mechanically stable elastic solid remains poorly understood.

In this chapter, we introduce a minimal realization of an active elastic solid, in which we characterize the emergence of selective and collective actuation resulting from the interplay between activity and elasticity. Polar active agents exert forces on the nodes of a $2d$ elastic lattice. The resulting displacement field nonlinearly reorients the active agents. For large enough coupling, a collective oscillation of the lattice nodes around their equilibrium position emerges. Only a few elastic modes are actuated, and crucially, they are not necessarily the lowest energy ones. Combining experiments with the numerical and theoretical analysis of an agents model, we unveil the bifurcation scenario and the selection mechanism by which the Collective Actuation (CA) takes place. We perform large-scale simulations, demonstrating that CA persists in the continuum limit, and show that the transition to CA is essentially discontinuous, with a spatial coexistence between frozen and collectively actuated regions. Finally, we coarse-grain the microscopic model, and find its homogeneous, mean-field-like solutions.

5.2 Collective actuation in active networks

Combining the active elastic building blocks described in chapter 2 with *soft* springs, we construct active triangular and kagome lattices. To avoid the presence of zero modes, we entirely pin the edges of those structures, so their spectrum is only composed of harmonic modes (see Appendix A). Therefore, each node has a well-defined reference position, but will be displaced by the active particles. In contrast, the polarization of each particle is free to rotate and reorients towards its displacement via self-alignment. Remember that this nonlinear feedback between deformations and polarizations is characterized by two length scales: (i) the typical elastic deformation caused by active forces l_e (Fig.2.4-c), and (ii) the self-alignment length l_a (Fig.2.4-d), see chapters 2 and 3.

We complement the experiments with numerical simulations of elastically coupled self-aligning active particles (see chapter 3). In the overdamped, harmonic, and noiseless limit, the model reads:

$$\dot{\boldsymbol{u}}_i = \pi \hat{\boldsymbol{n}}_i - \mathbb{M}_{ij}\boldsymbol{u}_j, \tag{5.1a}$$
$$\dot{\boldsymbol{n}}_i = (\hat{\boldsymbol{n}}_i \times \dot{\boldsymbol{u}}_i) \times \hat{\boldsymbol{n}}_i, \tag{5.1b}$$

where the ratio of the elasto-active and self-alignment lengths, $\pi = l_e/l_a$, which we refer to as the elasto-active coupling, is the unique control parameter. The $\hat{\boldsymbol{n}}_i$'s are the polarization unit vectors, $\boldsymbol{u}_i$ is the displacement field with respect to the reference configuration, and $\mathbb{M}$ is the dynamical matrix.

5.2.1 CA regime

For both the triangular (Fig.5.1-top) and the kagome (Fig.5.1-bottom) lattice, we observe a regime where all the lattice nodes spontaneously break chiral symmetry and rotate around their equilibrium position in a collective steady state (Fig.5.1-a), a so-called CA regime. All the particles perform circular-like orbits, with an amplitude that decreases as we consider particles closer to the boundary condition. This CA regime, in the form of Synchronized Chiral Oscillations (SCO), is reminiscent of oscillations in biological tissues [8, 77, 169], and is clearly different from collective motion in active fluids [43, 59] and rigid body motion in active solids [90, 92, 112].

The two dynamics are best described when projected on the normal modes of the elastic structures sorted by order of growing energies (see Appendix A). Thus, we measure the

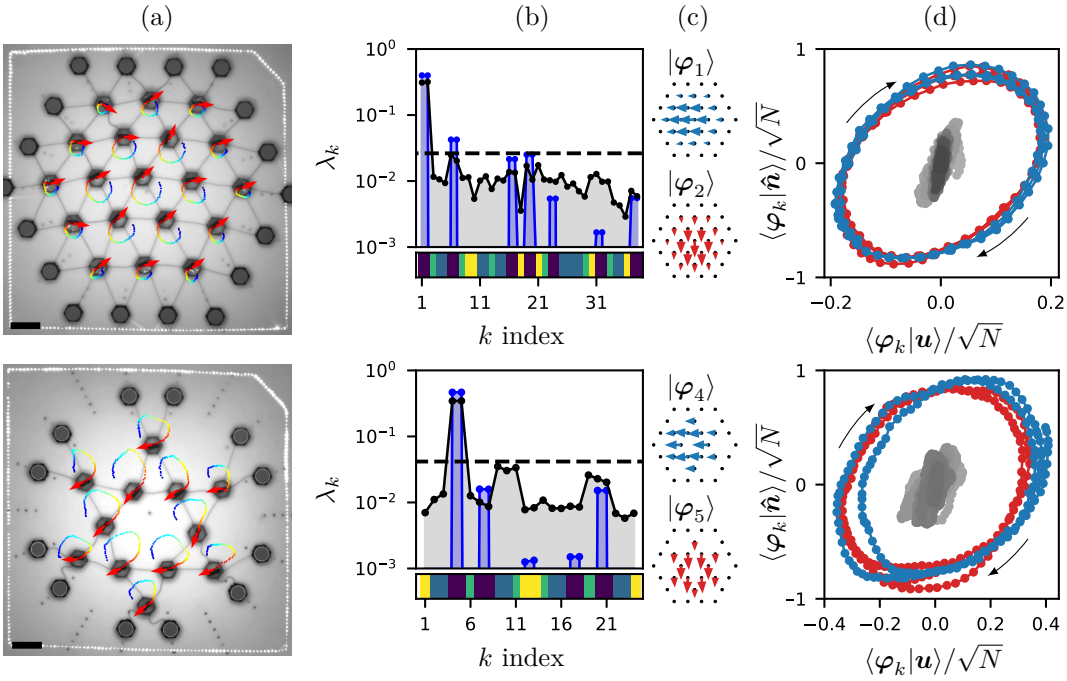


FIG. 5.1. **Selective and collective actuation in 2d elastic lattices, pinned at the edges.** (top) Triangular lattice, $N = 19$, $\alpha = 1.27$; (bottom) kagome lattice, $N = 12$, $\alpha = 1.02$. (a) When doped with active units, a large enough elasto-active feedback π drives the system towards collective actuation dynamics (red arrows: polarities $\hat{\boldsymbol{n}}_i$; trajectories color-coded from blue to red by increasing time; scale bars: 10 cm). (b) Condensation fraction λ_k on the normal modes of the lattices, sorted by order of growing energies (grey: experiments; blue: numerics). The horizontal dashed lines indicate equipartition. The bottom color bars code for the symmetry class of the modes (see appendix A). (c) Sketch of the two most excited modes, which are not necessarily the lowest energy ones. (d) Normal modes components of the active forces as a function of the normal modes components of the displacements (blue/red: projection on the modes shown in (c), shades of grey: all the other modes).

condensation fraction λ_k on mode $|\boldsymbol{\varphi}_k\rangle$:

$$\lambda_k = \left\langle (\tilde{a}_k^n)^2 \right\rangle_t = \frac{1}{T}\int^T \left[\frac{\langle \boldsymbol{\varphi}_k | \hat{\boldsymbol{n}}(t)\rangle}{\sqrt{N}}\right]^2 dt, \tag{5.2}$$

where $\tilde{a}_k^n = \langle \boldsymbol{\varphi}_k | \hat{\boldsymbol{n}}\rangle/\sqrt{N}$ is the normalized projection of the polarity field on mode $|\boldsymbol{\varphi}_k\rangle$, and satisfies $|\tilde{a}_k^n| < 1$ (see chapter 3). λ_k corresponds to the fraction of active force injected on average into mode $|\boldsymbol{\varphi}_k\rangle$. Said differently, it measures how much the polarity field is aligned with mode $|\boldsymbol{\varphi}_k\rangle$ on average and is bounded between 0 and 1.

The dynamics condensate mostly on two modes (Fig. 5.1-b), and describe a limit cycle driven by the misalignment between the active forces and the displacements (Fig. 5.1-d). In the case of the triangular lattice, the selected modes are the two lowest energy ones. Interestingly, in the case of the kagome lattice, these are the fourth and fifth modes, not the lowest energy ones. For both lattices, the selected pair of degenerated modes are strongly polarized along one spatial direction; they are extended, and the polarization of the modes in each pair is locally quasi-orthogonal (Fig. 5.1-c). Numerical simulations of the overdamped dynamics in the harmonic approximation confirm the experimental observations indicating that CA is already present for linear elasticity and is not of inertial origin. It also allows for the observation of additional secondary peaks in the spectrum, which belong to the same symmetry classes as the two most actuated modes (Fig. 5.1-b and Appendix A), i.e. $(1/2, \pm 1)$, and of even smaller peaks in the classes $(-1, \pm 1)$. As we shall see below, all these properties are at the root of the selection principle of the actuated modes.

5.2.2 Transition to CA

The transition to the CA regime (Fig. 5.2) is controlled by the elasto-active coupling π. The larger it is, the more the particles reorient upon elastic deformations. Experimentally, π is varied by changing the length of the springs, as discussed in chapter 2. We characterize the transition by measuring the average individual oscillation frequencies/rotation rates $\langle \omega_i \rangle_t$ through a fit of the long-time behavior of $\langle \theta_i(t+\tau) - \theta_i(t)\rangle_t(\tau)$ with a linear power law, where θ_i refers to the orientation of particle i. With the help of those quantities, we define the average collective oscillation frequency as $\Omega = \frac{1}{N}\sum_i \langle \omega_i \rangle_t$. Note that it measures the amount of rotation rate the active system collectively experiences, but not the phase synchronization of the particles from a Kuramoto point-of-view [170, 171], as such a description seems extraneous[1] here and is replaced by the projections on the normal modes, discussed above.

We find that below a first threshold π_{FD}, the active solid freezes in a disordered state, with random polarizations and angular diffusion. In noiseless numerical simulations, this state corresponds to a zero-frequency regime $\Omega = 0$, that stands on a stable fixed point. Beyond a second threshold π_{CA}, collective actuation sets in: synchronized oscillations at frequency $\Omega > 0$ take place, and the noiseless dynamics follow a limit cycle, composed of several frequencies in rational ratios (Figs. 5.3-a,b, and c). In between, the system is heterogeneous (Fig. 5.2-b), with the oscillating dynamics being favored close to the center, while the frozen disordered regime invades the system layer by layer, from the edges towards the center, as π decreases. Interestingly, in the noiseless simulations, we find coexisting frozen disordered regimes for π beyond π_{FD}, in a range that depends on

[1] Because the active particles only exert polar forces and are not driven at a constant rotation rate as Kuramoto-like oscillators do.

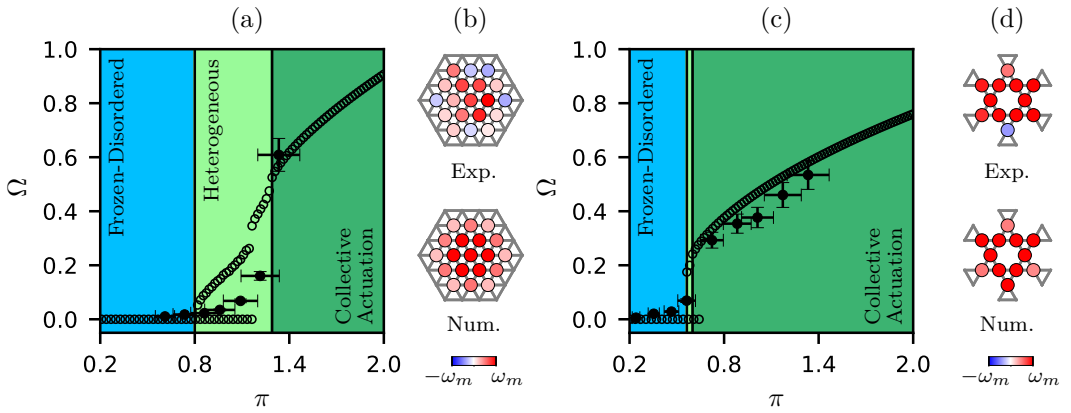


FIG. 5.2. **Transition to collective actuation in 2d elastic lattices, pinned at the edges.** (a/b) Triangular lattice, $N = 19$, $\alpha = 1.27$; (c/d) kagome lattice, $N = 12$, $\alpha = 1.02$. (a/c) Collective oscillation frequency Ω as a function of π. Black markers are experimental data, the error bars corresponding to the 1-σ confidence intervals, inherited from the uncertainty on the measurements of the microscopic parameters. Open circles are numerical data, obtained from several random initial conditions at each value of π. Background colors code for the dynamical regime (light blue: frozen and disordered; light green: heterogeneous (H); dark green: CA). Triangular: $\pi_{FD} = 0.800$, $\pi_{CA} = 1.29$; kagome: $\pi_{FD} = 0.564$, $\pi_{CA} = 0.600$. (b/d) Scaled individual oscillation frequencies ω_i/ω_m, where ω_m is the maximum individual oscillation frequency, illustrating the spatial coexistence in experiments and numerical simulations; (triangular lattice: $\pi_{\text{exp}}/\pi_{\text{num}} = 1.22/1.09$; kagome lattice: $\pi_{\text{exp}}/\pi_{\text{num}} = 0.723/0.564$).

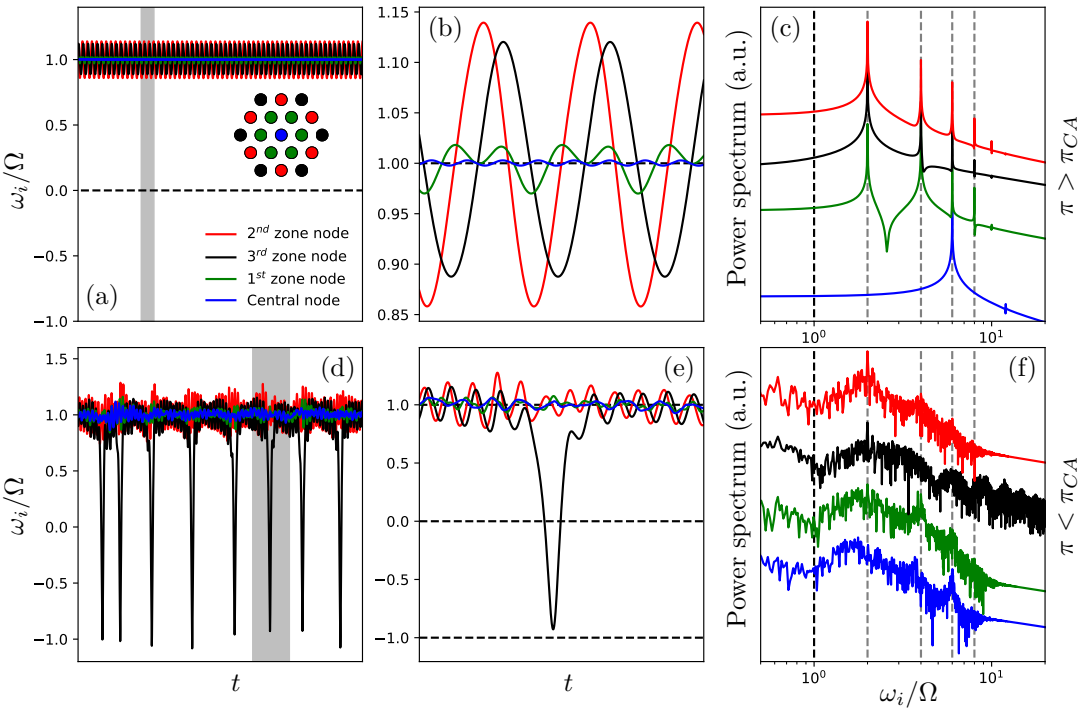


FIG. 5.3. **Transition to the heterogeneous regime in the triangular lattice pinned at the edges.** Noiseless simulations, just before the desynchronization, $\pi > \pi_{CA}$ (top); and just after the desynchronization, $\pi < \pi_{CA}$ (bottom). (a/d) Scaled individual oscillation frequencies ω_i/Ω as a function of time. The dynamics is restricted to four particles, representative of the four spatial zones of equivalent particles shown in the inset of panel (a). (b) and (e) are zooms on the gray zones of (a) and (d). (c/f) Power spectrums of the signals shown in panels (a/d), shifted vertically for clarity reasons. The dashed vertical black line represents the collective oscillation frequency Ω, and the dashed gray lines are even multiples of Ω.

the structure.

Fig. 5.3 describes the details of the discontinuous transition from the CA to the heterogeneous regime at $\pi = \pi_{CA}$. In the CA regime, the polarities rotate at a given mean frequency Ω, dressed with periodic modulations (Figs. 5.3-a and b). Indeed, as the selected modes are not strictly locally orthogonal, the oscillation cannot occur at a single-frequency, and is modulated by even multiples of the mean rotation rate (Fig. 5.3-c). As π decreases below π_{CA}, the periodic CA regime turns unstable, and the most-outer particles desynchronize from the mean oscillation. This yields a discontinuous jump in the collective oscillation frequency Ω, and aperiodic turnarounds of the most-outer polarities (Figs. 5.3-d and e). The system has entered into the heterogeneous regime, where the CA and the frozen regimes coexist spatially. This desynchronization process repeats layer-by-layer as π decreases, and the system abruptly stops at π_{FD}, when the central particles stop sustaining the synchronized oscillation.

5.2.3 Large N systems

Simulations with increasing values of N, while keeping the physical size L constant indicate that CA subsists for large N (Figs. 5.4 and 5.5).

We perform numerical simulations of Eqs. (5.1) for triangular, respectively kagome, lattices, increasing the number of active units, up to $N = 1141$, respectively $N = 930$, while keeping L constant, with an overall size L, such that the lowest energy modes have unity squared eigenfrequencies. For $\pi = 10$, starting from random initial conditions, we

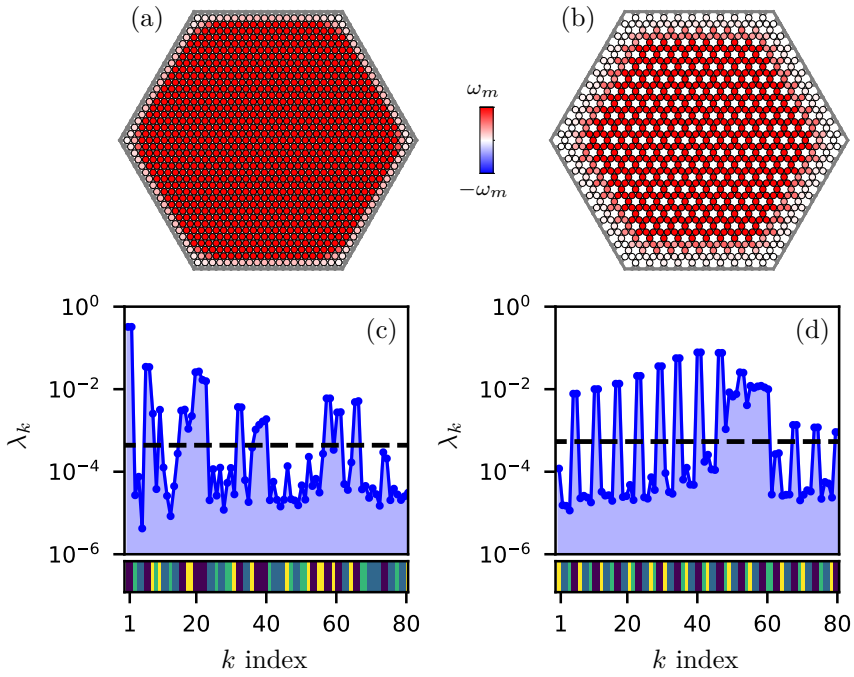


FIG. 5.4. **Collective actuation in large N lattices.** (left) Triangular lattice pinned at the edges, $N = 1141$, $\alpha = 1.0$, and (right) kagome lattice pinned at the edges $N = 930$, $\alpha = 1.0$; both for $\pi = 10$. (a/b) Scaled individual oscillation frequencies ω_i/ω_m, where ω_m is the maximum individual oscillation frequency. (c/d) Condensation fraction λ_k of the dynamics on the normal modes of the lattices, sorted by order of growing energies (only the first 80 modes are shown). The bottom color bars code for the symmetry class of the modes.

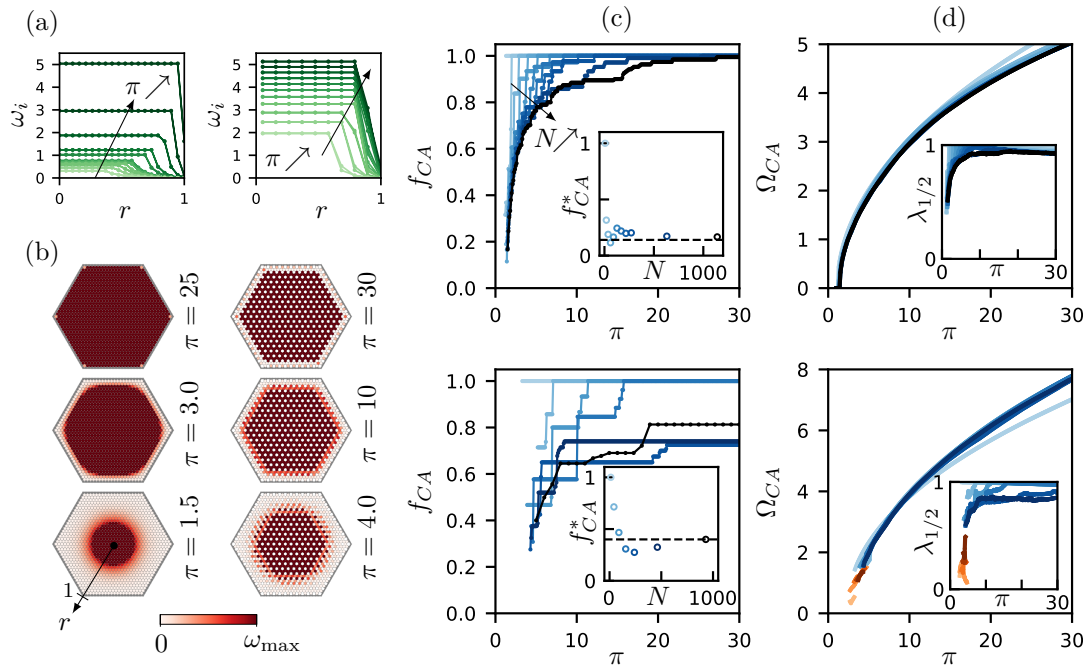


FIG. 5.5. **Transition to collective actuation in large N lattices.** (a) Radial distribution of the individual oscillation frequencies ω_i (left: triangular lattice, $N = 1141$; right: kagome lattice, $N = 930$). Plots are color-coded from light to dark green as π increases (triangular lattice: for $\pi \in [1.5, 1.6, 1.7, 1.8, 1.9, 2.0, 2.5, 3.0, 5.0, 10, 30]$; kagome lattice: for $\pi \in [4.0, 5.0, 6.0, 7.0, 8.0, 9.0, 10, 11, 12, 13, 14]$). (b) Spatial distribution of $|\omega_i|$ (left: triangular lattice, $N = 1141$; right kagome lattice, $N = 930$), π values as indicated. (c) Collective actuation fraction f_{CA} as a function of π for increasing N, color-coded from light to dark blue. Inset: f_{CA} at onset of collective actuation saturates to a finite value at large N. (d) Collective oscillation frequency Ω_{CA} as a function of π for increasing N, same color code (triangular lattices, $N = 7, 19, 37, 61, 91, 127, 169, 217, 271, 631, 1141$; kagome lattice, $N = 12, 42, 90, 156, 240, 462, 930$). Inset: condensation fraction on the selected symmetry classes, $\lambda_{1/2}$ as a function of π for increasing N. For panels (c) and (d): top row, triangular lattice; bottom row, kagome lattice. All simulations are performed with $\alpha = 1.0$.

find that the system converges toward the CA regimes represented in Figs. 5.4, corresponding to SCO. Most importantly, the spectrum demonstrates that inside the CA regime, the symmetry class of modes that are selected is independent of the system size (Figs. 5.4-c and d). The selection of the most actuated modes is again dictated by the geometry of the modes, and not only by their energies. For the sake of illustration, in the large kagome lattice pinned at the edges, the most activated modes are $|\varphi_{40}\rangle$ and $|\varphi_{41}\rangle$. Note that this holds even though there is some spatial coexistence with a frozen phase close to the boundary condition (Figs. 5.4-a and b), which contributes to thermalizing the spectral decomposition.

To better characterize the transition to CA when π varies, we measure the fraction of nodes activated in the center of the system, f_{CA}, defined as the ratio of the number of active units rotating at least at 90% of the maximum rotation frequency, over the total number of active units. The collective actuation oscillation frequency Ω_{CA} is defined as the average of the individual rotation rates inside the collectively actuated region. We quantify the condensation level by computing the averaged condensation fraction in the symmetry classes $(1/2, \pm 1)$: $\lambda_{1/2} = \sum_{i \in [1/2]} \lambda_i$, where $[1/2]$ refers to the modes belonging to the $(1/2, \pm 1)$ symmetry classes. This quantity, bounded between 0 and 1,

is the fraction of the dynamics condensed in the classes of the selected modes.

The successive de-actuation steps converge toward a regular variation of the fraction of nodes activated in the center of the system, f_{CA} (Fig. 5.5-c and d). At the transition to the frozen disordered state, when $\pi = \pi_{FD}$, the fraction of actuated nodes drops discontinuously to zero, from a finite value f^*_{CA}, which decreases with N, but saturates at large N (Fig. 5.5-c, inset). In the case of the triangular lattices, the collective oscillation frequency Ω_{CA} decreases continuously to zero (Fig. 5.5-d, top). This is however non-generic: in the case of the kagome lattices, very close to the transition, the dynamics condensate on a different set of modes, pointing at the possible multiplicity of periodic solutions. The transition is essentially discontinuous. In all cases, the condensation level remains significant, with a large condensation fraction $\lambda_{1/2}$ for a wide range of values of π (Fig. 5.5-d, inset).

5.2.4 Role of noise

The role of angular noise is another matter of interest. In the noiseless and overdamped framework, CA has been identified as an ordered dynamical regime, corresponding to a limit cycle. In the presence of noise, Eqs. (5.1) turn into coupled non-linear SDEs, with a Langevin term $\xi_i(t)$ in the polarity dynamics, Eq. (5.1b), with zero mean and correlations $\langle \xi_i(t)\xi_j(t')\rangle = 2D\delta_{ij}\delta(t-t')$. We focus on the case of the triangular lattice, and compute the collective oscillation frequency in absolute value, $\langle|\Omega|\rangle_t = \frac{1}{N}\sum_i \langle|\omega_i|\rangle_t$, where $\langle|\omega_i|\rangle_t$ is measured by fitting the long-time behavior of $\langle|\theta_i(t+\tau)-\theta_i(t)|\rangle_t(\tau)$ with linear power law[2].

In the frozen disordered regime, the noise is responsible for the angular diffusion of the polarities amongst the fixed points. In the CA regime, the noise level present in the experiment does not significantly alter the dynamics. Numerical simulations confirm a sharp transition at a finite noise amplitude D_c, below which collective actuation is sustained (Fig. 5.6-a). For noise amplitude much lower than D_c, the noise merely

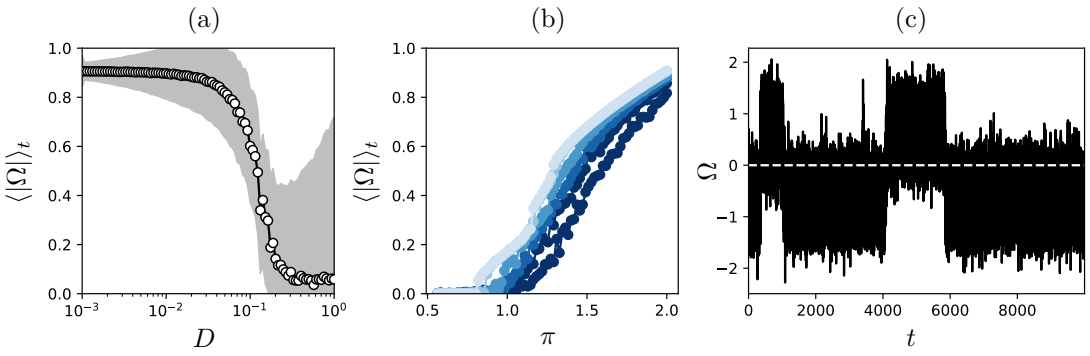


FIG. 5.6. **Effect of the noise on the collective actuation regime**. Simulations of a triangular lattice pinned at the edges, $N = 19$, $\alpha = 1.27$ (experimental conditions), including angular noise. (a) Average oscillation frequency in absolute value $\langle|\Omega|\rangle_t$ as a function of D, for $\pi = 2.0$. (b) Average oscillation frequency in absolute value $\langle|\Omega|\rangle_t$ as a function of π for increasing angular noise D. From top to bottom, $D = 0, 10^{-3}, 10^{-2}, 2.10^{-2}, 5.10^{-2}$. (c) Instantaneous oscillation frequency Ω as a function of time, for $\pi = 2.0$ and $D = 10^{-1}$; and we denote $\Omega(t) = \frac{1}{N}\sum_i (\theta_i(t+\delta t) - \theta_i(t))$.

[2]This quantity is still quite bad at measuring the average rotation rate close to the transition, because the long-time behavior of $\langle|\theta_i(t+\tau)-\theta_i(t)|\rangle_t(\tau)$ is no longer linear due to the frequent stochastic inversions.

reduces the mean angular frequency Ω, and shifts the transition to CA to larger values of elasto-active coupling π (Fig. 5.6-b). Closer to the transition, the noise allows for stochastic inversions of the direction of rotation, restoring the chiral symmetry (Fig. 5.6-c). Exploring further the nature and the universality class of this transition would be interesting but requires further numerical investigations.

5.2.5 Summary of observations

Altogether, our experimental and numerical findings demonstrate the existence of a selective and collective actuation in active solids. This new kind of collective behavior specifically takes place because of the elasto-active feedback, the reorientation of the active units by the displacement field. The salient features of collective actuation are three-fold:

(i) The transition from the disordered phase leads to a chiral phase with spontaneously broken symmetry.

(ii) The actuated dynamics are not of inertial origin, take place on a few modes, not always the lowest energy ones, and therefore obey non-trivial selection rules.

(iii) The transition follows a coexistence scenario, where the fraction of actuated nodes discontinuously falls to zero.

In the remainder of the chapter, we unveil the physical origins of these three attributes.

5.3 A few exact results for N particles systems

This section gives general results for N particle systems, including the complete fixed points linear stability analysis, selection rules from symmetry considerations, and a framework of condensation on two modes.

5.3.1 Fixed points stability analysis

Equilibrium configurations of Eqs. (5.1) are given by:

$$\pi|\hat{\boldsymbol{n}}\rangle - \mathbb{M}|\boldsymbol{u}\rangle = 0, \tag{5.3a}$$

$$\mathbb{K}^T\mathbb{K}\mathbb{M}|\boldsymbol{u}\rangle = 0, \tag{5.3b}$$

where the braket notations were introduced in chapter 3. Eq. (5.3a) imposes $|\boldsymbol{u}\rangle = \pi\mathbb{M}^{-1}|\hat{\boldsymbol{n}}\rangle$, where the matrix $\mathbb{M}$ is invertible as we consider mechanically stable elastic structures. Eq. (5.3b) is always satisfied since $\mathbb{K}^T\mathbb{K}|\hat{\boldsymbol{n}}\rangle = 0$ by construction (remember that $\mathbb{K}^T\mathbb{K}$ is the projector on $|\hat{\boldsymbol{n}}^\perp\rangle$, see chapter 3). Therefore, to any configuration of the polarity field $|\hat{\boldsymbol{n}}\rangle$ corresponds the fixed point $\{|\boldsymbol{u}\rangle = \pi\mathbb{M}^{-1}|\hat{\boldsymbol{n}}\rangle, |\hat{\boldsymbol{n}}\rangle\}$, and the set of fixed points is isomorphic to the N-torus.

Generally, the linear destabilization threshold $\pi_c(|\hat{\boldsymbol{n}}\rangle)$ depends on the fixed point configuration (see Appendix C). We show that a given configuration is stable for:

$$\pi \leq \pi_c(|\hat{\boldsymbol{n}}\rangle) = \frac{1}{\max \mathrm{Spec}\left(\mathbb{L}\left(|\hat{\boldsymbol{n}}\rangle\right)\right)}, \tag{5.4}$$

where the matrix $\mathbb{L}$ reads:

$$\mathbb{L}_{ij} = \frac{\langle\boldsymbol{\varphi}_i|\mathbb{K}^T\mathbb{K}|\boldsymbol{\varphi}_j\rangle}{\omega_i\omega_j}. \tag{5.5}$$

where ω_k is the square root of mode k's energy ω_k^2. Therefore, the knowledge of the dynamical matrix allows for assessing the linear stability properties of any fixed points. We also find that these thresholds are bounded $\pi_c^{\min} \leq \pi_c(|\hat{\boldsymbol{n}}\rangle) \leq \pi_c^{\max}$ (see Appendix C). A first fixed point becomes unstable for $\pi = \pi_c^{\min} = \omega_{\min}^2$, where $\omega_{\min}^2$ is the smallest eigenvalue of the dynamical matrix $\mathbb{M}$. This first unstable fixed point corresponds to the configuration locally orthogonal to $|\boldsymbol{\varphi}_{\min}\rangle$. An upper bound for $\pi_c^{\max}$ reads :

$$\pi^{\text{upp}} = \min_{\{i,j\}} \left(\frac{\omega_i^2 + \omega_j^2}{c(|\boldsymbol{\varphi}_i\rangle, |\boldsymbol{\varphi}_j\rangle)} \right), \tag{5.6}$$

where the function

$$c(|\boldsymbol{\varphi}_j\rangle, |\boldsymbol{\varphi}_k\rangle) = 1 - \frac{1}{2} \sum_i \left(\left[\left(\boldsymbol{\varphi}_j^i\right)^2 + \left(\boldsymbol{\varphi}_k^i\right)^2 \right]^2 - 4 \left[\boldsymbol{\varphi}_j^i \times \boldsymbol{\varphi}_k^i \right]^2 \right)^{1/2}, \tag{5.7}$$

only depends on the normal modes $\{|\boldsymbol{\varphi}_k\rangle\}$. It is bounded between 0 and 1 and is maximal when the modes $|\boldsymbol{\varphi}_j\rangle$ and $|\boldsymbol{\varphi}_k\rangle$ are extended and locally orthogonal. More specifically, the pair of modes which dominates the dynamics, $\{|\boldsymbol{\varphi}_1\rangle, |\boldsymbol{\varphi}_2\rangle\}$ for the triangular and $\{|\boldsymbol{\varphi}_4\rangle, |\boldsymbol{\varphi}_5\rangle\}$ for the kagome lattice, is precisely the one that optimizes the bound (Figs. 5.7-a and b). The construction of this bound is very general. It demonstrates that for any stable elastic structure, there is a strength of the elasto-active feedback above which the frozen dynamics is unstable, and a dynamical regime must set in. It also captures

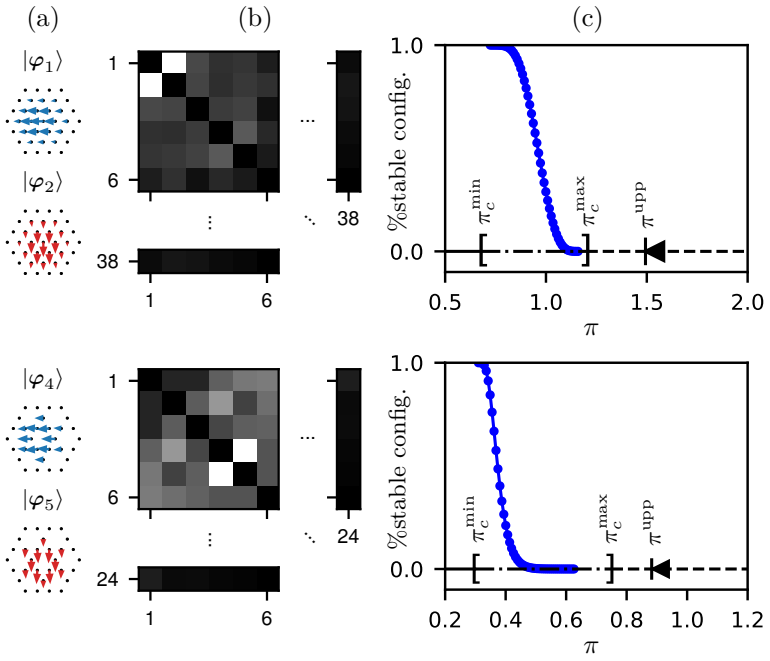


FIG. 5.7. **Fixed points stability thresholds for the experimental structures.** (top) Triangular lattice pinned at the edges; (bottom) kagome lattice pinned at the edges. (b) Stability thresholds upper-bound $\pi_{c,u}^{\{j,k\}}$ computed from Eq. (5.6) for every pair of modes. The darker the pixel, the greater the upper bound found. Remarkably, the best bound is always achieved for the pair of modes concerned by the condensation (a). (c) Fraction of stable fixed points as a function of π. The fraction of stable fixed points (blue markers) is computed by integrating the histogram of the stability thresholds found with Eq. (5.4) for one million configurations of the polarity field, drawn randomly and independently. For the triangular lattice pinned at the edges ($\alpha = 1.27$); $\pi_c^{\min} = 0.676$, $\pi_c^{\max} = 1.20$, $\pi_c^{\text{upp}} = 1.49$. For the kagome lattice pinned at the edges ($\alpha = 1.02$); $\pi_c^{\min} = 0.375$, $\pi_c^{\max} = 0.751$, $\pi_c^{\text{upp}} = 0.883$.

the mode selection in the strongly condensed regime.

We confirm the above results by evaluating the stability thresholds numerically for both experimental structures. We do so for one million configurations of the polarity field, sampled by drawing randomly and independently the orientations of each active unit according to a uniform distribution in $[0, 2\pi[$. The results are shown in Figs. 5.7-c, and highlight the fraction of configurations that remain stable for a given value of π. As expected, we find no configurations destabilizing for $\pi < \pi_c^{\min} = \omega_{\min}^2$, where the first configurations, locally orthogonal to the lowest energy mode, become unstable. The values of $\pi_c^{\max}$ were found through a numerical optimization process of $\pi_c(|\hat{\boldsymbol{n}}\rangle)$. The upper bound obtained by evaluating Eq. (5.6) for all pairs of modes captures mode selection but could be sharper. As a final remark, note that the fact that some fixed points lose stability does not imply that CA sets in: from these fixed points, the system can either slide to a neighboring stable fixed point or condensate on some dynamical attractor.

5.3.2 Symmetry considerations

Symmetry considerations contribute to the mode selection in two ways. First, the normalization condition of the polarity field imposes the actuation of some specific symmetry classes. Second, it sets the allowed nonlinear transfers between symmetry classes.

Let us first remind we sort the modes according to the classes of symmetry of the elastic structures, as explained in chapter 3. The symmetry group of the triangular and kagome lattices with hexagonal boundaries is the dihedral group D_6, generated by the rotation τ of angle $\pi/3$ and a reflection σ (say, of axis $y = 0$). Remember that for this symmetry group, the symmetry of a normal mode $|\boldsymbol{\varphi}_k\rangle$ is characterized by two real numbers,

$$\langle\boldsymbol{\varphi}_k|\tau|\boldsymbol{\varphi}_k\rangle \in \{1, 1/2, -1/2, -1\}, \tag{5.8a}$$

$$\langle\boldsymbol{\varphi}_k|\sigma|\boldsymbol{\varphi}_k\rangle \in \{1, -1\}. \tag{5.8b}$$

Moreover, we have seen that the CA regime in triangular and kagome lattices pinned at the edges corresponds to a condensation of the dynamics on modes belonging to the classes $(1/2, \pm 1)$.

Normalization constraint

The normalization of the polarity field, or in other words, the fact that the active forces are of constant modulus at every node imposes that the set of activated modes, as a whole, must contain non-zero amplitude displacements on every single node. For instance, in the case of the triangular lattice, the only modes for which the displacement is non-zero on the central node are those which are eigenvectors of τ, the rotation in the dihedral group D_6, with eigenvalues $e^{\pm i\pi/3}$ (see Appendix A). The dynamics must therefore have a finite projection on these modes. This demonstrates that the CA regimes encountered in the triangular lattice pinned at the edges will necessarily include actuations of the $(1/2, \pm 1)$ modes, as indeed observed. These considerations do not apply to the kagome lattice, which has no central node.

Nonlinear transfers

Assuming a condensation on a given symmetry class[3], the nonlinear couplings control the transfer of active force and elastic energy toward the other symmetry classes (Fig. 5.8).

The nonlinearities central to the present work come from the elasto-active feedback in the polarity dynamics, which redistribute the active force between the normal modes. Also, they are the only ones present in the numerical simulations of the harmonic dynamics. Remember the polarity dynamics, written in mode space (see chapter 3):

$$\frac{da_k^n}{dt} = -\sum_{lpq} \omega_q^2 \Gamma_{pqlk} a_q^u a_l^n a_p^n, \tag{5.9}$$

where a_k^n (resp. a_k^u) is the projection of the polarity (resp. displacement) field on mode $|\boldsymbol{\varphi}_k\rangle$, and where Γ_{pqlk} are the inter-modal geometrical coupling coefficients. A mode with eigenvalue λ with respect to a symmetry operation g can receive active force from modes with eigenvalues λ' only if they satisfy the relationship $\lambda = \lambda'^3$. For every symmetry class, we construct a table of allowed couplings (blue triangles in Fig. 5.8). We say class i couples with class j if, assuming all the active force projects on modes belonging to the class i, transfers are allowed toward class j.

Therefore, the elasto-active feedback allows for active force transfer from the selected classes $(1/2, \pm 1)$ to themselves and to the classes $(-1, \pm 1)$. This explains the precise selection of the secondary peaks in the residual pattern of actuation (Figs. 5.1-b and Appendix A). In the simulations of large triangular and kagome lattices (Figs. 5.4-c and d), it is also clear that the modes belonging to the selected classes $(1/2, \pm 1)$ are the

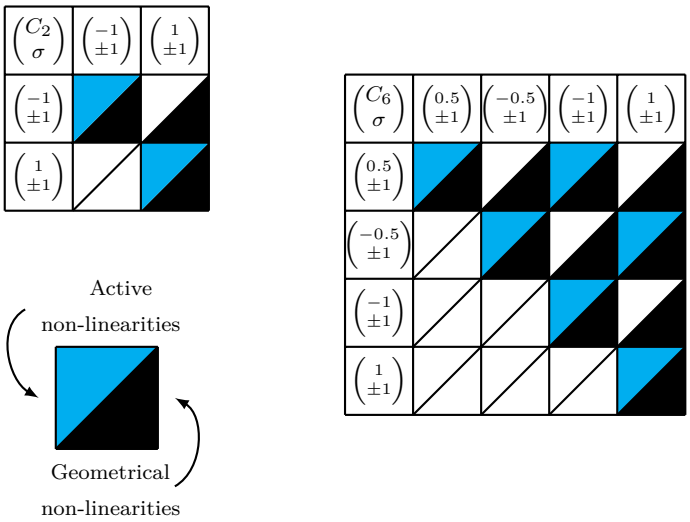


FIG. 5.8. **Nonlinear couplings between symmetry classes.** (left) Inter-class couplings for the dihedral group D_2. (right) Inter-class couplings for the dihedral group D_6. The upper left blue (resp. lower right black) triangles correspond to the elasto-active feedback nonlinearities (resp. geometrical nonlinearities) transferring active force (resp. elastic energy) from the class of row i to the class of column j, assuming active force and elastic energy only projects on modes belonging to the class of row i.

[3]Which means that the polarity and displacement fields have finite projections only on modes belonging to said symmetry class.

most activated ones, followed by modes belonging to the classes $(-1, \pm 1)$. Importantly, note that the interplay between heterogeneity and the normalization condition of the polarity field is responsible for the selection of the whole $(1/2, \pm 1)$ classes: to construct a normalized polarity field with a given symmetry, given that all the modes are heterogeneous, one must combine all those with the correct symmetry.

Finally, in the experimental system, there are large deformations of the springs for which the harmonic approximation is not valid, and nonlinear elastic couplings between the modes, so-called geometrical nonlinearities, also arise. The symmetries also restrict the possible couplings (Fig. 5.8), but we find that the selected classes can transfer elastic energy to all the other classes. Therefore, geometrical nonlinearities partly explain why the selection of the classes $(1/2, \pm 1)$ is less pronounced experimentally. Finally, the angular noise in the polarity dynamics also plays an essential role in thermalizing the system.

5.3.3 N particles dynamics restricted to two modes

The strong condensation of the dynamics on a pair of modes cannot be strict, in general, because of the normalization condition of each polarity. This is only possible if the two modes $\boldsymbol{\varphi}_1$ and $\boldsymbol{\varphi}_2$ are fully delocalized and locally orthogonal: $|\boldsymbol{\varphi}_k^i| = |\boldsymbol{\varphi}_k^j|$ for every sites i and j and $k \in \{1, 2\}$, and $\boldsymbol{\varphi}_1^i \perp \boldsymbol{\varphi}_2^i$ for every site i. Apart from very specific cases, like the one particle dynamics, the pairs of modes of an elastic structure pinned at its boundary do not satisfy such conditions exactly. However, investigating the dynamics restricted to two modes can still provide interesting insights into the transition to CA.

Starting from the equations of motion projected on the normal modes, Eqs. (3.49), the dynamics restricted to two modes reads:

$$\dot{a}_1^u = \pi a_1^n - \omega_1^2 a_1^u, \tag{5.10a}$$

$$\dot{a}_2^u = \pi a_2^n - \omega_1^2 a_2^u, \tag{5.10b}$$

$$\dot{a}_1^n = -\Gamma_{12} \left(\omega_1^2 a_1^u a_2^n - \omega_2^2 a_2^u a_1^n \right) a_2^n, \tag{5.10c}$$

$$\dot{a}_2^n = \Gamma_{12} \left(\omega_1^2 a_1^u a_2^n - \omega_2^2 a_2^u a_1^n \right) a_1^n, \tag{5.10d}$$

where there is only one coupling constant (see Eq. (3.50)):

$$\Gamma_{12} = \Gamma_{1212} = -\Gamma_{2112} = -\Gamma_{1221} = \Gamma_{2121} = \sum_i \left(\boldsymbol{\varphi}_1^i \times \boldsymbol{\varphi}_2^i \right)^2. \tag{5.11}$$

We note that $a_1^n \dot{a}_1^n + a_2^n \dot{a}_2^n = 0$, hence the norm $|a^n| = \left({a_1^n}^2 + {a_2^n}^2 \right)^{1/2}$ is constant; however, it is not necessarily 1. Introducing the rescaled quantities $\bar{a}_k^n = a_k^n / |a^n|$, where $\bar{a}_k^n$ is now normalized, $\bar{a}_k^u = \Gamma_{12} |a^n| a_k^u$ and $\bar{\omega}_k^2 = \omega_k^2 / (\Gamma_{12} |a^n|^2)$, the above equations read

$$\left(\Gamma_{12} |a^n|^2 \right)^{-1} \dot{\bar{a}}_1^u = \pi \bar{a}_1^n - \bar{\omega}_1^2 \bar{a}_1^u, \tag{5.12a}$$

$$\left(\Gamma_{12} |a^n|^2 \right)^{-1} \dot{\bar{a}}_2^u = \pi \bar{a}_2^n - \bar{\omega}_2^2 \bar{a}_2^u, \tag{5.12b}$$

$$\left(\Gamma_{12} |a^n|^2 \right)^{-1} \dot{\bar{a}}_1^n = -\left(\bar{\omega}_1^2 \bar{a}_1^u \bar{a}_2^n - \bar{\omega}_2^2 \bar{a}_2^u a_1^n \right) \bar{a}_2^n, \tag{5.12c}$$

$$\left(\Gamma_{12} |a^n|^2 \right)^{-1} \dot{\bar{a}}_2^n = \left(\bar{\omega}_1^2 \bar{a}_1^u \bar{a}_2^n - \bar{\omega}_2^2 \bar{a}_2^u a_1^n \right) \bar{a}_1^n. \tag{5.12d}$$

Up to a rescaling of the time, these are the equations of motion of a single active particle trapped in an elliptic harmonic potential (Eqs. (5.14)). In the degenerate case $\bar{\omega}_1^2 = \bar{\omega}_2^2 = \bar{\omega}_0^2$, rotating solutions exist for (see section 5.4)

$$\pi > \bar{\omega}_0^2 = \frac{\omega_0^2}{\Gamma_{12}|a^n|^2}. \tag{5.13}$$

When the modes 1 and 2 are fully delocalized and locally orthogonal, the condensation can be strict, and the restriction to these modes is exact. In this case $\Gamma_{12} = 1/N$ and $|a^n| = \sqrt{N}$, and one recovers the result obtained for one particle in the degenerate case (see section 5.4). When these conditions are not satisfied, $|a^n| < \sqrt{N}$ and thus more modes are activated, which are selected by the other Γ couplings. For the sake of illustration, from the normal modes of the triangular lattice pinned at the edges, we find that $|a^n_{12}| < 0.93\sqrt{N}$.

Altogether, one notes that the higher the scaled condensation level $|a^n_{12}|/\sqrt{N}$ and the stronger the scaled coupling $N\Gamma_{12}$, the lower the threshold for the existence of a periodic dynamics. Therefore, less homogeneous and less locally-orthogonal normal modes shift the transition to CA to larger values of π.

To conclude on the above N particles considerations, we found a connection between the linear stability analysis of fixed points and the selection rules in the strongly condensed regime. Long story short, the dynamics favor the selection of a pair of modes of low energy, extended, and locally orthogonal. Moreover, using symmetry arguments, we explained the pattern of secondary peaks and the selection of symmetry classes. However, the connection we found cannot be made rigorous, and the discontinuity of the transition forbids weakly nonlinear approaches. To proceed further, one must consider particular and simpler systems, or way larger ones.

5.4 Single particle in a harmonic potential

The simplest instance of a system evolving according to Eqs. (5.1) consist of a single active particle trapped in a harmonic potential. Given its trivial geometry, it is the poor man, thus the first ingredient of understanding. In this case, as we shall see below, all quantities of interest can be computed analytically, and we find a relatively exotic bifurcation scenario from a frozen to a chiral oscillating regime. Note that this model was already studied by *Dauchot and Démery* [143], including the effects of inertia and angular noise, which will both be neglected here.

5.4.1 Experiments

The experimental setup is made of a single active unit connected to the three static vertices of a regular triangle using *soft* springs (Figs. 5.9-a,d, and f). From symmetry, the reference configuration satisfying mechanical equilibrium lies at the barycenter of the three pinning points. Within the harmonic approximation, the elasticity of this structure is isotropic, and the normal modes consist of two orthogonal vectors, corresponding to a pair of degenerated modes of energy ω_0^2. The spring extension in the reference configuration is always kept fixed, equal to $\alpha = l_{eq}/l_0 = 1.29$, imposing $\omega_0^2 = 1.77$. Once again, the elasto-active coupling π is varied by tuning the length of the *soft* springs. Eventually, we use polar coordinates to express the polarity $\hat{\boldsymbol{n}} = (\cos\theta, \sin\theta)$ and the

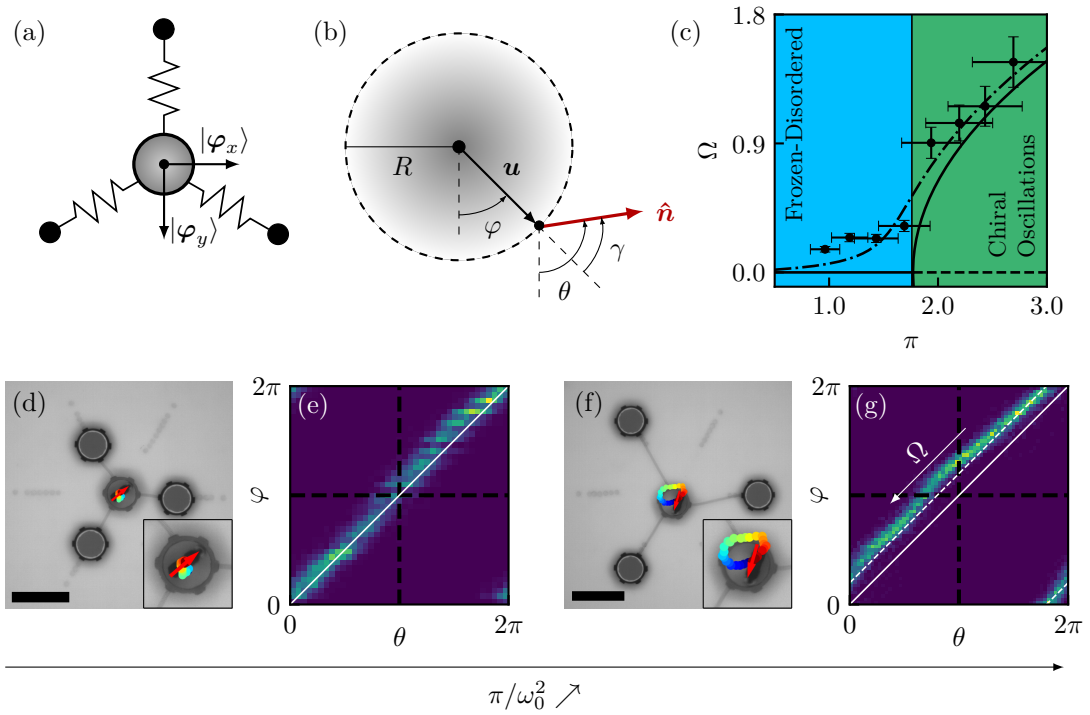


FIG. 5.9. **Single particle experiments.** (a) A single active unit connected to the three static vertices of a regular triangle. (b) Notations in an isotropic harmonic potential. R and φ are the polar-coordinate components of the displacement vector $\boldsymbol{u}$, θ is the orientation of the polarity vector $\hat{\boldsymbol{n}}$, and we denote $\gamma = \theta - \varphi$. (c) Rotation frequency Ω as a function of π. Black markers are experimental data, the error bars corresponding to the 1-σ confidence intervals, inherited from the uncertainty on the measurements of the microscopic parameters. The continuous line represents Eq. (5.20c), and the dot-dashed line corresponds to numerical values in the presence of a dimensional bias $\tilde{\omega}_B = 0.4$ rad/s; $\pi_c = \omega_0^2 = 1.77$. (d-g) Experimental dynamics for $\pi = 1.19 < \omega_0^2$ (d-e), and $\pi = 2.69 > \omega_0^2$ (f-g). (d/f) Dynamics in real space; red arrow: polarity $\hat{\boldsymbol{n}}$; trajectories color-coded from blue to red by increasing time; scale bar: 10 cm. Inset: zoom on the active unit. (e/g) pdf in the plane (θ,φ), integrated over the full dynamics. The solid white line represents the fixed points ($\theta = \varphi$). In panel (g), the white arrows indicate the main dynamics direction, and the dashed white line represents the prediction from Eq. (5.20b).

displacement with respect to the reference configuration $\boldsymbol{u} = R\,(\cos\varphi, \sin\varphi)$, and define the angle $\gamma = \theta - \varphi$ (Fig. 5.9-b).

For small activity, the system is *Frozen-Disordered* (FD): the active particle points radially, $\theta = \varphi$, and its polarity dynamics is mostly diffusive (Fig. 5.9-d). This is clear when measuring the probability density for the angles θ-φ integrated over the whole dynamics (Fig. 5.9-e): the system fluctuates around $\theta = \varphi$, and angular noise allows visiting all possible orientations. In contrast, as activity increases, the system transition to a *Chiral Oscillation* (CO) regime (Fig. 5.9-f), with the active particle spontaneously rotating around the reference configuration. We find that this regime is associated with a finite and constant misalignment $\gamma = \theta - \varphi$ (Fig. 5.9-g), driving the system in rotation at a constant rate Ω. This rotation rate Ω increases as activity increases, and the transition between the two regimes happens around $\pi/\omega_0^2 = 1$ (Fig. 5.9-c). The initial condition selects the left-or-right chirality of the oscillating regime, which can also spontaneously reverse because of angular noise. Finally, note that the rotation rate measured for the frozen regimes cannot be zero, because of the finite left/right bias of the *hexbug*.

Now, let us explain the above observations, determining solutions of Eqs. (5.1) for this simple geometry.

5.4.2 Governing ODEs

A single particle in $2d$ has two normal modes, which we denote $|\boldsymbol{\varphi}_1\rangle$ and $|\boldsymbol{\varphi}_2\rangle$ (respectively along $\hat{\boldsymbol{x}}$ and $\hat{\boldsymbol{y}}$), with corresponding eigenvalues ω_1^2 and ω_2^2. We decompose $|\boldsymbol{u}\rangle = a_1^u(t)|\boldsymbol{\varphi}_1\rangle + a_2^u(t)|\boldsymbol{\varphi}_2\rangle$ and $|\hat{\boldsymbol{n}}\rangle = a_1^n(t)|\boldsymbol{\varphi}_1\rangle + a_2^n(t)|\boldsymbol{\varphi}_2\rangle$. The fact that there is only one particle simplifies the problem:

- There is only one normalization condition $a_1^{n\,2} + a_2^{n\,2} = 1$.
- The only non-zero coupling coefficients (see Eq. (3.50)) are

$$\Gamma_{1212} = -\Gamma_{2112} = -\Gamma_{1221} = \Gamma_{2121} = \Gamma = \sum_i \left(\boldsymbol{\varphi}_1^i \times \boldsymbol{\varphi}_2^i\right)^2 = 1.$$

General case

Using the above simplification in Eqs. (3.49), we find the ODEs governing the amplitude of the displacement and polarity fields on each mode:

$$\dot{a}_1^u = \pi a_1^n - \omega_1^2 a_1^u, \tag{5.14a}$$
$$\dot{a}_2^u = \pi a_2^n - \omega_2^2 a_2^u, \tag{5.14b}$$
$$\dot{a}_1^n = -\left(\omega_1^2 a_1^u a_2^n - \omega_2^2 a_2^u a_1^n\right) a_2^n, \tag{5.14c}$$
$$\dot{a}_2^n = \left(\omega_1^2 a_1^u a_2^n - \omega_2^2 a_2^u a_1^n\right) a_1^n. \tag{5.14d}$$

Degenerate case

In the degenerate case, $\omega_1^2 = \omega_2^2 = \omega_0^2$, it is more convenient to use polar coordinates. We introduce R, φ and θ such that $a_1^u = R\cos(\varphi)$, $a_2^u = R\sin(\varphi)$, $a_1^n = \cos(\theta)$ and $a_2^n = \sin(\theta)$ (see Fig. 5.9-b). Using $\gamma = \theta - \varphi$, the angle between the displacement and polarity vectors, Eqs. (5.14) become:

$$\dot{R} = \pi\cos(\gamma) - \omega_0^2 R, \tag{5.15a}$$
$$\dot{\varphi} = \frac{\pi}{R}\sin(\gamma), \tag{5.15b}$$
$$\dot{\gamma} = \left(\omega_0^2 R - \frac{\pi}{R}\right)\sin(\gamma). \tag{5.15c}$$

5.4.3 Fixed Points

General case

We use the polar angle of the polarity θ, such that $a_1^n = \cos(\theta)$ and $a_2^n = \sin(\theta)$. The fixed points of Eqs. (5.14) are given by

$$\omega_1^2 a_1^u = \pi\cos(\theta_0), \tag{5.16a}$$
$$\omega_2^2 a_2^u = \pi\sin(\theta_0), \tag{5.16b}$$

for any orientation θ_0. The stability of the fixed points can be determined with Eq. (5.4). The matrix $\mathbb{L}$, from Eq. (5.5), reads

$$\mathbb{L} = \begin{pmatrix} \frac{\sin(\theta_0)^2}{\omega_1^2} & -\frac{\cos(\theta_0)\sin(\theta_0)}{\omega_1\omega_2} \\ -\frac{\cos(\theta_0)\sin(\theta_0)}{\omega_1\omega_2} & \frac{\cos(\theta_0)^2}{\omega_2^2} \end{pmatrix}, \tag{5.17}$$

where the eigenvalues of $\mathbb{L}$ are 0 and $\frac{\sin(\theta_0)^2}{\omega_1^2} + \frac{\cos(\theta_0)^2}{\omega_2^2}$, so that this state is stable for

$$\pi \leq \pi_c(\theta_0) = \frac{\omega_1^2\omega_2^2}{\omega_2^2\sin(\theta_0)^2 + \omega_1^2\cos(\theta_0)^2}. \tag{5.18}$$

Degenerate case

In the degenerate case, the fixed points are given by $R = \pi/\omega_0^2$, $\varphi = \theta = \theta_0$. The rotational symmetry ensures that they are all equivalent and stable for

$$\pi \leq \pi_c = \omega_0^2. \tag{5.19}$$

5.4.4 Orbiting solutions in the degenerate case

Orbiting solutions are defined by $\dot{R} = 0$, $\dot{\gamma} = 0$ and $\dot{\varphi} = \Omega \neq 0$. From Eqs. (5.15), we obtain

$$R = \frac{\sqrt{\pi}}{\omega_0}, \tag{5.20a}$$

$$\gamma = \pm \arccos\left(\frac{\omega_0}{\sqrt{\pi}}\right), \tag{5.20b}$$

$$\Omega = \pm\omega_0\sqrt{\pi - \omega_0^2}, \tag{5.20c}$$

where the $\pm$ indicates the two possible chiralities. This oscillating solution exists for $\pi > \omega_0^2$, i.e. when the fixed points are unstable. Note that we recover the results from [143], with $\omega_0^2 = 1$.

5.4.5 Bifurcation scenario

Below $\pi_c = \omega_0^2$, the phase space for the displacements contains an infinite set of marginally stable fixed points, organized along a circle of radius $R = \pi/\omega_0^2$ (Fig. 5.10-a). At π_c, the escape rate of the polarity, away from its frozen orientation, becomes faster than the restoring dynamics of the displacement (Fig. 5.10-b). As a result, the latter permanently chases the polarity, and the stable rotation sets in. All fixed points become unstable at once, and a limit cycle of radius $R = \left(\pi/\omega_0^2\right)^{1/2}$ and oscillation frequency, $\Omega = \omega_0\sqrt{\pi - \omega_0^2}$ branches off continuously (Figs. 5.9-c and 5.10-a). Note that the oscillating dynamics does not arise from a Hopf bifurcation, but from the global bifurcation of a continuous set of fixed points into a limit circle.

5.4.6 Influence of the bias

The hexbugs can be biased: they may preferentially turn to the right or the left. This is due to fabrication imperfections and intrinsic asymmetry brought by the rotating motor (see chapter 2). We take this effect into account by considering a constant dimensional

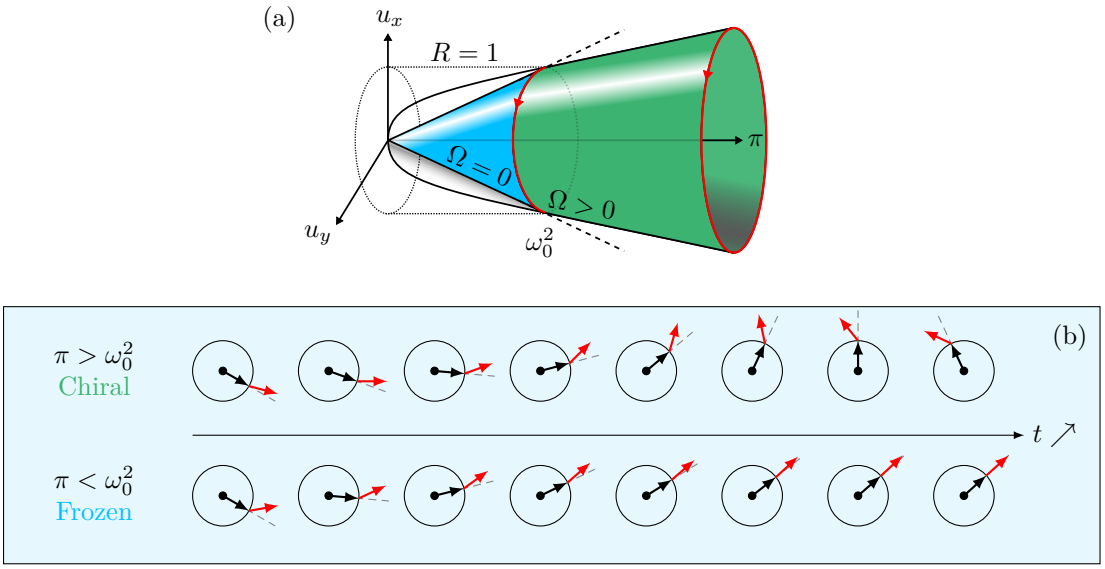


FIG. 5.10. **Single-particle instability mechanism.** (a) Phase space structure of the displacements: for $\pi < \omega_0^2$, an infinite set of marginally stable fixed points forms a circle of radius $R = \pi/\omega_0^2$; for $\pi > \omega_0^2$, all such fixed points are unstable and a limit cycle of radius $R = \left(\pi/\omega_0^2\right)^{1/2}$ branches off continuously. (b) Instability mechanism cartoon. The black (resp. red) arrows indicate the displacement $\boldsymbol{u}$ (resp. polarity $\hat{\boldsymbol{n}}$) vector. For $\pi > \omega_0^2$, any perturbation of γ explodes and reaches the limit cycle amplitude $\gamma = \arccos(\omega_0/\sqrt{\pi})$. The displacement vector ends up chasing the polarity vector at rotation rate Ω. For $\pi < \omega_0^2$, any perturbation of γ vanishes at long time, and all fixed points are marginally stable along φ. Note that the dynamics of R is omitted here.

rotation rate $\tilde{\omega}_B$ in the equation describing the dynamics of the particle's polarity. Eq. (5.15c) becomes

$$\dot{\gamma} = \left(\omega_0^2 R - \frac{\pi}{R}\right)\sin(\gamma) + \omega_B, \tag{5.21}$$

where $\omega_B = t_0\tilde{\omega}_B$ is the dimensionless bias, with the characteristic time $t_0 = \gamma/k$. Looking again for orbiting solution, Eq. (5.15a) and Eq. (5.15b) lead to the rotation rate

$$\Omega = \omega_0\sqrt{\left(\frac{\pi}{R\omega_0}\right)^2 - \omega_0^2}, \tag{5.22}$$

and, after substitution, Eq. (5.21) reads

$$(\rho - 1)^2\left(\rho - \frac{\pi}{\omega_0^2}\right) + \frac{\omega_B^2}{\omega_0^4}\rho = 0, \tag{5.23}$$

where we have introduced the variable $\rho = R^2\omega_0^2/\pi$. The latter satisfies the following conditions: by definition $\rho \geq 0$. Moreover, from the angular velocity $\rho \leq \pi/\omega_0^2$, and assuming that $\sin(\gamma)$ and ω_B are positive implies that $\rho \leq 1$. Only the smallest solution of the last equation satisfies these conditions, and the corresponding rotation rate is shown in Fig. 5.11-a.

In Fig. 5.9-c, we show the rotation rate Ω as a function of π, and compare it to the result of the above calculation. To do so, one must consider that, experimentally, $\pi = F_0/kl_a$ is varied by changing k, and keeping all other experimental parameters constant. Therefore, the characteristic time $t_0 = \gamma/k$ also varies, so that the dimensionless bias ω_B is not

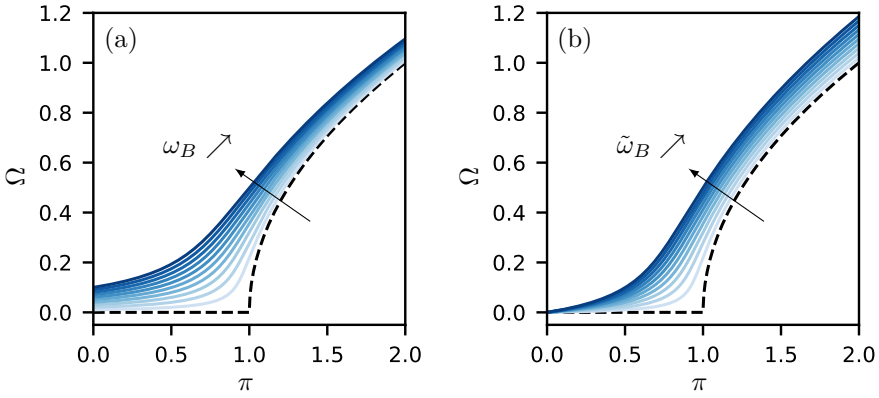


FIG. 5.11. **Biased single particle in a harmonic trap.** (a) Rotation rate Ω as a function of π for increasing dimensionless biases $\omega_B \in [0.01, 0.1]$ by steps of 0.01 (blue solid lines). (b) Rotation rate Ω as a function of π for increasing dimensional bias $\tilde{\omega}_B \in [0.01, 0.1]$ by steps of 0.01 (blue solid lines). In (a) and (b), the dashed black curve represents the unbiased case of Eq. (5.20). Here we use $l_a/v_0 = 1$.

constant. To obtain the curve corresponding to the experimental data, one must therefore compute the angular velocity at constant dimensional bias $\tilde{\omega}_B = \omega_B k/\gamma$, namely at constant $\omega_B v_0/\pi l_a$, as illustrated in Fig. 5.11-b. In the presence of bias, the supercritical pitchfork bifurcation in frequency transforms into an imperfect bifurcation.

As a final remark, we find that the transition to the chiral phase with spontaneously broken symmetry is already present at the single particle level. However, the two remaining observations discussed in section 5.2.5, i.e., the non-trivial selection, and the coexistence scenario at the transition to CA, cannot be explained within this framework, as they clearly involve the geometry of the elastic structures. In the next section, we study simple toy models where the effect of geometry can be taken into account analytically.

5.5 Simple models with heterogeneity

An exact theory to describe the condensation process leading to CA is still missing in the general case, but can be formulated in the simpler, yet rich enough, cases of a linear chain of N active particles fixed at both ends, and of two particles in a harmonic potential. As we shall see, in both cases, the system's geometry ensures the existence of pairs of locally-orthogonal normal modes, hence allowing for further analytical progress in the study of the dynamics.

5.5.1 Linear structures

Definition of the 1d chain, eigenmodes

Let us first consider a chain with N free particles $1 \leq i \leq N$ and pinned edges $i = 0$ and $i = N + 1$. The chain is oriented along $\hat{\boldsymbol{x}}$, so that the equilibrium positions are $x_i = \alpha i$, $y_i = 0$. The parameter α is the ratio between the length of the springs in the equilibrium configuration l_{eq} and the natural length of the springs l_0. The chain thus bears a dimensionless tension $T = \alpha - 1$. The dynamical matrix is equal to minus the discrete Laplacian matrix in both directions, modulo a factor $A_\alpha = 1 - \alpha^{-1}$ in the y

direction, and reads

$$\mathbb{M} = \begin{pmatrix} 2 & 0 & -1 & 0 & 0 & 0 & \cdots & 0 \\ 0 & 2A_\alpha & 0 & -A_\alpha & 0 & 0 & & 0 \\ -1 & 0 & 2 & 0 & -1 & 0 & & 0 \\ 0 & -A_\alpha & 0 & 2A_\alpha & 0 & -A_\alpha & & 0 \\ \vdots & & & & & & \ddots & \vdots \\ 0 & 0 & 0 & 0 & \cdots & -A_\alpha & 0 & 2A_\alpha \end{pmatrix}, \tag{5.24}$$

where odd (resp. even) lines and columns correspond to displacements along $\hat{\boldsymbol{x}}$ (resp. $\hat{\boldsymbol{y}}$). Notably, the directions x and y decouple. As a consequence, there are N eigenmodes along $\hat{\boldsymbol{x}}$ (resp. $\hat{\boldsymbol{y}}$), which we denote $\boldsymbol{\varphi}_{x,k}$ (resp. $\boldsymbol{\varphi}_{y,k}$) with eigenfrequencies $\omega_{x,k}$ (resp. $\omega_{y,k}$):

$$\boldsymbol{\varphi}^i_{x,k} = \sqrt{\frac{2}{N+1}} \sin\left(\frac{ik\pi}{N+1}\right) \hat{\boldsymbol{x}}; \qquad \omega^2_{x,k} = 4 \sin\left(\frac{k\pi}{2(N+1)}\right)^2, \tag{5.25a}$$

$$\boldsymbol{\varphi}^i_{y,k} = \sqrt{\frac{2}{N+1}} \sin\left(\frac{ik\pi}{N+1}\right) \hat{\boldsymbol{y}}; \qquad \omega^2_{y,k} = 4A_\alpha \sin\left(\frac{k\pi}{2(N+1)}\right)^2. \tag{5.25b}$$

The eigenmodes and eigenfrequencies for $N = 2, 3, 4$ and 5 are shown in Fig. 5.12. The modes in the directions x and y are obviously locally-orthogonal. Moreover, modes with the same index k have the same norm on each site, so that we introduce $\varphi^i_k = \boldsymbol{\varphi}^i_{x,k} \cdot \hat{\boldsymbol{x}} = \boldsymbol{\varphi}^i_{y,k} \cdot \hat{\boldsymbol{y}}$. Finally, in the limit $\alpha \to \infty$, which corresponds to infinite tension or zero-rest-

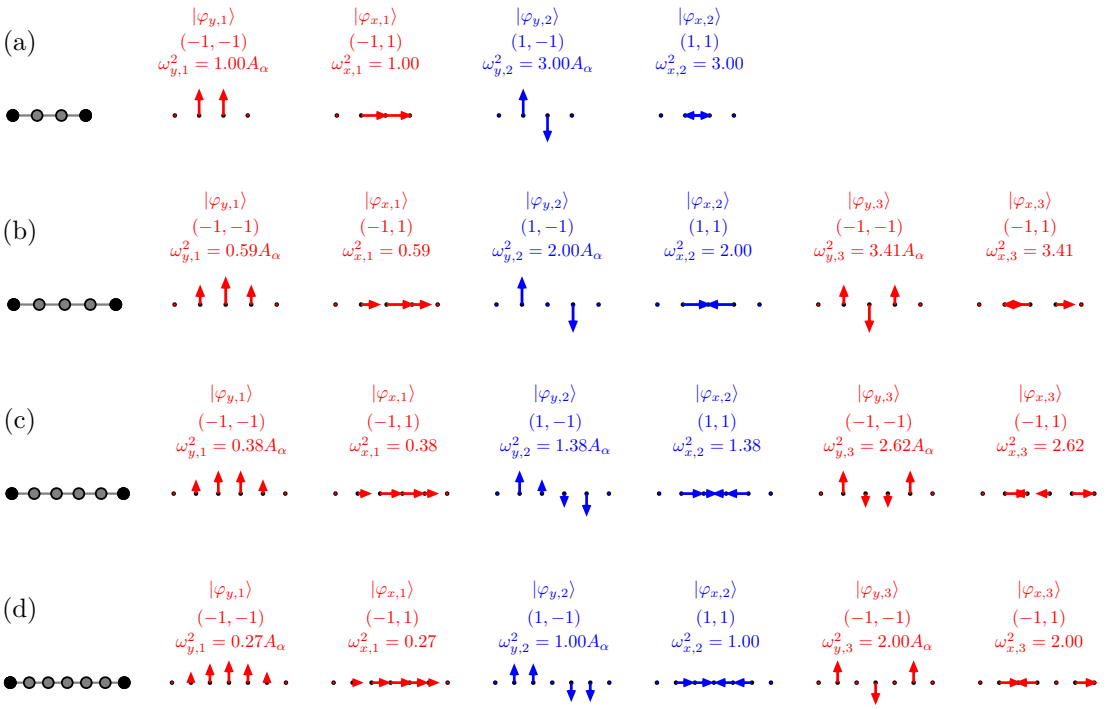


FIG. 5.12. **Normal modes for linear structures.** (a) $N = 2$, (b) $N = 3$, (c) $N = 4$, (d) $N = 5$, sorted by order of growing energies, and colored by their associated eigenvalues with respect to the rotation operation of the dihedral group D_2, characterizing the symmetry of the elastic structure (see chapter 3). Only the six first modes are shown. For every mode, we show the mode's index k, the eigenvalues associated with the symmetry operations (τ, σ), and the associated squared eigenfrequency ω^2_k.

length, $A_\alpha \to 1$ and the modes are degenerated: $\omega_{x,k} = \omega_{y,k} = \omega_k$ for $1 \leq k \leq N$. We restrict ourselves to this case in the following, which ensures rotational invariance.

CA regime

The specific geometry of the normal modes of zero-rest-length chains, which come in pairs of degenerated and locally-orthogonal modes, allows us to find the explicit expression and stability of the CA regime for arbitrary N (see Appendix D). Using this framework and numerical simulations, we find a unique solution corresponding to a periodic actuation of the pair of modes $|\boldsymbol{\varphi}_{x,1}\rangle$ and $|\boldsymbol{\varphi}_{y,1}\rangle$ at frequency Ω (Fig. 5.14). We have checked numerically that this periodic solution is the only one present, up to $N = 20$.

Moreover, we find that particles perform circular trajectories with radii R_i. The spatial distribution of the R_i is set by that of the modes selected by the collective actuation, with particles closer to the boundaries having typically a smaller radius of rotation than the ones at the center. The threshold value π_{CA}, below which the dynamics leave the limit cycle, is precisely met when the particles at the boundary reach a radius of rotation $R = 1$ (see Appendix D).

Linear stability thresholds

Let us elaborate on the linear stability thresholds $\pi_c(|\hat{\boldsymbol{n}}\rangle)$. The general bounds derived above for $\pi_c^{\min}$ and π_c^{upp} translate here into

$$\omega_1^2 \leq \pi_c\left(|\hat{\boldsymbol{n}}\rangle\right) \leq 2\omega_1^2, \tag{5.26}$$

where the upper bound π_c^{upp} is obtained with the pair of modes $|\boldsymbol{\varphi}_{x,1}\rangle$ and $|\boldsymbol{\varphi}_{y,1}\rangle$, which are locally-orthogonal. Therefore, like in the triangular and kagome lattices, the pair of modes optimizing the bound π_c^{upp} is also the one selected by the active dynamics.

The evolution of the stability of the fixed points and of their basins of attraction can be largely understood by studying the $N = 2$ and $N = 3$ cases. For $N = 2$, the eigenfrequencies are $\omega_1^2 = 1$ and $\omega_2^2 = 3$ (Fig. 5.12-a). Given the normal mode spectrum knowledge, we use Eq. (5.4) to determine the stability threshold for an arbitrary configuration of the line $\pi_c(\theta_1, \theta_2)$. The results are represented in Figs. 5.13-b and c, top. From invariance by rotation, we find that the instability threshold $\pi_c(\theta_1, \theta_2)$ only depends on the difference $\theta_1 - \theta_2$, and in particular:

$$\pi_c(\theta_1 - \theta_2) = \frac{3}{2 + |\cos(\theta_1 - \theta_2)|}. \tag{5.27}$$

Therefore, for $\pi < 1$, all fixed points are stable, and for $\pi > 1.5$, they are all unstable. In the range $1 < \pi < 1.5$, we find a phase space coexistence between stable and unstable fixed points. There are two basins of unstable fixed points, which can either slide to a neighboring stable fixed point or meet the nonlinear limit cycle, that exists and is stable for $\pi > \pi_{CA} = 1$. Note that $\pi_c^{\min} = \pi_{CA}$.

For $N = 3$, invariance by rotation allows us to draw the landscape of stability thresholds $\pi_c(\theta_c + \Delta\theta_1, \theta_c, \theta_c + \Delta\theta_2)$, where θ_c is the orientation of the central node, see Figs. 5.13-b and c, bottom. Restricting our analytical calculations to $\Delta\theta_1 = \Delta\theta_2 = \Delta\theta$, we find:

$$\pi_c(\Delta\theta) = \frac{2}{2 + \sqrt{2}|\cos(\Delta\theta)|}. \tag{5.28}$$

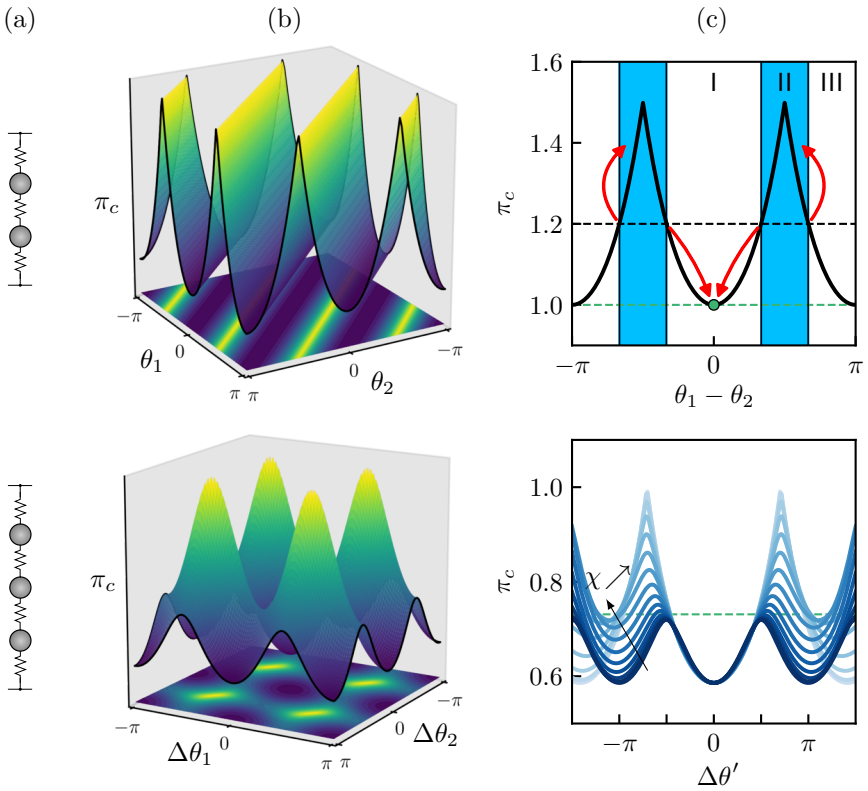


FIG. 5.13. **Linear instability thresholds of small chains.** (top) $N = 2$ chain, (bottom) $N = 3$ chain. (a) Linear structure cartoon. Springs have zero rest length to ensure infinite tension. (b/c) Linear instability thresholds $\pi_c(|\hat{\boldsymbol{n}}\rangle)$ computed from Eq. (5.4) for all configurations. For the $N = 2$ chain, configurations are parametrized by the two angles θ_1 and θ_2. Invariance by rotation decreases the number of degrees of freedom by one. Therefore, for the $N = 3$ chain, configurations are parametrized by the two angles $\Delta\theta_1 = \theta_1 - \theta_c$ and $\Delta\theta_2 = \theta_2 - \theta_c$ the outer particles make with the central one. (c) The green marker and its associated dashed horizontal line represent π_{CA}. (c, top) The dashed black line represents an arbitrary value of π chosen for the sake of illustration. Zones I and III: unstable configurations; zone II: stable configurations. The final configuration reached depends on the initial configuration $\theta_1 - \theta_2$. The red arrows indicate where the corresponding fixed point goes once it destabilizes. (c, bottom) $\Delta\theta' = (\Delta\theta_1^2 + \Delta\theta_2^2)^{1/2}$ and $\tan\chi = \Delta\theta_1/\Delta\theta_2 \in [0, \pi/4]$ are the polar-coordinate components of the vector $(\Delta\theta_1, \Delta\theta_2)$.

The stability threshold ranges from $\pi_c(\Delta\theta = 0[\pi]) = 2 - \sqrt{2}$ to $\pi_c(\Delta\theta = \pm\pi/2) = 1$. We note that $\pi_c(\Delta\theta = 0[\pi]) = \pi_c^{\min} = \omega_{\min}^2$, confirming that these are the most unstable fixed points. On the other hand, we confirm numerically that $\Delta\theta = \pm\pi/2$ corresponds to the most stable fixed points (Fig. 5.13-c, bottom). Similarly to the $N = 2$ case, there exists a phase space coexistence between stable and unstable fixed points in some range of π. However, here, $\pi_{CA} > \pi_c^{\min}$, which is a generic feature of heterogeneous systems.

Transition to CA

Now that we have understood the phase space structure, let us consider the nature of the transition to CA as N increases, and draw the phase diagrams.

In the $N = 2$ case, we find a continuous transition (Fig. 5.14-a). The CA regime corresponds to a strict condensation of the active force on modes $|\boldsymbol{\varphi}_{x,1}\rangle$ and $|\boldsymbol{\varphi}_{y,1}\rangle$, and therefore maps with the oscillation of the single particle. As π decreases, the oscillation frequency $\Omega = \sqrt{\pi - 1}$ and the trajectory radii $R_i = \sqrt{\pi}$ both decrease. Given that modes $|\boldsymbol{\varphi}_{x,1}\rangle$ and $|\boldsymbol{\varphi}_{y,1}\rangle$ are completely delocalized (Fig. 5.12-a), the two particles have

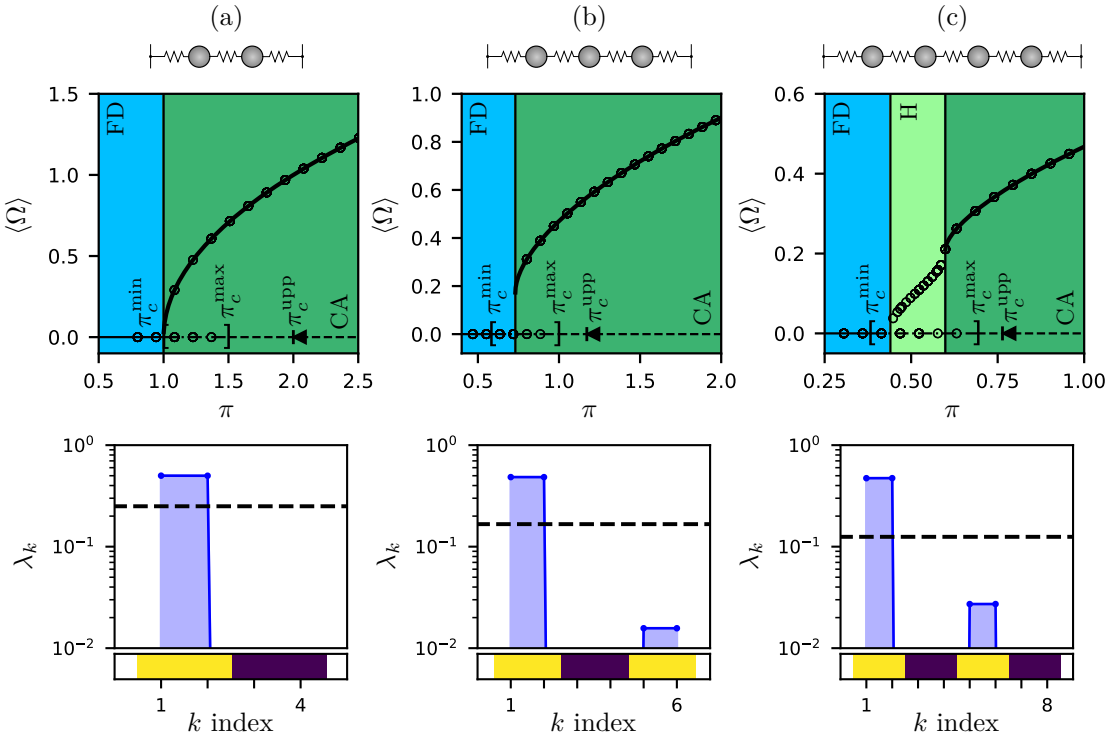


FIG. 5.14. **Transition to CA in zero-rest-length chains.** (a) $N = 2$. (b) $N = 3$. (c) $N = 4$. (top) Elastic structure cartoon. (middle) Bifurcation diagrams of stationary solutions corresponding to single frequency limit cycles. Continuous line: limit cycle found analytically; horizontal lines ($\Omega = 0$): range of existence of only stable (continuous), only unstable (dashed) and coexisting stable and unstable (dot-dashed) fixed points; (open markers): numerical data; same background color as for Fig. 5.1. In (a), $\pi_c^{\min} = 1.0$, $\pi_c^{\max} = 1.5$, $\pi_c^{\text{upp}} = 2.0$, $\pi_{FD} = \pi_{CA} = 1$. In (b), $\pi_c^{\min} = 0.586$, $\pi_c^{\max} = 1.0$, $\pi_c^{\text{upp}} = 1.17$, $\pi_{FD} = \pi_{CA} = 0.731$. In (c), $\pi_c^{\min} = 0.382$, $\pi_c^{\max} = 0.691$, $\pi_c^{\text{upp}} = 0.764$, $\pi_{FD} = 0.440$, $\pi_{CA} = 0.599$. (bottom) Condensation fraction of simulated CA dynamics (for $\pi = 2.0$) on the normal modes of the different linear structures, sorted by order of growing energies. The horizontal dashed lines indicate equipartition. The bottom color bars code for the symmetry class of the modes (see Figs. 5.12), the yellow ones corresponding to the classes $(-1, \pm 1)$.

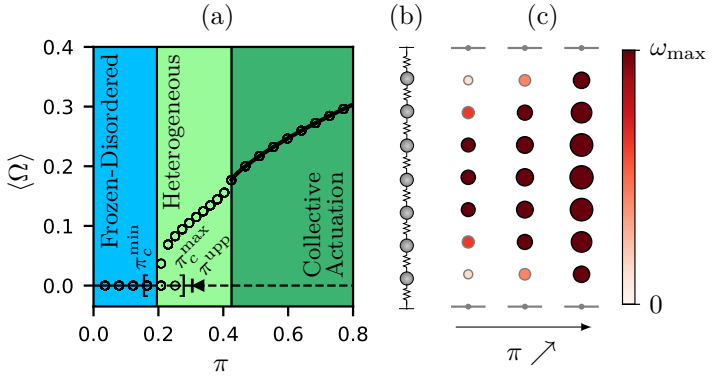


FIG. 5.15. **CA in a zero rest length chain of $N = 7$ nodes.** (a) Average oscillation frequency Ω as a function of π. Continuous line: limit cycle found analytically; horizontal lines ($\Omega = 0$): range of existence of only stable (continuous), only unstable (dashed) and coexisting stable and unstable (dot-dashed) fixed points; (open markers): numerical data; same background color as for Fig. 5.1; $\pi_c^{\min} = 0.152$, $\pi_c^{\max} = 0.280$, $\pi_c^{\text{upp}} = 0.304$, $\pi_{FD} = 0.195$, $\pi_{CA} = 0.426$. (b) Elastic structure cartoon. (c) Individual oscillation frequencies ω_i for increasing values of $\pi \in [0.20, 0.33, 1.0]$, in the $N = 7$ chain. Radii of the colored circles code for the average trajectory radius. Black, respectively gray, contours indicate $R_i \geq 1$ and $R_i \leq 1$.

the same trajectory radii, thus the stability condition $R_i = 1$ is reached everywhere in the system at $\pi = \pi_{CA}$, where the oscillation frequency simultaneously vanishes, and the periodic solution ceases to exist. In the range $1 < \pi < 1.5$, stable and unstable fixed points coexist with the limit cycle.

In the $N = 3$ case, we find a discontinuous transition (Fig. 5.14-b). In this case, modes $|\boldsymbol{\varphi}_{x,1}\rangle$ and $|\boldsymbol{\varphi}_{y,1}\rangle$ are not completely delocalized (Fig. 5.12-b); thus, even if the dynamics select those modes, some active force projects on all the modes belonging to the same symmetry classes. The modes heterogeneity is at the origin of the discontinuity: while the oscillation frequency is still finite at π_{CA}, the outer particles simultaneously reach the stability condition $R_i = 1$, and the steady rotation ceases to exist. For $\pi < \pi_{CA}$, the whole system abruptly stops and finds a stable fixed point.

Eventually, for $N \geq 4$, we find a discontinuous transition and a heterogeneous regime (Figs. 5.14-c and 5.15). In this case, the selected modes heterogeneity is large enough so that, when the outer particles reach the stability condition $R_i = 1$ at $\pi = \pi_{CA}$, the competition between outer particles, which want to freeze, and the central particles, which want to cycle, leads to the sequential layer by layer de-actuation, illustrated in Fig. 5.15-c for a linear chain with $N = 7$, and observed experimentally and numerically in triangular and kagome lattices. The threshold value π_{FD} is reached when, eventually, the remaining particles at the center freeze and the system discontinuously falls into the frozen disordered state. The physical origin of the spatial coexistence lies in the normalization constraint of the polarity field, $|\hat{\boldsymbol{n}}_i| = 1$, which translates into a strong constraint over the radii of rotation. Whenever R_i becomes unity, the polarity and displacement vectors become parallel, freezing the dynamics locally.

To conclude, the selected modes' heterogeneity dictates the nature of the transition to CA. For strictly homogeneous modes, we find that the transition is continuous. In contrast, heterogeneity induces a discontinuous transition to CA, and allows for the spatial coexistence between the oscillating and frozen phases.

5.5.2 Two coupled particles in a parabolic potential

We have seen above that the spatial heterogeneity of the most actuated modes governs the nature of the transition to CA. However, for linear structures, both the number of particles N and the spatial heterogeneity of the modes are varied; and, it is hard to disentangle their respective effects. Therefore, we introduce below a model of two coupled particles in a harmonic potential, in which the spatial heterogeneity can be varied continuously, at fixed N.

The model consists of $N = 2$ active particles embedded in the elastic structure represented in Fig. 5.16-a. The two particles are connected with a spring of stiffness k, and they are also connected to the origin with springs of stiffnesses k_1 and k_2, respectively; all having zero rest length. Let us discuss the normal mode spectrum of this structure. The first step is to write down the dynamical matrix $\mathbb{M}$ and compute its eigenvectors. Here the x and y components decouple: writing the displacements as $\boldsymbol{u} = (x_1, x_2, y_1, y_2)$, the dynamical matrix is:

$$\mathbb{M} = \begin{pmatrix} \mathbb{M}_x & 0 \\ 0 & \mathbb{M}_y \end{pmatrix}, \tag{5.29}$$

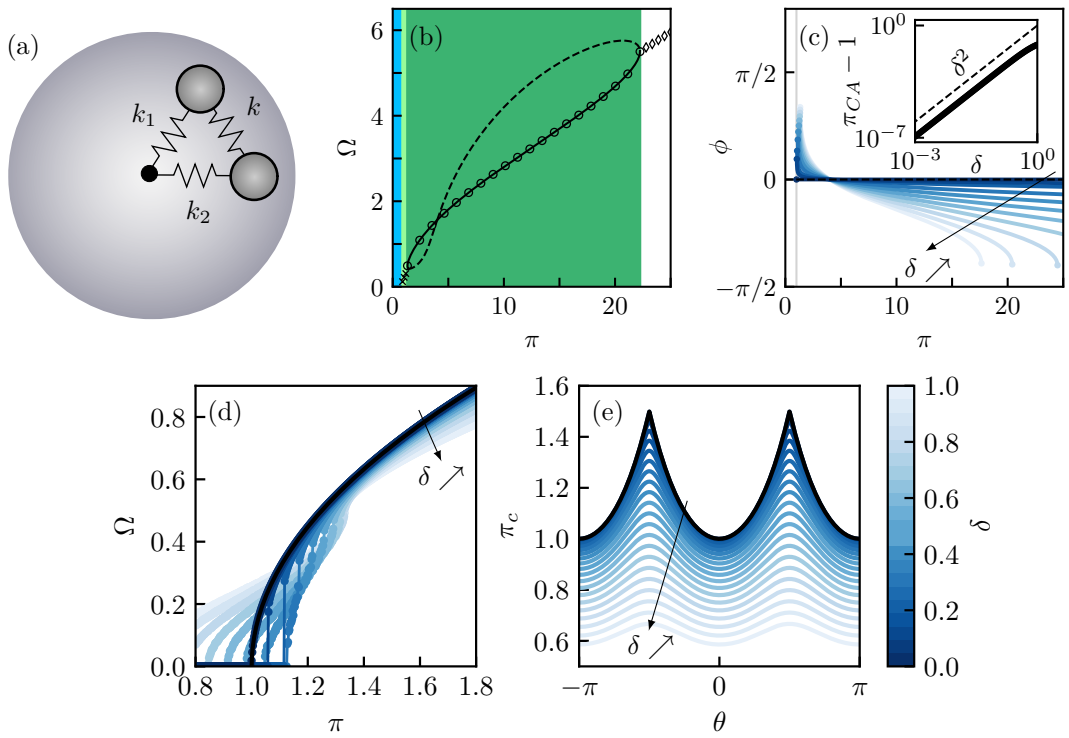


FIG. 5.16. **Two coupled particles in a harmonic potential.** (a) Elastic structure cartoon. All springs' rest lengths are zero. (b) Oscillation frequency as a function of the elasto-active coupling π for $\delta = 0.75$, as given by Eqs. (5.36) (black lines), and as obtained by numerical integration of the equations of motion, Eqs. (5.35) (markers). The solid (resp. dashed) lines represent stable (resp. unstable) solutions. The circle markers highlight steady orbiting regimes, the plus markers heterogeneous regimes, and the diamond markers large-π aperiodic regimes. Same background color as for Fig. 5.1. (c) Phase difference between the two particles as a function of the elasto-active coupling π in stable steady orbiting regimes, for different asymmetry $\delta \in [0, 1]$ by steps of 0.1, as given by the solutions of Eqs. (5.36). The gray vertical line represents $\pi = 1$. Inset: log-log plot of the minimum elasto-active coupling for steady orbiting regimes π_{CA} as a function of asymmetry δ, as given by the solutions of Eqs. (5.36). The dashed black line represents the square power law. (d) Oscillation frequency as a function of the elasto-active coupling π, for different asymmetry $\delta \in [0, 1]$ by steps of 0.1, as obtained by numerical integration of the equations of motion, Eqs. (5.35). The solid black line represents the prediction of Eq. (5.37) for $\delta = 0$. (e) Instability thresholds π_c as given by Eq. (5.4) for all configurations, parametrized by the angle θ between the two active particles' orientations; and for different asymmetry $\delta \in [0, 1]$ by steps of 0.05. The solid black line represents the prediction of Eq. (5.34) for $\delta = 0$. The color bar indicates the value of δ associated with the blue color code in panels (c-e).

with

$$\mathbb{M}_x = \mathbb{M}_y = \begin{pmatrix} k + k_1 & -k \\ -k & k + k_2 \end{pmatrix}. \tag{5.30}$$

Introducing $\delta = (k_1 - k_2)/2k$, $a = \delta + \sqrt{1 + \delta^2}$ and $b = \delta - \sqrt{1 + \delta^2}$, the eigenvectors of $\mathbb{M}_x$ can be written as:

$$\begin{aligned} \boldsymbol{\psi}_1 &= \frac{1}{\sqrt{1 + a^2}} \begin{pmatrix} 1 \\ a \end{pmatrix}, \\ \boldsymbol{\psi}_3 &= \frac{1}{\sqrt{1 + b^2}} \begin{pmatrix} 1 \\ b \end{pmatrix}, \end{aligned} \tag{5.31}$$

with eigenvalues

$$\begin{aligned}\omega_1^2 &= k_1 + k(1-a),\\ \omega_3^2 &= k_1 + k(1-b).\end{aligned} \tag{5.32}$$

The matrix $\mathbb{M}$ has four eigenvectors, two with $\boldsymbol{\psi}_1$ and $\boldsymbol{\psi}_3$ for the x-components, which we denote $|\boldsymbol{\varphi}_1\rangle$ and $|\boldsymbol{\varphi}_3\rangle$, and two with $\boldsymbol{\psi}_1$ and $\boldsymbol{\psi}_3$ for the y-components, which we denote $|\boldsymbol{\varphi}_2\rangle$ and $|\boldsymbol{\varphi}_4\rangle$. Their energies are $\omega_1^2 = \omega_2^2$ and $\omega_3^2 = \omega_4^2$. Like for zero-rest-length chains, the normal modes are locally-orthogonal, and the system is invariant by rotation. Also, from Eqs. (5.31) and (5.32), it is clear that the symmetric case $\delta = 0$ strictly maps with the $N = 2$ chain. In the general case $\delta > 0$, the larger the springs' asymmetry, the larger the heterogeneity of the normal modes over the two particles.

Linear stability analysis

Given the knowledge of the normal mode spectrum, from Eq. (5.4), we find the linear destabilization threshold of any configuration of the polarity field $\pi_c(\theta_1, \theta_2)$. From invariance by rotation, we can choose $\hat{\boldsymbol{n}}_1$ along $\hat{\boldsymbol{x}}$ and $\hat{\boldsymbol{n}}_2 = (\cos\theta, \sin\theta)$. The explicit expression of the destabilization thresholds is very hairy in the general case[4], but can be found numerically (Fig. 5.16-e). In the symmetric case $\delta = 0$, we recover the result of the $N = 2$ zero-rest-length chain:

$$\pi_c(\theta) = \frac{3}{2 + |\cos(\theta)|}, \tag{5.34}$$

and in the general case, we find that larger asymmetry decreases the stability thresholds of the fixed points.

Steady orbiting solutions

Starting from the general noiseless equations within the harmonic approximation:

$$\dot{\boldsymbol{u}}_i = \pi\hat{\boldsymbol{n}}_i + \boldsymbol{F}_i^{el}[\boldsymbol{u}], \tag{5.35a}$$

$$\dot{\boldsymbol{n}}_i = (\hat{\boldsymbol{n}}_i \times \boldsymbol{F}_i^{el}) \times \hat{\boldsymbol{n}}_i, \tag{5.35b}$$

we look for steady solutions orbiting at a rate Ω. This means that $\dot{\boldsymbol{u}} = \Omega\boldsymbol{u}^\perp$ and $\dot{\boldsymbol{n}} = \Omega\boldsymbol{n}^\perp$. Moreover, from invariance by rotation, we can set the phase of the orientation of particle 1, say $\phi_1 = 0$. In the rest, we focus on $k = 1$, $k_1 = 1-\delta$, $k_2 = 1+\delta$, even though the calculation can be done in the general case (see Appendix E). After some algebra, we find that for a phase difference between the two particles $\phi_2 = \phi$, the elasto-active coupling π and the rotation rate Ω of the steady orbiting solution satisfy:

$$\Omega_\pm = \frac{-2\sin\phi \pm \sqrt{4\sin(\phi)^2 + 3\delta^2 - \delta^4}}{\delta}, \tag{5.36a}$$

$$\pi = 2 + \delta - \cos\phi + \frac{\Omega^2(2 - \delta + \cos\phi) - 4\Omega\sin\phi - (2 + \delta - \cos\phi)\sin(\phi)^2}{3 - \delta^2 + \sin(\phi)^2}, \tag{5.36b}$$

[4]From the spectrum of the matrix:

$$L_{ij}(\theta) = \begin{pmatrix} \frac{a^2s^2}{\omega_1^2(1+a^2)} & \cdot & \cdot & \cdot \\ \frac{-a^2sc}{\omega_1^2(1+a^2)} & \frac{1+a^2c^2}{\omega_1^2(1+a^2)} & \cdot & \cdot \\ \frac{-s^2}{\omega_1\omega_3\sqrt{(1+a^2)(1+b^2)}} & \frac{sc}{\omega_1\omega_3\sqrt{(1+a^2)(1+b^2)}} & \frac{b^2s^2}{\omega_3^2(1+b^2)} & \cdot \\ \frac{sc}{\omega_1\omega_3\sqrt{(1+a^2)(1+b^2)}} & \frac{1-c^2}{\omega_1\omega_3\sqrt{(1+a^2)(1+b^2)}} & \frac{-b^2sc}{\omega_3^2(1+b^2)} & \frac{1+b^2c^2}{\omega_3^2(1+b^2)} \end{pmatrix}, \tag{5.33}$$

where $c = \cos\theta$ and $s = \sin\theta$, and where the matrix $\mathbb{L}$ is symmetric.

The solutions are parametrized by an angle ϕ, ranging in $[-\pi, \pi[$; however, each angle ϕ is not always associated with a solution. The numerical solution to Eqs. (5.36) is compared to the numerical integration of the equations of motion in Fig. 5.16-b for $\delta = 0.75$. For each value of π in the CA regime, two solutions Ω are predicted in our calculation. However, only one of them corresponds to a steady state observed in the numerical integration, and the other one is unstable, as discussed below. Moreover, from local-orthogonality, within the steady orbiting regimes, the particles perform circular trajectories of radii R_i. We also observe a discontinuity at the transition to CA, as the minimal value of Ω for steady oscillating solutions is not 0. This transition can once again be understood as a threshold for the radii of the particles' trajectories, i.e. $R_i = 1$.

In the limiting case of homogeneous modes, $\delta \to 0$, we find that $\phi = 0$ is the only phase difference allowing for steady orbiting regimes (Fig. 5.16-c) and recover the mapping with the single particle's oscillation. In particular, the oscillation frequency expresses as follows:

$$\Omega = \pm\sqrt{\pi - 1}. \tag{5.37}$$

For finite but small asymmetry, the minimum value of the elasto-active coupling allowing for steady orbiting solutions converge toward 1, indicating that the discontinuity must vanish as asymmetry goes to zero (Fig. 5.16-c, inset).

To study the stability of limit cycles, we introduce a small perturbation:

$$\boldsymbol{u}_i = \left[\boldsymbol{u}_i^0 + \boldsymbol{u}_i^1(t)\right] e^{i\Omega t}, \tag{5.38a}$$

$$\phi_i(t) = \phi_i^0 + \Omega t + \phi_i^1(t). \tag{5.38b}$$

Linearizing the dynamics around the limit cycle, we find the matrix governing the evolution of the vector $(u^1_{1,x}, u^1_{2,x}, u^1_{1,y}, u^1_{2,y}, \phi^1_1, \phi^1_2)$, see Appendix F. Computing numerically the eigenvalues of this matrix for the two branches discussed above, we find the picture shown in Fig. 5.16-b, which perfectly matches the numerical simulations in the CA regime.

Interestingly, we also find that there is a maximal value of Ω, associated with a maximal value of π above which the steady orbiting solution ceases to exist. In this range of π, the system is dynamical but aperiodic. Note that such a maximal value of π for CA is also found in the zero-rest-length chain model, and in simulations of triangular and kagome lattices. The large-π aperiodic regime is clearly a generic feature of heterogeneous systems, but was completely out of range experimentally, and thus omitted up to now.

Finally, to explore the transition to CA beyond steady orbits and fixed points, we perform numerical simulations of the equations of motion, annealing from large to small π for different asymmetries $\delta \in [0, 1]$ (Fig. 5.16-d). In the symmetric case, the transition is continuous, and is in perfect agreement with Eq. (5.37). In contrast, we confirm that small enough asymmetry leads to a discontinuous transition from CA to the fixed points, and large enough asymmetry leads to the emergence of an unsteady heterogeneous regime with a discontinuous transition on both sides. However, in this simple system, the heterogeneous regime remains a limit cycle. This two-particle toy model convincingly demonstrates that the heterogeneity of the normal modes governs the nature of the transition to CA, and is in qualitative agreement with the zero-rest-length chain toy model and the numerical simulations of the triangular and kagome lattices.

5.6 Coarse-grained description

At large scales, the dynamics of the displacement and polarization fields, $\mathbf{U}(\mathbf{r},t)$ and $\mathbf{m}(\mathbf{r},t)$, the local averages of, respectively, the microscopic displacements $\mathbf{u}_i$ and the polarizations $\hat{\mathbf{n}}_i$, are obtained from a coarse-graining procedure explained in detail below.

5.6.1 Continuous fields

Instead of a discrete elasticity problem, we consider a $2d$ continuous elastic sheet, defined by the deformation field $\boldsymbol{U}(\boldsymbol{r},t)$, and densely doped with active units. The orientation of the particles is described by a polarization field $\boldsymbol{m}(\boldsymbol{r},t)$, which can be understood as the mean over the mesoscopic scale of the polarity vectors. Thus we can get rid of the normalization condition the discrete formulation requires, and consider a polarization field with varying amplitude at any point of the sheet, and whose orientation and amplitude are governed by the elastic forces. First, we define the average over the mesoscopic scale:

$$\rho(\boldsymbol{r},t)\boldsymbol{m}(\boldsymbol{r},t) = \frac{1}{S}\int_{v(\boldsymbol{r})} \hat{\boldsymbol{n}}(\boldsymbol{r},t)d\boldsymbol{r} = \sum_{i\in v(\boldsymbol{r})} \hat{\boldsymbol{n}}_i(t)\delta(\boldsymbol{r}_i-\boldsymbol{r}), \tag{5.39}$$

$$\boldsymbol{U}(\boldsymbol{r},t) = \frac{1}{S}\int_{v(\boldsymbol{r})} \boldsymbol{u}(\boldsymbol{r},t)d\boldsymbol{r} = \sum_{i\in v(\boldsymbol{r})} \boldsymbol{u}_i(t)\delta(\boldsymbol{r}_i-\boldsymbol{r}), \tag{5.40}$$

where $v(\boldsymbol{r})$ is a disk of small radius, centered at position $\boldsymbol{r}$ and of surface S; and where $\rho(\boldsymbol{r},t)$ is the surface density of active force. Note that for a particle i inside $v(\boldsymbol{r})$, the local fields equal the average value plus the fluctuations, thus $\hat{\boldsymbol{n}}_i(t) = \boldsymbol{m}(\boldsymbol{r},t)+\delta\boldsymbol{m}_i(\boldsymbol{r},t)$ and $\boldsymbol{u}_i(t) = \boldsymbol{U}(\boldsymbol{r},t)+\delta\boldsymbol{U}_i(\boldsymbol{r},t)$, where $\langle\delta\boldsymbol{m}_i(\boldsymbol{r},t)\rangle_{v(\boldsymbol{r})} = \langle\delta\boldsymbol{U}_i(\boldsymbol{r},t)\rangle_{v(\boldsymbol{r})} = 0$. For the rest of this derivation, we consider the density of active force constant in time and space, equal at ρ_0. Moreover, we consider this average density equal to unity, as it simply rescales activity. Within such a framework, the normalization of the polarity vectors, $|\hat{\boldsymbol{n}}_i| = 1$, translates into the constraint $|\boldsymbol{m}(\boldsymbol{r},t)| \leq 1$ for the polarization.

5.6.2 Strain dynamics

The continuous limit of Eq. (5.1a) is obtained by averaging over $v(\boldsymbol{r})$, which is trivial as this equation is linear:

$$\partial_t\boldsymbol{U}(\boldsymbol{r},t) = \pi\boldsymbol{m} + \frac{1}{S}\int_{v(\boldsymbol{r})}\boldsymbol{f}^{el}(\boldsymbol{r},t)d\boldsymbol{r}, \tag{5.41}$$

$$\partial_t\boldsymbol{U}(\boldsymbol{r},t) = \pi\boldsymbol{m}(\boldsymbol{r},t) + \boldsymbol{F}^{el}(\boldsymbol{r},t), \tag{5.42}$$

where, assuming the average over the local elastic forces leads to the Hooke's law for the continuum elastic force, $\boldsymbol{F}^{el} = \mathrm{div}\sigma = -\mathbb{L}\boldsymbol{U}(\boldsymbol{r},t)$, with:

$$\sigma = \frac{E}{1+\nu}\left(\varepsilon + \frac{\nu}{1-2\nu}\mathrm{Tr}(\varepsilon)\mathbb{I}\right), \tag{5.43}$$

$$\varepsilon = \frac{1}{2}\left(\nabla\boldsymbol{U} + \nabla\boldsymbol{U}^t\right), \tag{5.44}$$

where E and ν are respectively the Young modulus and the Poisson's ratio of the elastic material. The displacement field dynamics is composed of a driving term along the polarization field direction, and a relaxation term, which is a second-order derivative in space of the displacement field. The elastic term thus smoothes the displacement field

on length scales smaller than $l^\star$, obtained from a scaling argument when balancing the two terms:

$$l^\star \sim 1/\sqrt{\pi}. \tag{5.45}$$

As a consequence, for a coarse-graining length smaller than $l^\star$, we can safely ignore the fluctuation of the displacement field. This assumption considerably simplifies the coarse-graining of the polarity dynamics below.

5.6.3 Polarity dynamics

Let us re-cast the dynamics for the polarity Eq. (5.1b) using the projector to the normal of $\hat{\boldsymbol{n}}_i$

$$\dot{\boldsymbol{n}}_i = (\mathbb{I} - \hat{\boldsymbol{n}}_i \otimes \hat{\boldsymbol{n}}_i)\dot{\boldsymbol{u}}_i, \tag{5.46}$$

where we neglect the angular noise, which is considered separately. Ignoring the fluctuations of the displacement field, we find:

$$\partial_t \boldsymbol{m} = (\mathbb{I} - \langle \hat{\boldsymbol{n}}_i \otimes \hat{\boldsymbol{n}}_i \rangle)\partial_t \boldsymbol{U}. \tag{5.47}$$

Now, we want to express the average $\langle \hat{\boldsymbol{n}}_i \otimes \hat{\boldsymbol{n}}_i \rangle$ as a function of the macroscopic field $\boldsymbol{m}$. By symmetry (in particular, from invariance by rotation), there are only two terms allowed:

$$\langle \hat{\boldsymbol{n}}_i \otimes \hat{\boldsymbol{n}}_i \rangle = \phi(m)\mathbb{I} + \psi(m)\boldsymbol{m} \otimes \boldsymbol{m}, \tag{5.48}$$

where $\phi(m)$ and $\psi(m)$ are two functions of m, which must satisfy one additional constraint: since $\mathrm{Tr}(\hat{\boldsymbol{n}}_i \otimes \hat{\boldsymbol{n}}_i) = 1$, one must have for any distribution of orientations:

$$\mathrm{Tr}\langle \hat{\boldsymbol{n}}_i \otimes \hat{\boldsymbol{n}}_i \rangle = 1. \tag{5.49}$$

Eventually, the functions $\phi(m)$ and $\psi(m)$ depend on the distribution of the orientations. The limiting cases $m = 0$ and $m = 1$ follow from Eqs (5.48) and (5.49):

- $m = 0 \Rightarrow \phi(0) = 1/2$ (from Eq. (5.49)).
- $m = 1 \Rightarrow \psi(1) = 1$ and $\phi(1) = 0$ (from the equality of all polarity vectors).

As a simple ansatz, we write $\langle \hat{\boldsymbol{n}}_i \otimes \hat{\boldsymbol{n}}_i \rangle$ as the only second-order polynomial in m that is compatible with the constraints above:

$$\langle \hat{\boldsymbol{n}}_i \otimes \hat{\boldsymbol{n}}_i \rangle = \frac{1 - m^2}{2}\mathbb{I} + \boldsymbol{m} \otimes \boldsymbol{m}. \tag{5.50}$$

We finally obtain

$$\mathbb{I} - \langle \hat{\boldsymbol{n}}_i \otimes \hat{\boldsymbol{n}}_i \rangle = \frac{1 + m^2}{2}\mathbb{I} - \boldsymbol{m} \otimes \boldsymbol{m} = \frac{1 - m^2}{2}\mathbb{I} + m^2(\mathbb{I} - \hat{\boldsymbol{m}} \otimes \hat{\boldsymbol{m}}), \tag{5.51}$$

where

$$m^2(\mathbb{I} - \hat{\boldsymbol{m}} \otimes \hat{\boldsymbol{m}})\boldsymbol{A} = (\boldsymbol{m} \times \boldsymbol{A}) \times \boldsymbol{m}, \tag{5.52}$$

hence

$$\partial_t \boldsymbol{m} = (\boldsymbol{m} \times \partial_t \boldsymbol{U}) \times \boldsymbol{m} + \frac{1 - m^2}{2}\partial_t \boldsymbol{U}. \tag{5.53}$$

The first term on the right-hand side corresponds to a self-alignment term of the polarization toward the displacement rate, and comes from the average values of displacements of polarizations. Note that, as in the microscopic model, only the elastic force contributes to rotating the polarization vector. In contrast, the second term on the right-hand side

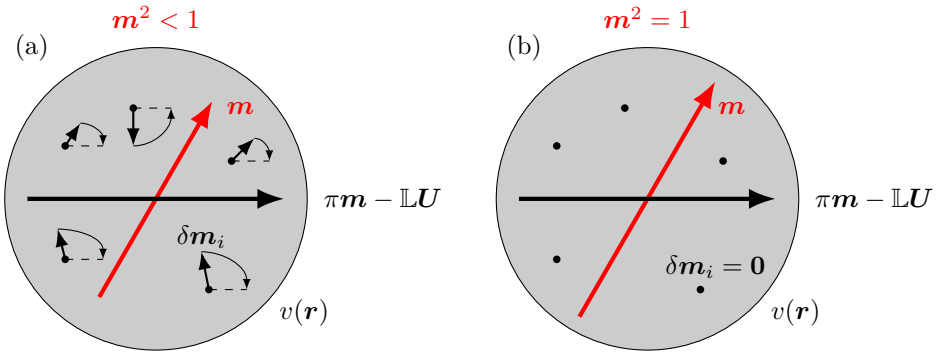


FIG. 5.17. **Representation of the effect of the polarization creation term**. (a) Arbitrary magnetization; the fluctuations reorient toward the averaged velocity $\partial_t \boldsymbol{U}$, which amplifies the magnetization along the direction of $\pi\boldsymbol{m} - \mathbb{L}\boldsymbol{U}$. (b) Fully magnetized; the fluctuations have to be zero and therefore have no effects. In all cases, $\boldsymbol{m}$ rotates toward the elastic force $-\mathbb{L}\boldsymbol{U}$ (not represented).

is a polarization creation term, acting on the amplitude of $\boldsymbol{m}$, and comes from the coarse-graining of the polarization's fluctuations. Note that the latter disappears as the system is fully magnetized ($|\boldsymbol{m}| = 1$), which is illustrated in Fig. 5.17. Altogether, the coarse-grained equations read:

$$\partial_t \boldsymbol{U} = \pi\boldsymbol{m} + \boldsymbol{F_{el}}, \tag{5.54a}$$

$$\partial_t \boldsymbol{m} = (\boldsymbol{m} \times \boldsymbol{F_{el}}) \times \boldsymbol{m} + \frac{1 - \boldsymbol{m}^2}{2} \partial_t \boldsymbol{U}. \tag{5.54b}$$

5.6.4 Polarization relaxation

Additionally considering angular noise in the microscopic polarity dynamics, we find that the polarization dynamics (Eq. 5.54b) is modified. Let us consider the following microscopic polarity dynamics:

$$\dot{\boldsymbol{n}}_i = \sqrt{2D}\xi_i \hat{\boldsymbol{n}}_i^{\perp}, \tag{5.55}$$

where ξ_i are i.i.d. Gaussian random variables with zero mean and correlations $\langle \xi_i(t)\xi_j(t')\rangle = \delta_{ij}\delta(t - t')$. It is possible to exactly coarse-grain this equation, following the approach of [134]. We find:

$$\partial_t \boldsymbol{m}(\boldsymbol{r}, t) = -D_r \boldsymbol{m}(\boldsymbol{r}, t), \tag{5.56}$$

where $D_r = D$ is inherited from the particles' angular diffusion coefficient, contributing to the polarization's relaxation toward zero.

Eventually, the final form for the coarse-grained equations, considering both self-alignment and microscopic angular noise, reads:

$$\partial_t \boldsymbol{U} = \pi\boldsymbol{m} + \boldsymbol{F}^{el}, \tag{5.57a}$$

$$\partial_t \boldsymbol{m} = (\boldsymbol{m} \times \boldsymbol{F}^{el}) \times \boldsymbol{m} + \frac{1 - \boldsymbol{m}^2}{2} \partial_t \boldsymbol{U} - D_r \boldsymbol{m}. \tag{5.57b}$$

5.6.5 Disordered phase

In the absence of the relaxation term, $D_r = 0$, any field $\boldsymbol{m}(\boldsymbol{r}, t)$ such that the elastic forces locally balance the activity ($\boldsymbol{F}^{el} = -\pi\boldsymbol{m}\ \forall r$) is again a fixed point. However,

any small amount of noise, of microscopic origin or effectively coming from the coarse-graining procedure, will induce a non-zero relaxation term $D_r > 0$. In that case, any stationary field with $m \neq 0$ relaxes to the only remaining fixed point $\boldsymbol{U} = \boldsymbol{m} = \boldsymbol{0}$.

The linearized equations of motion around this disordered rest state read, at leading order in small quantities:

$$\partial_t \delta \boldsymbol{U} = \pi \delta \boldsymbol{m} + \boldsymbol{F}^{el}\left[\delta \boldsymbol{U}\right], \tag{5.58a}$$

$$\partial_t \delta \boldsymbol{m} = \frac{1}{2}\left(\pi \delta \boldsymbol{m} + \boldsymbol{F}^{el}\left[\delta \boldsymbol{U}\right]\right) - D_r \delta \boldsymbol{m}. \tag{5.58b}$$

If $\delta \boldsymbol{U}(\boldsymbol{r},t) = \delta a(t)\boldsymbol{\phi}(\boldsymbol{r})$ and $\delta \boldsymbol{m}(\boldsymbol{r},t) = \delta b(t)\boldsymbol{\phi}(\boldsymbol{r})$, where $\boldsymbol{\phi}$ is an eigenmode of $\boldsymbol{F}^{el}$ such that $\boldsymbol{F}^{el}\left[\boldsymbol{\phi}\right] = -\omega_k^2 \boldsymbol{\phi}$, and where δa and δb are small quantities, we get:

$$\frac{d}{dt}\begin{bmatrix}\delta a(t)\\ \delta b(t)\end{bmatrix} = \begin{pmatrix}-\omega_k^2 & \pi\\ -\omega_k^2/2 & \pi/2 - D_r\end{pmatrix} \cdot \begin{bmatrix}\delta a(t)\\ \delta b(t)\end{bmatrix}. \tag{5.59}$$

The solutions λ to the eigenvalue problem satisfy:

$$\lambda^2 - \lambda(\pi/2 - \omega_k^2 - D_r) + D_r \omega_k^2 = 0, \tag{5.60}$$

and are represented in Figs. 5.18. In the limiting case $D_r \to 0$, we find two real eigenvalues $\lambda = 0$ and $\lambda = \pi/2 - \omega_k^2$ (Fig. 5.18-a). For $\pi < \min_k(2\omega_k^2) = 2\omega_{\min}^2$, the fixed point is marginally stable. For $\pi > 2\omega_{\min}^2$, it is unstable, and the dynamics grow along the lowest energy elastic mode. Therefore, the coarse-grained description, close to the disordered state, does not contain the non-trivial selection observed in discrete systems.

For $D_r > 0$, we find that the nature of the bifurcation is modified. First, any finite amount of noise creates a collision between the two eigenvalues below and above the instability, opening a range of π with complex conjugate eigenvalues (Figs. 5.18-b), and second, the instability threshold increases with the noise amplitude (Fig. 5.18-c).

Let us first focus on the small noise regime, for which the polarization relaxes much slower than the elastic modes $D_r \ll \omega_k^2$.

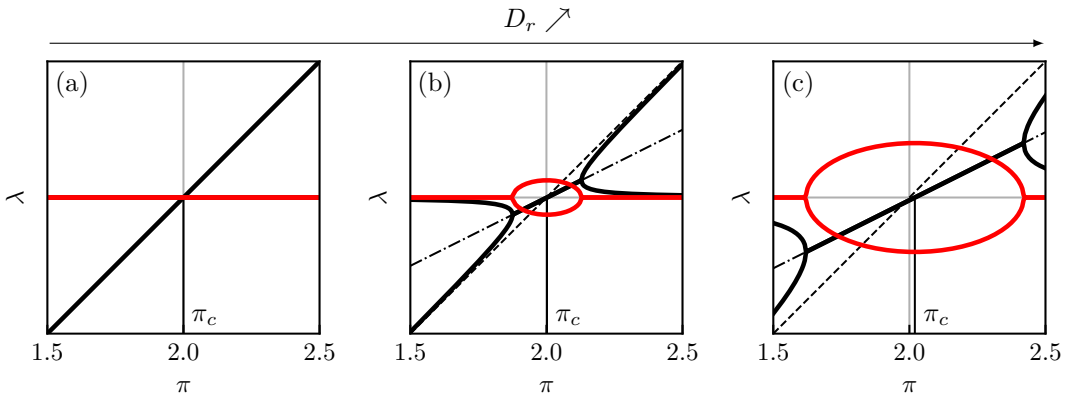


FIG. 5.18. **Disordered phase linear stability analysis.** Solutions of Eq. (5.60) as a function of the elasto-active feedback π, for $\omega_{\min}^2 = 1$. Black (resp. red) solid curves represent the real (resp. imaginary) parts of the solutions. The dashed and dashed-dotted black curves respectively represent the functions $\lambda = \pi/2 - 1$ and $\lambda = (\pi/2 - 1 - D)/2$. (a) $D_r = 0$, (b) $D_r = 10^{-3}$, (c) $D_r = 10^{-2}$.

- When $|\frac{\pi}{2} - \omega_{\min}^2| > 2\sqrt{D_r \omega_{\min}^2}$ (far enough from the noiseless instability threshold), the two eigenvalues are real, with the same sign:

$$\lambda = \frac{1}{2}\left(\frac{\pi}{2} - \omega_{\min}^2\right) \pm \frac{1}{2}\sqrt{\left(\frac{\pi}{2} - \omega_{\min}^2\right)^2 - 4D_r\omega_{\min}^2}. \tag{5.61}$$

- When $|\frac{\pi}{2} - \omega_{\min}^2| < 2\sqrt{D_r \omega_{\min}^2}$ (close enough to the noiseless instability threshold), the two eigenvalues are complex conjugate, with the same real part's sign:

$$\lambda = \frac{1}{2}\left(\frac{\pi}{2} - \omega_{\min}^2\right) \pm \frac{i}{2}\sqrt{4D_r\omega_{\min}^2 - \left(\frac{\pi}{2} - \omega_{\min}^2\right)^2}. \tag{5.62}$$

  Thus at the threshold $\pi = 2\omega_{\min}^2$, the imaginary part of the eigenvalues is equal to $\pm i\sqrt{D_r\omega_{\min}^2}$. When $\pi = \pi_c$, the fixed point turns unstable via a Hopf bifurcation.

Now, regarding the dependence of the instability threshold on the noise amplitude, a simple analysis of Eq. (5.60) reveals that in the general case, the instability threshold expresses as follows:

$$\pi_c = 2\left(\omega_k^2 + D_r\right). \tag{5.63}$$

Large noise stabilizes the disordered fixed point (Fig. 5.18-c). The oscillation frequency resulting from this Hopf bifurcation is finite at the bifurcation, with an amplitude proportional to $D_r^{1/2}$, decreasing when π moves away from the instability threshold. Unsurprisingly, the linear destabilization properties tell us very little about the disconnected nonlinear dynamics describing the SCO regime. In particular, the Hopf bifurcation's frequency has nothing to do with the limit cycle's frequency.

5.6.6 Homogeneous phases

We are here interested in describing the physics in the bulk of the material, far from the boundaries, where CA concentrates. In line with the physics of the triangular lattice, let us assume the dynamics condensate on two degenerated modes, which, far from the boundaries, are homogeneous and akin to two perpendicular translation modes. By convention, their geometry can be written as follows: $\langle i|\boldsymbol{\varphi}_1\rangle = \boldsymbol{e}_x$ and $\langle i|\boldsymbol{\varphi}_2\rangle = \boldsymbol{e}_y$. In this context and neglecting the contributions from all the other modes, the elastic force must be homogeneous $\boldsymbol{F}^{el}[\boldsymbol{U}] = -\omega_0^2\boldsymbol{U}$, where ω_0 is the eigenfrequency of the selected pair of modes. The coarse-grained equations then read:

$$\partial_t \boldsymbol{U} = \pi\boldsymbol{m} - \omega_0^2\boldsymbol{U}, \tag{5.64a}$$

$$\partial_t \boldsymbol{m} = -\omega_0^2(\boldsymbol{m}\times\boldsymbol{U})\times\boldsymbol{m} + \frac{1-\boldsymbol{m}^2}{2}\partial_t\boldsymbol{U} - D_r\boldsymbol{m}. \tag{5.64b}$$

We introduce the angles φ and θ, respectively, the angle of the displacement $\boldsymbol{U}$ with respect to the x-axis, and the angle of the polarization $\boldsymbol{m}$ with respect to the x-axis; and the norms R and m of the vectors $\boldsymbol{U}$ and $\boldsymbol{m}$. Once again, we denote $\gamma = \theta - \varphi$. These variables obey the following dynamical equations:

$$\partial_t R = \pi m\cos\gamma - \omega_0^2 R, \tag{5.65a}$$

$$R\partial_t\varphi = \pi m\sin\gamma, \tag{5.65b}$$

$$m\partial_t\theta = \frac{1+m^2}{2}\omega_0^2 R\sin\gamma, \tag{5.65c}$$

$$m\partial_t m = \frac{1-m^2}{2}\left[\pi m^2 - \omega_0^2 R m\cos\gamma\right] - D_r m^2. \tag{5.65d}$$

Fixed point

Due to the presence of the relaxation term in Eq. (5.65d), the only fixed point of Eqs. (5.65) expresses as ($R_0 = 0$, $m_0 = 0$) and corresponds to the disordered phase.

The linearized equations around the fixed point are:

$$\frac{d}{dt}\begin{pmatrix}\delta R\\ \delta m\end{pmatrix} = \begin{pmatrix}-\omega_0^2 & \pi\\ -\omega_0^2/2 & \pi/2 - D_r\end{pmatrix}\begin{pmatrix}\delta R\\ \delta m\end{pmatrix}, \tag{5.66}$$

and the eigenvalue problem reduces to solve the polynomial:

$$\lambda^2 - \lambda(\pi/2 - \omega_0^2 - D_r) + D_r\omega_0^2 = 0. \tag{5.67}$$

Thus we recover Eq. (5.60), with $\omega_{\min}^2 = \omega_0^2$; and the disordered fixed point is stable for $\pi < 2\omega_0^2$, unstable otherwise.

Oscillating solution

Now we look for oscillating solutions of Eqs. (5.65) at frequency $\Omega > 0$. It boils down to solving the equation for the amplitude of the polarization:

$$D_r m = \frac{1-m^2}{2} m^2 (\pi - \frac{2\omega_0^2}{1+m^2}). \tag{5.68}$$

Without relaxation. In the limiting case $D_r \to 0$, the only solution of Eq. (5.68) giving $\Omega > 0$ is $m = 1$. The non-linear saturation vanishes, and one recovers the equations for the single particle system, which predict a polarized solution with oscillation at frequency Ω, amplitude R_0 in displacements, and phase shift γ_0 between polarity and velocity vectors, such that:

$$m = 1, \tag{5.69a}$$
$$R_0 = \sqrt{\pi}/\omega_0, \tag{5.69b}$$
$$\cos\gamma_0 = 1/R_0, \tag{5.69c}$$
$$\Omega = \omega_0\sqrt{\pi - \omega_0^2}, \tag{5.69d}$$

when $\pi > \omega_0^2$.

With relaxation. The presence of a small relaxation rate of the polarization amplitude ($D_r = \varepsilon \ll 1$) modifies the picture. Assuming $m = 1 - \delta m$, we find, at leading order in small quantities:

$$\delta m = \frac{\varepsilon}{\pi - \omega_0^2}, \tag{5.70a}$$
$$R_0 = \frac{\sqrt{\pi}}{\omega_0}, \tag{5.70b}$$
$$\cos\gamma_0 = \frac{\omega_0}{\sqrt{\pi}}(1 + \frac{1}{2}\delta m), \tag{5.70c}$$
$$\Omega = \omega_0\sqrt{\pi - \omega_0^2}\left[1 - \delta m\left(1 + \frac{1}{2}\frac{\omega_0^2}{\pi - \omega_0^2}\right)\right], \tag{5.70d}$$

for $\pi > \omega_0^2$. As expected, a noisy microscopic dynamics decreases both the polarization and the phase shift γ_0. These two effect balance, resulting in an unmodified value for R_0. The oscillation frequency Ω also decreases with D_r. The effect of noise is as dramatic as the system is close to $\pi = \omega_0^2$.

5.6.7 Phase diagram

Combining the results obtained in the two previous sections, we find the mean-field phase diagram presented in Fig. 5.19, in the limiting case $D \to 0$. The latter captures the existence of the frozen-disordered and chiral phases and their phase space coexistence for a finite range of the elasto-active coupling π. However, the disordered $m = 0$, and the chiral $m = 1$ solutions being disconnected, the nature of the transition is controlled by inhomogeneous solutions, which cannot be investigated within perturbative approaches.

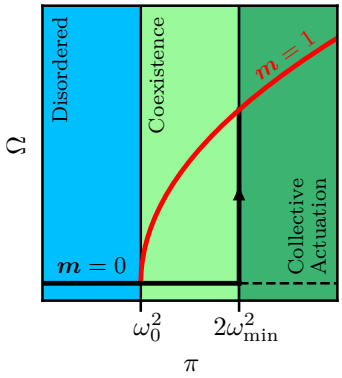


FIG. 5.19. **Coarse-grained model phase diagrams at the mean-field level.** The disordered, $\boldsymbol{m} = 0$, phase (black line) coexists with the fully polarized, $|\boldsymbol{m}| = 1$, chiral, $\Omega > 0$, phase (red line) for $\pi \in \left[\omega_0^2, 2\omega_{\min}^2\right]$. Note that we consider the general case where $\omega_{\min}^2$ is not necessarily the energy of the two degenerated translation-like modes ω_0^2.

5.6.8 Relation to non-reciprocal systems

It was recently shown that systems composed of microscopic degrees of freedom experiencing non-symmetrical interactions, together with non-conservative dynamics, are prone to develop chiral phases via a specific kind of phase transition, which *Fruchart et al.* called non-reciprocal [172]. Our model system, composed of active units connected by elastic springs, is a priori a good candidate for the study of this physics. Its dynamics results from the coupling of N polarity vectors $\hat{\boldsymbol{n}}_i$ and N displacement vectors $\boldsymbol{u}_i$, where one can recognize two abstract species A and B. We recall Eqs. (5.15), which govern the dynamics of a single particle in a harmonic potential:

$$\dot{R} = \pi \cos(\theta - \varphi) - \omega_0^2 R, \tag{5.71a}$$

$$\dot{\varphi} = \frac{\pi}{R} \sin(\theta - \varphi), \tag{5.71b}$$

$$\dot{\theta} = -\omega_0^2 R \sin(\varphi - \theta), \tag{5.71c}$$

where φ (resp. θ) represents the angle of the displacement (resp. polarity) vector with respect to the x-axis, and where R is the norm of the displacement vector. One sees that the phases φ and θ are coupled non-symetrically, as $J_{\hat{\boldsymbol{n}} \to \boldsymbol{u}} = \pi/R \neq J_{\boldsymbol{u} \to \hat{\boldsymbol{n}}} = -\omega_0^2 R$, in such a way that for $\pi > \pi_c$, the phase of the displacement vector chases that of the polarity (see Appendix F). It is therefore likely that the macroscopic dynamics for the order parameters associated with the mean polarization and mean displacement experience the kind of transition towards a chiral phase described in [172]. More precisely, the coarse-grained dynamics map on the general equations describing the dynamics of two

vector order parameters $\mathbf{v}_a(t,x)$, which serve as the starting point in [172] :

$$\partial_t \mathbf{v}_a = \mathbb{A}_{ab}\mathbf{v}_b + \mathbb{B}_{abcd}\left(\mathbf{v}_b \cdot \mathbf{v}_c\right)\mathbf{v}_d + \mathcal{O}(\nabla). \tag{5.72}$$

They read

$$\partial_t \boldsymbol{U} = \pi \boldsymbol{m} + \mathcal{O}(\nabla), \tag{5.73a}$$

$$\partial_t \boldsymbol{m} = \pi \frac{1-\boldsymbol{m}^2}{2}\boldsymbol{m} + \mathcal{O}(\nabla), \tag{5.73b}$$

where the non-zero coefficients, $\mathbb{A}_{um} = \pi$, $\mathbb{A}_{mm} = \pi/2$ and $\mathbb{B}_{mmmm} = -\pi/2$ are clearly non-symmetric.

This suggests a possible description of the transition to CA in terms of non-reciprocal phase transitions. If this were to be confirmed by a more involved analysis of the large-scale dynamics, it would motivate the study of the disordered to chiral phase transition in active solids, which has yet to be addressed theoretically. In the same vein, one may ask whether the coarse-grained system shall obey standard or odd elasticity [125].

5.7 Conclusion

In this chapter, we have seen that mechanically stable elastic structures doped with active units exhibit selective and collective actuation. This new kind of collective behavior arises explicitly because of the elasto-active feedback, the reorientation of the active units by the displacement field. For systems pinned at the edges, we find that a pair of degenerated, translation-like modes are spontaneously selected, resulting in a chiral regime oscillating between these two modes. Let us remind the three salient features of CA in triangular and kagome lattices: (i) the transition from the disordered phase leads to a chiral phase with spontaneously broken symmetry; (ii) the actuated dynamics are not of inertial origin, take place on a few modes, not always the lowest energy ones, and therefore obey non-trivial selection rules; (iii) the transition follows a coexistence scenario, where the fraction of actuated nodes discontinuously falls to zero.

We have shown that the chiral phase with spontaneously broken symmetry, i.e. point (i), is already present at the single particle level. Moreover, points (ii) and (iii) originate from the crucial role played by the normal modes' geometry. In particular, the non-trivial selection is inherited from the fact that the dynamics favor the activation of modes that are delocalized and locally-orthogonal, two properties met by the pair of translation-like modes. Moreover, with the help of simple toy models, we demonstrated that the heterogeneity of the selected modes is at the origin of the discontinuity in the transition to CA, and of the spatial coexistence between frozen and oscillating phases. Finally, we introduced a coarse-grained model to describe the large-scale physics of polar active solids. The coarse-graining procedure leads to an additional term in the polarization dynamics, in the form of a polarization creation term in the direction of the local displacement rate.

Much work remains to be done to understand better the transition to CA at large scales, which is generically governed by inhomogeneous solutions. Simulating the coarse-grained equations in triangular elastic networks pinned at the edges, we find that the polarization creation term indeed allows for sharp transition regions between the polarized-oscillating phase and the frozen-disordered phase, in a way reminiscent of the large-N simulations of the microscopic dynamics. This calls for simulations and theoretical analysis of the

coarse-grained equations in simple settings, like disk-shaped active solids [77], and for studying the non-trivial selection on continuum scales. Determining the critical exponents related to the transition to CA, and the influence of orientational elasticity [173], are other exciting avenues for future research.

Chapter 6

Tension-controlled switch between collective actuation

6.1 Introduction

Collective actuation (CA) takes place when spontaneous activation of a few harmonic modes occur, and was first reported in a numerical study of jammed active particles [79]. In the previous chapter, the experimental realization and theoretical study of CA in stable elastic structures demonstrated the key role of a nonlinear elasto-active feedback between the deformations of the structure and the orientations of the active units. A typical realization of CA is illustrated in Fig. 6.1-b. When an active triangular lattice is pinned at the edges, its nodes perform a Synchronized Chiral Oscillation (SCO) around their reference positions.

Very similar SCO dynamics have been reported in confined epithelial cells [8] and dense bacterial suspensions [77, 174] (see chapter 1). Another collective dynamics, with the system performing Global Alternating Rotation (GAR) around its center, was even reported in bacterial bio-films [77, 175], and, quite remarkably, a transition from SCO to GAR could be observed as activity decreases [77]. Nonetheless, its origin has yet to be fully understood. From a biomimetic point of view, active metamaterials are therefore a promising framework for creating multifunctional materials [103, 106, 108–110] with bona fide autonomy [107]. However, an explicit realization of active metamaterials exhibiting different CA regimes, with a good control of the transition between these regimes, is still lacking.

In this chapter, we bridge this gap by (i) demonstrating the existence of both SCO and GAR in the same active elastic structure, (Figs. 6.1-a and b), (ii) showing how mechanical tension can be harnessed to manipulate the vibrational spectrum of an active solid and control the transition between these different CA regimes. We first establish the experimental proof of concept using a toy-model active solid (Figs. 6.1-e and f). We then dissect the underlying mechanism and extend our findings to more general geometries, on the basis of an agents model and theoretical arguments. Apart from being a simple design principle and an intuitive way to interact with active solids, mechanical tension is of significant biological interest, as it is known to play a crucial role in growth processes and mechanical responses [176–180], especially during morphogenesis.

6.2 Boundary-condition-controlled dynamics

Our first, simple but important result, is that the GAR regime is readily obtained in the same active network of springs by changing the boundary conditions.

We construct another active triangular lattice, connecting the active elastic building blocks with *stiff* springs (see chapter 2). As discussed in chapter 4, when a given node of the elastic structure is pinned, suppressing its translational degrees of freedom, the system performs a collective steady rotation around the pinning point. Interestingly, when a given node of the elastic structure, here the central one, is embedded, i.e. pinned both in translation and rotation, the structure periodically alternates between clockwise and counter-clockwise rotations around this node (Fig 6.1-a). Note that these observations are qualitatively preserved if the embedded node is arbitrary. Such a CA regime is a GAR, contrasting sharply with the SCO observed for the active lattice of *soft* springs pinned at the edges (Fig 6.1-b).

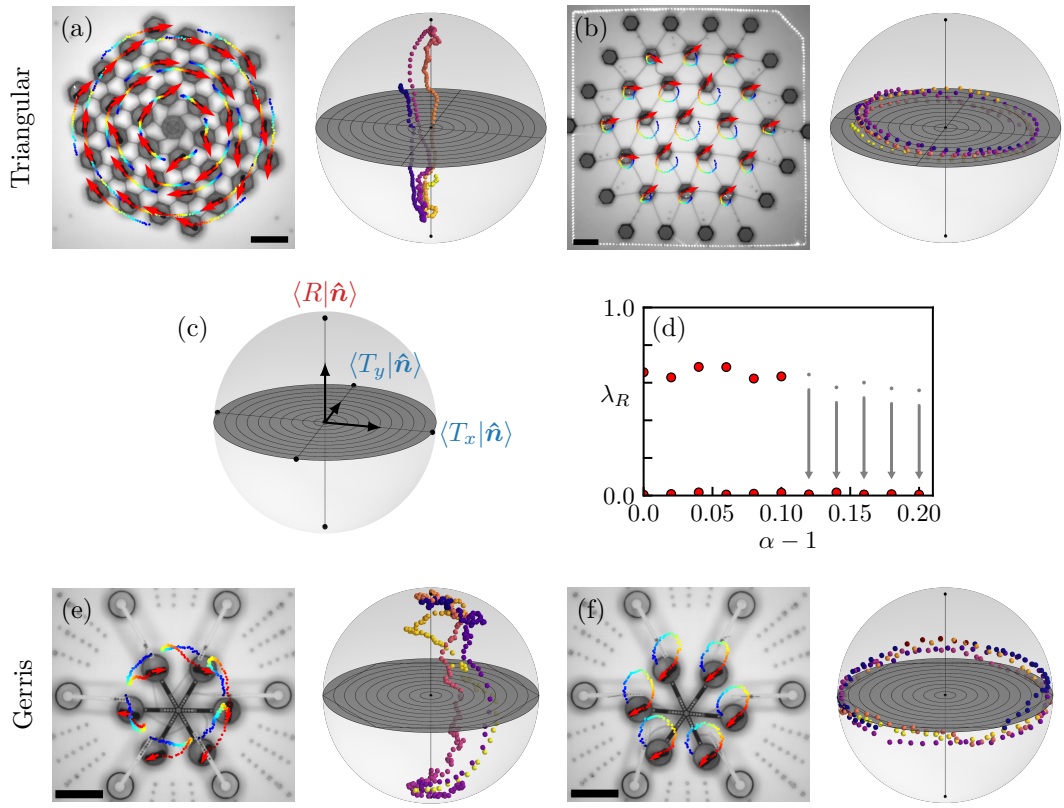


FIG. 6.1. **Experimental realization of a controlled switch between collective actuations**. (a) GAR in a triangular lattice with embedded central pinning; $N = 36$, $\alpha = 1.0$. (b) SCO in a triangular lattice under edge pinning; $N = 19$, $\alpha = 1.27$. Left panel: dynamics in real space (red arrows: polarities $\hat{\boldsymbol{n}}_i$; trajectories color-coded from blue to red with increasing time; scale bars: 10 cm); right panel: polarity dynamics projected on the translation and rotation modes of the structures (vertical axis: $\langle R|\hat{\boldsymbol{n}}\rangle$, equatorial plane: $\langle T_{x/y}|\hat{\boldsymbol{n}}\rangle$), see notations and convention in panel (c). (d) A switch between GAR and SCO is obtained in a model elastic structure, the active *Gerris*, by tuning mechanical tension: condensation fraction on the rotation mode λ_R as a function of tension $\alpha - 1$ (red bullets are obtained from data averaged in the steady state; the gray dots and arrows sketch the transitory regime when initials conditions enforce rotation at large tension). (e-f) GAR, resp. SCO in the active *Gerris* at low ($\alpha = 1.0$), resp. large ($\alpha = 1.8$) tension; $N = 6$.

These two dynamics are best illustrated when decomposed on the elastic modes of the structures (see Appendix A), which are the eigenvectors, $|\boldsymbol{\varphi}_k\rangle$, associated with the eigenvalues, ω_k^2, of the dynamical matrix, $\mathbb{M}$. More specifically, we represent the dynamics in the space spanned by the amplitude of the polarity field projected on three modes of interest: the vertical axis represents the normalized projection on the rotation mode $a_R = \langle R|\hat{\boldsymbol{n}}\rangle/\sqrt{N}$, whereas the equatorial plane represents the normalized projections on the two translational like modes $a_{T_{x/y}} = \langle T_{x/y}|\hat{\boldsymbol{n}}\rangle/\sqrt{N}$ (Fig. 6.1-c). From the polarity field normalization, the projections are confined inside the 3-sphere of radius $\sqrt{N}$, normalized to 1. Note that the rotation and translational modes are the three lowest energy modes for both boundary conditions (see Appendix A).

In the GAR regime, obtained from the central pinning condition, the polarity dynamics alternatively condensate on the clockwise and counter-clockwise rotation mode (the poles of the sphere), separated by fast reversal motion (Fig. 6.1-a). Conversely, in the SCO regime, obtained from the edge pinning condition, the polarity dynamics condensate on the translational modes spanning the equatorial plane of the sphere (Fig. 6.1-b), and rotate clockwise or counter-clockwise on this plane, spontaneously breaking the chiral symmetry.

As we shall now see, applying mechanical tension at the boundary allows switching between the SCO and GAR regimes, while keeping the boundary condition and the elasto-active coupling π fixed.

6.3 Active *Gerris*

We design a toy-model active elastic structure, which consists of $N = 6$ active units at the vertices of a rigid inner hexagon, each connected radially to the vertices of an outer pinned hexagon via *soft* springs (Figs. 6.2). We term this structure the active *Gerris* in reference to the water strider bug. As we will see, even though it could appear somewhat artificial, this structure allows studying the competition between two translational modes and a third mode, here a rotation. It is therefore the simplest instance allowing for a

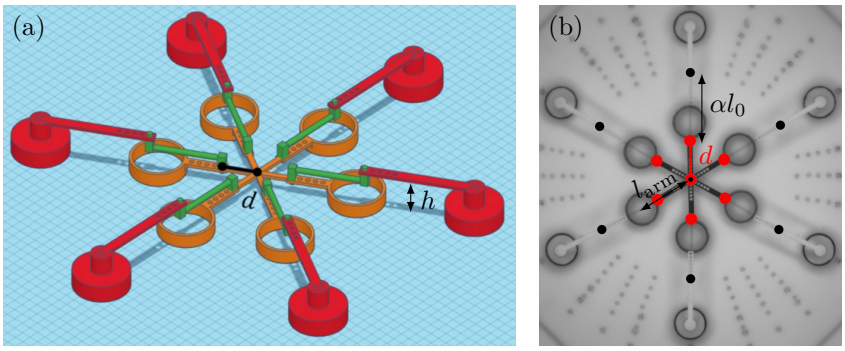


FIG. 6.2. **Active *Gerris*' structure**. (a-b) Experimental active *Gerris*. (a) 3d representation of the setup. Green cylinders represent springs, red structures are the six pinning points, and the orange structure is the rigid inner structure. The distance between the structure's barycenter and the springs connections on the rigid inner structure is denoted d. The height $h \simeq 30$ mm of the pinning points allows the *Gerris* to move without touching the pinning structures. (b) Top view of the experiment. The spring ends are attached to the red (connection with the arm) and black (connection with the pinning point) markers with freely-rotating pins.

behavior switch.

6.3.1 Structure

The active *Gerris* structure is made of a 3d printed stiff frame with six regularly spaced arms ($l_{\text{arm}} \simeq 97$ mm long), at the end of which are embedded the active units (Figs. 6.2-a, orange structure); which therefore sit at the vertices of a regular hexagon. Activity cannot deform the arms as they are made of ABS, and their bending rigidity is large compared to the active force produced by the hexbugs. This frame constitutes the rigid inner structure of the active *Gerris*. It is connected to six pinning points (Figs. 6.2-a, red structures) by *soft* springs (Figs. 6.2-a, green structures), on a plane above the experiment. This way, there are no steric interactions between the rigid inner frame and the pinning structures. The pinning points are located at the vertices of a regular outer hexagon, larger than the inner one. There is one spring per arm, whose ends are attached with freely rotating joints to the pinning point and the arm, at a distance d ($\simeq 33$ mm) from the barycenter. We model the active *Gerris* with the structure shown in Figs. 6.4-a and 6.3. It describes well the experimental reality, modulo two approximations:

- The arm length l_{arm} is assumed to be equal to the soft springs' rest length l_0 for simplicity.
- The distance d is chosen to be equal to l_{arm}, the rigid inner hexagon's side length. Indeed, choosing a shorter than l_{arm} distance d would just decrease the rotation's mode energy by a factor d/l_{arm} (and no effect on the translational modes), which does not modify the picture qualitatively.

6.3.2 Normal mode spectrum

To explicit the normal mode spectrum, we must first determine the reference configuration and the pre-stress. The pinning condition imposes $\alpha \geq 1$: the *soft* external springs are elongated at mechanical equilibrium (Fig. 6.4-a). It is also mandatory to prescribe how the inner structure dilates as tension is imposed on the structure. We call the inner structure's elongation factor α_I. Assuming it is strictly rigid, the inner structure does not dilate, thus $\alpha_I = 1$.

The *Gerris* is characterized by the three degrees of freedom of its inner structure: the spatial coordinates of its barycenter $\boldsymbol{u}_0$ and its angular orientation ϕ (Fig. 6.3). The

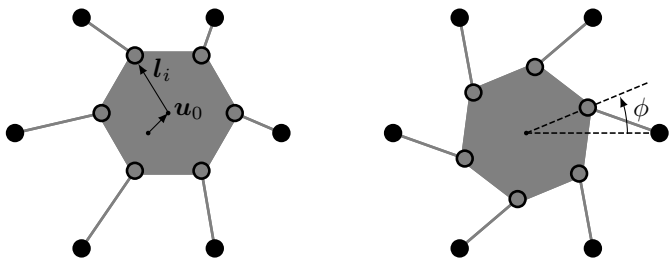


FIG. 6.3. **Notations for the *Gerris*.** (left) The position of the active *Gerris* inner rigid hexagon barycenter is denoted $\boldsymbol{u}_0$. (right) The angle ϕ characterizes the rotation of the active *Gerris* inner rigid hexagon. The vectors $\boldsymbol{l}_i$ are the positions of the active nodes with respect to $\boldsymbol{u}_0$.

three associated normal modes are two degenerated translation modes $|\boldsymbol{T}_{x/y}\rangle$ and one rotation mode $|\boldsymbol{R}\rangle$, which are illustrated in Fig. 6.4-b, together with their energies as a function of the imposed tension. Both the rotation and translation energies increase with tension, but the energetic ordering of the modes is preserved, and their geometries are unaffected. The three modes end up degenerated at infinite tension.

6.3.3 Tension-controlled switch

Experimentally, mechanical tension is controlled by a stepwise elongation of the *soft* external springs. At low tension, GAR and SCO regimes are both observed and are stable on the experimental timescale (Figs. 6.1-d and e). At large tension, only the SCO regime is stable (Fig. 6.1-f), while the GAR regime is metastable (arrows on Fig. 6.1-d); allowing for a one-way switch from GAR to SCO as tension increases.

Analyzing the dynamics in mode space, we find that the active *Gerris* convincingly explores the same dynamics under the control of tension as the triangular lattices (Figs. 6.1-e and f). The dynamics are quantified by the condensation fraction on the rotation mode, computed in the rotating frame of the *Gerris*[1]:

$$\lambda_R = \frac{1}{T}\int^T \left[\frac{\langle \boldsymbol{R}(t)|\hat{\boldsymbol{n}}(t)\rangle}{\sqrt{N}}\right]^2 dt, \tag{6.1}$$

where the vector $|\boldsymbol{R}\rangle(t)$ is always azimuthal with respect to the inner structure. The active *Gerris* switch is illustrated by the abrupt drop of this condensation fraction on the rotation mode λ_R as tension increases (Fig. 6.1-d).

6.3.4 Numerical model

We investigate numerically the switch in the active *Gerris*, using the overdamped equations of motion (see chapter 3):

$$\dot{\boldsymbol{u}}_i = \pi\hat{\boldsymbol{n}}_i + \boldsymbol{F}_i^{el}, \tag{6.2a}$$

$$\dot{\boldsymbol{n}}_i = (\hat{\boldsymbol{n}}_i \times \dot{\boldsymbol{u}}_i)\times\hat{\boldsymbol{n}}_i + \sqrt{2D}\xi_i\hat{\boldsymbol{n}}_i^{\perp}, \tag{6.2b}$$

where $\boldsymbol{F}_i^{el}$ is the sum of the elastic forces acting on node i, and ξ_i are i.i.d gaussian variables with zero mean and correlations $\langle\xi_i(t)\xi_j(t')\rangle = \delta_{ij}\delta(t-t')$. We set $\pi = 2.0$, a value consistent with previous calibrations (see chapter 3), and investigate the effect of mechanical tension. The *Gerris*' inner structure being rigid, the $2N$ equations for the position dynamics, Eqs. (6.2a), reduce to the equations of motion for the degrees of freedom $\boldsymbol{u}_0$ and ϕ (see Appendix H):

$$N\dot{\boldsymbol{u}}_0 = \sum_i \left[\pi\hat{\boldsymbol{n}}_i + \boldsymbol{F}_i^{el}\right], \tag{6.3a}$$

$$N\dot{\phi} = \sum_i \left[\pi\sin(\theta_i-\phi_i) + |\boldsymbol{F}_i^{el}|\sin(\psi_i-\phi_i)\right]. \tag{6.3b}$$

where θ_i is the orientation of the polarity vector $\hat{\boldsymbol{n}}_i$, ψ_i is the orientation of the elastic force vector $\boldsymbol{F}_i^{el}[\boldsymbol{u}_0,\phi]$, and ϕ_i is the orientation of the position vector $\boldsymbol{r}_i = \boldsymbol{u}_0 + \sigma_\phi\boldsymbol{l}_i$, with σ_ϕ the rotation matrix of angle ϕ.

[1]This avoids considering the geometrical nonlinearities coming from the large rotation angles, which virtually transfer active force from the rotation to the dilation mode.

Harmonic approximation level

We first simulate the noiseless, $D = 0$, active *Gerris* equations in the *harmonic approximation* (see Appendix H), annealing back and forth between small and large tensions. We find two linearly stable actuation branches, which we denote the TT and RT regimes (Fig. 6.4-c, circle markers).

The TT regime is a strict condensation of the polarity field on the equator (Fig. 6.4-d), with $\lambda_R = 0$, corresponding to a SCO of the *Gerris*. This is possible because the translational modes are fully delocalized $Q_{T_x} = Q_{T_y} = 1$, and locally orthogonal. Because they also are degenerated, the TT regime strictly maps onto the spontaneous oscillation of a single particle in a harmonic potential [143], as discussed in chapter 5. All quantities of interest can be calculated analytically, e.g., its oscillation frequency Ω expresses as follows:

$$\Omega = \pm\omega_T\sqrt{\pi - \omega_T^2}, \tag{6.4}$$

for $\pi > \omega_T^2$, where ω_T^2 refers to the squared eigenfrequency of the two degenerated translational modes. Surprisingly, despite the presence of a mode of lower energy than the

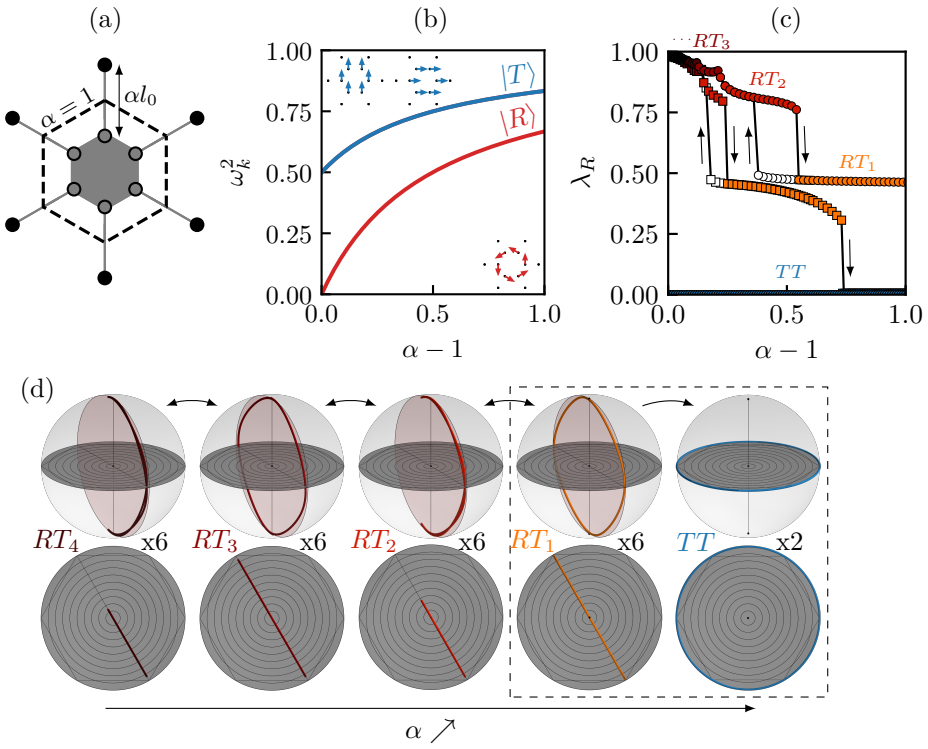


FIG. 6.4. **Active *Gerris*'s dynamics as a function of lattice tension.** (a) Elastic architecture cartoon. In gray: the rigid inner hexagon. The external springs are elongated by a factor α at mechanical equilibrium. (b) Normal modes spectrum as a function of springs tension $\alpha - 1$. The red (resp. blue) solid line corresponds to the rotation mode (resp. degenerated translational modes), shown in inset. (c) Condensation fraction on the rotation mode λ_R as a function of lattice tension $\alpha - 1$ (yellow-orange to black symbols: the different RT regimes; blue symbols: TT regimes; (circles): harmonic approximation; (squares): including geometrical nonlinearities; empty markers: backward annealing). (d) Side and top view of the $3d$ representations of the polarity field steady dynamics projected on the rotation and translation modes for the regimes RT_4, RT_3, RT_2, RT_1, TT, from left to right (vertical axis: $\langle R|\hat{\boldsymbol{n}}\rangle$, equatorial plane: $\langle T_{x/y}|\hat{\boldsymbol{n}}\rangle$). The dashed black square highlights the switch of interest.

translational ones, the TT regime is always stable, emphasizing the non-trivial selectivity of this SCO regime at the collective level. We can show that this effect is absent at the single particle level, underlining the role of geometry in the non-trivial selection (see Appendix J).

The RT regimes consist of a condensation of the polarity field on a plane, defined by the rotation vector $|\boldsymbol{R}\rangle$ and one of the six translational vector $|\boldsymbol{T}\rangle$, pointing toward one of the hexagon's main axis, in the equatorial plane (Fig. 6.4-d). They correspond to a GAR of the *Gerris*. The six possible orientations of this plane define six equivalent attractors, one of which is selected, spontaneously breaking the 6-fold symmetry of the system (Figs. 6.5). Depending on the tension, we actually report different RT dynamics, separated by hysteretic transitions, which differ in the precise trajectory of the alternating rotation. While the two selected modes are fully-delocalized $Q_R = Q_T = 1$, they are not locally orthogonal. This prevents a strict condensation: during the turnarounds, some active force must be transformed into mechanical stress of the rigid inner structure, and the polarity field enters inside the circle in the plane of the two selected modes (Figs. 6.4-d and 6.6-a). More importantly, the translational and rotation modes are not degenerated (Fig. 6.4-b): tension changes the energy ratio between the two selected modes.

Most of the RT regimes phenomenology can be understood qualitatively by studying the dynamics of a single particle trapped in elliptic harmonic potentials ([181] and Appendix I). As the energy ratio between the two modes increases, the single active particle orbits along circles, ellipses, lemniscates, and higher-order lemniscates [181], the so-called elliptic regimes E_n (see Appendix I). In mode space, these limit cycles are more and more condensed along the soft direction. Moreover, similarly to the active *Gerris*' RT_n regimes, the E_n regimes are separated by hysteretic and discontinuous transitions. Such a toy model is enough to explain the qualitative features of the dynamics in the selected RT plane, as illustrated in Fig. 6.6 for regimes RT_2 and E_2.

Within the linear level of description, there is however no switch between the coexisting RT and TT regimes.

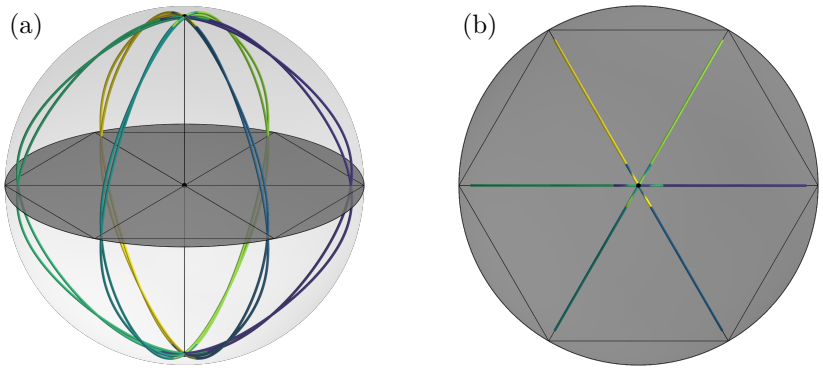


FIG. 6.5. **Multiplicity of the RT regimes**. Simulated harmonic dynamics of the active *Gerris* with $\pi = 2.0$ and $\alpha = 1.1$, shown in mode space; vertical axis: $\langle R|\hat{\boldsymbol{n}}\rangle$, equatorial plane: $\langle T_{x/y}|\hat{\boldsymbol{n}}\rangle$. The six RT_4 attractors are found by simulating numerous random initial conditions. Only the RT stationary states are shown. The black hexagon illustrates the orientation of the inner hexagon with respect to the axis. (a) Top-side view. (b) Top view.

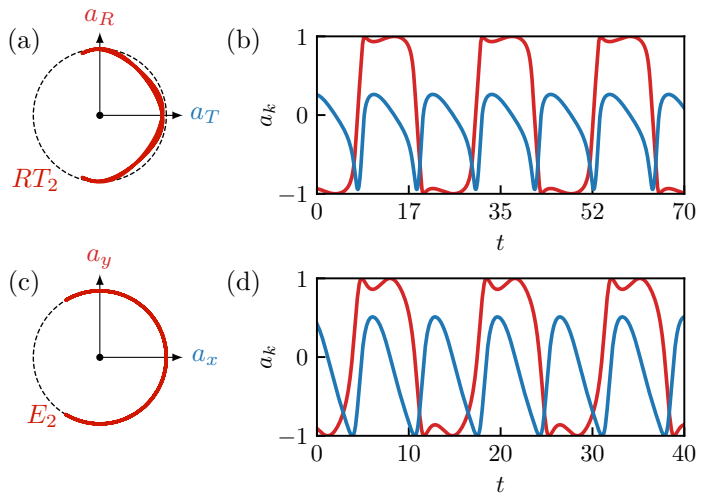


FIG. 6.6. **Mapping between the active *Gerris*' RT regimes and the dynamics of a single particle trapped in an elliptic harmonic potential.** Illustration in the case of regimes $RT_2 \leftrightarrow E_2$. (a-b) Active *Gerris*'s RT_2 regime ($\alpha = 1.4$), see Fig. 6.4-d. Polarity field dynamics, restricted to the plane of the two selected modes (a), and as a function of time (b). The solid red line (resp. solid blue line) represents a_R (resp. a_T), where T refers to the linear combination of the two translational modes giving the orientation of the plane in Fig. 6.4-d). E_2 dynamics of a single particle trapped in an elliptic harmonic potential, softer along the y-direction ($\omega_x^2 = 1.0$, $\omega_y^2 = 0.36$, $\pi = 2.0$), see Appendix I. Polarity field dynamics in the $x - y$ plane (a), and as a function of time (b). The solid red line (resp. solid blue line) represents a_y (resp. a_x). In (a/c), the dashed black circle represents the unit circle.

Including geometrical nonlinearities

Including the geometrical nonlinearities of the elastic forces (see Appendix H), we find that the TT regime is unaffected, while the stability ranges of the RT regimes are shifted toward smaller tensions (Fig. 6.4-c, square markers). More significantly, the RT regime destabilizes towards the TT regime for large enough tension. We thus find that geometrical nonlinearities allow for an irreversible, one-way switch, from the RT to the TT regime as tension increases. Coming back to the analogy with the single particle in asymmetric harmonic potentials, the switch is a discontinuous transition from an elliptic regime E_1 to a circular one E_0, standing on planes perpendicular to one another (Fig. 6.4-d).

Including angular noise

The TT regime persists for all values of the tension and coexists with the RT regime. We discuss the relative stability of the two attractors by adding a small noise, $D = 10^{-2}$, consistent with existing calibrations (see chapter 3). Starting from the RT regime, the system first remains close to the initial RT attractor, then visits the six equivalent RT attractors, before it eventually destabilizes into the TT regime at long times (Fig. 6.7-a). The smaller the tension, the longer it takes for this destabilization to occur. We evaluate the metastability of the RT regime, by simulating 80 independent runs with random initial condition, for each value of the tension. At small tension, the probability of ending up in a RT regime at $t = 10000$, $\mathbb{P}_{RT}$, is close to one and slowly decreases with increasing tension. This is due to both the increasing size of the attraction basin of the TT regime and the decreasing lifetime of the metastable RT regime. For tensions $\alpha \geq 1.2$, $\mathbb{P}_{RT}$ vanishes abruptly: all initial conditions end up in the TT regime at long

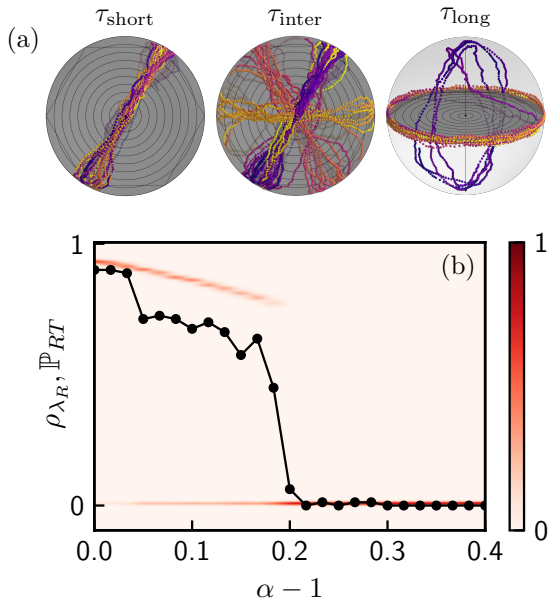


FIG. 6.7. **Active *Gerris*'s dynamics in the presence of noise** (a) Projection of the polarity field dynamics illustrating the effect of noise on the RT_1 regime, at short, intermediate, and long times (vertical axis: $\langle R|\hat{\boldsymbol{n}}\rangle$, equatorial plane: $\langle T_{x/y}|\hat{\boldsymbol{n}}\rangle$). (b) Density of condensation fraction on the rotation mode ρ_{λ_R} (color-coded as given by the color bar) and probability to end in a RT regime at long times $\mathbb{P}_{RT}$ (black markers) as a function of tension $\alpha - 1$.

time.

As a final remark, let us comment on the comparison between the experimental results (Fig. 6.1-d) and the numerical simulations, including geometrical nonlinearities and angular noise (Fig. 6.7-b), which are the most *realistic*. There is clearly no quantitative agreement, but note that this was not the point of the above analysis. We deciphered one by one the ingredients that are necessary to capture the experimental phenomenology in the correct range of parameter values: geometrical nonlinearities allow for a one-way switch between the RT and TT regimes as tension increases, and noise governs the metastability of the RT regimes at the transition.

6.4 Material-scale switch

Altogether the active *Gerris* establishes the proof of concept for the experimental control of CA using mechanical tension. Its structure, which results from several experimental compromises, is however admittedly rather artificial, raising the question of the possible generalization of the above results to a genuine active material.

6.4.1 Homogeneously dilating structures

We theoretically show below that the tension-controlled switch is generically expected even in the harmonic approximation. Consider an arbitrary lattice undergoing homogeneous dilation of factor $\alpha \in [1, +\infty[$, the dynamical matrix of which reads (see Appendix G):

$$\mathbb{M}(\alpha) = \frac{1}{\alpha}\mathbb{M}_0 + \left(1 - \frac{1}{\alpha}\right)\mathbb{M}_1. \tag{6.5}$$

$\mathbb{M}_0$ is the dynamical matrix of the structure at zero tension, and $\mathbb{M}_1$ reads:

$$\mathbb{M}_1 = \begin{pmatrix} \mathbb{M}_1^{xx} & 0 \\ 0 & \mathbb{M}_1^{yy} \end{pmatrix}, \tag{6.6}$$

where $\mathbb{M}_1^{xx} = \mathbb{M}_1^{yy}$ is the Laplacian matrix of the structure network $\mathbb{M}_{1,ii}^{\alpha\alpha} = Z(i)$, $\mathbb{M}_{1,ij}^{\alpha\alpha} = -1$ if i and j are neighbors and zero otherwise. Since $\mathbb{M}_1$ decouples the x and y directions, its eigenvectors φ_n come in degenerated pairs with identical form, respectively polarized along x and y. In particular, as a result of a discrete nodal domain theorem [182–184] (see Appendix G), the lowest energy modes of $\mathbb{M}_1$ have the geometry of translational modes. Increasing the mechanical tension, the spectral properties of $\mathbb{M}_1$ progressively dictate that of the elastic structure, thereby favoring the emergence of two degenerated low energy modes, with geometries akin to translation: extended and locally-orthogonal. These are the perfect conditions for selecting the SCO regime at large tension (see chapter 5). This is why any elastic structure, which, in the absence of tension, exhibits some form of CA, different from the condensation on modes akin to translation, will eventually switch to the SCO regime, when mechanical tension is large enough.

This argument/recipe is strictly valid in the case of a homogeneous dilation, but one expects it to persist as a design principle for CA switch in elastic structures which do not dilate homogeneously, as long as tension is relatively evenly distributed. In the case of the Gerris, the inner ring is rigid, thus the dilation is not homogeneous, and Eq. 6.5 does not apply. Would it hold, the two branches of eigenfrequencies, corresponding to the TT and R modes, meet at infinite tension, and one would expect a transition at infinite α. We however saw that geometrical nonlinearities enforce it at tensions, which can be reached experimentally.

6.4.2 Large honeycomb

We confirm this design principle by considering a large regular honeycomb lattice, composed of $N = 180$ nodes, pinned at its hexagonal edges (Fig. 6.8-a). Under small tension, this lattice has a rotation mode $|R\rangle$ that lies at the bottom of its vibrational spectrum (Fig. 6.8-b). As tension increases, the energies of both the degenerated translational modes and the rotation mode increase, but at different paces, and eventually cross each other for $\alpha = \alpha^* \simeq 1.1$, as expected from Eq. (6.5). When simulating the dynamics of the active honeycomb, *within the harmonic approximation*, with $\pi = 0.055$, we confirm the presence of a tension-controlled switch between two linearly stable actuation regimes, SCO and GAR (Fig. 6.8-c). Note that the condensation of the dynamics taking place on modes that are not fully delocalized, the condensation fraction must be strictly smaller than one: $\lambda_k \leq Q_k < 1$, with $Q_k = \left(\sum_i |\boldsymbol{\varphi}_k^i|\right)^2 / N$ [158]. Therefore, we normalize the condensation fraction by the participation ratio of the modes: $\tilde{\lambda}_k = \lambda_k / Q_k$ (see chapter 3).

The SCO is a *TT* regime, very similar to the one discussed above (Fig. 6.8-d), except for additional fluctuations taking place outside of the equatorial plane. Indeed, the translational modes being heterogeneous, there is room for a spatial coexistence of a collectively actuated region at the center of the system with a frozen/disordered one close to the boundary (see chapter 5), which tends to thermalize the polarity dynamics. The GAR regimes, with strictly positive $\tilde{\lambda}_R$, exhibit richer dynamics than in the case of the *Gerris*: for small enough tension, the GAR regimes are aperiodic, because of the

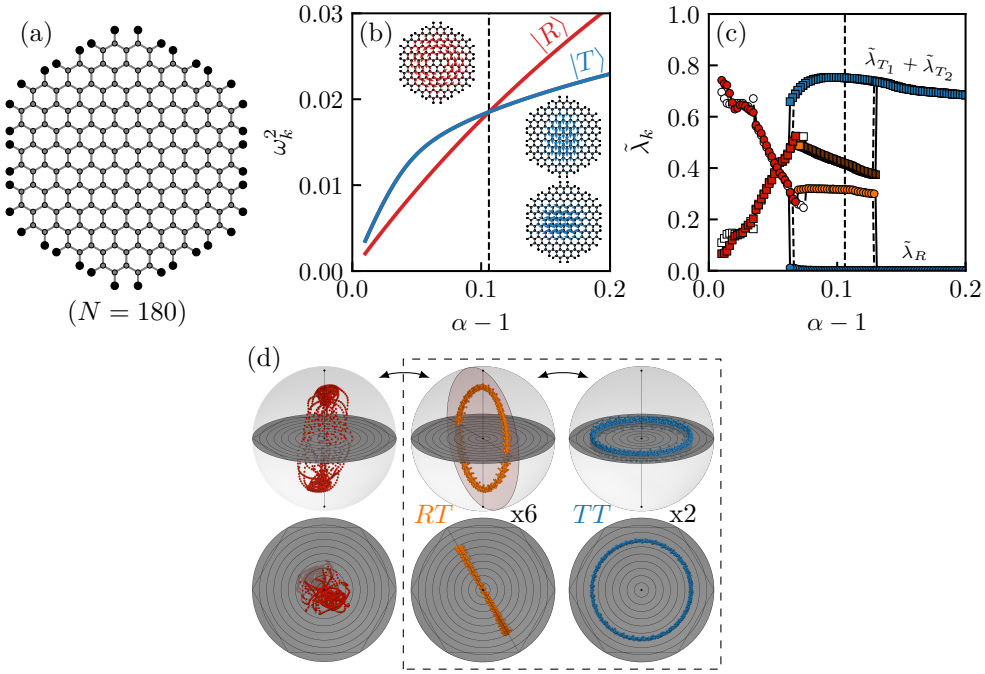


FIG. 6.8. **Active honeycomb dynamics as a function of lattice tension.** (a) Elastic architecture cartoon ($N = 180$). (b) Normal modes spectrum as a function of lattice tension $\alpha - 1$. The red (resp. blue) solid line corresponds to the rotation mode (resp. degenerated translational modes), shown in inset; see Appendix A for the full spectrum. The dashed black vertical line highlights the crossing of energies. (c) Normalized condensation fractions on the rotation mode $\tilde{\lambda}_R$ (circles) and on the translational modes $\tilde{\lambda}_{T_1} + \tilde{\lambda}_{T_2}$ (squares) as a function of lattice tension $\alpha - 1$; for $\pi = 0.055$. Colored markers and solid lines (resp. empty markers and dashed lines) stand for simulations performed within the harmonic approximation (resp. including geometrical nonlinearities). The dark red (resp. orange) branch represents the aperiodic (resp. periodic RT) GAR regime, while the blue branches represent the TT regime. (d) Projection of the polarity field dynamics in the steady states for the aperiodic GAR, RT and TT regimes, from left to right (vertical axis: $\langle R|\hat{\boldsymbol{n}}\rangle$, equatorial plane: $\langle T_{x/y}|\hat{\boldsymbol{n}}\rangle$). The dashed black square highlights the switch of interest.

many low energy modes, which couple to the rotational and translational modes (see Appendix A). At large enough tension, one recovers the RT_1 regime, condensed on a RT plane in mode space (Fig. 6.8-d), modulo some fluctuations of the same origin than in the TT regime. Annealing from small to large tension, the RT regime switches to the TT one for a tension $\alpha > \alpha^*$ (Fig. 6.8-c). Additionally, performing the backward annealing, the TT branch becomes unstable for a tension $\alpha < \alpha^*$. In the absence of geometrical nonlinearities, the observed hysteretic switch must be attributed to the non-trivial selectivity of CA: CA preferably takes place on low-energy modes, but also favors pairs of modes that are maximally extended and locally orthogonal. As demonstrated by the open symbols and dashed lines in Fig. 6.8-c, geometrical nonlinearities do not alter the above picture.

6.5 Conclusion

Altogether, having unveiled a new CA regime arising in active solids with a low-energy rotation mode (GAR), we demonstrate that mechanical tension is a robust control parameter to switch to a regime dominated by a pair of degenerated translational modes

(SCO). This phenomenon is inherited from passive mechanics: for structures dilating homogeneously, at large tension, the normal modes spectrum favors the SCO regime because it generically contains a pair of degenerated, extended, and locally orthogonal normal modes. Therefore, regardless of the low-tension CA regime, which can be designed by playing with the normal mode spectrum, an abrupt switch can be engineered by applying mechanical tension to the structure. It opens the path toward designing more complex behavior switches, using different sets of mechanical efforts or different low-tension CA regimes. Moreover, we find that the properties and stability of GAR and SCO regimes depend on the elasto-active coupling π. Exploring the physics of the above systems in the entire parameter space (α, π) could give rise to more subtle selection mechanisms.

On the meta-material science side, this work proposes a new way to construct multifunctional active mechanical metamaterials, with bona fide autonomy and the possibility to switch between drastically different actuation regimes, robust to dissipation and attenuation. In the realm of bio-physics, it sheds light on the emergence of SCO and GAR regimes, and suggests the possibility of such switching behavior, when contractility or confinement generates internal stresses. The recent observations of GAR and SCO regimes in bacterial bio-films and epithelial monolayers, and of a switch between the two as activity increases, offer a wide range of perspectives and applications for this work.

Chapter 7

Polarization by an external field

7.1 Introduction

The active units composing biological active solids have the ability to respond to various types of environmental cues and can polarize towards or away from these signals, e.g. by *chemotaxis*[1] or *galvanotaxis*[2]. Yet, the effect of an external field on the collective dynamics of active solids remains, until today, largely unexplored. In this chapter, we explore the effect of a polarizing field on the dynamics of our model active solids. Fine-tuning the tilt of the experimental setup with respect to the horizontal plane, we first demonstrate that a frozen single active unit polarizes opposite to the gravity force. We use this gravity-induced polarization mechanism as a tool to apply homogeneous polarizing fields to active solids in different settings.

We start exploring how polarization affects Synchronized Chiral Oscillations (SCO) in a triangular lattice pinned at the edges. As polarization increases, the SCO regime is replaced by synchronized transverse oscillations of all the active units, the so-called Synchronized Windscreen Wiper (SWW) regime. For large enough polarization, however, the amplitude of the transverse oscillations vanishes, and the system ends up frozen, polarized opposite to gravity, in the so-called *Frozen-Polarized* (FP) regime. Then, we focus on square lattices pinned at opposite ends. Without gravity, as activity increases in such systems, CA along the lowest-energy mode emerges from the balance between activity, elasticity, and angular noise. This third CA regime, different from SCO and GAR, is denoted Noise-Induced Collective Actuation (NICA). Similarly to the observations done with SCO, we find that increasing polarization transforms NICA into SWW, and eventually leads to a FP regime. Crucially, polarization decreases the activity threshold for CA, leading to a so-called Polarization-Induced Reentrance (PIR).

These observations are rationalized by performing the complete analysis of the single particle with a polarizing field, which sheds light on the physics of the triangular lattice pinned at the edges. As activity increases, we find that the FP regime destabilizes through a Hopf bifurcation. Interestingly, this system exhibits an exceptional point at zero-polarization and critical activity, close to which all the regimes can be found explicitly. Eventually, using the coarse-grained model derived in chapter 5, we explain the origin of NICA, and show that PIR is a purely collective effect, inherited from the differential stability of the *Frozen-Disordered* (FD) and *Frozen-Polarized* (FP) phases.

[1] Migration towards diffusible chemical cues.
[2] Migration towards or away from electric fields.

7.2 Gravity-induced polarization

In this chapter, we propose to use gravity to polarize active solids. The gravity force is varied by tilting the experimental setup with respect to the horizontal plane, as illustrated in Fig. 2.3-a. The originally flat PMMA substrate is replaced with two plywood plates[3] connected by hinges on one side to allow for a tilt α between them[4]. The tilt is held fixed using two aluminum feet pinned on the other side of the plates, and is varied from 0° to 21.4°, by steps of roughly 1.0°[5]. The PMMA plate is then placed back on top, and the active solids experiments are performed the same way as in the rest of this manuscript. As the camera attached to the ceiling is held vertically, movies acquired with a finite slope must be processed to correct for perspective distortions. This is done using planar homography (see Appendix K and [185]), which allows for changing the perspective of a tilted experimental movie and sending it back to the perspective of a flat experimental movie, given the position of at least four reference points on the pictures.

7.2.1 Experimental observations

Let us consider a frozen single active unit as a benchmark to characterize the effect of gravity. We employ the elastic structure used in chapter 2 to measure the self-alignment properties of the *hexbugs* as a stiff elastic structure. It consists of a stiff square frame, in the middle of which lies a square active elastic building block connected to the frame with four *stiff* springs (Fig. 7.1-a). The frame is held fixed using double-sided scotch, and the spring stiffness is such that the *hexbug* is completely *frozen* ($\pi \ll \omega_0^2$, where $\omega_0^2 = 2$ is the energy of the pair of degenerated modes of this structure). The angle between the particle's orientation and the gravity direction is denoted θ.

As expected, without gravity, the particle is in the *Frozen-Disordered* (FD) regime, and the orientation θ is diffusing (Fig. 7.1-c, dark red line). This is confirmed by computing the Mean Squared angular Displacement $\langle(\theta(t+\tau) - \theta(t))^2\rangle_t$ (MSD), which shows diffusive behavior at short time (Fig. 7.1-d, $\tau < 1$ s). At long time, we find a ballistic regime, because the *hexbug*'s bias ends up dominating over diffusion at long time. We also find that "switching on" gravity induces a polarization of the active unit's orientation against gravity (Fig. 7.1-c, light red line), which is centered on π rad modulo fluctuations originating from the angular noise. The system is *Frozen-Polarized* (FP). The long-time ballistic regime is replaced by caging, and angular displacements saturate (Fig. 7.1-d). The angular confinement is as strong and arises at as short lag times τ as gravity increases. Note that the experiments were performed several times with differently biased *hexbugs*, and Fig. 7.1 illustrates the results for the less biased of them. We find that additional bias induces an average misalignment, and, when strong enough, a long-time ballistic motion, while in the same conditions, the less biased *hexbug* remains caged (Fig. 7.1-d). This will drastically affect the measurements, so we restrict ourselves to the less biased *hexbug*. For this one, all experiments performed at finite gravity exhibit long-time caging.

To better characterize the polarization mechanism, we measure the experimental orientation distributions for four minutes acquisitions with tilts ranging from 0° to 10.7° (Fig. 7.1-e). As one increases gravity, the orientation distribution is more and more peaked

[3] Thickness 5 cm to prevent any bending.

[4] The two hinges are visible in Fig. 2.3-a, and are bolted on both sides.

[5] $\alpha \in [0°, 1.1°, 2.2°, 3.2°, 4.3°, 5.3°, 6.4°, 7.5°, 8.5°, 9.5°, 10.7°, 12.8°, 15.0°, 17.1°, 19.3°, 21.4°]$

around $\theta = \pi$ rad, illustrating the average polarization against gravity. However, as gravity vanishes, we find an orientation distribution that is not statistically compatible with the fully homogeneous one. This apparently paradoxical situation is simply due to the presence of a finite initial tilt of our frame, that is of the order of 1°[6]: while we impose no slope, the setup's initial tilt generates a preferred orientation against apparent gravity, which is small, but finite.

The localization of these distributions (Fig. 7.1-e) is measured using the magnetization $m\,[P(\theta)]$. It is a function of the full orientation distribution and is defined as:

$$m\,[P(\theta)] = \left| \int_0^{2\pi} e^{i\theta} P(\theta) d\theta \right|. \tag{7.1}$$

For an utterly homogeneous orientation distribution, such that $P(\theta) = 1/2\pi$, we find $m = 0$; while for a completely localized distribution, say at $\theta = \theta_0$ and such that $P(\theta) = \delta(\theta - \theta_0)$, we find $m = 1$. The magnetization can also be seen as the orientational order parameter computed over time. Fig. 7.1-f illustrates the magnetization, measured from the distributions of Fig. 7.1-e, as a function of the tilt α. We find that it increases

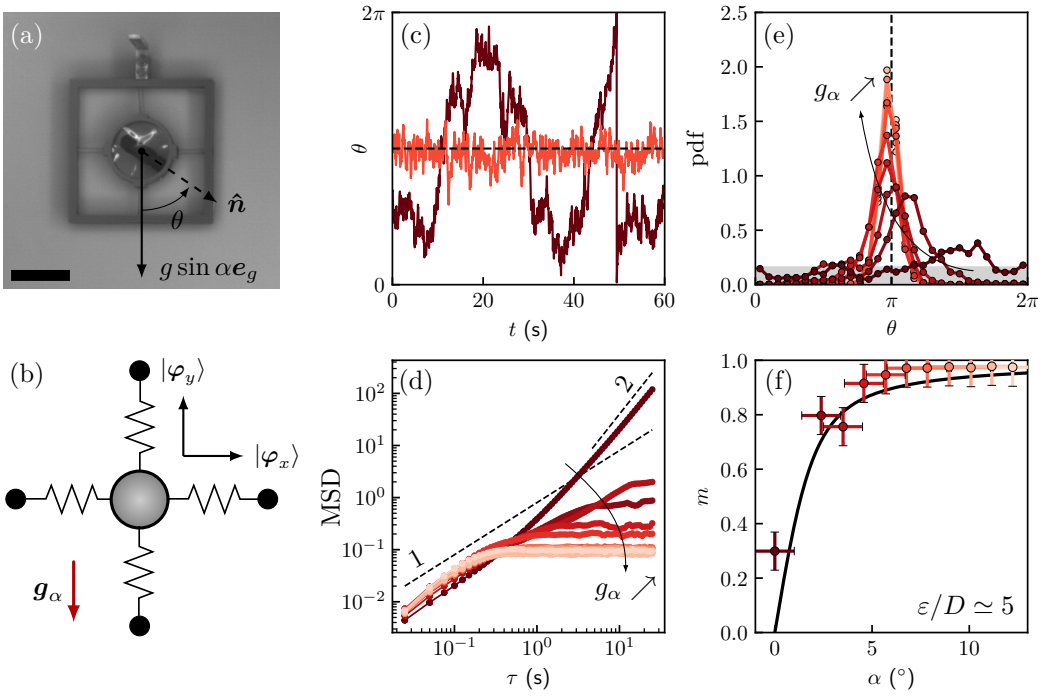


FIG. 7.1. **A frozen single particle polarizes against gravity.** (a) Experimental setup picture. The orientation of the polarity vector with respect to gravity is denoted θ; scale bar: 10 cm. (b) Model elastic structure's cartoon and normal mode spectrum. (c) Active unit's orientation θ as a function of time t for small gravity (dark red), i.e. $\alpha = 0^{\circ}$ (regime FD), and large gravity (light red), i.e. $\alpha = 5.3^{\circ}$ (regime FP). (d) Mean squared angular displacement $\langle(\theta(t+\tau) - \theta(t))^2\rangle_t$ as a function of lag time τ for different gravity. Curves are color-coded from dark to light red as gravity increases. The two dashed black lines represent the slopes 1 and 2. (e) Distributions of orientation θ for different tilts α. Curves are color-coded from dark to light red as gravity increases. The gray area corresponds to $1/2\pi$. (f) Magnetization m as a function of the tilt α; as obtained from experiments (markers, color-coded as in (d) and (e)), and from Eq. (7.10) assuming zero initial tilt and $\varepsilon/D = 5.0$ (solid black line).

[6]Without imposing any tilt, a smartphone inclinometer indicates an angle of 0.5° in the direction of gravity, and 1.3° orthogonally to it.

from 0.3 to roughly 1 within the range 0 to 5°, and saturates to a value close to 1 for larger tilts. Again, the value 0.3 obtained from $\alpha = 0°$ translates the presence of a small initial tilt of our frame.

7.2.2 Discussion

As displacements induced by the polar forces and gravity are very small in this system, we can safely use the harmonic approximation. We start with the equations of motion for a single active unit in a harmonic trap (see chapter 5):

$$\dot{\boldsymbol{u}} = \pi\hat{\boldsymbol{n}} - \omega_0^2\boldsymbol{u}, \tag{7.2a}$$

$$\dot{\boldsymbol{n}} = (\hat{\boldsymbol{n}} \times \dot{\boldsymbol{u}}) \times \hat{\boldsymbol{n}} + \sqrt{2D}\xi\hat{\boldsymbol{n}}^{\perp}, \tag{7.2b}$$

where $\pi = l_e/l_a = F_0/kl_a$ is the elasto-active coupling, $\boldsymbol{u}$ (resp. $\hat{\boldsymbol{n}}$) is the displacement vector with respect to the reference configuration (resp. polarity vector), ω_0^2 is the squared eigenfrequency associated with the two degenerated normal modes of the single particle, $D = \alpha\gamma/k\tau^2 = D_\theta l_e/v_0$ is the noise amplitude and ξ is a Gaussian random variable with zero mean and correlations $\langle\xi(t)\xi(t')\rangle = \delta(t-t')$.

Gravity relevance within the harmonic approximation

In this section, we show that (i) gravity induces a force and a torque, the latter reorienting the active unit against gravity; and that (ii) for small enough gravity, the gravity term in the force balance does not affect the dynamics of active solids and can be recasted into a change of reference configuration.

Gravity plays two roles in this system. The first one is an additional constant force in the position dynamics, Eq. (7.2a). The second one is an additional torque in Eq. (7.2b), reorientating the *hexbugs* in the direction opposite to gravity. The mechanism is similar to the relaxation of a non-linear pendulum in a gravity field (Fig. 7.2-a). The angle θ of a pendulum with the vertical direction obeys the following relaxation dynamics:

$$\tau\dot{\theta} = -\sin(\theta), \tag{7.3}$$

where we have considered the overdamped limit, and where τ is the relaxation time. This relaxation mechanism of the pendulum towards the vertical direction comes from the mass distribution of the body the pendulum is made of (Fig. 7.2-b). Similarly, an *hexbug* in its annulus can be seen as a pendulum in a gravity field (Fig. 7.2-c). Because of its asymmetry, the mass of the *hexbug* is not distributed evenly along the body's axis. The barycenter being close to the tail, a torque is generated when the polarity is not aligned with the gravity direction, reorientating the active unit. The new equations of motions, considering these two effects, yield:

$$\dot{\boldsymbol{u}} = \pi\hat{\boldsymbol{n}} - \omega_0^2\boldsymbol{u} + \tilde{g}_\alpha\hat{\boldsymbol{e}}_g, \tag{7.4a}$$

$$\dot{\boldsymbol{n}} = (\hat{\boldsymbol{n}} \times \dot{\boldsymbol{u}}) \times \hat{\boldsymbol{n}} - \varepsilon(\hat{\boldsymbol{n}} \times \boldsymbol{g}_\alpha) \times \hat{\boldsymbol{n}} + \sqrt{2D}\xi\hat{\boldsymbol{n}}^{\perp}, \tag{7.4b}$$

where $\tilde{g}_\alpha = mg_\alpha/kl_a$ is the dimensionless gravity force in the scheme chosen for Eqs. (7.2), $g_\alpha = g\sin\alpha$, and ε compares the relative strength of the self-alignment and polarization terms. This quantity can be seen as the inverse relaxation time toward gravity.

Changing variable to $\tilde{\boldsymbol{u}} = \boldsymbol{u} - \tilde{g}_\alpha\boldsymbol{e}_g/\omega_0^2$ in Eq. (7.4a) allows to find back Eqs. (7.2), the single particle's position dynamics without gravity, while Eq. (7.4b) remains unchanged.

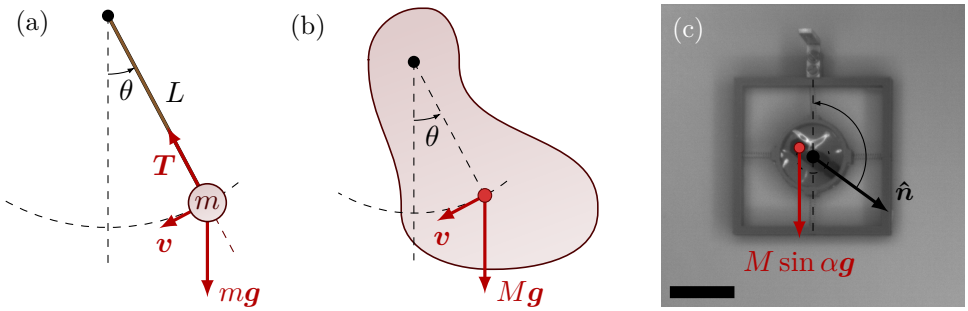


FIG. 7.2. **Gravity-induced polarization mechanism.** (a-b) Relaxation of a non-linear pendulum toward gravity, in the case of an idealized (a) and of a physical (b) pendulum. The black markers (resp. red marker) represent the pinning points (resp. the center of mass) (c) Polarization of a *hexbug* opposite to gravity. It originates from the *hexbug*'s mass asymmetry (the center of mass lies close to the particle's tail), which induces a torque reorienting the active unit in the direction opposite to gravity; scale bars: 10 cm.

Therefore, within the harmonic approximation, gravity in the force balance boils down to a change of reference configuration. However, and quite importantly, the new reference configuration[7] is different from the zero-gravity one, affecting the vibrational properties of the underlying elastic structure. This effect is characterized by the parameter mg_α/kl_0: if the typical deformations induced by gravity mg_α/k are small compared to the rest length l_0, then the reference configuration can be considered mostly unchanged. Otherwise, full elasticity should be considered to properly take into account gravity and determine the new reference configuration, around which the harmonic approximation can still be used to model the dynamics, given the new vibrational properties.

Altogether, within the harmonic approximation, and considering small mg_α/k such that the harmonic well remains isotropic, the equations of motion read:

$$\dot{\boldsymbol{u}} = \pi\hat{\boldsymbol{n}} - \omega_0^2\boldsymbol{u}, \tag{7.5a}$$

$$\dot{\boldsymbol{n}} = (\hat{\boldsymbol{n}} \times \dot{\boldsymbol{u}}) \times \hat{\boldsymbol{n}} - \varepsilon(\hat{\boldsymbol{n}} \times \boldsymbol{g}_\alpha) \times \hat{\boldsymbol{n}} + \sqrt{2D}\xi\hat{\boldsymbol{n}}^\perp, \tag{7.5b}$$

where we have omitted the tilda on the displacement vector $\boldsymbol{u}$ (denoting the change of reference configuration). The second term on the right-hand side of Eq. (7.5b) is a polarization term, originating from gravity. It is equivalent to a change of Galilean frame of reference traveling at velocity $\boldsymbol{V} = -\varepsilon\boldsymbol{g}_\alpha$ with respect to the reference frame of the lab[8], or to an interaction between the polarity vectors and a homogeneous magnetic field.

Strictly frozen active unit in a gravity field

Let us focus on the frozen single-particle experiments described above. Consistently with observations in real space, we consider that activity is very small as compared to the elastic forces $\pi \ll \omega_0^2$, which implies that we can safely neglect the displacement dynamics ($\dot{\boldsymbol{u}} \simeq 0$) and focus on Eq. (7.5b). Neglecting the contribution from the self-alignment term (first term on the right-hand side), we obtain the following simple Langevin equation:

$$\dot{\theta} = g_\alpha\varepsilon\sin\theta + \sqrt{2D}\xi. \tag{7.6}$$

[7] Obtained from spring-like elastic forces and gravity, in the absence of active forces.

[8] A tilted active solid experiment is equivalent to the same experiment without tilt, performed on a treadmill moving at velocity $\boldsymbol{V} = -\varepsilon\boldsymbol{g}_\alpha$

The Fokker-Planck equation associated with Eq. (7.6) reads:

$$\frac{\partial P}{\partial t}(\theta,t) = \frac{\partial}{\partial \theta}\Big(- g_\alpha \varepsilon \sin\theta P(\theta,t)\Big) + D\frac{\partial^2 P}{\partial \theta^2}(\theta,t), \tag{7.7}$$

where $P(\theta,t)$ is the probability distribution of the angle θ at time t. The stationary probability distribution $P_{ss}(\theta)$ satisfies:

$$P_{ss}(\theta) = \mathcal{N}\exp\left(-\frac{g_\alpha \varepsilon}{D}\cos(\theta)\right), \tag{7.8}$$

where $\mathcal{N}$ is a pre-factor. As expected, the distribution $P_{ss}(\theta)$ is centered on $\theta = \pi$ rad, and is as peaked as $g_\alpha\varepsilon/D$ is large. Imposing normalization of the probability density, we find:

$$\mathcal{N} = I_0(g_\alpha\varepsilon/D), \tag{7.9}$$

where $I_n(x)$ are the modified Bessel functions of first kind. With this explicit expression of the probability density, we find the magnetization for a given ratio $g_\alpha\varepsilon/D$:

$$m(g\varepsilon/D) = \frac{|I_1(g_\alpha\varepsilon/D) - I_1(-g_\alpha\varepsilon/D)|}{I_0(g_\alpha\varepsilon/D) + I_0(-g_\alpha\varepsilon/D)}. \tag{7.10}$$

Interestingly, this is exactly the expression for the magnetization of an XY spin submitted to an external field and thermal fluctuations, which respectively play the role of the polarization term and angular noise. The prediction from Eq. (7.10) correctly describes the experimental data (Fig. 7.1-f), and provides an approximate value for the ratio $\varepsilon/D \simeq 5.0$.

Altogether, gravity boils down to a polarization term in the polarity dynamics of *hexbugs*, which is equivalent to a change of Galilean frame of reference. Increasing the amplitude of the polarizing field, we find that a single active unit in the FD regime continuously transitions to a FP regime, polarized opposite to gravity. Below, we use gravity-induced polarization as a tool to study the dynamics of active solids in the presence of a polarizing field.

7.3 N particle systems with a polarizing field

7.3.1 Triangular lattices pinned at the edges

We start characterizing the effect of a polarizing field on a triangular lattice pinned at the edges. Without gravity, we have seen in chapter 5 that this system is FD for small enough activity, and performs *Synchronized Chiral Oscillations* (SCO) for large enough activity, with a transition between the two that is essentially discontinuous.

We start exploring the influence of polarization on the SCO regime. We progressively increase the polarizing field, i.e. gravity, in the direction represented in Figs 7.3-b and c, denoted $\hat{\boldsymbol{e}}_g$. To characterize the tendency of the active units to point along or perpendicularly to gravity at the collective level, we define the longitudinal (resp. transverse) polarizations:

$$M_{\parallel/\perp}(t) = \frac{1}{N}\sum_i \hat{\boldsymbol{n}}_i(t)\cdot\left(-\boldsymbol{e}_g/\boldsymbol{e}_g^\perp\right), \tag{7.11}$$

where the vector $\boldsymbol{e}_g^\perp$ is the unit vector orthogonal to $\boldsymbol{e}_g$. These quantities are bounded

between -1 and 1 and say how strongly polarized the active units are, along or orthogonally to the direction opposite to gravity.

For small enough polarizing fields, we find that SCO is preserved (Fig. 7.3-a). SCO is characterized by a spontaneous polarization in a direction that rotates with time. Therefore, the transverse and longitudinal polarizations oscillate with a phase shift of $\pi/2$ or $3\pi/2$ depending on the spontaneously broken chirality (Fig. 7.3-d). As the amplitude of the polarizing field increases, we find that SCO transforms into a new dynamical regime: the system polarizes longitudinally, and performs synchronized oscillations in the transverse direction (Fig. 7.3-b). In this regime, the so-called Synchronized Windscreen Wiper (SWW), the transverse polarization oscillates with a smaller frequency than SCO, and the longitudinal polarization is large and never changes sign, while being modulated at twice the frequency of the transverse oscillations (Fig. 7.3-e). Finally, for large enough polarizing fields, the amplitude of the transverse oscillations vanishes, and the system freezes with a longitudinal polarization close to one (Figs. 7.3-c and f). This is the so-called *Frozen-Polarized* (FP) regime. Altogether, we find that the presence of a polarizing field transforms SCO into SWW, and large enough polarization stabilizes the FP regime in the direction opposite to gravity.

Motivated by the above preliminary observations, we now study square lattices pinned at opposite ends. Such systems have the advantage of exhibiting pairs of locally-orthogonal normal modes, respectively the transverse and longitudinal modes (see chap-

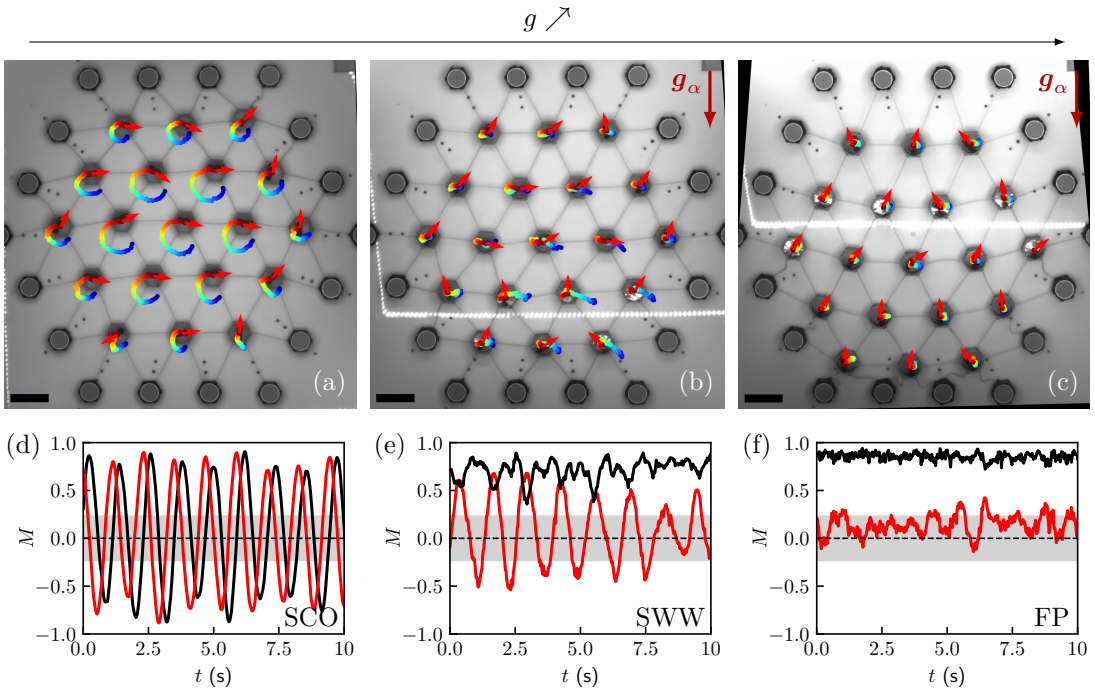


FIG. 7.3. **Synchronized Chiral Oscillations (SCO) with a polarizing field.** Triangular lattice pinned at the edges ($N = 19$, $\alpha = 1.27$) for different gravity. As the amplitude of the polarizing field increases, SCO (a) are replaced by SWW (b), and finally by a FP regime (c). (a-c) Experimental snapshots. Red arrows: polarities $\hat{\mathbf{n}}_i$; trajectories color-coded from blue to red with increasing time; scale bars: 10 cm. (d-f) Transverse $M_\perp$ (red) and longitudinal $M_\parallel$ (black) polarizations as a function of time, in the same conditions as (a-c). The gray areas illustrate the range inside which is expected to lie the polarizations for purely random spins, that is $\left[-1/\sqrt{N}, 1/\sqrt{N}\right]$. (a/d) $\alpha = 0°$, (b/e) $\alpha = 10.7°$, (c/f) $\alpha = 21.4°$.

ter 5). Therefore, gravity can be assigned to be strictly perpendicular to the activated modes of those systems, which could arguably simplify the physics.

7.3.2 Square lattices pinned at opposite ends

We consider square lattices of *stiff* springs with rectangular shapes, composed of L (resp. W) active units along the long (resp. short) direction of the structure (Fig. 7.4). The pinning condition imposes that the first and last columns of the square lattice are fixed, so that the extension of the springs in the structure along the long direction is $(l_{eq}-l_0)/l_0 \simeq 0.28$[9] in the stressed reference configuration. Once doped with active units, we call such structures active *ladders*. Their normal mode spectrum is very gapped: the first transverse mode $|\boldsymbol{\varphi}_{\perp,1}\rangle$ (Fig. 7.4, bottom) has a low energy $\omega^2_{\perp,1}$, comparable with π, and all the other modes have way larger energies and cannot be activated.

Eventually, in order to vary both the amplitude of the polarizing field, and the ratio between the elasto-active coupling π and the energy of the first transverse mode $\omega^2_{\perp,1}$, we keep the size L and springs extension constants and perform the experiments with W going from 2 to 4. The wider the structure, the stiffer the first transverse mode[10], and thus, the lower the ratio $\pi/\omega^2_{\perp,1}$.

Experimental observations

The polarizing field is applied along the longitudinal direction, i.e. $\boldsymbol{e}_g = -\boldsymbol{e}_\parallel$, so that the longitudinal (resp. transverse) polarization defined in Eq. (7.11) corresponds to the polarization along the long direction, i.e. $\boldsymbol{e}_\parallel$ (resp. short direction, i.e. $\boldsymbol{e}_\perp$) of the ladder (Fig. 7.4). Let us start by describing the observations at zero gravity.

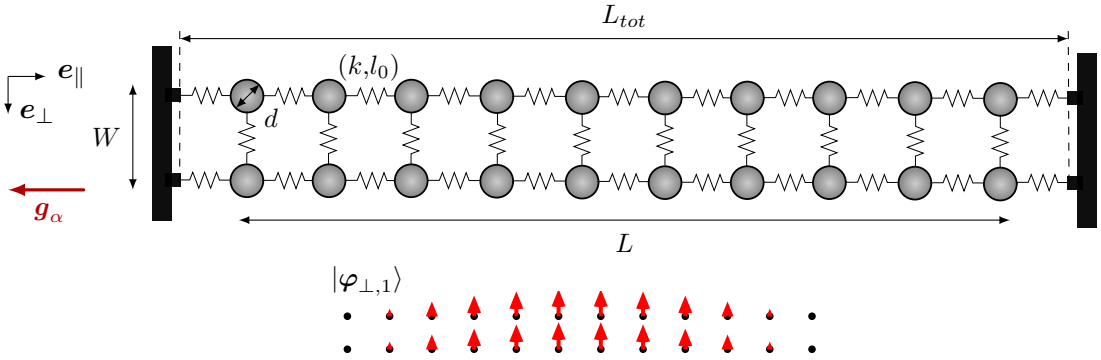


FIG. 7.4. **Active *ladder* architecture.** Experimentally, the length $L = 12$, and $W \in [2, 3, 4]$. The unit vector $\boldsymbol{e}_\perp$ (resp. $\boldsymbol{e}_\parallel$) denotes the direction transverse (resp. longitudinal) to the long direction of the *ladder*. The gravity force is applied along $-\hat{\boldsymbol{e}}_\parallel$. (bottom) Representation of the lowest-energy, first transverse mode $|\boldsymbol{\varphi}_{\perp,1}\rangle$.

[9] The pinning condition imposes $L_{tot} \simeq 109.8$ cm; while, in the absence of pre-stress $L_{tot,0} = Ld + (L+1)l_0 \simeq 99.0$ cm. Therefore, $(L_{tot} - L_{tot,0})/L_{tot,0} \simeq 0.11$, and because the annuli are inextensible:

$$\frac{l_{eq} - l_0}{l_0} = \frac{L_{tot} - L_{tot,0}}{L_{tot,0}} \left(1 + \frac{L}{L+1}\frac{d}{l_0}\right),$$

where l_{eq} is the length of the longitudinal springs is the stressed reference configuration. The other quantities are defined in Fig. 7.4.

[10] Note that this stiffening is not present if one considers simply central-forces springs on an idealized springs network, but is related to the finite bending and shear moduli of the real springs used, and to the finite size of the annuli.

NICA. At zero gravity, we find that large enough activity triggers the emergence of a new form of CA along the first transverse mode, which we shall call *Noise-Induced CA* (NICA), as we will see that it only takes place in the presence of angular noise.

On the one hand, for stiff enough transverse modes (large enough W), the system is *Frozen-Disordered* (FD): both the transverse and the longitudinal polarizations are small (Fig. 7.5-f), and so are displacements (Fig. 7.5-c). On the other hand, for soft enough structures ($\pi/\omega_{\perp,1}^2$ large enough), the system oscillates spontaneously along the transverse direction (Figs. 7.5-a and d). The longitudinal polarization remains relatively small, and lies within the range expected for random independent spins (Figs. 7.5-d and e), confirming that no longitudinal modes are spontaneously activated. We also find that the period is not completely well-defined.

This CA regime is very different from SCO and GAR in the sense that it corresponds to the activation of a single mode. We have shown in chapters 5 and 6 that CA requires at least two modes to develop spontaneously in the absence of noise. We thus conjecture that this new dynamical regime is noise-induced. We checked numerically that, indeed,

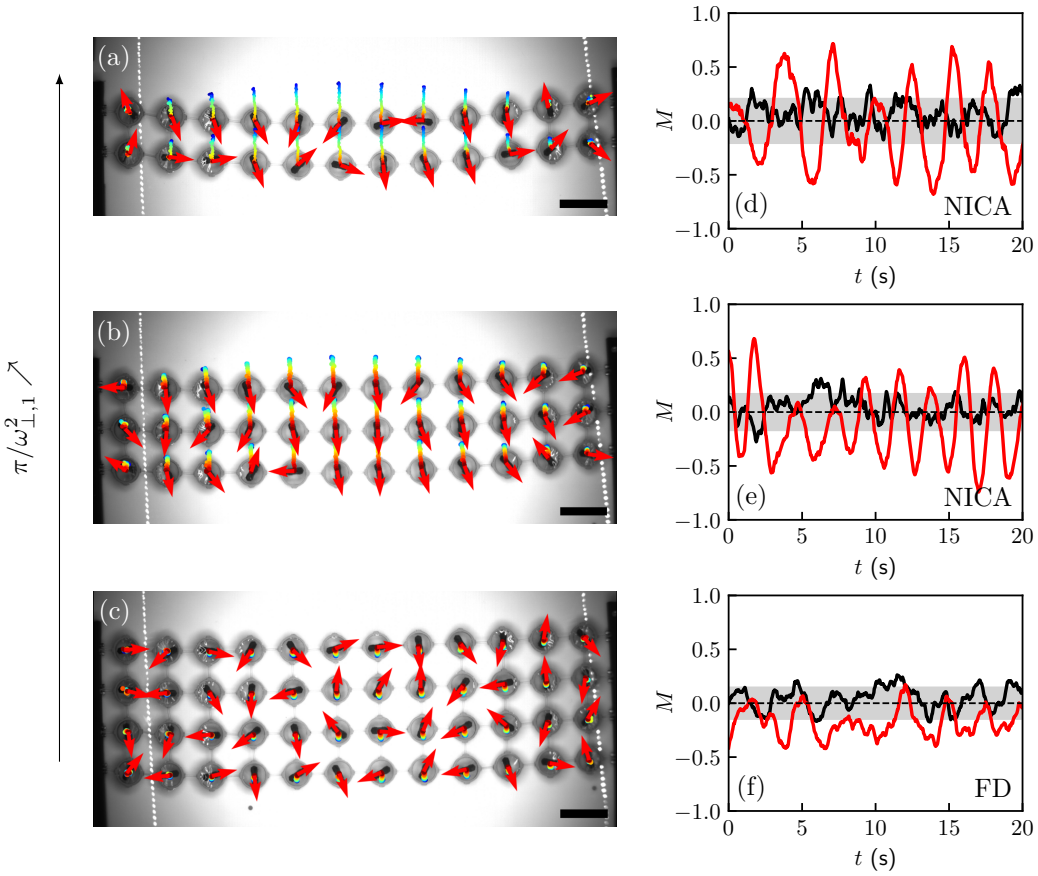


FIG. 7.5. **Noise-Induced Collective Actuation (NICA) in square lattices.** Active *ladders* at zero gravity for different widths. For soft enough *ladders* (small enough W), the system performs NICA. (a/d) $W = 2$ ($N = 24$), (b/e) $W = 3$ ($N = 36$), (c/f) $W = 4$ ($N = 48$). (a-c) Experimental snapshots of the active *ladder* dynamics. Red arrows: polarities $\hat{\boldsymbol{n}}_i$; trajectories color-coded from blue to red with increasing time; scale bars: 10 cm. (d-f) Transverse $M_\perp$ (red) and longitudinal $M_\parallel$ (black) polarizations as a function of time, in the same conditions as (a-c). The gray areas illustrate the range inside which is expected to lie the polarizations for purely random spins, that is $\left[-1/\sqrt{N}, 1/\sqrt{N}\right]$.

if the elasto-active coupling π is larger than $\omega_{\perp,1}^2$ but smaller than the energy of any of the longitudinal modes, CA emerges only in the presence of angular noise; otherwise, the system is frozen, polarized along the transverse direction. It is thus angular noise that is responsible for the transverse polarization reversal at each period: every spin reverses direction from $\hat{\boldsymbol{e}}_\perp$ to $-\hat{\boldsymbol{e}}_\perp$ independently, choosing randomly the direction $\hat{\boldsymbol{e}}_\parallel$ or $-\hat{\boldsymbol{e}}_\parallel$ at every turnaround. This is why the longitudinal polarization remains small during the dynamics. Finally, note that the oscillation frequency seems to increase as the transverse mode gets stiffer (Figs. 7.5-d and e).

NICA with a polarizing field. Now, we switch on the polarizing field in the longitudinal direction (Fig. 7.4). For soft enough structures ($\pi/\omega_{\perp,1}^2$ large enough), NICA emerges, as discussed above (Figs. 7.6-c and f). Increasing the amplitude of the polarizing field in the longitudinal direction, we find that NICA progressively transforms into SWW (Figs. 7.6-a,b,d, and e). Indeed, instead of alternatively activating the first transverse mode with stochastic turnarounds, the turnarounds are more and more biased in the longitudinal direction $\hat{\boldsymbol{e}}_\parallel$, which changes the nature of the oscillation. Progressively, the role of angular noise vanishes, and the turnarounds result from orientational elasticity, which induces a restoring torque in the longitudinal direction. In the SWW regime, the longitudinal polarization is large, oscillating at twice the frequency of the transverse one (Fig. 7.6-d). Increasing the amplitude of the polarizing field, we find that the longitudinal polarization increases monotonically (Figs. 7.7-b and c). However, we find very little effect of gravity on the transverse oscillations, whose amplitudes are mostly constants, roughly equal to $0.4\sqrt{2} \simeq 0.57$ (Figs. 7.7-a and b). Eventually, as observed for triangular lattices, for even larger polarization fields, the amplitude of the transverse oscillations vanishes, and the system is FP (Fig. 7.8-a and e).

Polarization-induced reentrance. We now apply a polarizing field to the FD regime, observed for small enough $\pi/\omega_{\perp,1}^2$ (with $W = 4$). First, we find that small polarizing fields transform the FD regime into a FP regime: the transverse polarization remains small, and the longitudinal polarization increases monotonically (Figs. 7.8-c and g). Crucially, we find that increasing the amplitude of the polarizing field at fixed activity can induce a transition from the FP to the SWW regime (Figs. 7.8-b and f). This is illustrated in Fig. 7.7-a, where we find that for great enough polarizing fields, the transverse polarization abruptly increases while the longitudinal polarization decreases, highlighting a change of regime. This phenomenon is denoted *Polarization-Induced Reentrance* (PIR) transition to SWW. Therefore, polarized frozen phases are more prone to destabilize transversally than disordered ones: the geometry of the frozen phase affects its stability.

7.3.3 Summary of observations

First, we have found a new CA regime, which corresponds to the spontaneous back-and-forth activation of the lowest energy mode. In this so-called NICA regime, angular noise plays a crucial role, allowing for polarization reversal at each period. Then, we applied homogeneous polarizing fields to triangular and square lattices. In agreement with the benchmark experiments of section 7.2, we find that the FD regime continuously transforms into FP regimes, polarized along the direction opposite to gravity. In contrast, the salient features of CA with a polarizing field are three-fold:

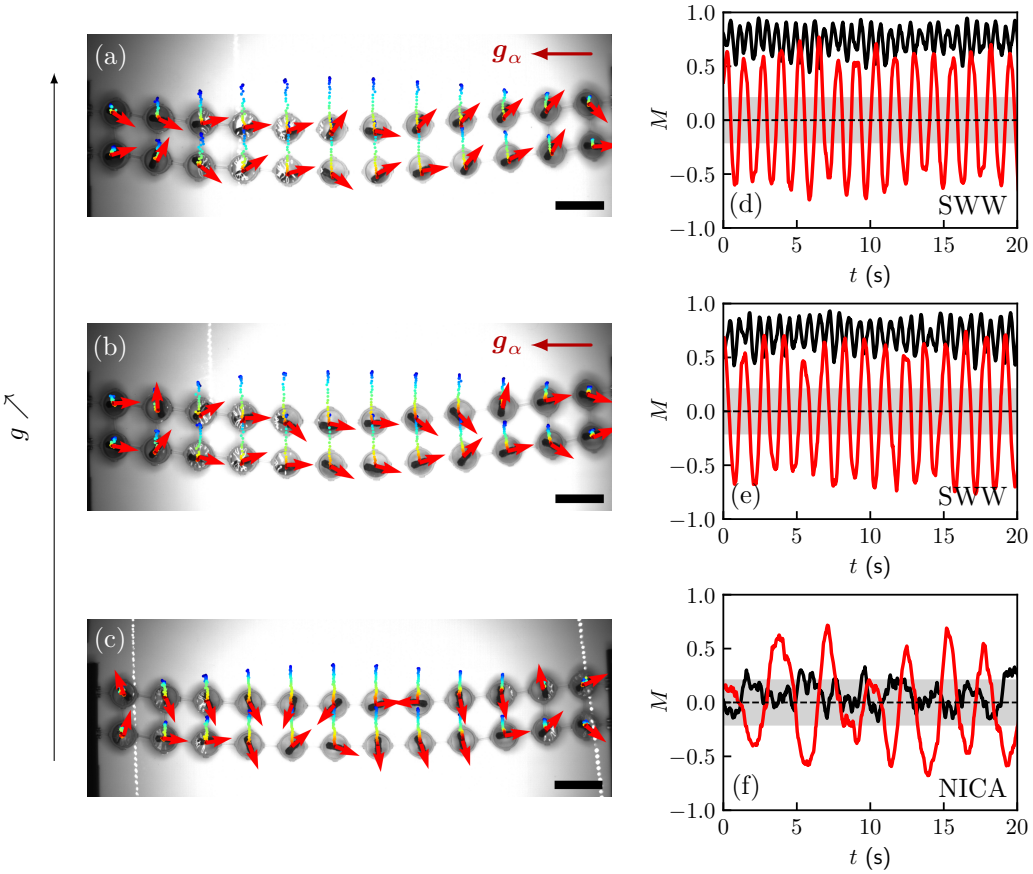


FIG. 7.6. **NICA with a transverse polarizing field.** Experimental snapshots of the $W = 2$ active *ladder* ($N = 48$) for small, i.e. $\alpha = 0°$ (c), intermediate, i.e. $\alpha = 8.5°$ (b), and large, i.e. $\alpha = 10.7°$ (a), gravity. Red arrows: polarities $\hat{\boldsymbol{n}}_i$; trajectories color-coded from blue to red with increasing time; scale bars: 10 cm. (d-f) Transverse $M_\perp$ (red) and longitudinal $M_\parallel$ (black) polarizations as a function of time, in the same conditions as (a-c). The gray areas illustrate the range inside which is expected to lie the polarizations for purely random spins, that is $\left[-1/\sqrt{N}, 1/\sqrt{N}\right]$.

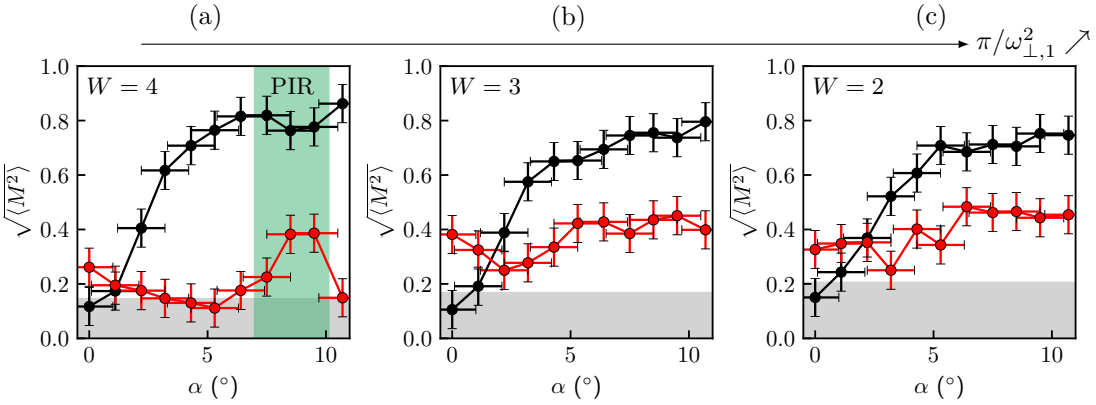


FIG. 7.7. **Polarizations as a function of gravity.** Root mean squared transverse $\sqrt{\langle M_\perp^2 \rangle}$ (red) and longitudinal $\sqrt{\langle M_\parallel^2 \rangle}$ (black) polarizations as a function of the imposed tilt α; for $W = 4$ (a), $W = 3$ (b), $W = 2$ (c). The gray areas illustrate the range inside which is expected to lie the root mean squared polarizations for purely random spins, that is $\left[0, 1/\sqrt{N}\right]$. The green area in (a) highlights the range inside which PIR transition is observed.

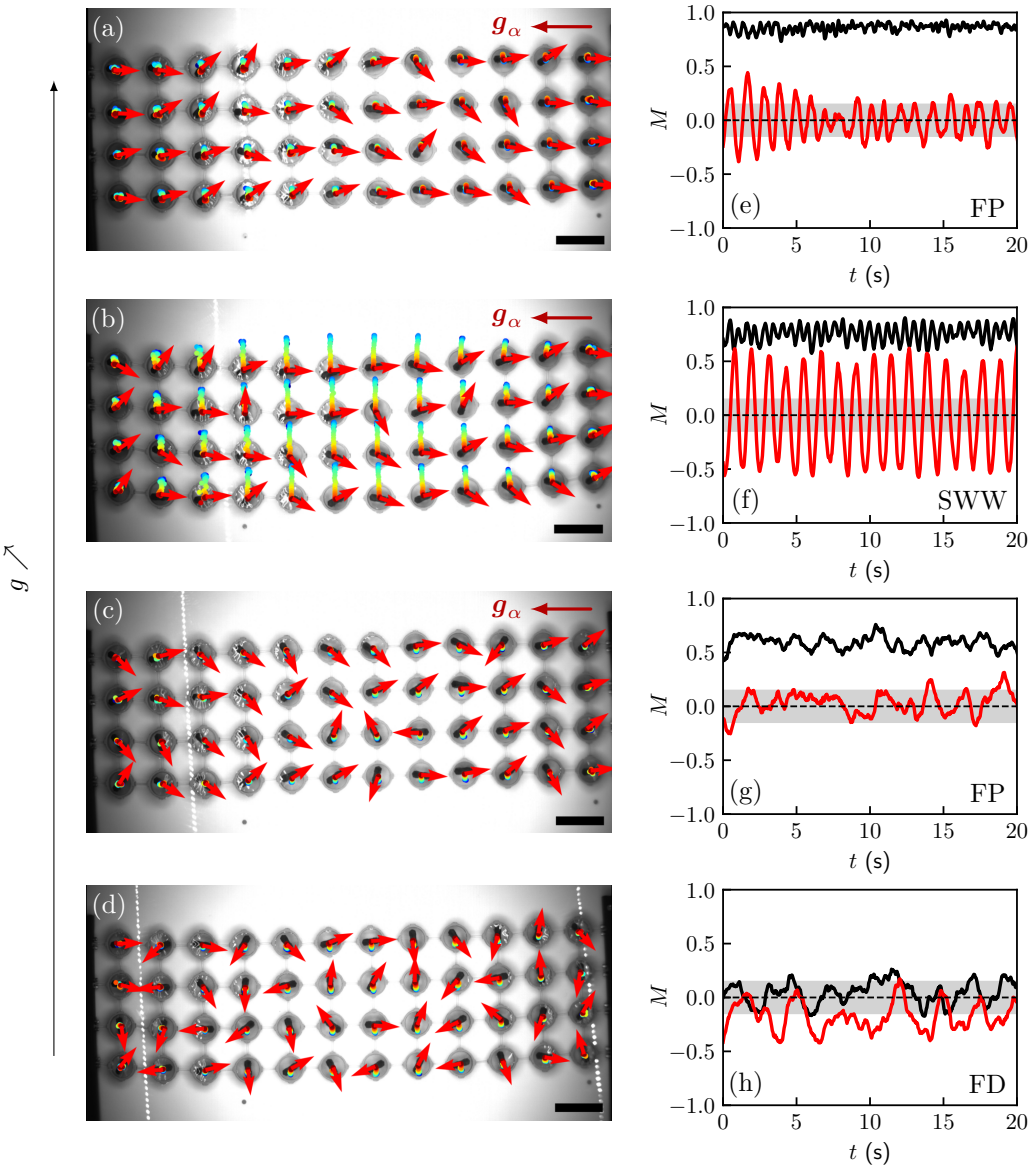


FIG. 7.8. **Polarization induces reentrance transition to collective actuation.** (a-d) Experimental snapshots of the $W = 4$ active *ladder* ($N = 48$) for increasing amplitude of the polarizing field. From bottom to top, $\alpha = 0°$ (d); $\alpha = 4.3°$ (c), $\alpha = 8.5°$ (b), and $\alpha = 10.7°$ (a). At intermediate gravity, regime SWW emerges. Red arrows: polarities $\hat{\boldsymbol{n}}_i$; trajectories color-coded from blue to red with increasing time; scale bars: 10 cm. The red arrows indicate the direction of the gravity force. (e-h) Transverse $M_\perp$ (red) and longitudinal $M_\parallel$ (black) polarizations as a function of time, in the same conditions as (a-d). The gray areas illustrate the range inside which is expected to lie the polarizations for purely random spins, that is $\left[-1/\sqrt{N}, 1/\sqrt{N}\right]$.

(i) Independently of the zero-gravity CA regime, increasing the polarizing field's amplitude leads to SWW regimes, which correspond to spontaneous transverse oscillations with a large longitudinal polarization.

(ii) Large enough polarizing fields stabilize the FP regime.

(iii) Polarization decreases the activity threshold for CA, leading to PIR.

In the rest of this chapter, combining numerical simulations and theoretical analysis, we decipher the mechanisms at the origin of NICA and of the three attributes of CA with

a polarizing field. First, we perform the complete analysis of the single particle with a polarizing field. Then, using the coarse-grained model derived in chapter 5, we explain the origin of NICA, and show that PIR is a purely collective effect, inherited from the differential stability of the FD and FP phases.

7.4 Single particle actuation with a polarizing field

We start by analyzing the physics of a single particle with a polarizing field, which is the first ingredient of understanding. We consider the elastic structure discussed in chapter 5 in the absence of gravity, and represented in Figs. 7.10-c, e, g and i. It is made of a single active unit connected to the three static vertices of a regular triangle (Fig. 7.10), using *soft* springs (see chapter 2). This structure has two degenerated normal modes, whose energy is denoted ω_0^2. The springs extension in the reference configuration is always kept fixed, equal to $\alpha = l/l_0 \simeq 1.16$, imposing $\omega_0^2 \simeq 1.70$, and the elasto-active coupling π is varied by tuning the length of the *soft* springs, like in chapter 5. The displacement and polarity vectors are expressed in polar coordinates, notations being defined in Fig. 7.9.

Let us remind the results without gravity (see chapter 5). For $\pi < \omega_0^2$, an infinite set of marginally stable fixed points forms a circle of radius $R = \pi/\omega_0^2$: the system is *frozen*. In the presence of angular noise, the particle can explore all the equivalent orientations, and we say the system is FD. For $\pi > \omega_0^2$, all such fixed points are unstable, and a limit cycle of radius $R = (\pi/\omega_0^2)^{1/2}$ and frequency $\Omega = \omega_0\sqrt{\pi - \omega_0^2}$, the so-called *Chiral Oscillations* (CO) regime, branches off continuously.

7.4.1 Experimental observations

At small enough gravity, the zero-gravity regimes are just decorated. As activity increases, the system goes from a FD regime, where angular diffusion allows to visit all possible fixed points configurations $\theta = \varphi$ (Fig. 7.10-g), to a CO regime (Fig. 7.10-i), with finite $\gamma = \theta - \varphi$, driving the system in rotation. These two regimes are best illustrated by measuring the probability density in the plane $\theta - \varphi$, integrated over four minutes acquisitions. In the FD regime, the system indeed always lies close to $\theta = \varphi$ (Fig. 7.10-h). However, the presence of a small polarization term, originating from the tilt of our frame, induces a preferred orientation close to $\theta = 3\pi/2$ rad. For the same reason, in the CO regime, γ is not constant but is modulated in time at the same rate as the rotation frequency (Fig. 7.10-j). Consistently with the results of chapter 5, the

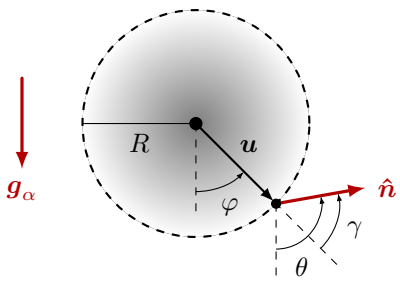


FIG. 7.9. **Notations for the single particle with gravity.** R and φ are the polar coordinates components of the displacement vector $\mathbf{u}$, and θ is the orientation of the polarity vector $\hat{\mathbf{n}}$. All angles are defined with respect to gravity, and we denote $\gamma = \theta - \varphi$.

transition happens around $\pi/\omega_0^2 = 1$ (Fig. 7.10-a).

For larger gravity, however, the scenario is entirely different. Consistently with the

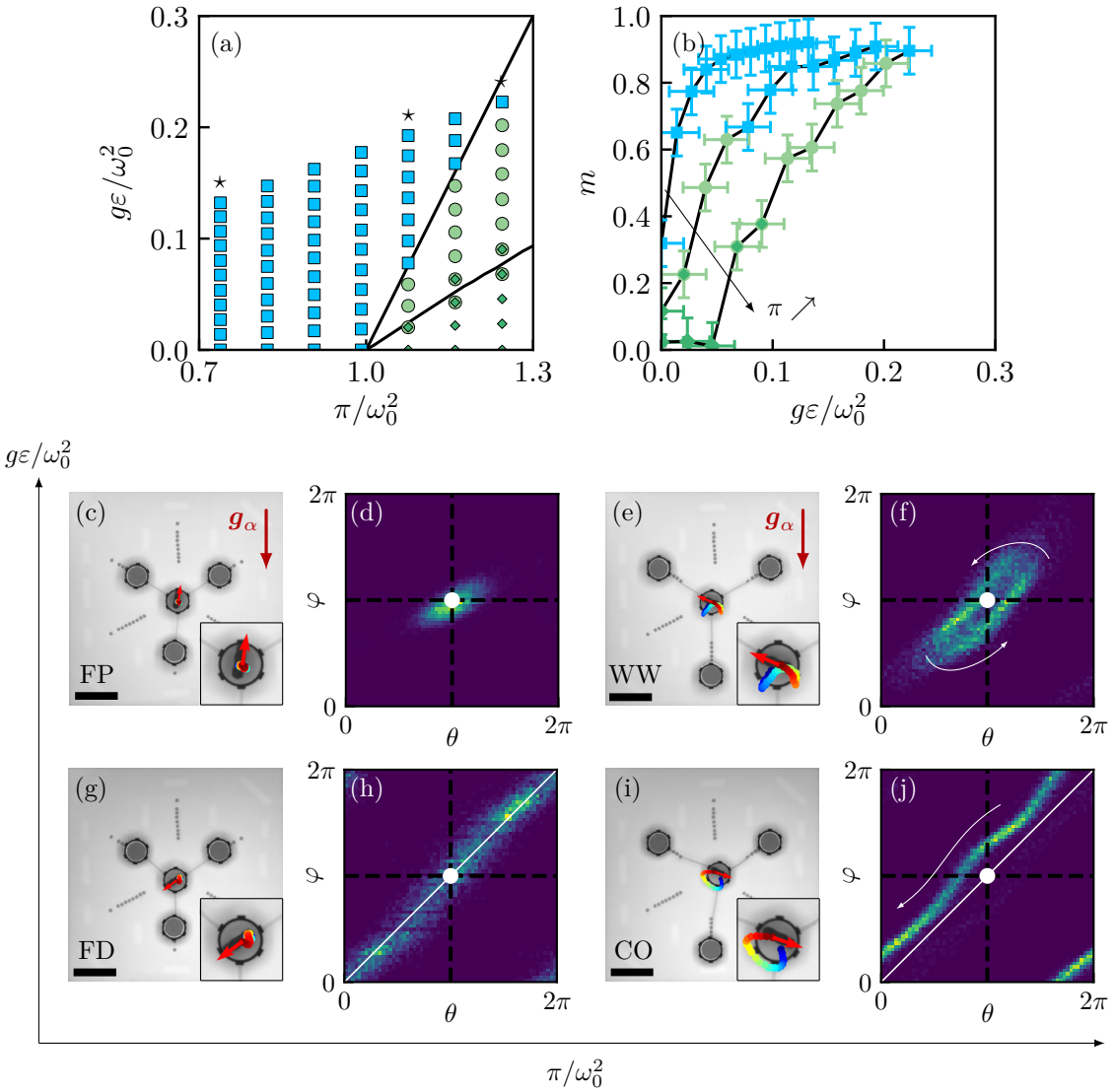


FIG. 7.10. **Single particle experiments with a polarizing field.** (a) Experimental phase diagram. Markers represent the different experiments and are color-coded by the dominant dynamical regime; blue squares: *frozen* (FD and FP), light green circles: WW, dark green diamonds: CO, dark green diamond inside light green circles: coexistence between WW and CO. The top and bottom solid black lines represent respectively $\pi = \omega_0^2 + g\varepsilon$ and $\pi = \omega_0^2 + 3g\varepsilon$. (b) Magnetization m as a function of gravity $g\varepsilon/\omega_0^2$ for various activity $\pi/\omega_0^2 \in [0.74, 1.08, 1.24]$ (stars in (a)), as obtained from experiments; same color and marker code as (a). (c/e/g/i) Experimental realizations of the four different dynamical regimes in real space. Red arrows: polarities $\hat{\mathbf{n}}_i$; trajectories color-coded from blue to red with increasing time; scale bars: 10 cm. (d/f/h/j) pdf in the plane (θ,φ), integrated over the whole dynamics. The white dot (resp. solid white line) represents the configuration $(\theta,\varphi)=(\pi,\pi)$ (resp. $\theta = \varphi$). When relevant, the white arrows indicate the main dynamics direction (it is omitted in panels (d) and (h) because the dynamics are diffusive or frozen). (i/j) CO regime ($\pi/\omega_0^2 = 1.24$, $g\varepsilon/\omega_0^2 = 0.0$). (e/f) WW regime ($\pi/\omega_0^2 = 1.24$, $g\varepsilon/\omega_0^2 = 0.11$). (g/h) FD regime ($\pi/\omega_0^2 = 0.91$, $g\varepsilon/\omega_0^2 = 0.0$). (c/d) FP regime ($\pi/\omega_0^2 = 0.91$, $g\varepsilon/\omega_0^2 = 0.08$).

benchmark experiments of section 7.2, we find that the small-activity FD regime polarizes against gravity: angular noise does not allow the active unit to visit all orientations anymore, and the system is FP, i.e. sits close to $\theta = \varphi = \pi$ rad (Figs. 7.10-c and d). Increasing activity leads to a new dynamical regime, the so-called *Windscreen Wiper* (WW) regime (Figs. 7.10-e and f). In this regime, the system oscillates around the configuration $\theta = \varphi = \pi$ rad in the $\theta - \varphi$ plane, which translates in real space into a back-and-forth motion perpendicularly to gravity, polarized opposite to gravity. We also find that the activity threshold below which the *frozen* regime is the only stable one increases with gravity (Fig. 7.10-a). For the largest gravity explored experimentally, we only find FP regimes. Eventually, increasing further activity leads, after some coexistence region, to the CO regime.

Lastly, we measure the magnetization m as a function of gravity $g\varepsilon/\omega_0^2$ for various values of activity π/ω_0^2, above and below the threshold $\pi = \omega_0^2$ (Fig. 7.10-b). Consistently with the previous section, for $\pi < \pi_c$, the system is *frozen* and progressively polarizes according to Eq. (7.10), which solely relies on the ratio $g\varepsilon/D$. For $\pi > \pi_c$, the magnetization increases from 0 to 1 over a typical gravity range that now depends on and increases with activity.

7.4.2 Numerical simulations

Our understanding of the different phases and transitions between them is limited by our ability to fine-tune the experiment's parameters. We escape this by simulating Eqs. (7.5), without noise ($D = 0$), and start by identifying precisely the phase boundaries. This is done by performing annealing simulations with decreasing gravity and various values of activity π/ω_0^2 between 1 and 10. We find the phase diagram presented in Fig. 7.11-a.

Numerical observations are consistent with experiments within the gravity and activity ranges explored. Below the threshold $\pi = \omega_0^2$, the system is FP; any finite amount of gravity polarizes the *frozen* regime. Above the threshold, we find the CO, then WW and FP regimes as one increases gravity (Fig. 7.11-a). In particular, for $\pi < \pi_c = \omega_0^2 + g\varepsilon$, we only find FP regimes. Notably, for large enough activity/gravity, in between the WW (Fig. 7.11-e) and CO (Fig. 7.11-c) regimes, we find a stable limit cycle that alternates in time between their respective properties (Fig. 7.11-d), and that is termed the *Second Windscreen Wiper* (WW2) regime. Below a certain activity threshold, this regime disappears, and the system transitions directly from CO to WW as gravity increases or activity decreases (Fig. 7.11-a); around $\pi = \pi^\star = \omega_0^2 + 3g\varepsilon$, which is consistent with experimental observations (Fig. 7.10-a). We also perform three gravity annealing simulations with the same parameters as the experiments shown in Fig. 7.10-b. The magnetization m as a function of gravity found numerically (Fig. 7.11-b) is consistent with experimental results, but essential differences must be noted. While, in noiseless simulations, the magnetization of FP regimes is strictly 1; in the experiments, angular noise imposes that it saturates below 1. Moreover, the time coexistence between the CO and the WW regimes observed in experiments is replaced by clearly separated dynamical regimes, with well-defined magnetization m.

7.4.3 Discussion

Altogether, the experimental and numerical study of the single particle with a polarizing field is consistent with the preliminary observations in triangular lattices pinned at the

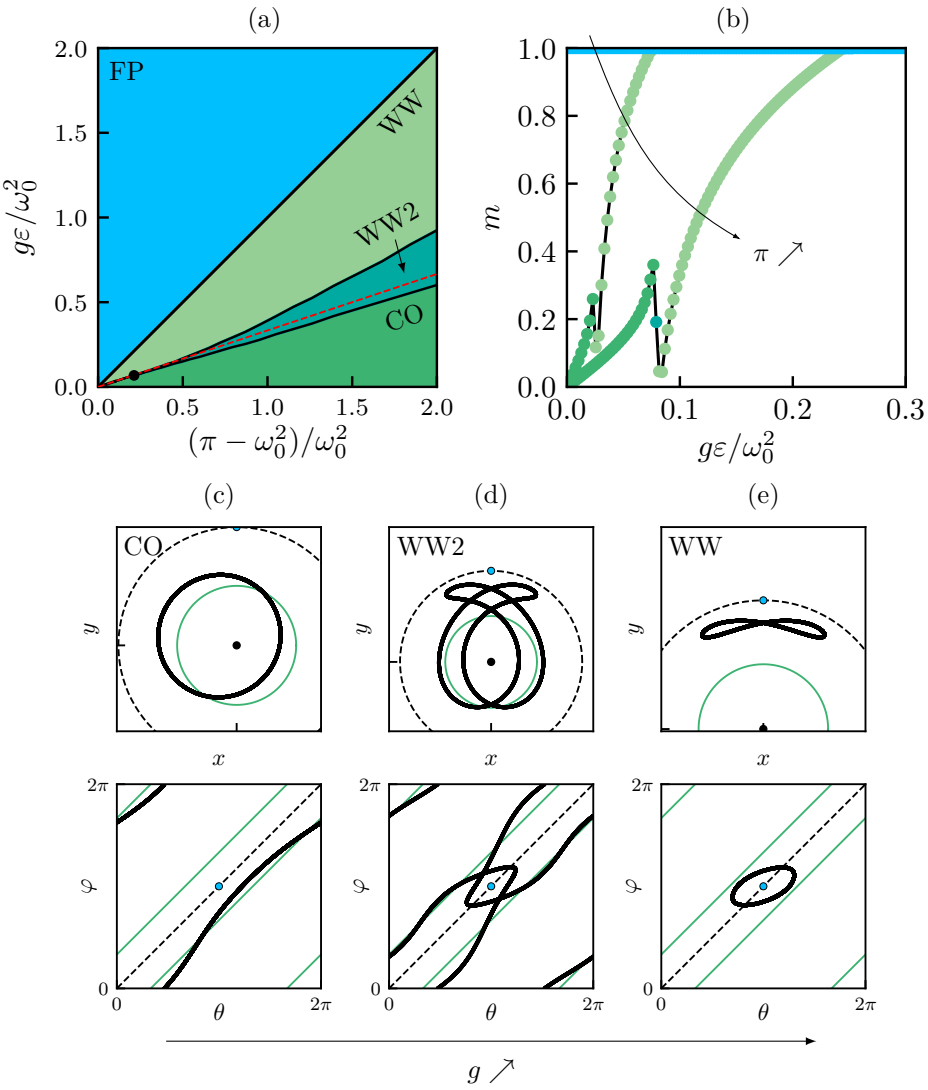


FIG. 7.11. **Noiseless single-particle with a polarizing field.** (a) Numerical phase diagram. The different colored regions correspond to different regimes; blue: FP, dark green: CO, light green: WW, gray: WW2. The top solid black (resp. dashed red) line represents $\pi = \omega_0^2 + g\varepsilon$ (resp. $\pi = \omega_0^2 + 3g\varepsilon$), and the black dot highlights the last stable WW2 regime. (b) Magnetization m as a function of gravity $g\varepsilon/\omega_0^2$ for various activity $\pi/\omega_0^2 \in [0.74, 1.08, 1.24]$ (the same as Fig. 7.10-b), as obtained from simulations. (c-e) Different dynamical regimes attractors in the XY (top) and θ-φ planes (bottom) for $\pi/\omega_0^2 = 3.95$; (c) CO regime ($g\varepsilon/\omega_0^2 = 0.62$), (d) WW2 regime ($g\varepsilon/\omega_0^2 = 1.15$), (e) WW regime ($g\varepsilon/\omega_0^2 = 2.23$). The dashed black lines represent the different zero-gravity fixed points ($R_0 = \pi/\omega_0^2, \gamma_0 = 0$), the blue dots highlighting the one pointing against gravity. The green lines represent the two CO regimes ($R = \sqrt{\pi}/\omega_0, \cos\gamma = \pm\omega_0/\sqrt{\pi}$).

edges. The four regimes observed at the collective level - FP, FD, SCO, and SWW - find analogous regimes at the single particle level, the regimes FP, FD, CO, and WW.

In the following, we analyze Eqs. (7.5) and explain the origin of the different dynamical regimes at the single particle level. Note that this work was done in collaboration with Vincent Démery, who determined the mapping with the underdamped nonlinear pendulum close to the exceptional point (see below).

One particle dynamics in a gravity field

Real space. We remind the equations discussed at the beginning of this chapter, Eqs. (7.5), describing the dynamics of the single particle with a polarizing gravity field:

$$\dot{\boldsymbol{u}} = \pi\hat{\boldsymbol{n}} - \omega_0^2\boldsymbol{u}, \tag{7.12a}$$

$$\dot{\boldsymbol{n}} = (\hat{\boldsymbol{n}} \times \dot{\boldsymbol{u}}) \times \hat{\boldsymbol{n}} - \varepsilon(\hat{\boldsymbol{n}} \times \boldsymbol{g}_\alpha) \times \hat{\boldsymbol{n}}, \tag{7.12b}$$

where we have omitted angular noise. Note that we have placed ourselves within the harmonic approximation and assumed that the change of reference configuration induced by gravity is small enough to be neglected. Nevertheless, this assumption can be approximatively assessed for the experiments presented in Fig. 7.10. We estimate the reference configuration by measuring the average position of the active unit over the whole dynamics. We find that, for the largest gravity explored, the reference configuration is shifted toward gravity by typically $0.2l_0$, which induces an increase (resp. decrease) of the energy of the transverse (resp. longitudinal) mode by typically 18%. Notwithstanding this effect, we still neglect it in the following for simplicity.

Polar real space. In polar coordinates, the above equations yield:

$$\dot{R} = \pi\cos(\gamma) - \omega_0^2 R, \tag{7.13a}$$

$$\dot{\varphi} = \frac{\pi}{R}\sin(\gamma), \tag{7.13b}$$

$$\dot{\gamma} = \left(\omega_0^2 R - \frac{\pi}{R}\right)\sin(\gamma) + g_\alpha\varepsilon\sin(\gamma+\varphi), \tag{7.13c}$$

where we remind the definitions of R, φ and $\gamma = \theta - \varphi$ in Fig. 7.9.

Fixed points stability analysis

We look for fixed points of the dynamics such that $\dot{R} = \dot{\varphi} = \dot{\gamma} = 0$. We find that they satisfy:

$$R_0 = \frac{\pi}{\omega_0^2}\cos(\gamma_0), \tag{7.14a}$$

$$\sin(\varphi_0) = 0, \tag{7.14b}$$

$$\sin(\gamma_0) = 0, \tag{7.14c}$$

where the only possible value of γ_0 is zero, because the solution $\gamma_0 = \pi$ rad gives negative radius R. Contrary to the zero-gravity case, we find that all configurations of the polarity field are not fixed points: only the configurations along ($\varphi_0 = 0$ rad) and against ($\varphi_0 = \pi$ rad) gravity are fixed points of the dynamics. Let us evaluate their stability. We introduce $R = R_0 + \delta R$, $\varphi = \varphi_0 + \delta\varphi$, $\gamma = \delta\gamma$, and write, at first order in small quantities, the linearized dynamics around the fixed points. It gives:

$$\dot{\delta R} = -\omega_0^2\delta R, \tag{7.15a}$$

$$\dot{\delta\varphi} = \omega_0^2\delta\gamma, \tag{7.15b}$$

$$\dot{\delta\gamma} = g_\alpha\varepsilon\cos\varphi_0\delta\varphi + \left(\pi - \omega_0^2 + g_\alpha\varepsilon\cos\varphi_0\right)\delta\gamma. \tag{7.15c}$$

The eigenvalue problem reduces to find λ such that

$$(\lambda + \omega_0^2)\left[\lambda^2 - \lambda\left(\pi - \omega_0^2 + g_\alpha\varepsilon\cos\varphi_0\right) - g_\alpha\varepsilon\cos\varphi_0\right] = 0. \tag{7.16}$$

The eigenvalue along the radial direction is always negative ($\lambda_R = -\omega_0^2$). The stability of the configurations $\varphi_0 = \{0, \pi\}$ rad is encoded in the two eigenvalues along φ and γ.

Without gravity $g_\alpha = 0$. With this sanity check, we recover the usual result of the symmetric single particle ($\lambda_\varphi = 0$, $\lambda_\gamma = \pi - \omega_0^2$), see Figs. 7.12-a and d. All fixed points are equivalent and marginally stable for $\pi < \omega_0^2$, and unstable for $\pi > \omega_0^2$. The bifurcation results from one eigenvalue turning positive and invariance by rotation.

Finite gravity $g_\alpha > 0$. For $g_\alpha > 0$, one finds that the nature of the bifurcation is modified:

- **Configuration along gravity $\varphi_0 = 0$ rad.** Eq. (7.16) transforms into:

$$(\lambda + \omega_0^2)\left[\lambda^2 - \lambda\left(\pi - \omega_0^2 + g_\alpha\varepsilon\right) - g_\alpha\varepsilon\right] = 0. \tag{7.17}$$

  For any finite g_α, a positive eigenvalue always exists (Figs. 7.12-b and c), and the configuration is unconditionally unstable.

- **Configuration against gravity $\varphi_0 = \pi$ rad.** Eq. (7.16) transforms into:

$$(\lambda + \omega_0^2)\left[\lambda^2 - \lambda\left(\pi - \omega_0^2 - g_\alpha\varepsilon\right) + g_\alpha\varepsilon\right] = 0. \tag{7.18}$$

  Stability now depends on π/ω_0^2 and $g_\alpha\varepsilon/\omega_0^2$ (Figs. 7.12-e and f). We find that the stability threshold expresses as follows:

$$\pi_c = \omega_0^2 + g_\alpha\varepsilon, \tag{7.19}$$

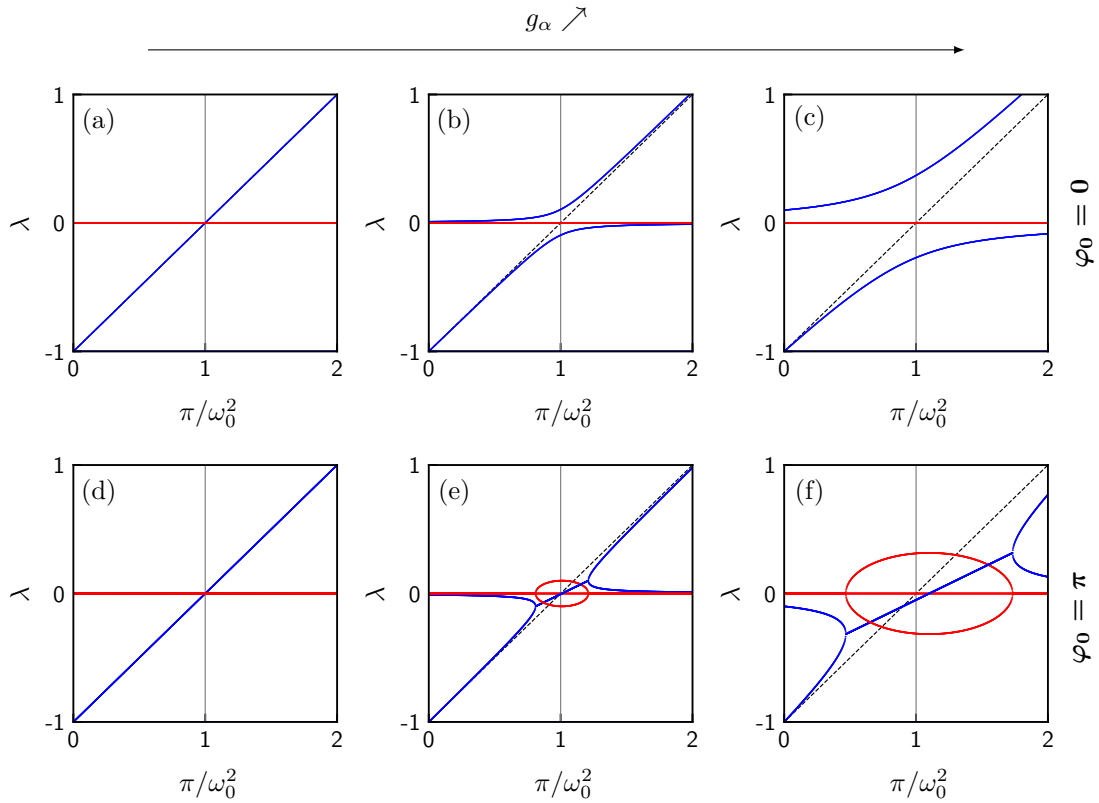


FIG. 7.12. **Fixed points stability analysis with a polarizing field.** Solutions of the eigenproblem Eq. (7.16) as a function of activity π/ω_0^2 for increasing amplitude of the polarizing field. Blue (resp. red) curves represent the solutions' real (resp. imaginary) part. The squared eigenfrequency ω_0^2 is fixed and equals one. (a-c) Fixed point along gravity $\varphi_0 = 0$. (d-f) Fixed point against gravity $\varphi_0 = \pi$ rad. (a/d) No gravity $g_\alpha\varepsilon = 0.0$; (b/e) small gravity $g_\alpha\varepsilon = 0.01$; (c/f) larger gravity $g_\alpha\varepsilon = 0.1$.

which corresponds to the numerical data (Figs. 7.11-a and 7.12-f). Consistently with observations in large N lattices, gravity stabilizes the FP regime. Close to this threshold, the general form of the eigenvalues solutions of Eq. (7.18) are:

$$\lambda_{\varphi,\gamma} = \frac{1}{2}(\pi - \pi_c) \pm \frac{i}{2}\sqrt{4g_\alpha\varepsilon - (\pi - \pi_c)^2}. \tag{7.20}$$

Therefore, in the absence of noise, any finite gravity g_α polarizes the frozen configurations, and the only remaining fixed point is oriented against gravity. When activity exceeds the threshold $\pi_c = \omega_0^2 + g_\alpha\varepsilon$, the FP regime destabilizes through a Hopf bifurcation. Indeed, at threshold $\pi = \pi_c = \omega_0^2 + g_\alpha\varepsilon$, the eigenvalues are complex conjugate, equal to $\pm i\sqrt{g_\alpha\varepsilon}$, and their real parts turn positive (Figs. 7.12-e and f).

Close to the exceptional point

Now we focus on the physics close to $(\pi/\omega_0^2 = 1, g\varepsilon = 0)$, which is an exceptional point, as demonstrated below. Starting from Eqs. (7.13), we change variables to $\theta = \theta + \pi$, $\varphi = \varphi + \pi$ so that the polarized fixed point is $\theta = \varphi = 0$:

$$\dot{R} = \pi\cos(\gamma) - \omega_0^2 R, \tag{7.21a}$$

$$\dot{\varphi} = \frac{\pi}{R}\sin(\gamma), \tag{7.21b}$$

$$\dot{\gamma} = \left(\omega_0^2 R - \frac{\pi}{R}\right)\sin(\gamma) - g_\alpha\varepsilon\sin(\gamma + \varphi). \tag{7.21c}$$

We define $\Delta = (\pi - \omega_0^2)/\omega_0^2$, $\rho = R - 1$, $G = g\varepsilon/\omega_0^2$. Rescaling time by ω_0^2, we obtain:

$$\dot{\rho} = (1 + \Delta)\cos(\gamma) - 1 - \rho \tag{7.22a}$$

$$\dot{\varphi} = \frac{1 + \Delta}{1 + \rho}\sin(\gamma), \tag{7.22b}$$

$$\dot{\gamma} = \left(\rho - \frac{\rho - \Delta}{\rho + 1}\right)\sin(\gamma) - G\sin(\gamma + \varphi). \tag{7.22c}$$

We are interested in the limit $\Delta \to 0$, $G \to 0$. Based on numerical simulations, we expect the following regimes:

- $\Delta > 3G$: regime CO.
- $G < \Delta < 3G$: regime WW.
- $\Delta < G$: regime FP.

Rescaling. The scaling of the transition lines suggests different limit behavior when $\Delta \to 0$ with G/Δ constant, as a function of G/Δ. To identify the asymptotic solutions to the equations of motion, we rescale the different quantities with Δ. The case without gravity suggests:

$$\rho(t) = \Delta\tilde{\rho}(\sqrt{\Delta}t), \tag{7.23a}$$

$$\phi(t) = \tilde{\phi}(\sqrt{\Delta}t), \tag{7.23b}$$

$$\gamma(t) = \sqrt{\Delta}\tilde{\gamma}(\sqrt{\Delta}t), \tag{7.23c}$$

$$G = \Delta\tilde{G}. \tag{7.23d}$$

Inserting these scaling forms in the equations of motion and taking the limit $\Delta \to 0$, we next separate the different orders in Δ.

Zeroth-order: the pendulum. At zeroth order, we find:

$$\tilde{\rho} = 1 - \frac{\tilde{\gamma}^2}{2}, \tag{7.24a}$$

$$\dot{\tilde{\varphi}} = \tilde{\gamma}, \tag{7.24b}$$

$$\dot{\tilde{\gamma}} = -\tilde{G}\sin(\tilde{\varphi}). \tag{7.24c}$$

$\tilde{\rho}$ is actually a fast variable, which relaxes instantaneously to $1-\tilde{\gamma}^2/2$ in the limit $\Delta \to 0$ (Eq. (7.24a)). The equations for $\tilde{\varphi}$ and $\tilde{\gamma}$ describe an underdamped pendulum (Eqs. (7.24b) and (7.24c)): $\ddot{\tilde{\varphi}} = -\tilde{G}\sin\tilde{\varphi}$. Interestingly, the pendulum contains both a small-energy oscillating regime, which would correspond to the WW regime, and a large-energy running regime, which would correspond to the CO regime. However, there is nothing to select the orbit, which only depends on the initial conditions. For instance, the energy

$$E = \frac{\tilde{\gamma}^2}{2} - \tilde{G}\cos\tilde{\varphi}, \tag{7.25}$$

is conserved.

Exceptional point. Exceptional points are spectral singularities in the parameter space of a system in which two or more eigenvalues, and their corresponding eigenvectors, simultaneously coalesce [172, 186]. Such degeneracies are peculiar features of nonconservative systems that exchange energy with their surrounding environment.

Let us show that $(g\varepsilon/\omega_0^2 = 0, \pi/\omega_0^2 = 1)$ is an exceptional point of Eqs. (7.13). We start from the zeroth-order equations close to $(g\varepsilon/\omega_0^2 = 0, \pi/\omega_0^2 = 1)$:

$$\dot{\tilde{\varphi}} = \tilde{\gamma}, \tag{7.26a}$$

$$\dot{\tilde{\gamma}} = -\tilde{G}\sin\tilde{\varphi}, \tag{7.26b}$$

where we restrict to $\tilde{\varphi}$ and $\tilde{\gamma}$, $\tilde{\rho}$ being a fast variable at zeroth-order. Linearizing close to the FP fixed points, we find:

$$\frac{d}{dt}\begin{pmatrix}\tilde{\varphi}\\ \tilde{\gamma}\end{pmatrix} = \begin{pmatrix}0 & 1\\ -\tilde{G} & 0\end{pmatrix}\begin{pmatrix}\tilde{\varphi}\\ \tilde{\gamma}\end{pmatrix}. \tag{7.27}$$

The eigenvalues of the above matrix are $\pm i\sqrt{\tilde{G}}$, and are respectively associated with the eigenvectors ${}^{\mathrm{t}}(1, \pm i\sqrt{\tilde{G}})$. This convincingly demonstrates that $(g\varepsilon/\omega_0^2 = 0, \pi/\omega_0^2 = 1)$ is an exceptional point.

First-order: energy drift. To the next order in Δ, Eq. (7.24c) for $\tilde{\gamma}$ has another term:

$$\dot{\tilde{\gamma}} = -\tilde{G}\sin\tilde{\varphi} + \sqrt{\Delta}\tilde{\gamma}\left[1 - \tilde{\gamma}^2 - \tilde{G}\cos\tilde{\varphi}\right], \tag{7.28}$$

where we have used Eq. (7.24a) to eliminate $\tilde{\rho}$. Eqs. (7.24a) and (7.24b) are modified only at order Δ. This new term introduces an energy drift:

$$\dot{E} = \sqrt{\Delta}\tilde{\gamma}^2\left[1 - \tilde{\gamma}^2 - \tilde{G}\cos\tilde{\varphi}\right] = 2\sqrt{\Delta}\left[E + \tilde{G}\cos\tilde{\varphi}\right]\left[1 - 2E - 3\tilde{G}\cos\tilde{\varphi}\right], \tag{7.29}$$

which can be computed for any orbit of energy E using the exact expressions of the pendulum solutions[11]. Eq. (7.29) is the central result of this section. Using it, one can

[11] The exact solutions of the underdamped pendulum equation:

$$\frac{d^2\theta}{dt^2} = -\tilde{G}\sin\theta \tag{7.30}$$

find the energy drift averaged over one period (remember that the drift is slow, so that the energy is almost constant over a period):

$$\delta E = \langle \dot{E} \rangle_T = \int_0^T \dot{E}(t) dt. \tag{7.33}$$

For a given value of $\tilde{G}$, to any orbit of energy E is associated an averaged energy drift $\delta E(E, \tilde{G})$. If, for such orbit, $\delta E > 0$ (resp. $\delta E < 0$), the energy drift increases (resp. decreases) energy over time. Equilibrium orbits satisfy $\delta E = 0$, and to be stable they also require $\partial \delta E / \partial E < 0$. Therefore, for a given value of $\tilde{G} = G/\Delta$, one can find the stable orbits spontaneously selected by the energy drift (Figs. 7.13-a and b). We can study explicitly the limiting cases of very large and very small energies.

- $E \gg \tilde{G}$. When the energy is very large, we are in the fast chiral state with $\tilde{\varphi}(t) \simeq \sqrt{2E}t$. Averaging over a period the energy drift, we get at leading order:

$$\delta E = 2\sqrt{\Delta} E(1 - 2E). \tag{7.34}$$

  This is negative for large $E > 1/2$, hence the energy decays.

- $E \ll \tilde{G}$. On the contrary, if the energy is small, then the amplitude $\tilde{\varphi}_m \ll 1$, and we can expand the cosine in Eq. (7.29). At leading order, we get:

$$\dot{E} = \sqrt{\Delta} \tilde{G}(1 - \tilde{G})(\tilde{\varphi}_m^2 - \tilde{\varphi}^2). \tag{7.35}$$

  Averaging over a period with $\langle \tilde{\varphi}^2 \rangle_T = \tilde{\varphi}_m^2/2$, we get:

$$\delta E = \frac{\sqrt{\Delta}}{2} \tilde{G}(1 - \tilde{G}) \tilde{\varphi}_m^2. \tag{7.36}$$

  We find that if $\tilde{G} > 1$, $\delta E < 0$: the minimum energy state is stable; this is the FP regime. Conversely, if $\tilde{G} < 1$, the minimal energy state is unstable, so we are in regimes WW or CO.

---

can be expressed using the Jacobi elliptic functions [187]. Defining the total energy $E = \dot{\theta}^2/2 - \tilde{G}\cos\theta$, it can be shown that:

- For $E < \tilde{G}$, solutions are bounded, and:

$$T = 4K(k^2)/\sqrt{\tilde{G}}, \tag{7.31a}$$

$$\theta(t) = 2\arcsin\left(ksn\left\{ \sqrt{\tilde{G}} \left(\frac{T}{4} - t \right); k^2 \right\} \right). \tag{7.31b}$$

- For $E > \tilde{G}$, solutions are unbounded, and:

$$T = 4K(1/k^2)/\sqrt{2\left(E + \tilde{G}\right)}, \tag{7.32a}$$

$$\theta(t) = 2\arcsin\left(sn\left\{ t\sqrt{\left(E + \tilde{G}\right)/2}; 1/k^2 \right\} \right). \tag{7.32b}$$

where $k = \frac{1}{\sqrt{2}}\sqrt{\left(1 + \frac{E}{\tilde{G}}\right)}$, $K(m)$ is the complete elliptic integral of the first kind, and where $sn(u; m)$ refers to the Jacobi elliptic functions. The solutions are represented in Fig. 7.13-c

Energy drift on the heteroclinic orbit. In order to decide whether the system is in the WW or CO regime, we compute the energy drift for the heteroclinic orbit, $E = \tilde{G}$. For $E \geq \tilde{G}$, $\tilde{\varphi}$ explores $[0, 2\pi]$, so that we can change variables in Eq. (7.33):

$$\delta E = \int_0^{2\pi} \dot{E}(\tilde{\varphi}) \frac{dt}{d\tilde{\varphi}} d\tilde{\varphi}, \tag{7.37}$$

where

$$\frac{dt}{d\tilde{\varphi}} = \tilde{\gamma}^{-1} = \left(2\left[E + \tilde{G}\cos\tilde{\varphi}\right]\right)^{-1/2}, \tag{7.38}$$

so that

$$\delta E = \sqrt{2\Delta} \int_0^{2\pi} \left[E + \tilde{G}\cos\tilde{\varphi}\right]^{1/2} \left[1 - 2E - 3\tilde{G}\cos\tilde{\varphi}\right] d\varphi. \tag{7.39}$$

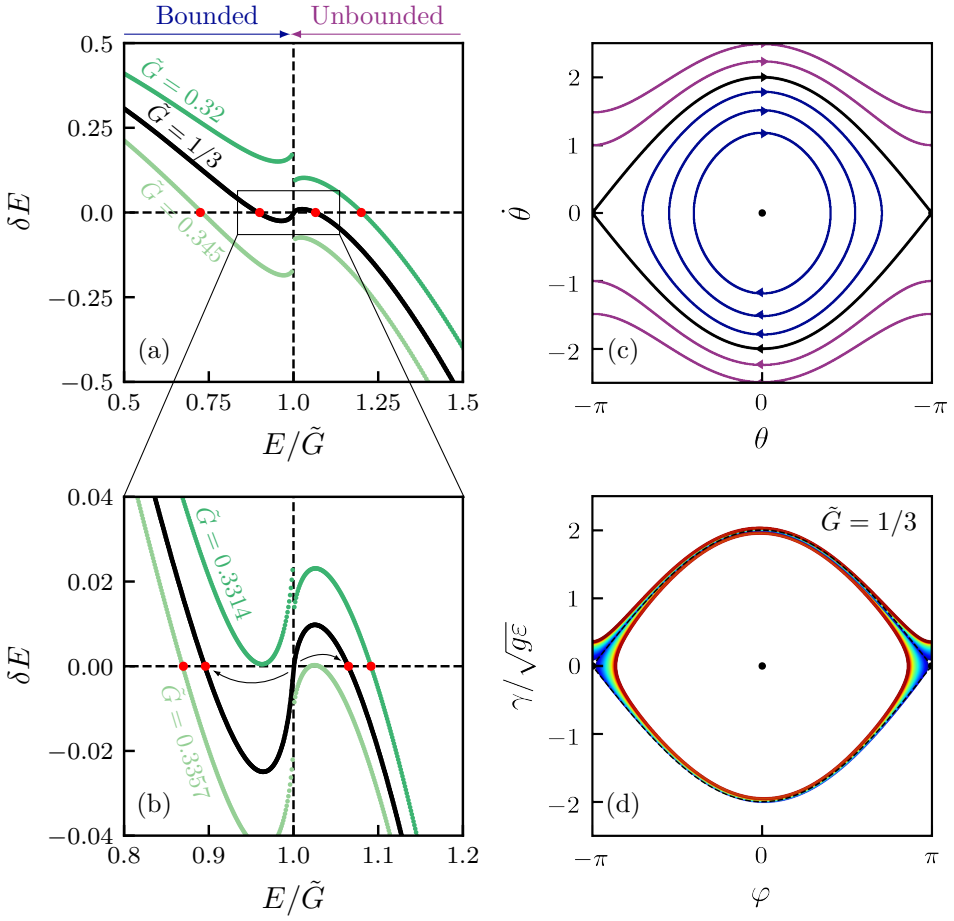


FIG. 7.13. **Mapping with the underdamped nonlinear pendulum.** (a) Energy drift δE as a function of $E/\tilde{G}$ for different values of $\tilde{G}$, as obtained from Eq. (7.29). Stable orbits are highlighted with a red marker. (b) Zoom on (a) close to $E/\tilde{G} = 1$ for different values of $\tilde{G}$; emphasizing the hysteresis range. (c) Exact solutions to the pendulum equation $\ddot{\theta} = -\tilde{G}\sin\theta$ [187] for different energies $E/\tilde{G}$ in the plane $\theta - \dot{\theta}$, where $E = \tilde{G}$ denotes the heteroclinic orbit's energy (solid black line). (d) Phase portrait of two transient regimes at $\tilde{G} = 1/3$, with initial energies $E = \tilde{G} \pm \delta$, i.e. slightly above and slightly below the heteroclinic orbit's energy. The trajectories are color-coded from blue to red as time increases. The dashed black line represents the separatrix. The stationary regimes obtained correspond to the stable orbits shown in panels (a-b) for $\tilde{G} = 1/3$.

Applying to the heteroclinic orbit, $E = \tilde{G}$, we have:

$$\delta E = \sqrt{2\Delta\tilde{G}} \int_0^{2\pi} [1+\cos\tilde{\varphi}]^{1/2} \left[1 - 2\tilde{G} - 3\tilde{G}\cos\tilde{\varphi}\right] d\varphi. \tag{7.40}$$

This last integral can be computed exactly and yields:

$$\delta E = 8\sqrt{\tilde{G}}(1-3\tilde{G}). \tag{7.41}$$

Hence:

- if $\tilde{G} > 1/3$, the energy decays on the heteroclinic orbit: this is regime WW;
- if $\tilde{G} < 1/3$, the energy increases on the heteroclinic orbit: this is regime CO.

Semi-analytic general solutions. Computing Eq. (7.33) using Eq. (7.29) and the exact expressions of the pendulum solutions, Eqs. (7.31) and (7.32), we find the energy drift δE for any value of $\tilde{G}$ (Figs. 7.13-a and b). The results confirm the asymptotic and heteroclinic cases. For $\tilde{G} = 1/3$, we actually report two stable solutions, one bounded ($E < \tilde{G}$) and one unbounded ($E > \tilde{G}$). This is the hallmark of a hysteresis: two stable solutions coexist within a given range of $\tilde{G}$. For large enough gravity $\tilde{G} > \tilde{G}_+ \simeq 0.3357$, the only stable solution is bounded, corresponding to a WW regime. In contrast, for small enough gravity $\tilde{G} < \tilde{G}_- \simeq 0.3314$, the only stable solution is unbounded, corresponding to a CO regime. Within the range $\tilde{G}_- < \tilde{G} < \tilde{G}_+$, the initial condition sets the stationary solution reached by the system. Eventually, note that in the limit $\Delta \to 0$, the dynamics is slow as it scales like $\sqrt{\Delta}$. The energy drift is even slower and scales as Δ, indicating that the transient regime is slower and slower as the exceptional point is approached.

Numerical simulations. First, we confirm the predicted hysteresis. We simulate Eqs. (7.5), placing ourselves at $\tilde{G} = 1/3$ for very small gravity $g\varepsilon = 10^{-4}$. We simulate twice the dynamics, starting from two initial conditions, which, within the above mapping, have energies $E = \tilde{G} \pm \delta$, i.e. slightly below and slightly above the heteroclinic orbit's energy. We find that both initial conditions converge toward the stable orbits predicted using the semi-analytic approach (Fig. 7.13-d). The transient regime is very long, as expected close to the exceptional point. Having confirmed the hysteresis, we now perform an annealing simulation, slowly varying $\tilde{G}$ back-and-forth around 1/3, keeping $g\varepsilon = 10^{-4}$. We compare the main frequency of oscillation of φ (obtained from the largest peak of its FFT) to the frequency of the stable pendulum solutions found from the semi-analytic approach. We find a perfect agreement between the predictions and the numerical data (Fig. 7.14-b), with an evident hysteresis loop, that span a very small range of $\tilde{G}$. Note that this hysteresis was not seen in the simulations of Fig. 7.11, because the stepwise variations of parameters were way too large. Interestingly, as one approaches the transitions, the WW and CO regimes' frequency never vanishes, meaning that there are no stable pendulum orbits selected in the vicinity of the heteroclinic orbit. This explains why we find that the oscillation amplitude of regime WW saturates as it approaches the CO regime: θ and φ do not explore all the angles up to $\theta = \varphi = \pm\pi$, but plateau at $\pm(\pi - \theta^\star)$, where $\theta^\star \simeq 17°$ (Fig. 7.14-c).

Perturbative approaches

We have seen above that the physics close to the exceptional point reduces to that of an underdamped nonlinear pendulum, whose orbits are selected according to an energy

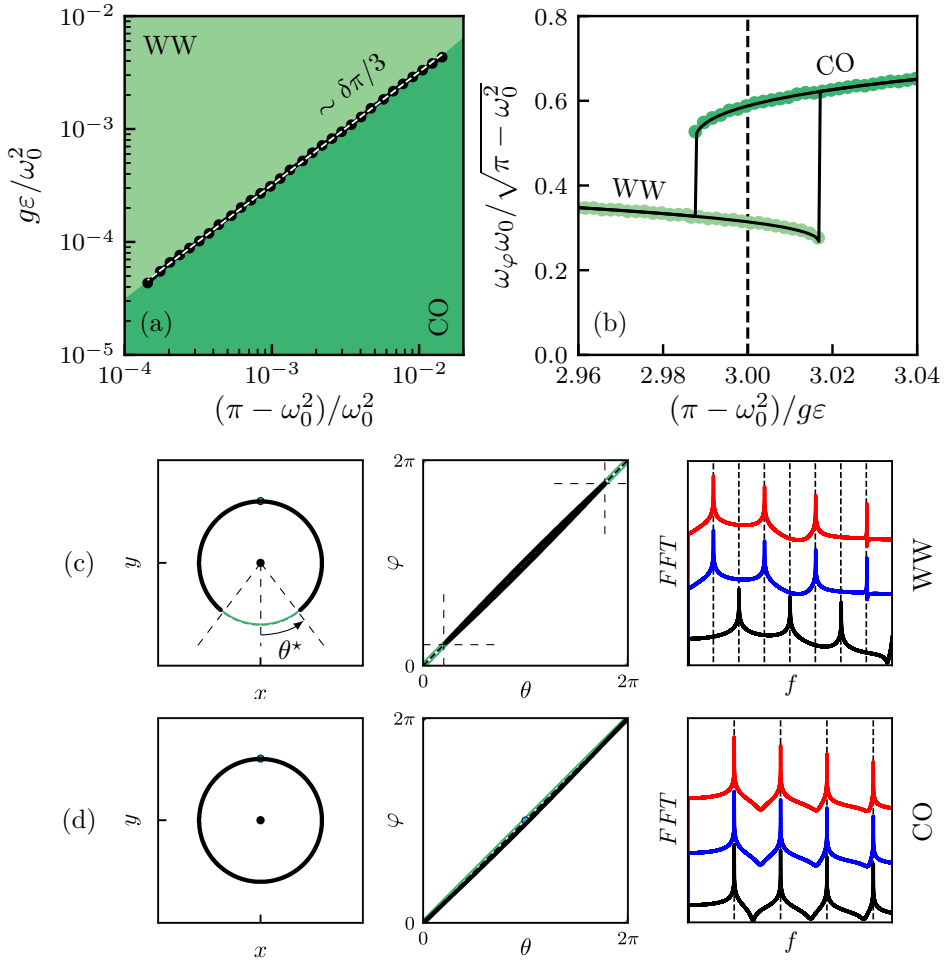


FIG. 7.14. **Physics close to the exceptional points.** (a) Zoom on the numerical phase diagram close to $(g\varepsilon/\omega_0^2,\, \pi/\omega_0^2) = (0,\, 1)$. The different colored regions correspond to different regimes; dark green: CO, light green: WW. The black dots represent the transition found in numerics. The dashed white line represents $\pi = \omega_0^2 + 3g\varepsilon$. (b) Rescaled fundamental frequency of oscillation of φ as a function of rescaled distance to threshold, for small gravity $g\varepsilon/\omega_0^2 = 10^{-4}$. Colored markers represent numerical simulations, and the solid black lines are the solutions of Eq. (7.29), using the exact expressions of the pendulum solutions. (c/d) WW (c) and CO (d) regimes just above and below the transition line, for $g\varepsilon/\omega_0^2 = 10^{-2}$. From left to right: attractor in the XY plane, in the θ-φ plane, and FFT of $\gamma(t) - \langle\gamma\rangle_t$ (red), $\dot\varphi(t) - \langle\dot\varphi\rangle_t$ (blue), and $R(t) - \langle R\rangle_t$ (black), shifted vertically for the sake of clarity. The dashed black lines represent the fundamental frequency and its harmonics.

drift, and found the exact expressions of the dynamical solutions in this limit. While the exact expressions of the dynamical solutions are out of reach in the general case, they can be found perturbatively close to the lines $\pi = \pi_c = \omega_0^2 + g\varepsilon$ (regime WW) and $g\varepsilon = 0$ (regime CO), and far enough from the exceptional point.

For $\pi = \pi_c + \delta$, with $\delta \ll 1$, the FP regime turns unstable through a Hopf bifurcation, and any perturbation of θ or φ diverges. The amplitude of the nonlinear limit cycle branching off from the FP regime, corresponding to regime WW, can be computed analytically using multiple-scale analysis (see Appendix L). We find that θ and φ oscillate according

to:

$$\begin{pmatrix}\varphi(t,T)\\ \theta(t,T)\end{pmatrix} = A(T)\begin{pmatrix}a\\1\end{pmatrix}e^{i\Omega t} + A^\star(T)\begin{pmatrix}a^\star\\1\end{pmatrix}e^{-i\Omega t}, \tag{7.42}$$

where $a = \frac{1-i\sqrt{G}}{1+G}$, $G = g_\alpha\varepsilon/\omega_0^2$, $\Omega = \sqrt{g_\alpha\varepsilon\omega_0^2}$; and where the complex number $A(T)$ depends on the slow timescale T and can be written:

$$|A| \simeq 2.8284\sqrt{\frac{\delta}{\omega_0^2}}\sqrt{\frac{G+0.25}{8G^2+3G-1}}. \tag{7.43}$$

For $G > G^\star = (\sqrt{41}-3)/16 \simeq 0.21$, the denominator of Eq. (7.43) is strictly positive, and the amplitude of the square-root power law is well-defined: this is a supercritical Hopf bifurcation. Nevertheless, as G approaches $G^\star$, the pre-factor of the square-root power law diverges, and the multiple-scale analysis fails to predict the amplitude of regime WW. As a matter of fact, comparing Eq. (7.43) with simulations of Eqs. (7.5) close to the Hopf bifurcation (see Appendix L), we find that the prediction is faithful to observations only for $G > 1$. Nevertheless, we find from the numerical simulations that the bifurcation is always a supercritical Hopf, whatever the amplitude of gravity.

Finally, for very small gravity and far enough from the exceptional point, the gravity term in Eq. (7.13c) can be seen as a small sinusoidal forcing perturbing the CO regime at its own oscillation frequency. Therefore, the linear response of the system in the CO regime provides an asymptotic expression of the dynamical solution (see Appendix L).

7.5 Coarse-grained description

To rationalize the observations done in *large* N square lattices, we now consider the coarse-grained dynamics in the presence of a polarizing field. We are here interested in describing the physics in the bulk of the material, far from the boundaries, where CA concentrates. In line with the developments of chapter 5, let us assume the dynamics condensate on two modes, which, far from the boundaries, are homogeneous and akin to two perpendicular translation modes. By convention, their geometry can be written as follows: $|\boldsymbol{\varphi}_{\perp/\parallel}\rangle = \hat{\boldsymbol{e}}_{\perp/\parallel}/\sqrt{N}$. We also consider that they have different energies: the transverse mode has a relatively low energy $\omega_\perp^2$, and the longitudinal mode, a relatively large energy $\omega_\parallel^2 \geq \omega_\perp^2$. Consistently with the active *ladder* experiments, gravity expresses as $\boldsymbol{g}_\alpha = -g_\alpha\hat{\boldsymbol{e}}_\parallel$. In the coarse-grained framework, the polarity field is described by the magnetization $\boldsymbol{m}$, which can take any value between -1 and 1 along the two directions of the plane. The displacement $\boldsymbol{U} = U_\perp\hat{\boldsymbol{e}}_\perp + U_\parallel\hat{\boldsymbol{e}}_\parallel$; and the magnetization $\boldsymbol{m} = m_\perp\hat{\boldsymbol{e}}_\perp + m_\parallel\hat{\boldsymbol{e}}_\parallel$, obey the following equations (see chapter 5):

$$\partial_t\boldsymbol{U} = \pi\boldsymbol{m} + \boldsymbol{F}^{el}[\boldsymbol{U}], \tag{7.44a}$$

$$\partial_t\boldsymbol{m} = (\boldsymbol{m}\times[\partial_t\boldsymbol{U} - \boldsymbol{g}_\alpha\varepsilon])\times\boldsymbol{m} + \frac{1-\boldsymbol{m}^2}{2}[\partial_t\boldsymbol{U} - \boldsymbol{g}_\alpha\varepsilon] - D\boldsymbol{m}. \tag{7.44b}$$

Projected on the two axes, they yield:

$$\partial_t U_\perp = \pi m_\perp - \omega_\perp^2 U_\perp, \tag{7.45a}$$

$$\partial_t U_\parallel = \pi m_\parallel - \omega_\parallel^2 U_\parallel, \tag{7.45b}$$

$$\partial_t m_\perp = \omega_\parallel^2 m_\parallel m_\perp U_\parallel - \omega_\perp^2 m_\parallel^2 U_\perp - g_\alpha \varepsilon m_\perp m_\parallel + \frac{1-\boldsymbol{m}^2}{2}\left(\pi m_\perp - \omega_\perp^2 U_\perp\right) - D m_\perp, \tag{7.45c}$$

$$\partial_t m_\parallel = -\omega_\parallel^2 m_\perp^2 U_\parallel + \omega_\perp^2 m_\perp m_\parallel U_\perp + g_\alpha \varepsilon m_\perp^2 + \frac{1-\boldsymbol{m}^2}{2}\left(\pi m_\parallel - \omega_\parallel^2 U_\parallel + g_\alpha \varepsilon\right) - D m_\parallel, \tag{7.45d}$$

where the polarization term has been coarse-grained together with the self-alignment term, which results in a magnetization creation term opposite to gravity, along the longitudinal direction. In the rest of this section, we decipher the respective effects of the different ingredients composing the toy model (noise, polarization, activity).

7.5.1 Noise-induced collective actuation at zero-gravity

At zero gravity, we can restrict the analysis to the transverse direction, given that the system cannot spontaneously mobilize the longitudinal direction ($\omega_\perp^2 < \pi \ll \omega_\parallel^2$). We find that $U_\perp$ and $m_\perp$ evolve according to:

$$\partial_t U_\perp = \pi m_\perp - \omega_\perp^2 U_\perp, \tag{7.46a}$$

$$\partial_t m_\perp = \frac{1-m_\perp^2}{2}\left(\pi m_\perp - \omega_\perp^2 U_\perp\right) - D m_\perp. \tag{7.46b}$$

Fixed point

As discussed in chapter 5, in the coarse-grained model, and *a fortiori* in Eqs. (7.46), any finite amount of noise D enforces the existence of a single fixed point ($U_\perp = 0$,$m_\perp = 0$), which corresponds to the disordered phase. For $\pi < \pi_c = 2\left(\omega_\perp^2 + D\right)$, the disordered phase is stable; otherwise, it is unstable.

NICA limit cycle

We can apply the method of multiple-scales once again to compute the amplitude of the nonlinear NICA limit cycle emerging as π exceeds π_c (see Appendix L). For $\pi = \pi_c + \delta$, with $\delta \ll 1$, the disordered phase turns unstable through a Hopf bifurcation, and $U_\perp$ and $m_\perp$ oscillate according to:

$$\begin{pmatrix} U_\perp(t,T) \\ m_\perp(t,T) \end{pmatrix} = A(T)\begin{pmatrix} a \\ 1 \end{pmatrix} e^{i\Omega t} + A^\star(T)\begin{pmatrix} a^\star \\ 1 \end{pmatrix} e^{-i\Omega t}, \tag{7.47}$$

where $a = 2\left(1 - i\sqrt{\mu}\right)$, $\mu = D/\omega_\perp^2$, $\Omega = \sqrt{D\omega_\perp^2}$, and where the complex number $A(T)$ depends on the slow timescale T and is solution of the amplitude equation:

$$\frac{1}{\omega_\perp^2}\frac{d|A|}{dT} = |A|\frac{\delta}{\omega_\perp^2}\frac{3+2\mu}{4\left(1+\mu\right)} - |A|^3\frac{3\mu}{2}. \tag{7.48}$$

Eq. (7.48) is the normal form of a supercritical Hopf bifurcation: for $\delta < 0$, the only stable solution is $|A| = 0$, and for $\delta > 0$, the linear Hopf instability leads the system to a nonlinear limit cycle whose amplitude is given by Eq. (7.48), and is set by the balance of activity, noise and elasticity. Importantly, in contrast with SCO, at the level of homogeneous solutions, we find that the transition from the disordered phase to NICA is continuous.

7.5.2 Fixed points with a polarizing field

We look for the fixed points of Eqs. (7.45), i.e., in the presence of a polarizing field along $\hat{\boldsymbol{e}}_\parallel$. We find only one, which satisfies ($m_\perp = 0$, $m_\parallel > 0$, $U_\perp = 0$, $U_\parallel = \pi m_\parallel/\omega_\parallel^2$), where the value of $m_\parallel$ is imposed by Eq. (7.45d):

$$Dm_\parallel = \frac{1 - m_\parallel^2}{2} g_\alpha \varepsilon. \tag{7.49}$$

The equilibrium magnetization, $m_\parallel^0(g_\alpha, D)$, for which noise balances the polarization by gravity, can be written as follows:

$$m_\parallel^0 = -\frac{D}{g_\alpha \varepsilon} + \sqrt{\left(\frac{D}{g_\alpha \varepsilon}\right)^2 + 1}. \tag{7.50}$$

The equilibrium magnetization is solely a function of the ratio $g_\alpha\varepsilon/D$ (Fig. 7.15-a). For $g_\alpha\varepsilon/D \to +\infty$, $m_\parallel^0 \to 1$, while for $g_\alpha\varepsilon/D \to 0$, $m_\parallel^0 \to 0$. The crossover between these two regimes arises for $g_\alpha\varepsilon \simeq D$. We thus find a single fixed point corresponding to a FP or FD regime, depending on the noise amplitude.

7.5.3 Stability of the frozen phase

We now study the stability of the *frozen* fixed point discussed above. We denote $m_\perp = \delta m_\perp$, $m_\parallel = m_\parallel^0 + \delta m_\parallel$, $U_\perp = \delta U_\perp$, $U_\parallel = \pi m_\parallel^0/\omega_\parallel^2 + \delta U_\parallel$; where $m_\parallel^0$ is solution of Eq.

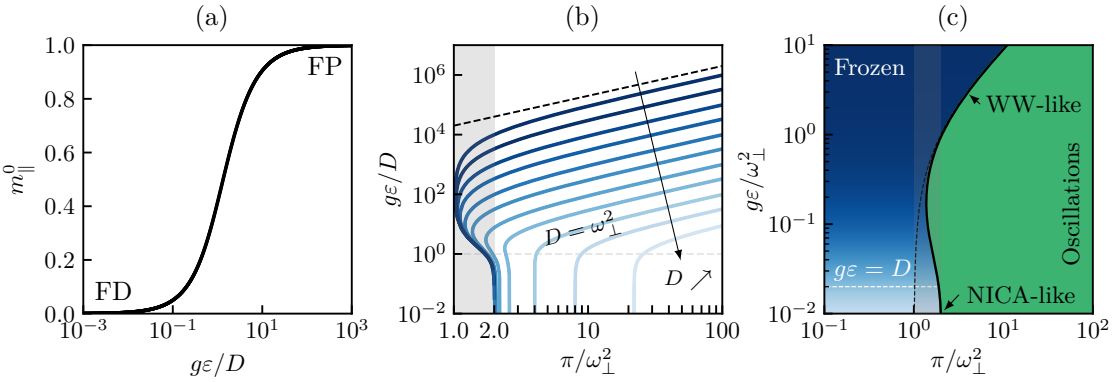


FIG. 7.15. **Toy model's results.** We restrict to $\omega_\perp^2 < \omega_\parallel^2$, and set $\omega_\perp^2 = 1$. (a) Equilibrium longitudinal magnetization in the *frozen* phase $m_\parallel^0$, solution of Eq. (7.50), as a function of $g\varepsilon/D$. (b) Toy model's instability threshold π_c as a function of $g\varepsilon/D$ for various noise intensity $D \in [\, 10^{-4}, 3.10^{-4}, 10^{-3}, 3.10^{-3}, 10^{-2}, 3.10^{-2}, 10^{-1}, 3.10^{-1}, 10^{0}, 3.10^{0}, 10^{1}\,]$, color-coded from dark to light blue as noise increases. The dashed black line represents a linear function. (c) Phase diagram. Noise amplitude is set to $D = 0.02$ to be consistent with experiments. The stability region of the *frozen* phase (FD and FP) is color-coded from dark to light blue as polarization decreases. The solid black line represents the stability threshold, as given by Eqs. (7.51); the dashed white line highlights $g\varepsilon = D$, and the dashed black line represents $\pi = \omega_\perp^2 + g\varepsilon$. The gray areas in (b-c) illustrate the range $\pi/\omega_\perp^2 \in [1, 2]$.

(7.50). At first order in small quantities, Eqs. (7.45) become:

$$\partial_t \delta U_\perp = \pi \delta m_\perp - \omega_\perp^2 \delta U_\perp, \tag{7.51a}$$

$$\partial_t \delta U_\parallel = \pi \delta m_\parallel - \omega_\parallel^2 \delta U_\parallel, \tag{7.51b}$$

$$\partial_t \delta m_\perp = -\delta U_\perp \left(\frac{1+m_\parallel^{02}}{2} \omega_\perp^2 \right) + \delta m_\perp \left(-g_\alpha \varepsilon m_\parallel^0 - D + \frac{1+m_\parallel^{02}}{2} \pi \right), \tag{7.51c}$$

$$\partial_t \delta m_\parallel = -\delta U_\parallel \left(\frac{1-m_\parallel^{02}}{2} \omega_\parallel^2 \right) + \delta m_\parallel \left(-g_\alpha \varepsilon m_\parallel^0 - D + \frac{1-m_\parallel^{02}}{2} \pi \right). \tag{7.51d}$$

The solutions to this general eigenvalue problem can be found numerically. Fig. 7.15-b shows the instability threshold π_c above which the fixed point becomes unstable (at least one eigenvalue has a positive real part), as a function of gravity and for various noise amplitudes.

For small noise $D \ll g_\alpha \varepsilon$, the system is polarized longitudinally, thus mapping with the single particle discussed in section 7.4. We find that the instability threshold reads $\pi_c = \omega_\perp^2 + g_\alpha \varepsilon$. On the contrary, for large noise $D \gg g_\alpha \varepsilon$, we find that the instability threshold is shifted toward larger values of activity $\pi_c = 2(\omega_\perp^2 + D)$. In both asymptotic cases (derived below), the instability threshold π_c is monotonous in g. However, for intermediate noise amplitude $D \simeq g_\alpha \varepsilon$, given that $D < \omega_0^2$, we find a non-monotonous variation of the instability threshold, which first decreases with gravity and then increases back (Fig. 7.15-b). This behavior is at the origin of PIR. Note that the above results do not depend on $\omega_\parallel^2$, as soon as $\omega_\parallel^2 \geq \omega_\perp^2$.

Asymptotic cases

Bifurcation in π in the limit $g_\alpha \varepsilon / D \ll 1$. Let us consider that noise is large as compared to gravity. In that case, from Eq. (7.49), $m_\parallel^0 = 0$, and the system is disordered. Eqs. (7.51) transform into:

$$\partial_t \delta U_\perp = \pi \delta m_\perp - \omega_\perp^2 \delta U_\perp, \tag{7.52a}$$

$$\partial_t \delta U_\parallel = \pi \delta m_\parallel - \omega_\parallel^2 \delta U_\parallel, \tag{7.52b}$$

$$\partial_t \delta m_\perp = -\delta U_\perp \omega_\perp^2/2 + \delta m_\perp \left(\frac{\pi}{2} - D \right), \tag{7.52c}$$

$$\partial_t \delta m_\parallel = -\delta U_\parallel \omega_\parallel^2/2 + \delta m_\parallel \left(\frac{\pi}{2} - D \right). \tag{7.52d}$$

Note that the transverse and longitudinal directions completely decouple. Without loss of generality, we focus on the transverse direction. Eqs. (7.52a) and (7.52c) reduce to the following eigenvalue problem:

$$\lambda^2 - \lambda \left[\frac{\pi}{2} - \left(\omega_\perp^2 + D \right) \right] + D\omega_\perp^2 = 0. \tag{7.53}$$

And we recover the result discussed in chapter 5 for the disordered phase stability. The disordered phase is stable for $\pi < \pi_c = 2(\omega_{\min}^2 + D) = 2(\omega_\perp^2 + D)$, unstable otherwise. Note the importance of the factor $1/2$ found in the derivation of the coarse-grained equations.

Bifurcation in π in the limit $g_\alpha\varepsilon/D \gg 1$. Let us consider that noise is small as compared to gravity. In that case, from Eq. (7.49), $m_\parallel^0 = 1$, and the system is polarized. Eqs. (7.51) transform into:

$$\partial_t \delta U_\perp = \pi \delta m_\perp - \omega_\perp^2 \delta U_\perp, \tag{7.54a}$$

$$\partial_t \delta U_\parallel = \pi \delta m_\parallel - \omega_\parallel^2 \delta U_\parallel, \tag{7.54b}$$

$$\partial_t \delta m_\perp = -\delta U_\perp \omega_\perp^2 + \delta m_\perp \left(\pi - g_\alpha \varepsilon\right), \tag{7.54c}$$

$$\partial_t \delta m_\parallel = -\delta m_\parallel g_\alpha \varepsilon. \tag{7.54d}$$

Once again, the transverse and longitudinal directions decouple. Along the longitudinal direction, the two eigenvalues are strictly negative. However, along the transverse direction, we find the following eigenvalue problem:

$$\lambda^2 - \lambda \left[\pi - \left(\omega_\perp^2 + g_\alpha \varepsilon\right)\right] + g_\alpha \varepsilon \omega_\perp^2 = 0. \tag{7.55}$$

And we recover the result discussed in section 7.4. The FP phase is stable for $\pi < \pi_c = \omega_\perp^2 + g_\alpha \varepsilon$, unstable otherwise.

Phase diagram

Considering a value of noise consistent with experiments, $D = 0.02$, we solve numerically the eigenvalue problem Eqs. (7.51) and draw the phase diagram illustrated in Fig. 7.15-c. For low enough activity/gravity, the system is *frozen*, and the longitudinal polarization increases with gravity at $g\varepsilon = D$, when the FD phase transforms into the FP phase. As gravity or activity exceeds a certain threshold, the system crosses the stability limit of the *frozen* phase, and the system starts oscillating in the transverse direction. In experiments, the presence of angular noise allows for PIR for $W = 4$, because in that case $1 < \pi/\omega_{\perp,1}^2 < 2$, while for $W = 2$ and $W = 3$, $\pi/\omega_{\perp,1}^2 > 2$.

7.5.4 Beyond fixed points

As activity increases, the *frozen* phase turns unstable. An exact description of the dynamical phases setting in as a function of gravity and activity is still lacking. The vast majority of the technical challenge comes from the non-degeneracy of the two modes $|\boldsymbol{\varphi}_\perp\rangle$ and $|\boldsymbol{\varphi}_\parallel\rangle$, which, already at the single-particle level and at zero gravity, leads to elliptic regimes E_n, which are out of reach analytically (see Appendix I and [181]). Yet, it is possible to determine qualitatively the nature of the dynamical regime which sets in close to the instability, in the limiting cases of large enough and small enough gravity.

For large enough gravity, $g\varepsilon/D \gg 1$; and below the instability $\pi_c = \omega_\perp^2 + g\varepsilon$, the system is FP, $m_\parallel^0 \to 1$. In this limit, the coarse-grained model (Eqs. (7.44)) maps with the single particle in an elliptic harmonic potential with a polarizing field. We studied this model in the degenerate case above. In the non-degenerate case, little can be done. However, we have seen that the longitudinal rigidity plays no role in the linear instability of the FP phase, as illustrated by the decoupling of the longitudinal and transverse linearized equations. Therefore, the dynamical regime setting in at the instability threshold for large enough gravity has to be qualitatively analogous to regime WW (Fig. 7.15-c, top). The SWW regimes observed in the square lattices at large gravity (Figs. 7.6 and 7.8) convincingly demonstrate the qualitative similarity with the regime WW in the symmetric single-particle (Figs. 7.10-e and f).

For very small gravity, $g\varepsilon/D \gg 1$; and below the instability $\pi_c = 2(\omega_\perp^2 + D)$, the system is FD, $m_\parallel^0 \to 0$. As activity increases and exceeds the stability threshold π_c, the system exhibits transverse oscillations which emerge via a transition to NICA (Fig. 7.15-c, bottom). As activity increases even further, the transverse polarization increases because NICA develops, and the coarse-grained model resembles more and more the single-particle in an elliptic harmonic potential. Assuming we can neglect the polarizing field for small enough gravity, we anticipate the emergence of collective elliptic regimes for $\pi > \omega_\parallel^2$ (see Appendix I), so-called SE_n, which are analogous to the elliptic regimes E_n in the plane $(|\boldsymbol{\varphi}_\perp\rangle,|\boldsymbol{\varphi}_\parallel\rangle)$. Interestingly, such SE_n regimes might be seen as the generalization of the GAR regime[12] to an arbitrary pair of non-degenerated normal modes.

7.6 Conclusion

Let us summarize here the main results of this chapter.

First, we have introduced a new CA regime, NICA, which corresponds to a spontaneous actuation of the lowest-energy mode of a structure at large enough activity. In contrast with SCO and GAR, NICA allows for periodic activation of a single normal mode, thanks to angular noise. Using multiple-scale analysis, we found the explicit expression of the NICA limit cycle emerging as π exceeds $\pi_c = 2(\omega_0 + D)$, the stability threshold of the FD phase. In contrast with SCO, at the level of homogeneous solutions, the transition from the FD phase to NICA is continuous.

We also introduced gravity-induced polarization, a tool to apply homogeneous polarizing fields to model active solids. This new ingredient induces a torque in the polarity dynamics of the active units, which reorients them in the direction opposite to the gravity force, and is analogous to a change of Galilean frame of reference. Therefore, in the presence of a polarizing field, both the positional and orientational degrees of freedom have a reference configuration. Applying polarizing fields to triangular and square lattices, we find that both NICA and SCO regimes transform into SWW regimes, and eventually, large enough polarizing fields stabilize the FP regime. These observations are well captured by a single particle with a polarizing field. We performed the linear stability analysis of the only remaining fixed point in the presence of gravity, the FP regime, and found a Hopf bifurcation at $\pi_c = \omega_0^2 + g\varepsilon$. Close to the exceptional point, the system maps with the underdamped nonlinear pendulum, whose orbits are selected via a small energy drift. The boundary $\pi^\star = \omega_0^2 + 3g\varepsilon$ separates the CO from the WW regimes, and is found analytically, in agreement with experimental and numerical observations.

Crucially, we also find that polarization decreases the activity threshold for CA, leading to PIR. We rationalized this observation using the coarse-grained model, and demonstrated that PIR is inherited from the differential stability of the FD and FP phases. Finally, we determined qualitatively the phase diagram of the coarse-grained model restricting to homogeneous solutions with a pair of non-degenerated normal modes. Much work remains to be done to understand precisely how SCO and SE_n regimes connect to the other regimes at the collective level.

The study of active solids with a polarizing field offers interesting and powerful analogies,

[12]For GAR regimes, the rotation mode plays the role of the soft mode of the elliptic potential.

and allows for a better control of the collective behaviors emerging in such systems. Moreover, the coupling between the polarity dynamics of active units and an external field is biologically relevant. Indeed, cells can respond to various environmental cues, and in many cases these cues induce directed cell migration towards or away from these signals [188]. Typical realizations are chemotaxis or galvanotaxis. This may allow for strong connections between this chapter and genuine biological systems, where external fields play essential functions in wound-healing or embryogenesis [188].

Chapter 8

Perspectives

8.1 Counter-rotating squares mechanism

Auxetic materials exhibit the very unusual properties of becoming wider when stretched and narrower when squashed: they have negative Poisson's ratios. Consider the paradigmatic metamaterial realizing a negative Poisson's ratio (Fig. 8.1), which is based on a mechanism consisting of counter-rotating hinged squares [102, 189–194]. As this mechanism is actuated, the system compresses in both directions, up to reaching half its initial area. When the counter-rotating squares touch each other, we say the system has *reconfigured* (Fig. 8.1-d). In contrast, in the initial state, we say the system is completely *open* (Fig. 8.1-a).

In the following, we demonstrate that active units embedded at the nodes of a square lattice spontaneously actuate the counter-rotating square mechanism, first in the case of quasi-freely-rotating hinges, and then for a square spring network.

8.1.1 Case of a zero mode

Let us start with the simplest instance of the counter-rotating square mechanism: a 2×2 square lattice. To make this structure active, we combine four active elastic building blocks. However, instead of connecting the blocks with springs, we embed them into a frame made of rigid squares, connected by very flexible hinges (Fig. 8.2-a). The frame's

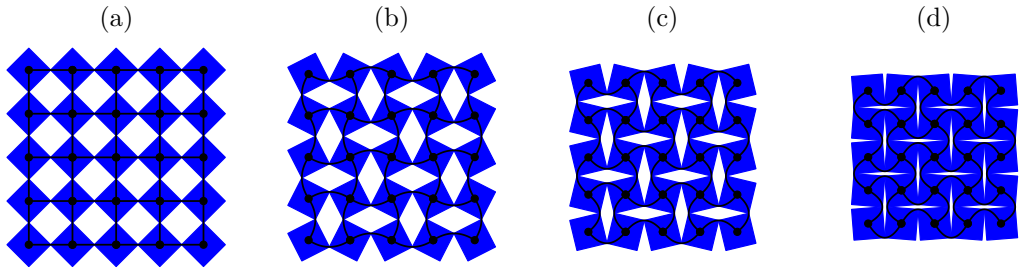


FIG. 8.1. **Counter-rotating squares mechanism.** Mechanism consisting of counter-rotating hinged squares. From left to right, the mechanism is more and more actuated, and the compression in both directions illustrates the negative Poisson's ratio of the structure. At (a), we say the structure is *open*, and we say it has *reconfigured* in the limiting case where the squares touch each other (d). The solid black lines illustrate the mapping with a square lattice of bending springs.

squares are designed to fit the active elastic building blocks perfectly, so this system is a genuine realization of the metamaterial shown in Fig. 8.1, doped at every square center with an active unit. The 3*d* printed frame (3 mm thick) is made of two materials. On the one hand, the square's bulk is made of VeroWhite© resin, a stiff material that does not deform under the action of the hexbugs; on the other hand, the connections between the squares are made of Agilus©[1], a very soft plastic that plays the role of the freely rotating hinges. However, we say they are only quasi-freely rotating because the material has finite viscoelastic properties. The frame resting on top of the active elastic building blocks, the hexbugs support an additional mass that slightly changes the physics, resulting in a smaller angular diffusion coefficient for the active units' orientations. Finally, to kill the collective translation and rotation regimes described in chapter 4, we pin a given node of the network, freezing its positional and rotational degrees of freedom.

Once the three remaining nodes are doped with active agents, the counter-rotating squares mechanism is spontaneously actuated back-and-forth (Figs. 8.2-a to d). This CA regime is best illustrated when considering the area spanned by the system as a function of time (Fig. 8.2-e). We find that the latter alternates between two values, a large area corresponding to the system completely *open* (Fig. 8.2-a), and a smaller area, half of the large one, corresponding to the two system's reconfigurations, clockwise (Fig. 8.2-b) or counter-clockwise (Fig. 8.2-d) around the pinning point. Note that the CA regime observed is not completely periodic: while the reversals between two reconfigurations are very similar, the time spent trapped in the states reconfigured fluctuates.

These observations can be understood considering that this system is rigid and exhibits a single *bounded* zero mode (defined below). First, the hinges are very soft, therefore

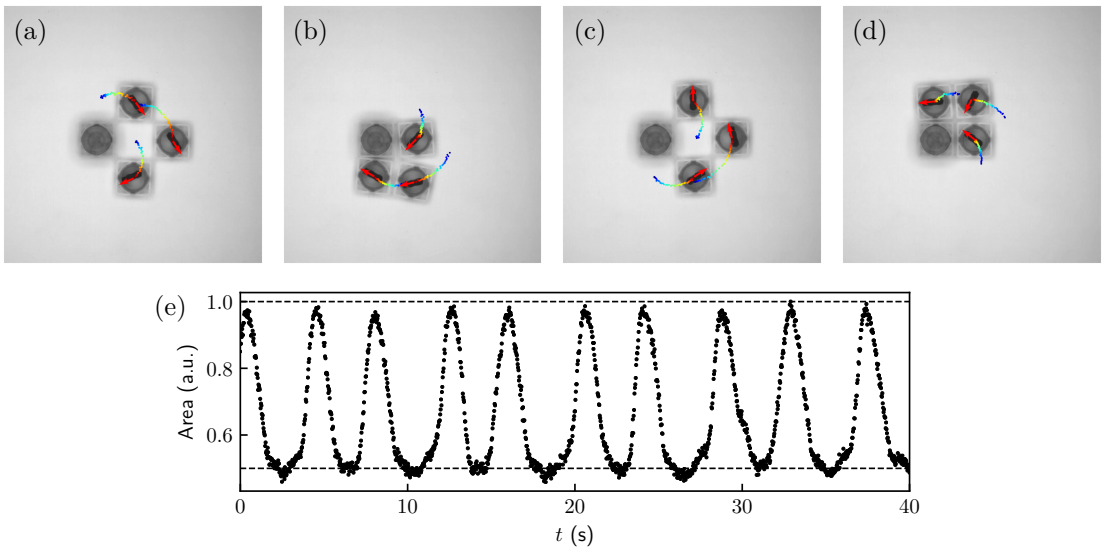


FIG. 8.2. **Spontaneous back-and-forth actuation of the counter-rotating squares mechanism for a hinged square lattice.** Collective actuation of an active 2×2 hinged square lattice with a single embedded node ($N = 3$). (a-d) Snapshots of the dynamics; time increases from left to right; red arrows: polarities $\hat{\boldsymbol{n}}_i$; trajectories color-coded from blue to red by increasing time. (e) Area of the polygon defined by the outer particles as a function of time. The area is normalized by its maximum. The dashed black lines represent the system completely *open* and completely *reconfigured*.

[1] Agilus30, FLX935.

the auxetic mode can safely be considered a zero mode. Being the only one of this rigid structure, according to the results of chapter 4, any perturbation of the polarity field along that mode explodes, and thus the system must actuate it. However, once the metamaterial reaches its reconfigured state, the auxetic mode becomes rigid in the direction chosen initially, because of steric repulsion, and motion stops. The auxetic zero mode is *bounded*: it consists of a flat elastic potential energy landscape with infinite energy barriers on both sides, corresponding to the two reconfigurations. Angular noise then allows for the polarity field to relax and fluctuate. Once the projection of the polarity field on the auxetic mode reverses direction, it amplifies via self-alignment, and the motion starts the other way around. Note the essential role played by angular noise during the motion reversals. This scenario explains well the experimental observations. Note that this CA can also be interpreted as a NICA regime. Indeed, a single normal mode is activated back and forth, and the reversals are triggered by angular noise. However, the activated mode is not a simple harmonic mode, but a *bounded* zero mode, with a strongly non-linear response.

The above system convincingly demonstrates that self-aligning active particles spontaneously actuate the counter-rotating square mechanism in the case where it is a bounded zero mode of the structure. Let us now show that this observation also holds in the case of a soft harmonic auxetic mode.

8.1.2 Case of a harmonic mode

To construct a harmonic auxetic mode, we return to the initial design and connect the active elastic building blocks with *stiff* springs in a 5×5 square lattice (Fig. 8.3-a). As shown in Fig. 8.1, a square spring network exhibits the same auxetic mode as counter-rotating hinged squares, with a direct mapping between the two when the springs can

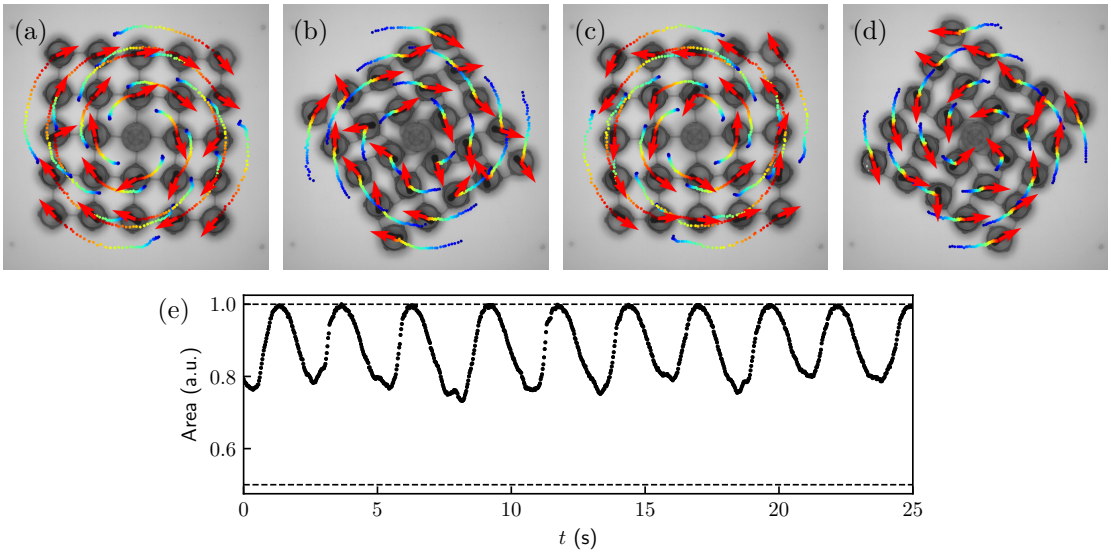


FIG. 8.3. **Spontaneous back-and-forth actuation of the counter-rotating squares mechanism for a spring square lattice.** Collective actuation of an active 5×5 spring square lattice with embedded central pinning ($N = 24$). (a-d) Snapshots of the dynamics; time increases from left to right; red arrows: polarities $\hat{\boldsymbol{n}}_i$; trajectories color-coded from blue to red by increasing time. (e) Area of the polygon defined by the outer particles as a function of time. The area is normalized by its maximum. The dashed black lines represent the system completely *open* and completely *reconfigured*

only bend [194]. However, when the springs' bending rigidity is finite, the rotating squares mechanism transforms into a harmonic mode: its actuation accumulates elastic potential energy in bending the springs. Finally, we again prevent the system from collectively rotating or translating by embedding the central node.

Once doped with active agents, the active square network spontaneously actuates back-and-forth the auxetic mode (Figs. 8.3-a to d). First, we find that the CA regime is more periodic than the 2×2 network (Fig. 8.3-e). Second, the system only partially reconfigures (Figs. 8.3-b and d). This is clear when considering the system's area as a function of time: the reconfiguration is only halfway at the motion reversal. This last observation has two origins: (i) the auxetic mode is harmonic, and thus motion stops when the elastic and active forces balance; (ii) the counter-rotations decay away from the center, which is reminiscent of the observations of *Coulais et al.* [194]. At the passive level, mechanism-based metamaterials have an intrinsic length scale that depends on the ratio between the shear and bending moduli of the springs, and diverges in the pure mechanism limit. Such a length scale quantifies the spatial extension of the auxetic mode, which localizes near inhomogeneities such as boundaries, here the embedded center. Therefore, when the springs used have a finite shear modulus, like in the experiments, the auxetic mode must decay away from the center, bounding the maximum reconfiguration level. Indeed, when steric repulsion stops the motion of the first layer around the pinning point, the second layer has not entirely reconfigured.

Let us make a few final comments. First, the above system has the potential to become a tunable and truly autonomous active mechanical metamaterial. It is not yet clear, however, if this CA regime, and in particular the turnarounds, are the results of angular noise only, similarly to the NICA regimes discussed in chapter 7, or if other modes of the system contribute to these events, similarly to the GAR regimes discussed in chapter 6. More numerical work is required to answer this intriguing question. Eventually, it could be interesting to study the effect of noise on the spontaneous activation of bounded harmonic and zero modes; for example, by combining the present active solid's framework and first-passage time tools to predict the turnarounds and the period of the CA regime in large systems.

8.2 Mechanical response

In this section, we explore the mechanical response of active elastic structures in simple settings. These experiments were realized in collaboration with Corentin Coulais and Jonas Veenstra during a visit to Amsterdam in February 2022.

8.2.1 Setup

We study the mechanical response of a 2×10 square lattice pinned at both ends. The square lattice is oriented along $\hat{\boldsymbol{e}}_y$, and the top end is sheared back-and-forth along $\hat{\boldsymbol{e}}_x$ using a custom translating stage (Fig. 8.4-a). The translating stage imposes motion speed from 6 cm/s to 18 cm/s, such that the top end moves alternatively to the left or right with amplitude h and constant speed V (Fig. 8.4-b). Moreover, the vertical separation W between the two force sensors is larger than the rest length of the spring network: the whole structure is elongated by a factor $\alpha \simeq 0.09$. The translating stage is mounted with force sensors on both ends of the structure. On the one hand, the top, moving force sensor measures the shear force exerted on the moving pinning point,

$F_m = \boldsymbol{F}_m \cdot \hat{\boldsymbol{e}}_x$, where $\boldsymbol{F}_m$ is the total force exerted on the moving pinning point. On the other hand, the bottom, static force sensor measures the shear force exerted on the

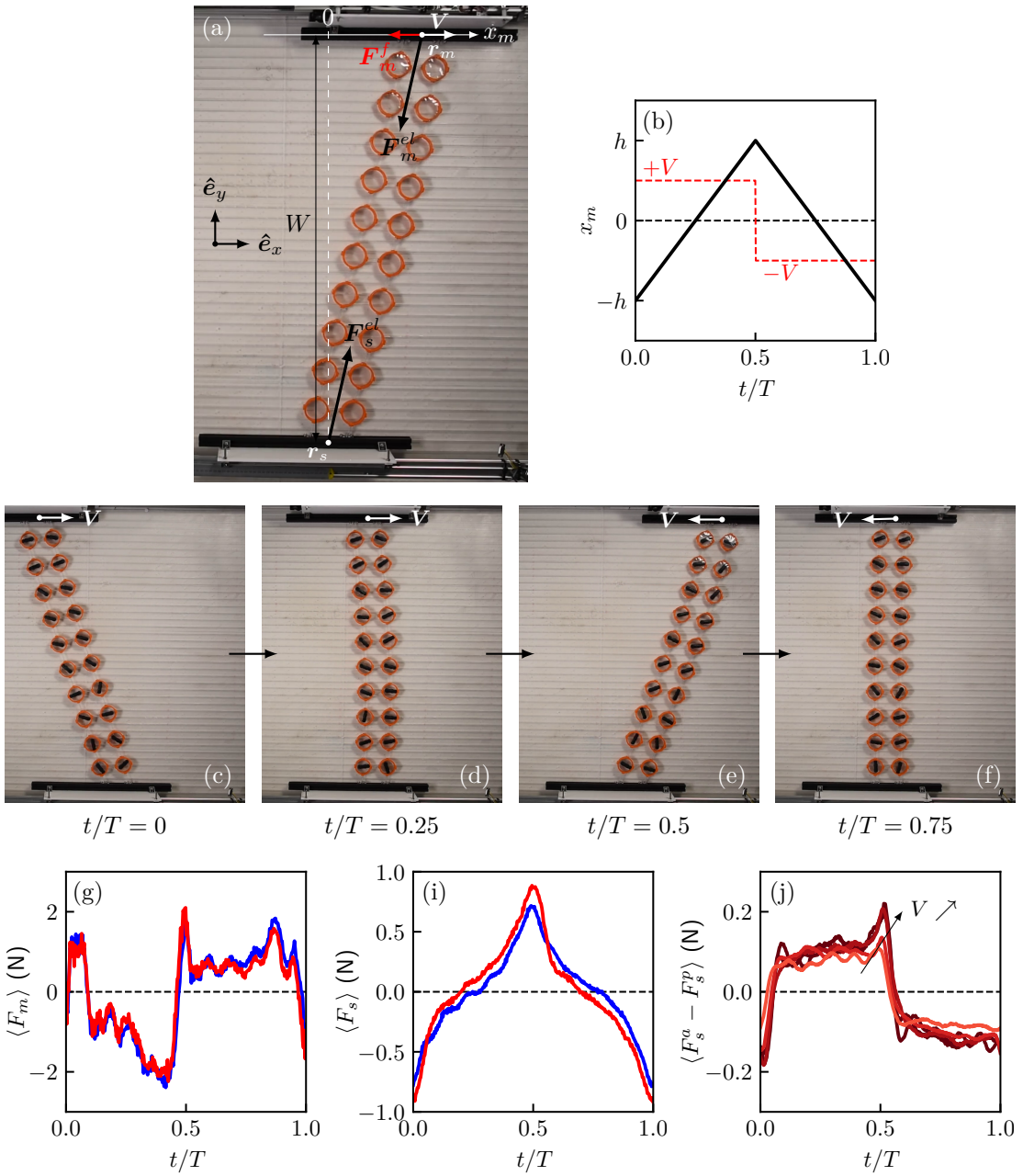


FIG. 8.4. **Mechanical response of active and passive square lattices.** (a) Experimental setup in the passive case and notations. The ladder is pinned at both ends. The bottom pinning is the static probe, fixed at $\boldsymbol{r}_s$, and measures $F_s = \boldsymbol{F}_s \cdot \hat{\boldsymbol{e}}_x$. In contrast, the top pinning is the moving probe, measuring $F_m = \boldsymbol{F}_m \cdot \hat{\boldsymbol{e}}_x$. (b) Motion of the moving probe (black line) as a function of time. The dashed red line represents the instantaneous velocity of the moving probe. For $0 < t < T/2$ (resp. $T/2 < t < T$), the moving probe travels to the right (resp. left) with speed V. (c-f) Snapshots of the mechanical test for an active square lattice with $V = 18$ cm/s, at different times. The white arrows represent the instantaneous velocity of the moving probe. (g-i) Average shear force measured with the moving (g) and static (i) probes as a function of time; in the passive (blue line) and active (red line) cases, for $V = 18$ cm/s. (j) Average difference between the active and passive cases for the shear force measured by the static probe, for different speeds $V \in [6, 9, 12, 15, 18]$ cm/s. Curves are color-coded from light to dark red as V increases.

static pinning point, $F_s = \boldsymbol{F}_s \cdot \hat{\boldsymbol{e}}_x$, where $\boldsymbol{F}_s$ is the total force exerted on the static pinning point. The static probe only measures the elastic forces exerted by the network, $\boldsymbol{F}_s = \boldsymbol{F}_s^{el}$, while the moving probe is also submitted to friction, opposite to the motion direction, $\boldsymbol{F}_m = \boldsymbol{F}_m^{el} + \boldsymbol{F}_m^{f}$ (Fig. 8.4-a). Finally, note that $\boldsymbol{F}_s^{el}$ and $\boldsymbol{F}_m^{el}$ are the opposite of one another only in the passive and static case. We measure the shear forces exerted by the active elastic network on the static and moving probes for 20 shear periods at $V = 18$ cm/s (Figs. 8.4-c to f), and average the signals (Fig. 8.4-g and i, red curves). Note that we can perform the same measurements in the passive case, i.e. running the mechanical tests with empty annuli (Fig. 8.4-g and i, blue curves).

Let us discuss a critical aspect of comparing measurements performed in the passive and active cases: solid friction. When the structure is doped with active agents, it does not exhibit solid friction with the substrate as it is constantly vibrated by the robots. An accurate comparison thus requires killing the static friction in the passive case. Importantly, we can take advantage of the translating stage designed by Corentin and Jonas: it is constructed on top of an air table, that blows air vertically through little holes that are small enough not to affect the hexbugs propulsion. For every measurement in the passive case, we switch on this feature, and switch it off in the active case.

Next, we separate the discussion into two. We first explain the measurements performed in the passive case, and then elaborate on the differences observed in the active case.

8.2.2 Discussion

Passive case

The response measured in the passive case can largely be explained by considering the complete nonlinear elasticity of the spring network. Let us consider that the system has no inertia, or that the measurements are performed quasi-statically. The elastic forces exerted by the structure on the probes are equal and opposite, and proportional to the elongation of the structure. The proportionality constant can be found explicitly by combining the spring stiffness in series and parallel. Finally, the moving probe also measures an effective friction force, opposite to the direction of motion. Altogether, the forces on the moving and static probes can be written as:

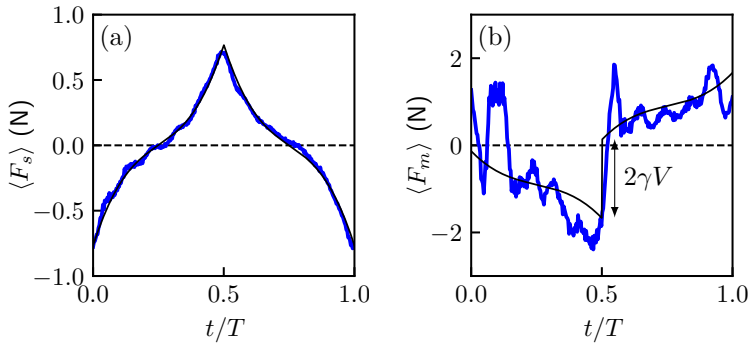


FIG. 8.5. **Mechanical response of passive square lattices.** Average shear force measured with the static (a) and moving (b) probes as a function of time, as given by the experimental measurements in the passive case, for $V = 18$ cm/s (blue line); and by Eqs. (8.1) (black line), with $\gamma = 5$ kg.s^{-1}.

$$F_s^{el} = \kappa \left(\sqrt{x_m^2 + W^2} - L_0 \right) \sin \alpha, \tag{8.1a}$$

$$F_m^{el} = -\kappa \left(\sqrt{x_m^2 + W^2} - L_0 \right) \sin \alpha - \gamma V, \tag{8.1b}$$

where κ (resp. L_0) is the system's stiffness (resp. rest length), γ is a friction coefficient, and α is the angle of the structure with the vertical axis when the moving probe is at x_m ($\tan \alpha = x_m/W$). Notably, we already know all the parameters of the Eqs. (8.1), except for the effective friction coefficient on the moving probe γ; an estimate of which is obtained by manually adjusting Eq. (8.1b) to the experimental data. We find a very good correspondence between the measurements and the prediction for the static probe (Fig. 8.5-a). In contrast, Eq. (8.1b) cannot be perfectly adjusted to the measurements performed on the moving probe (Fig. 8.5-b). We attribute this discrepancy to the presence of inertia, coming from the mass of the moving probe but also from the elastic structure being tested, which induces oscillations of the force measured, more pronounced on the moving than on the static probe. Overall, the response measured on the moving (resp. static) probe is dominated by friction (resp. elasticity of the network).

Influence of activity

When the structure is doped at every node with active units, we find that the signal of the moving probe is not significantly different from the passive case (Fig. 8.4-g). Conversely, the signal on the static probe sheds light on the influence of activity (Fig. 8.4-i). We measure the average difference of shear force between the active and passive cases for the static probe, $\langle F_s^a - F_s^p \rangle$, at different speeds V (Fig. 8.4-j). During the first half-period, the moving probe translates to the right. At the same time, the active force measured on the static probe is larger in the active than in the passive case, indicating that the active particles, polarized toward the direction of motion through self-alignment (Fig. 8.4-d), contribute to push/pull to the right the static probe. At $t = T/2$, the moving probe abruptly changes direction. During a short transitory regime, the excess of force measured in the active case reorients toward the new direction of motion, and ends up saturating in the opposite direction, contributing once again to the motion imposed by the moving probe. Therefore, activity might be interpreted as a negative friction coefficient, relaxing toward the direction of motion. This is clear when comparing the response measured on the moving probe, dominated by friction, and $\langle F_s^a - F_s^p \rangle$: in first approximation, they are simply the opposite of each other.

Interestingly, we measure a small dependence of $\langle F_s^a - F_s^p \rangle$ on the motion speed. First, note that the transitory regime's duration does not depend on the motion speed (Fig. 8.4-j), thus the latter happens over a characteristic distance, that is typically 2.6 cm. This value clearly corresponds to the alignment length of the hexbugs, which reorient toward the new direction of motion through *self-alignment*, as measured in chapter 2. Second, the larger the motion speed, the larger the average negative friction, with a saturation of $\langle F_s^a - F_s^p \rangle$ to typically 0.1 N at large speed. This observation can be interpreted at the coarse-grained level. Remember from chapter 7 that a change of Galilean frame of reference induces a net polarization toward the direction of motion, which balances with the relaxation induced by angular noise. Here, the system is forced to translate to the right or left, with a linear velocity profile, maximum at the moving probe, and zero at the static probe. The larger the imposed motion speed, the larger the polarizing field, thus the larger the active force contributing to the direction of motion. This is confirmed by visual inspection of the orientational order for different velocities: the larger the motion speed, the larger the polarization. Note that this polarization is also expected to

saturate, as discussed in chapter 7, consistently with experimental observations.

The above interpretation of activity in simple terms of a negative friction coefficient is not completely satisfying. *Scheibner et al.* demonstrated the existence of *odd* elastic moduli (for example, a coupling between the two shear deformations) in active solids that conserve linear momentum [125]. This motivates constructing an experimental system that could measure such *odd* moduli, which is not the case with the above system. Altogether, more theoretical and experimental work is required to understand the mechanical properties of *dry* and *polar* active solids.

8.3 Walking grains experiments

In this section, we exploit the *walking grains* experimental setup to demonstrate the possibility of downsizing our active solid's design principle, i.e. a network of annuli connected by coil springs and doped with active units.

8.3.1 Setup

The walking grains were already discussed in chapter 1, and were historically introduced as a model system of active liquids. They allowed for a better understanding of the mechanisms leading to CM [55–58], but also shed light on the $2d$ crystallization [92, 135] and mechanical pressure [136] of active systems. The experimental setup is made of two parallel and horizontal glass plates, the bottom one being vertically vibrated. In the gap between the two plates evolve little disks with a built-in polar asymmetry, which enables them to move persistently in the $2d$ plane (Fig. 8.6-b). The polar particles are micromachined copper-beryllium disks (diameter $d = 4$ mm) with an off-center tip and a glued rubber skate located at diametrically opposite positions (total height $h = 2$ mm). These two "legs", with different mechanical responses, endow the particles with a polar axis. Under proper vibration, the self-propelled polar (SPP) disks perform a persistent random walk, the persistence length of which is set by the vibration parameters. We also use plain rotationally invariant disks (same metal, diameter, and height), hereafter called the "isotropic" (ISO) disks, as a control to ensure that all the effects reported here are indeed due to the self-propulsion induced by the built-in polarity (Fig. 8.6-a).

The SPP walking grains have similar properties to the hexbugs: they are self-propelled along their polarity vector $\hat{\boldsymbol{n}}$, and the latter reorients toward the direction of motion via a *self-aligning* torque. The equations of motion for walking grains and hexbugs are thus the same at the effective level. However, the walking grains are less *active* than the hexbugs. First, the polar force they exert is way smaller than hexbugs[2], making it more complicated to find soft enough springs to construct the active elastic lattices. Moreover, the polarity dynamics of the walking grains is noisier, favoring the emergence of disordered regimes. Finally, the walking grains are more sophisticated to manipulate because of their small size, and are therefore also more sensitive to imperfections of the experimental conditions (parallelism and horizontality of the different plates, cleanliness, heterogeneity of the walking grains). For all the above reasons, we initially decided to use hexbugs as model active units. However, in this section, we show how the walking grains can still be used as active units by downsizing the design principle introduced in chapter 2.

[2]The polar force exerted by such bristle bots is typically proportional to their mass, and the walking grains are very light compared to hexbugs.

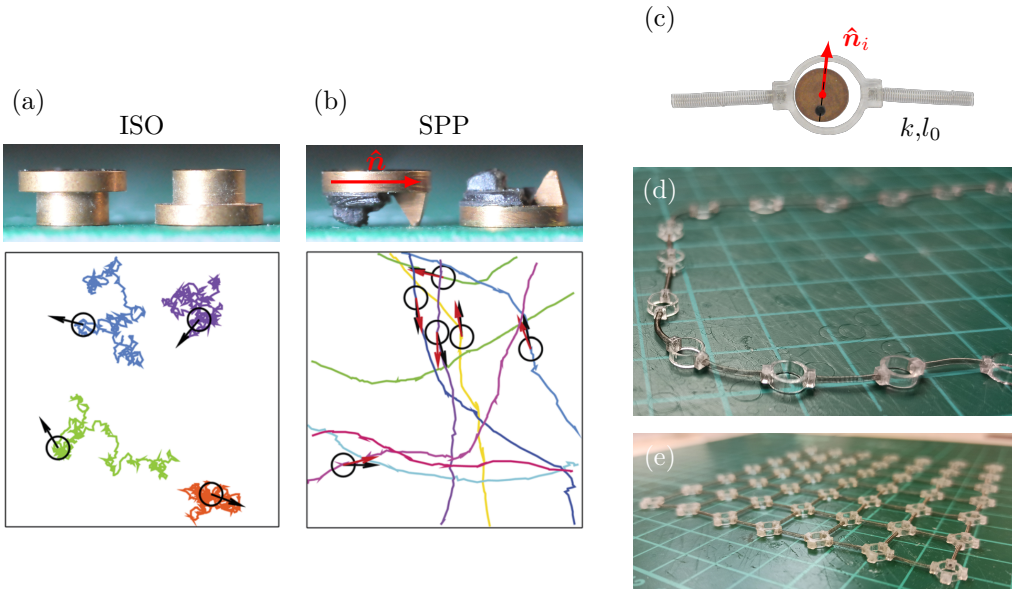


FIG. 8.6. **Walking grains-based active solids.** (a) Isotropic (ISO) grains. Under proper vertical vibration, the walker performs a random walk (bottom). (b) Self-propelled (SPP) walking grains: a hard metallic disc with an off-center tip and a glued rubber skate located at diametrically opposite positions (top); the velocity $\boldsymbol{v}$ is in general not perfectly aligned with the polarity $\hat{\boldsymbol{n}}$. Under proper vertical vibration, the walker performs a persistent random walk (bottom). (c) Design principle for the walking grains experiments: the active units exert polar forces along the polarity vectors $\hat{\boldsymbol{n}}_i$, and are embedded in $3d$ printed annuli connected with coil springs of stiffness k and rest length l_0. The black dot indicates the tail of the SPP walking grain. (d-e) The active elastic building blocks are combined into $2d$ lattices; (d) linear chain, (e) square lattice. The bottom panels of (a) and (b) and adapted from [55].

8.3.2 Design principle

The design principle again consists of $3d$ printed annuli, made of VeroClear© resin[3], with the same height as the walking grains, and 0.5 mm thick (Fig. 8.6-c). The internal diameter is slightly larger than the walking grains' diameter, allowing the units to rotate freely inside their cages. We use helical compression springs[4] (diameter: 1 mm, length: 10 mm) to connect the active elastic building blocks, attached manually with commercial glue inside a hole (diameter: 1.2 mm, depth: 1 mm) designed in the overhangs. We then construct different networks of active elastic building blocks, like linear chains (Fig. 8.6-d), square lattices (Fig. 8.6-e), and honeycomb lattices (Fig. 8.8).

We first optimize the geometry of the design principle to make the active elastic building blocks as active as possible. We explore a few parameters: the internal diameter of the annuli, denoted d_i, the gap between the two plates, denoted h, and the vibration parameters. This exploration was not completely systematic; however, we could find that the correct range of vibration frequency is $f = 95$ Hz, with an amplitude $\Gamma \simeq 2.7$, where $\Gamma = 2\pi f A/g$ is the dimensionless acceleration amplitude with respect to gravity. The best design, which *optimizes*[5] the spontaneous actuation of the lowest energy mode of a linear chain (see below), is $d_i = 4.4$ mm, for a gap $h = 2.5$ mm. For this final

[3]VeroClear© is a transparent resin with similar mechanical properties to PMMA.

[4]Schweizer Federntechnik, stiffness: 1 N/m, wire diameter: 50 μm, number of windings: 67.

[5]The one maximizing the projection of the polarity field on that mode, while keeping the angular noise as low as possible. The smaller d_i, the smaller the angular noise, but the larger the alignment length, thus the less active the structure. The *optimal* design is therefore a compromise.

design, we could estimate the value of the elasto-active coupling $\pi \simeq 5.10^{-3}$ (see below), highlighting that walking grains are less active than hexbugs, even considering hexbugs connected with *stiff* springs (see chapter 2). For the elasto-active coupling π to exceed the energy of some normal mode, we should consider larger structures than ever before.

Now, let us illustrate the collective dynamics observed in experiments for linear chains and large honeycomb lattices, which are still ongoing work, but illustrate the potential and generality of our design principle.

8.3.3 Linear chains

We construct linear chains composed of $N = 18$ active elastic building blocks, pinned at both ends (Fig. 8.7-a). The chain is oriented along $\hat{\boldsymbol{x}}$ (denoted $\hat{\boldsymbol{e}}_{\parallel}$), so that the equilibrium positions are $x_i = \alpha i$, $y_i = 0$. The parameter α is the ratio between the length of the springs in the equilibrium configuration l_{eq} and the natural length of the springs l_0. The chain thus bears a dimensionless tension $T = \alpha - 1$. The normal mode spectrum of linear structures was discussed in chapter 5. There are N eigenmodes along $\hat{\boldsymbol{e}}_{\parallel}$ (resp. $\hat{\boldsymbol{e}}_{\perp}$), which we denote $|\boldsymbol{\varphi}_{\parallel,k}\rangle$ (resp. $|\boldsymbol{\varphi}_{\perp,k}\rangle$) with eigenfrequencies $\omega_{x,k}$ (resp. $\omega_{y,k}$):

$$\boldsymbol{\varphi}^i_{\parallel,k} = \sqrt{\frac{2}{N+1}} \sin\left(\frac{jk\pi}{N+1}\right) \hat{\boldsymbol{x}}; \qquad \omega^2_{\parallel,k} = 4 \sin\left(\frac{k\pi}{2(N+1)}\right)^2, \tag{8.2a}$$

$$\boldsymbol{\varphi}^i_{\perp,k} = \sqrt{\frac{2}{N+1}} \sin\left(\frac{jk\pi}{N+1}\right) \hat{\boldsymbol{y}}; \qquad \omega^2_{\perp,k} = 4A_\alpha \sin\left(\frac{k\pi}{2(N+1)}\right)^2. \tag{8.2b}$$

Longitudinal (along $\hat{\boldsymbol{e}}_{\parallel}$) and transverse (along $\hat{\boldsymbol{e}}_{\perp}$) modes are thus locally-orthogonal. Moreover, modes with the same index k have the same norm on each site, so that we introduce $\varphi^i_k = \boldsymbol{\varphi}^i_{\parallel,k} \cdot \hat{\boldsymbol{x}} = \boldsymbol{\varphi}^i_{\perp,k} \cdot \hat{\boldsymbol{y}}$. Finally, in the limit $\alpha \to \infty$, which corresponds to infinite tension or zero-rest-length, $A_\alpha = 1 - \alpha^{-1} \to 1$ and the modes are degenerated: $\omega_{x,k} = \omega_{y,k} = \omega_k$ for $1 \leq k \leq N$.

For small tension, $\alpha \leq \alpha_c \simeq 1.1$, the system performs CA: the lowest energy mode, $|\boldsymbol{\varphi}_{\perp,1}\rangle$, is spontaneously activated back-and-forth (Fig. 8.7-h), resulting in transverse oscillations of the chain (Fig. 8.7-d). In contrast, for large enough tension $\alpha > \alpha_c$, the oscillation stops, and the system is frozen and apparently disordered (Figs. 8.7-g and k). The transition is best illustrated by considering the transverse condensation fraction $\sum_k \lambda_{\perp,k}$, where $\lambda_{\perp,k}$ is the condensation fraction on mode $|\boldsymbol{\varphi}_{\perp,k}\rangle$, as a function of tension (Fig. 8.7-b). We find that the low-tension CA regimes have an excess of transverse condensation fraction with respect to the large-tension frozen regimes, indicating that the spontaneous transverse oscillations induce self-alignment. However, note that the effect is relatively weak (only a few percent), because of the significant noise present in the experiments.

These observations agree with the results of chapter 7 concerning the spontaneous activation of a single normal mode in the presence of angular noise, i.e. Noise-Induced CA (NICA). Let us consider a large system with a single normal mode of energy ω_0^2. For $\pi < \pi_c = 2(\omega_0^2 + D)$, activity is too small and the system is *Frozen-Disordered* (FD). For $\pi > \pi_c$, the disordered phase becomes linearly unstable through a Hopf bifurcation, and a nonlinear NICA limit cycle of finite frequency $f \sim \sqrt{D\omega_0^2}$ and amplitude $A \sim \sqrt{\pi - \pi_c}$ branches-off continuously.

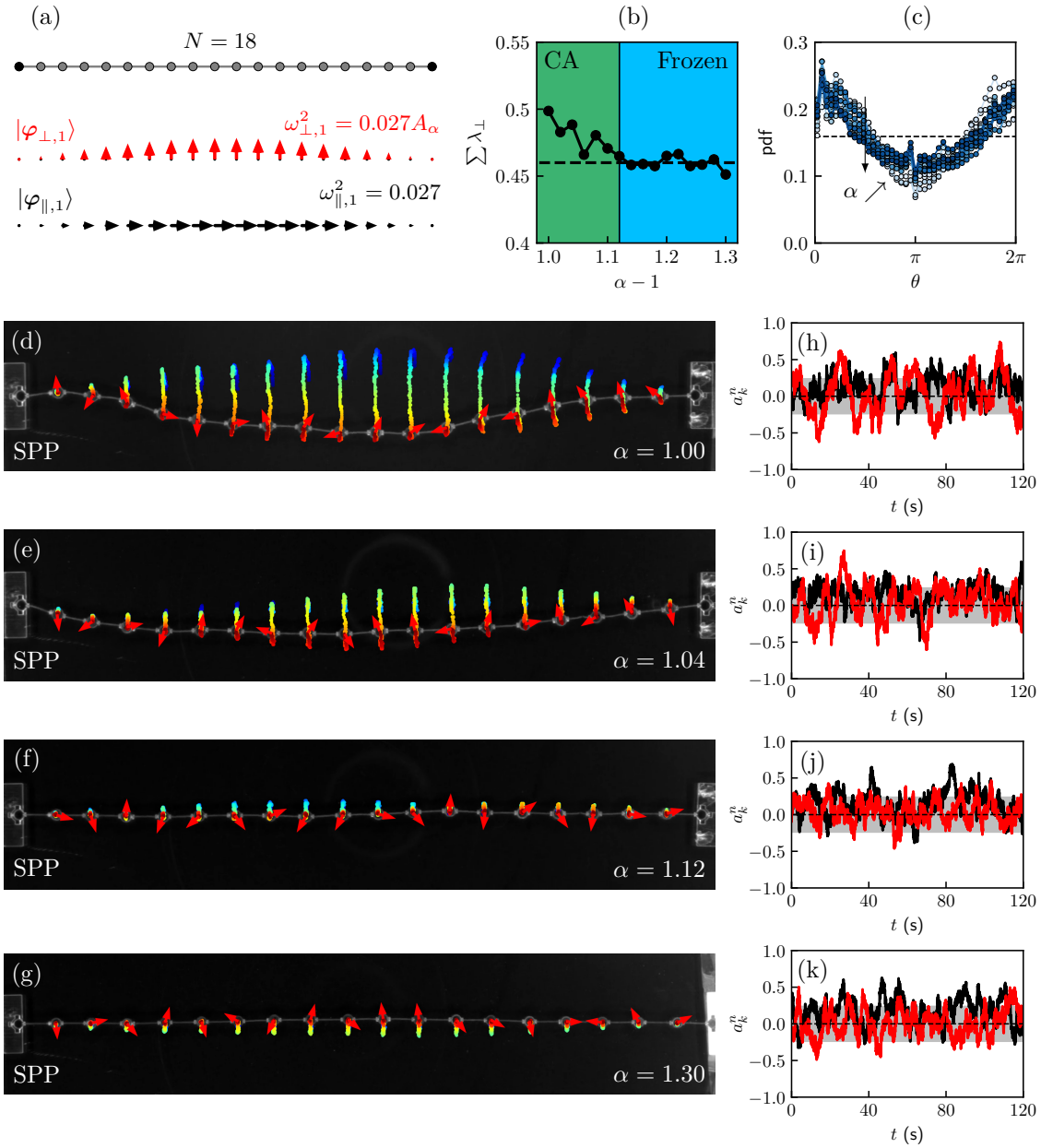


FIG. 8.7. **Transition to CA in walking grains-based active chains.** (a) Elastic structure cartoon, $N = 18$ (top), and sketch of the two lowest energy and most activated modes (bottom). (b) Transverse condensation fraction $\sum_{k\in\perp} \lambda_k$ as a function of tension $\alpha - 1$. Background colors code for the dynamical regime (light blue: frozen and disordered; dark green: CA) (c) Ensemble averaged probability density function of orientations θ; $\theta = 0$ (resp. $\theta = \pi/2$) represents the orientation parallel (resp. perpendicular) to the chain. Curves are color-coded from light to dark blue as tension increases. (d-g) Snapshots of the experiments for different tensions $\alpha - 1$; red arrows: polarities $\hat{\boldsymbol{n}}_i$; trajectories color-coded from blue to red by increasing time. (h-k) Polarity field projections on the two lowest energy modes as a function of time for the tensions indicated in (d-g). The solid black (resp. red) line represents the projection of the polarity field on mode $|\varphi_{\parallel,1}\rangle$ (resp. $|\varphi_{\perp,1}\rangle$). The gray areas illustrate the range inside which is expected to lie the polarizations for purely random spins, that is $\left[-1/\sqrt{N}, 1/\sqrt{N}\right]$.

Therefore, in the chains, the transition from the CA to the FD regime is attributed to the increase of the transverse modes' energy as tension increases. For $\alpha < \alpha_c$, $\pi > \pi_c = 2(\omega^2_{\perp,1} + D)$: the disordered phase is unstable and the system self-oscillates

along $|\boldsymbol{\varphi}_{\perp,1}\rangle$. As α increases, $\omega^2_{\perp,1}$ becomes larger and larger. For $\alpha > \alpha_c$, $\pi < \pi_c$, and the disordered phase is the only stable solution. Note that the selection of $|\boldsymbol{\varphi}_{\perp,1}\rangle$ over the other transverse modes in the CA regime is not completely trivial: at the linear level, without tension, they are all zero-modes. Mode $|\boldsymbol{\varphi}_{\perp,1}\rangle$ might be favored because it is relatively extended, or because of geometrical nonlinearities. Interestingly, the value of α at the transition gives an estimate of the elasto-active coupling for the walking grains active solids: $\pi \simeq 5.10^{-3}$.

However, this set of experiments exhibits a problem of horizontality. Indeed, the transverse condensation fraction does not converge toward 0.5 in the frozen regime, as expected from a disordered regime, but a smaller value, indicating that the polarity dynamics is biased toward the right end of the chain in the absence of motion (Fig. 8.7-b). This is even clearer when measuring the distribution of orientations, averaged over particles and time (Fig. 8.7-c). Surprisingly, for all regimes, the active units are more prone to be oriented along $\hat{\boldsymbol{e}}_{\parallel}$, even when the system spontaneously oscillates transversally. The educated reader might remember from chapter 7 that this bias could be attributed to a problem of horizontality. Being unable to determine a systematic method to solve this problem, we did not exploit the experimental data further.

8.3.4 Large honeycomb

Finally, we construct the largest structure studied experimentally in this manuscript: a large honeycomb lattice pinned at the edges ($N = 180$). To minimize the energy of the normal modes, we impose zero tension on the structure. Note that at the linear level, such a honeycomb lattice is not mechanically stable as it contains 73 IZMs. Unfortunately, SPP grains embedded in the lattice do not perform a large-scale CA regime as described in chapters 5 and 6 (Fig. 8.8-b). We find that the system is very disordered, but exhibits complex correlation patterns, in the form of intermittent and localized motions. Those resemble rotations of the inner hexagons, or also motion along the lines of the structure, and might be attributed to the spontaneous activation of localized low-energy modes. As tension increases, we only observe frozen regimes.

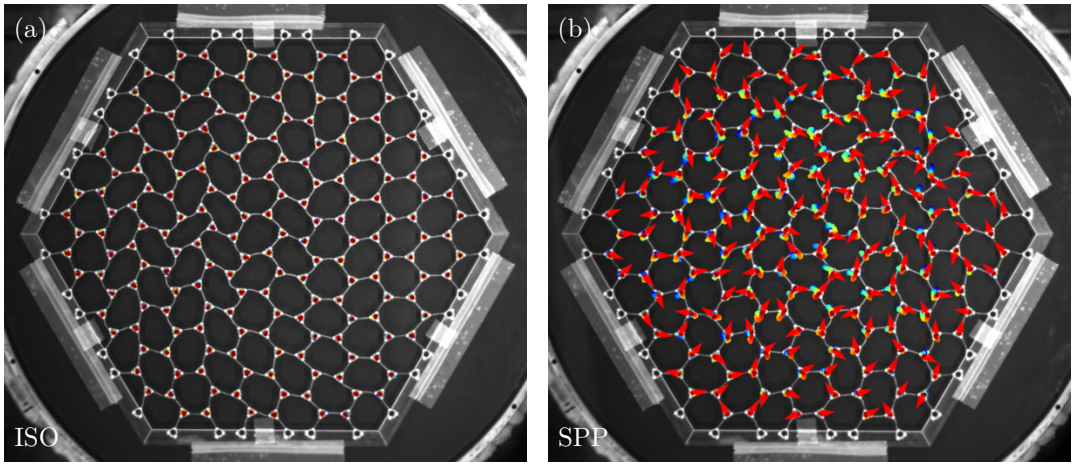


FIG. 8.8. **Experiments with walking grains-based active honeycomb lattices.** Snapshots of the experiments with large honeycomb lattices ($N = 180$, $\alpha \simeq 0$), constructed out of ISO grains (a); and SPP walking grains (b); red arrows: polarities $\hat{\boldsymbol{n}}_i$; trajectories color-coded from blue to red by increasing time.

A few comments are in order. First, those observations must be related to the active forces generated by the SPPs, given that the same system built out of ISO grains performs thermal fluctuations around the reference configuration, without noticeable exotic behavior (Fig. 8.8-a). Second, the experimental system is not ideal: the lattice is clearly not regular, as seen in Fig. 8.8-a; and the mechanical tension is controlled modulo a few percent, which has dramatic consequences on the normal mode spectrum. Further experimental and numerical developments should allow for determining the origin of the phenomena observed in this fascinating system.

Conclusion

Intermediate conclusions and discussions have been made in this manuscript. In this final conclusion, we intend to bring together and synthesize the main results of this work.

Within the harmonic approximation, the emergence of collective behaviors is dictated by the elasto-active coupling $\pi = l_e/l_a$ (see chapter 3), and the normal mode spectrum of the underlying elastic structure. In the presence of rigid body motion zero modes, any finite amount of activity leads to the emergence of collective translation and rotation regimes, which could arguably be interpreted as collective motions (see chapter 4). However, when the structure is mechanically stable, and all the modes are harmonic, we find a more subtle physics. First, at small enough activity, any configuration of the polarity field is a marginally stable fixed point; the system is *frozen*. As activity increases, these fixed points destabilize one by one, more disordered configurations being generally more stable (we found the general expression of the stability thresholds in chapter 5). Eventually, when activity is large enough and stable fixed points no longer exist, the system is attracted toward nonlinear limit cycles, which may coexist with the fixed points. They are utterly different from collective motion in active liquids and rigid body motions in active solids, and shall be called *Collective Actuation* (CA).

A CA regime is characterized by the tendency of the polarity field to only explore a subset of normal modes, and in particular, selects one or two modes that completely dominate the dynamics, resulting in a periodic actuation of the structure. In the absence of angular noise, at least two modes are required to perform a limit cycle. The nontrivial feature of this selection mechanism is that it is not only based on the energy of the modes, but also on their geometries, and how strongly they couple. As a rule of thumb, the geometrical coupling between two modes is as strong as they are spatially extended and locally orthogonal, which is inherited from the microscopic properties. Indeed, each polarity vector is normalized, thus the modes which can make the most of this homogeneous force field are those which are themselves the most extended. Moreover, reorientation via self-alignment is fueled by perpendicular motion.

Motivated by the observation that the dynamics generally condensate on two modes, we extensively studied the physics of a single particle, which has two locally-orthogonal normal modes, $|\boldsymbol{\varphi}_x\rangle$ and $|\boldsymbol{\varphi}_y\rangle$:

(i) **Degenerate single particle.** In that case, $\omega_x^2 = \omega_y^2 = \omega_0^2$ (Fig. Cl.1-a, see chapter 5).

Deterministic dynamics. For $\pi < \pi_c$, the phase space is composed of a continuous set of marginally stable fixed points, organized along a circle (Fig. Cl.1-a, left). At $\pi = \pi_c$, the system is at an exceptional point and the dynamics is infinitely slow (Fig. Cl.1-a, middle). For $\pi > \pi_c$, all fixed points destabilize, and a limit cycle branches off continuously, corresponding to the *Chiral Oscillation* (CO) regime (Fig. Cl.1-a, right). This global bifurcation results from one eigenvalue turning positive, and invariance by rotation. The frequency of oscillation reads $\Omega = \pm\omega_0\sqrt{\pi - \pi_c}$, where the the $\pm$ indicates the two possible chiralities.

Effect of noise. For $\pi < \pi_c$, angular noise is responsible for the diffusion amongst the fixed points (because they are marginally stable), leading to a *Frozen-Disordered* (FD) regime. For $\pi > \pi_c$, a small angular noise merely affects the CO limit cycle, but the presence of a marginally stable direction leads to a diffusion of the oscilla-

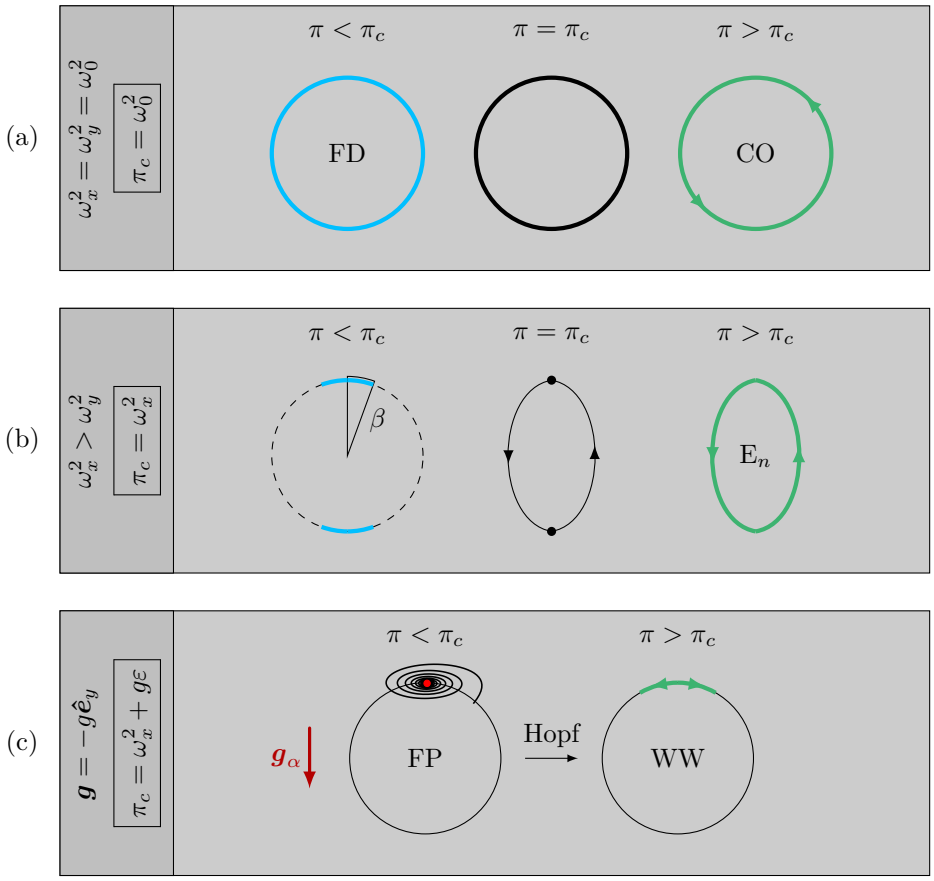


FIG. Cl.1. **Summary of the different bifurcations at the single-particle level.** Schematic of the different fixed points and limit cycles as π increases (from left to right), in the space of displacements. (a) Degenerate case, i.e. $\omega_x^2 = \omega_y^2 = \omega_0^2$; transition to regime CO. (b) Non-degenerate case, considering $\omega_x^2 > \omega_y^2$; transition to an elliptic regime E_n. (c) Case with a polarizing field along $|\boldsymbol{\varphi}_y\rangle$; transition to regime WW. (left) Fixed points for $\pi < \pi_c$. Blue dots and solid lines represent marginally stable fixed points; the red dot represents a linearly stable fixed point; dashed black lines represent unstable fixed points. The angle β goes from $\pi/2$ rad to 0 as π goes from ω_y^2 to ω_x^2. (middle) Heteroclinic orbits for $\pi = \pi_c$, represented by solid black lines and arrows. The dynamics is infinitely slow in the thick regions. (right) Limit cycles for $\pi > \pi_c$, represented by solid green lines and arrows.

tion's phase. Moreover, close to the threshold, angular noise allows for stochastic inversions of the direction of rotation, restoring the chiral symmetry.

(ii) **Non-degenerate single particle.** In that case, $\omega_x^2 > \omega_y^2$ (Fig. Cl.1-b, see chapter 6 and Appendix I).

Deterministic dynamics. In the non-degenerate case, the stability threshold of the fixed points depends on the configuration. At $\pi = \omega_y^2$, the first fixed points, orthogonal to the lowest-energy mode, thus along and opposite to $|\boldsymbol{\varphi}_x\rangle$, destabilize. For $\omega_y^2 < \pi < \omega_x^2$, the fixed points progressively lose stability, up to the last stable ones, along and opposite to $|\boldsymbol{\varphi}_y\rangle$, which turn unstable at $\pi = \omega_x^2$ (Fig. Cl.1-b, left). At $\pi = \pi_c = \omega_x^2$, a zero-frequency heteroclinic orbit connecting these two fixed points emerge (Fig. Cl.1-b, middle), leading to elliptic regimes E_n for $\pi > \pi_c$ (Fig. Cl.1-b, right), whose frequency also scale like $\sqrt{\pi - \pi_c}$.

Effect of noise. The effect of noise strongly depends on the range of activity. Similarly to the degenerate case, for $\pi < \omega_y^2$, angular noise is responsible for the diffusion amongst the fixed points, leading to a *Frozen-Disordered* (FD) regime. For $\omega_y^2 < \pi < \omega_x^2$, angular noise also allows for stochastic turnarounds between the two basins of marginally stable fixed points. Finally, for $\pi > \pi_c$, the elliptic regimes E_n are merely affected by angular noise, the same way as CO regime.

(iii) **Single particle with a polarizing field.** In that case, there exists a polarizing gravity field along $|\boldsymbol{\varphi}_y\rangle$ (Fig. Cl.1-c, see chapter 7):

Deterministic dynamics. For $\pi < \pi_c = \omega_x^2 + g\varepsilon$, any finite amount of gravity polarizes the fixed points of the single particle: there is one unstable fixed point oriented along gravity, i.e. along $-|\boldsymbol{\varphi}_y\rangle$, and only one linearly stable fixed point, oriented opposite to gravity, i.e. along $|\boldsymbol{\varphi}_y\rangle$ (Fig. Cl.1-c, left). At $\pi = \pi_c$, the fixed point turns unstable through a Hopf bifurcation at a frequency scaling like $\sqrt{g\varepsilon}$, leading to *Windscreen Wiper* (WW) limit cycles oscillating at the same frequency (Fig. Cl.1-c, right). In contrast with the above cases, the frequency is finite at the onset of oscillations.

Effect of noise. For $\pi < \pi_c$, noise allows for exploring the vicinity of the linearly stable *Frozen-Polarized* (FP) regime, and for $\pi > \pi_c$, the WW limit cycle is merely affected by angular noise.

At the collective level, we discovered four different CA regimes, the nature of which are dictated by the set of selected modes, and which resonate with the different regimes observed at the single particle level:

1. Selection of a pair of degenerated and locally-orthogonal normal modes (SCO).

   This first scenario was introduced in chapter 5 and extended in chapter 6. In real space, this CA regime is characterized by Synchronized Chiral Oscillations (SCO) of all the active units around their reference configuration (Fig. Cl.2-a). In mode space, the polarity field rotates in the plane spanned by the two selected modes, clockwise or counter-clockwise, depending on the chosen chirality. The selection of a degenerated pair of modes arises preferentially when they are both maximally locally-orthogonal and maximally extended. Crucially, we find that SCO arises even in instances where this pair of modes is not the lowest energy one, illustrating the nontrivial selectivity of this regime. At the level of homogeneous solutions and for locally-orthogonal modes, SCO maps with the CO regime of the single particle. However, in large-scale simulations and in the coarse-grained model, we find that the transition from FD to SCO is essentially discontinuous and exhibits hysteresis.

2. Selection of one mode + turnarounds using other selected modes (GAR).

   This second scenario was reported in chapter 6. This CA regime corresponds to Global Alternating Rotations (GAR) of the structure around its pinning point: the rotation mode is selected and activated back and forth (Fig. Cl.2-b). However, CA cannot take place on a single mode in a noiseless framework, and other modes must play a role in the turnarounds of the polarity field at each new rotation. The modes selected for the turnarounds must couple with the rotation mode, thus they must be as extended and as locally-orthogonal with the rotation mode as possible. This regime also exhibits a nontrivial selectivity in the sense that it is

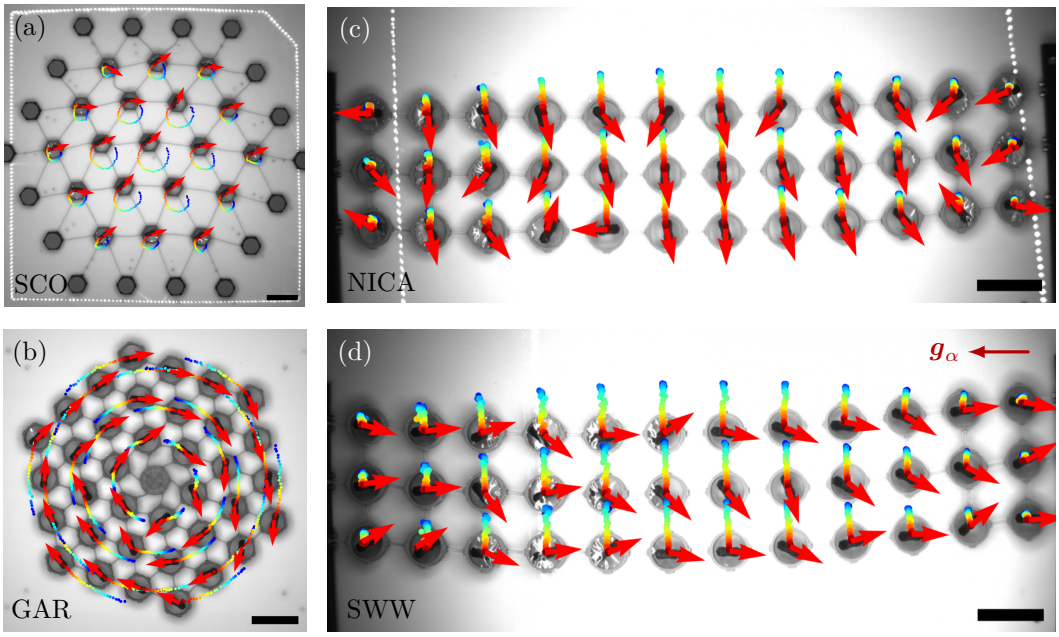


FIG. Cl.2. **Summary of the different CA regimes.** (a) Synchronized Chiral Oscillations (SCO) in a triangular lattice pinned at the edges, see chapter 5. (b) Global Alternating Rotation (GAR) in a triangular lattice with embedded central pinning, see chapter 6. (c) Noise-Induced Collective Actuation (NICA) in a square lattice pinned at opposite ends, without gravity, see chapter 7. (d) Synchronized Windscreen Wiper (SWW) in a square lattice pinned at opposite ends, with a longitudinal polarizing gravity field (as indicated by the top right red arrow), see chapter 7. Red arrows: polarities $\hat{\mathbf{n}}_i$; trajectories color-coded from blue to red with increasing time; scale bars: 10 cm.

observed even for instances where the rotation mode is not the lowest energy one. We did not study in detail the transition to GAR as activity increases. At the level of homogeneous solutions and for locally-orthogonal modes, GAR maps with the elliptic regimes E_n of the asymmetric single particle. Therefore, the generalization of GAR regimes to arbitrary pairs of non-degenerated normal modes shall be called SE_n regimes. However, we anticipate that the transition from FD to GAR/SE_n is also discontinuous for large systems.

3. Selection of the lowest energy mode + turnarounds with angular noise (NICA).

This scenario was reported in chapters 7 and 8. This CA regime is characterized by self-oscillations of the system along a single normal mode, the turnarounds being driven by the balance between activity, elasticity, and crucially, angular noise (Fig. Cl.2-c). Noise-induced Collective Actuation (NICA) arises when a given normal mode is very gapped with respect to the rest of the spectum, and must preferentially take place along a mode that is maximally extended. This regime apparently exhibits a trivial selection: it is only observed with the lowest energy mode of the structure. Finally, the transition to NICA as activity increases results from the destabilization of the FD phase through a Hopf bifurcation at $\pi = \pi_c = 2(\omega_0^2 + D)$ at frequency $\Omega = \omega_0\sqrt{D}$, where ω_0^2 is the energy of the selected mode. At the level of homogeneous solutions, the transition is continuous (both the magnetization and displacements grow continuously), but in large systems, we also anticipate that this transition becomes discontinuous.

4. Polarization + selection of a transverse mode (SWW).

   This last scenario originates from the presence of a polarizing gravity field, which polarizes the active units' orientations in a given direction. SWW is characterized by spontaneous oscillations in the direction transverse to the polarizing field (Fig. Cl.2-d). The selected transverse mode must couple with the polarizing field, thus it must be as extended and as locally-orthogonal with gravity as possible. We did not study the possibility of a nontrivial selection in that case. At the level of homogeneous solutions and for large enough gravity, SWW maps with regime WW of the single particle. However, as gravity decreases and the longitudinal polarization becomes small, SWW transforms into NICA, and may exhibit Polarization-Induced Reentrance (PIR).

Much work remains to understand precisely how CA regimes emerge and grow in large-scale active solids, and also to predict which one is selected by the active dynamics. Looking ahead, the recent miniaturization of autonomous active units [195] and the study of large biological active solids [77] opens the path toward extending our design principle to the scale of material science. In this context, expanding the relationship between the structural design of active materials – including the geometry and topology of the lattice, the presence of disorder, the inclusion of doping agents – and their spontaneous actuation offers a wide range of perspectives. It is now time for active matter to become solid.

Appendix A

Normal modes

In this appendix, we provide the normal mode spectrum of the structures studied experimentally in the different result chapters. The method used to compute the normal modes and sort them by symmetry classes is explained in chapter 3.

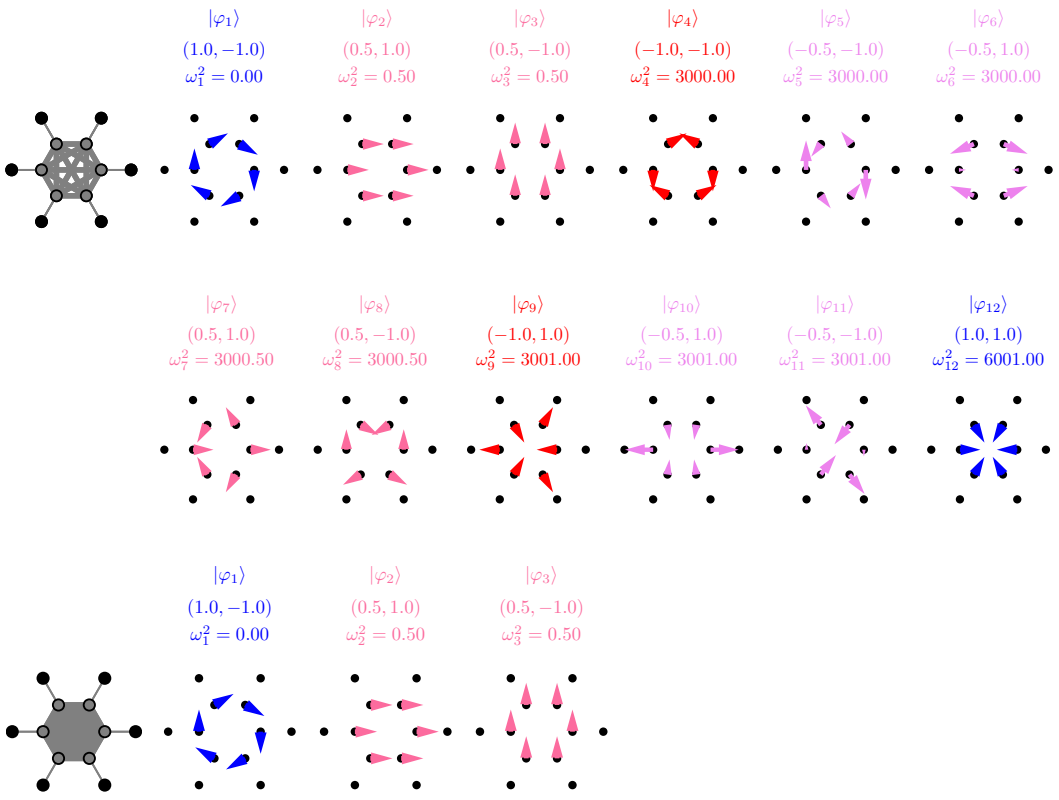


FIG. A.1. **Normal modes spectrum of the *Gerris*.** (top) Stiff heterogeneous hexagon pinned from outside, without tension ($\alpha = 1.0$). The thin outer springs have stiffness 1, the inner thick springs have stiffness 1000. The inner structure's neighboring graph is the complete one. (bottom) Rigid heterogeneous hexagon pinned from outside, without tension ($\alpha = 1.0$). The inner structure is assumed to be fully rigid, thus all the harmonic modes whose energy scale with the inner structure springs stiffness ($k \geq 4$) have infinite energies. The modes are sorted by order of growing energies, and colored by their associated eigenvalues with respect to the rotation operation of the dihedral group of symmetry D_6 of the structure. For every mode, the figure highlights the mode's index k, the eigenvalues associated with the symmetry operations (τ, σ), and the associated squared eigenfrequency ω_k^2.

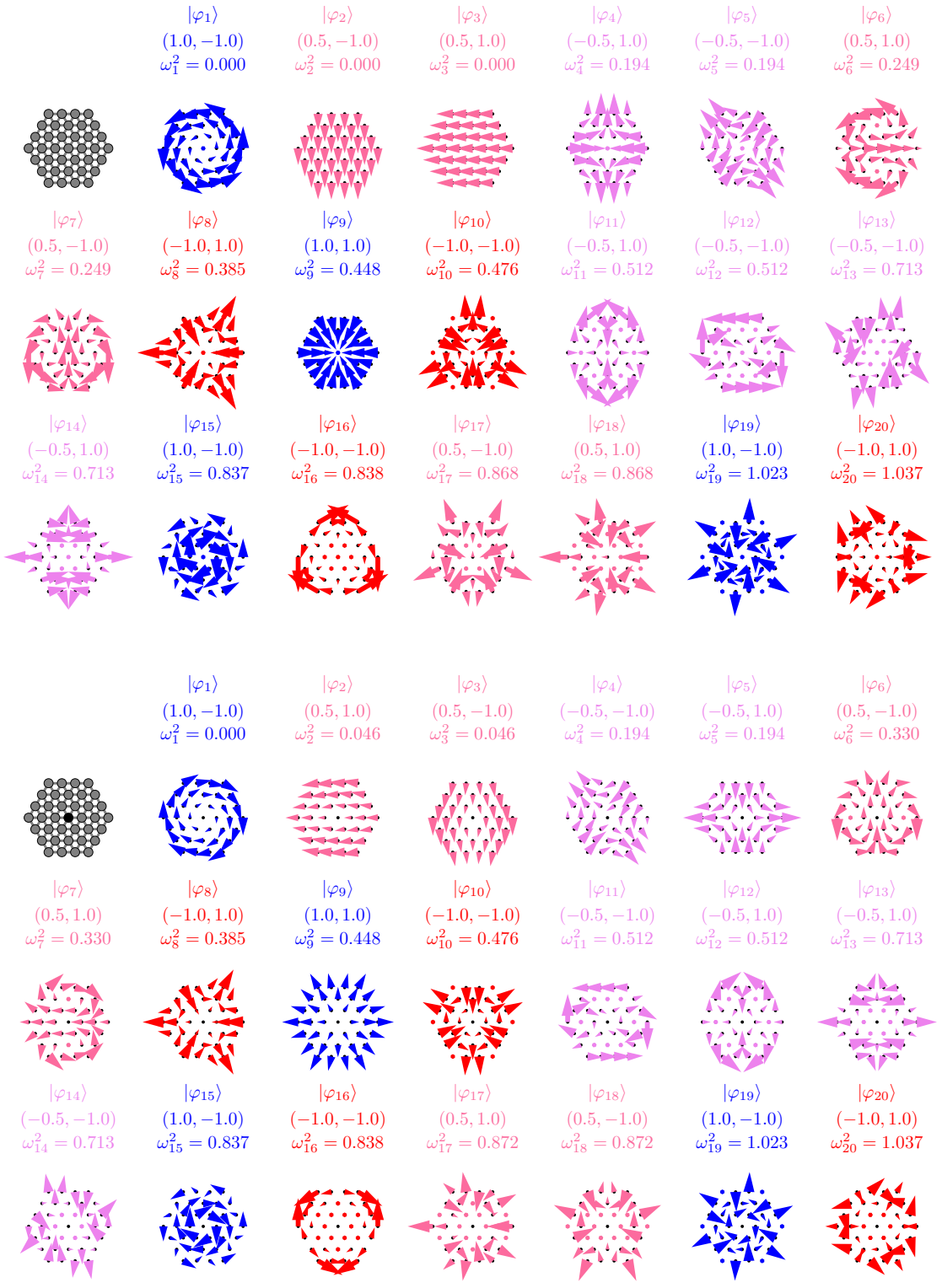


FIG. A.2. **Normal modes spectrum of lattices with zero modes** (top) Triangular lattice in free boundary conditions ($\alpha = 1.0$), and (b) with central pinning ($\alpha = 1.0$). The modes are sorted by order of growing energies, and colored by their associated eigenvalues with respect to the rotation operation of the dihedral group of symmetry D_6 of the structure. The modes are computed for the experimental values of the tension, and only the twentieth first modes are shown. For every mode, the figure highlights the mode's index k, the eigenvalues associated with the symmetry operations (τ, σ), and the associated squared eigenfrequency ω_k^2.

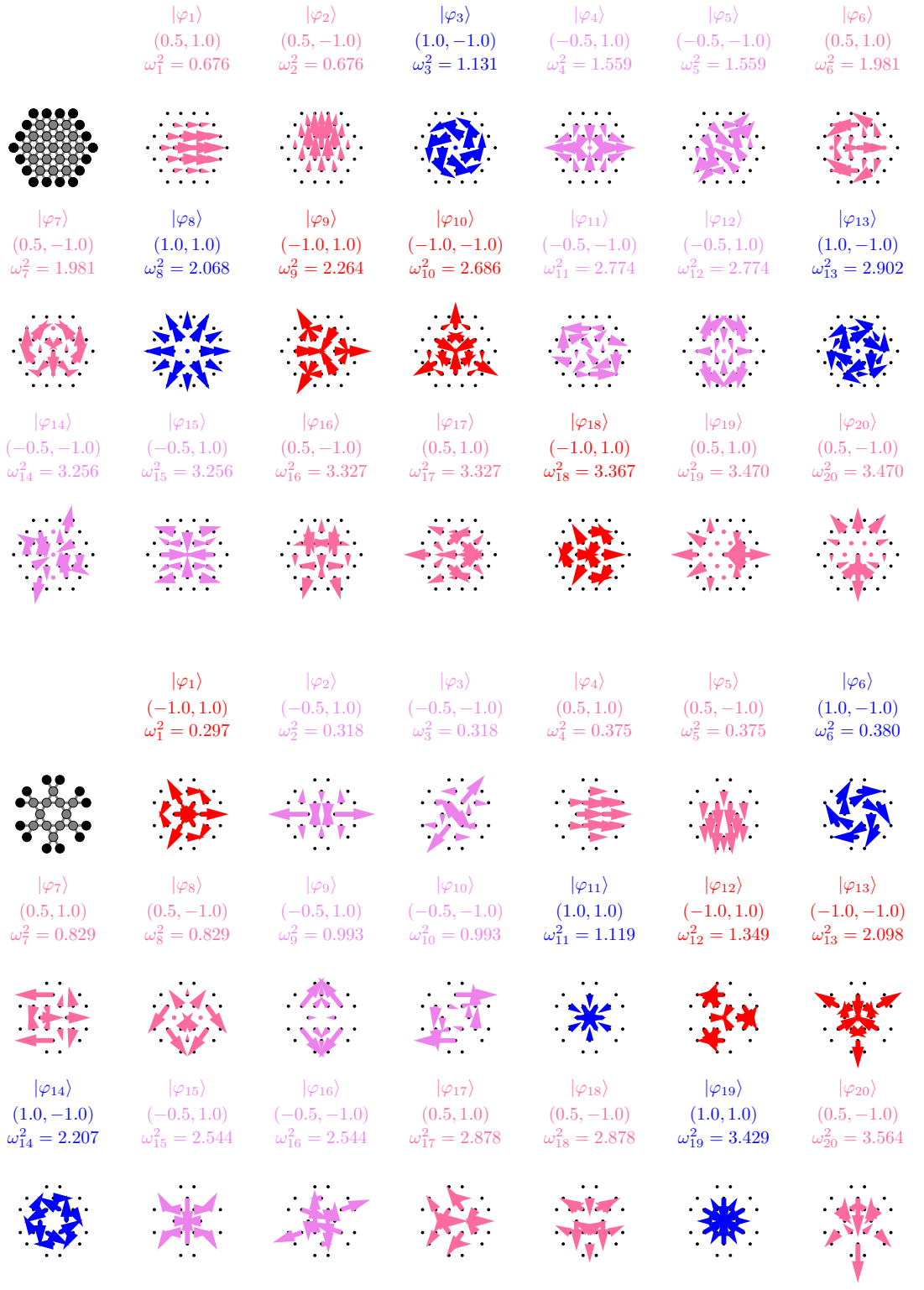


FIG. A.3. **Normal modes spectrum of lattices pinned at the edges** (top) Triangular lattice pinned at the edges ($\alpha = 1.27$), and (bottom) kagome lattice pinned at the edges ($\alpha = 1.02$). The modes are sorted by order of growing energies, and colored by their associated eigenvalues with respect to the rotation operation of the dihedral group of symmetry D_6 of the structure. The modes are computed for the experimental values of the tension, and only the twentieth first modes are shown. For every mode, the figure highlights the mode's index k, the eigenvalues associated with the symmetry operations (τ, σ), and the associated squared eigenfrequency ω_k^2.

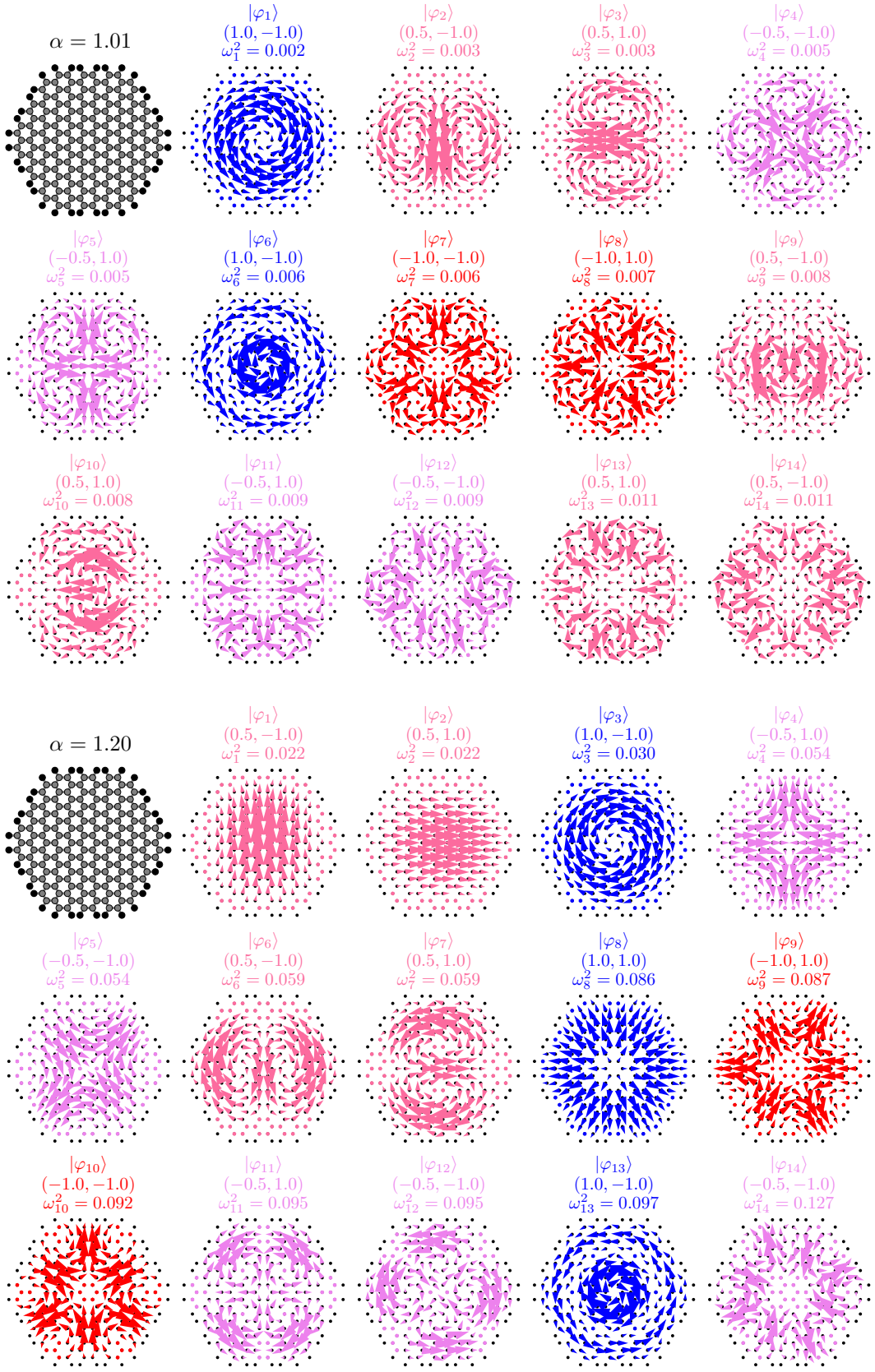


FIG. A.4. **Normal modes spectrum of large honeycomb lattices.** Large honeycomb lattice pinned at the edges ($N = 180$); (top) for low tension ($\alpha = 1.01$); and (bottom) large tension ($\alpha = 1.2$). The modes are sorted by order of growing energies, and colored by their associated eigenvalues with respect to the rotation operation of the dihedral group of symmetry D_6 of the structure. Only the fourteenth first modes are shown. For every mode, the figure highlights the mode's index k, the eigenvalues associated with the symmetry operations (τ, σ), and the associated squared eigenfrequency ω_k^2.

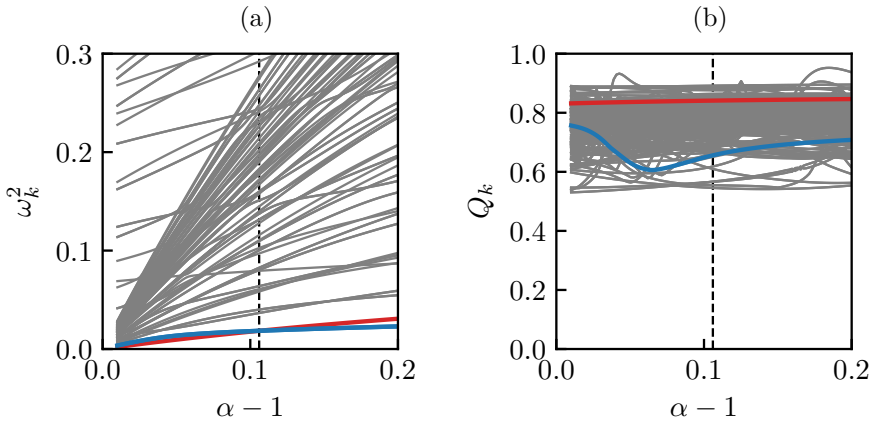


FIG. A.5. **Properties of the large honeycomb lattice's normal modes.** (a) Modes' squared eigenfrequencies ω_k^2 as a function of tension $\alpha - 1$. (b) Modes' particiation ratio Q_k as a function of tension $\alpha - 1$. The black dashed vertical line highlights the energy switch. The solid blue line (resp. solid red line) corresponds to the rotation mode (resp. translational modes), and the solid gray lines to all the other modes.

Appendix B

Rigid limit

In this appendix, complementing chapter 4, we provide the derivation of the rigid limit in the general case of pairwise radially symmetric forces between agents. We then perform the linear stability analysis of the rotating and translating solutions for different boundary conditions. Finally, we elaborate on the derivarion of the Fokker-Planck equation and on the calculation of the Landau-Ginzburg-like free energy.

B.1 Rigid theoretical framework

B.1.1 Dimensionless scheme

The derivation of the rigid limit by Gustavo Düring and Claudio Hernández López is written in a more general context of position-based interactions. The total elastic force acting on particle i, $\boldsymbol{F}_i$, considers the sum of pairwise radially symmetric interaction forces $f_{ij}\hat{\boldsymbol{e}}_{ij}$, where $\hat{\boldsymbol{e}}_{ij}$ is a unit vector pointing from particle i to j, and $f_{ij}(\boldsymbol{r}_i - \boldsymbol{r}_j)$ represents the exact position dependence and sets the force amplitude. Thus, the total force $\boldsymbol{F}_i = \sum_{j\in\partial i} f_{ij}\hat{\boldsymbol{e}}_{ij}$ where the sum runs over all interacting active units. Moreover, they rescale the elastic forces by the amplitude of the active forces $\boldsymbol{F}_i \to F_0\boldsymbol{F}_i$. Note that those differences completely vanish in the rigid limit.

Moreover, they use a different dimensionless scheme than the one of chapter 4: length are rescaled by $r_0 = l_0$ (instead of l_a), and time by $t_0 = l_0/v_0$ (instead of l_a/v_0), resulting in a global rescaling of units by τ_n. For the sake of consistency, the entire Appendix is written in this dimensionless scheme. In this context, the overdamped equations of motion read:

$$\dot{\boldsymbol{r}}_i = \hat{\boldsymbol{n}}_i + \boldsymbol{F}_i, \tag{B.1a}$$

$$\dot{\theta}_i = \frac{1}{\tau_n}\left(\hat{\boldsymbol{n}}_i^{\perp}\cdot\dot{\boldsymbol{r}}_i\right) + \sqrt{\frac{2D}{\tau_n}}\xi_i, \tag{B.1b}$$

Note that this scheme is simpler when actually performing numerical calculations, because this way particles are connected by bonds of unit length, and τ_n appears as one parameter in the equations.

B.1.2 Force determination

Let i and j be two agents connected by a rigid link. We may express the geometrical inextensibility condition as:

$$\frac{\mathrm{d}}{\mathrm{d}t}|\boldsymbol{r}_i - \boldsymbol{r}_j| = \hat{\boldsymbol{e}}_{ij}\cdot(\dot{\boldsymbol{r}}_i - \dot{\boldsymbol{r}}_j) = 0, \tag{B.2}$$

where $\hat{\boldsymbol{e}}_{\boldsymbol{ij}} = (\boldsymbol{r}_i - \boldsymbol{r}_j)/|\boldsymbol{r}_i - \boldsymbol{r}_j|$. If j refers to a pinned site, then the above condition reads:

$$\hat{\boldsymbol{e}}_{ij} \cdot \dot{\boldsymbol{r}}_i = 0. \tag{B.3}$$

There exist M such equations, where M is the number of edges of the system. We can put them in a compact form using braket notation. Let m denote the link between agents i and j. Eq. (B.2) can be re-casted as:

$$\langle m|\mathcal{S}|\dot{\boldsymbol{r}}\rangle = 0, \tag{B.4}$$

where $|\dot{\boldsymbol{r}}\rangle$ is a particle-space ket satisfying:

$$\langle a|\dot{\boldsymbol{r}}\rangle = \dot{\boldsymbol{r}}_a, \tag{B.5}$$

and:

$$\langle m|\mathcal{S}|a\rangle = \hat{\boldsymbol{e}}_{ij}^T(\delta_{ai} - \delta_{aj}), \tag{B.6}$$

or, if j refers to a pinned site:

$$\langle m|\mathcal{S}|a\rangle = \hat{\boldsymbol{e}}_{ij}^T\delta_{ai}, \tag{B.7}$$

are the matrix elements of the $M \times 2N$ operator $\mathcal{S}$. The set of all such equations can be expressed succinctly as:

$$S\,|\dot{\boldsymbol{r}}\rangle = 0. \tag{B.8}$$

The same matrix can be utilized to decompose the net force on each agent as the sum of the tensions along each edge. Indeed, given the generic elastic force expression:

$$\boldsymbol{F}_i = \sum_{j\in\partial i} f_{ij}\hat{\boldsymbol{e}}_{ij}. \tag{B.9}$$

Let m denote the link between active particles k and j. Then:

$$\begin{aligned}
\boldsymbol{F}_i &= \sum_m \hat{\boldsymbol{e}}_m\delta_{ik}\,\langle m|f\rangle\,, && \text{(B.10)}\\
&= \sum_m \left(\langle m|\mathcal{S}|i\rangle\right)^T\langle m|f\rangle\,, && \text{(B.11)}\\
&= \sum_m \langle i|\mathcal{S}^T|m\rangle\,\langle m|f\rangle\,, && \text{(B.12)}\\
&= \langle i|\mathcal{S}^T|f\rangle\,, && \text{(B.13)}
\end{aligned}$$

where we have used the completeness of the edge-space basis:

$$\sum_m |m\rangle\,\langle m| = \mathbb{I}. \tag{B.14}$$

Finally, as $\boldsymbol{F}_i = \langle i|\boldsymbol{F}\rangle$:

$$|\boldsymbol{F}\rangle = \mathcal{S}^T\,|f\rangle\,. \tag{B.15}$$

Using (B.8) and (B.15) in Eq. (B.1a), we find:

$$\mathcal{S}\mathcal{S}^T\,|f\rangle = -\mathcal{S}\,|\hat{\boldsymbol{n}}\rangle\,. \tag{B.16}$$

We can now decompose $|f\rangle$ in the eigenkets of $\mathcal{S}\mathcal{S}^T$:

$$|f\rangle = \sum_q f_q\,|\phi^q\rangle = \sum_{q\in\mathfrak{F}} f_q\,|\phi^q\rangle + \sum_{q\notin\mathfrak{F}} f_q\,|\phi^q\rangle\,, \tag{B.17}$$

where $\mathfrak{F}$ is the set of zero modes of $\mathcal{S}\mathcal{S}^T$. We can then replace this expansion in B.16:

$$\sum_{q\notin\mathfrak{F}} f_q\omega_q^2\,|\phi^q\rangle = -\mathcal{S}\,|\hat{\boldsymbol{n}}\rangle\,, \tag{B.18}$$

so that:

$$f_q = -\frac{\langle\phi^q|\mathcal{S}|\hat{\boldsymbol{n}}\rangle}{\omega_q^2}\;\forall q\notin\mathfrak{F}. \tag{B.19}$$

Then:

$$|f\rangle = \sum_{q\in\mathfrak{F}} f_q\,|\phi^q\rangle - \sum_{q\notin\mathfrak{F}}\frac{\langle\phi^q|\mathcal{S}|\hat{\boldsymbol{n}}\rangle}{\omega_q^2}\,|\phi^q\rangle\,. \tag{B.20}$$

Before continuing, it is important to realize that $\mathcal{S}\mathcal{S}^T$ shares a common set of eigenvalues with $\mathcal{S}^T\mathcal{S}$, the dynamical matrix. Let $|\boldsymbol{\varphi}^p\rangle$ be the p-th eigenket of the latter, then we can write:

$$\mathcal{S}^T\mathcal{S}\,|\boldsymbol{\varphi}^p\rangle = \omega_p^2\,|\boldsymbol{\varphi}^p\rangle\,, \tag{B.21}$$

such that:

$$\mathcal{S}\mathcal{S}^T\left(\mathcal{S}\,|\boldsymbol{\varphi}^p\rangle\right) = \omega_p^2\left(\mathcal{S}\,|\boldsymbol{\varphi}^p\rangle\right). \tag{B.22}$$

If $|\boldsymbol{\varphi}^p\rangle\notin\ker(\mathcal{S})$, then $\mathcal{S}\,|\boldsymbol{\varphi}^p\rangle$ is an eigenket of $\mathcal{S}\mathcal{S}^T$ with eigenvalue ω_p^2. Then, every nonzero eigenvalue of $\mathcal{S}^T\mathcal{S}$ is also in $\mathcal{S}\mathcal{S}^T$, same with the zero eigenvalues associated with kets that are not in the kernel of $\mathcal{S}$. We can also go the other way around, consider the q-th eigenket of $\mathcal{S}\mathcal{S}^T$. Then:

$$\mathcal{S}\mathcal{S}^T\,|\phi^q\rangle = \widetilde{\omega}_q^2\,|\phi^q\rangle\,, \tag{B.23}$$

such that:

$$\mathcal{S}^T\mathcal{S}\left(\mathcal{S}^T\,|\phi^q\rangle\right) = \widetilde{\omega}_q^2\left(\mathcal{S}^T\,|\phi^q\rangle\right). \tag{B.24}$$

If $|\phi^q\rangle\notin\ker(\mathcal{S}^T)$, then $\mathcal{S}^T\,|\phi^q\rangle$ is an eigenket of $\mathcal{S}^T\mathcal{S}$ with eigenvalue $\widetilde{\omega}_q^2$. Then, every nonzero eigenvalue of $\mathcal{S}\mathcal{S}^T$ is also in $\mathcal{S}^T\mathcal{S}$, same with the zero eigenvalues associated to kets that are not in the kernel of $\mathcal{S}^T$. With this, we conclude that the two matrices have the same nonzero eigenvalues, and share a subset of their zero eigenvalues, with the non-shared part being associated with kets in the kernel of $\mathcal{S}$ or $\mathcal{S}^T$. We can then write the following:

$$\mathcal{S}^T\,|\phi^q\rangle = \alpha_q\,|\boldsymbol{\varphi}^q\rangle\,, \tag{B.25}$$

$$\mathcal{S}\,|\boldsymbol{\varphi}^q\rangle = \beta_q\,|\phi^q\rangle\,, \tag{B.26}$$

so that:

$$\mathcal{S}\mathcal{S}^T\,|\phi^q\rangle = \alpha_q\beta_q\,|\phi^q\rangle\,, \tag{B.27}$$

$$\mathcal{S}^T\mathcal{S}\,|\boldsymbol{\varphi}^q\rangle = \beta_q\alpha_q\,|\boldsymbol{\varphi}^q\rangle\,. \tag{B.28}$$

We have established that $\widetilde{\omega}_q^2 = \omega_q^2$ for eigenkets not in the kernel of $\mathcal{S}$ or $\mathcal{S}^T$. With this, we conclude that:

$$\mathcal{S}^T\,|\phi^q\rangle = \omega_q\,|\boldsymbol{\varphi}^q\rangle\,, \tag{B.29}$$

$$\mathcal{S}\,|\boldsymbol{\varphi}^q\rangle = \omega_q\,|\phi^q\rangle\,, \tag{B.30}$$

which works even if $\mathcal{S}^T\,|\phi^q\rangle = 0$ or $\mathcal{S}\,|\boldsymbol{\varphi}^q\rangle = 0$ as in that case $\omega_q = 0$. Finally:

$$|\boldsymbol{F}\rangle = \mathcal{S}^T\,|f\rangle = -\sum_{q\notin\mathfrak{F}}\langle\boldsymbol{\varphi}^q|\hat{\boldsymbol{n}}\rangle\,|\boldsymbol{\varphi}^q\rangle\,, \tag{B.31}$$

and using the resolution of the identity:

$$|\boldsymbol{F}\rangle = -\,|\hat{\boldsymbol{n}}\rangle + \sum_{q\in\mathfrak{F}}\langle\boldsymbol{\varphi}^q|\hat{\boldsymbol{n}}\rangle\,|\boldsymbol{\varphi}^q\rangle\,. \tag{B.32}$$

B.2 Stability of translational and rotational solutions in rigid structures

Let ϕ denote the angle of a certain point of the structure with respect to the horizontal axis. We can define $\theta'_i = \theta_i - \phi$ and $\phi'_i = \phi_i - \phi$ as angles measured from the frame co-rotating with the structure. From the rigid limit, ϕ'_i is fixed, and we can write the temporal evolution of θ'_i from Eqs. (4.7b) and (4.12):

$$\dot{\theta}'_i = \dot{\theta}_i - \dot{\phi}, \tag{B.33}$$

$$= \frac{1}{\tau_n} \sum_{q \in \mathfrak{F}} \langle \boldsymbol{\varphi}^q | \hat{\boldsymbol{n}} \rangle \left(\hat{\boldsymbol{n}}_i^{\perp} \cdot \boldsymbol{\varphi}_i^q \right) - \frac{1}{I} \left(\sum_k \boldsymbol{r}_k^{\perp} \cdot \hat{\boldsymbol{n}}_k \right). \tag{B.34}$$

B.2.1 Pinned structure

The equation of motion for the angular degrees of freedom can be written as follows:

$$\dot{\theta}'_i = \left(\frac{1}{\tau_n} r_i \cos(\theta'_i - \phi'_i) - 1 \right) \frac{1}{I} \sum_k r_k \sin(\theta'_k - \phi'_k) = f_i(\theta'_1, \ldots, \theta'_N), \tag{B.35}$$

where the steady-state rotational solution satisfies:

$$r_i \cos(\theta'_i - \phi'_i) = \tau_n \, \forall \, i. \tag{B.36}$$

Let us designate this solution as $\widetilde{\theta}'_i$. We will now perform a Taylor series expansion of f_i centered around this solution:

$$f_i \approx \sum_j \mathcal{A}_{ij} (\theta'_j - \widetilde{\theta}'_j), \tag{B.37}$$

where:

$$\mathcal{A}_{ij} = \left. \frac{\partial f_i}{\partial \theta'_j} \right|_{\theta'_k = \widetilde{\theta}'_k \ \forall k}. \tag{B.38}$$

We have the following:

$$\frac{\partial f_i}{\partial \theta'_j} = -\frac{1}{\tau_n} r_i \sin(\theta'_i - \phi'_i) \frac{1}{I} \sum_k r_k \sin(\theta'_k - \phi'_k) + \left(\frac{1}{\tau_n} r_i \cos(\theta'_i - \phi'_i) - 1 \right) \frac{1}{I} r_j \cos(\theta'_j - \phi'_k). \tag{B.39}$$

Now, from B.36, we can see that:

$$r_i \sin(\theta'_i - \phi'_i) = \pm \sqrt{r_i^2 - \tau_n^2}, \tag{B.40}$$

where every particle shares the same sign as we are studying a global rotation. Replacing in B.39:

$$\mathcal{A}_{ij} = -\frac{\sqrt{r_i^2 - \tau_n^2}}{I} \sum_k \left(\sqrt{r_k^2 - \tau_n^2} \right) \delta_{ij}. \tag{B.41}$$

This matrix is diagonal, and every entry is negative. Therefore, the rotating solution in a pinned structure is always linearly stable.

B.2.2 Non-pinned structure translational solution

The equation of motion for the angular degrees of freedom can be written as follows:

$$\dot{\theta}'_i = -\frac{1}{\tau_n}\frac{1}{N}\sum_k \sin(\theta'_i - \theta'_k) + \left(\frac{1}{\tau_n} r_i \cos(\theta'_i - \phi'_i) - 1\right)\frac{1}{I}\sum_k r_k \sin(\theta'_k - \phi'_k) = f_i(\theta'_1, \ldots, \theta'_N), \tag{B.42}$$

with the steady state solution $\theta'_i = \theta' \ \forall i$. We have:

$$\begin{aligned}\frac{\partial f_i}{\partial \theta'_j} = &-\frac{1}{\tau_n}\frac{1}{N}\sum_k \cos(\theta'_i - \theta'_k)\delta_{ij} + \frac{1}{\tau_n}\frac{1}{N}\sum_k \cos(\theta'_i - \theta'_k)\delta_{kj} \\ &- \frac{1}{\tau_n} r_i \sin(\theta'_i - \phi'_i)\frac{1}{I}\sum_k r_k \sin(\theta'_k - \phi'_k) + \left(\frac{1}{\tau_n} r_i \cos(\theta'_i - \phi'_i) - 1\right)\frac{1}{I} r_j \cos(\theta'_j - \phi'_k).\end{aligned} \tag{B.43}$$

Thus:

$$\mathcal{A}_{ij} = -\frac{1}{\tau_n}\delta_{ij} + \frac{1}{\tau_n}\frac{1}{N} + \frac{1}{I} r_j \cos(\theta' - \phi'_j)\left(\frac{1}{\tau_n} r_i \cos(\theta' - \phi'_i) - 1\right). \tag{B.44}$$

Consider the sum of the columns of matrix $\mathcal{A}_{ij}$:

$$\sum_j \mathcal{A}_{ij} = -\frac{1}{\tau_n} + \frac{1}{\tau_n} + \frac{1}{I}\left(\frac{1}{\tau_n} r_i \cos(\theta' - \phi'_i) - 1\right)\sum_j r_j \cos(\theta' - \phi'_j) = 0, \tag{B.45}$$

where the last sum is equal to zero as it corresponds to the position of the barycenter with respect to itself along the x-axis. Therefore, $\mathcal{A}_{ij}$ has at least one null eigenvalue. Let us now demonstrate that the matrix has $N-2$ eigenvalues $\lambda = -1/\tau_n$. If $v_i \ \forall i$ represent the components of one of these eigenvectors, then:

$$\sum_j \mathcal{A}_{ij} v_j = -\frac{1}{\tau_n} v_i, \tag{B.46}$$

which implies that:

$$\frac{1}{\tau_n}\frac{1}{N}\sum_j v_j + \frac{1}{I}\left(\frac{1}{\tau_n} r_i \cos(\theta' - \phi'_i)\right)\sum_j r_j \cos(\theta' - \phi'_j) v_j = 0. \tag{B.47}$$

As the components v_j cannot depend on i, then the eigenvector must satisfy two conditions:

$$\sum_j v_j = 0, \tag{B.48}$$

$$\sum_j r_j \cos(\theta' - \phi'_j) v_j = 0. \tag{B.49}$$

These two restrictions imply that there exist $N-2$ eigenvectors with eigenvalue $\lambda = -1/\tau_n$. Now, the characteristic polynomial of $\mathcal{A}$ reads:

$$\lambda\left(\lambda + \frac{1}{\tau_n}\right)^{N-2}(\lambda - \lambda_N) = 0, \tag{B.50}$$

where λ_N is the last unknown eigenvalue. We may recognize that $\left(\frac{1}{\tau_n}\right)^{N-2}\lambda_N$ is the coefficient of the linear term in this polynomial, and thus, it is equal to the trace of $\mathcal{A}$:

$$\lambda_N = \tau_n^{N-2}\left(-\frac{1}{\tau_n}N + \frac{1}{\tau_n} + \frac{1}{\tau_n}\frac{1}{I}\sum_i \left(r_i \cos(\theta' - \phi'_i)\right)^2\right) \leq \tau_n^{N-3}(2 - N), \tag{B.51}$$

which proves that the stability of the translational solution is assured for any structure.

B.2.3 Non-pinned structure rotating solution

We consider equation B.43 with the rotating condition given by B.36. We can write:

$$\cos(\theta_i' - \theta_k') = \cos((\theta_i' - \phi_i') - (\theta_k' - \phi_k') + (\phi_i' - \phi_k')), \tag{B.52}$$

$$= \cos((\theta_i' - \phi_i') - (\theta_k' - \phi_k'))\cos((\phi_i' - \phi_k')) \tag{B.53}$$
$$- \sin((\theta_i' - \phi_i') - (\theta_k' - \phi_k'))\sin((\phi_i' - \phi_k')),$$

$$= \cos(\phi_i' - \phi_k')\left(\cos(\theta_i' - \phi_i')\cos(\theta_k' - \phi_k') + \sin(\theta_i' - \phi_i')\sin(\theta_k' - \phi_k')\right)$$
$$- \sin(\phi_i' - \phi_k')\left(\sin(\theta_i' - \phi_i')\cos(\theta_k' - \phi_k') - \cos(\theta_i' - \phi_i')\sin(\theta_k' - \phi_k')\right), \tag{B.54}$$

$$= \frac{\cos(\phi_i' - \phi_k')}{r_i r_k}\left(1 + \sqrt{r_i^2 - \tau_n^2}\sqrt{r_k^2 - \tau_n^2}\right) \tag{B.55}$$
$$\mp \frac{\sin(\phi_i' - \phi_k')}{r_i r_k}\left(\sqrt{r_i^2 - \tau_n^2} - \sqrt{r_k^2 - \tau_n^2}\right),$$

$$= \alpha_{ik}. \tag{B.56}$$

Then:

$$\mathcal{A}_{ij} = \frac{1}{N}\alpha_{ij} - \left[\frac{\sqrt{r_i^2 - \tau_n^2}}{I}\sum_k\left(\sqrt{r_k^2 - \tau_n^2}\right) + \frac{1}{N}\sum_k \alpha_{ik}\right]\delta_{ij}. \tag{B.57}$$

B.3 Fokker-Planck equation

Consider a system described by a set of W random variables y_i evolving under the following stochastic differential equation:

$$\dot{y}_i(t) = L_i(y_1, \ldots, y_W|t) + \sigma_i \xi_i(t), \tag{B.58}$$

where ξ_i is a Gaussian white noise with zero mean and correlations $\langle \xi_i(t)\xi_j(t')\rangle = \delta_{ij}\delta(t - t')$. Let $Q(y_1, \ldots, y_W|t)$ be the probability density function of a particular system configuration at time t. The Fokker-Planck equation describing the spatio-temporal evolution of Q reads:

$$\frac{\partial Q}{\partial t} = -\sum_i \frac{\partial}{\partial y_i}(L_i Q) + \sum_i \frac{\sigma_i^2}{2}\frac{\partial^2 Q}{\partial y_i^2}. \tag{B.59}$$

In our particular case, $W = 3N$. Furthermore, $\sigma_i = 0$ for all the equations describing the particle positions. From the dimensionless dynamical equations in the rigid limit, the Fokker-Planck equation reads:

$$\frac{\partial}{\partial t}Q(\boldsymbol{r}_1, \ldots, \boldsymbol{r}_N|\theta_1, \ldots, \theta_N|t) =$$
$$- \sum_{i,q} \boldsymbol{\nabla}_{\boldsymbol{x}_i} \cdot (\langle \boldsymbol{\varphi}^q|\hat{\boldsymbol{n}}\rangle \boldsymbol{\varphi}_i^q Q) + \sum_i \frac{\partial}{\partial \theta_i}\left(\frac{1}{\tau_n}\frac{\partial V}{\partial \theta_i}Q\right) + \frac{D}{\tau_n}\sum_i \frac{\partial^2 Q}{\partial \theta_i^2}. \tag{B.60}$$

Let us take a system in free boundary conditions, with two translational modes and a rotational one. Then, the relevant variables are the position of the center of mass $\boldsymbol{R}$, the rotation of the structure ϕ and the polarization of each agent θ_i. We must write the dynamical equation for each one of them. From the definition of the center of mass, we

find the equation governing its temporal evolution:

$$\dot{\boldsymbol{R}} = \frac{1}{N}\sum_i \dot{\boldsymbol{r}}_i, \tag{B.61}$$

$$= \frac{1}{N}\sum_i \hat{\boldsymbol{n}}_i, \tag{B.62}$$

where the last equality is obtained because the sum of all the inter-particle forces vanishes from reciprocity. In summary, the set of variables of interest evolves according to the following equations:

$$\dot{X} = \frac{1}{N}\sum_j \cos(\theta'_j + \phi), \tag{B.63}$$

$$\dot{Y} = \frac{1}{N}\sum_j \sin(\theta'_j + \phi), \tag{B.64}$$

$$\dot{\phi} = \frac{1}{I}\sum_j r_j \sin(\theta'_j - \phi'_j), \tag{B.65}$$

$$\tau_n\dot{\theta}'_i = -\frac{\partial V}{\partial \theta'_i} - \tau_n\dot{\phi} + \sqrt{2D\tau_n}\xi_i = -\frac{1}{N}\sum_j \sin(\theta'_i - \theta'_j) + \left(r_i\cos(\theta'_i - \phi'_i) - \tau_n\right)\dot{\phi} + \sqrt{2D\tau_n}\xi_i, \tag{B.66}$$

where X and Y and respectively the x and y components of the barycenter's position vector $\boldsymbol{R}$. Then, $Q(X, Y, \phi, \theta'_1, \ldots, \theta'_N|t)$ evolves according to the following equation:

$$\frac{\partial Q}{\partial t} = -\frac{\partial}{\partial X}\left[\frac{1}{N}\sum_i \cos(\theta'_i + \phi)Q\right] - \frac{\partial}{\partial Y}\left[\frac{1}{N}\sum_i \sin(\theta'_i + \phi)Q\right] - \frac{\partial}{\partial \phi}\left[\frac{1}{I}\sum_i r_j \sin(\theta'_i - \phi'_i)Q\right] + \sum_i \frac{\partial}{\partial \theta'_i}\left[\left(\frac{1}{\tau_n}\frac{\partial V}{\partial \theta'_i} + \dot{\phi}\right)Q\right] + \frac{D}{\tau_n}\sum_i \frac{\partial^2 Q}{\partial \theta'^2_i}. \tag{B.67}$$

Let us define the reduced probability distribution $\mathcal{Q}(\theta'_1, \ldots, \theta'_N|t)$ such that:

$$\mathcal{Q} = \int Q \,\mathrm{d}X\,\mathrm{d}Y\mathrm{d}\phi, \tag{B.68}$$

and as neither $\partial V/\partial\theta'_i$ nor $\dot{\phi}$ depend on these variables, we are left with:

$$\frac{\partial \mathcal{Q}}{\partial t} = \sum_i \frac{\partial}{\partial \theta'_i}\left[\left(\frac{1}{\tau_n}\frac{\partial V}{\partial \theta'_i} + \dot{\phi}\right)\mathcal{Q}\right] + \frac{D}{\tau_n}\sum_i \frac{\partial^2 \mathcal{Q}}{\partial \theta'^2_i}. \tag{B.69}$$

If $\dot{\phi} = 0$ the stationary distribution can be found exactly and it corresponds to the Boltzmann distribution:

$$\mathcal{Q} \propto \exp(-\beta V), \tag{B.70}$$

with $\beta = 1/D$. We now perform a scaling analysis to study the magnitudes of terms $\partial V/\partial\theta'_i$ and $\dot{\theta}$. Note that:

$$\frac{\partial V}{\partial \theta'_i} \sim -1 + h\dot{\phi}, \tag{B.71}$$

$$\dot{\phi} \sim \frac{1}{h}, \tag{B.72}$$

where h is the characteristic agent distance from the center of mass. Therefore, if $\tau_n \ll h$, the approximation $\dot{\phi} = 0$ is reasonably accurate. We introduce a series expansion of $\mathcal{Q}$ as follows:

$$\mathcal{Q} = \mathcal{Q}^{(0)} + \tau_n \mathcal{Q}^{(1)} + \dots \tag{B.73}$$

By plugging Eq. (B.73) back in Eq. (B.69), at order $\mathcal{O}(\tau_n)$, we recover the steady-state solution given by B.70. For any higher order $\mathcal{O}(\tau_n^p)$, the steady-state solution satisfies the following equation:

$$\boldsymbol{\nabla} \cdot \left(e^{-\beta V} \boldsymbol{\nabla} \left(e^{\beta V} \mathcal{Q}^{(p)} \right) \right) = \beta \sum_i \frac{\partial}{\partial \theta_i'} \left(\dot{\phi} \mathcal{Q}^{(p-1)} \right). \tag{B.74}$$

B.4 Statistics of the adiabatic approximation

We can calculate the partition function as follows:

$$\mathcal{Z} = \int_0^{2\pi} \exp\left(\beta \left(\frac{1}{2} \sum_q \left(\langle \boldsymbol{\varphi}^q | \hat{\boldsymbol{n}} \rangle \right)^2 + \sqrt{N} \sum_q h_q \langle \boldsymbol{\varphi}^q | \hat{\boldsymbol{n}} \rangle \right) \right) d^N\theta. \tag{B.75}$$

where we have introduced a conjugated field h_q. Note that, for a globally extended mode, $\langle \boldsymbol{\varphi}^q | \hat{\boldsymbol{n}} \rangle$ is $\mathcal{O}(\sqrt{N})$. To recast this integral, we define the parameter μ_q via the integral of the Gaussian function:

$$\exp\left(\frac{\beta}{2N} \left(\sqrt{N} \langle \boldsymbol{\varphi}^q | \hat{\boldsymbol{n}} \rangle \right)^2 \right) = \sqrt{\frac{N\beta}{2\pi}} \int_{-\infty}^{\infty} \exp\left(-\frac{N\beta}{2} \mu_q^2 + \left(\beta \sqrt{N} \langle \boldsymbol{\varphi}^q | \hat{\boldsymbol{n}} \rangle \right) \mu_q \right) \mathrm{d}\mu_q, \tag{B.76}$$

so that:

$$\mathcal{Z} = \left(\frac{N\beta}{2\pi} \right)^{\frac{M}{2}} \int_{-\infty}^{\infty} \exp\left(\frac{N\beta}{2} \sum_q \mu_q^2 \right) I(\mu_1, \dots, \mu_M) \, \mathrm{d}^M\mu, \tag{B.77}$$

where:

$$I = \int_0^{2\pi} \exp\left(\beta \sum_k \left(\sqrt{N} \langle \boldsymbol{\varphi}^q | \hat{\boldsymbol{n}} \rangle \right) (\mu_q + h_q) \right) \mathrm{d}^N\theta. \tag{B.78}$$

For any of the global modes, we can write:

$$|\boldsymbol{\varphi}^q\rangle = \frac{1}{\sqrt{N}} \sum_i r_{qi} \left(\cos(\phi_{qi}) \hat{\boldsymbol{x}} + \sin(\phi_{qi}) \hat{\boldsymbol{y}} \right), \tag{B.79}$$

then:

$$I = \int_0^{2\pi} \prod_i \left[\exp\left(a_i \cos(\theta_i) + b_i \sin(\theta_i) \right) \mathrm{d}\theta_i \right], \tag{B.80}$$

where:

$$a_i = \sum_q (\mu_q + h_q) r_{qi} \cos(\phi_{qi}), \tag{B.81}$$

$$b_i = \sum_q (\mu_q + h_q) r_{qi} \sin(\phi_{qi}). \tag{B.82}$$

Thus:

$$I = (2\pi)^N \prod_i I_0\left(\beta \sqrt{a_i^2 + b_i^2} \right). \tag{B.83}$$

This expression can be rewritten in a more tractable way:

$$a_i^2 + b_i^2 = \sum_{q,l} (\mu_q + h_q)(\mu_l + h_l) r_{qi} r_{li} \left(\cos(\phi_{qi})\cos(\phi_{li}) + \sin(\phi_{qi})\sin(\phi_{li})\right), \tag{B.84}$$

$$= \sum_{q,l} (\mu_q + h_q)(\mu_l + h_l) r_{qi} r_{li} \cos(\phi_{qi} - \phi_{li}), \tag{B.85}$$

$$= N \sum_{q,l} (\mu_q + h_q)(\mu_l + h_l) \left(\boldsymbol{\varphi}_i^q \cdot \boldsymbol{\varphi}_i^l\right), \tag{B.86}$$

then we can define:

$$\mathcal{D}_i = \left(N \sum_{q,l} (\mu_q + h_q)(\mu_l + h_l) \left(\boldsymbol{\varphi}_i^q \cdot \boldsymbol{\varphi}_i^l\right) \right)^{1/2}, \tag{B.87}$$

so that, up to a multiplicative constant:

$$\mathcal{Z} = \int_{-\infty}^{\infty} \exp\left(-N\beta f(\mu_1, \ldots, \mu_M)\right) \mathrm{d}^M \mu, \tag{B.88}$$

where:

$$f = \frac{1}{2} \sum_q \mu_q^2 - \frac{1}{N\beta} \sum_i \ln\left(I_0(\beta \mathcal{D}_i(\mu_1, \ldots, \mu_M))\right). \tag{B.89}$$

$\mathcal{D}_i$ is $\mathcal{O}(1)$, hence the free energy per particle in the thermodynamic limit is given by the minimum of f. This minimum satisfies, for every mode q:

$$\widetilde{\mu}_q = \frac{1}{N\beta} \sum_i \left. \frac{\partial \ln(I_0(\beta \mathcal{D}_i))}{\partial \mu_q} \right|_{\substack{h_l = 0 \ \forall l \\ \mu_l = \widetilde{\mu}_l \ \forall l}}. \tag{B.90}$$

We are interested in calculating the mean values of the projections of each mode over the polarity field. From the partition function definition in B.75:

$$\langle\langle \boldsymbol{\varphi}^q | \hat{\boldsymbol{n}} \rangle\rangle = \frac{1}{\sqrt{N}\beta} \left. \frac{\partial \ln(\mathcal{Z})}{\partial h_q} \right|_{h_l = 0 \ \forall l}. \tag{B.91}$$

Note that $\mathcal{Z}$ depends on h_q only through f. Then:

$$\langle\langle \boldsymbol{\varphi}^q | \hat{\boldsymbol{n}} \rangle\rangle = \frac{1}{\mathcal{Z}} \frac{1}{\sqrt{N}\beta} \int_{-\infty}^{\infty} \exp\left(-N\beta f\right) \left(-N\beta \frac{\partial f}{\partial h_q}\right) \mathrm{d}^M \mu \Big|_{h_l = 0 \ \forall l}. \tag{B.92}$$

Thus:

$$\frac{\langle\langle \boldsymbol{\varphi}^q | \hat{\boldsymbol{n}} \rangle\rangle}{\sqrt{N}} = \frac{1}{N\beta} \frac{1}{\mathcal{Z}} \int_{-\infty}^{\infty} \exp\left(-N\beta f\right) \left(\sum_i \frac{\partial \ln(I_0(\beta \mathcal{D}_i))}{\partial h_q} \right) \mathrm{d}^M \mu \Big|_{h_l = 0 \ \forall l}. \tag{B.93}$$

From the explicit form of $\mathcal{D}_i$:

$$\frac{\partial \ln(I_0(\beta \mathcal{D}_i))}{\partial h_q} = \frac{\partial \ln(I_0(\beta \mathcal{D}_i))}{\partial \mu_q}. \tag{B.94}$$

Finally, ignoring fluctuations up to first order in the saddle point approximation:

$$\frac{\langle\langle \boldsymbol{\varphi}^q | \hat{\boldsymbol{n}} \rangle\rangle}{\sqrt{N}} = \frac{1}{N\beta} \sum_i \left. \frac{\partial \ln(I_0(\beta \mathcal{D}_i))}{\partial \mu_q} \right|_{\substack{h_l = 0 \ \forall l \\ \mu_l = \widetilde{\mu}_l \ \forall l}}. \tag{B.95}$$

Then, the values:

$$\widetilde{\mu}_q = \frac{\langle\langle \boldsymbol{\varphi}^q | \hat{\boldsymbol{n}} \rangle\rangle}{\sqrt{N}}, \tag{B.96}$$

define a minimum of the free energy.

Appendix C

Fixed point stability analysis for mechanically stable structures

In this appendix, we provide the complete linear stability analysis of an arbitrary fixed point for mechanically stable structures (see chapter 5), and derive the lower and upper bounds of stability thresholds.

C.1 Dynamics linearized around a given fixed point

To study the stability of a given fixed point $\left\{|\boldsymbol{u}^0\rangle, |\hat{\boldsymbol{n}}^0\rangle\right\}$ we consider small perturbations $|\hat{\boldsymbol{n}}\rangle = |\hat{\boldsymbol{n}}^0\rangle + |\boldsymbol{\delta}\hat{\boldsymbol{n}}\rangle$ and $|\boldsymbol{u}\rangle = |\boldsymbol{u}^0\rangle + |\boldsymbol{\delta u}\rangle$, where $\hat{\boldsymbol{n}}_i^0 = (\cos\theta_i^0, \sin\theta_i^0)$ and $\boldsymbol{\delta}\hat{\boldsymbol{n}}_i = (-\sin\theta_i^0, \cos\theta_i^0)\delta\theta_i = \hat{\boldsymbol{n}}_i^{0\perp}\delta\theta_i = \langle i|\mathbb{K}_0^T|\delta\theta\rangle$. Linearizing Eqs. (3.46) one gets:

$$|\dot{\boldsymbol{\delta u}}\rangle = -\mathbb{M}|\boldsymbol{\delta u}\rangle + \pi\mathbb{K}_0^T|\delta\theta\rangle, \tag{C.1a}$$

$$|\dot{\delta\theta}\rangle = -\mathbb{K}_0\mathbb{M}|\boldsymbol{\delta u}\rangle - \pi\delta\mathbb{K}|\hat{\boldsymbol{n}}^0\rangle. \tag{C.1b}$$

Since $\boldsymbol{\delta}\hat{\boldsymbol{n}}_i^{\perp} = (-\cos\theta_i^0, -\sin\theta_i^0)\delta\theta_i = -\hat{\boldsymbol{n}}_i^0\delta\theta_i$, we use the contraction $\delta\mathbb{K}|\hat{\boldsymbol{n}}^0\rangle = -|\delta\theta\rangle$. Finally, rescaling time $t \to \pi^{-1}t$ leads to the following system:

$$|\dot{\boldsymbol{\delta u}}\rangle = -\pi^{-1}\mathbb{M}|\boldsymbol{\delta u}\rangle + \mathbb{K}_0^T|\delta\theta\rangle, \tag{C.2a}$$

$$|\dot{\delta\theta}\rangle = -\pi^{-1}\mathbb{K}_0\mathbb{M}|\boldsymbol{\delta u}\rangle + |\delta\theta\rangle. \tag{C.2b}$$

Therefore the stability of the configuration $|\hat{\boldsymbol{n}}^0\rangle$ is encoded in the $3N$ eigenvalues of the matrix

$$\mathbb{D} = \begin{pmatrix} -\pi^{-1}\mathbb{M} & \mathbb{K}_0^T \\ -\pi^{-1}\mathbb{K}_0\mathbb{M} & \mathbb{I} \end{pmatrix}. \tag{C.3}$$

The matrix $\mathbb{D}$ depends on the parameter π, the network geometry, and the equilibrium configuration of the polarities encoded in the matrix $\mathbb{K}_0$. In the following, we drop the subscript 0, but one should remember that $\mathbb{K}$ depends on the configuration of the polarities.

C.2 Properties of the spectrum valid for all fixed points

Consider the eigenvector $|\Psi\rangle = (|\boldsymbol{b}\rangle, |\boldsymbol{c}\rangle)$ of the matrix $\mathbb{D}$ with eigenvalue λ, then:

$$-\pi^{-1}\mathbb{M}|\boldsymbol{b}\rangle + \mathbb{K}^T|\boldsymbol{c}\rangle = \lambda|\boldsymbol{b}\rangle, \tag{C.4a}$$

$$-\pi^{-1}\mathbb{K}\mathbb{M}|\boldsymbol{b}\rangle + |\boldsymbol{c}\rangle = \lambda|\boldsymbol{c}\rangle. \tag{C.4b}$$

Multiplying Eq. (C.4a) by $\mathbb{K}$ and noting that $\mathbb{K}\mathbb{K}^T = \mathbb{I}$ leads to:

$$-\pi^{-1}\mathbb{K}\mathbb{M}|\boldsymbol{b}\rangle + |\boldsymbol{c}\rangle = \lambda\mathbb{K}|\boldsymbol{b}\rangle. \tag{C.5}$$

Comparing with Eq. (C.4b), we obtain that either $\mathbb{K}|\boldsymbol{b}\rangle = |\boldsymbol{c}\rangle$ or $\lambda = 0$.

- First, we consider the case $\lambda = 0$. From Eq. (C.5), $|\boldsymbol{c}\rangle = \pi^{-1}\mathbb{K}\mathbb{M}|\boldsymbol{b}\rangle$; using this relation in Eq. (C.4a) leads to

$$\left(\mathbb{I} - \mathbb{K}^T\mathbb{K}\right)\mathbb{M}|\boldsymbol{b}\rangle = 0. \tag{C.6}$$

  This means that $\mathbb{M}|\boldsymbol{b}\rangle$ must be an eigenvector of $\mathbb{K}^T\mathbb{K}$ with eigenvalue 1. The operator $\mathbb{K}^T\mathbb{K}$ is the projector on the space spanned by $(|\hat{\boldsymbol{n}}_i^\perp\rangle)_i$: it has N eigenvectors $|\boldsymbol{\kappa}_i\rangle = |\hat{\boldsymbol{n}}_i\rangle = \hat{\boldsymbol{n}}_i|i\rangle$ with eigenvalue 0 and N eigenvectors $|\boldsymbol{\kappa}_i\rangle = |\hat{\boldsymbol{n}}_i^\perp\rangle = \hat{\boldsymbol{n}}_i^\perp|i\rangle$ with eigenvalue 1. Hence, for any equilibrium configuration, there are N eigenvectors with eigenvalue 0, given by

$$|\boldsymbol{b}\rangle = \mathbb{M}^{-1}\hat{\boldsymbol{n}}_i^\perp|i\rangle, \tag{C.7a}$$
$$|\boldsymbol{c}\rangle = \pi^{-1}|i\rangle. \tag{C.7b}$$

  These eigenvectors span the tangent space of the N-dimensional fixed points manifold. We also note that, consequently, the equilibrium configurations are all marginally stable.

- Second, we consider the case $\mathbb{K}|\boldsymbol{b}\rangle = |\boldsymbol{c}\rangle$. Inserting this relation in Eq. (C.4a), we obtain

$$\left(-\pi^{-1}\mathbb{M} + \mathbb{K}^T\mathbb{K}\right)|\boldsymbol{b}\rangle = \lambda|\boldsymbol{b}\rangle. \tag{C.8}$$

  λ should thus be an eigenvalue of the symmetric matrix

$$\tilde{\mathbb{D}} = -\pi^{-1}\mathbb{M} + \mathbb{K}^T\mathbb{K}. \tag{C.9}$$

Since $\tilde{\mathbb{D}}$ is symmetric, λ is real; hence, the spectrum of $\mathbb{D}$, $\mathrm{Spec}(\mathbb{D})$, is real and is given by

$$\mathrm{Spec}(\mathbb{D}) = \{0\} \cup \mathrm{Spec}\left(\tilde{\mathbb{D}}\right). \tag{C.10}$$

Since the eigenvalues of $\mathbb{M}$ are bounded between $\omega_{\min}^2$ and $\omega_{\max}^2$, and the eigenvalues of $\mathbb{K}^T\mathbb{K}$ are 0 and 1, the eigenvalues of $\tilde{\mathbb{D}}$ are bounded by

$$-\frac{\omega_{\max}^2}{\pi} \leq \mathrm{Spec}\left(\tilde{\mathbb{D}}\right) \leq 1 - \frac{\omega_{\min}^2}{\pi}. \tag{C.11}$$

When $\pi \to 0$, we see from Eq. (C.11) that $\mathrm{Spec}(\tilde{\mathbb{D}}) \to -\infty$. When $\pi \to \infty$, $\tilde{\mathbb{D}} \to \mathbb{K}^T\mathbb{K}$, which has eigenvalues 0 and 1 with N associated eigenvectors each.

C.3 Stability threshold of a given fixed point

A given fixed point is stable if $\mathrm{Spec}(\tilde{\mathbb{D}}) \leq 0$, which is equivalent to the fact that for any vector $|\boldsymbol{b}\rangle$,

$$\langle\boldsymbol{b}|\tilde{\mathbb{D}}|\boldsymbol{b}\rangle \leq 0. \tag{C.12}$$

With the explicit expression of $\tilde{\mathbb{D}}$, this reads

$$\langle\boldsymbol{b}| - \pi^{-1}\mathbb{M} + \mathbb{K}^T\mathbb{K}|\boldsymbol{b}\rangle \leq 0. \tag{C.13}$$

We now project $|\boldsymbol{b}\rangle$ on the eigenvectors of $\mathbb{M}$; denoting $b_k = \langle \boldsymbol{\varphi}_k | \boldsymbol{b} \rangle$, this reads

$$\sum_{jk} b_j b_k \left(-\pi^{-1} \omega_j \omega_k + \langle \boldsymbol{\varphi}_j | \mathbb{K}^T \mathbb{K} | \boldsymbol{\varphi}_k \rangle \right) \leq 0. \tag{C.14}$$

Now defining $\tilde{b}_k = \omega_k b_k$, this becomes

$$\sum_{jk} \tilde{b}_j \tilde{b}_k \left(-\pi^{-1} + \frac{\langle \boldsymbol{\varphi}_j | \mathbb{K}^T \mathbb{K} | \boldsymbol{\varphi}_k \rangle}{\omega_j \omega_k} \right) \leq 0. \tag{C.15}$$

Introducing the matrix

$$\mathbb{L}_{jk} = \frac{\langle \boldsymbol{\varphi}_j | \mathbb{K}^T \mathbb{K} | \boldsymbol{\varphi}_k \rangle}{\omega_j \omega_k}, \tag{C.16}$$

the stability condition reads

$$\mathrm{Spec} \left(-\pi^{-1} \mathbb{I} + \mathbb{L} \right) \leq 0. \tag{C.17}$$

But $\mathrm{Spec} \left(-\pi^{-1} \mathbb{I} + \mathbb{L} \right) = -\pi^{-1} + \mathrm{Spec}(\mathbb{L})$. Finally, the fixed point $|\hat{\boldsymbol{n}}\rangle$ is stable if

$$\pi \leq \pi_c \left(|\hat{\boldsymbol{n}}\rangle \right) = \frac{1}{\max \mathrm{Spec} \left(\mathbb{L} \left(|\hat{\boldsymbol{n}}\rangle \right) \right)}. \tag{C.18}$$

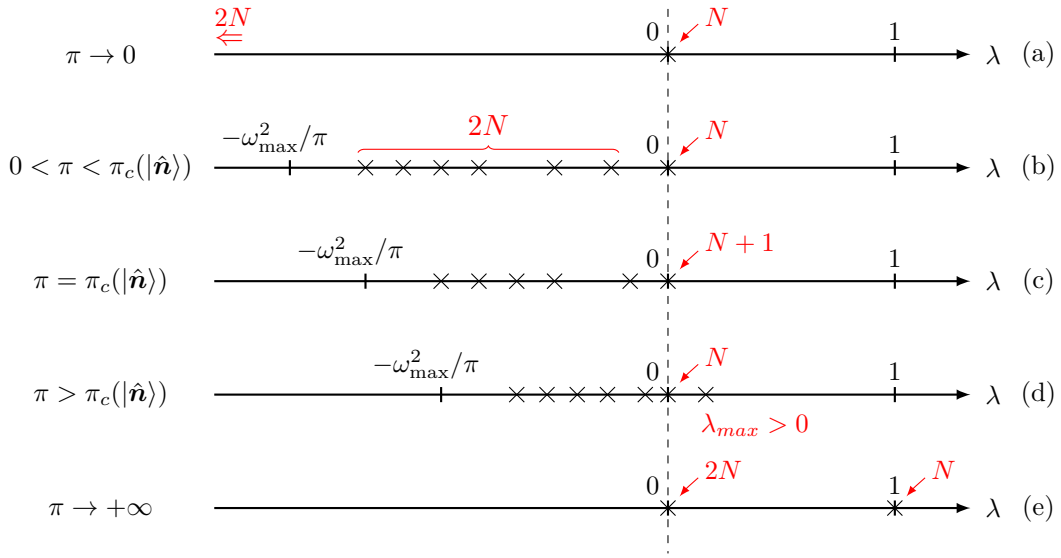


FIG. C.1. **Eigenvalue spectrum for an arbitrary fixed point $\{|\boldsymbol{u}\rangle = \pi \mathbb{M}^{-1} |\hat{\boldsymbol{n}}\rangle, |\hat{\boldsymbol{n}}\rangle\}$.** The fixed point is stable for $\pi < \pi_c(|\hat{\boldsymbol{n}}\rangle)$, where $\pi_c(|\hat{\boldsymbol{n}}\rangle)$ is given by Eqs. (C.18). (a) $\pi \to 0$, N zero eigenvalues and the $2N$ which are left are strictly negative, given by $-\omega_k^2/\pi$. (b) $0 < \pi < \pi_c(|\hat{\boldsymbol{n}}\rangle)$, N zero eigenvalues, and the $2N$ which are left are strictly negative. (c) $\pi = \pi_c(|\hat{\boldsymbol{n}}\rangle)$, $N+1$ zero eigenvalues, and the $2N-1$ which are left are strictly negative. (d) $\pi > \pi_c(|\hat{\boldsymbol{n}}\rangle)$, the greatest eigenvalue is strictly positive. (e) $\pi \to +\infty$, $2N$ zero eigenvalues, N one eigenvalues.

C.4 First linear destabilization

We then determine a lower bound of the stability thresholds and show that this bound is sharp.

Let $\pi_c^{\min}$ be the smallest value of π for which there exists an unstable configuration. We thus have $\pi_c\left(|\hat{\boldsymbol{n}}\rangle\right) \geq \pi_c^{\min}$ for all $|\hat{\boldsymbol{n}}\rangle$. From Eq. (C.11) there can be a positive eigenvalue only if $\pi > \omega_{\min}^2$, hence we have

$$\pi_c\left(|\hat{\boldsymbol{n}}\rangle\right) \geq \pi_c^{\min} = \omega_{\min}^2. \tag{C.19}$$

We now exhibit a configuration $|\hat{\boldsymbol{n}}_{\min}\rangle$ that does destabilize at $\omega_{\min}^2$. Consider the eigenmode of $\mathbb{M}$ associated to the eigenvalue $\omega_1^2 = \omega_{\min}^2$, $|\boldsymbol{\varphi}_1\rangle$; and a configuration $|\hat{\boldsymbol{n}}_{\min}\rangle$ where the orientation $\hat{\boldsymbol{n}}_i$ is orthogonal to $\boldsymbol{\varphi}_1^i$ for every particle i. For this configuration, $\mathbb{L}_{11} = \omega_{\min}^{-2}$, hence $\max \mathrm{Spec}(\mathbb{L}) \geq \omega_{\min}^{-2}$ and $\pi_c(|\hat{\boldsymbol{n}}\rangle) \leq \omega_{\min}^2$. With the lower bound (C.19), we conclude that $\pi_c^{\min} = \pi_c(|\hat{\boldsymbol{n}}_{\min}\rangle) = \omega_{\min}^2$: the lower bound (C.19) is sharp and the first configuration to destabilize is related to the lowest energy mode in a simple way.

C.5 Upper bound of the stability thresholds

We don't have an explicit analytical expression for the largest destabilization threshold, $\pi_c^{\max}$, but we can determine an upper bound π_c^{upp} of it above which there exists no stable fixed point.

To do so, we look for a $|\hat{\boldsymbol{n}}\rangle$-independent lower bound of the maximal eigenvalue of $\tilde{\mathbb{D}}$. We use the restriction of the matrix $\tilde{\mathbb{D}}$ to the two modes j and k, which is a 2×2 matrix that we denote $\tilde{\mathbb{D}}_{\{j,k\}}$. We have

$$\begin{aligned}
\max \mathrm{Spec}\left(\tilde{\mathbb{D}}\left(|\hat{\boldsymbol{n}}\rangle\right)\right) &\geq \max \mathrm{Spec}\left(\tilde{\mathbb{D}}_{\{j,k\}}\left(|\hat{\boldsymbol{n}}\rangle\right)\right), \\
&= \frac{\tilde{\mathbb{D}}_{jj}+\tilde{\mathbb{D}}_{kk}}{2} + \sqrt{\frac{(\tilde{\mathbb{D}}_{jj}-\tilde{\mathbb{D}}_{kk})^2}{4} + \tilde{\mathbb{D}}_{jk}^2}, \\
&\geq \frac{\tilde{\mathbb{D}}_{jj}+\tilde{\mathbb{D}}_{kk}}{2}.
\end{aligned} \tag{C.20}$$

Explicitly,

$$\frac{\tilde{\mathbb{D}}_{jj}+\tilde{\mathbb{D}}_{kk}}{2} = -\frac{\omega_j^2+\omega_k^2}{2\pi} + \frac{1}{2}\left(\langle\boldsymbol{\varphi}_j|\mathbb{K}^T\mathbb{K}|\boldsymbol{\varphi}_j\rangle + \langle\boldsymbol{\varphi}_k|\mathbb{K}^T\mathbb{K}|\boldsymbol{\varphi}_k\rangle\right), \tag{C.21}$$

$$= -\frac{\omega_j^2+\omega_k^2}{2\pi} + \frac{1}{2}\sum_i \left[(\boldsymbol{\varphi}_j^i \times \hat{\boldsymbol{n}}_i)^2 + (\boldsymbol{\varphi}_k^i \times \hat{\boldsymbol{n}}_i)^2\right]. \tag{C.22}$$

Now we have to minimize the term in the sum over the orientations $\hat{\boldsymbol{n}}_i$. This amounts to finding the minimal eigenvalue of the matrix

$$\begin{aligned}
\boldsymbol{\varphi}_j^i(\boldsymbol{\varphi}_j^i)^T + \boldsymbol{\varphi}_k^i(\boldsymbol{\varphi}_k^i)^T &= \begin{pmatrix} (\varphi_{j,x}^i)^2 + (\varphi_{k,x}^i)^2 & (\varphi_{j,x}^i)(\varphi_{j,y}^i) + (\varphi_{k,x}^i)(\varphi_{k,y}^i) \\ (\varphi_{j,x}^i)(\varphi_{j,y}^i) + (\varphi_{k,x}^i)(\varphi_{k,y}^i) & (\varphi_{j,y}^i)^2 + (\varphi_{k,y}^i)^2 \end{pmatrix}, \\
&= \begin{pmatrix} c_{11} & c_{12} \\ c_{12} & c_{22} \end{pmatrix},
\end{aligned} \tag{C.23}$$

which is

$$\lambda_{\min} = \frac{1}{2}\left[c_{11}+c_{22} - \sqrt{(c_{11}-c_{22})^2 + 4c_{12}^2}\right], \tag{C.24}$$

$$= \frac{1}{2}\left[\left(\boldsymbol{\varphi}_j^i\right)^2 + \left(\boldsymbol{\varphi}_k^i\right)^2 - \left(\left[\left(\boldsymbol{\varphi}_j^i\right)^2 + \left(\boldsymbol{\varphi}_k^i\right)^2\right]^2 - 4\left[\boldsymbol{\varphi}_j^i \times \boldsymbol{\varphi}_k^i\right]^2\right)^{1/2}\right]. \tag{C.25}$$

Using the fact that the modes are normalized, we finally get the bound

$$\max \mathrm{Spec}\left(\tilde{\mathbb{D}}\left(|\hat{\boldsymbol{n}}\rangle\right)\right) \geq -\frac{\omega_j^2+\omega_k^2}{2\pi}+\frac{1}{2}\left[1-\frac{1}{2}\sum_i\left(\left[\left(\boldsymbol{\varphi}_j^i\right)^2+\left(\boldsymbol{\varphi}_k^i\right)^2\right]^2-4\left[\boldsymbol{\varphi}_j^i\times\boldsymbol{\varphi}_k^i\right]^2\right)^{1/2}\right]. \tag{C.26}$$

All the fixed points are unstable when this bound is positive, which happens for

$$\pi \geq \pi_{c,u}^{\{j,k\}} = \frac{\omega_j^2+\omega_k^2}{c(|\boldsymbol{\varphi}_j\rangle,|\boldsymbol{\varphi}_k\rangle)}, \tag{C.27}$$

with

$$c(|\boldsymbol{\varphi}_j\rangle,|\boldsymbol{\varphi}_k\rangle) = 1-\frac{1}{2}\sum_i\left(\left[\left(\boldsymbol{\varphi}_j^i\right)^2+\left(\boldsymbol{\varphi}_k^i\right)^2\right]^2-4\left[\boldsymbol{\varphi}_j^i\times\boldsymbol{\varphi}_k^i\right]^2\right)^{1/2}. \tag{C.28}$$

Finally, the bound for π, above which there exists no stable fixed point is

$$\pi_c^{\mathrm{upp}} = \min_{\{j,k\}}\left(\frac{\omega_j^2+\omega_k^2}{c(|\boldsymbol{\varphi}_j\rangle,|\boldsymbol{\varphi}_k\rangle)}\right). \tag{C.29}$$

Note that the function $c(\bullet,\bullet)$ is bounded between 0, when $j=k$, and 1, when the pair of modes $(|\boldsymbol{\varphi}_j\rangle,|\boldsymbol{\varphi}_k\rangle)$ are locally orthogonal and of the same norm.

Appendix D

Zero-rest-length chains

In this appendix, we provide the derivation of the CA regime's explicit expression in the general case of a normal mode spectrum composed of pairs of degenerated and locally-orthogonal eigenmodes (see chapter 5). We then analyze its stability. Eventually, we apply this framework to zero-rest-length chains with $N = 2$, 3, and 4.

D.1 Single-frequency limit cycles.

We look for a CA regime such that all the particles turn with the same constant angular velocity: the orientation $\theta_j(t)$ of the particle j follows

$$\theta_j(t) = \Omega t + \phi_j, \tag{D.1}$$

where ϕ_j is a constant phase. Integrating Eq. (3.49a), we deduce that:

$$a^u_{x,k}(t) = a^u_{x,k}(0)e^{-\omega_k^2 t} + \pi \sum_j \int_0^t \varphi^j_k \cos(\theta_j(t-t'))e^{-\omega_k^2 t'}\ \mathrm{d}t', \tag{D.2a}$$

$$a^u_{y,k}(t) = a^u_{y,k}(0)e^{-\omega_k^2 t} + \pi \sum_j \int_0^t \varphi^j_k \sin(\theta_j(t-t'))e^{-\omega_k^2 t'}\ \mathrm{d}t'. \tag{D.2b}$$

In the long time limit,

$$a^u_{x,k}(t) = \frac{\pi}{\omega_k^4 + \Omega^2} \sum_j \varphi^j_k f_k(\Omega t + \phi_j), \tag{D.3a}$$

$$a^u_{y,k}(t) = \frac{\pi}{\omega_k^4 + \Omega^2} \sum_j \varphi^j_k f_k\left(\Omega t + \phi_j - \frac{\pi}{2}\right), \tag{D.3b}$$

where we have defined

$$f_k(\theta) = \omega_k^2 \cos(\theta) + \Omega \sin(\theta). \tag{D.4}$$

Using the above expressions in the equation for $\dot{\theta}_j = \Omega$, Eq. (3.47b), we get

$$\Omega = \sum_k \omega_k^2 \varphi^j_k \left[\sin(\theta_j) a^u_{x,k} - \cos(\theta_j) a^u_{y,k}\right] = \sum_{k,i} \frac{\pi \omega_k^2}{\omega_k^4 + \Omega^2} \varphi^i_k \varphi^j_k f_k \left(\phi_i - \phi_j + \frac{\pi}{2}\right). \tag{D.5}$$

We obtain a set of N equations with N unknowns: Ω and $N-1$ phases (we can always fix one of them). $\Omega = 0$ is always a solution, corresponding to a fixed point. Depending on π, there may be other solutions. Note that the radii of rotation of the particles can be computed at any time by summing over the modes:

$$R_j = \sqrt{\boldsymbol{u}_j^2} = \sqrt{\sum_{k,l} \varphi^j_k \varphi^j_l (a_{x,k} a_{x,l} + a_{y,k} a_{y,l})}. \tag{D.6}$$

D.2 Stability of the limit cycles.

Each solution may be tested for stability. To determine the stability of a rotating solution, we use the comoving frame and introduce the coefficients β such that:

$$a^u_{x,k}(t) = \beta_{x,k}(t)\cos(\Omega t) - \beta_{y,k}(t)\sin(\Omega t), \tag{D.7a}$$
$$a^u_{y,k}(t) = \beta_{x,k}(t)\sin(\Omega t) + \beta_{y,k}(t)\cos(\Omega t). \tag{D.7b}$$

We now write these coefficients as the rotating solution plus a perturbation:

$$\beta_{x,k}(t) = \beta^{(0)}_{x,k} + \beta^{(1)}_{x,k}(t), \tag{D.8a}$$
$$\beta_{y,k}(t) = \beta^{(0)}_{y,k} + \beta^{(1)}_{y,k}(t), \tag{D.8b}$$
$$\theta_j(t) = \theta^{(0)}_j(t) + \theta^{(1)}_j(t), \tag{D.8c}$$

with

$$\beta^{(0)}_{x,k} = \frac{\pi}{\omega_k^4 + \Omega^2}\sum_j \varphi^j_k f_k(\phi_j), \tag{D.9a}$$
$$\beta^{(0)}_{y,k} = \frac{\pi}{\omega_k^4 + \Omega^2}\sum_j \varphi^j_k f_k\left(\phi_j - \frac{\pi}{2}\right), \tag{D.9b}$$
$$\theta^{(0)}_j = \Omega t + \phi_j. \tag{D.9c}$$

The dynamical equations for these perturbations are derived from (3.49a) and (3.47b):

$$\dot\beta^{(1)}_{x,k} = -\omega_k^2\beta^{(1)}_{x,k} + \Omega\beta^{(1)}_{y,k} - \pi\sum_i \varphi^i_k \sin(\phi_i)\theta^{(1)}_i, \tag{D.10a}$$
$$\dot\beta^{(1)}_{y,k} = -\omega_k^2\beta^{(1)}_{y,k} - \Omega\beta^{(1)}_{x,k} + \pi\sum_i \varphi^i_k \cos(\phi_i)\theta^{(1)}_i, \tag{D.10b}$$
$$\dot\theta^{(1)}_j = \sum_k \omega_k^2\varphi^j_k\left[\sin(\phi_j)\beta^{(1)}_{x,k} - \cos(\phi_j)\beta^{(1)}_{y,k}\right] + \sum_{k,i}\frac{\pi\omega_k^2}{\omega_k^4+\Omega^2}\varphi^i_k\varphi^j_k f_k(\phi_i-\phi_j)\theta^{(1)}_j. \tag{D.10c}$$

D.3 Geometrical restriction on the existence of rotating solutions

A simple condition can be derived to determine the stability of the rotating solution found above. Let us remind the equations for a single particle:

$$\dot{\boldsymbol{x}}_i = \pi\hat{\boldsymbol{n}}_i + \boldsymbol{F}^{el}_i, \tag{D.11a}$$
$$\dot\theta_i = \boldsymbol{F}_i\cdot\hat{\boldsymbol{n}}^\perp_i, \tag{D.11b}$$

where we may express Eq. (D.11b) as:

$$\dot\theta_i = \dot{\boldsymbol{x}}_i\cdot\hat{\boldsymbol{n}}^\perp_i. \tag{D.12}$$

Consider an active particle in the condensed state of the linear chain (i.e. circular motion). From the dynamics periodicity, the angular speed of the position and polarity vectors are the same. Thus:

$$\dot{\boldsymbol{x}}_i = \Omega R_i\hat{\boldsymbol{r}}^\perp_i, \tag{D.13a}$$
$$\dot\theta_i = \Omega, \tag{D.13b}$$

where R_i is the radius of particle i's trajectory. Then, replacing in Eq (D.12), and discarding the $\Omega = 0$ case:

$$\frac{1}{R_i} = \hat{\boldsymbol{r}}_i^{\perp} \cdot \hat{\boldsymbol{n}}_i^{\perp} = \hat{\boldsymbol{r}}_i \cdot \hat{\boldsymbol{n}}_i \leq 1. \tag{D.14}$$

This means rotating solutions exist only when the trajectory radius of all the particles is greater than 1. As π decreases, the radii of rotation of the active units in the rotating solution decrease until the outer-most particles cross the threshold, and the steady rotating solution does not exist anymore. In this state, the whole system may stop abruptly or transition to a heterogeneous regime, where those polarity vectors are frozen and spatially coexist with oscillating ones.

D.4 Application to the chains

In the following, we apply the above framework to the example of the zero-rest-length chains introduced in chapter 5.

$N = 2$ chain

Setting $\phi_1 = 0$ rad, Eqs. (D.5) for Ω and ϕ_2 read

$$\Omega = \pi \left[\frac{\Omega(1+\cos(\phi_2)) - \sin(\phi_2)}{2(1+\Omega^2)} + 3\frac{\Omega(1-\cos(\phi_2)) + 3\sin(\phi_2)}{2(9+\Omega^2)} \right], \tag{D.15a}$$

$$= \pi \left[\frac{\Omega(1+\cos(\phi_2)) + \sin(\phi_2)}{2(1+\Omega^2)} + 3\frac{\Omega(1-\cos(\phi_2)) - 3\sin(\phi_2)}{2(9+\Omega^2)} \right]. \tag{D.15b}$$

We see that $\phi_2 = 0$ rad or $\phi_2 = \pi$ rad. For $\phi_2 = 0$ the angular velocity is given by

$$\Omega = \sqrt{\pi - 1}, \tag{D.16}$$

which is a valid solution as long as $\pi \geq 1$ (Fig. 5.14). To determine the stability of this solution, we need to study the spectrum of the matrix

$$\mathbb{C}_2 = \begin{pmatrix} -1 & \Omega & 0 & 0 & 0 & 0 \\ -\Omega & -1 & 0 & 0 & \frac{\pi}{\sqrt{2}} & \frac{\pi}{\sqrt{2}} \\ 0 & 0 & -3 & \Omega & 0 & 0 \\ 0 & 0 & -\Omega & -3 & \frac{\pi}{\sqrt{2}} & -\frac{\pi}{\sqrt{2}} \\ 0 & -\frac{1}{\sqrt{2}} & 0 & -\frac{3}{\sqrt{2}} & 1 & 0 \\ 0 & -\frac{1}{\sqrt{2}} & 0 & \frac{3}{\sqrt{2}} & 0 & 1 \end{pmatrix}. \tag{D.17}$$

We are interested in particular in the zero eigenvalues. This matrix always admits one that corresponds to global rotations, which does not preclude the stability of the solution. There is another null eigenvalue when $\pi = 1$, meaning that the rotating solution is stable on its whole range of existence. We can also compute the radius of rotation and obtain $R = \sqrt{\pi}$. This rotating solution strictly maps with the one of the single particle, which is expected given the geometry of modes $|\boldsymbol{\varphi}_{x,1}\rangle$ and $|\boldsymbol{\varphi}_{y,1}\rangle$, which are completely delocalized and locally orthogonal. Finally, one can show that the rotating solution corresponding to $\phi_2 = \pi$ rad is unstable.

$N = 3$ **chain**

For symmetry reasons, we assume that $\phi_1 = \phi_3$, and set these phases to 0. From Eqs. (D.5), we can establish the relation between Ω and π:

$$\frac{4 + 12\Omega^2 + \Omega^4}{2\pi} = 2 + \Omega^2 \pm \frac{8\Omega(\Omega^2 - 2)}{\sqrt{4 + 140\Omega^2 + \Omega^4}}. \tag{D.18}$$

Plotting Ω versus π reveals a bifurcation that occurs for $\pi_{CA} \simeq 0.7310$, $\Omega^{CA} \simeq 0.1733$ (Fig. 5.14): there is no rotating solution for $\pi < \pi_{CA}$, while there are two solutions for $\pi > \pi_{CA}$, a stable one and an unstable one. Contrary to the $N = 2$ chain, the rotation starts with a finite angular velocity Ω_{CA}.

$N = 4$ **chain**

Assuming that $\phi_1 = \phi_4$ and $\phi_2 = \phi_3$, we derive from Eqs. (D.5) the equation for the rotating solution:

$$\frac{1 + 7\Omega^2 + \Omega^4}{\pi} = \frac{3}{2}(1 + \Omega^2) \pm (1 - \Omega^2)\sqrt{1 - \left(\frac{1 - \Omega^2}{6\Omega}\right)^2}. \tag{D.19}$$

The solution presents a bifurcation $\pi_{CA} \simeq 0.5987$, $\Omega_{CA} \simeq 0.2082$ (Fig. 5.14).

Appendix E

Two coupled particles in a harmonic potential

In this appendix, we provide the complete derivation of the orbiting solution expression for the two-particles toy model (see chapter 5), and study its stability.

Orbiting solutions

Equations. Starting from the general noiseless equations within the harmonic approximation:

$$\dot{\boldsymbol{u}}_i = \pi \hat{\boldsymbol{n}}_i + \boldsymbol{F}_i^{el}\left[\boldsymbol{u}\right], \tag{E.1a}$$

$$\dot{\boldsymbol{n}}_i = (\hat{\boldsymbol{n}}_i \times \boldsymbol{F}_i^{el}\left[\boldsymbol{u}\right]) \times \hat{\boldsymbol{n}}_i. \tag{E.1b}$$

We look for steady solutions orbiting at a rate Ω. This means that $\dot{\boldsymbol{u}} = \Omega \boldsymbol{u}^{\perp}$ and $\dot{\boldsymbol{n}} = \Omega \boldsymbol{n}^{\perp}$. The evolution equations become

$$\Omega \boldsymbol{u}^{\perp} = \pi \hat{\boldsymbol{n}}_i + \boldsymbol{F}_i^{el}\left[\boldsymbol{u}\right], \tag{E.2a}$$

$$\Omega \hat{\boldsymbol{n}}^{\perp} = (\hat{\boldsymbol{n}}_i \times \boldsymbol{F}_i^{el}) \times \hat{\boldsymbol{n}}_i. \tag{E.2b}$$

The right-hand side of Eq. (E.2b) is a projection of $\boldsymbol{F}_i^{el}$ on $\hat{\boldsymbol{n}}_i^{\perp}$. Taking the scalar product with $\hat{\boldsymbol{n}}_i^{\perp}$, it becomes

$$\Omega = \hat{\boldsymbol{n}}_i^{\perp} \cdot \boldsymbol{F}_i^{el}\left[\boldsymbol{u}\right]. \tag{E.3}$$

Taking the scalar product of Eq. (E.2a) with $\hat{\boldsymbol{n}}_i^{\perp}$, we get

$$\hat{\boldsymbol{n}}_i \cdot \boldsymbol{u}_i = 1. \tag{E.4}$$

Hence our final equations are

$$\Omega \boldsymbol{u}_i^{\perp} - \boldsymbol{F}_i^{el}\left[\boldsymbol{u}\right] = \pi \hat{\boldsymbol{n}}_i, \tag{E.5a}$$

$$\boldsymbol{n}_i \cdot \boldsymbol{u}_i = 1. \tag{E.5b}$$

There are 6 equations with 7 unknowns: the positions $\boldsymbol{u}_i$ (4 unknowns), the polarities $\hat{\boldsymbol{n}}_i$ (2 unknowns), and the orbiting rate Ω. From invariance by rotation, we can set the phase of the orientation of particle 1, say $\phi_1 = 0$. This leaves us with 6 equations with 6 unknowns. However, this system is non-linear.

Resolution. From Eq. (E.5b), we see that:

$$\boldsymbol{u}_i = \hat{\boldsymbol{n}}_i + \lambda_i \hat{\boldsymbol{n}}_i^{\perp}. \tag{E.6}$$

Projecting Eq. (E.5a) on $\hat{\boldsymbol{n}}_i$ leads to

$$-\lambda_i \Omega - \hat{\boldsymbol{n}}_i \cdot \boldsymbol{F}_i^{el}[\boldsymbol{u}] = \pi. \tag{E.7}$$

We can get rid of the parameter π by taking the difference between the two equations (for $i = 1$ and $i = 2$):

$$(\lambda_1 - \lambda_2)\Omega + \hat{\boldsymbol{n}}_1 \cdot \boldsymbol{F}_1^{el}[\boldsymbol{u}] - \hat{\boldsymbol{n}}_2 \cdot \boldsymbol{F}_2^{el}[\boldsymbol{u}] = 0. \tag{E.8}$$

Now, projecting Eq. (E.5a) on $\hat{\boldsymbol{n}}_i^{\perp}$ leads to:

$$\Omega - \hat{\boldsymbol{n}}_i^{\perp} \cdot \boldsymbol{F}_i^{el}[\boldsymbol{u}] = 0. \tag{E.9}$$

Formally, the set of Eqs. (E.8) and (E.9) is of the form:

$$A \begin{pmatrix} \lambda_1 \\ \lambda_2 \end{pmatrix} = B, \tag{E.10}$$

where A and B are 3×2 and 3×1 matrices. The 2 columns of A and B are vectors in $\mathbb{R}^3$. If a solution to Eq. (E.10) exists, then B lies in the vector space spanned by the 2 columns of A, meaning that these 3 vectors span only a $2d$ space. Hence, the determinant of the 3×3 matrix $\bar{A}$ composed of the 2 columns of A and the vector B is 0. The converse is not true, but we assume that it is true most of the time, and use the determinant of $\bar{A}$ to determine whether a solution exists. Here:

$$\bar{A} = \begin{pmatrix} k + k_1 & -k\cos(\phi) & -\Omega + k\sin(\phi) \\ -k\cos(\phi) & k + k_2 & -\Omega - k\sin(\phi) \\ \Omega - k\sin(\phi) & -\Omega - k\sin(\phi) & k_1 - k_2 \end{pmatrix}, \tag{E.11}$$

where $\phi = \phi_2$ is the phase difference between the two particles, and

$$\det(\bar{A}) = (k_2 - k_1)\left[\Omega^2 - \frac{2k(2k + k_1 + k_2)\sin(\phi)}{k_2 - k_1}\Omega - k(k_1 + k_2) - k_1 k_2\right]. \tag{E.12}$$

In particular, when $k = 1$, $k_1 = 1 - \delta$, $k_2 = 1 + \delta$, we find:

$$\det(\bar{A}) = -2\delta\left[\Omega^2 + \frac{4\sin(\phi)}{\delta}\Omega - 3 + \delta^2\right]. \tag{E.13}$$

The roots of this second-order polynomial are:

$$\Omega_{\pm} = \frac{-2\sin\phi \pm \sqrt{4\sin(\phi)^2 + 3\delta^2 - \delta^4}}{\delta}. \tag{E.14}$$

Once the value of Ω is known, solving Eq. (E.9) gives the value of λ_i:

$$\begin{pmatrix} \lambda_1 \\ \lambda_2 \end{pmatrix} = \frac{1}{k^2\sin(\phi)^2 + kk_1 + kk_2 + k_1k_2} \begin{pmatrix} k + k_2 & k\cos(\phi) \\ k\cos(\phi) & k + k_1 \end{pmatrix} \begin{pmatrix} -\Omega + k\sin(\phi) \\ -\Omega - k\sin(\phi) \end{pmatrix}. \tag{E.15}$$

Then, using Eq. (E.7) with $i = 1$ gives the value of π:

$$\pi = k\left[1 - \cos(\phi)\right] + k_1 - \Omega\lambda_1 + k\sin(\phi)\lambda_2. \tag{E.16}$$

Inserting the value of λ_i above, we get an explicit expression for π. When $k = 1$, $k_1 = 1 + \delta$, $k_2 = 1 - \delta$, it reads:

$$\pi = 2 + \delta - \cos\phi + \frac{\Omega^2(2 - \delta + \cos\phi) - 4\Omega\sin\phi - (2 + \delta - \cos\phi)\sin(\phi)^2}{3 - \delta^2 + \sin(\phi)^2}. \tag{E.17}$$

Below, we study the stability of the orbiting solution.

Stability analysis. We introduce a small perturbation:

$$\boldsymbol{u}_i = \mathcal{R}_{\Omega t}\left[\boldsymbol{u}_i^0 + \boldsymbol{u}_i^1(t)\right], \tag{E.18a}$$

$$\phi_i(t) = \phi_i^0 + \Omega t + \phi_i^1(t), \tag{E.18b}$$

where $\mathcal{R}_{\Omega t}$ is the rotation matrix of angle Ωt. Injecting in the equations of motion leads to:

$$\dot{\boldsymbol{u}}_i^1(t) = -\Omega \boldsymbol{u}_i^{\perp} + \pi\phi_i^1(t)\hat{\boldsymbol{n}}_i^{0\perp} + \boldsymbol{F}_i^{el}\left[\boldsymbol{u}^1(t)\right], \tag{E.19a}$$

$$\dot{\phi}_i^1(t) = -\hat{\boldsymbol{n}}_i^0 \cdot \boldsymbol{F}_i^{el}\left[\boldsymbol{u}^0\right]\phi_i^1(t) + \hat{\boldsymbol{n}}_i^{0\perp} \cdot \boldsymbol{F}_i^{el}\left[\boldsymbol{u}^1(t)\right]. \tag{E.19b}$$

Using Eq. (E.5a) for the rotating state, we obtain:

$$\hat{\boldsymbol{n}}_i^0 \cdot \boldsymbol{F}_i^{el}\left[\boldsymbol{u}^0\right] = \Omega \boldsymbol{u}_i^{0\perp} \cdot \hat{\boldsymbol{n}}_i^0 - \pi = -\Omega\lambda_i - \pi, \tag{E.20}$$

where we have used Eq. (E.6). The evolution of the vector $(u_{1,x}^1,\, u_{2,x}^1,\, u_{1,y}^1,\, u_{2,y}^1,\, \phi_1^1,\, \phi_2^1)$ is linear and is given by the matrix:

$$\begin{pmatrix}
-(k+k_1) & k & \Omega & 0 & 0 & 0 \\
k & -(k+k_2) & 0 & \Omega & 0 & -\pi\sin(\phi) \\
-\Omega & 0 & -(k+k_1) & k & \pi & 0 \\
0 & -\Omega & k & -(k+k_2) & 0 & \pi\cos(\phi) \\
0 & 0 & -(k+k_1) & k & \pi+\lambda_1 & 0 \\
-k\sin(\phi) & (k+k_2)\sin(\phi) & k\cos(\phi) & -(k+k_2)\cos(\phi) & 0 & \pi+\lambda_2
\end{pmatrix}, \tag{E.21}$$

where we have used $\phi_1^0 = 0$ and $\phi_2^0 = \phi$. The eigenvalues of this matrix can be calculated numerically for a given rotating state.

Appendix F

Single particle mapping to non-reciprocal systems

In this appendix, we draw connections between the dynamics of a single particle trapped in a harmonic potential and non-reciprocal systems, specifically the model introduced by *Fruchart et al.* [172] of non-reciprocally coupled XY spins. Assuming that the dynamics along the radial variable is very fast, we first demonstrate the existence of an exceptional point at the transition to spontaneous oscillations, and then provide the mapping between the two models.

F.1 Single particle dynamics

Our starting point is the equations of motion for a single particle trapped in a harmonic potential (see chapter 5):

$$\dot{R} = \pi \cos\gamma - \omega_0^2 R, \tag{F.1a}$$

$$\dot{\varphi} = \frac{\pi}{R} \sin(\theta - \varphi), \tag{F.1b}$$

$$\dot{\theta} = \omega_0^2 R \sin(\theta - \varphi), \tag{F.1c}$$

where R and φ are the polar-coordinate components of the displacement vector, and θ denotes the orientation of the active unit.

F.2 Exceptional points

Assuming the dynamics along R quickly relaxes to its stationary value R_0, we restrict ourselves to the equations for θ and φ. Copy-pasting Eqs. (F.1), we have:

$$\dot{\varphi} = \frac{\pi}{R_0} \sin(\theta - \varphi), \tag{F.2a}$$

$$\dot{\theta} = \omega_0^2 R_0 \sin(\theta - \varphi). \tag{F.2b}$$

Let us linearize Eqs. (F.2) around the stationary states of the single particle above and below the instability $\pi = \omega_0^2$, and write the Lagrangian of the system:

Fixed points. For $\pi \leq \omega_0^2$, we linearize around the fixed point ($R_0 = \pi/\omega_0^2$, $\varphi_0 = \theta_0$). The Lagrangian can be written as follows:

$$L = \begin{pmatrix} -\omega_0^2 & \omega_0^2 \\ -\pi & \pi \end{pmatrix}, \tag{F.3}$$

which is diagonalizable for any $\pi \neq \omega_0^2$. However, at instability onset $\pi = \omega_0^2$, the Lagrangian expresses as:

$$L = \omega_0^2 \begin{pmatrix} -1 & 1 \\ -1 & 1 \end{pmatrix}, \tag{F.4}$$

which is not diagonalizable, highlighting the presence of an exceptional point.

Orbiting solution. For $\pi \geq \omega_0^2$, we linearize around the orbiting solution ($R_0 = \sqrt{\pi}/\omega_0$, $\varphi_0 = \Omega t$, $\cos\gamma_0 = \omega_0/\sqrt{\pi}$), where $\Omega = \omega_0\sqrt{\pi - \omega_0^2}$ is the oscillation frequency and $\gamma_0 = \theta_0 - \varphi_0$. The Lagrangian expresses as:

$$L = \begin{pmatrix} -\sqrt{\pi\omega_0^2} & \sqrt{\pi\omega_0^2} \\ -\sqrt{\pi\omega_0^2} & \sqrt{\pi\omega_0^2} \end{pmatrix} = \sqrt{\pi\omega_0^2} \begin{pmatrix} -1 & 1 \\ -1 & 1 \end{pmatrix}, \tag{F.5}$$

which is not diagonalizable. The orbiting solution lies on a line of exceptional points.

F.3 Mapping of j_+ and j_-

The model of two non-reciprocally coupled XY spins introduced by *Fruchart et al.* [172] reads:

$$\dot{\theta}_A = J_{AB}\sin(\theta_A - \theta_B), \tag{F.6a}$$
$$\dot{\theta}_B = J_{BA}\sin(\theta_B - \theta_A), \tag{F.6b}$$

which can be rewritten

$$\dot{\bar{\theta}} = j_-\sin(\Delta\theta), \tag{F.7a}$$
$$\dot{\Delta\theta} = j_+\sin(\bar{\theta}), \tag{F.7b}$$

where $\bar{\theta} = (\theta_A + \theta_B)/2$ and $\Delta\theta = (\theta_A - \theta_B)/2$, and where $j_+ = (J_{AB} + J_{BA})/2$ and $j_- = (J_{AB} - J_{BA})/2$. Once again, assuming the dynamics along R quickly relaxes to its equilibirum value R_0, we restrict ourselves to the equations for θ and φ. We have:

$$\dot{\varphi} = \frac{\pi}{R_0}\sin(\theta - \varphi) \leftrightarrow \theta_A, \tag{F.8a}$$
$$\dot{\theta} = \omega_0^2 R_0 \sin(\theta - \varphi) \leftrightarrow \theta_B, \tag{F.8b}$$

where, on the right-hand side, we specify the mapping with Eqs. (F.6). In the general case, in the one particle system, the coefficients J_{AB} and J_{BA} of Eqs. (F.8) can be written as follows

$$\begin{cases} J_{AB} = \pi/R_0(\pi, \omega_0^2) \\ J_{BA} = -\omega_0^2 R_0(\pi, \omega_0^2) \end{cases} \tag{F.9}$$

Fixed points. For $\pi \leq \omega_0^2$, the system lies on the fixed points with $R_0 = \pi/\omega_0^2$. Eqs. (F.9) turn into

$$\begin{cases} J_{AB} = \omega_0^2 \\ J_{BA} = -\pi \end{cases} \Rightarrow \begin{cases} j_- = \frac{\omega_0^2 + \pi}{2} \\ j_+ = \frac{\omega_0^2 - \pi}{2} \end{cases} \tag{F.10}$$

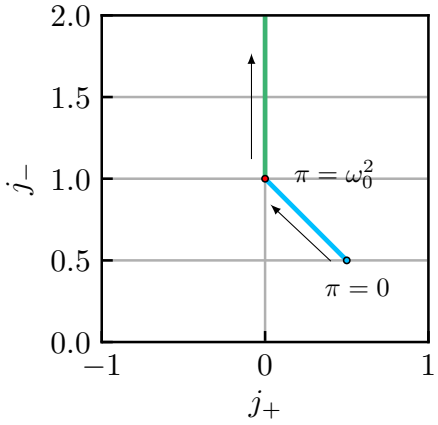


FIG. F.1. **Mapping of Eqs. (F.8) in the j_+/j_- plane.** Graphical representation of the results of Eqs. (F.10) and (F.11). The red (resp. blue) dot highlights the change of stability of the fixed points at $\pi = \omega_0^2$ (resp. $\pi = 0$)

Orbiting solution. For $\pi \geq \omega_0^2$, the system oscillates with $R_0 = \sqrt{\pi/\omega_0^2}$. Eqs. (F.9) turn into

$$\begin{cases} J_{AB} = \sqrt{\pi\omega_0^2} \\ J_{BA} = -\sqrt{\pi\omega_0^2} \end{cases} \Rightarrow \begin{cases} j_- = \sqrt{\pi\omega_0^2} \\ j_+ = 0 \end{cases} \tag{F.11}$$

Interestingly enough, in the oscillating regime, the radius R_0 is "fine-tuned" so that j_+ exactly vanishes.

To conclude, some connections can be drawn between non-reciprocally coupled XY spins and the dynamics of a single particle trapped in a harmonic potential. However, remember that we neglected the dynamics of the radial variable, which plays a crucial role, and therefore, all the above conclusions should be taken with a grain of salt.

Appendix G

Dynamical matrix of an homogeneously dilated structure

In this appendix, we derive the expression of the dynamical matrix for structures dilating homogeneously as a function of tension (see chapter 6).

We consider an elastic structure of springs with homogeneous rest length l_0 and stiffness k (which are both equal to 1 in the following). We denote $\boldsymbol{R}_i$ the reference configuration of node i at zero tension, and $\mathbb{M}_0$ the dynamical matrix at zero tension. As in the experimental settings, we consider that tension is applied on the lattice by stretching uniformly its boundaries, such that springs are elongated by a factor α. The new reference configuration of node i reads $\boldsymbol{R}_i(\alpha)$. Due to lattice pre-stress, its normal modes and their corresponding eigenvalues change via two mechanisms [157]: (i) tension $\alpha - 1$ stiffens the bonds, changing the normal modes energy and geometry; (ii) force balance on the nodes changes their rest positions - modifying the structure of the dynamical matrix. For homogenous dilation, the new positions are simply $\boldsymbol{R}_i \to \alpha \boldsymbol{R}_i$ for the extension $\alpha = l_{eq}/l_0$. We consider small deviations from the equilibrium positions and define the position of each particle $\boldsymbol{r}_i = \boldsymbol{R}_i + \boldsymbol{u}_i$, where $\boldsymbol{R}_i = (\alpha x_i^{eq}, \alpha y_i^{eq})$ and $\boldsymbol{u}_i = (u_i^x, u_i^y)$. The elastic force particle j exerts on particle i is:

$$\mathbf{F}_{ij} = \left(1 - \frac{1}{|\boldsymbol{r}_j - \boldsymbol{r}_i|}\right)(\boldsymbol{r}_j - \boldsymbol{r}_i)\,. \tag{G.1}$$

Using the positions we defined and keeping only leading terms in u, we get:

$$\begin{aligned}
|\mathbf{r}_j - \mathbf{r}_i| &= \sqrt{\begin{array}{l}\left[\alpha\left(x_j^{eq} - x_i^{eq}\right) + u_j^x - u_i^x\right]^2 \\ + \left[\alpha\left(y_j^{eq} - y_i^{eq}\right) + u_j^y - u_i^y\right]^2\end{array}}, \\
&\approx \sqrt{\begin{array}{l}\alpha^2\left[\left(x_j^{eq} - x_i^{eq}\right)^2 + \left(y_j^{eq} - y_i^{eq}\right)^2\right] \\ + 2\alpha\left(x_j^{eq} - x_i^{eq}\right)\left(u_j^x - u_i^x\right) \\ + 2\alpha\left(y_j^{eq} - y_i^{eq}\right)\left(u_j^y - u_i^y\right)\end{array}}, \\
&= \alpha\sqrt{\begin{array}{l}1 + \frac{2}{\alpha}\left(x_j^{eq} - x_i^{eq}\right)\left(u_j^x - u_i^x\right) \\ + \frac{2}{\alpha}\left(y_j^{eq} - y_i^{eq}\right)\left(u_j^y - u_i^y\right)\end{array}},
\end{aligned}$$

$$\left(1-\frac{1}{|\boldsymbol{r}_j-\boldsymbol{r}_i|}\right)\approx 1-\frac{1}{\alpha}+\frac{\left(x_j^{eq}-x_i^{eq}\right)\left(u_j^x-u_i^x\right)}{\alpha^2} + \frac{\left(y_j^{eq}-y_i^{eq}\right)\left(u_j^y-u_i^y\right)}{\alpha^2}. \tag{G.2}$$

For simplicity, we focus on the forces along the x-axis, reduced so far to:

$$F_{ij}^x\approx\left(1-\frac{1}{|\boldsymbol{r}_j-\boldsymbol{r}_i|}\right)\left[\alpha\left(x_j^{eq}-x_i^{eq}\right)+\left(u_j^x-u_i^x\right)\right]. \tag{G.3}$$

Let us decompose the elastic force in orders of u. To 0^{th} order in u we get $\left(x_j^{eq}-x_i^{eq}\right)(1-\alpha)$. This contribution will cancel when summing over all the neighbors of particle i as the lattice is in mechanical equilibrium at its reference configuration. To 1^{st} order in u we get:

$$F_{ij}^x\approx\frac{1}{\alpha}\begin{bmatrix}\left(x_j^{eq}-x_i^{eq}\right)^2\left(u_j^x-u_i^x\right)\\+\left(x_j^{eq}-x_i^{eq}\right)\left(y_j^{eq}-y_i^{eq}\right)\left(u_j^y-u_i^y\right)\\+(\alpha-1)\left(u_j^x-u_i^x\right)\end{bmatrix}. \tag{G.4}$$

We recognize the first two contributions to be the unstressed dynamical matrix divided by factor α. We conclude that the dynamical matrix of the stressed lattice is:

$$\mathbb{M}(\alpha)=\frac{1}{\alpha}\mathbb{M}_0+\left(1-\frac{1}{\alpha}\right)\mathbb{M}_1, \tag{G.5}$$

where the correction $\mathbb{M}_1$ has elements: $\mathbb{M}_{1,ij}^{\beta\gamma}=-\delta_{\beta\gamma}$ if i and j are neighbors, zero otherwise; $\mathbb{M}_{1,ii}^{\beta\gamma}=Z(i)\,\delta_{\beta\gamma}$ for $Z(i)$ the number of neighbors of node i; and $\beta,\gamma=\hat{x},\hat{y}$ is the axis. At large tension $\mathbb{M}_1$ dominates the behavior. Note that $\mathbb{M}_1$ decouples the x and y axes. Its eigenvectors φ_n would thus come in degenerated pairs with identical form, once in the x-direction only and once in the y-direction only. It is also topological - it is determined by the structure of neighbors in the lattice, independent of geometry. We can decompose $\mathbb{M}_1$ to identical block matrices for x and y, each of them is a submatrix of the Laplacian matrix of the connected graph that represents the lattice:

$$\mathbb{M}_1=\begin{pmatrix}\mathbb{M}_1^{xx} & 0\\ 0 & \mathbb{M}_1^{yy}\end{pmatrix}. \tag{G.6}$$

The spectrum of $\mathbb{M}_1$ is the combined spectra of $\mathbb{M}_1^{xx}$ and $\mathbb{M}_1^{yy}$. Both are also real, symmetric, and indecomposable (as the network is fully connected), with nonpositive off-diagonal elements. As such, a discrete analog of Courant's nodal domain theorem applies - eigenvectors φ_n of $\mathbb{M}_1^{\alpha\alpha}$ must have no more than n domains - subsets of adjacent elements carrying the same sign, and $n-1$ nodes [182–184].

We can now conclude that the first vibrational modes φ_1 and φ_2 are akin to translational modes in the large tension limit: they are degenerated, rather delocalized, locally orthogonal, and have all elements in the same sign - all arrows pointing the same direction. This holds for any homogeneously dilated structure. For structures that do not dilate homogeneously, the calculation cannot be done in the general case as the stressed reference configuration is unknown. Nevertheless, for large systems, even for amorphous structures, we expect the dilation to be homogeneous at large scale, broadening the previous result's range of application.

Appendix H

Active *Gerris*' equations of motion

In this appendix, we give further details on the active *Gerris* model and derive its equations of motion (see chapter 6).

Let us remind Eqs. (6.2), which govern the overdamped dynamics of N elastically-coupled active particles:

$$\begin{aligned}\dot{\boldsymbol{u}}_i &= \pi\hat{\boldsymbol{n}}_i + \boldsymbol{F}_i^{el},\\ \dot{\boldsymbol{n}}_i &= (\hat{\boldsymbol{n}}_i \times \dot{\boldsymbol{u}}_i) \times \hat{\boldsymbol{n}}_i + \sqrt{2D}\xi_i\hat{\boldsymbol{n}}_i^{\perp},\end{aligned}$$

and apply it to the model active *Gerris*. Thus, we transform the set of Eqs. (6.2) into a set governing the dynamics of:

- $\boldsymbol{u}_0$ the position vector of the inner structure's barycenter,
- ϕ the solid rotation angle of the whole rigid inner structure,

These notations and other notations introduced later in these notes are shown in Fig. H.1.

Position and velocity. The first step is to express the position and velocity of all particles as a function of solely $\boldsymbol{u}_0$ and ϕ. We define the vectors $\boldsymbol{l}_i = \boldsymbol{R}_i - \boldsymbol{R}_0$, going from the inner structure barycenter $\boldsymbol{R}_0$ to the particles reference configuration $\boldsymbol{R}_i$, and illustrated in Fig. H.1. The new positions and velocities express as:

$$\boldsymbol{r}_i = \boldsymbol{u}_0 + \sigma_\phi \boldsymbol{l}_i, \tag{H.2a}$$

$$\dot{\boldsymbol{r}}_i = \dot{\boldsymbol{u}}_0 + \dot{\phi}\sigma_\phi \boldsymbol{l}_i^{\perp}, \tag{H.2b}$$

where σ_ϕ is the rotation matrix of angle ϕ.

Polarity dynamics. The polarity dynamics equations read:

$$\dot{\boldsymbol{n}}_i = (\hat{\boldsymbol{n}}_i \times \dot{\boldsymbol{r}}_i) \times \hat{\boldsymbol{n}}_i, \tag{H.3}$$

where $\dot{\boldsymbol{r}}_i$ is given by Eq. H.2b in term of $\boldsymbol{u}_0$ and ϕ only, and where we have omitted angular noise. Note that there are $N = 6$ of these equations, one for each polarity vector.

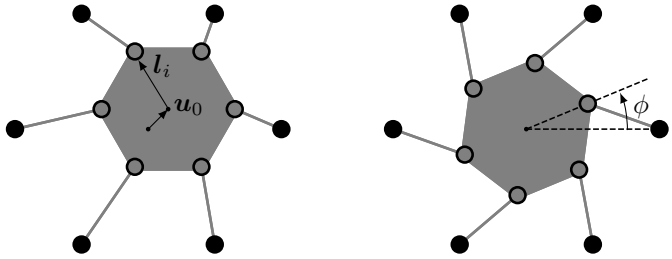


FIG. H.1. **Notations for the *Gerris*.** (left) The position of the active *Gerris* inner rigid hexagon barycenter is denoted $\boldsymbol{u}_0$. (right) The angle ϕ characterizes the rotation of the active *Gerris* inner rigid hexagon. The vectors $\boldsymbol{l}_i$ are the positions of the active nodes with respect to $\boldsymbol{u}_0$.

Barycenter. The dynamics of the system's barycenter is given by the balance of the whole system's dissipation and the sum of all the forces on the system's nodes. It gives:

$$N\dot{\boldsymbol{u}}_0 = \sum_i \left[\pi\hat{\boldsymbol{n}}_i + \boldsymbol{F}_i^{el}\right], \tag{H.4}$$

Solid body rotation. The dynamics of the system's orientation ϕ is given by the torque equation.

$$I\dot{\phi} = \sum_i r_i \left[\pi\sin(\theta_i - \phi_i) + |\boldsymbol{F}_i^{el}|\sin(\psi_i - \phi_i)\right], \tag{H.5}$$

where $I = \sum_i r_i^2$ is the (massless) inertia, r_i is the distance from node i to the system's barycenter, θ_i is the orientation of the polarity vector $\hat{\boldsymbol{n}}_i$, ϕ_i is the orientation of the vector $\boldsymbol{r}_i$, and ψ_i is the orientation of the vector $\boldsymbol{F}_i^{el}$. Note that the rigid condition imposes that the nodes are at a fixed distance from the system barycenter, i.e. 1 in the dimensionless model. Thus the previous equation simplifies to:

$$N\dot{\phi} = \sum_i \left[\pi\sin(\theta_i - \phi_i) + |\boldsymbol{F}_i^{el}|\sin(\psi_i - \phi_i)\right]. \tag{H.6}$$

Elastic force. Finally, one has to write the elastic forces as a function of solely $\boldsymbol{u}_0$ and ϕ. In the following two paragraphs, we express the elastic force at the linear elasticity (harmonic approximation) and full elasticity (including geometrical nonlinearities) levels.

- **Full elasticity level.** The general expression of the elastic force particle i is submitted to reads:

$$\boldsymbol{F}_i^{el} = \sum_{j\in\partial i}(|\boldsymbol{r}_i - \boldsymbol{r}_j| - 1)\hat{\boldsymbol{e}}_{ij}, \tag{H.7}$$

  where ∂i denotes the set of neighbors of node i, and $\hat{\boldsymbol{e}}_{ij}$ is the unit vector going from node j to node i. Note that ∂i can be decomposed into the neighbors of i belonging to the stiff inner structure $\partial_I i$, and the neighbors of i belonging to the external pinned ring $\partial_E i$. Only the latter contributes to the elastic forces, as the stiff inner structure is assumed not to deform. As the external pinned ring is held fixed, we end up with a closed form for the elastic force on particle i:

$$\boldsymbol{F}_i^{el} = \sum_{j\in\partial_E i}(|\boldsymbol{r}_i - \boldsymbol{r}_j| - 1)\hat{\boldsymbol{e}}_{ij} = \left(|\boldsymbol{r}_i - \boldsymbol{R}_{i_p}| - 1\right)\hat{\boldsymbol{e}}_{ii_p}, \tag{H.8}$$

where i_p refers to the only node of the external pinning ring particle i is connected to. Note that $\hat{\boldsymbol{e}}_{ii_p}$ is the unit vector going from $\boldsymbol{R}_{i_p}$ to $\boldsymbol{r}_i$, where $\boldsymbol{r}_i$ is the instantaneous position of node i.

- **Harmonic approximation level.** At the linear level, the elastic force acting on node i can be written as follows:

$$\boldsymbol{F}_i^{el} = -\sum_j \mathbb{M}_{ij}\boldsymbol{u}_j, \tag{H.9}$$

where $\mathbb{M}$ is the dynamical matrix. The rigid limit makes all the modes deforming the inner structure infinitely energetics. Only the three trivial translations and rotation of the rigid inner structure have finite energies (see Appendix A). From orthonormality, one can write:

$$\boldsymbol{F}_i^{el} = -\sum_k a_k\omega_k^2|\boldsymbol{\varphi}_k\rangle, \tag{H.10}$$

where $a_k = \langle\boldsymbol{\varphi}_k|\boldsymbol{u}\rangle$ is the projection of the displacement field on mode k, and where the summation is done only on the translations and the rotation, all the other contributions being zero from the rigid limit imposed to the inner structure. Finally, one has to express the projections a_k solely as a function of $\boldsymbol{u}_0$ and ϕ. The first step is to compute the displacement field at first order in $\boldsymbol{u}_0$ and ϕ:

$$\boldsymbol{u}_i = \boldsymbol{r}_i - \boldsymbol{R}_i = \boldsymbol{u}_0 + (\sigma_\phi - \mathbb{I})\boldsymbol{l}_i. \tag{H.11}$$

Linearizing the second term:

$$\boldsymbol{u}_i = \boldsymbol{u}_0 + \tilde{\sigma}_\phi\boldsymbol{l}_i + o(\boldsymbol{u}_0, \phi), \tag{H.12}$$

where

$$\tilde{\sigma}_\phi = \begin{pmatrix} 0 & -\phi \\ \phi & 0 \end{pmatrix}. \tag{H.13}$$

Last, we compute the projections mode by mode:

  - Translation along $\hat{\boldsymbol{x}}$ (T_x). The mode geometry reads $\boldsymbol{\varphi}^i_{T_x} = \hat{\boldsymbol{x}}/\sqrt{N}$. A simple calculation leads to:

$$a_{T_x} = \sqrt{N}u_x, \tag{H.14}$$

    where $u_x = \boldsymbol{u}\cdot\hat{\boldsymbol{x}}$ is the x-axis component of the barycenter's displacement.
  - Translation along $\hat{\boldsymbol{y}}$ (T_y). The mode geometry reads $\boldsymbol{\varphi}^i_{T_y} = \hat{\boldsymbol{y}}/\sqrt{N}$. Symmetrically, it gives:

$$a_{T_y} = \sqrt{N}u_y, \tag{H.15}$$

    where $u_y = \boldsymbol{u}\cdot\hat{\boldsymbol{y}}$ is the y-axis component of the barycenter's displacement.
  - Rotation (R). The mode geometry reads $\boldsymbol{\varphi}^i_R = \boldsymbol{l}_i^\perp/\sqrt{N}$. A similar calculation gives:

$$a_R = \sqrt{N}\phi. \tag{H.16}$$

Finally, reminding that $\omega^2_{T_x} = \omega^2_{T_y} = \omega^2_T(\alpha)$ and $\omega^2_R = \omega^2_R(\alpha)$, where α is the elongation imposed to the external springs at mechanical equilibrium; and injecting Eqs. (H.14), (H.15) and (H.16) in Eq. (H.10), one finds:

$$\boldsymbol{F}_i^{el} = -\boldsymbol{u}_0\omega_T^2 - \phi\omega_R^2\boldsymbol{l}_i^\perp, \tag{H.17}$$

which is the expression of the elastic force acting on node i at the linear level. Only the term coming from the rotation mode depends on the given particle.

H.1 Full elasticity level

$$\boldsymbol{r}_i = \boldsymbol{u}_0 + \sigma_\phi \boldsymbol{l}_i, \tag{H.18a}$$
$$\dot{\boldsymbol{r}}_i = \dot{\boldsymbol{u}}_0 + \dot{\phi}\sigma_\phi \boldsymbol{l}_i^\perp, \tag{H.18b}$$
$$\dot{\boldsymbol{n}}_i = (\hat{\boldsymbol{n}}_i \times \dot{\boldsymbol{r}}_i) \times \hat{\boldsymbol{n}}_i, \tag{H.18c}$$
$$\dot{\boldsymbol{u}}_0 = \frac{1}{N}\sum_i \left[\pi \hat{\boldsymbol{n}}_i + \boldsymbol{F}_i^{el}\right], \tag{H.18d}$$
$$\dot{\phi} = \frac{1}{N}\sum_i \left[\pi \sin(\theta_i - \phi_i) + |\boldsymbol{F}_i^{el}| \sin(\psi_i - \phi_i)\right], \tag{H.18e}$$
$$\boldsymbol{F}_i^{el} = \left(|\boldsymbol{r}_i - \boldsymbol{R}_{i_p}| - 1\right) \hat{\boldsymbol{e}}_{ii_p}. \tag{H.18f}$$

Here, only the vectors $\boldsymbol{R}_{i_p}$ depend on the elongation α. Their expression is $\boldsymbol{R}_{i_p} = \boldsymbol{l}_i(1+\alpha)$.

H.2 Harmonic approximation level

$$\boldsymbol{r}_i = \boldsymbol{l}_i, \tag{H.19.1}$$
$$\dot{\boldsymbol{r}}_i = \dot{\boldsymbol{u}}_0 + \dot{\phi}\boldsymbol{l}_i^\perp, \tag{H.19.2}$$
$$\dot{\boldsymbol{n}}_i = (\hat{\boldsymbol{n}}_i \times \dot{\boldsymbol{r}}_i) \times \hat{\boldsymbol{n}}_i, \tag{H.19.3}$$
$$\dot{\boldsymbol{u}}_0 = \frac{1}{N}\sum_i \left[\pi \hat{\boldsymbol{n}}_i + \boldsymbol{F}_i^{el}\right], \tag{H.19.4}$$
$$\dot{\phi} = \frac{1}{N}\sum_i \left[\pi \sin(\theta_i - \phi_i) + |\boldsymbol{F}_i^{el}| \sin(\psi_i - \phi_i)\right], \tag{H.19.5}$$
$$\boldsymbol{F}_i^{el} = -\boldsymbol{u}_0\omega_T^2 - \phi\omega_R^2 \boldsymbol{l}_i^\perp. \tag{H.19.6}$$

Here, only the squared eigenfrequencies ω_R^2 and ω_T^2 depend on the elongation α (see chapter 6).

H.3 Additionally considering angular noise

$$\dot{\boldsymbol{n}}_i = (\hat{\boldsymbol{n}}_i \times \dot{\boldsymbol{r}}_i) \times \hat{\boldsymbol{n}}_i + \sqrt{2D}\xi_i \hat{\boldsymbol{n}}_i^\perp, \tag{H.20.1}$$
$$\dot{\boldsymbol{u}}_0 = \frac{1}{N}\sum_i \left[\pi \hat{\boldsymbol{n}}_i + \boldsymbol{F}_i^{el}\right], \tag{H.20.2}$$
$$\dot{\phi} = \frac{1}{N}\sum_i \left[\pi \sin(\theta_i - \phi_i) + |\boldsymbol{F}_i^{el}| \sin(\psi_i - \phi_i)\right], \tag{H.20.3}$$

where D is the amplitude of the angular noise, and the ξ_i are i.i.d. Gaussian variables with zero mean and correlations $\langle \xi_i(t)\xi_j(t')\rangle = \delta_{ij}\delta(t-t')$.

Appendix I

Asymmetric single particle

In this appendix, we discuss the different results obtained for the dynamics of a single particle trapped in an elliptic harmonic potential. The symmetric case was studied in [143] and chapter 5. Here we remind the main conclusions and additionally perform numerical simulations of the dynamical regimes in the asymmetric case.

We study the different dynamical regimes and fixed points of Eqs. (3.49) in the case of a system of one particle in dimension $d = 2$, which consequently has two eigenmodes (Fig. I.1-a). We denote these eigenmodes $|\boldsymbol{\varphi}_1\rangle$ and $|\boldsymbol{\varphi}_2\rangle$ (respectively along $\hat{\boldsymbol{x}}$ and $\hat{\boldsymbol{y}}$), with corresponding eigenvalues ω_1^2 and ω_2^2. We decompose $|\boldsymbol{u}\rangle = a_1^u(t)|\boldsymbol{\varphi}_1\rangle + a_2^u(t)|\boldsymbol{\varphi}_2\rangle$ and $|\hat{\boldsymbol{n}}\rangle = a_1^n(t)|\boldsymbol{\varphi}_1\rangle + a_2^n(t)|\boldsymbol{\varphi}_2\rangle$. The fact that there is only one particle simplifies the problem: there is only one normalization condition ${a_1^n}^2 + {a_2^n}^2 = 1$. Therefore, the polarity vector strictly stands on the 2-circle of radius 1 in the space of projections on the normal modes.

Governing equations. We remind the ODEs governing the amplitude of the displacement and polarity on each mode (see chapter 5):

$$\dot{a}_1^u = \pi a_1^n - \omega_1^2 a_1^u, \tag{I.1a}$$

$$\dot{a}_2^u = \pi a_2^n - \omega_2^2 a_2^u, \tag{I.1b}$$

$$\dot{a}_1^n = -\left(\omega_1^2 a_1^u a_2^n - \omega_2^2 a_2^u a_1^n\right) a_2^n, \tag{I.1c}$$

$$\dot{a}_2^n = \left(\omega_1^2 a_1^u a_2^n - \omega_2^2 a_2^u a_1^n\right) a_1^n, \tag{I.1d}$$

where π is the elasto-active coupling.

I.1 Fixed points stability analysis

We use the polar angle of the polarity θ, such that $a_1^n = \cos(\theta)$ and $a_2^n = \sin(\theta)$. The fixed points are given by

$$\omega_1^2 a_1^u = \pi \cos(\theta_0), \tag{I.2a}$$

$$\omega_2^2 a_2^u = \pi \sin(\theta_0), \tag{I.2b}$$

for any orientation θ_0. The stability of the fixed points in the general case was determined in chapter 5: the configuration oriented along θ_0 is stable for

$$\pi \leq \pi_c(\theta_0) = \frac{\omega_1^2 \omega_2^2}{\omega_2^2 \sin(\theta_0)^2 + \omega_1^2 \cos(\theta_0)^2}. \tag{I.3}$$

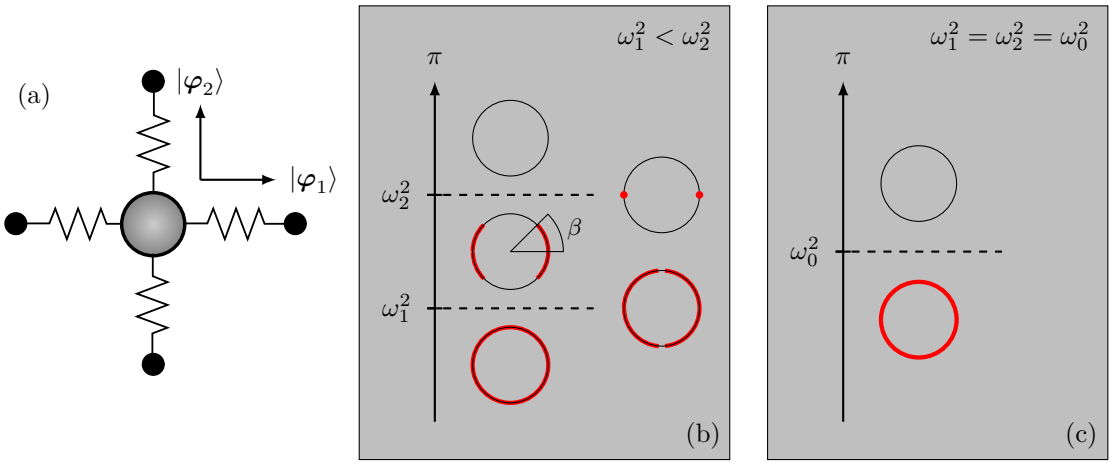


FIG. I.1. **Fixed point stability analysis for single particles in elliptic harmonic potentials**. (a) Elastic structure cartoon. (b/c) Summary of the stable fixed points depending on π in the asymmetric (b) and symmetric (c) cases. Red areas highlight orientations corresponding to stable fixed points.

This result is represented graphically in Fig. I.1-b. The angle β below which fixed points are stable (considering that the soft direction is along $\hat{\boldsymbol{x}}$) is given by:

$$\cos(\beta) = \sqrt{\frac{\omega_2^2(\omega_1^2 - \pi)}{\pi(\omega_1^2 - \omega_2^2)}}, \tag{I.4}$$

for $\omega_1^2 < \pi < \omega_2^2$. For $\pi < \omega_1^2$, all the fixed points are stable. At $\pi = \omega_1^2$, the first configuration, perpendicular to $|\boldsymbol{\varphi}_1\rangle$, thus along $|\boldsymbol{\varphi}_2\rangle$, destabilizes. At $\pi = \omega_2^2$, the last configuration, along $|\boldsymbol{\varphi}_1\rangle$, destabilizes. For $\pi > \omega_2^2$, all the fixed points are unstable.

In the degenerate case, $\omega_1^2 = \omega_2^2 = \omega_0^2$, the rotational symmetry ensures that the fixed points are all equivalent and stable for $\pi \leq \pi_c = \omega_0^2$ (Fig. I.1-c).

I.2 Dynamical regimes

I.2.1 Degenerate case

In the degenerate case, thoroughly discussed in chapter 5, there exist oscillating solutions in the form of circular orbits of frequency:

$$\Omega = \pm\omega_0\sqrt{\pi - \omega_0^2}, \tag{I.5}$$

for $\pi > \omega_0^2$, and of radius $R = \sqrt{\pi}/\omega_0$.

I.2.2 General case

In the case of a single particle in an asymmetric harmonic potential ($\omega_1^2 < \omega_2^2$), determining the expression of the dynamical solutions analytically requires a more involved analysis. Thus, we turn toward numerical simulations to understand the influence of asymmetry on the possible dynamical solutions. We consider that the $\hat{\boldsymbol{y}}$ direction is softer than the $\hat{\boldsymbol{x}}$ direction, so that $\omega_y^2 = \omega_x^2/\delta < \omega_x^2$. The potential the active particle is submitted to is no longer a parabola, but an elliptical paraboloid, elongated in the $\hat{\boldsymbol{y}}$ direction. We simulate the dynamics of an active particle in such a well, with

$1 < \delta < 10$, and with varying distances to the threshold above the instability $\pi > \omega_x^2 = 1$.

First, let us discuss the geometry of the dynamical solutions the system finds when asymmetry is plugged in. We perform an annealing simulation, initializing the system with $\delta = 1$ (symmetric parabola), and let the system finds the circular orbit, namely solution E_0 (Fig. I.3-a). In that case, the condensation fraction along the y-direction is 1/2 (Fig. I.2-a): the active force is evenly shared among the two directions. We then slowly increase δ and study the new dynamical solutions. Figs. I.2 and I.3 summarize the main results. For small asymmetry, we find that the circular orbit turns to an ellipse, which belongs to the same branch as E_0, but that is termed solution E_1 (Fig. I.3-b). For larger asymmetry, the ellipse destabilizes, and the system finds a new dynamical solution, called E_2, with a lemniscate geometry (Fig. I.3-c). At the transition between the two regimes, there is a sharp increase in condensation fraction along the y-direction. As asymmetry further increases, solution E_2 also destabilizes and leads to a new branch of solution, namely E_3 (Fig. I.3-d), that is even more elongated in the y-direction (the authors of [181] call such trajectories generalized higher order lemniscates), and with an even greater condensation fraction along the y-direction, and so on. In summary, we find a family of dynamical solutions that are stable for different ranges of asymmetry, and as elongated in the y-direction as the asymmetry is strong. The family of solutions is represented in Fig. I.3 up to regime E_4. Note that there exists an equivalent of each of these attractors turning the other way around, whose geometry is obtained by reflecting the attractors of Fig. I.3 with respect to the y-axis. Once $\delta = 10$ is reached, we also perform the backward annealing. We find that the forward and backward transitions are not happening at the same asymmetry values, highlighting some hysteresis from one elliptical regime to the other (Fig. I.2-a).

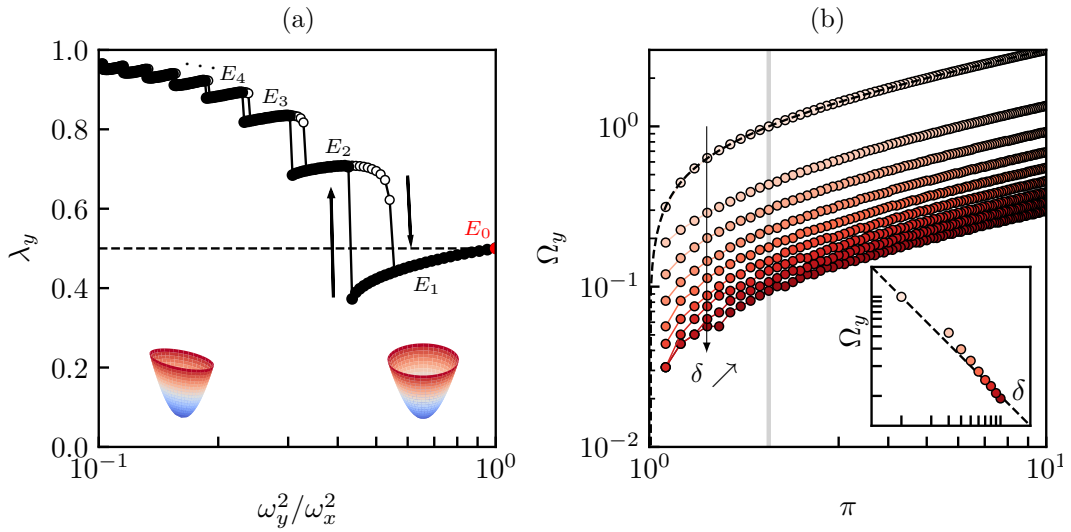


FIG. I.2. **Elliptic regimes in asymmetric elliptic harmonic potentials**. (a) Condensation fraction on the soft direction ($\hat{\boldsymbol{y}}$) as a function of the potential asymmetry ($\omega_y^2/\omega_x^2 = 1/\delta$). The forward (resp. backward) annealing is shown with empty (resp. full) markers. The two annealings were performed with fixed active-elastic coupling $\pi = 2.0$. (b) Main frequency of oscillation along the soft direction Ω_y as a function of the active-elastic feedback π for several asymmetry values $\delta \in [1, 3, 4, 5, 6, 7, 8, 9, 10]$. The black dotted line corresponds to the prediction of Eq. (I.5). The vertical gray line corresponds to $\pi = 2.0$. Inset: main frequency of oscillation along the soft direction Ω_y as a function of asymmetry δ for fixed active-elastic coupling $\pi = 2.0$. The dotted black line corresponds to the inverse power law.

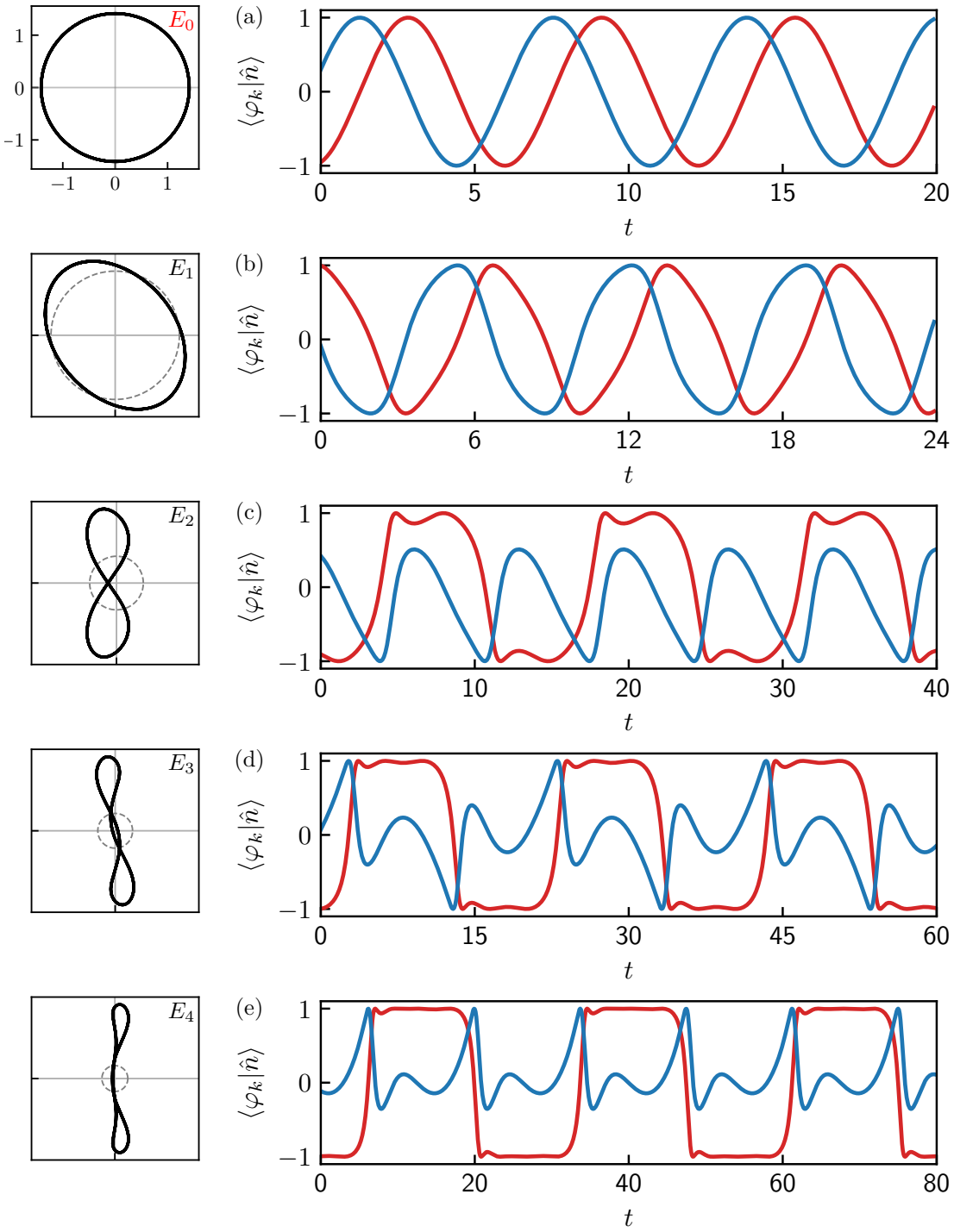


FIG. I.3. **Elliptic regimes phenomenology**. Single particle simulations in asymmetric elliptic harmonic potentials for $\pi = 2.0$, fixed $\omega_x^2 = 1$, and varying $\omega_y^2 \leq \omega_x^2$. (left) Attractors' representation in real space. The circular attractor shown in (a) is superposed on all the dynamics to compare the attractors' sizes. (right) Polarity vector projections on $\hat{\boldsymbol{x}}$ (solid blue line) and $\hat{\boldsymbol{y}}$ (solid red line) as a function of time. (a) $\delta = 1.0$, regime E_0. (b) $\delta = 1.5$, regime E_1. (c) $\delta = 2.75$, regime E_2. (d) $\delta = 3.75$, regime E_3. (e) $\delta = 4.75$, regime E_4.

Now, let us discuss the frequency variations due to the asymmetry. For several asymmetry values δ, we simulate the dynamics of the single particle, starting with $\pi = 10$, and

slowly decrease π up to the stabilization threshold of the first fixed point, $\pi_c = \omega_x^2 = 1.0$, at which the dynamical regime stops. We measure the main Fourier component of the displacement along the y-direction, namely Ω_y. The results are shown in Fig. I.2-b. We find that for $\delta = 1.0$ (symmetric parabola), the frequency variations are perfectly described by Eq. (I.5). For increasing asymmetry values, we find that the frequency is still critically slowing down at the same threshold $\pi = 1.0$, and that the large-π regime has a square root dependence with π, like in the symmetric case. However, the asymmetric curves are shifted in frequency by some prefactor compared to the symmetric case. In the range of asymmetry explored, the prefactor scales like $1/\delta$, as shown in the inset of Fig. I.2-b.

Appendix J

Single particle in $3d$

In this appendix, complementing chapter 6, we study a single particle in $3d$ with a pair of degenerated normal modes. We find that the TT regime, which corresponds to a chiral oscillation condensed on the pair of degenerated modes, is unstable in the presence of a third mode of lower energy.

Let us consider a single active unit evolving in a $3d$ space. The three normal modes of the elastic structure, respectively along $\hat{\boldsymbol{x}} = |\boldsymbol{\varphi}_{T_1}\rangle$, $\hat{\boldsymbol{y}} = |\boldsymbol{\varphi}_{T_2}\rangle$ and $\hat{\boldsymbol{z}} = |\boldsymbol{\varphi}_R\rangle$, have energies $\omega_x^2 = \omega_y^2 = \omega_T^2$ and $\omega_z^2 = \omega_R^2$. Consequently, in the equatorial plane, the two normal modes are degenerated, mimicking two translation modes; and the third mode plays the role of the rotation mode. The main difference with the active *Gerris* model is that here the system has a trivial geometry.

J.1 General equations

The active unit is characterized by its position $\boldsymbol{u} = (u_{T_1}, u_{T_2}, u_R)$ and orientation $\hat{\boldsymbol{n}} = (n_{T_1}, n_{T_2}, n_R)$. These variables obey the following dynamical equations:

$$\dot{\boldsymbol{u}} = \pi\hat{\boldsymbol{n}} - \omega_T^2 u_{T_1}\hat{\boldsymbol{e}}_x - \omega_T^2 u_{T_2}\hat{\boldsymbol{e}}_y - \omega_R^2 u_R\hat{\boldsymbol{e}}_z, \tag{J.1a}$$

$$\dot{\boldsymbol{n}} = (\hat{\boldsymbol{n}} \times \dot{\boldsymbol{u}}) \times \hat{\boldsymbol{n}}, \tag{J.1b}$$

where we have omitted angular noise.

J.1.1 In cartesian coordinates

Expliciting the vectorial product in Eq. (J.1b), and projecting on the three space directions, we find:

$$\dot{u}_{T_1} = \pi n_{T_1} - \omega_T^2 u_{T_1}, \tag{J.2a}$$

$$\dot{u}_{T_2} = \pi n_{T_2} - \omega_T^2 u_{T_2}, \tag{J.2b}$$

$$\dot{u}_R = \pi n_R - \omega_R^2 u_R, \tag{J.2c}$$

$$\dot{n}_{T_1} = -n_R^2 u_{T_1}\omega_T^2 + n_R n_{T_1} u_R \omega_R^2 + n_{T_2} n_{T_1} u_{T_2}\omega_T^2 - n_{T_2}^2 u_{T_1}\omega_T^2, \tag{J.2d}$$

$$\dot{n}_{T_2} = -n_{T_1}^2 u_{T_2}\omega_T^2 + n_{T_1} n_{T_2} u_{T_1}\omega_T^2 + n_R n_{T_2} u_R \omega_R^2 - n_R^2 u_{T_2}\omega_T^2, \tag{J.2e}$$

$$\dot{n}_R = -n_{T_2}^2 u_R\omega_R^2 + n_R n_{T_2} u_{T_2}\omega_T^2 + n_R n_{T_1} u_{T_1}\omega_T^2 - n_{T_1}^2 u_R\omega_R^2. \tag{J.2f}$$

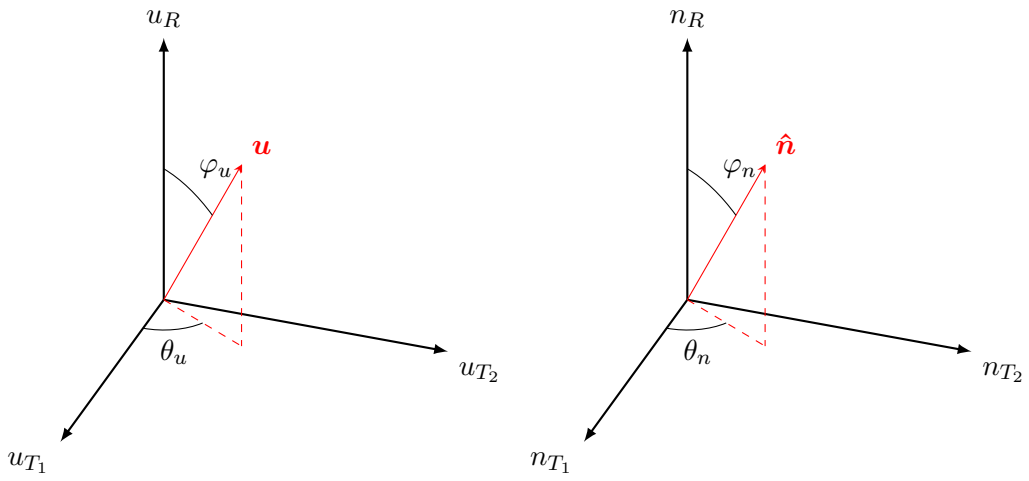


FIG. J.1. **Notations in spherical coordinates.** (left) Spherical coordinates for the position vector. (right) Spherical coordinates for the polarity vector.

J.1.2 In spherical coordinates

We introduce the spherical coordinates θ_u, θ_n, φ_u, φ_n and R, such that

- $n_{T_1} = \cos\theta_n \sin\varphi_n$, $n_{T_2} = \sin\theta_n \sin\varphi_n$, $n_R = \cos\varphi_n$,
- $u_{T_1} = R\cos\theta_u \sin\varphi_u$, $u_{T_2} = R\sin\theta_u \sin\varphi_u$, $u_R = R\cos\varphi_u$,

where $\theta_{u/n}$ (resp. $\varphi_{u/n}$) are the polar angles (azimuthal angles) in spherical coordinates (see Fig. J.1). They obey the following dynamical equations:

$$\dot{R} = \pi\cos\gamma\sin\varphi_u\sin\varphi_n + \pi\cos\varphi_u\cos\varphi_n - \omega_R^2 R\cos^2\varphi_u - \omega_T^2 R\sin^2\varphi_u, \tag{J.3a}$$

$$\dot{\theta}_u = \frac{\pi}{R}\frac{\sin\varphi_n}{\sin\varphi_u}\sin\gamma, \tag{J.3b}$$

$$\dot{\theta}_n = R\omega_T^2\frac{\sin\varphi_u}{\sin\varphi_n}\sin\gamma, \tag{J.3c}$$

$$\dot{\varphi}_u = \frac{\pi}{R}\left(\cos\gamma\cos\varphi_u\sin\varphi_n - \cos\varphi_n\sin\varphi_u\right) + \cos\varphi_u\sin\varphi_u\left(\omega_R^2 - \omega_T^2\right), \tag{J.3d}$$

$$\dot{\varphi}_n = R\omega_R^2\cos\varphi_u\sin\varphi_n - R\omega_T^2\sin\varphi_u\cos\varphi_n\cos\gamma. \tag{J.3e}$$

Introducing $\gamma = \theta_n - \theta_u$, the previous equations become:

$$\dot{R} = \pi\cos\gamma\sin\varphi_u\sin\varphi_n + \pi\cos\varphi_u\cos\varphi_n - \omega_R^2 R\cos^2\varphi_u - \omega_T^2 R\sin^2\varphi_u, \tag{J.4a}$$

$$\dot{\theta}_u = \frac{\pi}{R}\frac{\sin\varphi_n}{\sin\varphi_u}\sin\gamma, \tag{J.4b}$$

$$\dot{\gamma} = \sin\gamma\left(R\omega_T^2\frac{\sin\varphi_u}{\sin\varphi_n} - \frac{\pi}{R}\frac{\sin\varphi_n}{\sin\varphi_u}\right), \tag{J.4c}$$

$$\dot{\varphi}_u = \frac{\pi}{R}\left(\cos\gamma\cos\varphi_u\sin\varphi_n - \cos\varphi_n\sin\varphi_u\right) + \cos\varphi_u\sin\varphi_u\left(\omega_R^2 - \omega_T^2\right), \tag{J.4d}$$

$$\dot{\varphi}_n = R\omega_R^2\cos\varphi_u\sin\varphi_n - R\omega_T^2\sin\varphi_u\cos\varphi_n\cos\gamma. \tag{J.4e}$$

J.2 Oscillating regime on the equatorial plane

We study the oscillating regime, strictly condensed on the equatorial plane ($\varphi_u = \varphi_n = \pi/2$).

J.2.1 Stationary solution

The stationary solution with $\dot{\theta}_u = \Omega > 0$, for which $\dot{R} = \dot{\gamma} = \dot{\varphi}_u = \dot{\varphi}_n = 0$, verifies ($R_0 = \sqrt{\pi}/\omega_T$, $\cos\gamma_0 = \omega_T/\sqrt{\pi}$, $\Omega = \omega_T\sqrt{\pi - \omega_T^2}$). We recover the regular orbiting solution on a pair of degenerated normal modes, which exists for $\pi > \omega_T^2$.

J.2.2 Stability

To analyze the stability of the orbiting solution, we can restrict the analysis to Eqs. (J.4e) and (J.4d) for the two azimuthal angles. We introduce the small quantities $\varphi_u = \pi/2 + \delta\varphi_u$, $\varphi_n = \pi/2 + \delta\varphi_n$. At first order in small quantities, we find:

$$\dot{\delta\varphi_u} = -\omega_R^2 \delta\varphi_u + \sqrt{\pi\omega_T^2}\delta\varphi_n, \tag{J.5a}$$

$$\dot{\delta\varphi_n} = \omega_T^2 \delta\varphi_u - \sqrt{\pi\omega_R^4/\omega_T^2}\delta\varphi_n. \tag{J.5b}$$

The stability of the orbits is set by the solutions to the eigenvalue problem:

$$\lambda^2 - \lambda\left(\omega_T^2 - \omega_R^2\right) + \omega_R^2\left(\pi - \omega_T^2\right) = 0. \tag{J.6}$$

- If $\omega_R^2 = 0$, we find $(\lambda = 0, \omega_T^2)$, thus the orbiting solution is unstable.
- If $\omega_R^2 > 0$, we find that the eigenvalues have negative real parts for $\omega_T^2 < \omega_R^2$. Conversely, if the degenerated normal modes are not the lowest energy ones, the eigenvalues have positive real parts, and the orbiting solution is linearly unstable.

At the single particle level, we find that the TT regime is *not selective*: in the presence of a third mode of energy $\omega_R^2 < \omega_T^2$, it is unstable.

Appendix K

Perspective distortions

In this appendix, we explain the backbone of the method used to correct perspective distortions in chapter 7.

As the camera attached to the ceiling is held vertically, acquisitions from experiments tilted with respect to the horizontal plane must be corrected for perspective distortions. This is done using planar homography [185], which allows for changing the perspective of a tilted experimental movie and sending it back to the perspective of a flat experimental movie, given the knowledge of at least four reference points in both frames.

In a picture, every pixel is assigned a position $(u,\ v)$ (measured in pixel units) in the reference frame of the camera sensor. The coordinates of such points in the reference frame of the experiments are called $(x,\ y,\ z)$ (measured in meters). Noting that our images were captured with a long focal length and from far enough, we neglect the lens's optical distortion. Given this assumption, the mapping between the experiments and camera sensor coordinates takes the linear form:

$$\begin{pmatrix} u \\ v \\ 1 \end{pmatrix} = \mathbb{C} \cdot \begin{pmatrix} x \\ y \\ z \\ 1 \end{pmatrix}, \tag{K.1}$$

where the so-called camera matrix $\mathbb{C}$ depends on the camera's intrinsic parameters and the precise location of the camera in space. To invert this relationship, we have to further neglect the spatial extent of the experimental scene in the z-direction (defined as perpendicular to the experimental plane), and assume that every point we see on the image belongs to the $z = 0$ plane. Therefore, the mapping reduces to:

$$\begin{pmatrix} u \\ v \\ 1 \end{pmatrix} = \mathbb{H} \cdot \begin{pmatrix} x \\ y \\ 1 \end{pmatrix} \tag{K.2}$$

where $\mathbb{H}$, usually called the homography matrix, is a priori invertible. The inversion is performed using the functions *cv2.findHomography* and *cv2.warpPerspective* from the Python package *OpenCV*, which take as input the coordinates of a set of at least four points on a source image and a destination image, and explicitly performs the inversion. Eventually, note that perspective distortions coming from the finite extension of the system in the z-direction are not corrected for, leading to additional tracking errors on the displacement detection, but with minimal effect on the orientation detection.

Appendix L

Perturbative approaches

In this appendix, complementing chapter 7, we provide the perturbative approaches used to determine the explicit expression of the dynamical regimes. First, using multiple-scale analysis, we determine the expression of NICA at the level of homogeneous solutions of the coarse-grained model, for zero-gravity. Then, again using multiple-scale analysis, we determine the expression of regime WW for the single particle, far enough from the exceptional point. Finally, we study the linear response to a small polarizing field in the CO regime of the single particle.

L.1 Multiple-scale analysis

L.1.1 Coarse-grained toy model: NICA regime at zero-gravity

In this section, we consider the coarse-grained model, as presented in chapter 7 in simple settings (see Eqs. (7.44)), i.e. restricting to homogeneous solutions. We focus on the emergence of NICA at zero gravity, as one increases activity. For $\pi < \pi_c = 2\left(\omega_\perp^2 + D\right)$, the only solution is the disordered, $|\mathbf{m}| = 0$, fixed point. Using multiple-scale analysis, we find the amplitude equation for the nonlinear NICA limit cycle appearing as π exceeds π_c, and discuss its properties. We consider the coarse-grained Eqs. (7.44), and restrict to the equations projected along the first transverse mode:

$$\partial_t U = \pi m - \omega_0^2 U, \tag{L.1a}$$

$$\partial_t m = \frac{1-m^2}{2}\left(\pi m - \omega_0^2 U\right) - Dm, \tag{L.1b}$$

where $\omega_0^2 = \omega_\perp^2$. This restriction to one mode consists of assuming mode $|\boldsymbol{\varphi}_\perp\rangle$ is the only mode soft enough to be activated, so that we can neglect the projections elsewhere.

Scaling variables. We consider the elasto-active coupling very close to the stability threshold: $\pi = \pi_c + \delta$, where $\delta = \lambda\Delta$, with λ a small parameter; and introduce a slow timescale $T = \lambda t$. We propose the scalings $U = \sqrt{\lambda}U(t,T)$ and $m = \sqrt{\lambda}m(t,T)$, and look for solutions of the form:

$$U(t,T) = U_0(t,T) + \lambda U_1(t,T) + \dots \tag{L.2a}$$

$$m(t,T) = m_0(t,T) + \lambda m_1(t,T) + \dots \tag{L.2b}$$

Perturbation. Re-injecting Eqs. (L.2) into Eqs. (L.1), we next separate the different orders in λ:

- At zeroth order in λ, we find:

$$\frac{\partial}{\partial t}\begin{pmatrix} U_0(t,T) \\ m_0(t,T) \end{pmatrix} = \begin{pmatrix} -\omega_0^2 & \pi_c \\ -\omega_0^2/2 & \frac{\pi_c}{2} - D \end{pmatrix} \begin{pmatrix} U_0(t,T) \\ m_0(t,T) \end{pmatrix} = \mathbb{D} \begin{pmatrix} U_0(t,T) \\ m_0(t,T) \end{pmatrix}. \tag{L.3}$$

  The eigenvalues of $\mathbb{D}$ are $\pm i\Omega$, where $\Omega = \sqrt{D\omega_0^2}$. Imposing real solutions, we find:

$$\begin{pmatrix} U_0(t,T) \\ m_0(t,T) \end{pmatrix} = A(T) \begin{pmatrix} a \\ 1 \end{pmatrix} e^{i\Omega t} + A^\star(T) \begin{pmatrix} a^\star \\ 1 \end{pmatrix} e^{-i\Omega t}, \tag{L.4}$$

  where $a = 2\left(1 - i\frac{\sqrt{D}}{\omega_0}\right)$; where the complex number $A(T)$ depends on the slow timescale T; and where the two vectors ${}^{\mathrm{t}}(a,1)$ and ${}^{\mathrm{t}}(a^\star,1)$ are respectively the eigenvectors associated with the eigenvalues $i\Omega$ and $-i\Omega$.

- At first-order in λ, we find:

$$\frac{\partial}{\partial t}\begin{pmatrix} U_1(t,T) \\ m_1(t,T) \end{pmatrix} = \mathbb{D} \begin{pmatrix} U_1(t,T) \\ m_1(t,T) \end{pmatrix} + \begin{pmatrix} \Delta m_0 - \frac{\partial U_0}{\partial T} \\ \frac{1}{2}\Delta m_0 - \frac{\pi_c}{2} m_0^3 + \frac{\omega_0^2}{2} m_0^2 U_0 - \frac{\partial m_0}{\partial T} \end{pmatrix}, \tag{L.5}$$

  where the matrix $\mathbb{D}$ is the same as in Eqs. (L.3). There is no need to solve explicitly for U_1 and m_1: some terms drive the system at the resonance frequency $\omega = \pm\Omega$; and the system will generally have no solution. It will only have a solution, leading to a bounded solution for Eq. (L.5), if the right-hand side satisfies a certain constraint. This constraint we get from the Fredholm alternative theorem.

Fredholm alternative theorem. The resonant terms of the righthand side of Eqs. (L.5) must be orthogonal to any vector of the kernel of the matrix $(i\Omega\mathbb{I} - \mathbb{D})^\star$. A basis for this subspace is the vector ${}^{\mathrm{t}}(\frac{1}{2}\frac{\omega_0^2 + i\omega_0\sqrt{D}}{\omega_0^2 + D}, 1)$. Thus, the solvability condition reads:

$$\begin{pmatrix} \Delta m_0 - \frac{\partial U_0}{\partial T} \\ \frac{1}{2}\Delta m_0 + \frac{\omega_0^2}{2} m_0^2 U_0 - \frac{\pi_c}{2} m_0^3 - \frac{\partial m_0}{\partial T} \end{pmatrix}_{\Omega t} \cdot \begin{pmatrix} \frac{1}{2}\frac{\omega_0^2 + i\omega_0\sqrt{D}}{\omega_0^2 + D} \\ 1 \end{pmatrix} = 0, \tag{L.6}$$

where Ωt denotes that the associated expression is restricted to terms oscillating at Ωt. Actually performing the tedious algebra and the scalar product, we find:

$$\frac{1}{\omega_0^2}\frac{dA}{dT} = A\frac{\Delta}{\omega_0^2}\frac{2 + \mu + i\sqrt{\mu}}{4} - A|A|^2\frac{(1+\mu)\left(3\mu + i\sqrt{\mu}\right)}{2}, \tag{L.7}$$

where $\mu = D/\omega_0^2$.

Amplitude equation. Finally, introducing $A = Re^{i\Psi}$, we obtain the amplitude equation for the real amplitude R:

$$\frac{1}{\omega_0^2}\frac{dR}{dT} = R\frac{\Delta}{\omega_0^2}\frac{2+\mu}{4} - R^3\frac{3\mu(1+\mu)}{2}. \tag{L.8}$$

At first-order, we thus find that for $\pi < \pi_c$ ($\Delta < 0$), the only stable solution is the disordered fixed point; $A = 0$; and for $\pi > \pi_c$ ($\Delta > 0$), the only stable solution is the nonlinear limit cycle spontaneously oscillating along the soft mode. As one approaches the bifurcation from above, the activity-independent frequency $\Omega = \sqrt{D\omega_0^2}$ remains the same, while the amplitude vanishes like a square root. The normal form, Eq. (L.8), and the linear stability analysis are the hallmarks of a supercritical Hopf bifurcation. Importantly, in contrast with SCO, at the level of homogeneous solutions, we find that the transition from the disordered phase to NICA is continuous.

Timescales separation. The long timescale corresponds to the typical relaxation timescale of the transitory regime $\tau_{relax} \simeq 1/\delta$; and the short one to the period of the oscillations $\tau_{osc} \simeq 1/\omega_0^2\sqrt{\mu}$. The timescale separation condition can be written as follows:

$$\delta \ll \omega_0\sqrt{D}, \tag{L.9}$$

which is verified close enough to the threshold.

L.1.2 Single-particle: WW regime

In this section, we consider the single particle in a harmonic trap with a polarizing field (see Eqs. (7.13)). Using multiple-scale analysis, we find the amplitude equation for the nonlinear WW limit cycle appearing as π exceeds $\pi_c = \omega_0^2 + g_\alpha\varepsilon$, the stability threshold for the polarized fixed point; and discuss its properties. There are two technical challenges. First, the presence of an exceptional point at zero gravity and critical activity. Second, the multiple-scale method has to be applied to a system of three coupled nonlinear ODEs of very different natures; the radius dynamics Eq. (7.13a) boils down to a first-order relaxation with very weak driving, while Eqs. (7.13b) and (7.13c) for the angles φ and θ are very much coupled and strongly non-linear [196, 197].

Scaling variables. Starting from Eqs. (7.13), it is easier to describe the dynamics through the angles φ and θ. Moreover, we change variables to $\varphi \to \varphi + \pi$ and $\theta \to \theta + \pi$ in order to keep oscillations of θ and φ around 0. It yields:

$$\dot{R} = \pi\cos(\theta - \varphi) - \omega_0^2 R, \tag{L.10a}$$

$$\dot{\varphi} = \frac{\pi}{R}\sin(\theta - \varphi), \tag{L.10b}$$

$$\dot{\theta} = \omega_0^2 R\sin(\theta - \varphi) - g_\alpha\varepsilon\sin(\theta). \tag{L.10c}$$

We consider the elasto-active coupling very close to the stability threshold: $\pi = \pi_c + \delta$, where $\delta = \lambda\Delta$, with λ a small parameter; and introduce a slow timescale $T = \lambda t$. Inspired by simulation data, we propose the following scalings $R = R(t,T)$, $\varphi = \sqrt{\lambda}\varphi(t,T)$, $\theta = \sqrt{\lambda}\theta(t,T)$, and look for solutions of the form:

$$R(t,T) = R_0(t,T) + \lambda R_1(t,T) + \dots \tag{L.11a}$$

$$\varphi(t,T) = \varphi_0(t,T) + \lambda\varphi_1(t,T) + \dots \tag{L.11b}$$

$$\theta(t,T) = \theta_0(t,T) + \lambda\theta_1(t,T) + \dots \tag{L.11c}$$

Perturbation. Re-injecting Eqs. (L.11) into Eqs. (L.10), we next separate the different orders in λ:

- At zeroth order in λ, we find:

$$\frac{\partial R_0}{\partial t} + \omega_0^2 R_0 = \pi_c, \tag{L.12a}$$

$$\frac{\partial \varphi_0}{\partial t} + \omega_0^2\varphi_0 - \omega_0^2\theta_0 = 0, \tag{L.12b}$$

$$\frac{\partial \theta_0}{\partial t} + \pi_c\varphi_0 - \omega_0^2\theta_0 = 0. \tag{L.12c}$$

  Eq. (L.12a)'s general solution expresses as:

$$R_0(t,T) = \frac{\pi_c}{\omega_0^2} + B(T)e^{-\omega_0^2 t}, \tag{L.13}$$

where the exponential factor vanishes at short times and is therefore discarded in the following. Eqs. (L.12b) and (L.12c) can be recast into the following vectorial form:

$$\frac{\partial}{\partial t}\begin{pmatrix}\varphi_0(t,T)\\ \theta_0(t,T)\end{pmatrix} = \begin{pmatrix}-\omega_0^2 & \omega_0^2\\ -\omega_0^2 - g_\alpha\varepsilon & \omega_0^2\end{pmatrix}\begin{pmatrix}\varphi_0(t,T)\\ \theta_0(t,T)\end{pmatrix} = \mathbb{D}\begin{pmatrix}\varphi_0(t,T)\\ \theta_0(t,T)\end{pmatrix}. \tag{L.14}$$

The eigenvalues of $\mathbb{D}$ are $\pm i\Omega$, where $\Omega = \sqrt{g_\alpha\varepsilon\omega_0^2}$. Imposing real solutions, we find:

$$\begin{pmatrix}\varphi_0(t,T)\\ \theta_0(t,T)\end{pmatrix} = A(T)\begin{pmatrix}a\\ 1\end{pmatrix}e^{i\Omega t} + A^\star(T)\begin{pmatrix}a^\star\\ 1\end{pmatrix}e^{-i\Omega t}, \tag{L.15}$$

where $a = \frac{1-i\sqrt{G}}{1+G}$ and $G = g_\alpha\varepsilon/\omega_0^2$; where the complex number $A(T)$ depends on the slow timescale T; and where the two vectors ${}^{\mathrm{t}}(a,1)$ and ${}^{\mathrm{t}}(a^\star,1)$ are respectively the eigenvectors associated with the eigenvalues $i\Omega$ and $-i\Omega$. Eventually, at zeroth order in λ, we find:

$$R_0(t,T) = \pi_c/\omega_0^2, \tag{L.16a}$$
$$\varphi_0(t,T) = A(T)ae^{i\Omega t} + A^\star(T)a^\star e^{-i\Omega t}, \tag{L.16b}$$
$$\theta_0(t,T) = A(T)e^{i\Omega t} + A^\star(T)e^{-i\Omega t}. \tag{L.16c}$$

- At first-order in λ, we find:

$$\frac{\partial R_1}{\partial t} + \omega_0^2 R_1 = \Delta - \frac{\pi_c}{2}\left(\theta_0 - \varphi_0\right)^2, \tag{L.17a}$$
$$\frac{\partial\varphi_1}{\partial t} + \omega_0^2\varphi_1 - \omega_0^2\theta_1 = -\frac{\partial\varphi_0}{\partial T} + \left(\theta_0-\varphi_0\right)\left[\frac{\Delta}{R_0} - \frac{\pi_c R_1}{R_0^2}\right] - \frac{\pi_c}{6R_0}\left(\theta_0-\varphi_0\right)^3, \tag{L.17b}$$
$$\frac{\partial\theta_1}{\partial t} + \pi_c\varphi_1 - \omega_0^2\theta_1 = -\frac{\partial\theta_0}{\partial T} + \frac{g\varepsilon}{6}\theta_0^3 - \frac{\pi_c}{6}\left(\theta_0-\varphi_0\right)^3 + \omega_0^2 R_1\left(\theta_0-\varphi_0\right). \tag{L.17c}$$

First, note that Eq. (L.17a) illustrates the origin of the frequency doubling of $R(t)$ in regime WW. We find that R_1 is forced by constant terms and terms oscillating at 2Ω, and this equation being linear, R_1 oscillates at the same frequencies. We find:

$$R_1(t,T) = \frac{\Delta}{\omega_0^2} - G|A|^2 - \frac{A^2}{2}\frac{\left(G+i\sqrt{G}\right)^2}{(1+G)\left(1+2i\sqrt{G}\right)}e^{2i\Omega t} + \text{c.c.}, \tag{L.18}$$

where c.c. denotes the complex conjugate. Similarly, Eqs. (L.17b) and (L.17c) are forced at different frequencies. Again, there is no need to solve explicitly for φ_1 and θ_1: some terms drive the system at the resonance frequency $\omega = \pm\Omega$; and the system will generally have no solution: the right-hand side must satisfy the Fredholm alternative theorem.

Fredholm alternative theorem. The resonant terms of the right-hand side of Eqs. (L.17b) and (L.17c) must be orthogonal to any vector of the kernel of the matrix $(i\Omega\mathbb{I} - \mathbb{D})^\star$, where * indicates the adjoint matrix. A basis for this subspace is the vector ${}^{\mathrm{t}}(-1-i\sqrt{G},1)$. Thus, the solvability condition reads:

$$\begin{pmatrix}-\frac{\partial\varphi_0}{\partial T} + \left(\theta_0-\varphi_0\right)\left[\frac{\Delta}{R_0} - \frac{\pi_c R_1}{R_0^2}\right] - \frac{\pi_c}{6R_0}\left(\theta_0-\varphi_0\right)^3\\ -\frac{\partial\theta_0}{\partial T} + \frac{g\varepsilon}{6}\theta_0^3 - \frac{\pi_c}{6}\left(\theta_0-\varphi_0\right)^3 + \omega_0^2 R_1\left(\theta_0-\varphi_0\right)\end{pmatrix}_{\Omega t}\cdot\begin{pmatrix}-1-i\sqrt{G}\\ 1\end{pmatrix} = 0, \tag{L.19}$$

where Ωt denotes that the associated expression is restricted to terms oscillating at Ωt. Actually performing the tedious algebra and the scalar product, we find:

$$0 = A\frac{\Delta}{\omega_0^2}\left(G + i\sqrt{G}\right) - Gb|A|^2A, \tag{L.20}$$

where the complex number $b = b_R + ib_I$ has the following expression:

$$b = \frac{3}{2}\left(G + i\sqrt{G}\right) + \frac{1}{2}\frac{G + i\sqrt{G}}{1 + 2i\sqrt{G}} + \frac{\left(G + i\sqrt{G}\right)\left(1 + i\sqrt{G}\right)^2}{(1+G)\left(1 + 2i\sqrt{G}\right)} - \frac{1}{2}(1+G). \tag{L.21}$$

Amplitude equation. Finally, introducing $A = Re^{i\Psi}$, we obtain the amplitude equation for the real amplitude R:

$$0 = \frac{\Delta}{\omega_0^2}R - b_R R^3. \tag{L.22}$$

Note that $b_r > 0$ for $G > G^\star = (\sqrt{41} - 3)/16 \simeq 0.21$, and $b_r < 0$ for $0 < G < G^\star$. At first order, we thus find that for $\pi < \pi_c$ ($\Delta < 0$), the only stable solution is the polarized fixed point; $A = 0$; and for $\pi > \pi_c$ ($\Delta > 0$), we find two cases:

- For large enough gravity $G > G^\star$, the third order term in Eq. (L.22) provides the non-linear saturation. We find:

$$|A| = \sqrt{\frac{\Delta}{\omega_0^2}}\frac{1}{\sqrt{b_R}} \simeq 2.8284\sqrt{\frac{\Delta}{\omega_0^2}}\sqrt{\frac{G + 0.25}{8G^2 + 3G - 1}}, \tag{L.23}$$

  which is the hallmark of a supercritical Hopf bifurcation at frequency $\Omega = \sqrt{g_\alpha \varepsilon \omega_0^2}$. The predicted bifurcation scenario is illustrated in Fig. L.1-a for great enough gravity, and is compared to simulations close to the threshold for a broad range of gravity in Fig. L.1-b. We find that the first-order multiple-scale works well for great enough gravity ($G > 1$), but fails close to $G = G^\star$ and smaller gravity. Nevertheless, we find from the numerical simulations that the bifurcation remains a supercritical Hopf, even at small gravity, where the multiple-scale analysis fails to predict the amplitude of the limit cycle (Fig. L.1-b, inset).

- For small enough gravity $G < G^\star$, the third-order term in Eq. (L.22) is positive, and there is no non-linear saturation. Going to second order in λ should likely allow finding the amplitude $|A|(\delta)$ for some larger range of G. Nonetheless, as gravity decreases and the system gets closer to the exceptional point ($G = 0$, $\pi/\omega_0^2 = 1$), we expect the amplitude of the nonlinear limit cycle to diverge, and going to second order might not be enough to solve this problem. Close to the exceptional point, one should instead use the mapping with the nonlinear pendulum discussed in chapter 7.

Note that at first-order in λ, we also find a prediction for the radius of oscillations:

$$R(t) \simeq \frac{\pi_c}{\omega_0^2} + \frac{\lambda\Delta}{\omega_0^2} - \lambda G|A|^2 - \lambda\frac{A^2}{2}\frac{(G + i\sqrt{G})^2}{(1+G)(1+2i\sqrt{G})}e^{2i\Omega t} + \text{c.c.} \tag{L.24}$$

Timescales separation. The long timescale corresponds to the typical relaxation timescale of the transitory regime $\tau_{relax} \simeq 1/\delta$; and the short one to the period of the oscillations $\tau_{osc} \simeq 1/\omega_0^2\sqrt{G}$. The timescale separation condition can be written as follows:

$$\delta \ll \omega_0^2\sqrt{G}, \tag{L.25}$$

which is verified close enough to the threshold.

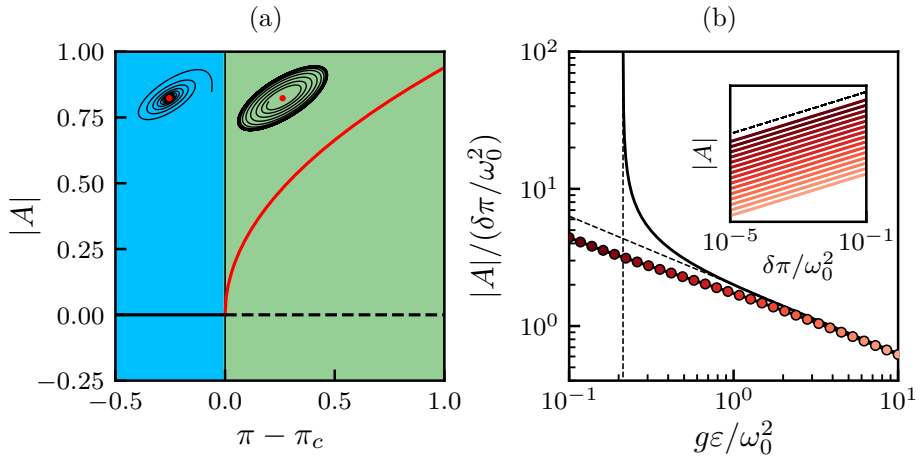


FIG. L.1. **Bifurcation scenario for the emergence of regime WW.** (a) Nonlinear limit cycle ampitude $|A|$ as a function of π, as given by Eq. (L.23) for great enough gravity (here $G = 1 > G^\star$). Solid (resp. dashed) lines represent stable (resp. unstable) branches. The insets represent typical trajectories in the (θ, φ)-plane, below (left) and above (right) the instability. (b) Prefactor of the supercritical Hopf bifurcation as a function of gravity $g_\alpha\varepsilon/\omega_0^2$ as obtained from simulations (red dots), and from Eq. (L.23) (solid black line). The markers are color-coded by gravity. The vertical (resp. oblique) dashed line represents the gravity threshold below which the first-order multiple-scale fails (resp. the large gravity asymptotic regime predicted by Eq. (L.23)). Inset: amplitude of the oscillation along θ as a function of the distance to the threshold $\delta\pi/\omega_0^2$, as obtained from simulations. The dashed black line represents the 1/2 power law. The color code indicates the associated gravity, as given by panel (b), and the curves are shifted vertically for clarity.

L.2 Linear response in the CO regime

Here, we find the linear response of the CO regime to a small polarizing field. Starting from Eqs. (7.13), we linearize the dynamics around the stationary CO regime ($R_0 = \sqrt{\pi}/\omega_0$, $\cos\gamma_0 = \omega_0/\sqrt{\pi}$, $\dot\varphi = \Omega_0 = \omega_0\sqrt{\pi - \omega_0^2}$), and introduce the small quantities $R(t) = R_0 + \delta R(t)$, $\gamma(t) = \gamma_0 + \delta\gamma$, $\varphi = \Omega_0 t + \delta\varphi$, $g_\alpha\varepsilon = \delta g_\alpha\varepsilon$. We find:

$$\frac{d}{dt}\begin{pmatrix}\delta R\\ \delta\varphi\\ \delta\gamma\end{pmatrix} = \begin{pmatrix}-\omega_0^2 & 0 & -\pi\sin\gamma_0\\ -\omega_0^2\sin\gamma_0 & 0 & \omega_0^2\\ 2\omega_0^2\sin\gamma_0 & 0 & 0\end{pmatrix}\begin{pmatrix}\delta R\\ \delta\varphi\\ \delta\gamma\end{pmatrix} + \delta g_\alpha\varepsilon\sin(\gamma_0 + \Omega_0 t)\begin{pmatrix}0\\ 0\\ 1\end{pmatrix}, \tag{L.26}$$

where the matrix on the right-hand side not only allows access to the stability of the CO regime, but also to the linear response of this regime to a small gravity field. We find that assessing the stability boilds down to the following eigenvalue problem:

$$\lambda\left[\lambda^2 + \lambda\omega_0^2 + 2\omega_0^2\left(\pi - \omega_0^2\right)\right] = 0, \tag{L.27}$$

which only has one zero solution in the $\delta\varphi$ direction. We denote $\Delta = \omega_0^4 - 8\omega_0^2\left(\pi - \omega_0^2\right)$ the determinant of Eq. (L.27) and $\delta\pi = \pi - \omega_0^2$ the distance to the threshold. For $\delta\pi/\omega_0^2 < 1/8$, the two remaining eigenvalues are reals and negatives: $\lambda = \left(-\omega_0^2 \pm \sqrt{\Delta}\right)/2$; and for $\delta\pi/\omega_0^2 > 1/8$, they are complex conjugates with negative real parts: $\lambda = \left(-\omega_0^2 \pm i\sqrt{-\Delta}\right)/2$. Thus, the zero-gravity CO regime is stable in its whole range of existence. Introducing the complex amplitudes A_R, A_φ and A_γ, we look for solutions of

the form $(\delta R,\, \delta\varphi,\, \delta\gamma) = (A_R,\, A_\varphi,\, A_\gamma)e^{i\Omega_0 t}$. We find the following condition:

$$\begin{pmatrix} -\omega_0^2 - i\Omega_0 & 0 & -\pi\sin\gamma_0 \\ -\omega_0^2\sin\gamma_0 & -i\Omega_0 & \omega_0^2 \\ 2\omega_0^2\sin\gamma_0 & 0 & -i\Omega_0 \end{pmatrix} \begin{pmatrix} A_R \\ A_\varphi \\ A_\gamma \end{pmatrix} = A_g \begin{pmatrix} 0 \\ 0 \\ 1 \end{pmatrix}, \tag{L.28}$$

where $A_g = \delta g_\alpha \varepsilon e^{i\Psi}$, and Ψ is an irrelevant phase shift. The matrix on the left-hand side of Eq. (L.28) is invertible for $\pi > \omega_0^2$. At lowest order in $\delta\pi = \pi - \omega_0^2$, the complex amplitudes expresses as:

$$\begin{pmatrix} |A_R| \\ |A_\varphi| \\ |A_\gamma| \end{pmatrix} \simeq |A_g| \begin{pmatrix} 1/\omega_0^2 \\ 1/\delta\pi \\ 1/\omega_0\sqrt{\delta\pi} \end{pmatrix}. \tag{L.29}$$

The complex amplitudes for the modulations along φ and γ diverge as one gets closer to the exceptional point, which induces a change of regime, well captured by the mapping with a nonlinear pendulum (see chapter 7).

Appendix M

Blueprints

Active elastic building block

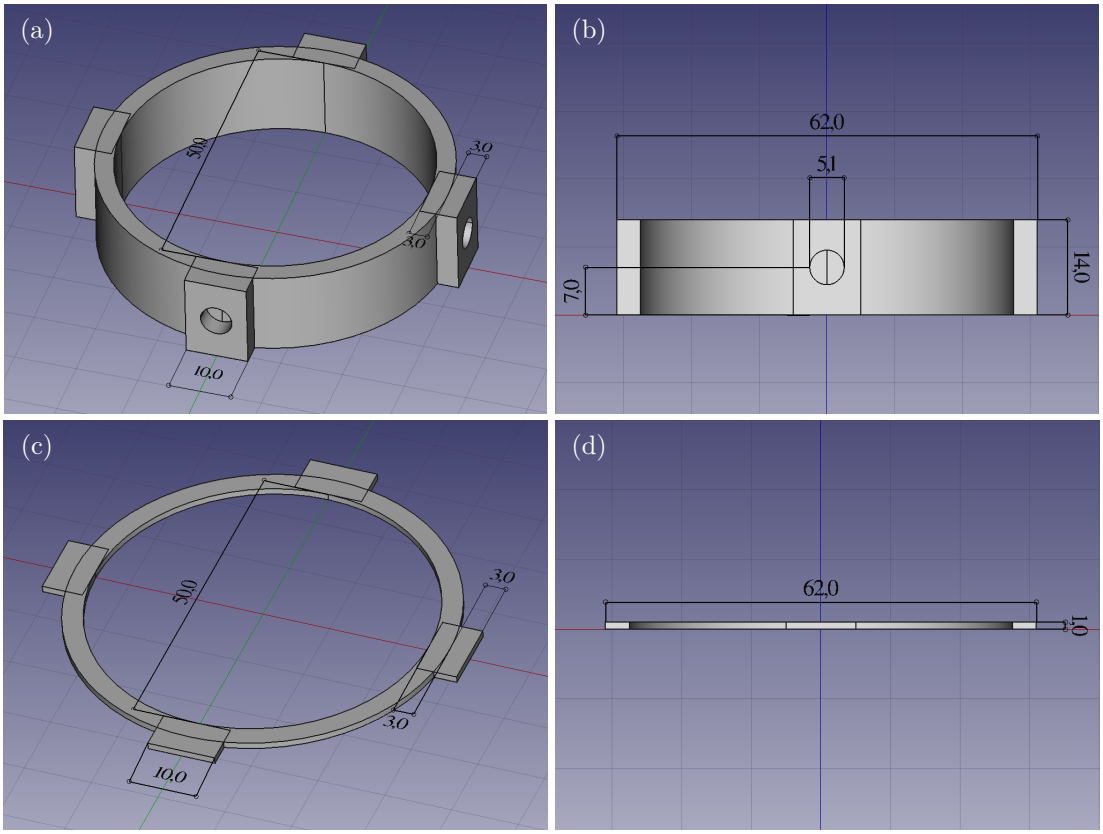


FIG. M.1. **3D plan for the square active elastic building block.** See section 2.2. (a-b) Active elastic building block's structure. (a) Top-side orthographic projection. (b) Side orthographic projection. (c-d) Active elastic building block's hat. (c) Top-side orthographic projection. (d) Side orthographic projection. Quotes are written in mm.

Pinner

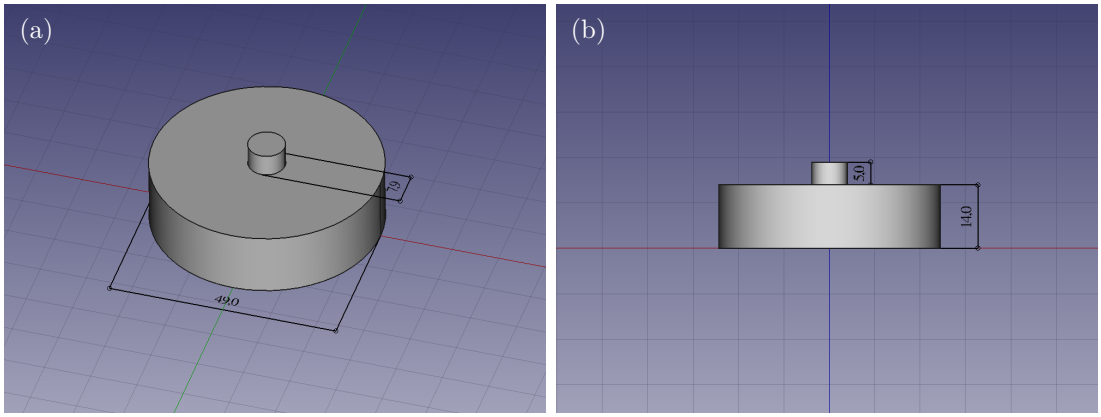


FIG. M.2. **3D plan for the pinner.** See section 2.4. (a) Top-side orthographic projection. (b) Side orthographic projection. Quotes are written in mm.

Self-alignment device

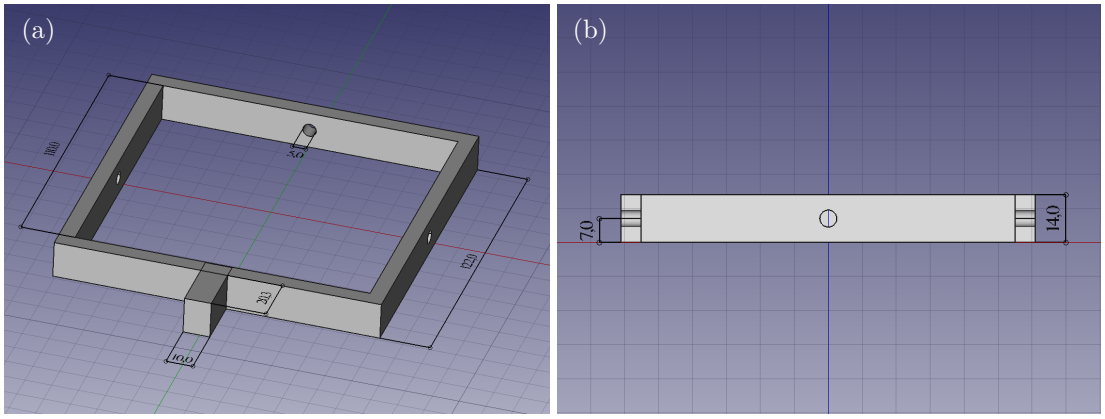


FIG. M.3. **3D plan for the alignment device.** See section 2.3.2. (a) Top-side orthographic projection. (b) Back side orthographic projection. Quotes are written in mm.

Active *Gerris*

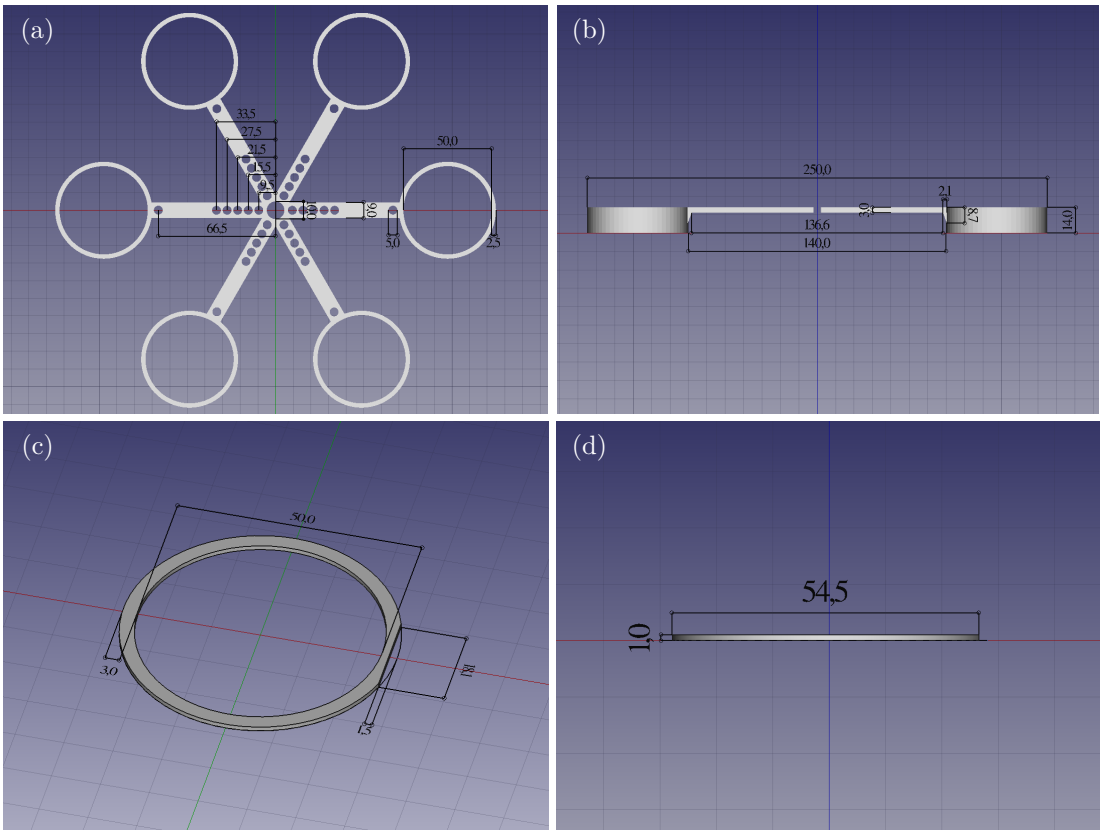


FIG. M.4. **3D plan for the active *Gerris*.** See section 6.3. (a-b) Active *Gerris*'s structure. (a) Top orthographic projection. (b) Side orthographic projection of a single arm. (c-d) Active *Gerris*'s hat (c) Top-side orthographic projection. (d) Side orthographic projection. Quotes are written in mm.

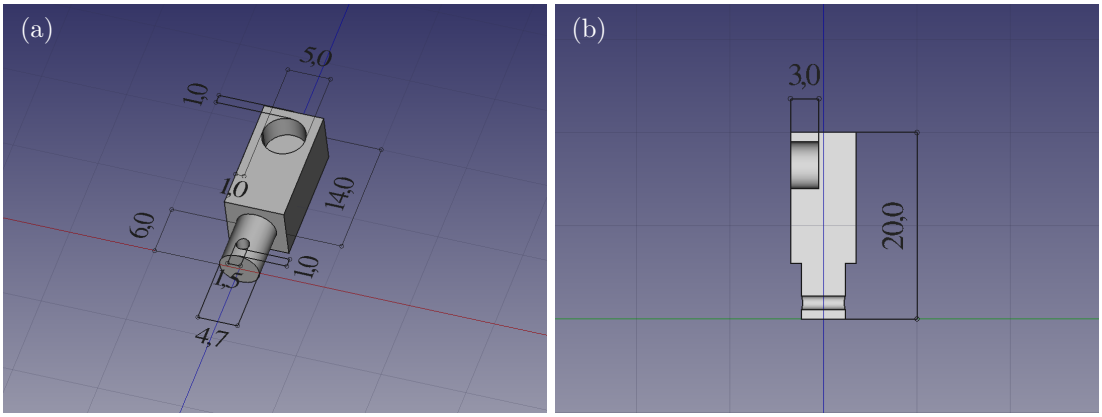


FIG. M.5. **3D plan for the active *Gerris*'s springs holder.** See section 6.3. (a) Top side orthographic projection. (b) Side orthographic projection. Quotes are written in mm.

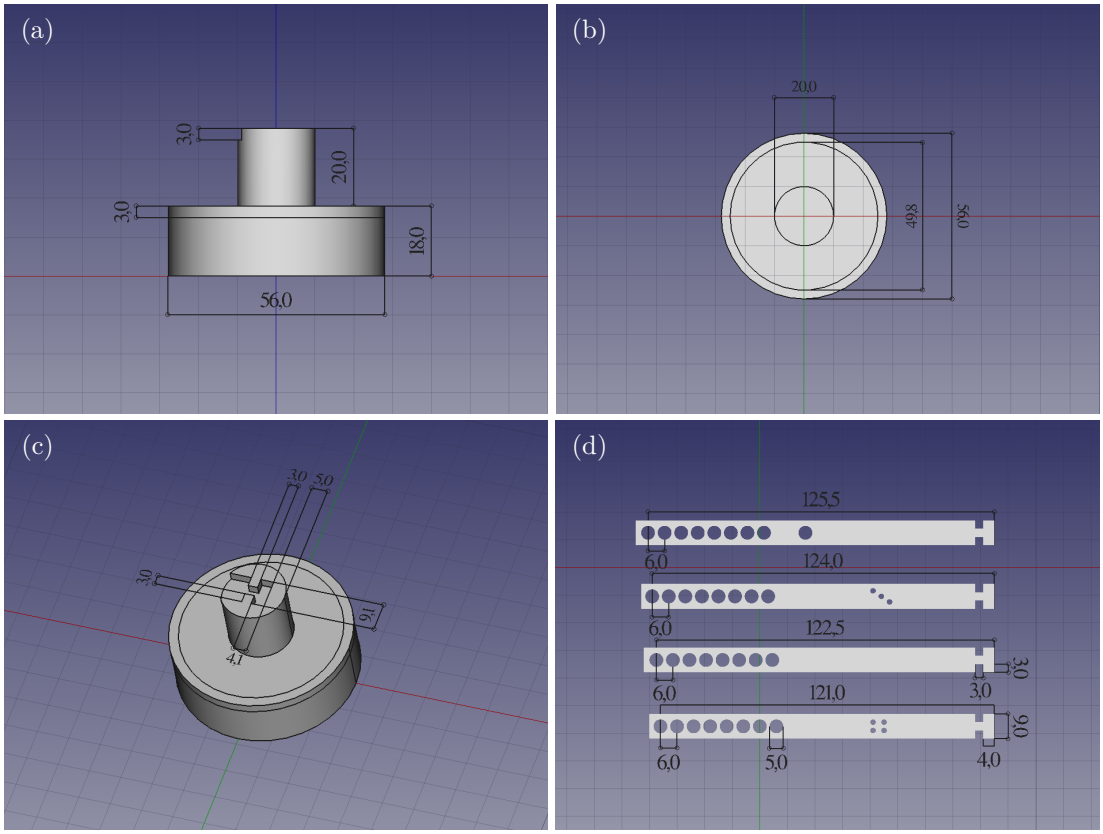


FIG. M.6. **3D plan for the active *Gerris*'s pinner.** See section 6.3. (a-c) Pinner's hat. (a) Side orthographic projection. (b) Bottom orthographic projection. (c) Top side orthographic projection. (d) Four pinner's arm. Quotes are written in mm.

Bibliography

1. Baconnier, P. *et al.* Selective and collective actuation in active solids. *Nat. Phys.* (2022).
2. Baconnier, P., Shohat, D. & Dauchot, O. Discontinuous Tension-Controlled Transition between Collective Actuations in Active Solids. *Physical Review Letters* **130,** 028201 (2023).
3. Helbing, D., Johansson, A. & Al-Abideen, H. Z. Dynamics of crowd disasters: An empirical study. *Physical review E* **75,** 046109 (2007).
4. Moussaïd, M., Helbing, D. & Theraulaz, G. How simple rules determine pedestrian behavior and crowd disasters. *Proceedings of the National Academy of Sciences* **108,** 6884–6888 (2011).
5. Mlot, N. J., Tovey, C. A. & Hu, D. L. Fire ants self-assemble into waterproof rafts to survive floods. *Proceedings of the National Academy of Sciences* **108,** 7669–7673 (2011).
6. Reid, C. R. *et al.* Army ants dynamically adjust living bridges in response to a cost–benefit trade-off. *Proc. Natl Acad. Sci.* **112,** 15113–15118 (2015).
7. Tennenbaum, M., Liu, Z., Hu, D. & Fernandez-Nieves, A. Mechanics of fire ant aggregations. *Nature materials* **15,** 54–59 (2016).
8. Peyret, G. *et al.* Sustained oscillations of epithelial cell sheets. *Biophys. J.* **117,** 464–478 (2019).
9. Vicsek, T., Czirók, A., Ben-Jacob, E., Cohen, I. & Shochet, O. Novel type of phase transition in a system of self-driven particles. *Physical review letters* **75,** 1226 (1995).
10. Tailleur, J & Cates, M. Statistical mechanics of interacting run-and-tumble bacteria. *Physical review letters* **100,** 218103 (2008).
11. Cates, M. E. & Tailleur, J. When are active Brownian particles and run-and-tumble particles equivalent? Consequences for motility-induced phase separation. *EPL (Europhysics Letters)* **101,** 20010 (2013).
12. Stenhammar, J., Tiribocchi, A., Allen, R. J., Marenduzzo, D. & Cates, M. E. Continuum theory of phase separation kinetics for active Brownian particles. *Physical review letters* **111,** 145702 (2013).
13. Fily, Y. & Marchetti, M. C. Athermal phase separation of self-propelled particles with no alignment. *Physical review letters* **108,** 235702 (2012).
14. Cates, M. E. & Tailleur, J. Motility-induced phase separation. *Annu. Rev. Condens. Matter Phys.* **6,** 219–244 (2015).
15. Liu, G. *et al.* Self-driven phase transitions drive Myxococcus xanthus fruiting body formation. *Physical review letters* **122,** 248102 (2019).
16. Redner, G. S., Hagan, M. F. & Baskaran, A. Structure and dynamics of a phase-separating active colloidal fluid. *Physical review letters* **110,** 055701 (2013).
17. Redner, G. S., Baskaran, A. & Hagan, M. F. Reentrant phase behavior in active colloids with attraction. *Physical Review E* **88,** 012305 (2013).
18. Stenhammar, J., Marenduzzo, D., Allen, R. J. & Cates, M. E. Phase behaviour of active Brownian particles: the role of dimensionality. *Soft matter* **10,** 1489–1499 (2014).
19. Farage, T. F., Krinninger, P. & Brader, J. M. Effective interactions in active Brownian suspensions. *Physical Review E* **91,** 042310 (2015).
20. Schnitzer, M. J. Theory of continuum random walks and application to chemotaxis. *Physical Review E* **48,** 2553 (1993).
21. Hohenberg, P. C. & Halperin, B. I. Theory of dynamic critical phenomena. *Reviews of Modern Physics* **49,** 435 (1977).

22. Chaikin, P. M., Lubensky, T. C. & Witten, T. A. *Principles of condensed matter physics* (Cambridge university press Cambridge, 1995).
23. Wittkowski, R. *et al.* Scalar φ 4 field theory for active-particle phase separation. *Nat. Commun.* **5,** 1–9 (2014).
24. Tjhung, E., Nardini, C. & Cates, M. E. Cluster phases and bubbly phase separation in active fluids: reversal of the Ostwald process. *Physical Review X* **8,** 031080 (2018).
25. Theurkauff, I., Cottin-Bizonne, C., Palacci, J., Ybert, C. & Bocquet, L. Dynamic clustering in active colloidal suspensions with chemical signaling. *Physical review letters* **108,** 268303 (2012).
26. Palacci, J., Sacanna, S., Steinberg, A. P., Pine, D. J. & Chaikin, P. M. Living crystals of light-activated colloidal surfers. *Science* **339,** 936–940 (2013).
27. Buttinoni, I. *et al.* Dynamical clustering and phase separation in suspensions of self-propelled colloidal particles. *Physical review letters* **110,** 238301 (2013).
28. Van Der Linden, M. N., Alexander, L. C., Aarts, D. G. & Dauchot, O. Interrupted motility induced phase separation in aligning active colloids. *Physical review letters* **123,** 098001 (2019).
29. Matas-Navarro, R., Golestanian, R., Liverpool, T. B. & Fielding, S. M. Hydrodynamic suppression of phase separation in active suspensions. *Physical Review E* **90,** 032304 (2014).
30. Zöttl, A. & Stark, H. Hydrodynamics determines collective motion and phase behavior of active colloids in quasi-two-dimensional confinement. *Physical review letters* **112,** 118101 (2014).
31. Ballerini, M. *et al.* Interaction ruling animal collective behavior depends on topological rather than metric distance: Evidence from a field study. *Proceedings of the national academy of sciences* **105,** 1232–1237 (2008).
32. Ballerini, M. *et al.* Empirical investigation of starling flocks: a benchmark study in collective animal behaviour. *Animal behaviour* **76,** 201–215 (2008).
33. Cavagna, A. *et al.* From empirical data to inter-individual interactions: unveiling the rules of collective animal behavior. *Mathematical Models and Methods in Applied Sciences* **20,** 1491–1510 (2010).
34. Cavagna, A. *et al.* Scale-free correlations in starling flocks. *Proceedings of the National Academy of Sciences* **107,** 11865–11870 (2010).
35. Procaccini, A. *et al.* Propagating waves in starling, Sturnus vulgaris, flocks under predation. *Animal behaviour* **82,** 759–765 (2011).
36. Bialek, W. *et al.* Statistical mechanics for natural flocks of birds. *Proceedings of the National Academy of Sciences* **109,** 4786–4791 (2012).
37. Cavagna, A. & Giardina, I. Bird flocks as condensed matter. *Annu. Rev. Condens. Matter Phys.* **5,** 183–207 (2014).
38. Yang, Y. *et al.* Dominating lengthscales of zebrafish collective behaviour. *PLOS Computational Biology* **18,** e1009394 (2022).
39. Buhl, J. *et al.* From disorder to order in marching locusts. *Science* **312,** 1402–1406 (2006).
40. Bazazi, S. *et al.* Collective motion and cannibalism in locust migratory bands. *Current biology* **18,** 735–739 (2008).
41. Zhang, H.-P., Be'er, A., Florin, E.-L. & Swinney, H. L. Collective motion and density fluctuations in bacterial colonies. *Proceedings of the National Academy of Sciences* **107,** 13626–13630 (2010).
42. Gachelin, J, Rousselet, A, Lindner, A & Clement, E. Collective motion in an active suspension of Escherichia coli bacteria. *New Journal of Physics* **16,** 025003 (2014).
43. Vicsek, T. & Zafeiris, A. Collective motion. *Physics reports* **517,** 71–140 (2012).
44. Chaté, H, Ginelli, F, Grégoire, G & Raynaud, F. Collective motion of self-propelled particles interacting without cohesion. *Phys. Rev. E* **77,** 046113 (2008).
45. Solon, A. & Tailleur, J. Revisiting the flocking transition using active spins. *Physical review letters* **111,** 078101 (2013).
46. Kosterlitz, J. M. & Thouless, D. J. Ordering, metastability and phase transitions in two-dimensional systems. *Journal of Physics C: Solid State Physics* **6,** 1181 (1973).
47. Mermin, N. D. & Wagner, H. Absence of ferromagnetism or antiferromagnetism in one-or two-dimensional isotropic Heisenberg models. *Physical Review Letters* **17,** 1133 (1966).

48. Toner, J. & Tu, Y. Long-Range Order in a Two-Dimensional Dynamical XY Model: How Birds Fly Together. *Phys. Rev. Lett.* **75,** 4326–4329 (1995).

49. Toner, J. & Tu, Y. Flocks, herds, and schools: A quantitative theory of flocking. *Physical review E* **58,** 4828 (1998).

50. Toner, J., Tu, Y. & Ramaswamy, S. Hydrodynamics and phases of flocks. *Annals of Physics* **318,** 170–244 (2005).

51. Bertin, E., Droz, M. & Grégoire, G. Boltzmann and hydrodynamic description for self-propelled particles. *Physical Review E* **74,** 022101 (2006).

52. Ihle, T. Kinetic theory of flocking: Derivation of hydrodynamic equations. *Physical Review E* **83,** 030901 (2011).

53. Kung, W., Marchetti, M. C. & Saunders, K. Hydrodynamics of polar liquid crystals. *Physical Review E* **73,** 031708 (2006).

54. Marchetti, M. C. *et al.* Hydrodynamics of soft active matter. *RMP* **85,** 1143 (2013).

55. Deseigne, J., Dauchot, O. & Chaté, H. Collective motion of vibrated polar disks. *Physical review letters* **105,** 098001 (2010).

56. Deseigne, J., Léonard, S., Dauchot, O. & Chaté, H. Vibrated polar disks: spontaneous motion, binary collisions, and collective dynamics. *Soft Matter* **8,** 5629–5639 (2012).

57. Weber, C. A. *et al.* Long-range ordering of vibrated polar disks. *Phys. Rev. Lett.* **110,** 208001 (2013).

58. Lam, K.-D. N. T., Schindler, M. & Dauchot, O. Self-propelled hard disks: implicit alignment and transition to collective motion. *New J. Phys.* **17,** 113056 (2015).

59. Bricard, A., Caussin, J.-B., Desreumaux, N., Dauchot, O. & Bartolo, D. Emergence of macroscopic directed motion in populations of motile colloids. *Nature* **503,** 95–98 (2013).

60. Bricard, A. *et al.* Emergent vortices in populations of colloidal rollers. *Nature communications* **6,** 1–8 (2015).

61. Geyer, D., Morin, A. & Bartolo, D. Sounds and hydrodynamics of polar active fluids. *Nature materials* **17,** 789–793 (2018).

62. Schaller, V., Weber, C., Semmrich, C., Frey, E. & Bausch, A. R. Polar patterns of driven filaments. *Nature* **467,** 73–77 (2010).

63. Schaller, V., Weber, C., Frey, E. & Bausch, A. R. Polar pattern formation: hydrodynamic coupling of driven filaments. *Soft Matter* **7,** 3213–3218 (2011).

64. Quincke, G. Ueber rotationen im constanten electrischen felde. *Annalen der Physik* **295,** 417–486 (1896).

65. Abercrombie, M. & Heaysman, J. E. Observations on the social behaviour of cells in tissue culture: II."Monolayering" of fibroblasts. *Experimental cell research* **6,** 293–306 (1954).

66. Smeets, B. *et al.* Emergent structures and dynamics of cell colonies by contact inhibition of locomotion. *Proceedings of the National Academy of Sciences* **113,** 14621–14626 (2016).

67. Stramer, B. & Mayor, R. Mechanisms and in vivo functions of contact inhibition of locomotion. *Nature reviews Molecular cell biology* **18,** 43–55 (2017).

68. Szabo, B. *et al.* Phase transition in the collective migration of tissue cells: experiment and model. *Phys. Rev. E* **74,** 061908 (2006).

69. Soumya, S. *et al.* Coherent motion of monolayer sheets under confinement and its pathological implications. *PLoS Comput. Biol.* **11,** e1004670 (2015).

70. Notbohm, J. *et al.* Cellular contraction and polarization drive collective cellular motion. *Biophys. J.* **110,** 2729–2738 (2016).

71. Hakim, V. & Silberzan, P. Collective cell migration: a physics perspective. *Rep. Prog. Phys* **80,** 076601 (2017).

72. Giavazzi, F. *et al.* Flocking transitions in confluent tissues. *Soft Matter* **14,** 3471–3477 (2018).

73. Petrolli, V. *et al.* Confinement-induced transition between wavelike collective cell migration modes. *Physical review letters* **122,** 168101 (2019).

74. Henkes, S., Kostanjevec, K., Collinson, J. M., Sknepnek, R. & Bertin, E. Dense active matter model of motion patterns in confluent cell monolayers. *Nat. Commun.* **11,** 1–9 (2020).

75. Shimoyama, N., Sugawara, K., Mizuguchi, T., Hayakawa, Y. & Sano, M. Collective motion in a system of motile elements. *Physical Review Letters* **76,** 3870 (1996).

76. Palmieri, B., Bresler, Y., Wirtz, D. & Grant, M. Multiple scale model for cell migration in monolayers: Elastic mismatch between cells enhances motility. *Scientific reports* **5,** 1–13 (2015).

77. Xu, H., Huang, Y., Zhang, R. & Wu, Y. Autonomous waves and global motion modes in living active solids. *Nature Physics,* 1–6 (2022).

78. Taylor, B. L. & Koshland Jr, D. Intrinsic and extrinsic light responses of Salmonella typhimurium and Escherichia coli. *Journal of bacteriology* **123,** 557–569 (1975).

79. Henkes, S., Fily, Y. & Marchetti, M. C. Active jamming: Self-propelled soft particles at high density. *Phys. Rev. E* **84,** 040301 (2011).

80. Bindschadler, M. & McGrath, J. L. Sheet migration by wounded monolayers as an emergent property of single-cell dynamics. *Journal of cell science* **120,** 876–884 (2007).

81. Poujade, M. *et al.* Collective migration of an epithelial monolayer in response to a model wound. *Proceedings of the National Academy of Sciences* **104,** 15988–15993 (2007).

82. Trepat, X. *et al.* Physical forces during collective cell migration. *Nature physics* **5,** 426–430 (2009).

83. Angelini, T. E., Hannezo, E., Trepat, X., Fredberg, J. J. & Weitz, D. A. Cell migration driven by cooperative substrate deformation patterns. *Physical review letters* **104,** 168104 (2010).

84. Petitjean, L. *et al.* Velocity fields in a collectively migrating epithelium. *Biophysical journal* **98,** 1790–1800 (2010).

85. Angelini, T. E. *et al.* Glass-like dynamics of collective cell migration. *Proceedings of the National Academy of Sciences* **108,** 4714–4719 (2011).

86. Mermin, N. D. Crystalline order in two dimensions. *Physical Review* **176,** 250 (1968).

87. Digregorio, P. *et al.* Full phase diagram of active Brownian disks: From melting to motility-induced phase separation. *Physical review letters* **121,** 098003 (2018).

88. Bialké, J., Speck, T. & Löwen, H. Crystallization in a dense suspension of self-propelled particles. *Physical review letters* **108,** 168301 (2012).

89. Klamser, J. U., Kapfer, S. C. & Krauth, W. Thermodynamic phases in two-dimensional active matter. *Nature communications* **9,** 1–8 (2018).

90. Menzel, A. M. & Löwen, H. Traveling and Resting Crystals in Active Systems. *Phys. Rev. Lett.* **110,** 055702 (2013).

91. Weber, C. A., Bock, C. & Frey, E. Defect-mediated phase transitions in active soft matter. *Physical review letters* **112,** 168301 (2014).

92. Briand, G., Schindler, M. & Dauchot, O. Spontaneously flowing crystal of self-propelled particles. *Phys. Rev. Lett.* **120,** 208001 (2018).

93. Janssen, L. M. Active glasses. *J. Condens. Matter Phys.* **31,** 503002 (2019).

94. Bi, D., Yang, X., Marchetti, M. C. & Manning, M. L. Motility-driven glass and jamming transitions in biological tissues. *Physical Review X* **6,** 021011 (2016).

95. Bi, D., Lopez, J. H., Schwarz, J. M. & Manning, M. L. Energy barriers and cell migration in densely packed tissues. *Soft matter* **10,** 1885–1890 (2014).

96. Bi, D., Lopez, J., Schwarz, J. M. & Manning, M. L. A density-independent rigidity transition in biological tissues. *Nature Physics* **11,** 1074–1079 (2015).

97. Merkel, M. & Manning, M. L. A geometrically controlled rigidity transition in a model for confluent 3D tissues. *New Journal of Physics* **20,** 022002 (2018).

98. Park, J.-A. *et al.* Unjamming and cell shape in the asthmatic airway epithelium. *Nature materials* **14,** 1040–1048 (2015).

99. Malinverno, C. *et al.* Endocytic reawakening of motility in jammed epithelia. *Nature materials* **16,** 587–596 (2017).

100. Chen, B. G.-g., Upadhyaya, N. & Vitelli, V. Nonlinear conduction via solitons in a topological mechanical insulator. *Proc. Natl Acad. Sci.* **111,** 13004–13009 (2014).

101. Paulose, J., Chen, B. G.-g. & Vitelli, V. Topological modes bound to dislocations in mechanical metamaterials. *Nature Physics* **11,** 153–156 (2015).

102. Florijn, B., Coulais, C. & van Hecke, M. Programmable mechanical metamaterials. *Phys. Rev. Lett.* **113,** 175503 (2014).

103. Bertoldi, K., Vitelli, V., Christensen, J. & Van Hecke, M. Flexible mechanical metamaterials. *Nature Reviews Materials* **2,** 1–11 (2017).

104. Zhai, Z., Wang, Y. & Jiang, H. Origami-inspired, on-demand deployable and collapsible mechanical metamaterials with tunable stiffness. *Proc. Natl Acad. Sci.* **115,** 2032–2037 (2018).

105. Kadic, M., Milton, G. W., van Hecke, M. & Wegener, M. 3D metamaterials. *Nat. Rev. Phys.* **1,** 198–210 (2019).

106. Liarte, D. B., Stenull, O. & Lubensky, T. Multifunctional twisted kagome lattices: tuning by pruning mechanical metamaterials. *Physical Review E* **101,** 063001 (2020).

107. Yuan, X. *et al.* Recent progress in the design and fabrication of multifunctional structures based on metamaterials. *Current Opinion in Solid State and Materials Science* **25,** 100883 (2021).

108. Bossart, A., Dykstra, D. M., van der Laan, J. & Coulais, C. Oligomodal metamaterials with multifunctional mechanics. *Proceedings of the National Academy of Sciences* **118** (2021).

109. Siéfert, E., Reyssat, E., Bico, J. & Roman, B. Bio-inspired pneumatic shape-morphing elastomers. *Nature materials* **18,** 24–28 (2019).

110. Kim, Y., Yuk, H., Zhao, R., Chester, S. A. & Zhao, X. Printing ferromagnetic domains for untethered fast-transforming soft materials. *Nature* **558,** 274–279 (2018).

111. Pishvar, M. & Harne, R. L. Foundations for soft, smart matter by active mechanical metamaterials. *Adv. Sci.* **7,** 2001384 (2020).

112. Ferrante, E., Turgut, A. E., Dorigo, M. & Huepe, C. Elasticity-based mechanism for the collective motion of self-propelled particles with springlike interactions: a model system for natural and artificial swarms. *Phys. Rev. Lett.* **111,** 268302 (2013).

113. Brambilla, M., Ferrante, E., Birattari, M. & Dorigo, M. Swarm robotics: a review from the swarm engineering perspective. *Swarm Intell.* **7,** 1–41 (2013).

114. Woodhouse, F. G., Ronellenfitsch, H. & Dunkel, J. Autonomous actuation of zero modes in mechanical networks far from equilibrium. *Phys. Rev. Lett.* **121,** 178001 (2018).

115. Fodor, É. & Marchetti, M. C. The statistical physics of active matter: From self-catalytic colloids to living cells. *Physica A: Statistical Mechanics and its Applications* **504,** 106–120 (2018).

116. Su, W., Schrieffer, J. & Heeger, A. J. Solitons in polyacetylene. *Physical review letters* **42,** 1698 (1979).

117. Kane, C. & Lubensky, T. Topological boundary modes in isostatic lattices. *Nature Physics* **10,** 39–45 (2014).

118. Erdmann, U., Ebeling, W., Schimansky-Geier, L. & Schweitzer, F. Brownian particles far from equilibrium. *The European Physical Journal B-Condensed Matter and Complex Systems* **15,** 105–113 (2000).

119. Forrow, A., Woodhouse, F. G. & Dunkel, J. Mode selection in compressible active flow networks. *Physical Review Letters* **119,** 028102 (2017).

120. Zheng, E. *et al.* Self-oscillation and synchronisation transitions in elasto-active structures. *arXiv preprint arXiv:2106.05721* (2021).

121. Machin, K. Wave propagation along flagella. *Journal of Experimental Biology* **35,** 796–806 (1958).

122. Brokaw, C. J. Molecular mechanism for oscillation in flagella and muscle. *Proceedings of the National Academy of Sciences* **72,** 3102–3106 (1975).

123. Camalet, S., Jülicher, F. & Prost, J. Self-organized beating and swimming of internally driven filaments. *Physical review letters* **82,** 1590 (1999).

124. Landau, L. e. a. *Theory of Elasticity* (Elsevier, 1986).

125. Scheibner, C. *et al.* Odd elasticity. *Nat. Phys.* **16,** 475–480 (2020).

126. Tan, T. H. *et al.* Odd dynamics of living chiral crystals. *Nature* **607,** 287–293 (2022).

127. Brandenbourger, M., Locsin, X., Lerner, E. & Coulais, C. Non-reciprocal robotic metamaterials. *Nat. Commun.* **10,** 1–8 (2019).

128. Ghatak, A., Brandenbourger, M., Van Wezel, J. & Coulais, C. Observation of non-Hermitian topology and its bulk–edge correspondence in an active mechanical metamaterial. *Proceedings of the National Academy of Sciences* **117,** 29561–29568 (2020).

129. Brandenbourger, M., Scheibner, C., Veenstra, J., Vitelli, V. & Coulais, C. Active impact and locomotion in robotic matter with nonlinear work cycles. *arXiv preprint arXiv:2108.08837* (2021).

130. Shankar, S., Souslov, A., Bowick, M. J., Marchetti, M. C. & Vitelli, V. Topological active matter. *Nature Reviews Physics* **4,** 380–398 (2022).

131. Palacci, J. *et al.* Light-activated self-propelled colloids. *Philosophical Transactions of the Royal Society A: Mathematical, Physical and Engineering Sciences* **372,** 20130372 (2014).

132. Aubret, A., Youssef, M., Sacanna, S. & Palacci, J. Targeted assembly and synchronization of self-spinning microgears. *Nature Physics* **14,** 1114–1118 (2018).

133. Wang, W., Lv, X., Moran, J. L., Duan, S. & Zhou, C. A practical guide to active colloids: choosing synthetic model systems for soft matter physics research. *Soft Matter* **16,** 3846–3868 (2020).

134. Lam, K.-D. N. T., Schindler, M. & Dauchot, O. Polar active liquids: a universal classification rooted in nonconservation of momentum. *Journal of Statistical Mechanics: Theory and Experiment* **2015,** P10017 (2015).

135. Briand, G & Dauchot, O. Crystallization of self-propelled hard discs. *Physical review letters* **117,** 098004 (2016).

136. Junot, G, Briand, G, Ledesma-Alonso, R & Dauchot, O. Active versus passive hard disks against a membrane: mechanical pressure and instability. *Phys. Rev. Lett.* **119,** 028002 (2017).

137. Lanoiselée, Y., Briand, G., Dauchot, O. & Grebenkov, D. S. Statistical analysis of random trajectories of vibrated disks: Towards a macroscopic realization of Brownian motion. *Physical Review E* **98,** 062112 (2018).

138. Chardac, A., Shankar, S., Marchetti, M. C. & Bartolo, D. Emergence of dynamic vortex glasses in disordered polar active fluids. *Proceedings of the National Academy of Sciences* **118** (2021).

139. Izri, Z., Van Der Linden, M. N., Michelin, S. & Dauchot, O. Self-propulsion of pure water droplets by spontaneous Marangoni-stress-driven motion. *Physical review letters* **113,** 248302 (2014).

140. Illien, P., de Blois, C., Liu, Y., van der Linden, M. N. & Dauchot, O. Speed-dispersion-induced alignment: A one-dimensional model inspired by swimming droplets experiments. *Physical Review E* **101,** 040602 (2020).

141. De Blois, C. *et al.* Swimming droplets in 1D geometries: an active Bretherton problem. *Soft Matter* **17,** 6646–6660 (2021).

142. Tapia-Ignacio, C., Gutierrez-Martinez, L. L. & Sandoval, M. Trapped active toy robots: theory and experiment. *Journal of Statistical Mechanics: Theory and Experiment* **2021,** 053404 (2021).

143. Dauchot, O. & Démery, V. Dynamics of a self-propelled particle in a harmonic trap. *Phys. Rev. Lett.* **122,** 068002 (2019).

144. Barois, T., Boudet, J.-F., Lintuvuori, J. S. & Kellay, H. Sorting and extraction of self-propelled chiral particles by polarized wall currents. *Physical Review Letters* **125,** 238003 (2020).

145. Sánchez, R & Díaz-Leyva, P. Self-assembly and speed distributions of active granular particles. *Physica A: Statistical Mechanics and its Applications* **499,** 11–19 (2018).

146. Boudet, J.-F. *et al.* From collections of independent, mindless robots to flexible, mobile, and directional superstructures. *Science Robotics* **6,** eabd0272 (2021).

147. Yang, X., Ren, C., Cheng, K. & Zhang, H. Robust boundary flow in chiral active fluid. *Physical Review E* **101,** 022603 (2020).

148. Giomi, L, Hawley-Weld, N & Mahadevan, L. Swarming, swirling and stasis in sequestered bristlebots. *Proceedings of the Royal Society A: Mathematical, Physical and Engineering Sciences* **469,** 20120637 (2013).

149. Cicconofri, G., Becker, F., Noselli, G., Desimone, A. & Zimmermann, K. *The inversion of motion of bristle bots: analytical and experimental analysis* in *Symposium on Robot Design, Dynamics and Control* (2016), 225–232.

150. Majewski, T., Szwedowicz, D. & Majewski, M. Locomotion of a mini bristle robot with inertial excitation. *Journal of Mechanisms and Robotics* **9,** 061008 (2017).

151. Zion, M. Y. B., Bredeche, N. & Dauchot, O. Distributed on-line reinforcement learning in a swarm of sterically interacting robots. *arXiv preprint arXiv:2111.06953* (2021).

152. Cohen, C., Texier, B. D., Quéré, D. & Clanet, C. The physics of badminton. *New Journal of Physics* **17,** 063001 (2015).

153. MathWorks. *Design Optimization of a Helical Compression Spring* `https://fr.mathworks.com/matlabcentral/fileexchange/64651-design-optimization-of-a-helical-compression-spring`. Accessed: 2022-05-10. 2022.

154. Maxwell, J. C. L. on the calculation of the equilibrium and stiffness of frames. *The London, Edinburgh, and Dublin Philosophical Magazine and Journal of Science* **27,** 294–299 (1864).

155. Calladine, C. R. Buckminster Fuller's "tensegrity" structures and Clerk Maxwell's rules for the construction of stiff frames. *International journal of solids and structures* **14,** 161–172 (1978).

156. Lubensky, T., Kane, C., Mao, X., Souslov, A. & Sun, K. Phonons and elasticity in critically coordinated lattices. *Reports on Progress in Physics* **78,** 073901 (2015).

157. Alexander, S. Amorphous solids: their structure, lattice dynamics and elasticity. *Physics reports* **296,** 65–236 (1998).

158. Bell, R., Dean, P & Hibbins-Butler, D. Localization of normal modes in vitreous silica, germania and beryllium fluoride. *Journal of Physics C: Solid State Physics* **3,** 2111 (1970).

159. Cho, M., Fleming, G. R., Saito, S., Ohmine, I. & Stratt, R. M. Instantaneous normal mode analysis of liquid water. *The Journal of chemical physics* **100,** 6672–6683 (1994).

160. Bembenek, S. D. & Laird, B. B. Instantaneous normal modes and the glass transition. *Physical review letters* **74,** 936 (1995).

161. Wang, L. *et al.* Low-frequency vibrational modes of stable glasses. *Nature communications* **10,** 1–7 (2019).

162. Fermi, E., Pasta, P, Ulam, S. & Tsingou, M. *Studies of the nonlinear problems* tech. rep. (Los Alamos National Lab.(LANL), Los Alamos, NM (United States), 1955).

163. Czirók, A., Ben-Jacob, E., Cohen, I. & Vicsek, T. Formation of complex bacterial colonies via self-generated vortices. *Physical Review E* **54,** 1791 (1996).

164. Kudrolli, A., Lumay, G., Volfson, D. & Tsimring, L. S. Swarming and swirling in self-propelled polar granular rods. *Physical review letters* **100,** 058001 (2008).

165. Zheng, Y., Huepe, C. & Han, Z. Experimental capabilities and limitations of a position-based control algorithm for swarm robotics. *Adaptive Behavior* **30,** 19–35 (2022).

166. Acuna, D. *et al.* A three step recipe for designing auxetic materials on demand. *Communications Physics* **5,** 1–9 (2022).

167. Mikhailov, A. S. & Zanette, D. H. Noise-induced breakdown of coherent collective motion in swarms. *Physical Review E* **60,** 4571 (1999).

168. Erdmann, U., Ebeling, W. & Mikhailov, A. S. Noise-induced transition from translational to rotational motion of swarms. *Physical Review E* **71,** 051904 (2005).

169. Vilfan, A. & Frey, E. Oscillations in molecular motor assemblies. *Journal of physics: Condensed matter* **17,** S3901 (2005).

170. Kuramoto, Y. *Self-entrainment of a population of coupled non-linear oscillators* in *International symposium on mathematical problems in theoretical physics* (1975), 420–422.

171. Strogatz, S. H. From Kuramoto to Crawford: exploring the onset of synchronization in populations of coupled oscillators. *Physica D: Nonlinear Phenomena* **143,** 1–20 (2000).

172. Fruchart, M., Hanai, R., Littlewood, P. B. & Vitelli, V. Non-reciprocal phase transitions. *Nature* **592,** 363–369 (2021).

173. Maitra, A. & Ramaswamy, S. Oriented active solids. *Phys. Rev. Lett.* **123,** 238001 (2019).

174. Chen, C., Liu, S., Shi, X.-q., Chaté, H. & Wu, Y. Weak synchronization and large-scale collective oscillation in dense bacterial suspensions. *Nature* **542,** 210–214 (2017).

175. Liu, S., Shankar, S., Marchetti, M. C. & Wu, Y. Viscoelastic control of spatiotemporal order in bacterial active matter. *Nature* **590,** 80–84 (2021).

176. Bunting, C. & Eades, C. C. The effect of mechanical tension upon the polarity of growing fibroblasts. *The Journal of experimental medicine* **44,** 147 (1926).

177. Kolega, J. Effects of mechanical tension on protrusive activity and microfilament and intermediate filament organization in an epidermal epithelium moving in culture. *The Journal of cell biology* **102,** 1400–1411 (1986).

178. Hinz, B., Mastrangelo, D., Iselin, C. E., Chaponnier, C. & Gabbiani, G. Mechanical tension controls granulation tissue contractile activity and myofibroblast differentiation. *The American journal of pathology* **159,** 1009–1020 (2001).

179. Ingber, D. E. Cellular mechanotransduction: putting all the pieces together again. *The FASEB journal* **20,** 811–827 (2006).

180. Anava, S., Greenbaum, A., Jacob, E. B., Hanein, Y. & Ayali, A. The regulative role of neurite mechanical tension in network development. *Biophysical journal* **96,** 1661–1670 (2009).

181. Damascena, R. H., Cabral, L. R. & de Souza Silva, C. C. Coexisting orbits and chaotic dynamics of a confined self-propelled particle. *Physical Review E* **105,** 064608 (2022).

182. Duval, A. M. & Reiner, V. Perron–Frobenius type results and discrete versions of nodal domain theorems. *Linear algebra and its applications* **294,** 259–268 (1999).

183. Davies, E. B., Leydold, J. & Stadler, P. F. Discrete nodal domain theorems. *arXiv preprint math/0009120* (2000).

184. Gladwell, G. M. & Zhu, H. Courant's nodal line theorem and its discrete counterparts. *Quarterly Journal of Mechanics and Applied Mathematics* **55,** 1–15 (2002).

185. Bain, N. & Bartolo, D. Dynamic response and hydrodynamics of polarized crowds. *Science* **363,** 46–49 (2019).

186. Miri, M.-A. & Alú, A. Exceptional points in optics and photonics. *Science* **363,** eaar7709 (2019).

187. Beléndez, A., Pascual, C., Méndez, D., Beléndez, T. & Neipp, C. Exact solution for the nonlinear pendulum. *Revista brasileira de ensino de física* **29,** 645–648 (2007).

188. SenGupta, S., Parent, C. A. & Bear, J. E. The principles of directed cell migration. *Nature Reviews Molecular Cell Biology* **22,** 529–547 (2021).

189. Grima, J. N. & Evans, K. E. Auxetic behavior from rotating squares (2000).

190. Mullin, T., Deschanel, S., Bertoldi, K. & Boyce, M. C. Pattern transformation triggered by deformation. *Physical review letters* **99,** 084301 (2007).

191. Bertoldi, K., Reis, P. M., Willshaw, S. & Mullin, T. Negative Poisson's ratio behavior induced by an elastic instability. *Advanced materials* **22,** 361–366 (2010).

192. Shim, J., Perdigou, C., Chen, E. R., Bertoldi, K. & Reis, P. M. Buckling-induced encapsulation of structured elastic shells under pressure. *Proceedings of the National Academy of Sciences* **109,** 5978–5983 (2012).

193. Coulais, C., Overvelde, J. T., Lubbers, L. A., Bertoldi, K. & van Hecke, M. Discontinuous buckling of wide beams and metabeams. *Physical review letters* **115,** 044301 (2015).

194. Coulais, C., Kettenis, C. & van Hecke, M. A characteristic length scale causes anomalous size effects and boundary programmability in mechanical metamaterials. *Nature Physics* **14,** 40–44 (2018).

195. Miskin, M. Z. *et al.* Electronically integrated, mass-manufactured, microscopic robots. *Nature* **584,** 557–561 (2020).

196. Kevorkian, J. K. & Cole, J. D. *Multiple scale and singular perturbation methods* (Springer Science & Business Media, 2012).

197. Jakobsen, P. Introduction to the method of multiple scales. *arXiv preprint arXiv:1312.3651* (2013).

RÉSUMÉ

Les solides actifs sont constitués d'unités hors équilibre couplées élastiquement. Ils sont centraux dans de nombreux processus biologiques comme la locomotion, les oscillations spontanées et la morphogenèse. De plus, leurs propriétés mécaniques et leur capacité à fournir du travail permettent d'imaginer de nouveaux métamatériaux, multifonctionnels, et dotés d'une véritable autonomie. Néanmoins, les mécanismes de rétroaction entre les forces actives et élastiques et la possible émergence de comportements collectifs, restent encore peu explorés. En tirant profit d'unités actives centimétriques, nous construisons une réalisation minimale de solide actif élastique. Les unités actives polaires exercent des forces sur les nœuds d'un réseau élastique bidimensionnel, et le champ de déplacement induit réoriente non-linéairement les agents actifs. De ce couplage, dit élasto-actif, émergent quantités de nouveaux comportements. Dans la première partie, nous montrons que, pour un faible couplage, la présence de modes zéros dicte la nature et la géométrie des comportements collectifs. Sans conditions aux limites, les solides actifs fournissent ainsi un moyen de mettre en mouvement collectif une population d'unités actives couplées rigidement. Dans un second temps, nous constatons, pour un couplage suffisamment grand, l'émergence d'une oscillation collective des nœuds du réseau autour de leurs positions d'équilibres. Nous appelons ce phénomène l'actuation collective. Seuls quelques modes élastiques sont activés et, de manière cruciale, ils ne sont pas nécessairement les modes de plus basses énergies. En combinant des expériences modèles avec l'analyse numérique et théorique d'un modèle d'agents, nous expliquons le scénario de bifurcation et le mécanisme de sélection par lequel l'actuation collective a lieu. Nous proposons une théorie hydrodynamique des solides actifs pour décrire leurs propriétés à grande échelle, et analysons certaines de ses conséquences. En jouant avec les propriétés de vibrations du réseau, nous explorons également la grande variété d'actuations collectives, et mettons en évidence les paramètres qui contrôlent la dynamique. Enfin, nous étudions la manière dont le couplage avec un champ extérieur polarise les solides actifs et affecte l'émergence de l'actuation collective. En définitive, au-delà de la compréhension de notre système particulier, ce manuscrit tente d'établir les fonctions mécaniques de la matière active à grande échelle.

MOTS CLÉS

Matière active, solides actifs, mouvements collectifs, actuation collective, métamatériaux.

ABSTRACT

Active solids consist of elastically coupled out-of-equilibrium units performing work. They are central to autonomous processes in biological systems, e.g. locomotion, self-oscillations and morphogenesis. Moreover, their shape-preserving property and their intrinsic non-equilibrium nature make active solids a promising framework to create multifunctional metamaterials with bona fide autonomy. Yet, the feedback mechanism between elastic and active forces, and the possible emergence of collective behaviors remains poorly understood. We take advantage of centimetric models of self-propelled active units and introduce a minimal realization of an active elastic solid. Polar active agents exert forces on the nodes of a two-dimensional elastic lattice, and the resulting displacement field nonlinearly reorients the active agents. From this so-called elasto-active feedback emerges numerous new collective behaviors. In the first part, we show that for weak enough coupling, the presence of zero modes dictates the nature and the geometry of the collective behaviors. Rigid body motions in free boundary conditions thus provide a way to set a population a rigidly coupled active units into collective motion. Then, we find that for large enough coupling, a collective oscillation of the lattice nodes around their equilibrium position emerges, the so-called collective actuation. We find that only a few elastic modes are actuated and, crucially, they are not necessarily the lowest energy ones. Combining experiments with the numerical and theoretical analysis of an agents model, we unveil the bifurcation scenario and the selection mechanism by which the collective actuation takes place. We propose a hydrodynamic theory of active solids to describe their large-scale properties, and analyze some of its consequences. Playing with the vibrational properties of the lattice, we also explore the wide variety of collective actuations, and find control parameters and design strategies for the emerging dynamics. Finally, we study how the coupling with an external field polarizes active solids and affects the emergence of collective actuation. Altogether, beyond the understanding of our particular system, this manuscript is an attempt to unveil the mechanical functionality of active matter as a continuum.

KEYWORDS

Active matter, active solids, collective motion, collective actuation, metamaterials.